IMPACT
Technical Design Report

Volume HIMB

PSI Bericht Nr. 25-02
December 2025
ISSN 3042-6391

PSI

Cover page description

View of the IMPACT installations within the HIPA accelerator facility, showing the HIMB production target and muon beamlines in green and the new cooling water and helium liquefaction installations in light green. On the left the high-power HIPA accelerator with its large ring cyclotron is shown. The second muon production target and the SINQ neutron source follow downstream of HIMB.
Image by PSI design engineers/M. Dzambegovic

Editorial Board

With contributions from

M. Aeschbacher
M. Bolzonella
B. Cvetkovic
G. Dal Maso
A. Di Giovanna
R. Dölling
R. Eichler
P. Fernandez Carmona
A. Gabard
R. Ganter
C. Geiselhart
S. Gerhardt
O. Gumenyuk
J. Hadobas
R. Häfeli
C. Harm
S. Harzmann
E. Hohmann
T. Höwler
E. Hüsler
A. Ivanov
S. Jaroslawzew
S. Jollet
M. Kalt
B. Keil
P.-R. Kettle
D. Kiselev
A. Knecht
R. Kobler
A. Koschik
R. Künzi
D. Laube
M. Leber
H. Luetkens
R. Martinie
A. Merkai
P. Meyer (OU 8441)
P. Meyer (OU 9642)
M. Müller
C. Nyfeler
A. Papa
L. Pedrazzi
T. Rauber
D. Reggiani
D. Reinhard
R. Riccioli
B. Ronner
O. Ruckli
Z. Salman
M. Sapinski
C. Sattler
C. Schmid
P. Simon
J. Snuverink
R. Sobbia
T. Stapf
S. Staudenmann
V. Talanov
R. Tan
M. Tisi
D. Treyer
L. Tröndle
N. van der Meulen
E. Valetov
X. Wang
A. Weber
G. Wehrle
U. Wellenkamp
J. Wickström
B. Zimmermann
E. Zehnder

Acknowledgements

Despite the extensive author list, many more individuals have contributed to the development of the HIMB technical design than are listed there. We extend our deepest gratitude to all of them for the remarkable work they have been undertaking over the past few years since the publication of the Conceptual Design Report in 2022.

We express our gratitude to the PSI divisions, management, and communication section for their unwavering support in the project. We extend our special appreciation to Michèle Erat for her invaluable assistance, insightful contributions, and guidance throughout the project.

We thank the members of the HIMB External Advisory Board – Johannes Bernhard (CERN, CH), Stephen Blundell (University of Oxford, UK), Yasuhiro Miyake (KEK, JP), Michele Weber (University of Bern, CH), and Robert Zwaska (FNAL, USA) – for their support, comments and guidance over the last five years.

The strong support of the ETH board, the Swiss parliament, and numerous other academic institutions, along with the potential end-users of HIMB, is acknowledged. As the long shutdown draws near, we believe that not only our excitement, but that of the entire international community, is growing in anticipation of the realization of HIMB.

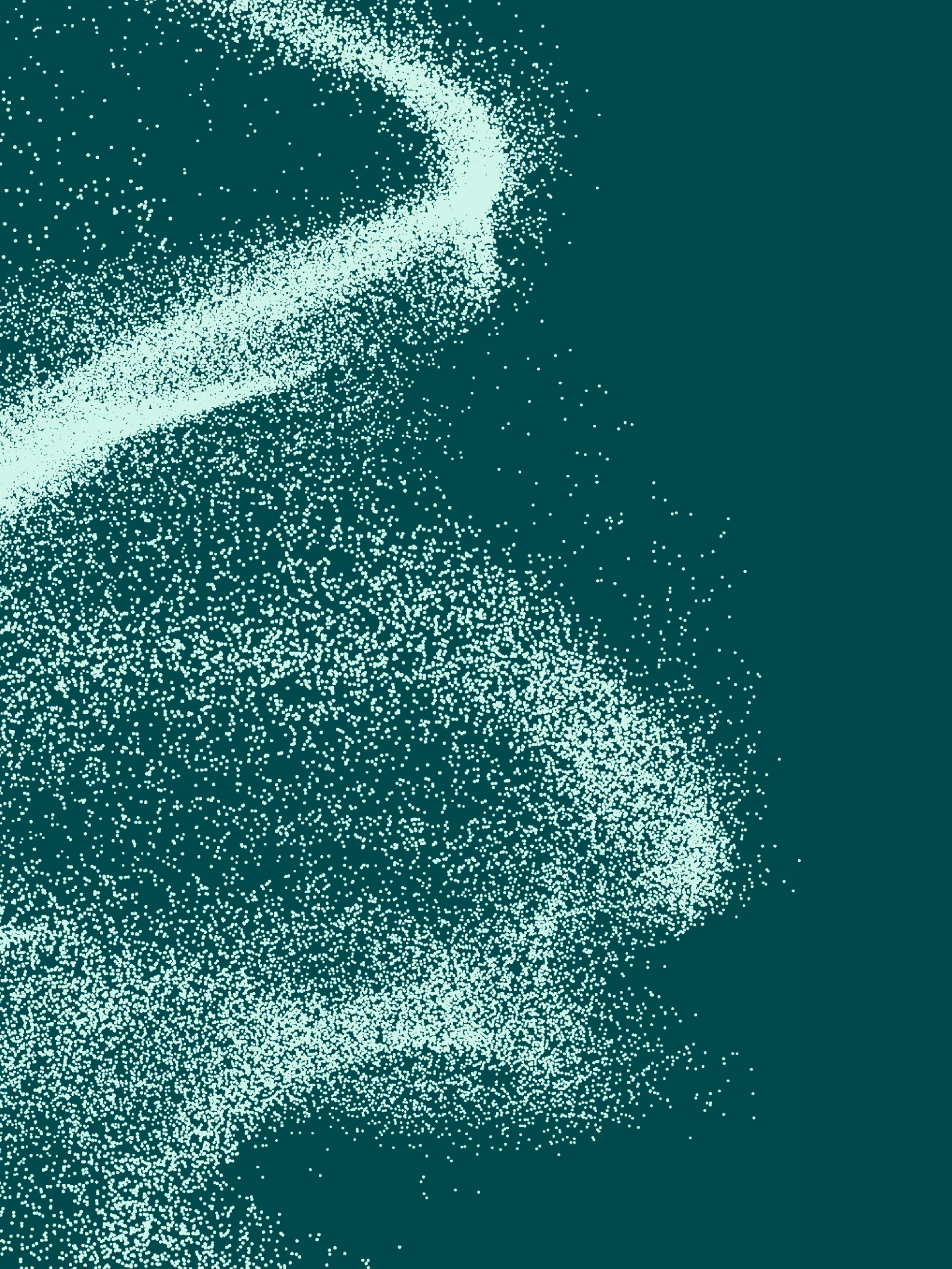

Executive Summary

Great progress was made in the years after the publication of the CDR for IMPACT (Isotope and Muon Production using Advanced Cyclotron and Target technologies) in 2022 for HIMB, the High-Intensity Muon Beamlines, which is the first part of IMPACT. The realization of the second part of IMPACT, TATTOOS, the Targeted Alpha Tumour Therapy and Other Oncological Solutions, is planned two years after HIMB and is therefore not part of this TDR.

HIMB aims to increase the surface muon rate by two orders of magnitude at HIPA (High Intensity Proton Accelerator) by upgrading the existing Target station M and its two secondary beamlines, PiM1 and PiM3, in the experimental hall WEHA.

The new target station H with beamlines, MuH2 and MuH3, are fully optimized for the main use cases. Conceptual ideas, as outlined in the CDR, were further developed to a realistic technical design enabling the goal of 10^{10} surface muons per second at the location of the particle detector in the experimental area of MuH2. This achievement could be confirmed by intensive and realistic beam transport calculations. The included multi-dimensional optimization of the parameter space in many iterations shapes the layout of the secondary beamlines. At the same time, an enormous number of calculations and multi-physics simulations[1] set challenging boundaries on the technical design and infrastructure of the secondary and proton beamlines as well as the target station H. The latter is known as the source of muons but also of other particles to get rid of by various means. Further difficult constraints are set by the harsh environment of high radiation fields for a long-lasting technical design reducing the need of unscheduled services during operational periods and subsequently the personal dose. Besides radiological measures and step-by-step planning as the basis for safe work, remote handling of highly radioactive components is required for maintenance and disposal, as regularly performed at HIPA using shielded exchange flasks and the service cells at the ATEC facility. The hall crane capacity of 60 t set the hard weight limit for the design of the new exchange flask H, which was challenged by the size and mass of the capture solenoid and the required shielding for its remnant dose rate.

Before the new HIMB installation, the existing target station M as well as both beamlines, PiM1 and PiM3, in operation since 1985, have to be dismantled. Part of the dismantling takes place in an under-pressure contamination protection equipped with a 32 t crane, cameras, radiation monitors, a personnel and material lock and specially designed containers for transport of radioactive material to the storage place and later to the shielded service cell for disposal. Moreover, about half of the experimental hall WEHA (6400 m^2 in total), which is full of shielding, infrastructure, beamlines etc., has to be remodeled to adapt for the new layouts of the MuH2 and MuH3 beamlines, which would otherwise not fit into the present setup.

Since 1990, the upgrade for higher proton currents at WEHA, no comparable work took place at HIPA. Preparational work already started in the beginning of 2025 and will continue until the final installation of HIMB. For the shielding, about 9000 t of blocks of concrete and steel have to be moved as well as large amounts of beamline equipment and infrastructure disposed. This requires solid and detailed planning and logistics as well as the design, procurement, manufacturing, installation, commissioning of new equipment for HIMB involving many expert groups of the Centers for Accelerator Science and Engineering CAS, Corporate Services CCS and Center for Neutron and Muon Sciences CNM.

The TDR is organized as follows:
In the first part, an overview from the perspective of the project management is given about IMPACT and the evolution of HIMB after the CDR in Jan. 2022 to date.
In the second part, the focus shifts to the particle transport calculations setting the requirements for the proton and secondary beamlines as well as on the shielding of beamlines and the exchange flask. Further input for the decision of radiation hard magnets, for the estimation of personal dose as well as for the cooling design is given. New detector developments, keeping up with the expected higher rates and experiments planned after the commissioning of the new experimental areas MuH2 and MuH3, are described. Furthermore, an overview of the HIMB layout based on the technical design, which is outlined in more detail in the following parts, as well as the implementation plan are presented.
In the third part the technical design, specifications of the components along the proton and secondary beamlines are presented, including the power supplies of the magnets, vacuum pumping system and girders as well as the exchange flask H. Simulations and calculations setting the requirements and checking the final designs are given as well.
The fourth part focuses on the necessary remodeling and dismantling of the existing infrastructure in the experimental hall WEHA and installation of the upgrade. This goes hand in hand with safety, in particular radiation protection, as well as the triage and processing of material to be disposed.

[1] ANSYS (CFD, cooling, stress, deformation, HV maps), BDSIM (proton beam dynamics), CADFEM (magnetic field distribution, cooling), Geant4 (muon, electron, pion beam transport), MCNP (shielding, dose rate maps, energy deposition, absorbed dose), MolFlow+ (vacuum pressure)

Contents

1. Project Overview and Timeline

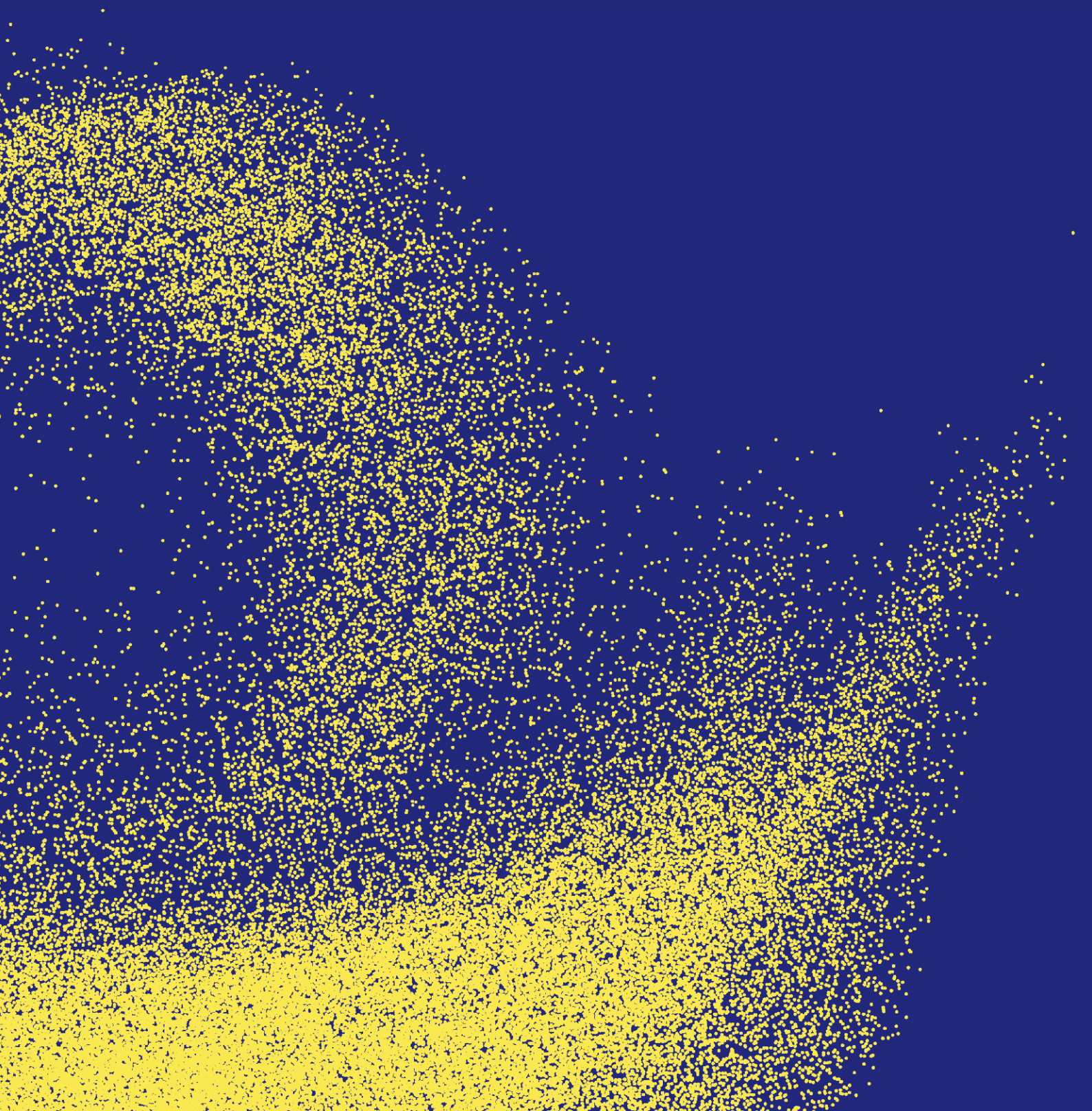

1.1 IMPACT

IMPACT (Isotope and Muon Production using Advanced Cyclotron and Target technologies) consists of two parts, namely, HIMB (High Intensity Muon Beams) and TATTOOS (Targeted Alpha Tumour Therapy and Other Oncological Solutions). Since IMPACT serves several research disciplines, besides the Centers for Accelerator Science and Engineering CAS and Corporate Services CCS, there are three research centers at PSI directly involved: Center for Life Sciences CLS, Center for Neutron and Muon Sciences CNM, and the Center for Nuclear Engineering and Sciences NES. Further jointly with PSI, the University of Zurich (UZH) center for Detector & Matter at Extremes Test and Research (DEMETER) will develop new instrumentation and establish new technologies for particle detection, while UZH and University Hospital Zurich (USZ) supports with novel radiolabeled biomolecules and the preparation of promising drug candidates. The TDR focuses solely on the PSI part.

HIMB upgrades the target station M, built in 1985 mainly for high energy pion production, and converts it into a highly intense surface muon production station aiming for intensities up to 10^{10} s^{-1}. It is important to note that this design goal has been confirmed by detailed simulations using realistic inputs from CAD models and the magnetic field distributions. The upgrade keeps PSI at the forefront of research requiring low-energy muon beams and makes it competitive and attractive for users, while other facilities aim for similar enhancements. Since both user communities from particle physics and materials science are most interested in low-energy muons, the new target station together with the two beamlines will be optimized for surface muons.

TATTOOS aims to produce radionuclides from high-energy proton-induced spallation reactions, whose decay properties are promising for the ultimate fight against cancer, i.e. for both diagnosing cancer and its therapy. In the first phase, a tantalum target will be used with focus on completing the PSI-based production of the so-called theragnostic "Terbium sisters" by ^{149}Tb and ^{152}Tb. The other two, ^{155}Tb and ^{161}Tb are already produced at PSI by irradiating enriched gadolinium targets at the IP2 irradiation station with 72 MeV protons and in the irradiation station at SINQ using thermal neutrons, respectively. In a second phase, other alpha-therapeutic radionuclides are going to be produced from Uranium or Thorium target irradiations. The TATTOOS facility exploits the ISOL (Isotope Separation OnLine) techniques, combining their isotopic mass separation abilities with highly optimized chemical separation processes, allowing for an introduction of radionuclidically and chemically pure products to preclinical research, as well as via GMP for the further production of labelled radiopharmaceuticals applied in clinical research.

Both target stations, HIMB and TATTOOS, are served by the 590 MeV proton beam from the Ring Cyclotron. However, while target station H for HIMB is designed for the full beam intensity, TATTOOS can take a maximum of 100 µA, which is split from the main beam by an electrostatic HV device. Both target stations are made for continuous beam supply. However, during a short period, where the full beam is sent to UCN for a few seconds, the beam is off for the rest of the facilities.

IMPACT is part of the Swiss Roadmap for Research Infrastructures 2023 and co-financed by the ETH-Board. The first tranche of 50 MCHF for 2025–2028 was confirmed with the financial approval of the ERI Dispatch for the same period by the Swiss Parliament on 18th December 2024 [1]. As of 2025, IMPACT is the large-scale project of PSI with highest priority [2]. The PSI pre-project phase 2022–2024 was supported solely by PSI financial and personnel resources. In late 2022 the ETH board decided that the financial profile of IMPACT should be stretched into the following four-year period, with 10 Mio. CHF from the original ETH-Board co-financing budget shifted to 2029. As a consequence, the TATTOOS installation is shifted by two years. Since then, the focus of the pre-project was on the preparation for the realization of HIMB. This also includes the remodeling of the experimental hall WEHA in the regular HIPA shutdowns in preparation of fitting the two new beamlines, MuH2 and MuH3, into the existing layout. The first stage was already completed in the first quarter of 2025.

1.1.1 References

[1] PSI, *"IMPACT: Upgrade at PSI research facility approved"*, PSI Media Release. [Online]. Available: https://www.psi.ch/en/news/media-releases/impact-upgrade-at-psi-research-facility-approved

[2] PSI, *"Strategic Planning: Development plan for 2025–2028"*, PSI intern. [Online]. Available: https://intranet.psi.ch/de/media/40256/download?attachment

1.2 HIMB design evolution from CDR to TDR

While the concept of HIMB was already well outlined in the CDR, the design of the HIMB components were mainly inspired from target station E located 18 m downstream of the new target station H. At the time of the CDR, 2022, proton as well as muon beam simulations were already well progressed due to its start a year in advance financed by a proposal between the PSI centers CNM and CAS. Therefore, the principal layout of the proton beamline did not change from the CDR to the TDR. However, the technical design of the components in the proton channel were only sketched and had to be developed further by simulations regarding e.g. the necessary cooling, which required first particle transport calculation for the power deposition. Both kinds of simulations had to be iterated many times for several components, on the one hand for optimization, on the other hand to account for design changes, which were – besides other reasons - also caused by the simulation results. Impressive views on the design at the stage of the CDR in comparison to today's version can be found in Chapter 3.1, e.g. Figure 3.1.52.

Main visible changes in the muon beamlines are the increase of the number of beam stoppers from two to four, due to the unexpected large streaming of neutrons along the almost straight beamline. All magnet types were carefully tuned according to the results of the muon beam transport simulations in many iterations optimizing for highest muon transmission. In addition, cooling of the coils had to be designed and checked by simulations, while the size of the magnets was reduced as much as possible. This was particularly important for the capture solenoid, a key player for the muon transport from the target to the muon beamline but also setting stringent constraints on the weight of the exchange flask. Finally, both, the capture solenoid and the exchange flask could be optimized for reduced weight while maintaining their functionality, such that the capture solenoid together with its shielding can be pulled into the exchange flask H in one piece.

Another key parameter, the distance between the beam-target interaction point and the first coil of the capture magnet, which was set to 250 mm in the CDR, could finally be achieved by several modifications to the target H insert, e.g. the shortening of the horizontal driving axis of the wheel compared to the target E insert. The small space available also required an innovative solution for the placement of the guiding rails keeping the necessary compatibility to the exchange flask E.

For highest muon transmission to the final detector the distances between solenoids, dipoles and beam blockers in the muon beamlines should be as small as possible. In the CDR, individual vacuum chambers were foreseen for each insert. However, due to the additional walls of the vacuum chambers and the required pillow seals in between, distances between components would be much larger. In addition, the many required pillow seals would be prone to vacuum leaks in the future, particularly due to thermal cycles induced by the proton beam. Therefore, it was decided to replace the individual small chambers by large chambers. Later, the MuH2 chamber between the first two dipoles was split in two due to its weight. As a positive side effect, the first chamber in the MuH2 and MuH3 beamline could be made almost identical. Altogether there are five big chambers, the target chamber (including the two capture solenoids and the collimator KHH0), the PK2 chamber with two profile monitors and two collimators, two chambers in the MuH2 and one in the MuH3 beamline.

However, the change to the large chambers required intensive simulations regarding the vacuum conditions and resulted in four additional turbopump stations. Besides five large vacuum chambers there are still many small chambers in the secondary beamlines required, e.g. for the dipoles, the neutron beam blockers as well as for the components outside the shielding.

1.3 HIMB Layout & Key Parameters

The basic design parameters for HIMB remained unchanged since the publication of the CDR in 2022. Here, we would like to summarize them again for convenience:

- The position of the new target TgH is at the same location as the old TgM. This is driven by the required extended collimation system, the existing proton channel downstream of the target (which should not be changed) and the needed length to refocus the proton beam properly onto the second production target TgE.
- Target H is designed as a slanted target with a 10-degree slant angle with respect to the proton beam, a 20 mm length in the proton beam direction and an overall rim length of 100 mm. The basic design of the target insert follows the design of the existing target TgE such that also the same, existing exchange flask can be used for the two targets.
- The two secondary beamlines MuH2 and MuH3 face the target at 90 degrees with respect to the proton beamline. The beamlines feature dipoles of moderate deflection angles to obstruct any direct line-of-sight from the experimental areas onto the production target. Additionally, the first dipole bends the secondary beam into the upstream direction (with respect to the proton beam) to reduce the amount of radiation being transported along the secondary beamlines and to better adapt to the existing layout of the experimental areas. The muon beamlines each feature a capture solenoid located close to the target with the edge of the coil being only 250 mm away from the proton beam.
- Two infrastructure installations are in the way of the new installations. The tertiary water-cooling loop 7 is in the way of the MuH3 beamline and thus needs to be moved to a different location. Additionally, the existing helium liquefier is located on top of the shielding just above the tertiary water-cooling loop 7. During the dismantling of the existing target station and shielding it has to be dismantled as well. It was decided to move it to a new and better location inside the experimental hall WEHA and not reinstall it at the previous location.
- All the new installations will be designed and laid out for a potential upgrade of the proton beam current to 3 mA.

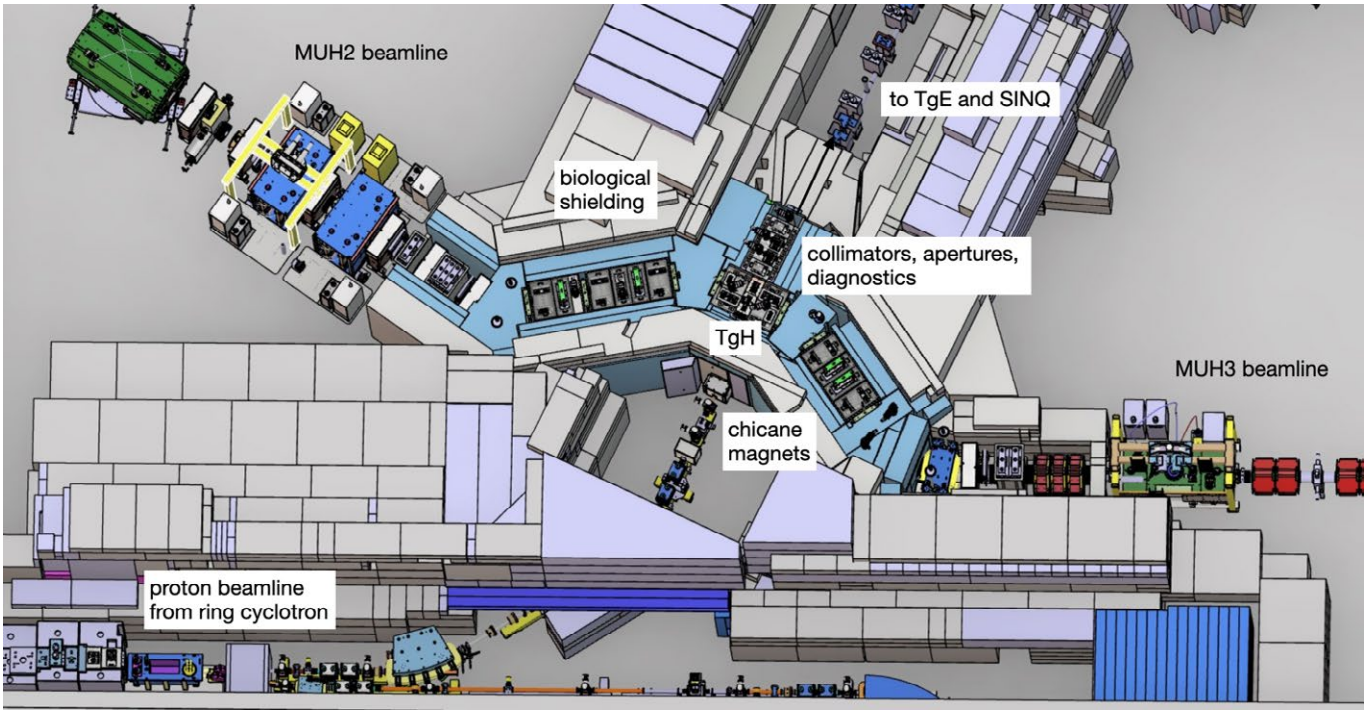

Figure 1.3.1: Overview of the HIMB Layout showing the proton beamline, target station and MUH2 and MUH3 beamlines.

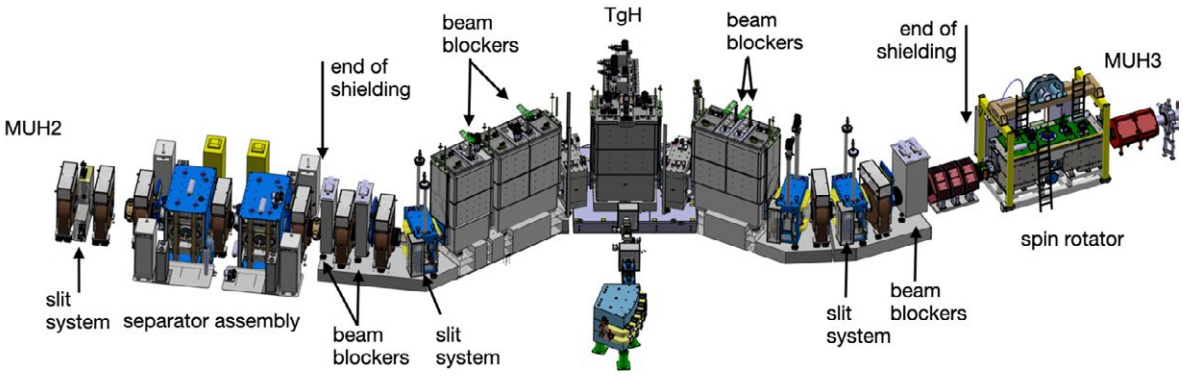

Figure 1.3.2: Overview of the components of the MUH2 and MUH3 beamlines.

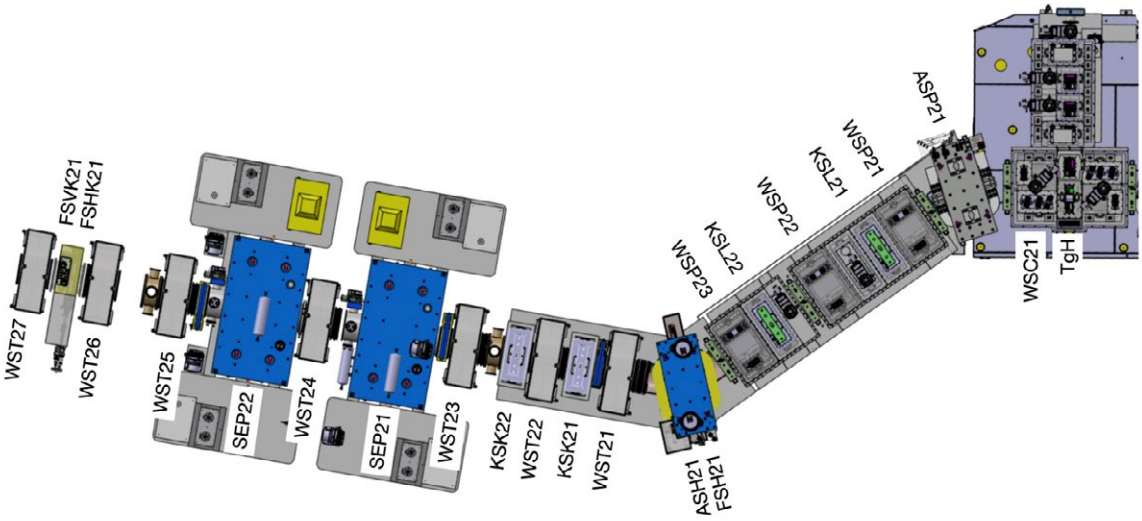

Figure 1.3.3: Detailed overview and naming conventions of components along the MuH2 beamline.

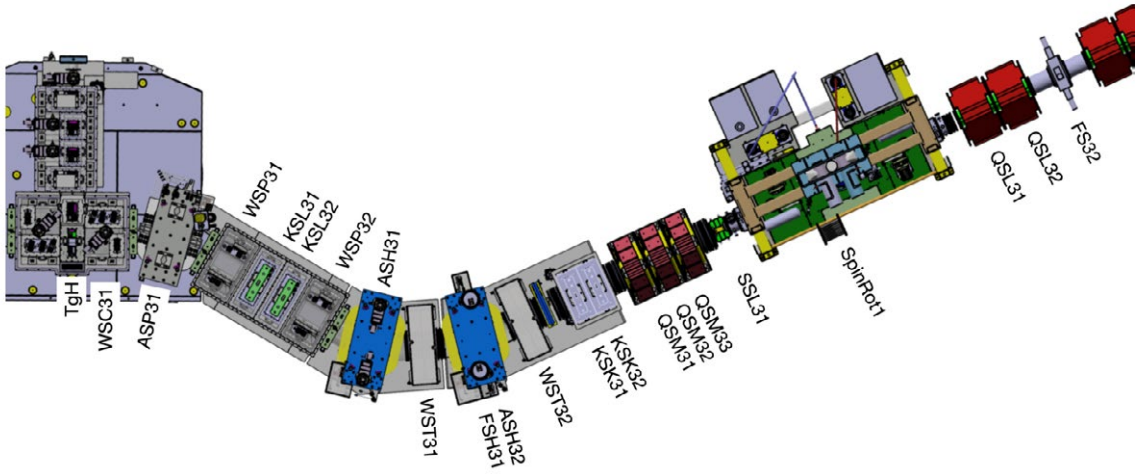

Figure 1.3.4: Detailed overview and naming conventions of components along the first part of the MuH3 beamline.

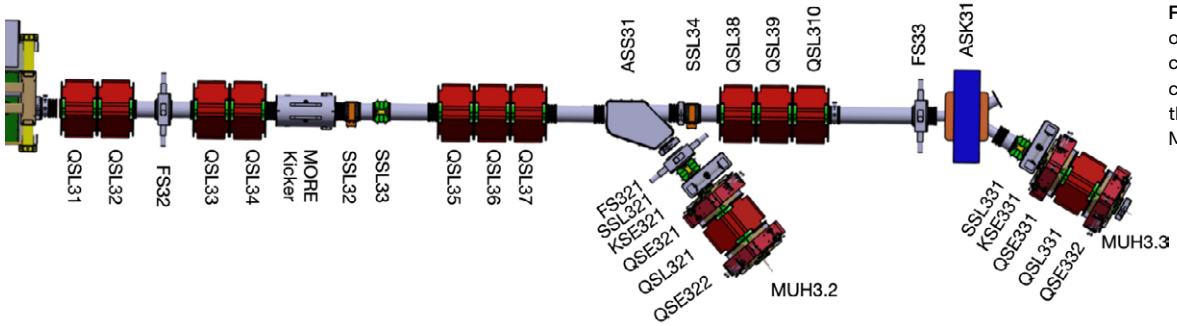

Figure 1.3.5: Detailed overview and naming conventions of components along the second part of the MuH3 beamline.

Figure 1.3.1 illustrates the general layout that fulfills the above requirements. Protons from the ring cyclotron pass through two new chicane magnets positioned in front of the target station, TgH. These chicane magnets counteract the influence of the field at target created by the two capture solenoids. After passing through TgH, the proton beam continues through a section of apertures, collimators, and diagnostic elements to ensure safe operation and high beam quality for the subsequent installations, TgE and SINQ. On either side of TgH, two secondary beamlines, MuH2 and MuH3, are installed. TgH, along with the initial sections of MuH2 and MuH3, is embedded within the biological shielding, which consists of steel and concrete.

Figure 1.3.2 illustrates the MuH2 and MuH3 beamlines, showcasing their components in more details and the naming conventions given in Figure 1.3.3, Figure 1.3.4 and Figure 1.3.5. The beamline begins with two capture solenoids (WSC) positioned on either side of the TgH target. Subsequently, a radiation-hard dipole (ASP) follows. The subsequent straight section comprises radiation-hard solenoids (WSP) and metal-based beam blockers (KSL). These elements are designed as inserts into large vacuum chambers. The straight section is followed by a non-radiation-hard dipole (ASH). On the MuH2 side, the dipole is followed by a transport solenoid (WST) and two borated polyethylene-based beam blockers (KSK), before entering the separator assembly and ending at the final focus. Slit systems located in the ASH dipole (FSH) and before the last solenoid (FSVK/FSHK) allow to control the intensity, size and momentum acceptance of the beam.

On the MuH3 side, an additional ASH dipole is sandwiched between two transport solenoids before connecting to a quadrupole-based beamline. This beamline consists of existing QSM, QSL, and QSE quadrupoles and the existing spin rotator. It also features several steering magnets (SSL) to counteract beam steering effects of stray magnetic fields. As MuH2, it features several slit systems (FS) to control the beam quality and intensity. The quadrupole-based beamline transports the muons through a septum magnet (ASS) to the two experimental areas MuH3.2 and MuH3.3 protected separately with two additional beam blockers (KSE). The two experimental areas host the muSR instruments GPS and FLAME.

Figure 1.3.6 shows the proton beamline along with its components. The 590 MeV proton beam coming from the ring cyclotron is bent using two large dipole magnets, AHD1 (not shown) and AHD2, towards the new target TgH. Two quadrupoles (QHB) are used for the final focusing onto the target. Proper setup of the two chicane magnets (AHE), which compensate the fringe field from the capture solenoids, is checked by means of the beam position and profile monitors (MHP/MHS). After the target, collimators (KHH) are used to catch the scattered protons and further, position and profile monitors ensure beam quality towards the downstream facilities.

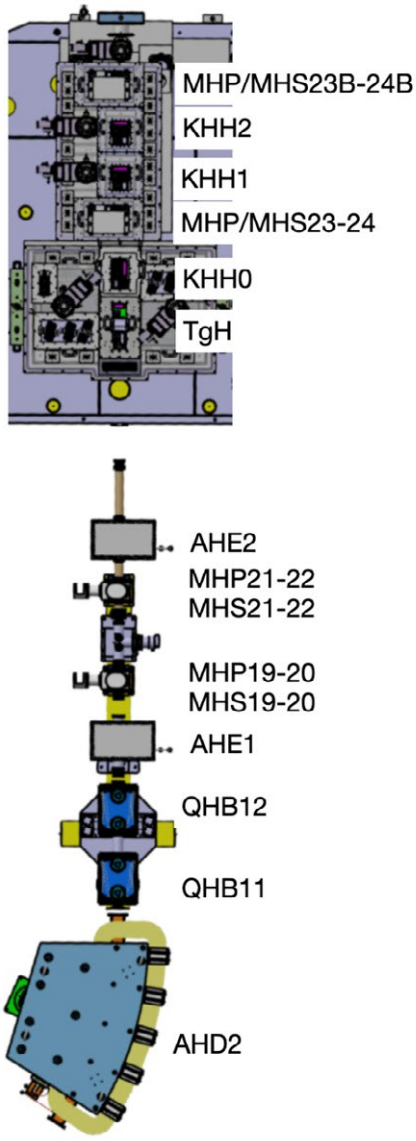

Figure 1.3.6: Detailed overview and naming conventions of components along the proton beamline.

1.4 Implementation Schedule

IMPACT is set to become an integral part of the HIPA infrastructure and its experimental stations; however, the preparation of the foreseen locations represents a major task. This includes not only the removal of the existing target station M and the two beamlines PiM1 and PiM3, but also the adjacent areas, which are affected due to the different geometry of the new beamlines MuH2 and MuH3. Moreover, the target region is activated, such that the dismantling has to be performed in a contamination protection area by remote handling. Consequently, a long shutdown of HIPA is planned, during which no proton beam will be available for an entire year. To keep this schedule, PiM1, MuE4 and PiM3 must be dismantled ahead of the long shutdown, starting in October (19.10., 16.11. and 23.11.2026, respectively).

The decision for the timing of the long shutdown will be taken at the steering committee meeting scheduled for 10.12.2025. A month before, a retreat is planned where all expert groups present their status. According to the current schedule, 2027 is foreseen for the long shutdown. A delay in the delivery of critical system components could result in a shift.

In 2026, components manufactured in-house or delivered from external companies will be assembled and tested. The five large chambers are pre-assembled on their girders in the northern area of the experimental hall, filled with the inserts and surveyed. A vacuum test is foreseen, along with additional functional tests. This procedure is intended to accelerate installation at the final location and to facilitate the early identification of any technical issues well in advance.

The setup of HIPA, followed by commissioning of the 590 MeV proton beamline up to SINQ, is planned from May on after the long shutdown. Since the proton beam passes through the new target station H and as well through the dismantled and reinstalled PK1 beamline, two months instead of the usual two weeks setup for HIPA are scheduled. Other infrastructure, which was removed during the long shutdown in preparation for the new TATTOOS building, also needs to be tested. Based on the current planning status, user operation for all experimental stations except for MuH2 and MuH3 would start on 1.7.2028 after the long shutdown.

To allow for operation of the 590 MeV proton beam, the secondary beamlines must be assembled up to the beam blockers with all shielding fully in place. Further installation, commissioning and pilot experiments at the two newly installed beamlines, MuH2 and MuH3, will take place until the end of the year. Normal user operation for MuH2 and MuH3 is scheduled for the following year, 2029.

Details of the schedule with a focus on HIMB are shown in Figure 1.4.1, which assumes the long shutdown in 2027 as planned. Important milestones are marked in the upper part.

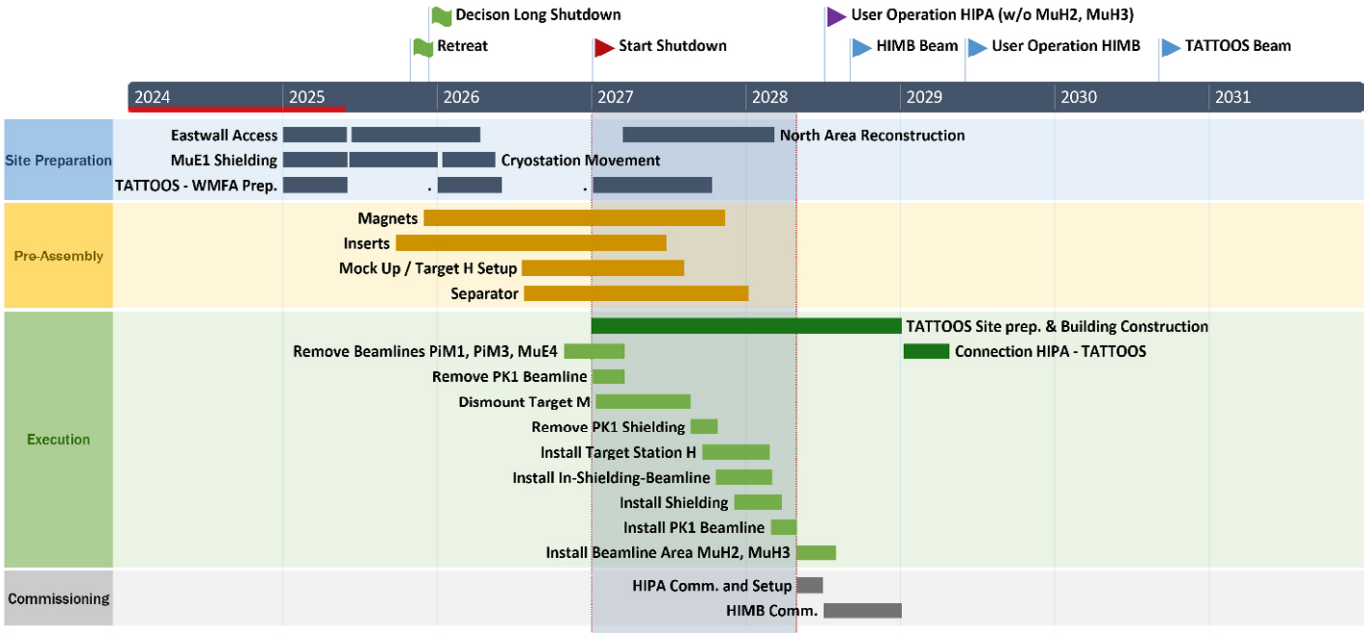

Figure 1.4.1: Schedule overview for the implementation of HIMB, including important milestones and activities.

2. Particle transport and radiation calculations: Beamlines and Areas

2.1 Proton Beamline

2.1.1 Optics and Beam Transport

2.1.1.1 Present Situation

After being extracted from the 590 MeV main ring cyclotron with an efficiency better than 99.98 %, the beam is transported in three different stages to impact three different targets: *The first stage* of the proton beamline delivers the beam to Target M: its transfer line consists of a 43 m long channel containing 5 bending magnets, 12 quadrupoles, 12 steerer magnets and 22 profile monitors (see also Figure 2.1.1). After impacting Target M, the beam is transported in a *second stage* to Target E. This section of the beamline is 18 m long and consists of 2 quadrupoles triplets that we will refer to as "Triplet 1" and "Triplet 2", 12 profile monitors (6 horizontal and 6 vertical) as well as 2 horizontal and 2 vertical steering magnets. In the *third and last stage*, the remaining primary proton beam is directed towards the SINQ target for neutron production: this section is 55 m long, and its components are 4 bending magnets, 12 quadrupoles, 9 profile monitors (horizontal and vertical), 5 horizontal steering magnets, 7 collimators and 3 pairs of slits. The latter were introduced at the dispersive region to block unwanted beam, which e.g. has a large energy spread or missed Target E, and to trigger an interlock for machine protection [1], [2].

In the present situation, the effective thickness of Target M is 5 mm only. Interactions with Target M therefore reduce the average kinetic energy of the 590 MeV beam only minimally by 2 MeV. For the secondary particles, muons and pions, there are two beamlines under 22.5° in forward direction. For comparison, in the target station E, a 40 mm or 60 mm graphite wheel-like target can be inserted.

Detailed benchmarking of the simulation tools for the present situation has been described in the IMPACT CDR (Section 8.3) and [3].

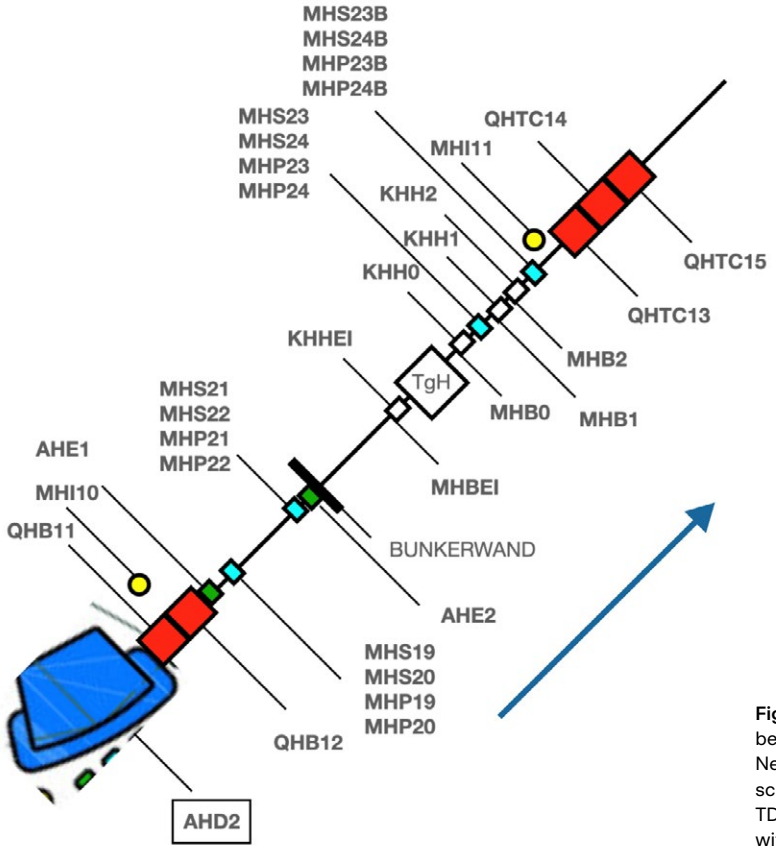

Figure 2.1.1: Layout of the HIPA proton beamline in the Target H region. New components for HIMB are described in the sections of Part 3 of this TDR. The beam direction is indicated with an arrow.

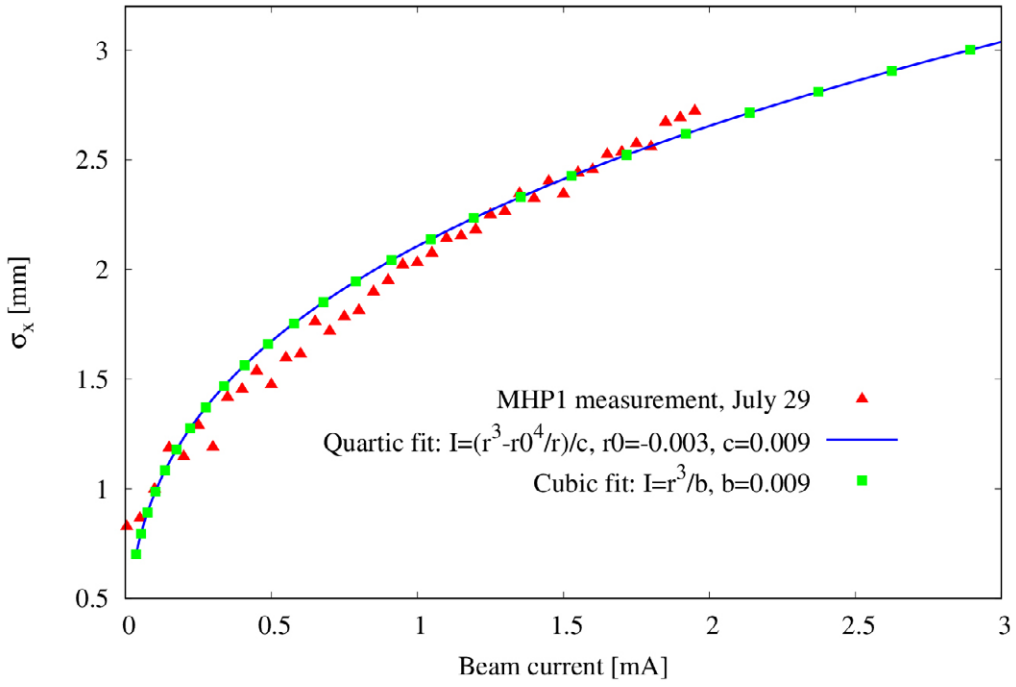

Figure 2.1.2: Beam size versus current at the location of the first profile monitor of the beamline after the 590 MeV ring cyclotron. The projected beam size at 3 mA is also shown.

2.1.1.2 Adaptations in p-channel

2.1.1.2.1 Basic Considerations, Requirements and Constraints

The purpose of the transport channels is to transport the high-power beam with minimum losses towards each target and to produce optimum matching conditions suitable for both the primary and the secondary beamlines. As discussed in previous chapters, one of the major changes in the IMPACT project consists in replacing the 5 mm Target M with the slanted 20 mm Target H. Such a thicker target will thus increase the beam divergence, lower the beam energy, and alter the downstream optics. Regarding Target H and Target E impact locations, the proton beam shall be focused to a waist ($\sigma'_x = \sigma'_y = 0$) with typical spot sizes of $\sigma_x \approx \sigma_y \approx 1$ mm . A much more focused beam could damage the target due to overheating, and a larger and more divergent beam could lead to large losses on the subsequent collimators. Furthermore, tails and halo of the beam might miss Target E, whose standard width is 6 mm only. The consequences could be locally higher, potentially damaging current densities at the SINQ target. In addition, upstream of Target H, the goal is to reduce the power depositions to a level below 1 W/m equivalent to a fractional beam loss of smaller than 1.7 nA/m for hands-on maintenance.

Although the nominal beam current for HIPA is 2.2 mA, an increase to 3 mA is considered. We aim to design the new target station for a future, possible increase. Beam studies showed that the size of the beam is increasing with current as it is shown Figure 2.1.2. The beamline must tolerate such variations, other imperfections and alignment errors. This indicates the need for a sensitivity study to assess the respective impact on power depositions along the beamline. Such a detailed study was performed and described in the IMPACT CDR (Section 8.4.5) and published in [3].

Furthermore, the density of the target material made of graphite might increase in the future if one extrapolates from the experience in the past. The first polycrystalline graphite target used at PSI in 1985 had a density of 1.7 g/cm^3 whereas the analysis performed between 2019 and 2021 on the manufactured targets showed that the density is lying in the range [1.80:1.82] g/cm^3. This is still far from the value of 2.26 g/cm^3 for natural graphite, however, it shows the progress in the manufacturing process achieving higher densities by decreasing the size of the crystals to about 10 µm nowadays. A density of 1.84 g/cm^3 is chosen as the reference value for all our simulations including the secondary beamline calculations, however, the influence on the optics due to an increase of the density, which we might expect in the future, is studied as well in the sensitivity analysis.

2.1.1.3 Adaptations before target H

2.1.1.3.1 Correction of the fringe field at the target

The fringing field produced by the solenoids surrounding Target H does alter the primary proton beam trajectory. Given that the main magnetic field component of the solenoid is in the x-direction i.e. perpendicular to the momentum direction of the primary beam, the only noticeable impact will be a vertical beam deflection. The fringe field is largest when the two solenoids contribute in the same direction, which if uncorrected, can sidetrack the primary beam nearly 30 mm at the location of the 1st quadrupole triplet downstream the target. The horizontal beam motion is unaffected.

In order to cure such an effect, two measures are employed: *the first one* consists of adding mirror plates adjacent to the solenoid entrances to reduce the fringing field extent i.e. the field integral seen by the primary beam. The effective extent of the fringing field can be limited to ±1 m around the target and its integrated value amounts to 45.5 mTm.

The second measure consists in canceling the impact that the remaining fringing field will have on the primary proton beam trajectory after the target. The idea is to modify the incoming beam trajectory towards the target by applying two vertical deflections that will compensate for the fringing field. Since the matching conditions required are for the beam to be back on axis after the target i.e. Y=Y'=0, at least two vertical steerers, called *chicane magnets*, are needed for the correction. The location of the two steerer magnets, one just before the target shielding block and one after the last quadrupole before the target, is chosen such to utilize the lowest field strength for such magnets while ensuring the beam trajectory remains as close as possible to the ideal one without interference from other magnetic elements and allowing direct access in the PK1 area.

To make place for the chicane magnets a small reshuffling of the beamline before the target is needed:

- Replace the long type-C (length 800 mm) QHC11 and QHC12 quadrupoles with shorter ones of type-B (length 530 mm).
- The current monitor MHC3 will be moved upstream before the bending magnet AHD2.
- The vertical steerer magnet SHA11Y will be removed. Its function, vertical steering for the automated steering, will be overtaken by the chicane magnets.
- The horizontal steerer magnet SHB10X will be removed. Its function, horizontal steering for the automated steering will be overtaken by the bending magnet AHD2.

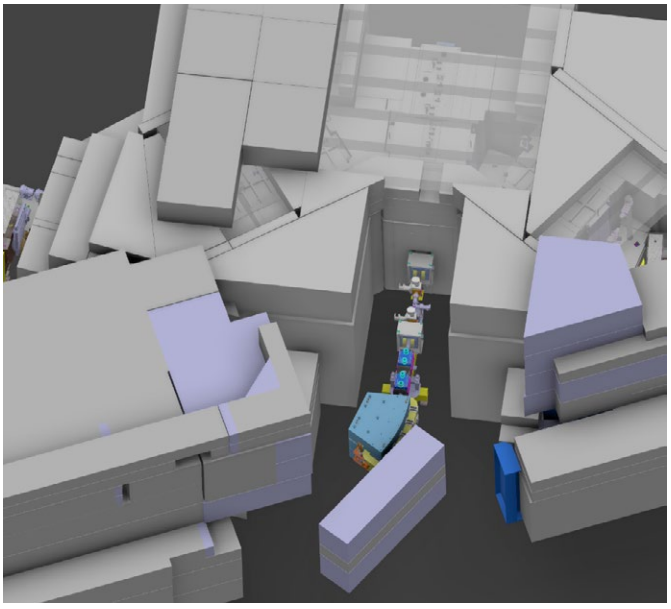

Figure 2.1.3: CAD layout of beamline before Target H.

2.1.1.3.2 Target protection collimator

To protect the cooling plate of the target from a badly misteered beam, a protection collimator is placed at the entrance towards Target H. Its apertures are chosen such as to accommodate for various fringing field strengths, thus for various vertically deflected beam trajectories compensating for it, as well as for possible beam size variations. The latter lies in the range 1 mm < $\sigma_{x,y}$ < 2 mm. Thus, allowing a safety margin of few millimeters, the apertures are chosen as follows: r_x = 10 mm and r_y = 15 mm. Compared to the IMPACT CDR (Section 8.4.2) the protection collimator was shortened to reduce the heat load and meet the temperature requirements. Also, with the shortened version the target cannot be bypassed since from aperture constraints, the maximum angle in the horizontal plane would be 0.43° and over 0.7° is needed to miss both the protection collimator and the target and hit directly KHH0.

2.1.1.4 Adaptations after target H

2.1.1.4.1 Collimator system

The collimator system is one of the most important elements of the high-power beamline. With the anticipated beam intensity upgrade of the cyclotron complex in the years to come, the new collimators shall be able to withstand the power depositions produced by the 3 mA beam. In addition, the collimators act both as local shielding and as absorbers by reducing the beam halo that might deposit its energy in some critical parts of the beamline downstream that are not sufficiently protected against high radiation levels. In doing so, the collimators should also not be very sensitive to beam misalignment errors of sub-millimeter level in order not to trigger frequent interlocks of the machine. The design of the collimators is driven by the beam simulation including power deposition calculations on the component and its shielding. Details about the collimator system optimization are described in the IMPACT CDR (Section 8.4.3).

2.1.1.5 Beam Envelopes and Transmission

The main consequences of the new Target H on the part of the beamline following Target E are:

1. The beam loses 8.45 MeV of its energy after impacting Target H in comparison with the 2 MeV energy loss with the existing Target M. Such an additional energy loss shall be corrected by lowering the bending fields of all magnets downstream of Target E. The field change amounts to −0.7 % and is a necessary condition for the beam to reach SINQ.
2. For the same extracted current from the cyclotron, the fraction reaching Target E is 5 % lower with Target H in comparison with Target M.

Since the beam matching conditions are almost identical at Target E, both consequences imply that the absolute beam

losses and the power depositions on Target E and its set of collimators will be lower with the new Target H. Nevertheless, the beam energy spread with Target H is nearly a factor of two higher than with Target M. Thus, the optics start to differ after the first bending magnet following Target E, namely AHL, as is illustrated in Figure 2.1.4. This impacts the power depositions on the slits KHNY21 and KHNX22 which may need to be opened slightly more: KHNY21 is placed inside the first magnet bending the beam vertically, namely AHL, while KHNX22 is located right afterwards. In addition, it should be verified that those slits can withstand a few kW of additional power deposition, since they were originally introduced to protect the subsequent beamline from the fraction of the beam that scatters off the Target E collimators. Since it is envisaged to use a slanted target type in the Target E station, which already demonstrated an increase of the surface muon rate of 30–50 %, the beam positioning on the target is more relaxed. In addition, a new development with grooves on the inner and outer side of the target, will certainly help to detect deviation of the beam from center immediately with high sensitivity [4].

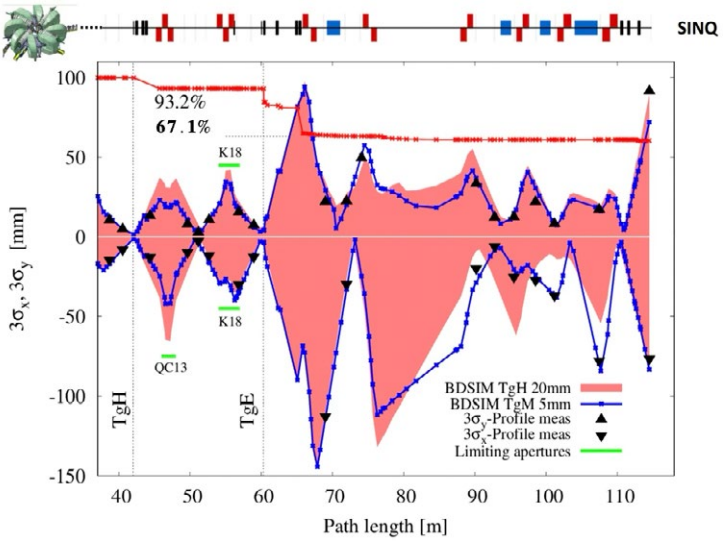

Figure 2.1.4: Comparison of the transverse beam envelopes obtained with the slanted Target H and with the standard Target M.

2.1.2 Imperfections: Tuning range and correction capability

One of the important questions to tackle is how sensitive the beam losses are to different sources of imperfections in the beamline. A detailed study was performed and described in the IMPACT CDR (Section 8.4.5). It was proven that, under realistic misalignment errors, none of the existing or newly designed elements in the beamline will be intercepting a substantial fraction of the primary beam, which is crucial to avoid frequent interlocks of the machine.

2.1.3 Power Deposition and Losses

The complete layout of the optics along with the beam transmission and energy deposition is summarized in Figure 2.1.4 and Figure 2.1.5 where we can see that the fraction of the beam reaching SINQ target amounts to 61 % of the total incoming beam from the cyclotron. At SINQ this represents a downgrade of 4 % only in comparison with the existing Target M, which is in apparent contradiction to the 5 % reduction at Target E. The relatively small downgrade lies in the fact that the newly introduced collimators after Target H will cut a large fraction of the halo beam that would have been cut otherwise by Target E collimators, which also means a lower power deposition in the

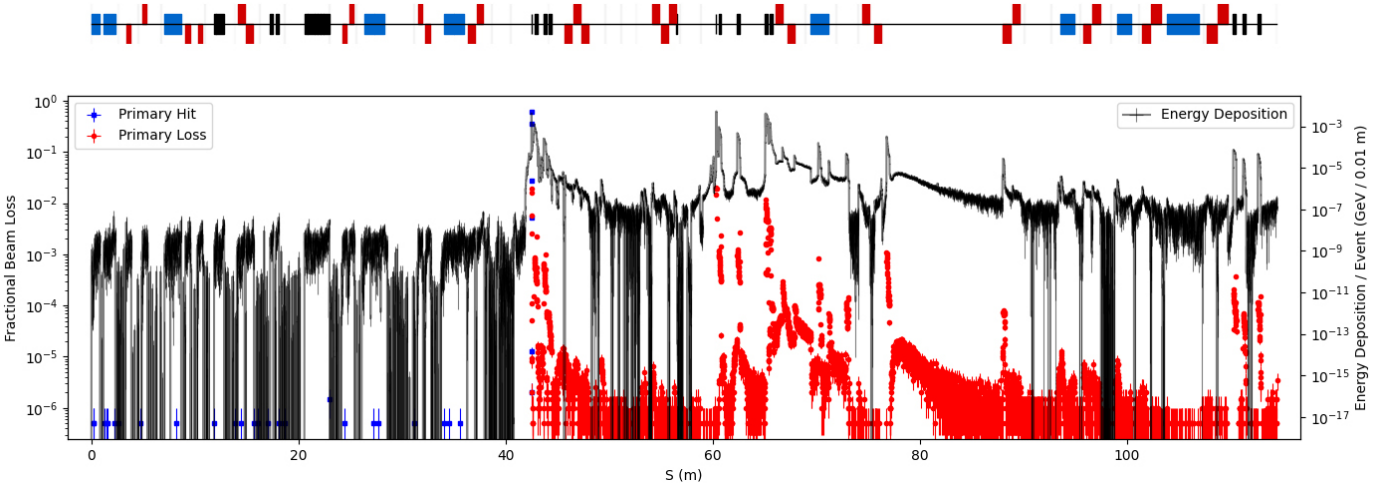

Figure 2.1.5: Energy deposition and beam losses chart from the Ring cyclotron to SINQ target. Primary hit indicates the first impact point, primary loss is the energy deposit from primary protons.

Target E collimators. Figure 2.1.4 gives a comparison of the optics with the present 5 mm Target M and the 20 mm Target H. In Figure 2.1.5, the losses along the beamline are shown. A comparison of the power depositions is given in the IMPACT CDR (Section 8.4.4).

2.1.4 Machine Protection System (MPS)

The protection of the beamlines, the target stations as well as the collimators from the high-power proton beam is of utmost importance. At 590 MeV, it takes about 10 ms to cause a meltdown of the beamline components with a mis-steered beam having a transverse distribution comparable to the ones at Target M and Target E [5]. Therefore, a fast and redundant interlock system, called machine protection system is in place to detect such losses and switch off the beam fast enough. Based on the PSI experience acquired over more than 40 years of operation [6], [5], [7], several types of diagnostic elements will ensure the safe and reliable operation with the new TgH station:

- **Beam profile monitors:** They are used temporarily to tune the optics and improve the understanding of the beamline, e.g. when comparing to simulations.
- **Beam position monitors (BPM):** The new profile monitors are combined with a BPM. The BPMs at both target stations are used for automatic centering the beam on Target H and E.
- **Current monitors:** They serve to determine the beam transmission at the different target stations and are of particular importance to prevent the possibility of having a fraction of the beam bypassing the target. An interlock is generated whenever the transmission deviates significantly from the usual one. There are two different types, one relative RF and fast resonator for triggering the interlock system and one absolute slower Bergoz monitor, which is used to calibrate the relative monitor.
- **4-segment aperture foil:** A thin four-sector aperture foil to measure the secondary emission currents is provided at the entrance of each collimator. An offset beam can be detected from the sector signal current ratios. By comparing the sector signal currents to a measurement of the full beam current, an overly focused or defocused beam can be detected. Aperture foils are in use for several of the targets and beamdumps in HIPA.
- **Beam loss monitors (BLM):** BLMs are ionization chambers filled with air and placed in the vicinity of the beam tube. Around 50 BLMs are installed in the proton channel. BLMs are very fast devices (response time of the order of 2 ms), hence their signals are employed by the MPS to trigger a machine interlock as soon as a threshold is exceeded. Since the beam losses depend on the beam current, the MPS provides dynamic windows for the loss threshold. This ensures the beam losses to stay within the allowed range (neither too high nor too low) during beam ramp up or whenever the beam current needs to be changed.
- **Temperature sensors:** Thermocouples are used to monitor temperatures of, mostly water-cooled, elements, such as beamline component, inserts and vacuum chambers. Some of the thermocouples are connected to the interlock system and can trigger an interlock to protect the component. See Chapter 3.1. for the thermocouples at the target station H.

The following diagnostic elements will be installed for safe operation of the Target H beamline, i.e. protection of all components from damage:

Upstream of Target H:

- The two new vertical chicane magnets (Section 3.2.3.4), AHE1 and AHE2, are each accompanied by a horizontal/vertical BPM/profile monitor system, MHS/MHP19-20 and MHS/MHP21-22 respectively. If a steering magnet fails or the capture solenoid current changes accidentally, there will be an interlock. Two systems for redundancy: Monitoring the magnet current and the beam deposited on the four-sector aperture monitor of the protection collimator, MHBEI.

At Target H:

- A very narrow protection collimator (Section 3.1.2.5), KHHEI, embedded in the target cooling plate and preceded by a 4-sector aperture foil, MHBEI. This collimator is not only equipped with thermocouples but also measures the secondary emission current created by the beam hitting the collimator at larger radii or non-axis-parallel, which can trigger a fast interlock.

Downstream of the Target H:

- A set of three copper collimators (Sections 3.1.3 and 3.1.6), KHH0-2, shields the subsequent beamline components and reshapes the beam after scattering off the Target H. KHH0 is a fully new element whereas KHH1-2 replace the existing ones at different positions. Each collimator is preceded by a 4-sector aperture foil, MHB0, MHB1 and MHB2 respectively, and equipped with at least four thermocouples to protect the collimator from damage.
- Two BPM/Profile monitor sets (Section 3.4.1), MHS/MHP23-24 and MHS/MHP23B-24B, will be installed between Target H and the first triplet. The first set represents a new diagnostic element and will be located between KHH0 and KHH1. The second new set that shall be installed after KHH2 will replace the currently existing one MHP/MHS23-24. Two devices are installed for redundancy and to check the position and profile before and after KHH1 and KHH2. Those elements will be useful to tune the optics whenever the fringing field of the solenoids changes due to the needs of the secondary beamlines. Due to their proximity to the targets, the power depositions on the profile monitors were calculated (Section 3.4.5.2) for later adequate cooling. With

the two BPMs a tilt of the beam can be detected and automatically corrected with the steerer magnets.
- The BLM (Section 3.4.3), MHI11, will be no longer on top of the second collimator (KHM2) but will be placed after the PK2 vacuum chamber next to the beampipe.

2.1.5 Magnet Requirements

The requirements can be found in the specification tables in Chapter 3.2.

2.1.6 Diagnostic Requirements

The requirements can be found in the specification tables in Chapter 3.4.

2.1.7 Control System Requirements

The main challenge of the IMPACT project for the control system is the integration into the existing control systems of the proton accelerator on the one hand and the new requirements and technical progress on the other hand. Therefore, the IMPACT control system will be rooted in the existing system while at the same time providing the capability to grow to accommodate new possibilities and developments.

2.1.7.1 The EPICS Framework

The control system will use the EPICS (Experimental Physics and Industrial Control System, described on https://epics-controls.org/) toolkit. Using a standard software toolkit will allow to make the best use of in-house know-how and to consolidate technical support services. Due to its collaborative nature, using EPICS enables to take advantage of work done at other laboratories.

2.1.7.2 Software Environment

The architecture of the control system software infrastructure will be based on experiences from other PSI accelerator facilities like the existing HIPA setup and new developments for SLS 2.0, but it will be adapted to the new needs of IMPACT. The basis for simple operator panels will be the caQtDM display manager. The expert groups, e.g. the beam dynamics and diagnostics team or the experiment scientists, will provide application software which requires a deep understanding of either accelerator physics or the experiments.

2.1.7.3 Hardware Strategy

At HIPA the hardware controllers are still exclusively based on VME. This concept has been revised already for other facilities at PSI and is replaced by a toolbox approach. The changes in computer technology result in different classes of devices that will be handled each by a different approach:
- A hardware toolbox will be provided for both
  - Simple devices that need no real-time capabilities and no connection to a global timing and event system.
  - Moderate to demanding devices that need real-time capabilities or connection to a global timing and event system.
- Devices that come with a network or serial interface like vacuum gauges and PLC systems will be integrated by using dedicated network protocols communicating directly with EPICS servers running on virtual machines in the server room.
- Highly demanding devices are developed according to specific and unique requirements.

Access to radiation protection areas and person safety is handled independently from the control system by a dedicated Person Safety System (PSYS) that solely grants read-only access to all other systems.

2.1.8 Commissioning and Operation

For the beam commissioning, the interlock thresholds will be set to very conservative values to prevent damage of machine components due to wrong diagnostic calibration or beam setting. The commissioning of the HIMB proton beam line will be carried out in steps of increasing beam intensity starting at very low current (around 20 μA). The capture solenoids shall be ramped to their nominal values for surface muon production and the chicane magnets shall be set such to compensate the fields at the target. Especially, the new diagnostic components, the BPMs and the profile monitors, shall be tested in detail and integrated in control room programs, in particular the automated steering and the fitting of the optics to the profile measurements. The beam optics and trajectory must be carefully checked such that the beam safely crosses Target H and Target E onto the beamdump and later to the SINQ target with the proper footprint. The optics in the beam sections between Target H and Target E as well as between Target E and SINQ shall be reconstructed by fitting beam profile measurements with the standard control room tools like TRANSPORT [8] and MINT [9]. If necessary, the beam optics and the interlock thresholds will be adjusted.

At this point, the beam current can be slowly increased iteratively. During each increase the beam transmission and losses shall be constantly monitored, and the optics and trajectory must be checked again.

2.1.9 References

[1] **U. Rohrer**, "A NOVEL METHOD TO IMPROVE THE SAFETY OF THE PLANNED MEGAPIE TARGET AT SINQ," 2001. [Online]. Available: http://aea.web.psi.ch/Urs_Rohrer/MyWeb/pdfs/megapie.pdf

[2] **U. Rohrer**, "FIRST BEAM TESTS WITH THE NEW SLIT COLLIMATOR IN THE PROTON BEAM LINE TO SINQ," *PSI Annu. Rep., 2004*.

[3] **M. Haj Tahar, D. Kiselev, A. Knecht, D. Laube, D. Reggiani, and J. Snuverink**, "Probing the losses for a high power beam," *Nucl. Instruments Methods Phys. Res. Sect. A Accel. Spectrometers, Detect. Assoc. Equip.*, vol. 1046, p. 167638 (11 pp.), Jan. 2023, doi: 10.1016/J.NIMA.2022.167638.

[4] **D. Kiselev *et al.***, "Progress and Challenges of the PSI Meson Targets and Relevant Systems," in *Proceedings of the 3rd J-PARC Symposium (J-PARC2019)*, 2021. doi: 10.7566/jpscp.33.011102.

[5] **R. Dölling *et al.***, "Beam diagnostics at the high power proton beam lines and targets at PSI," in *7th European Workshop on Beam Diagnostics and Instrumentation for Particle Accelerators, DIPAC 2005*, 2005, pp. 228–232. [Online]. Available: https://cds.cern.ch/record/924030

[6] **U. Rohrer**, "THE MULTILEVEL PROTECTION SYSTEM FOR THE VACUUM CHAMBERS OF THE HIGH-INTENSITY 590 MEV PROTON BEAM LINES," in *PSI*, 2005.

[7] **D. Reggiani *et al.***, "Improving beam simulations as well as machine and target protection in the SINQ beam line at PSI-HIPA," in *Journal of Neutron Research*, 2020, pp. 325–335. doi: 10.3233/jnr-200162.

[8] **U. Rohrer**, "Graphic Transport Framework User Manual," *PSI*, 2010, [Online]. Available: http://aea.web.psi.ch/Urs_Rohrer/MyWeb/trans.htm

[9] **C. Baumgarten**, "MinT user guide," PSI. [Online]. Available: https://gitea.psi.ch/baumgarten/MinT/src/branch/master/TeX/mint_user.pdf

2.2 Secondary Beamlines MuH2 & MuH3

2.2.1 Beam transport simulations MuH2

The MuH2 beam line is primarily conceived for particle physics experiments exploiting the unprecedented low-energy surface muon and sub-surface muon rates at momenta between approximately 14–30 MeV/c. MuH2 also gives access to a broad range of experiments [1] utilizing cloud muons, of both charge signs, derived from pion decay-in-flight in the target region, as well as electrons, positrons and pions with momenta up to 80 MeV/c. The transmitted particle yields, normalized to a proton current of 2.4 mA, for both positive & negative particles are shown in Figure 2.2.1 for the final focus.

2.2.1.1 Channel Overview

The MuH2 channel is based on the concept of a large acceptance solenoidal channel with wide-aperture dipole magnets and a multiple Wien-filter cleaning stage, with emphasis on a high transmission beam with reasonable phase space. This approach is superior to the traditional quadrupole channel approach, as the solenoids allow focusing in both transverse planes simultaneously, as opposed to the equivalent quadrupole triplet elements previously used, thus allowing for a more compact and shorter channel design.

Specially designed, high acceptance, radiation-hard, graded-field capture solenoids are enclosed in the new slanted target station H vacuum tank, at only 250 mm from the target, thus allowing the enhanced muon production from the slanted design to be efficiently captured by the upstream high-field coil, while allowing for an optimal optical coupling to the first dipole by means of the lower energized downstream coils.

The beam background cleaning stage, known as the Wien-filter assembly (WFA), consists of two separate crossed-field electromagnetic velocity separator stages (Wien-filters) with an intermediate focusing transport solenoid. The latter is required to allow optimal transmission over the effective long drift-length by refocusing. However, this refocusing effect also affects unwanted background particles, so that careful tuning is required to suppress the more than three times higher beam positron rate of the channel acceptance. The total beam positron suppression factor at the final focus, with respect to the channel acceptance value is a factor of 567x for the "Standard Mode" or 5528x for "Low-contamination Mode" (see below). Other background particles are electrons and gammas from positron and muon interactions with the walls of the vacuum pipes and elements. A further asset of the Wien-filter design is the movable electrode construction, allowing plate gaps of between 300 mm to 450 mm to be achieved, yielding electric field strengths ranging from 1.42 MV/m to 2.13 MV/m. This flexibility allows for various final focus modes to be defined, of which three have been established:

- "Standard Mode" – a compromise solution with high muon transmission and low beam background contamination (plate separation of WF1/WF2 of 400/400 mm)
- "High-intensity mode" – maximal transmission, with less emphasis on background suppression (plate separation of WF1/WF2 of 450/450 mm)

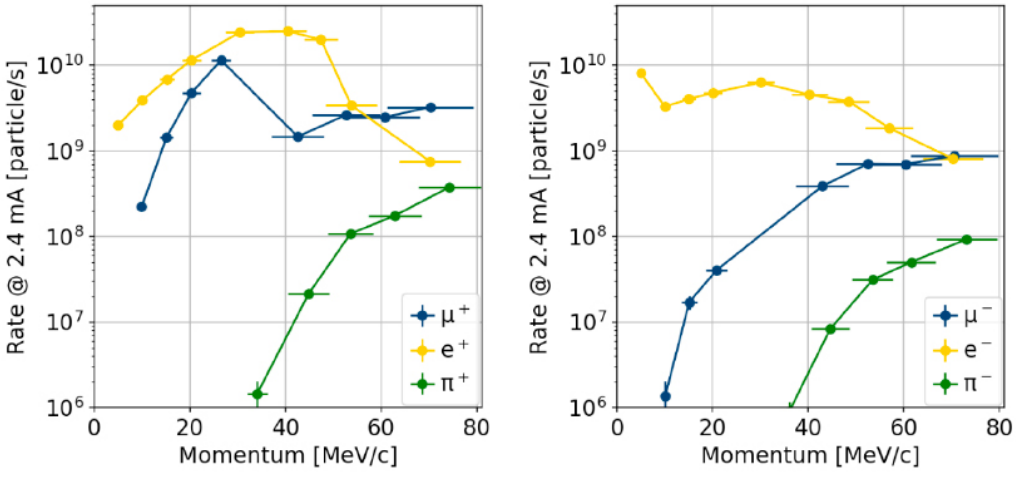

Figure 2.2.1: Figures show the momentum dependence of the different particle yields at the final focus of the MuH2 channel, split by charge sign, positive particles on the left-hand plot and negative on the right-hand plot.

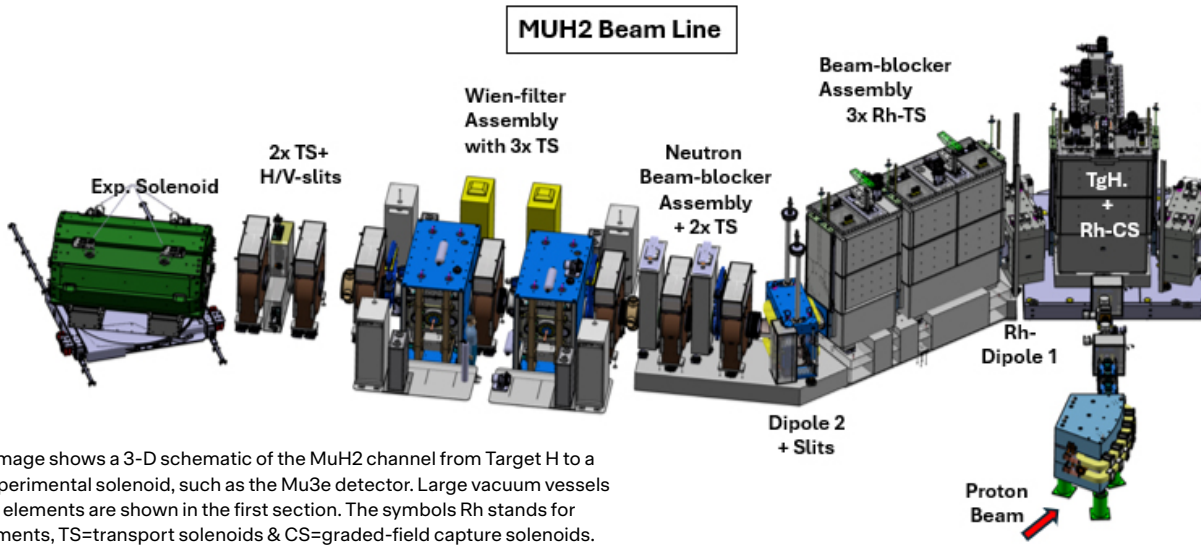

Figure 2.2.2: The image shows a 3-D schematic of the MuH2 channel from Target H to a final focus in an experimental solenoid, such as the Mu3e detector. Large vacuum vessels containing various elements are shown in the first section. The symbols Rh stands for radiation-hard elements, TS=transport solenoids & CS=graded-field capture solenoids.

- "Low-contamination Mode" - emphasis on the lowest contamination possible but at the cost of lower muon transmission (plate separation of WF1/WF2 of 300/300 mm)

A 3-D schematic layout of the MuH2 channel is shown in Figure 2.2.2.

2.2.1.2 Channel Modelling

The beam line design was a staged approach starting with optical modelling using the matrix-based package of Graphics Transport [2] and cross-checked using the charged particle ray-tracing program Graphics Turtle [3]. A detailed outline of the optical considerations is given in [4]. The main simulation code used was a custom-built version of the Geant4 (4.10.05.p01) toolkit code G4beamline (3.06), with parametrized pion production cross-sections [5], as well as G4beamline (3.08) [6]. All electromagnetic elements used in the code had generated 3D field maps derived from COMSOL Multiphysics (6.2.0.339) numerical modelling software.

Two optimization approaches were used to find the optimal transmission conditions, namely, a manual/automated sequential multiparameter maximization optimization using the Optima G4BL code [7], a python-based code with a GUI (graphical user interface) used to steer G4beamline to achieve a multi-parameter optimization with a spline fitter output. The second method used was a multi-objective optimization technique using the Non-dominated Sorting Genetic Algorithm NGSA-II [8], which allows higher dimensional problems to be tackled, while truly optimizing the multidimensional space.

2.2.1.3 MuH2 Characteristics

The channel comprises of five sections, split by the two dipole magnets ASP21 and ASH21. The initial straight capture section is followed by ASP21 and a second straight transport and beam-blocker section. The third straight section, after the second dipole magnet ASH21, comprises of three parts namely, a transport and neutron beam-blocker section, followed by a cleaning stage comprising of the Wien-filter assembly. This is followed by a final focus/injection stage. The G4beamline model of MuH2 is shown in Figure 2.2.3.

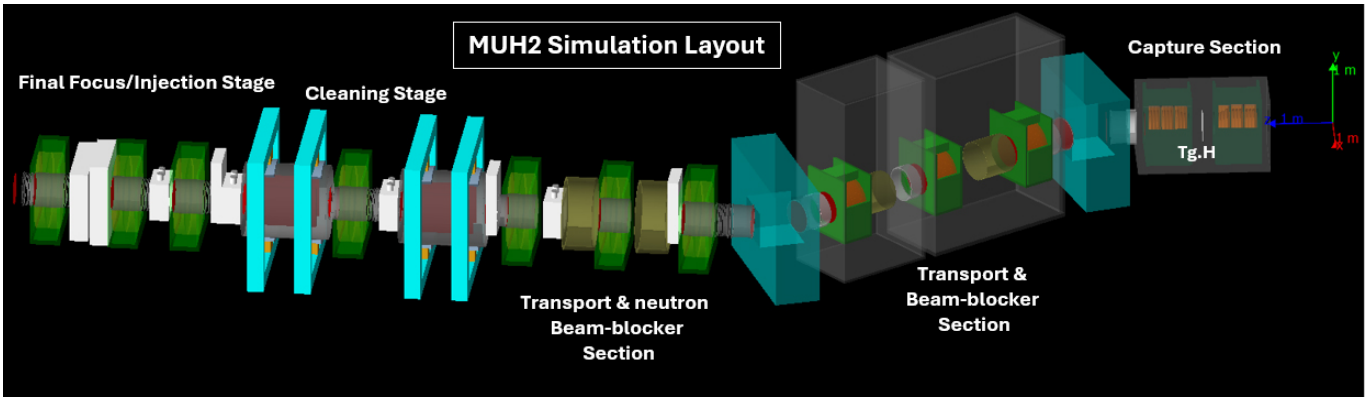

Figure 2.2.3: G4beamline model of MuH2, showing the three straight sections formed by the two dipole magnets and their five functions.

A total of seventeen magnet and two electrostatic elements are used for transmission of the beam from the target to the final focus:

- A radiation-hard, graded-field capture solenoid WSC21, placed at only 250 mm from Target H (TgH.). Figure 2.2.4 shows the axial graded-field configuration of the two symmetrically positioned, capture solenoids with respect to TgH., for two different magnet steel configurations, high-grade ARMCO steel and the lesser quality S355, virtually no difference is seen, allowing the lower grade steel to be used (see Section 3.2.2.2 for more details). The high field intensity close to the target (at 0 mm) enhances the muon capture probability, while the downstream lower intensity allows the optics to be matched to the injection into the first dipole.
- A set of two dipole magnets such that no direct line-of-sight is possible to the target, the first ASP21 is also a radiation-hard, mineral-insulated coil magnet with a bending angle of 35.5°. The second dipole ASH21, has conventional copper coils with a bending angle of 45°. It also has a built-in horizontal slit system for manipulation of the beam phase space.

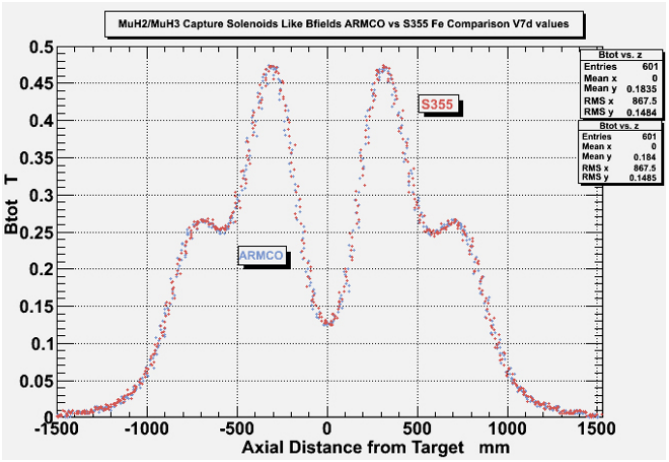

Figure 2.2.4: Graded-field capture solenoid showing the axial B-field profile from the target centre for two types of magnet steel ARMCO & S355.

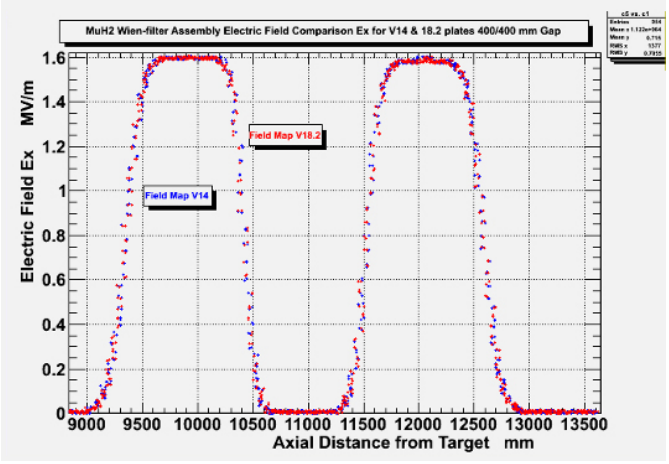

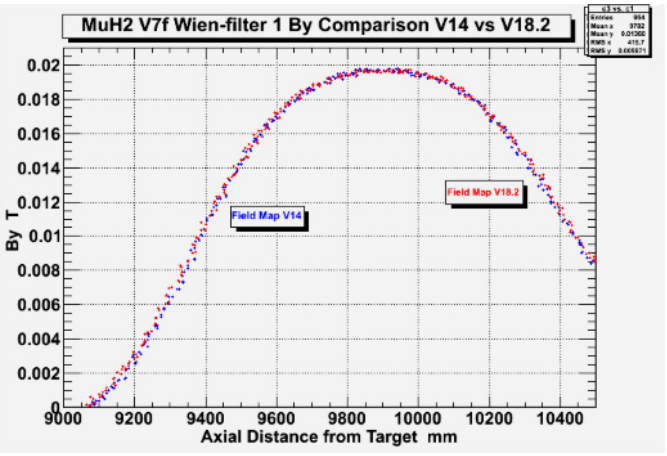

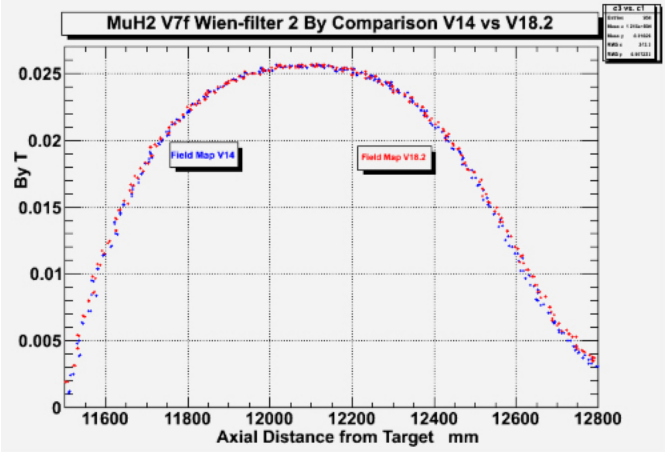

Figure 2.2.5: (Top) Shown is the electric field intensity EX versus axial distance from the target for Wien-filters 1 & 2. (Left) shows the magnetic field intensity BY for Wien-filter 1 versus axial distance from the target and (Right) shows the same for Wien-filter 2.

Table 2.2.1: Shows a comparison of beam characteristics at the final focus of MuH2 for different Wien-filter setting as well as the corresponding Mode classification.

WF1 Gap [mm]	WF 2 Gap [mm]	Electric Field [MV/m]	Muon Rate Hz @2.4mA Ip	Beam e+ [%]	Gamma [%]	Beam-spot σ(x/y) [mm]	Muon Polarization PolZ (PolX,PolY)	Operation Mode
450	450	1.422	$1.11 \cdot 10^{10}$	8.5	2.2	36.8x36.1	**-0.904** (-0.144, 0.279)	High-intensity
430	430	1.488	$1.10 \cdot 10^{10}$	6.6	2.1	36.4x36.2	**-0.898** (-0.119, 0.299)	
400	400	1.60	$1.07 \cdot 10^{10}$	4.1	2.0	36.9x36.7	**-0.888** (-0.123, 0.323)	Standard
300	300	2.13	(0.79-0.83) · 10^{10}	(0.6-1.4)	1.5	33.9x33.8	**-0.850** (-0.096, 0.411)	Low-contamination

- Between the two dipoles a series of three radiation-hard transport solenoids WSP21-WSP23 are placed and interleaved by two sets of beam-blockers made of a sandwich of stainless steel and copper plates.
- The third stage comprises of two transport solenoids interspaced between two neutron beam-blockers comprising of a steel, copper and polyethylene sandwich of plates, this marks the end of the shielding region and the entrance of the beam line to the experimental area, with the purpose of reducing the neutron and gamma backgrounds to the area.
- The cleaning stage section consists of two Wien-filters with 950 mm long electrodes of variable gap and are used to reduce the beam positron background stemming from the target region. The horizontal electric field is supplemented by two vertical dipole fields for each filter; the crossed fields act as a velocity selector for particles having the same momentum. Normal copper coiled transport solenoids are required in this section to allow the efficient transport of muons. It is important to both minimize the stray-field and optimize the spacing of these magnets, as they enable a refocussing of background particles, which must be minimized. The electric field component EX as well as the vertical magnetic field component BY for the Wien-filter Assembly are shown in Figure 2.2.5.
- Beam infrastructure components such as pumping stations, gate-valves are shown in white in Figure 2.2.3.
- Finally, in the injection /final-focus stage which couples to the experiment in the area, a slit system comprising of both horizontal and vertical plates allows the remote adjustment of the final phase space to suit the experimental conditions.

2.2.1.4 MuH2 Tune Characteristics

Having previously defined the three tune modes: "High-intensity", "Standard" and "Low-contamination" the final focus results are given in Table 2.2.1 above, while a more detailed overview of the "Standard Mode" is provided in the Figures 2.2.6-10.

The following presents a more detailed overview of the beam characteristics at the final focus of MuH2 for the "Standard Mode" settings shown in Table 2.2.1. The beam phase space plots, both in the horizontal and vertical planes, are shown in Figure 2.2.6, where x' vs. x and y' vs. y are shown respectively.

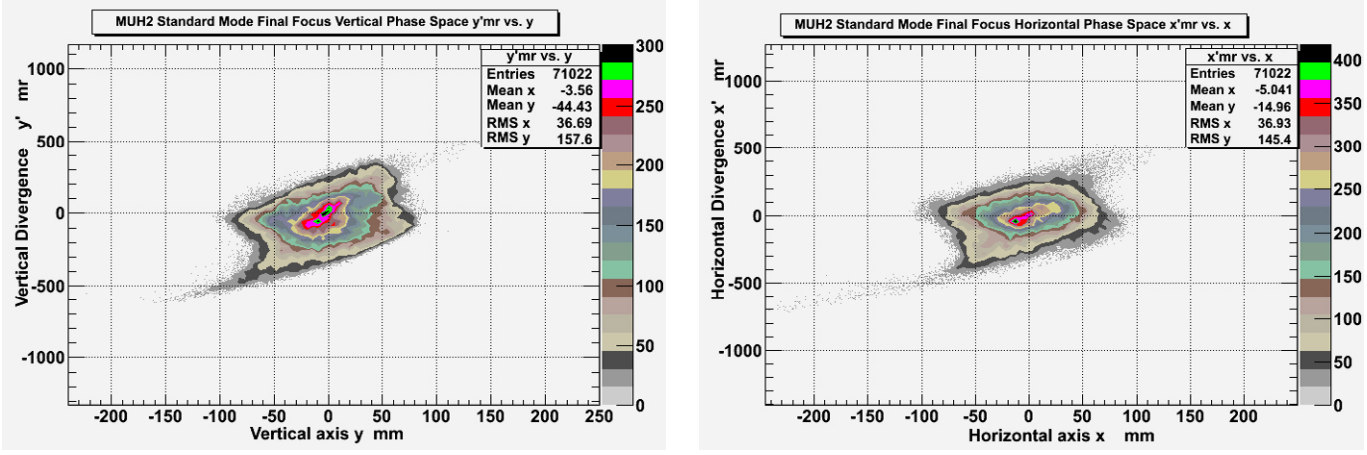

Figure 2.2.6: Shows the horizontal and vertical Phase space at the final focus of MuH2 for the standard mode. The vertical axes are the corresponding beam divergences measured in mr, whereas the horizontal axes are the respective beam-spot sizes in mm.

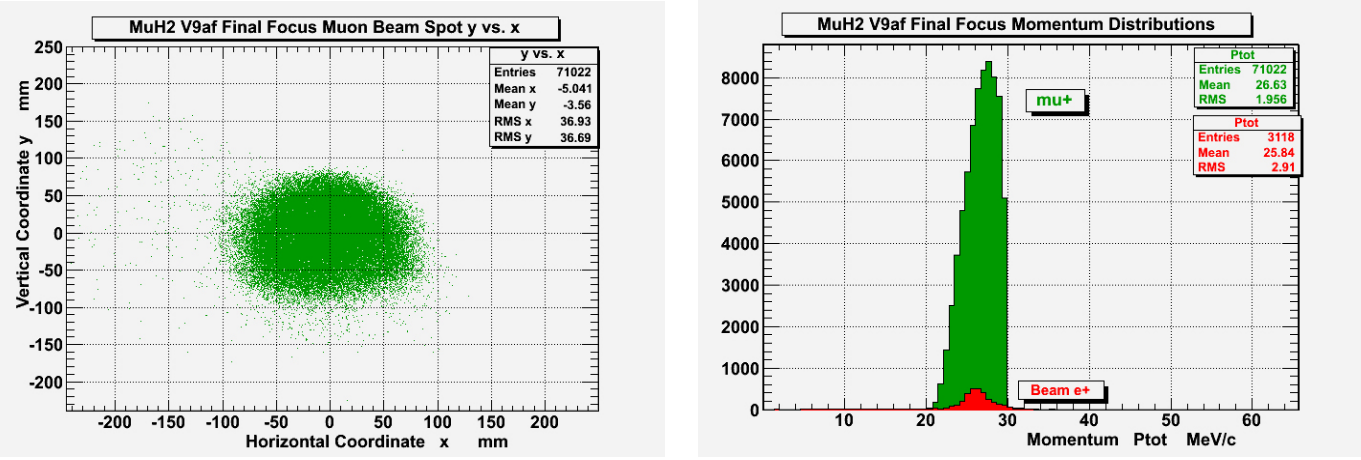

Figure 2.2.7: (Left) shows the final focus beam-spot for muons. (Right) shows the muon momentum Ptot in green, at the final focus, together with the beam positron momentum spectrum, shown in red. The e+ contamination amounts to 4.1%.

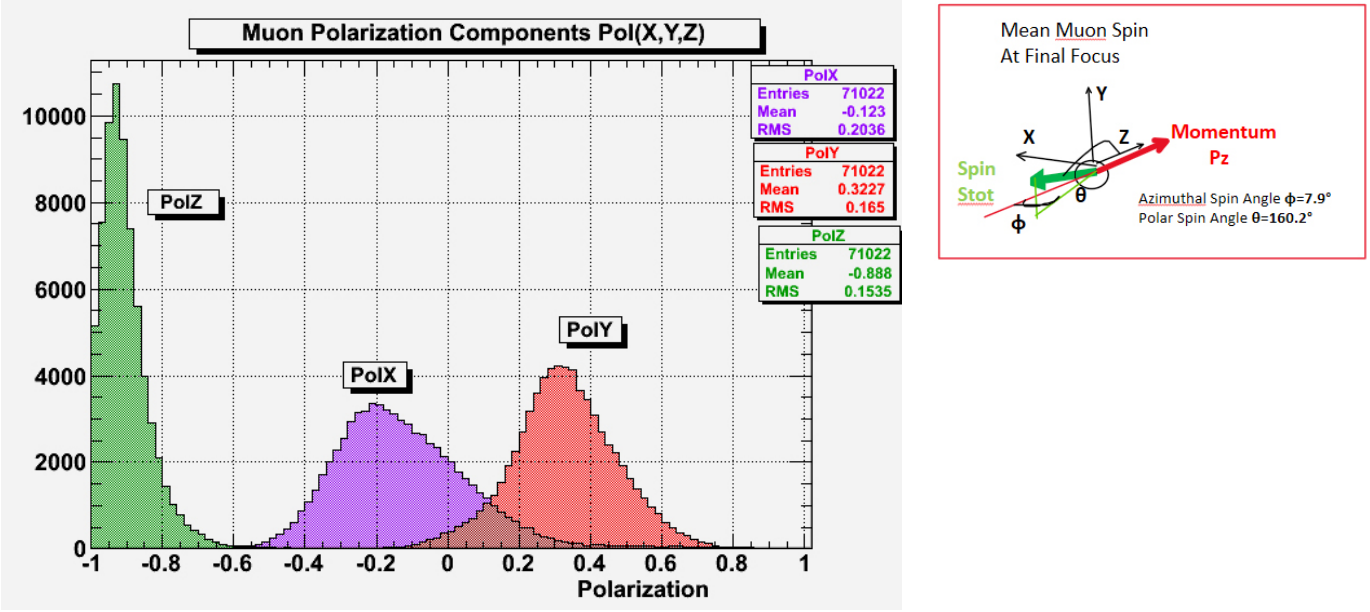

Figure 2.2.8: (Left) shows the distribution of muon polarization components PolX, PolY, PolZ at the final focus of MuH2. (Right) the corresponding mean muon spin orientation given by its polar and azimuthal angle with respect to the muon momentum along the beam axis (Pz).

The final-focus beam-spot (x,y) and momentum spectrum Ptot are shown in Figure 2.2.7. Muons are shown in green and the beam e+ contamination in red, which amounts to 4.1%.

The decomposition of the muon polarization into its components (PolX, PolY, PolZ) is displayed in Figure 2.2.8. Also shown in Figure 2.2.8 is the resultant average muon spin direction, derived from the polarization vectors, shown with respect to its momentum vector along the beam axis Pz.

The target muon momentum spectrum up to 100 MeV/c consists of sub-surface and surface muons, produced in the target, and cloud muons, produces by pion decay-in-flight predominantly around the target. These particles are filtered into a transmitted momentum spectrum at the end of the channel, centred around 27 MeV/c. This is mainly formed by the dipole central momentum settings, with a tight momentum-byte selected by the dispersion of the dipoles along the channel, so resulting in a surface muon beam between 20-30 MeV/c with virtually total suppression of the cloud muon content at the final focus (the cloud muon content below the surface muon peak, at most a few %, is not distinguished). Table 2.2.2 shows the muon beam momentum constituents versus position along the beam channel, while Figure 2.2.9 shows the momentum constituents at either end of the channel, Target H and the final focus.

A horizontal & vertical slit-system just in front of the last transport solenoid, allows the final phase space of the beam

to be matched to the experimental conditions. Figure 2.2.10 shows a horizontal & vertical slit-curve obtained by moving either set of plates by the same step-size and measuring the transmitted rate at the final focus. Also shown is the effect on the beam positron contamination at the final focus, which is slightly more favourable in the horizontal plane, consistent with the horizontal deflection of the beam positrons in the Wien-filter assembly.

Finally, the results for a coupled experimental solenoid, such as the Mu3e experiment are shown in Section 2.3.2.2 .

Muon p-spectrum Constituent change with Distance from Target						
P-Bins MeV/c	Target Yield%	Cap.Sol US Yield	Cap.Sol DS Yield %	Dipol 1 DS ASP21 Yield %	Dipole 2 DS ASH21 Yield %	Final Focus Yield %
(0-4) MeV/c	0.1	0.1	0.1	0.0	0.0	0.00
(5-9) MeV/c	0.7	1.3	1.0	0.1	0.0	0.00
(10-14) MeV/c	2.5	4.9	5.0	1.2	0.0	0.00
(15-19) MeV/c	5.7	10.4	11.9	4.0	0.1	0.00
(20-24) MeV/c	10.5	18.6	25.9	22.9	15.4	12.72
(25-30) MeV/c	20.0	35.4	47.6	68.5	83.9	87.18
(31-100) MeV/c Cloud Muons	60.5	29.3	8.5	3.3	0.7	0.10

Table 2.2.2: The table shows how the muon momentum spectrum, split into 7 momentum bins, changes along the channel length, with the dominant selection occurring at the dipoles. (US=upstream, DS=downstream, Cap.Sol= Capture solenoid).

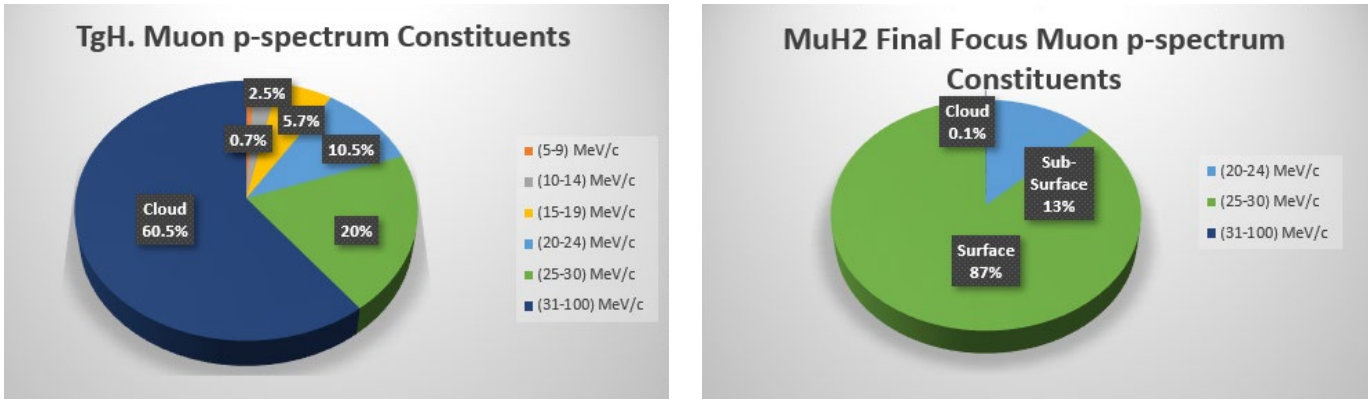

Figure 2.2.9: Schematic of part of Table 2, illustrating the %-composition of the 7 momentum bins. (Left) at TgH and (Right) at the final focus.

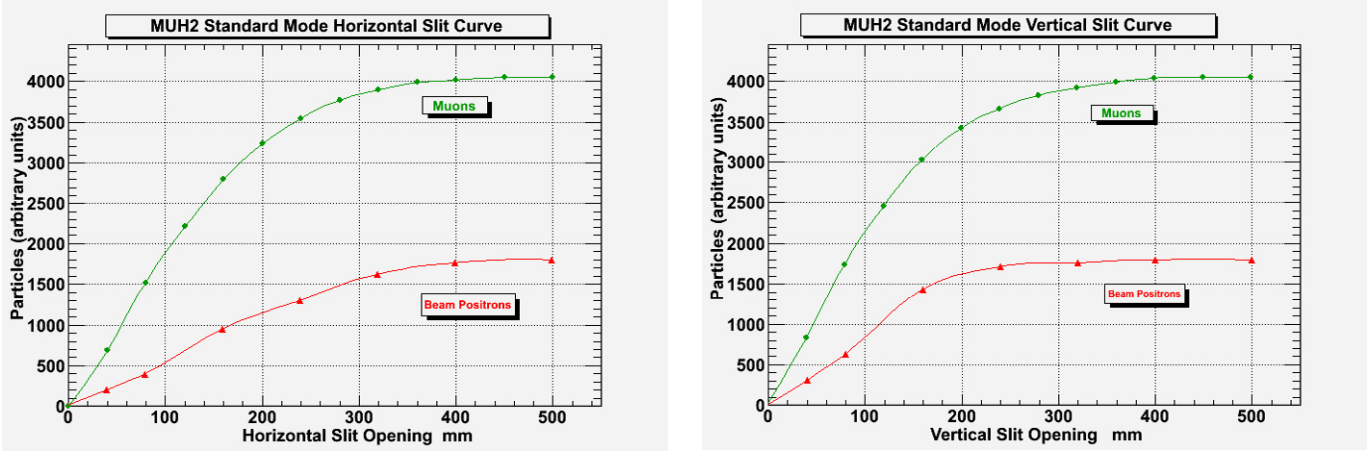

Figure 2.2.10: (LEFT) Horizontal Slit-curve showing the relative muon transmission to the final focus, together with the effect on the beam positron contamination. (RIGHT) Same plot but for vertical slits.

2.2.2 Beam transport simulations MuH3

The MuH3 beamline (Figure 2.2.11) is aimed at delivering surface muons to μSR experiments (see Section 2.3 and [1,4]). The first section of the beamline, including capture, consists of solenoidal elements to improve transmission. The solenoidal channel ends towards the end of the concrete shielding in the experimental area and couples into a quadrupole-based channel delivering the muons to the two μSR stations, GPS (MuH3.2) and FLAME (MuH3.3). A detailed description of the layout and the elements employed together with the expected performances of the proposed layout are given in the following Sections. The simulation of particle transmission has been performed with G4beamline (see [6]). Further details can also be found in [4].

2.2.2.1 MuH3 Layout

The capture part is analogous to that of MuH2 but mirrored across the proton beam axis. The captured muon beam is bent by 30° by the radiation-hard *ASP31* dipole, which is of the same type as the 36° bend *ASP21* dipole employed in MuH2.

The beam is propagated then through a short straight section consisting of two radiation-hard transport solenoids *WSP31* and *WSP32*. Two beam-blockers, *KSL31* and *KSL32*, are positioned between them to shield the experimental area and allow safe access.

Two non-radiation-hard dipoles, *ASH31* and *ASH32*, with an interposed non-radiation-hard transport solenoid *WST31*, provide 34.4° and 20.6° bends respectively and propagate the beam to the last solenoidal element of the beamline, *WST32*.

The *ASH32* dipole is equipped with a slits system to allow for rate moderation. A double beam blocker, *KSK31* and *KSK32*, with polyethylene layers is used to further suppress the neutron flux in the experimental area to grant safe access during accelerator operation. At this location rates higher than $1.2 \cdot 10^{10}$ μ^+/s can be achieved.

A triplet of large aperture quadrupole magnets, *QSM31-QSM32-QSM33*, is used to match the muon phase space into the spin rotator *SpinRot31* and maximize transmission through it. The spin rotator marks the first element of the existing beamline supplemented by a few additional quadrupoles taken from the removal of the PiM1 and PiM3 beamlines. Two *QSL* quadrupole doublets couple the muon beam through the *MORE* electrostatic kicker into a *QSL* triplet. A septum magnet, *ASS31*, is used to split the beam and bend it to the MuH3.2 area, where a triplet, *QSE321-QSL321-QSE322*, provides the final focusing into the GPS. The fraction of muon beam which is not captured by *ASS31* is delivered to the FLAME detector by a *QSL* triplet, a 30° bend, *ASK31*, and a final triplet, *QSE331-QSL331-QSE332*. Additionally, six *SSL* steering magnet are positioned along the beamline to compensate for beam deviations from the centerline.

2.2.2.2 Beamline optimization and results

Not including the steering magnets, the MuH3 beamline consists of 29 elements to define the optics and the transmission of the muons to the experimental stations. The MuH3 beamline will be operated analogously to the current PiM3 beamline, with three operation modes: a shared mode, where ideally the beam is equally split and delivered to the two μSR instru-

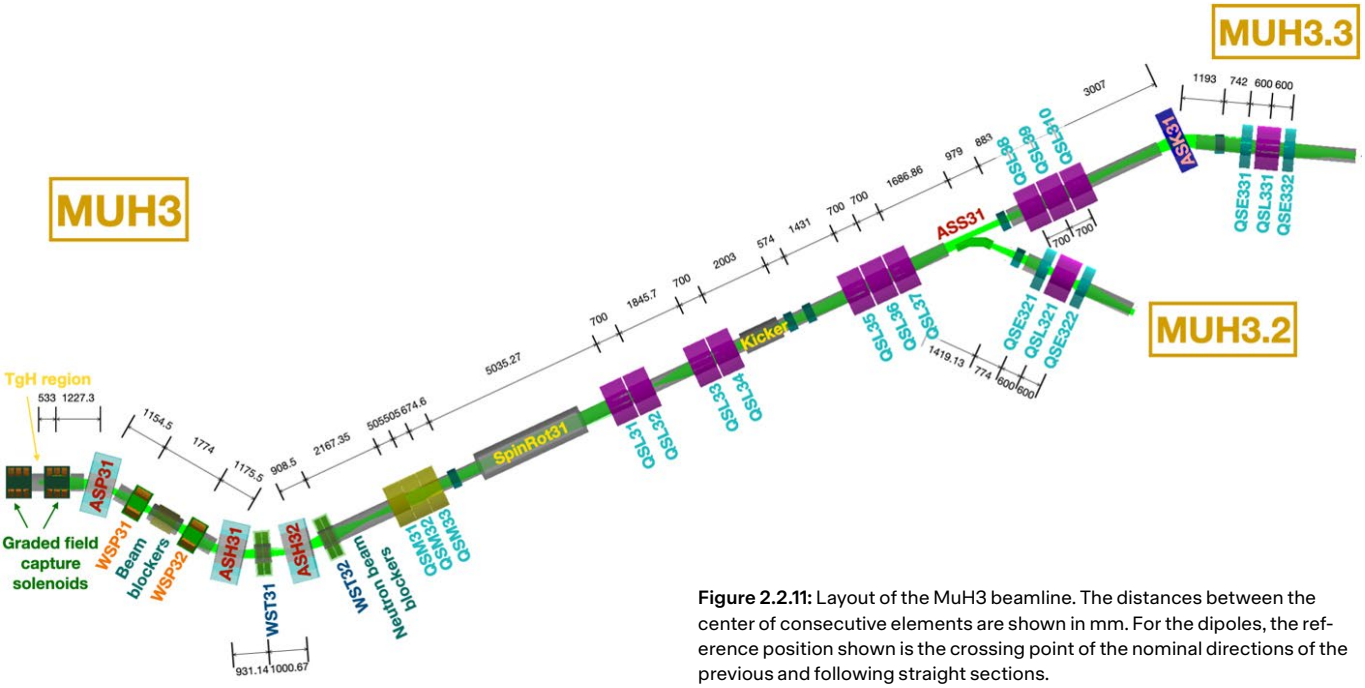

Figure 2.2.11: Layout of the MuH3 beamline. The distances between the center of consecutive elements are shown in mm. For the dipoles, the reference position shown is the crossing point of the nominal directions of the previous and following straight sections.

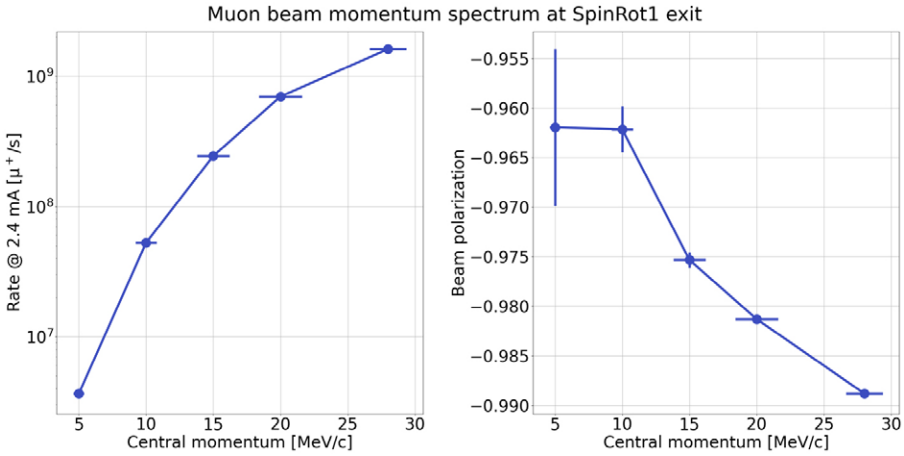

Figure 2.2.12: Rate and polarization dependence on central beam momentum for muons transmitted to the end of SpinRot31.

ments; two exclusive modes, where the beam is delivered only to either of the two detectors; the kicker mode, in which the beam is continuously delivered to either of the two areas and the *MORE* kicker is used to periodically deliver single muons to the other instrument. Although the problem has a high dimensionality and three operation modes, there are a few considerations which allow to simplify the optimization problem and reduce it to smaller scale ones. The first consideration is that the muon beam phase space downstream to *SpinRot31* is fixed due to its narrow acceptance. This means that the optimization of the elements before and after *SpinRot31* can be carried out independently. Secondly, due to the larger phase space accepted by the solenoidal channel, the rates delivered to the two branches differ in shared or exclusive mode only at a level of about 5%. Therefore, it is sufficient to find a suitable shared mode as a reference to benchmark the performances of the beamline.

To find the most suitable tunes for MuH3, first the transmission through *SpinRot31* was maximized, by varying the currents of all the elements upstream to it and by adjusting the position of *ASP31*, *ASH31*, *ASH32* and *WST31*.

The so-found parameters deliver a maximum surface muon rate of $1.62 \cdot 10^9\ \mu^+/s$ at 2.4 mA proton current. The muon implantation depth depends on the incoming muon energy. Figure 2.2.12 shows the maximum rates transmitted through *SpinRot31*, which is turned off in all optimizations and simulations reported here, and the resulting polarization for sub-surface and surface muon beams, obtained by scaling the excitation currents linearly with the desired momentum. To obtain highly polarized muon beams above 30 MeV/c further considerations are required, see Section 2.2.2.3.

Once an optimal operation mode was found, the parameters upstream to *SpinRot31* were fixed, and the rate before *ASS31* was maximized. This was done to fix the optics of

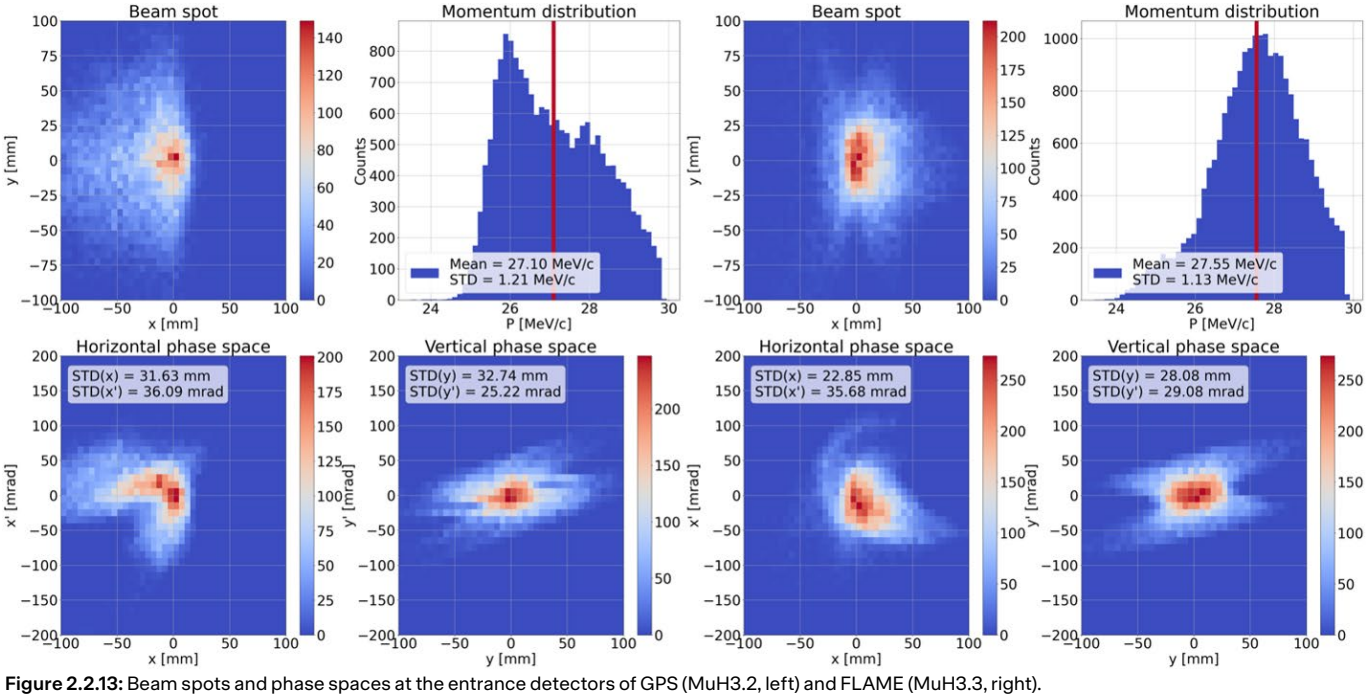

Figure 2.2.13: Beam spots and phase spaces at the entrance detectors of GPS (MuH3.2, left) and FLAME (MuH3.3, right).

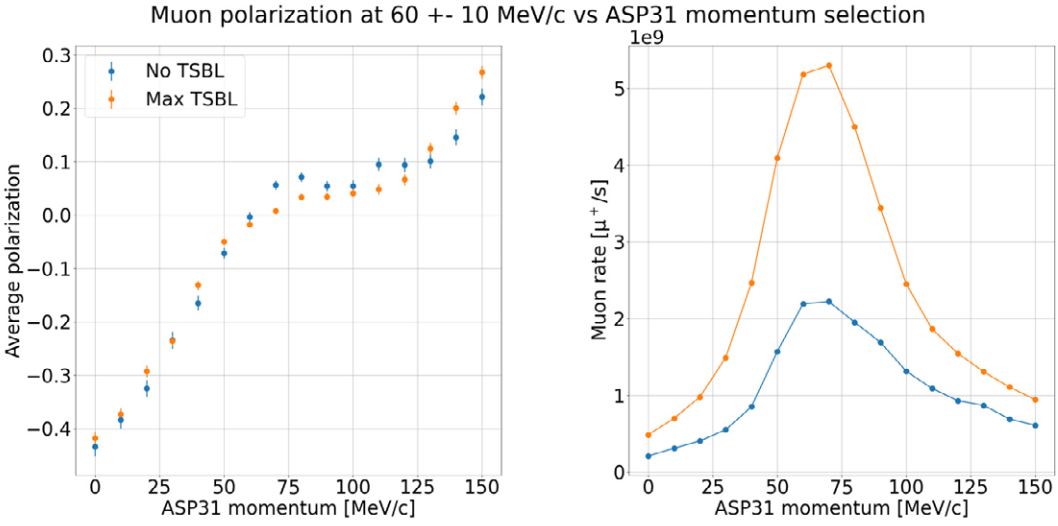

Figure 2.2.14: On the left, polarization of decay muons between 50 and 70 MeV/c in momentum, as a function of the central momentum setting of ASP31. On the right, decay muon rate within the same momentum range. Both plots are made between WSP31 and ASH31. TSBL refers to the two pyrotenax transport solenoids WSP31 and WSP32.

the two *QSL* doublets as further beam shaping to couple into *ASS31* can be provided by the *QSL35-QSL36-QSL37* triplet. The rate delivered to the two experimental areas was then maximized with a multi-objective optimization algorithm to fix the currents of the *QSL35-QSL36-QSL37* triplet.

The muons delivered to the μSR instruments are accepted by an 8 mm diameter plastic scintillator *entrance detector*. Two independent optimizations were run to maximize the rate on the two entrance detectors. The optimizations outlined above have all been performed with the Non-dominated Sorting Genetic Algorithm II (cite *NGSAII*).

Such a configuration delivers *3.6•10⁶ μ⁺/s (2.3•10⁸ μ⁺/s)* and *5.4•10⁶ μ⁺/s (2.6•10⁸ μ⁺/s)* to the GPS and FLAME entrance detectors (full beam spot) respectively. Figure 2.2.13 shows their final beam spots and phase spaces. Both branches deliver highly polarized muon beams at a 98.7% level.

2.2.2.3 High-polarization cloud muons tune

The high degree of polarization of surface muons is given by the kinematics of the pion decay: the pion being a scalar particle and the neutrinos always left-handed, the polarization of the muons in the rest frame of the decaying pion is fixed and they are always left-handed. In the laboratory frame, the polarization of the muon beam depends on the boost of the decaying pion and therefore on the acceptance of the beamline. A high degree of polarization can be obtained in MuH3 at 60 MeV/c by favoring pion capture from TgH with the first dipole and then selecting the polarized muons with the following two bends. Figure 2.2.14 shows the polarization of muons with momentum between 50 and 70 MeV/c as a function of the nominal momentum setting of the first dipole between WSP32 and ASH31. The plot shows that, to obtain a high degree of polarization, the best option is to turn off the first dipole ASP31.

An optimization aimed at maximizing both the rate and the polarization at the end of *SpinRot31* was run, with the result being shown in Figure 2.2.15. The study shows that 60 MeV/c muon beams exceeding 50% of polarization can be transmitted through *SpinRot31* with an expected maximum polarization of *55%*. The final rate and polarization expected at the FLAME experiment for such a beam are *~2.5•10⁴ μ⁺/s* (full beam spot) and *~57%*. Additionally, a vertical polarization of *~68%* is expected for the aforementioned case.

2.2.2.4 Low power surface muon tunes

The MuH3 beamline is expected to improve the surface muon rates delivered to the current μSR instruments by a factor of 40. So far, rate moderation has been performed by closing the slits systems present along the beamlines. Such an approach would, of course, work also for MuH3, but with a power consumption of *280 kW* for the nominal surface muon

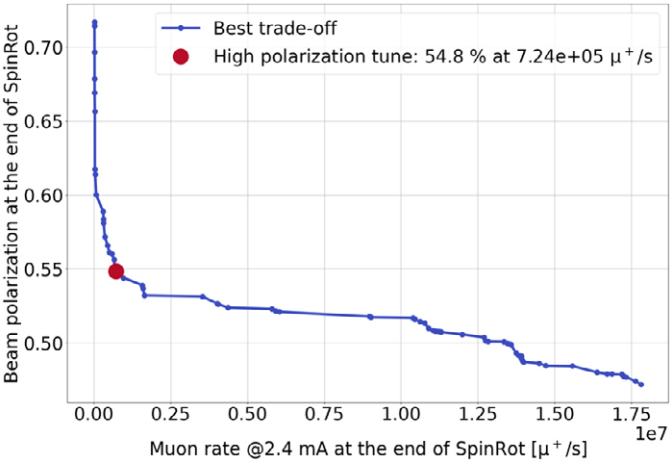

Figure 2.2.15: Muon beam polarization as a function of the rate at the exit of SpinRot31 for a 60 MeV/c decay muon beam. The higher polarization obtained at low rate is probably due to lack of statistics in the simulated beams for such tunes, leading to an under populated tail and a biased estimate.

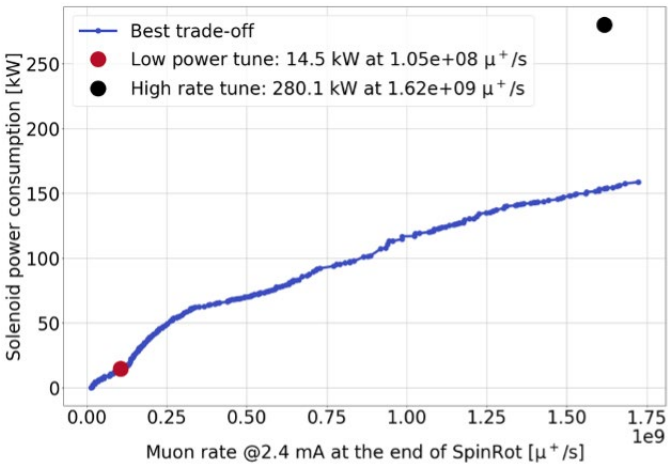

Figure 2.2.16: Solenoid power consumption in MuH3 as a function of the surface muon rate at the end of SpinRot31. The red point is chosen as an example of low power consumption tune. The black point is the reference tune for the maximum rate shared mode of MuH3.

tune, a better approach would be to reduce the magnetic fields in the solenoids. Figure 2.2.16 shows the dependence of the cumulative power consumption of the solenoidal section as a function of the rate transmitted through *SpinRot31*, obtained by running the genetic optimization algorithm to maximize the rate through the spin rotator and minimize the power consumption of the solenoids. A tune with power consumption close to the current energy consumption in PiM3, *~15 kW*, can deliver $1.0 \cdot 10^8$ μ^+/s to the end of the spin rotator and $\sim 2.3 \cdot 10^5$ *and* $3.5 \cdot 10^5$ to the GPS and FLAME entrance detectors respectively, which would be a viable option for lower rate measurements.

2.2.3 Control System Requirements

For normal user operation, the user accessible control system should allow the control of the following parameters such that the beamline can be set up and operated:

- currents of all magnets
- voltage applied to the separator
- position of the various slits
- position of the electrodes of the separator
- position of the beam blocker

A special case is the current applied to the capture solenoid, which will only be changeable by the HIPA operators as the two chicane magnets in the proton beamline (see Section 2.1.1.3) have to be adjusted accordingly.

Additionally, the control system is responsible for the operation of various other components along the beamline. All magnets feature temperature sensors that are readout and shut off the corresponding power supply in case a given temperature is exceeded. The vacuum control system operates the different pumps, reads the pressure gauges and allows manual and automatic movement of the vacuum valves given safe pressure levels. The separator and spin rotator control system allow for safe operation of these devices (see Section 3.8.7). They are locally installed close to the separators and spin rotator, respectively, but can also be controlled from the user control room. The PSYS system controls access to the experimental areas (see Section 4.6.2).

2.2.4 Commissioning and Operation

The commissioning of the two new MuH2 and MuH3 beamlines will aim at measuring beam profile and rate, as well as beam divergence, and beam particle fractions, for both positive and negative charged beams, at different momenta, and for different beam optics settings. Those measurements will assess the actual beam rate and properties to validate the Monte Carlo simulations.

A few strategic points have been identified where those measurements will take place. Having the MuH2 as a reference beam line:

- In front of the separator
- Behind the separator
- At the end of the beam line/at the experiment

Some of the main challenges of performing such measurements is to have detectors that will be able to sustain the expected high particle fluxes, doing particle identification (either directly, i.e. exploiting differences in particle energy deposit where possible, or indirectly, i.e. complementing it with time-of-flight techniques), working in the presence of high magnetic fields, and being vacuum compatible where needed.

2.2.4.1 Detectors for Commissioning and Operation

To address such a request, several detectors have been developed and other are still under investigation. More than one detector will be used at a same place along the beam line in order to have independent measurements and keep under control systematic effects.

The developed detectors have been tested and used along the piE5 beam line. They operated up to a flux of a few 10^8 muons/s, and some of them even up to a beam intensity of 10^9 particles/s (positron beam). A short summary of these detector characteristics and performances is given below. Ongoing R&D is also mentioned.

2.2.4.1.1 Pill Detector

This detector consists of an NE-102A scintillator, 1 mm in radius and 2 mm in length, coupled to a miniature Hamamatsu R9880U-110 photomultiplier. It is connected to a scanner system that allows a “raster” scan to be made with the possibility of having a few mm pitch and a 2D fine grid size allowing up to a thousand measured points per scan in a region of 160×160 mm^2

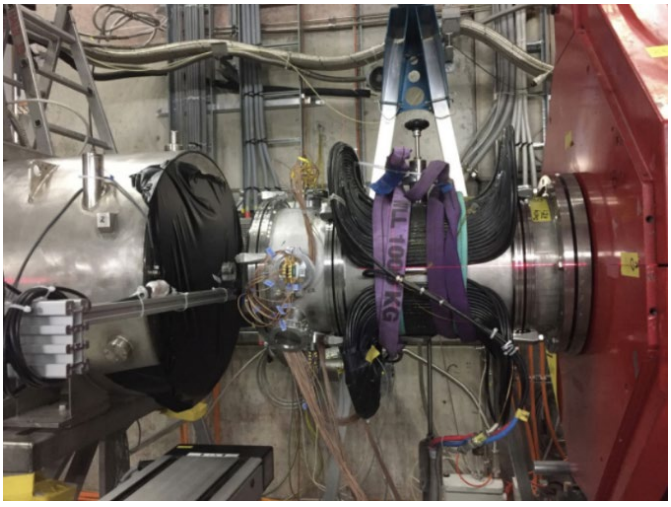

Figure 2.2.17: The pill detector mounted along the piE5 beam line at PSI.

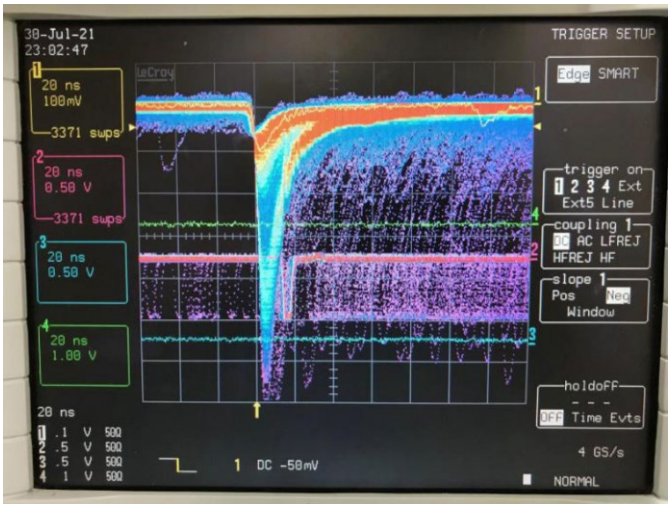

Figure 2.2.18: An example of the Pill signal at the oscilloscope. The beam momentum is 28 MeV/s. The high amplitude waveforms are associated with the muons while the low ones with the positrons (in this case cut by the trigger threshold). The separation between the two particle types is very clear.

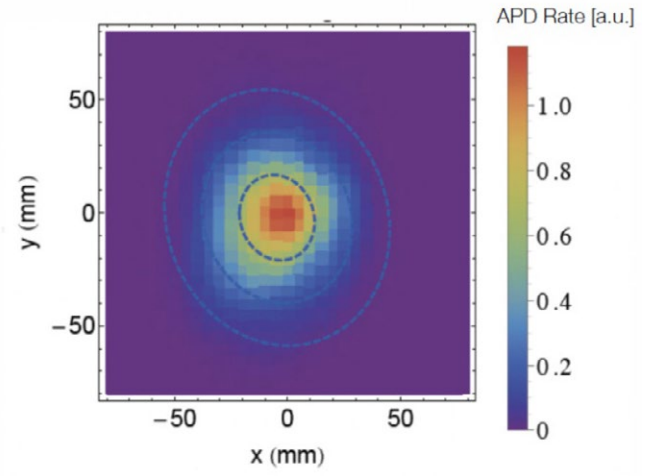

Figure 2.2.19: Muon beam profile at the center of the MEGII magnet as measured with the APD detector. The picture shows the collected measured points in "raster" scan mode.

with a pitch of 5 mm. The system is read-out by a 4-channel waveform digitizing board (the so-called DRS4 evaluation board) and fast electronics, with a LabVIEW-based acquisition system. This detector is operated in air; it allows for a clear separation between minimum ionizing particles and stopping muons, and it can be used only in low magnetic field regions to avoid compromising the functionality of the photomultiplier. Due to the setup, the impact on the beam is destructive. Thanks to the small active area of the detector, the high particle fluxes, even those expected at HIMB, can be measured without significant rate saturation.

Figure 2.2.17 shows a picture of the Pill detector, while Figure 2.2.18 shows some detector signals.

2.2.4.1.2 APD Detector

This detector is an avalanche photodiode of 1.5 mm active area radius, with a 130 µm depletion layer (SPL4419 Hamamatsu). It is the depletion layer that is the sensitive part of the detector. Since the depletion layer is relatively thick, it allows for a remarkable clear separation between minimum ionizing particles and stopping particles. A single detector coupled with a scanner, as described for the Pill detector, allows one to perform both X- and Y- beam profile scans, as well as 2D fine grid profile scans. The main advantage of the APD over the Pill is that it is insensitive to the magnetic fields, and can be used in high magnetic field environments, in our case deployed up to 1.25 Tesla. The front-end electronic board provides the first amplification stage and the proper bias delivery. The output signal is used, as in the Pill detector case, as an input to a DRS4 evaluation board and fast electronics and manipulated to extract the beam profile and rate measurements. Figure 2.2.19 shows a muon beam profile at the center of the MEGII magnet as measured with the APD at 1.25 T. A new generation of highly depleted APDs have been tested in view of HIMB, with a similar detector size and a depletion layer of 145 µm (S12453 Hamamatsu). While the current setup is used in air, we will investigate the possibility of having it compatible with a vacuum environment.

2.2.4.1.3 SciFi Detector

This detector is a quasi-non-invasive, high-rate sustainable beam monitoring tool, able to provide beam rate, profile measurements and particle identification in real time. It is based on scintillating fibres (SciFi) coupled to MPPC (SiPMs). It consists of a grid of two orthogonal fibre layers: one with the fibres running along the x-axis and the other with the fibres along the y-axis. Each fibre is independently coupled at both ends to MPPCs. A vacuum compatible version has been built and used while a movable configuration is now under construction.

Two detectors have been built and tested, the only main difference between the two being the type of mounted fibres (Saint-Gobain multi cladding BCF-12, 250×250 µm^2 and 500×500 µm^2) while in both cases S13360-1350CS MPPCs from Hamamatsu Photonics have been used (with an active area of 1.3×1.3 mm^2 and a pixel size of 50×50 µm^2). The relative

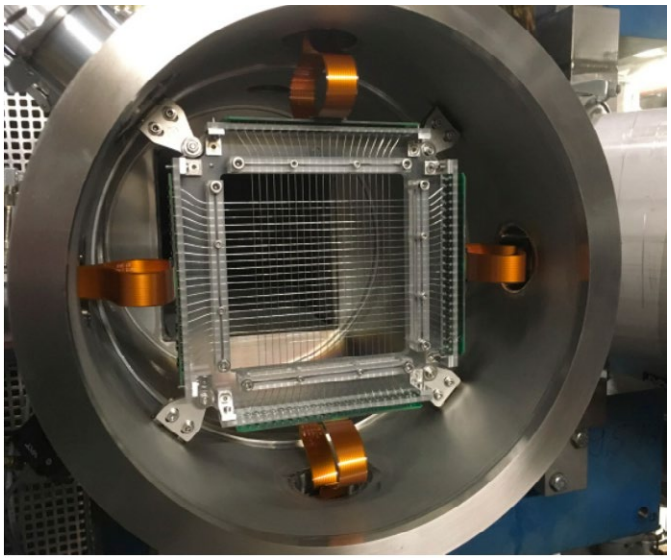

Figure 2.2.20: The SciFi detector mounted along the piE5 beamline at PSI.

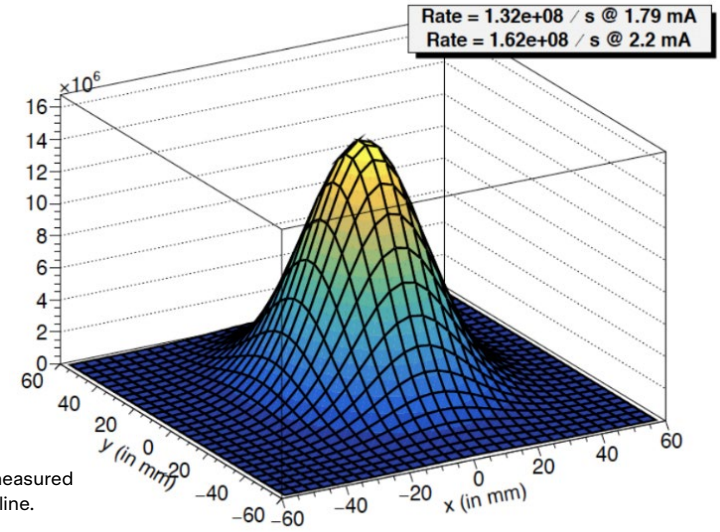

Figure 2.2.21: Muon beam profile as measured by the SciFi detector at the piE5 beamline.

distance between adjacent fibres mounted in the same layer is 4.75 mm, a pitch that satisfies the requirements for a precise measurement of the beam profile and rate. Furthermore, a large detector transparency T>92% (where 1–T = particles hitting the fibres/total incident particles) is achieved with a relatively small number of channels (≈100). In fact, for these detectors, we mounted 21 fibres per layer, giving a total number of 84 channels. The readout system is based on the WaveDAQ boards developed at PSI and the trigger boards of the MEGII experiment. It also includes the pre-amplifier and the voltage power for each MPPC. The system allows for the digitization of the waveform of each channel up to 5 Gigasamples per second. This feature is mainly useful during the setup of the detector. Normally, the beam profile and rate are extracted based only on the single fibre rate (for independent X- and Y-profiles) and the coincidence between fibres of different layers (to extract possible beam profile correlation). This feature has been proven to work with one of the two detectors (500 µm fibre detector-version) for a rate up to 7×10^7 muons/s.

A full Monte Carlo (MC) simulation code has been written, based on GEANT4. It also includes the response of the photosensors, going through the full electronic chain up to the waveform digitization, with a standalone code based on C++.

Figure 2.2.20 shows a picture of the SciFi detector, while Figure 2.2.21 shows some results.

2.2.4.1.4 MatriX Detector

The tested version of this detector is made of a matrix of 9×9 independent elements that act as a single detector, with a 6 mm pitch. Each element is made of $2\times2\times0.2$ mm^3 BC400 plastic scintillator, followed by a $2\times2\times2$ mm^3 plexiglass (light guide/MPPC protection) coupled to a S13360-1350PE (soon S13360-1325PE is to fully exploit the pixel dynamic range) Hamamatsu MPPC. The HiMB detector version foresees two different alternating plastic scintillator thicknesses, each thickness optimized for either minimum ionizing particles or low energy ones. In this way a simultaneously detection of these two kinds of particles can be detected, as well as their beam properties. The readout system is based on the WaveDAQ boards developed at PSI and the trigger boards of the MEGII experiment, following a similar approach to the one for the SciFi detector. The sensitive area coverage, the number of channels and the pitch can be optimized based on the expected beam characteristics. The main advantages associated with this detector are as follows.

1) A one-shot 2D grid scan from which both the beam profile and the rate can be extracted, as well as any beam correlations. The exposure to the beam will be just a few seconds, similar to the SciFi detector, and different to the Pill/APD scan that could require up to several hours, depending on the amount of requested measured points.
2) A detector compatible with both magnetic fields and vacuum.
3) A detector able to perform particle identification.
4) A full MC simulation code is also available for this detector. It is based on GEANT4 and it extends to the response of the photosensors, going through the full electronic chain up to the waveform digitization, with a standalone code based on C++.

The detector itself is beam-destructive. A movable version to operate it on demand and reduce the exposure to radiation to a minimum, allowing for a longer detector lifetime, is envisioned.

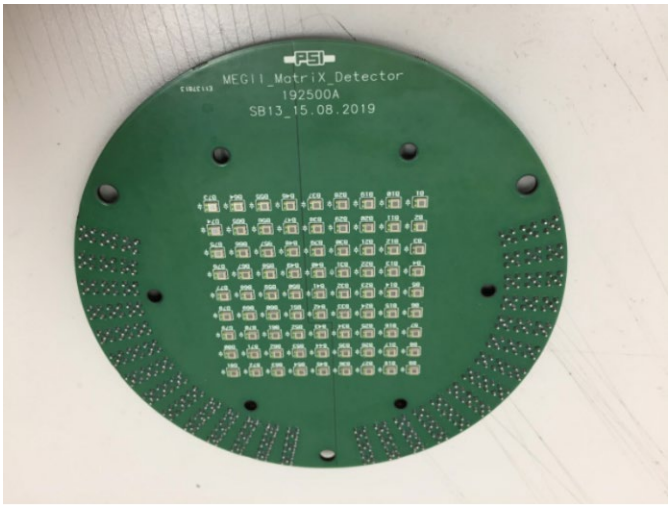

Figure 2.2.22: The MatriX detector prototype during assembly stage.

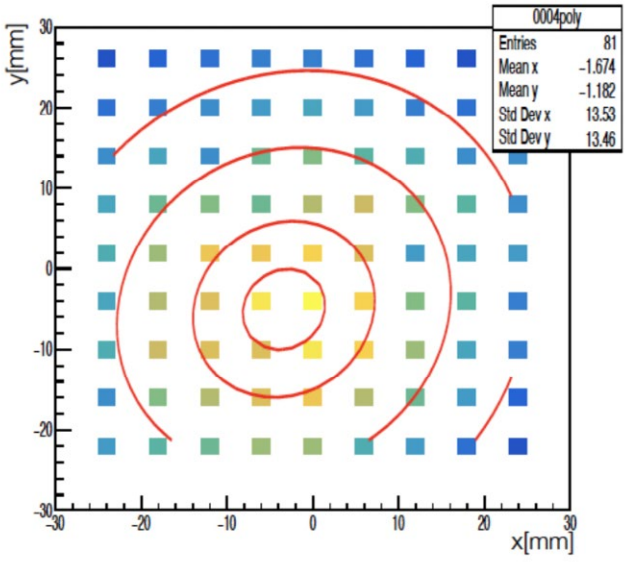

Figure 2.2.23: First test of the MatriX detector's capability along the piE5 beamline.

Figure 2.2.22 shows a picture of the matrix detector, while Figure 2.2.23 shows some results.

2.2.4.1.5 Luminophore Detector System

Based on scintillation light imaged by a CCD camera system, the ultra-thin 3 µm thick PET-foil substrate has a CSI(TI) layer of around 5 µm deposited on it using a thermal vapour deposition technique. An initial 130 mm diameter imaging foil was developed for use in high-intensity secondary beams of muons, pions and electrons, allowing both non-destructive and accurate beam profile imaging and together with a one-off independent intensity measurement, also allows beam intensity variations to be followed in real-time. Figure 2.2.24 shows the system developed for in-situ vacuum measurements developed for the MEG II and Mu3e experiments.

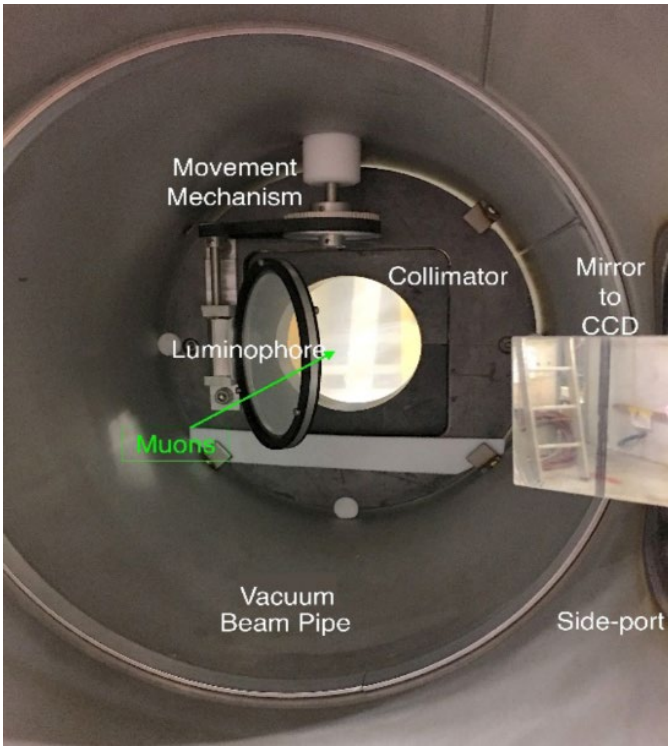

Figure 2.2.24: Luminophore setup used in the MEG II and Mu3e experiments. The foil is placed in the vacuum-pipe and can be moved in and out of the beam. It is imaged by a CCD camera system viewed via a side-port from outside of the vacuum system.

A calibration grid on the frame of the luminophore, which can be illuminated by an upstream UV-LED allows a pixel-to-mm ratio to be determined, as well as, allowing a perspective transformation to be made when viewing the foil off-axis. A beam profile image typically comprises of five consecutive exposures and five dark frames, taken with the beam-blocker closed, to produce a background subtracted image of the beam, using the high-resolution thermoelectric/water cooled 16-bit QSI RS-9.2S camera with a Canon EF-S 18-200 mm f/3.5-5.6 IS lens. The spatial resolution of the system has been measured to be better than 540 µm with a linear light-yield response over two-orders of magnitude in intensity reaching above 10^8 particles/s, only limited by the available beam. Comparative measurements with the pill-scanner system show comparative profile measurements to within 100 µm. The radiation hardness has also been tested up to 75 kGy.

Figure 2.2.25 shows the muon and positron beam profiles as measured with reduced separation-power of a Wien-filter to clearly show the separated muon and intense beam positron spots in the same field of view.

2.2.4.1.6 Future Detector Developments

While the detectors described in the previous Section can work at the expected HIMB intensities, with a fine-tuning of material thickness and size, as well as the number of channels, future beam tools based on different technologies, such as silicon devices, will be considered and investigated as well. In

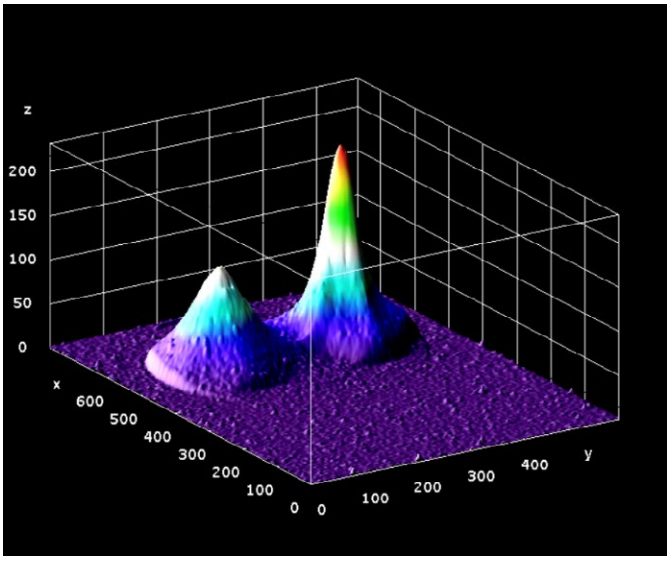

Figure 2.2.25: The surface muon and positron beam profiles at an intermediate focus position downstream of the Wien-filter, with reduced high-voltage so as to see both particles in the same frame.

fact, one of the main limitations of the scintillator coupled to silicon photomultiplier based detectors is the effect of radiation hardness, which strongly affects the lifetime of the detector itself. Furthermore, "transparent"/"super-thin" devices that could be permanently installed along the beamline would simplify the monitoring and operation of the beamline itself.

Among the other options, a first very promising test along the piE5 beamline has been recently done using the Jungfrau detector prototype, a 320 µm based silicon detector, with a 75×75 µm^2 pixel size and an active area of 80×80 mm^2, being developed at PSI for SwissFEL. Silicon wafers of 420 µm and 650 µm thickness are also available. A picture of the detector mounted along the piE5 beamline is shown in Figure 2.2.26. Some preliminary results are given in Figure 2.2.27.

2.2.5 References

[1] M. Aiba et al., *Science Case for new High-intensity Muon Beams HIMB at PSI*. arXiv:2111.05788v1, 10 Nov 2021.

[2] *PSI Graphic TRANSPORT Framework by* U. Rohrer *based on a CERN-SLAC-FERMILAB version by* K.L. Brown et al.

[3] *PSI Graphic TURTLE Framework by* U. Rohrer *based on a CERN-SLAC-FERMILAB version by* K.L. Brown et al.

[4] Eichler, R., Kiselev, D., Koschik, A., Knecht, A., van der Meulen, N., et al. (2022). *IMPACT conceptual design report*. (PSI Bericht, Report No.: 22-01). Paul Scherrer Institut. section 7.7, https://www.dora.lib4ri.ch/psi/islandora/object/psi%3A41209.

[5] Berg et al., *Target Studies for surface muon production*, Phys. Rev. Accel. Beams, 19(2), 024701, p.1-13, doi.org/10.1103/PhysRevAccelBeams.19.024701.

[6] T. J. Roberts and D. M. Kaplan, *G4beamline simulation program for matter-dominated beamlines*, 2007 IEEE Particle Accelerator Conference (PAC), Albuquerque, NM, USA, 2007, pp. 3468-3470, doi: 10.1109/PAC.2007.4440461 https://www.muonsinc.com/Website1/tiki-index.php?page=G4beamline#Documentation

[7] F. Berg, *CMBL – A High-intensity Muon Beam Line & Scintillation Target with Monitoring System for Next-generation Charged Lepton Flavour Violation Experiments*, PhD thesis 24547, ETH Zürich, Switzerland, 2017.

[8] K. Deb et al. *A fast and elitist multiobjective genetic algorithm: NSGAII*. In: IEEE Transactions on Evolutionary Computation 6.2 (2002), pp. 182–197. doi: 10.1109/4235.996017.

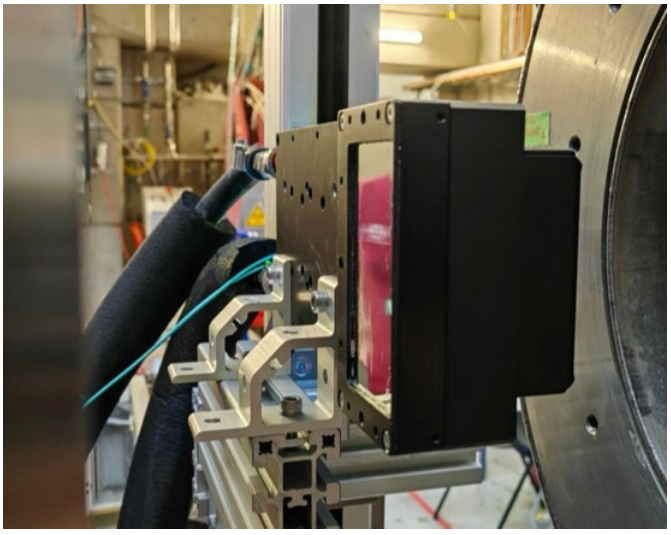

Figure 2.2.26: The Jungfrau detector prototype mounted along the piE5 beamline.

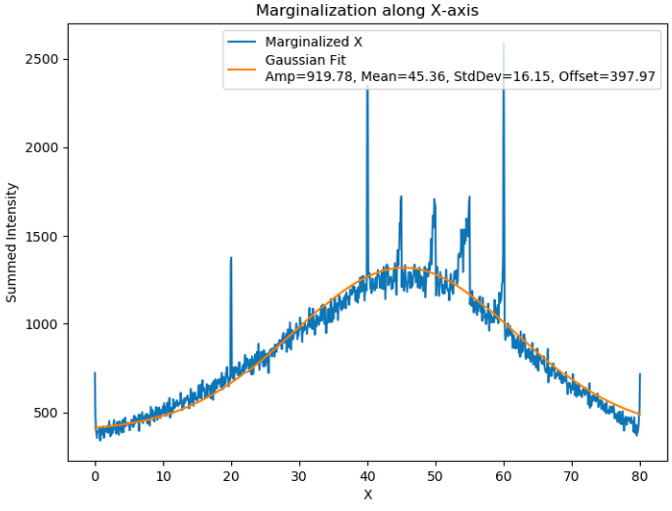

Figure 2.2.27: The x-coordinate surface muon beam profile as measured by the Jungfrau detector prototype.

2.3 Experimental Areas MuH2 and MuH3

2.3.1 General strategy

As part of the HIMB upgrade, two new secondary beamlines, MuH2 and MuH3 will be built. MuH2 will serve the particle physics experiments, while MuH3 is intended for μSR instruments. Figure 2.3.1 shows an overview of the two foreseen experimental areas connected to these beamlines.

General MuH2 infrastructure needs	
General electrical power distributors	Gas cabinet for storage of gas bottles
Fast ethernet connections	Helium return line
Liquid nitrogen	Dry, gaseous nitrogen
Distributor for experimental hall signals (proton current, proton RF, synchronization signals)	Patch panel for signals from area to counting house
Exhaust line for vacuum pumps	Workspace for small assemblies

Table 2.3.1: MuH2 general requirements

MuH2 replaces the current PiM1 beamline and area. As the overall layout of the MuH2 beamline is completely different to PiM1, the experimental area has to be rebuilt and adjusted to fit the beamline and potential new experiments taking place in this area.

MuH3 replaces the current PiM3 beamline, but in contrast to MuH2, the second part of the beamline remains largely in place and as such also the two experimental areas MuH3.2 and MuH3.3 with the μSR instruments GPS and FLAME remaining unchanged.

2.3.2 MuH2

2.3.2.1 Infrastructure

The MuH2 area will host various particle physics experiments over the years. Therefore, precise infrastructure cannot be provided, but the installations should be flexible and varied enough to adapt to different experiments. The existing PiE5 area can serve as a model for this. Table 2.3.1 lists the most important general requirements.

Figure 2.3.1: Overview of the three experimental areas MuH2, MuH3.2 and MuH3.3. MuH2 will host various particle physics experiments (shown here the Mu3e experiment), while MuH3.2 and MuH3.3 host the μSR instruments GPS and FLAME.

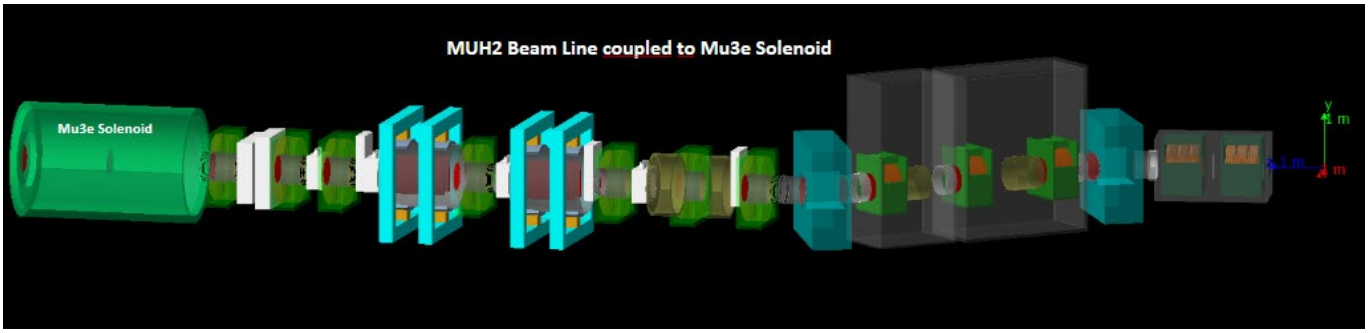

Figure 2.3.2: Shows the Mu3e solenoid coupled to the end of the MuH2 beam line.

To create a pleasant and functional workspace, it is essential to paint the concrete walls white wherever possible and install dedicated area lighting.

Additionally, it is crucial to consider the infrastructure requirements for the Mu3e experiment. Since the experiment will transition from PiE5 to MuH2 after the long shutdown, all its infrastructure currently installed primarily on two platforms above PiE5 will need to be relocated to MuH2. Furthermore, connections between the server room in front of PiE5 and the experiment in MuH2 using optical fiber cables will need to be reinstalled.

2.3.2.2 Potential experiments: Mu3e phase II and muCool

In the Science Case for HIMB [1], a wide range of possible experiments to be performed at the MuH2 beamline are presented. Here we focus as an example on two potential experiments running at MuH2: coupling into the Mu3e experiment, the main scientific driver of the project (see [2]), and into the MuCOOL device, aimed at compressing the muon beam phase space by ten orders of magnitude with a 10^{-4}~10^{-5} efficiency (see [1]).

Dedicated optimizations have been run for both cases to maximize the transmission to the two targets. A simple coupling into the two experimental magnets was assumed. More elaborate and improved couplings are conceivable.

2.3.2.2.1 Mu3e coupling

The Mu3e experiment aims to measure the forbidden decay μ→eee, heavily suppressed in the Standard Model of particle physics (see [2]). Any observation of such a decay would be a clear sign of new physics, and the experiment aims to take data in two phases: phase I, with a sensitivity goal of 10^{-15} on the branching ratio; phase II, with a sensitivity goal of 10^{-16} on the branching ratio. The first phase will take place in the PiE5 area, where rates up to ~10^8 μ^+/s can be delivered to the Mu3e target. Such muon rates however, will not suffice for the phase II experiment. This will require improving the current, deliverable muon rates, by at least one order of magnitude.

Two scenarios have been studied, the first with no restrictions on the internal structure of the Mu3e solenoid, allowing an upper limit on the transmission to be assessed. Figure 2.3.2 shows the MuH2 layout with the coupled Mu3e solenoid, without internal structure. The second scenario is with the current Phase I beam-related layout placed in the solenoid. This is not ideal as it is not matched to the HIMB phase space and only a Phase II experimental redesign will yield the required stopping rate.

The non-restrictive scenario, based on the high-intensity MuH2 mode with maximal Wien-filter gaps of 450 mm yields a total rate at the centre of the magnet of 1.07 10^{10} muons per second at a proton beam current of 2.4 mA. The rate on the very small Phase I target, of radius 19 mm, yields close to 3 10^9 mu^+s^1, well above the factor of 10 increase wanted for phase II experiment.

The non-optimal Phase I internal setup was tested with the MuH2 beam line as this is likely to be the initial layout at MuH2 for the Mu3e experiment. Figure 2.3.3 shows the r.m.s beam-spot sizes in the Mu3e solenoid, without internal structure, showing the double waist positions at the centre of the magnet, where the target is situated, as well as the possible locations for the 600-micron Mylar degrader and a 40 mm id Al collimator, placed in the small 60 mm id beam-pipe.

The optimized beam-related internal layout positions for the various features of the Phase I experiment: 600 μm thick Mylar degrader; 40 mm id Al collimator; 35 μm Mylar end vacuum window; double-cone Mylar target with an upstream

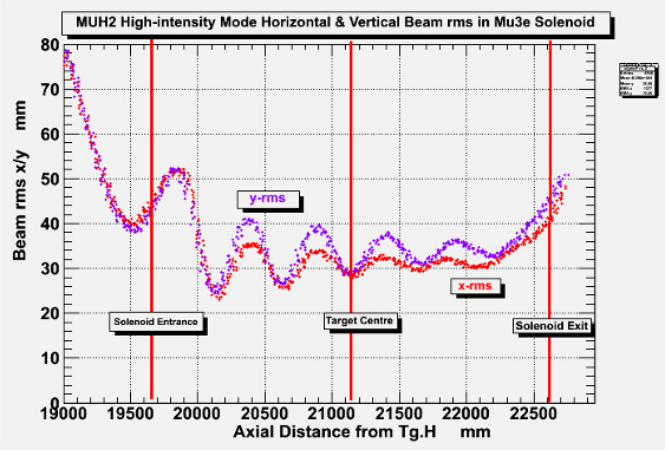

Figure 2.3.3: Shows the r.m.s horizontal and vertical beam sizes versus axial distance within the Mu3e solenoid. The muon beam double waist at the centre of the solenoid is clearly visible, together with possible further double waist/antinode locations for degrader and collimator positions respectively.

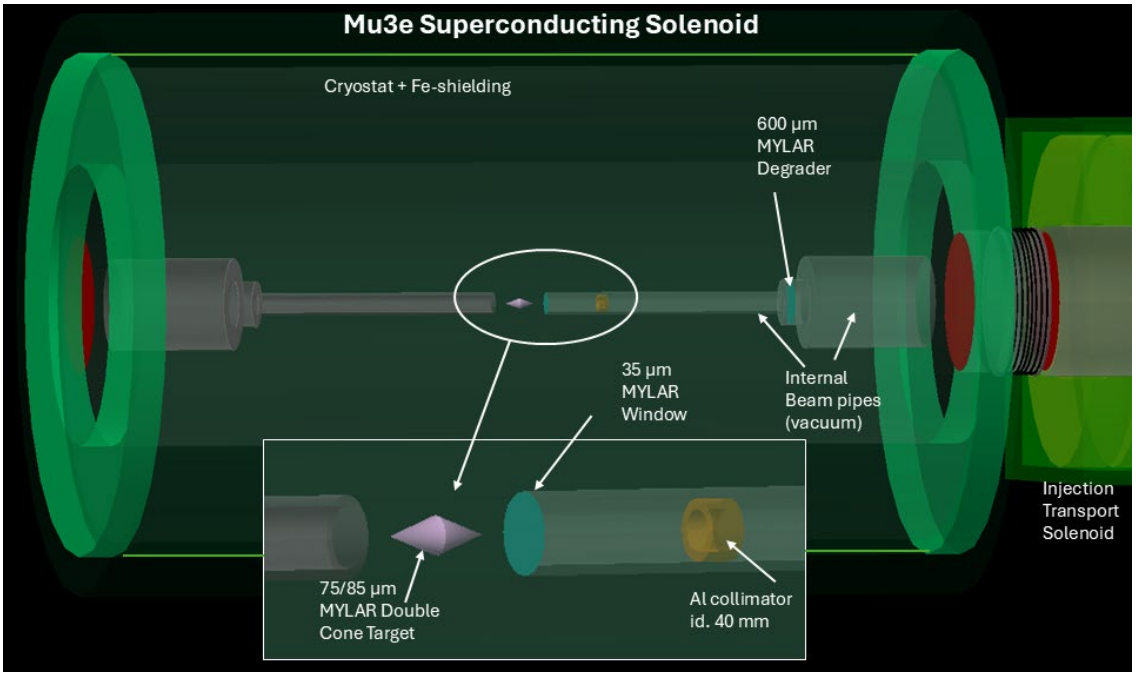

Figure 2.3.4: Shows the non-optimal beam-related internal layout of the Mu3e experiment Phase I, matched to the HIMB Mu3e Phase II beam line. The R=19 mm double cone target is placed at the double beam waist at the centre of the magnet, with the upstream vacuum window, degrader and collimator system shown.

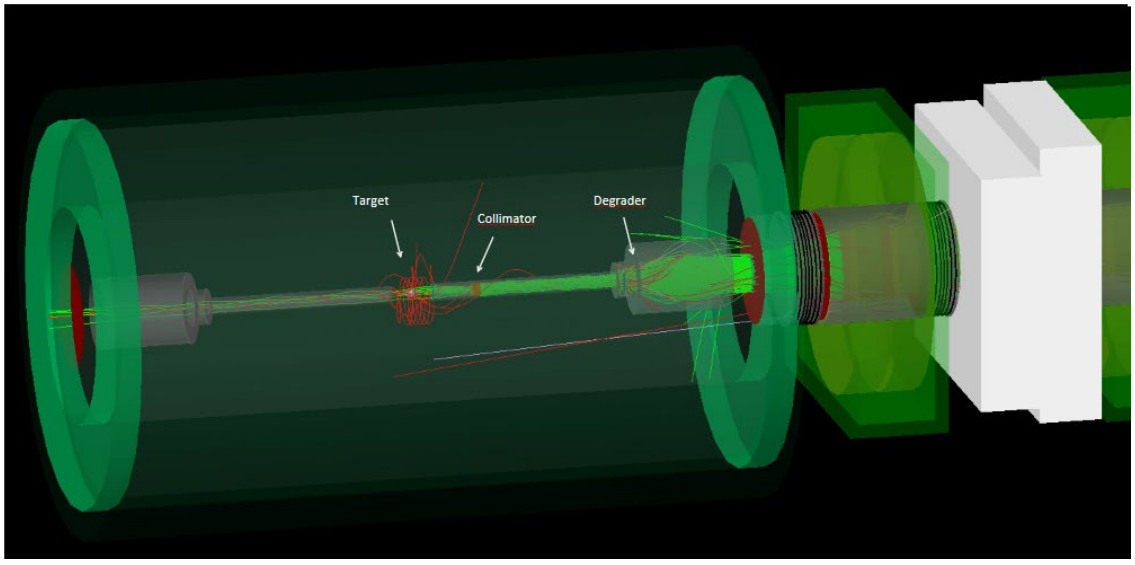

Figure 2.3.5: Mu3e Phase I internal beam-related components attached to the HIMB Mu3e Phase II beam line. A set of muon beam events (shown in green) are displayed interacting in the double-cone target and producing Michel positrons from their decay (shown in red).

wall thickness of 75 µm and a downstream wall thickness of 85 µm are shown in Figure 2.3.4.

In Figure 2.3.5 a sample of muon beam events can be seen focused on the degrader and interacting in the target producing decay Michel positions. The photon background has been suppressed here to show the optical properties of the muon beam. The target is surrounded by two double layers of silicon tracking detectors (not shown here).

The beam spot characteristics on the Mu3e Phase I target are shown in two forms, one the full beam spot size, which is slightly larger than the spot size on the R=19 mm target. Even though the Phase I setup is not optimally matched to the phase space of HIMB, more than a factor of 6.5 times the currently measured Mu3e rate in the PiE5 area is achieved with the same setup. On the R=19 mm target a factor of more than 5.3 is achieved, both for a Solenoid field of 1.1 T. Figure 2.3.6 shows the beam spot sizes at the centre of the detector (R=50 mm target, Green dots) and on the R=19 mm target (Purple dots). The respective r.m.s sizes are (10.5×10.6) mm and (8.7×8.8) mm.

Finally, the muon polarization with respect to the beam axis, PolZ is shown in Figure 2.3.7 for muons impinging on the R=19 mm target, a value of 89% is measured.

2.3.2.3 muCool coupling

The muCool target is a device aimed at compressing the positive muons' phase space by ten orders of magnitude with a 10^{-4}~10^{-5} efficiency. This is done with a triangularly shaped target

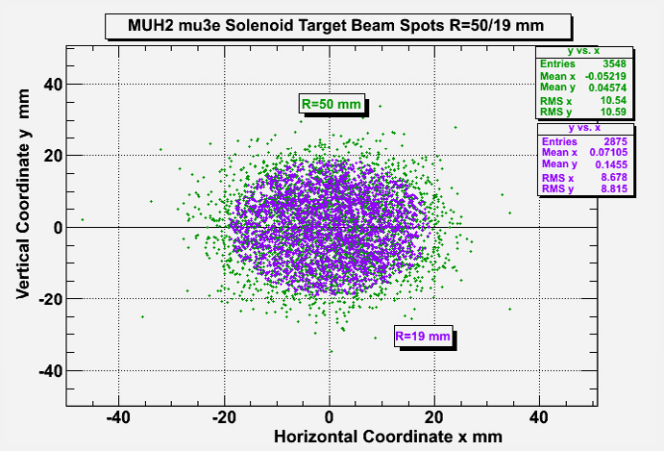

Figure 2.3.6: Shows the full beam spot at the centre of the detector measured on an R=50 mm target (Green dots), while the spot size on the Mu3e R=19 mm target is shown in purple.

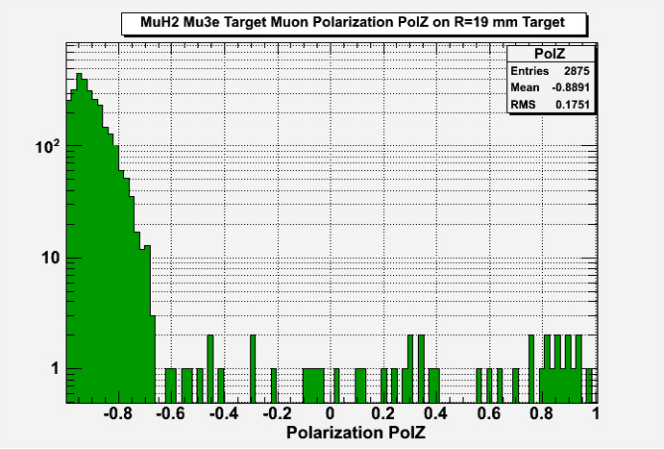

Figure 2.3.7: Shows the muon polarization PolZ on the Mu3e Phase I target of R=19 mm, measured with respect to the beam axis, yielding a value of -0.89 or 89%.

containing gaseous helium. The two inclined planes outlining the triangle are linked to two thermal sinks to introduce a thermal gradient in the helium, hence leading to a density gradient. The muons are stopped in the target and drift in helium following a cycloidal motion in an electromagnetic field. The density gradient allows to vary the average distance between consecutive collisions with the helium atoms, and control the drifting motion of the muons, which are collected at the exit of the target and reaccelerated up to a few tens of kV. The magnetic field is currently provided by the Phase Space Compression magnet, PSC, a 5 T superconducting solenoid, which has a bore radius of 100 mm and a length of 1 m. In the future, it will be substituted by a larger bore magnet, but here it is used as the reference for the results reported in the following.

The optimization has been performed considering a large acceptance muCool target, with a 60 mm high *back* panel. The PSC magnet has been included in the simulation at a 5 T field configuration, and its position has been included in the optimization. The maximum rate obtained in the muCool target is *7.1 10^9 μ^+/s at 2.4 mA of proton current*, hence leading to a ~60% acceptance. Figure 2.3.8 shows the beam spot at the center of the PSC magnet overlayed the muCool target profile and the momentum spectrum.

2.3.3 MuH3

2.3.3.1 Continuation of Existing Beamlines & Instruments

The Laboratory for Muon Spin Spectroscopy (LMU) at PSI operates the world leading μSR user facility (SμS) with six permanently installed instruments at five separate secondary muon beamlines of the HIPA proton cyclotron complex. The different

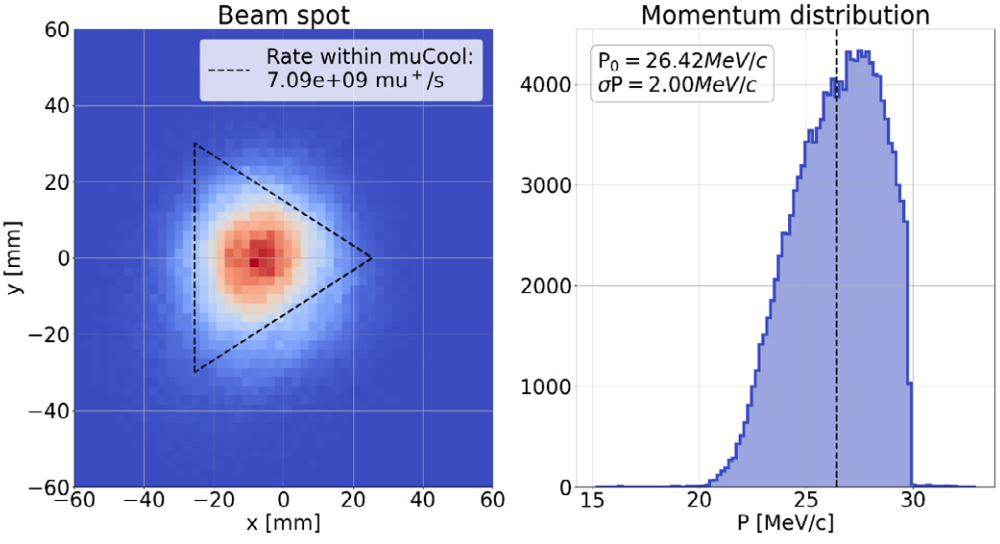

Figure 2.3.8: On the left: final beam spot transmitted to the muCool target. In black, the muCool target profile.On the right: momentum spectrum at the muCool target.

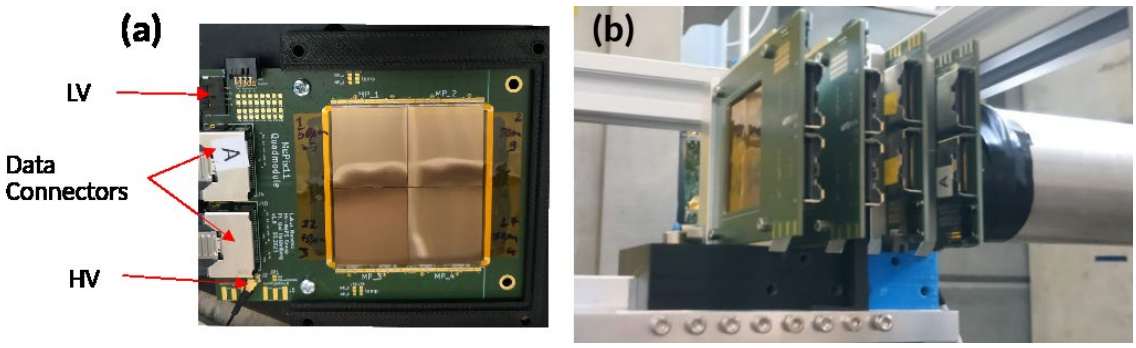

Figure 2.3.9: (a) A photo of a quad hosting four Si-pixel chips. (b) The arrangement of the quads in the prototype spectrometer with two upstream, two downstream, and the sample in the middle.

instruments provide the users with a wealth of different experimental capabilities with respect to e.g. temperature, magnetic field, pressure, time resolution, measurement geometry, probing depth and minimal sample size to fulfill the various requirements for the broad scientific spectrum addressed by the Swiss and international user community. Measurement time can be acquired by a proposal system which receives up to 300 new proposals per year.

Today, the two most demanded SμS facility instruments, GPS and FLAME, are located at the PiM3 beamlines. The beam of PiM3.1 is split by a septum magnet (ASS31) and provides both end stations, GPS in PiM3.2 and FLAME in PiM3.3, with equal rates of surface muons. With the HIMB upgrade, the naming of the beamline changes to MuH3. The muon production target region and the first part of the MuH3 secondary beamline up to the muon spin rotator will be completely modified while the remaining layout of the MuH3.1, MuH3.2 and MuH3.3 will stay mostly the same as today except for additional steering magnets, a change from quadrupole doublets to triplets and a relocation of the slit systems. The additional magnets needed for this second part of the beamline are either from the removal of the PiM1 and PiM3 beamlines or from stock.

GPS and FLAME instruments use the current state-of-the-art technology for time-differential μSR. However, to fully exploit the much higher muon rates provided by the MuH3 beamline, new concepts for fast data acquisition with temporally overlapping muon/positron events with spatial resolution of the order of 1 mm must be developed. Therefore, we will develop an instrument with vertex reconstruction for each muon/positron pair using Si-pixel detector technology. This development will be described in Section 2.3.3.2.

At the same time, the currently high scientific productivity of the two instruments shall be maintained during the transition stage until the new technology is fully established. Therefore, until the commissioning of HIMB, we will rebuild GPS into a hybrid instrument which will allow a quick changeover between a current state-of-the-art detector and data acquisition system and the newly developed Si-pixel based system. This modification requires a complete redesign of the magnetic and cryogenic sample environment as well as the actual particle detector systems. Once the new technique has proven successful, it shall be rolled-out to FLAME and other SμS instruments.

For the initial stage of HIMB, FLAME will still use the conventional way of conducting μSR experiments but will anyway benefit from the higher muon flux. It will be equipped with a novel passive movable collimation system allowing for selectable and smaller beam spot sizes than currently available allowing for measurements with lower background on considerably smaller samples.

2.3.3.2 Advanced μSR using Silicon Pixel Detectors

Measuring sub-millimeter samples using μSR is a dream for material scientists, in particular in the field of novel quantum materials which are difficult to produce in large quantities. In addition, data collection rates at continuous muon sources, which offer high time resolution measurements, have stagnated at a stopped muons rate of ~40 kHz since the development of the technique. As a part of the HIMB project, we aim at developing new concepts for μSR spectrometers which break these limitations ushering in a new era for muon spin spectroscopy and its applications. The main idea here is based on identifying corresponding pairs of an incoming muon and its decay positron by their common vertex, i.e. the hit position of the muon on the sample and the origin of the decay positron. To achieve this, one must track and reconstruct the trajectories of muons and positrons. With recent developments in silicon pixel detector chips used in particle physics experiments, such accurate tracking becomes possible for the first time, benefiting from a superb single hit spatial resolution of 23 μm and a timing resolution better than 15 ns, e.g., for the MuPix11 chip developed within the Mu3e collaboration.

Other potential breakthroughs for the above mentioned vertex reconstructed μSR (VR-μSR) technique include the ability to (I) obtain magnetic and electronic properties of materials on the sub-millimeter lateral resolution, (II) measure multiple

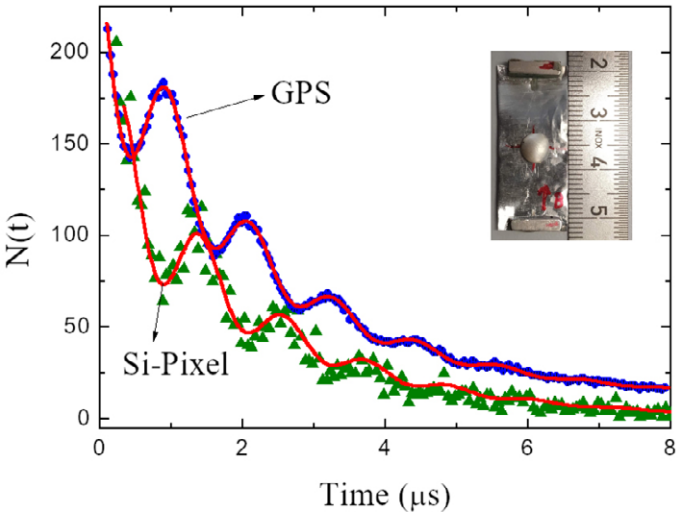

Figure 2.3.10: A first VR-μSR signal measured in a 6 mm diameter Al disc placed between two permanent magnets producing a transverse field of 6.3 mT at the center (inset). The number of counts as a function of time measured in the upstream detector of the Si-Pixel spectrometer (green triangles). This is compared to the counts in the upstream detector of GPS measured on the exact same sample (blue circles).

samples in parallel allowing, e.g., fast and efficient exploration of the phase space of a family of materials, (III) perform pump probe and transient measurements benefiting from the high data collection rate, and (IV) measurements of μSR signals with lower uncorrelated background, allowing longer time window measurements beyond the current 10 μs limit, without sacrificing the high time resolution or data rate.

Over the past two years, a prototype VR-μSR spectrometer has been constructed at PSI. The spectrometer uses four quad modules, each consisting of four MuPix11 Si-pixel chips mounted on a single PCB board (Figure 2.3.9 (a)). The thickness of the MuPix11 chips used in the quads varies between 50 μm and 100 μm. The quads were arranged such that two quads make an upstream detector set and two make a downstream detector set (Figure 2.3.9 (b)). The sample is mounted/suspended on a frame and placed in the middle between the two detector sets. The design of this spectrometer allows for flexible positioning of the quads and the sample relative to each other. The electronics and data acquisition (DAQ) software for the spectrometer were adapted from the Mu3e collaboration. The quad PCB is fed by a low voltage (LV) to operate the Si-pixels and a high voltage (HV) to bias their substrate. The data was read using a custom-made front-end board (FEB), converted to optical signals which is then fed into the DAQ PC hosting the DE5a-NET development board.

Since our prototype spectrometer does not have a magnet, we use permanent magnets placed above and below a 6 mm diameter Al disc to generate a perpendicular magnetic field (see inset of Figure 2.3.10). Measurements of this sample using the GPS spectrometer show a clear precession signal in an applied field of ~6.3 mT, as seen in Figure 2.3.10. We detect the same precession signal (with different phases due to the different geometries) in the GPS and the Si-Pixel prototype spectrometers. A fit of both spectra (single histogram fits, solid lines) gives a precession frequency and a damping rate which are equal (within the error bar).

It is important to point out here that the algorithm used to create the VR-μSR histograms from the Si-Pixel spectrometer has a negligible accidental background, compared to the currently used spectrometer technology, such as GPS (Figure 2.3.10). The primary advancement over conventional technology lies in the capability for spatial resolution, which allows for the reduction of accidental background noise. This clearly shows that using vertex reconstruction schemes will enable measurements to be performed with much longer data windows, without reducing the data rate or compromising on time resolution. We also note that the signal in the Si-Pixel detector is from data of ~35 seconds duration only as opposed to the ~25 minutes measurement time at GPS.

These are the first results obtained from the novel μSR spectrometer prototype based on Si-pixel chips [3]. With the added information about the lateral position of muon/decay positron events, VR-μSR promises to transform the way we do μSR spectroscopy at PSI. Therefore, we aim at upgrading the GPS spectrometer using Si-pixel detectors which will be available for use at day one of HIMB.

2.3.4 References

[1] M.Aiba et al., *Science Case for new High-intensity Muon Beams HIMB at PSI*. arXiv:2111.05788v1, 10 Nov 2021.

[2] K. Arndt et al., *Technical design of the phase I Mu3e experiment*, Nucl. Instr. Meth. A **1014**, 165679 (2021).

[3] L. Mandok et al., *Advanced muon-spin spectroscopy with high lateral resolution using Si-pixel detectors*, arXiv:2503.08891 (2025).

2.4 Radiation Simulations

2.4.1 Basic considerations

2.4.1.1 Tasks of radiation simulation

The HIMB project aims to provide experiments in particle physics and material science with unprecedented high muon flux. This goal is achieved by combining a high intensity particle production target with high transmission secondary beam lines for muon transport to the experiments.

As a result, the radiation environment during the HIMB operation is challenging. Thick radiation shielding around the target station and the secondary beamlines is needed to ensure that the operational dose rate does not exceed the regulatory limits. Beamline components exposed to the created secondary radiation shall be actively cooled and constructed from radiation hard materials to allow for the design lifetime. Technical design shall account for induced activation of components and resulting remanent gamma dose rate to keep the exposure of the personnel during the maintenance as low as reasonably achievable.

The task of radiation simulations is to provide the numerical estimates of the quantities of the secondary radiation field required for corresponding technical solutions that address these challenges.

2.4.1.2 Simulation codes and data libraries

Monte Carlo simulation of particle production and transport was done with the MCNP radiation transport code version 6.11 using the CEM03.03 model for neutron (above 20 MeV), proton, pion, and photon nuclear interactions and the LAQGSM03.03 model to handle all heavy ion interactions as well as all light ion interactions [1]. Neutron interactions at energies below 20 MeV were simulated using the ENDF/B-VIII.0 evaluated nuclear reaction data library [2]. Induced activation and decay gamma spectra were calculated with the FISPACT 2010 nuclide inventory code [3;4;5] using the EASY-2010 cross-section library [6]. Models for Monte Carlo calculations were converted from the CAD models using the CAD conversion tools TopMC [7] and GEOUNED [8]. Variance reduction parameters for MCNP simulations were calculated using the ADVANTG generator [9].

2.4.1.3 Energy balance at Target H and its impact on the radiation environment

The proton beam will lose some of its energy while passing through Target H. One fraction of the lost energy will be deposited locally in the target. Another fraction will be taken away by different species of secondary radiation produced through the interactions of the beam protons with the material of the target. The last fraction will define the radiation environment around the target.

The energy stored in the proton beam will be lost when the beam passes through the target. The energy balance at Target H is given in Table 2.4.1. The physical processes that lead to the loss of the stored energy may be grouped into two categories. The inelastic nuclear interactions of beam protons with the target will result in reducing the intensity of the proton beam. The MCNP simulation shows that 3.79 % of primary 590 MeV protons will be removed from the beam through this loss channel that is equivalent to the lost power of 66.6 kW ("Beam intensity loss" in Table 2.4.1). Beam protons that will avoid the inelastic interactions with the target will nevertheless lose their energy because of the continuous energy loss and elastic interactions. The MCNP simulation predicts the beam energy reduction to on average 581.88 MeV that gives additional 25.1 kW of the lost power ("Beam energy loss" in Table 2.4.1).

Out of the total power lost in the target only 30 kW will be absorbed locally in the target wheel itself. The remaining 62 kW will be taken away from the target by the secondary particles, mainly by protons and neutrons, created in the inelastic interactions in the target. The environment around Target H will be then featured by the following quantities:

- Prompt neutron dose rate at 50 cm from the target will exceed 3000 Sv/h and will have to be attenuated by the radiation shielding on the top of the target block and at the secondary beamlines.

Power, lost	**kW**
Beam intensity loss	66.6
Beam energy loss	25.1
Power, deposited	
Target H, wheel	30.0
Taken away by secondaries	61.7

Table 2.4.1: Energy balance at Target H at 590 MeV proton beam current of 3 mA.

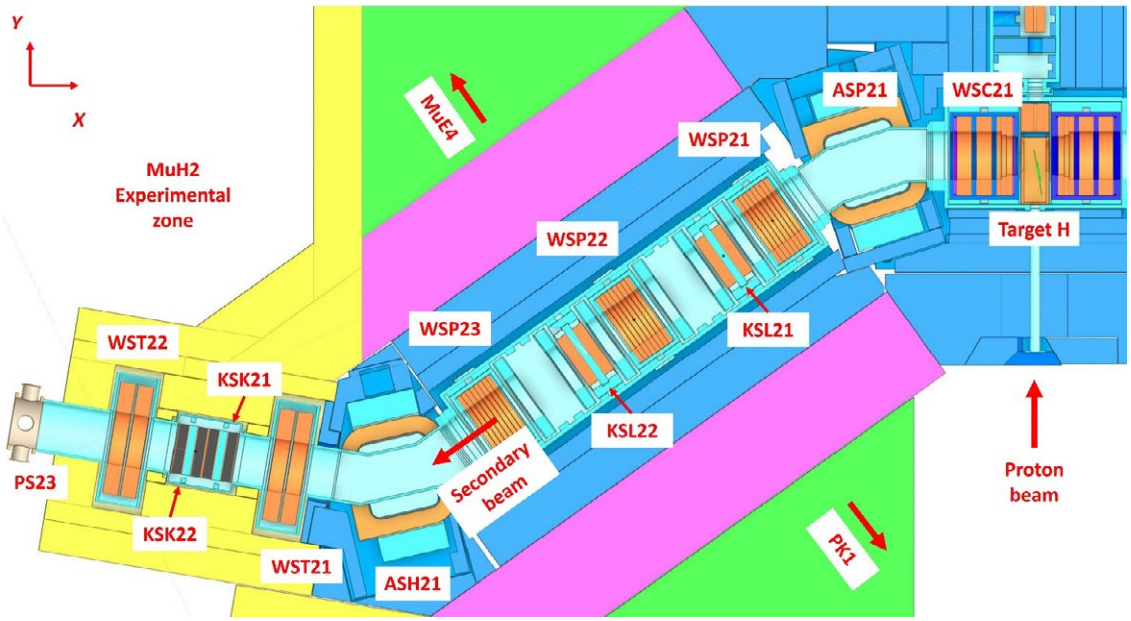

Figure 2.4.1: Layout of shielding at Target H and MuH2 beamline: iron (blue), concrete (yellow), support walls for the rails for the exchange flask (currently iron), and regions for further optimization (concrete or iron, green). Cyan marks stainless steel, orange are copper parts and black – polyethylene blocks.

- Power of 62 kW taken by the secondaries away from the target will be deposited in the neighboring beamline elements, vacuum chambers and shielding inserts among them, that will have to be actively cooled.
- Neutron fluence in the middle of the capture solenoids will reach 4×10^{17} n/cm^2 in a year that will require magnets with radiation hard coils.
- Remanent dose rate at the coils of capture solenoids will exceed 10 Sv/h after 20 years of operation that will require a special handling procedure using an exchange flask.

Simulation results are presented for the 3 mA beam current on Target H, except for the remanent gamma dose rate where the beam current of 2 mA per year is assumed that corresponds to the operation at 3 mA for 8 months in a year.

2.4.2 MuH2 radiation shielding

2.4.2.1 Shielding constraints

Radiation shielding at HIMB has been designed to match the constructional and operational constraints of the PK2 proton channel in the WEHA building.

On the roof above Target H and the MuH2 beamline the dose rate during the operation of PK2 proton channel shall not exceed the limit of 10 µSv/h for the permanent working place. The total height of the roof shielding shall not exceed the maximal distance of 8.5 m between the floor and the service crane. Otherwise, the exchange flask E cannot pass above the shielding (limited crane height). Lateral shielding in direction from the target block towards the MuH2 experimental zone shall also allow for decreasing the dose rate to 10 µSv/h but must be as compact as possible to provide additional space for the experimental equipment. The MuH2 beamline shall contain the system to block the aperture of the secondary beam to allow for obtaining the dose rate in the MuH2 experimental zone below 10 µSv/h during beam operation on Target H.

During data taking the MuH2 experimental zone will be closed, the secondary beam will be delivered to the experiment and the resulting dose rate outside the experimental zone shall not exceed 10 µSv/h. Special case are the tuning of the beamline magnets when the secondary beam can be lost on the separators in the center of the experimental zone (see Section 2.2.1). In this case the dose rate shall not exceed 10 µSv/h in the passages above the shielding walls of the MuH2 zone and in the WEHA building as whole because of the skyshine effect.

2.4.2.2 Shielding in the MuH2 beam plane

The iron shielding at the target block has been already evaluated for the IMPACT CDR and the reinforcement of the top shielding by 50 cm has been proposed that will give the total height of 4 m of the iron block. The layout of the lateral shielding of Target H and along the MuH2 beamline has been subject of the current optimization. The result is shown in Figure 2.4.1.

Directly at the MuH2 beamline up to the distance of 1.25 m from the beamline the shielding is iron along the height and the length of the MuH2 beamline. The ASP21 and ASH21 dipoles are surrounded by custom plates that are also made of iron. Next to the direct shielding of the beamline 1 m thick walls are located that shall support the installation of the exchange flask for replacing beamline components. During the shielding optimization these walls were calculated as iron blocks while changing the material to normal concrete may be also

KSL21	KSL22	KSK21	KSK22	d, µSv/h
OFF	OFF	OFF	OFF	83561.6
ON	ON	OFF	OFF	4344.5
ON	ON	ON	ON	10.6
ON	ON	OFF	ON	22.8
ON	OFF	OFF	ON	43.2

Table 2.4.2: Prompt neutron dose rate at the exit of the MuH2 beamline with different modes of the beam blocker system.

considered from the mechanical point of view. The end part of the MuH2 beamline is enclosed in the concrete hutch around the last two transport solenoids WST21 and 22. The wall, also made of concrete, closes the lateral shielding of the target block towards the MuH2 experimental zone.

Shielding towards the MuE4 experiment and the PK1 proton channel has been left for further optimization during the final integration with the shielding of the neighboring beamlines in WEHA.

2.4.2.3 Beam blockers system

During access of the MuH2 experimental zone, e.g. for maintenance, the large aperture of the beamline must be closed. The designed beam blockers system protects the MuH2 zone not only against the secondary beam but mainly against the neutral debris that will penetrate through the beamline aperture. The system contains two beam blockers of copper-steel-copper sandwich, KSL21 and KSL22 that will be located downstream from the first WSP21 and the second WSP22 transport solenoids. Next two beam blockers, KSK21 and KSK22, are copper-borated polyethylene-copper sandwich and are placed between the solenoids WST21 and 22.

Different beam blockers may be closed and opened independently. The variation of the prompt dose rate at the position of the PS23 vacuum pumping station at the exit of the MuH2 beamline depending on the beam blocker configuration is given in Table 2. With all four beam blockers closed the prompt dose rate is at the required operational limit. If one of the KSK beam blockers will fail the dose rate will increase by a factor of 2. In the worst-case of operating only one KSL and one KSK beam blocker the dose rate is still expected within the 100 µSv/h required for the temporary work in the MuH2 experimental zone as shown in Table 2.4.2.

2.4.2.4 Shielding above Target H and the MuH2 beamline

Iron shielding at Target H ends at the height of 4 m. The space of 1 m on top of the target block shall be left empty to provide room for beamline equipment and so the concrete shielding above the target may start from the height of 5 m. Figure 2.4.2 shows the upper view on the layout of the shielding at Target H and the MuH2 beamline. The bulky concrete shielding ends on the level of 8.5 m. With this arrangement of the shielding the limit of 10 µSv/h is exceeded only in the confined area directly above and downstream from Target H. To match the dose rate limit on the complete roof above Target H, an additional set of five 0.5 m thick and 4 m long standard concrete blocks can be installed there as shown in Figure 2.4.2. The two-dimensional distribution of the dose rate simulated on top of the concrete shielding at the total height of 9 m is shown in Figure 2.4.3.

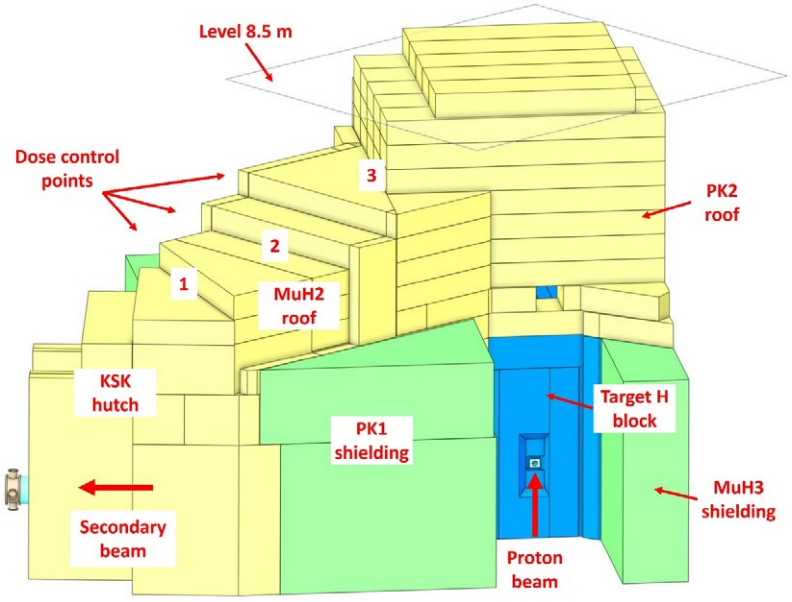

Figure 2.4.2: 3D Layout of shielding at Target H and the MuH2 beamline: iron (blue), concrete (yellow) and regions for further optimization (concrete or iron, green).

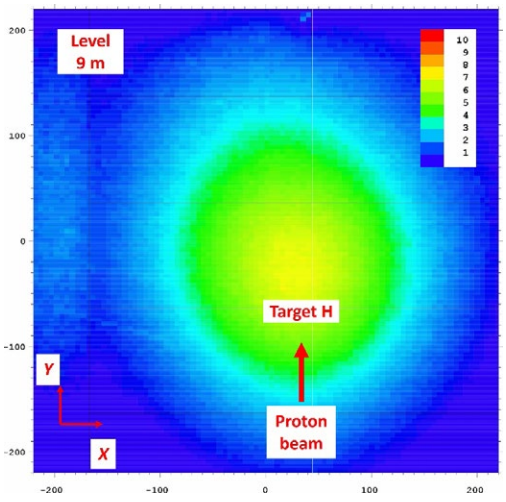

Figure 2.4.3: Prompt neutron dose rate (µSv/h) above Target H at the height of 9 m.

Point	d, μSv/h
1	1.2
2	4.6
3	10.8

Table 2.4.3: Prompt neutron dose rate at the control points on the MuH2 roof (see Figure 2.4.2).

Particle	rate, s^{-1}	dose, μSv/h
μ+	1.27E+10	27.2
e+	1.80E+10	24.5
π+	2.94E+07	0.24

Table 2.4.4: The rate of 26 MeV/c muon beam and its accompanying species and prompt gamma dose rate at control point 1 at the entrance from the courtyard resulting from dumping the beam into the shielding wall on the back.

Secondary particle flux along the MuH2 beamline is attenuated with the increase of the distance from Target H. Dose rates above the beamline shall exhibit the same behavior and so the concrete shielding above the MuH2 beamline has been designed in steps with the height decreasing along the secondary beam as seen from Figure 2.4.2. To evaluate the shielding performance, the dose rate has been controlled at different levels on the MuH2 roof and is given in Table 2.4.3. The dose rate limit of less than 10 μSv/h has been obtained over the whole roof surface and some negligible excess of the dose rate limit in the control point 3 can be straightforwardly mitigated by installing additional compact mobile shielding blocks.

2.4.2.5 Experimental zone of MuH2

Most of the shielding around the MuH2 experimental zone is composed of standard concrete blocks. The layout of the concrete parts around the MuH2 zone is shown in Figure 2.4.4. In the absence of experimental equipment (e.g. a detector) at the end of the beamline in the MuH2 zone, the worst-case scenario will be dumping the full secondary beam into the corner of the shielding next to the entrance to the MuH2 zone.

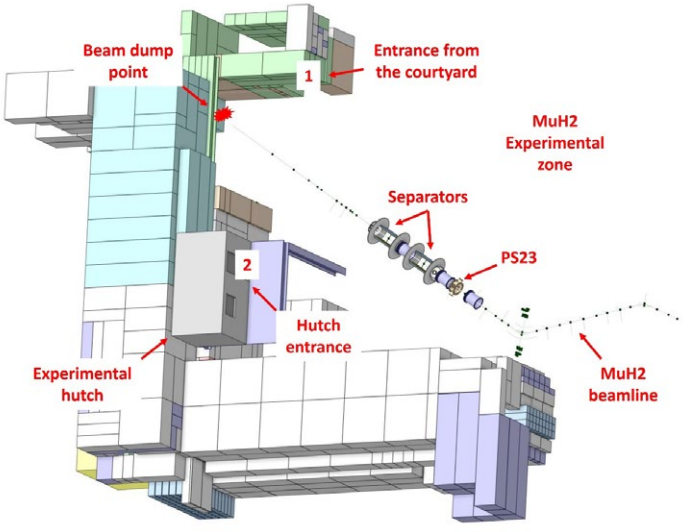

Figure 2.4.4: Layout of the concrete shielding around the MuH2 experimental zone. For orientation, the position of the PS23 vacuum pumping station at the end of the MuH2 beamline is shown. Dose control point 1 is at the entrance from the courtyard and control point 2 – at the hutch entrance.

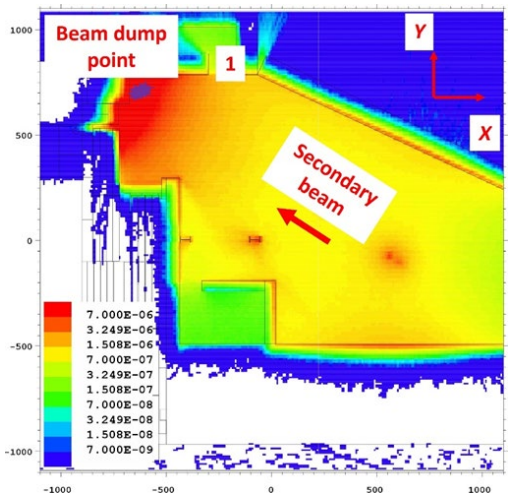

Figure 2.4.5: Prompt gamma dose rate in the MuH2 zone at the beam plane at 1.5 m (pSv per 1 lost positive muon) for a muon beam of 26 MeV/c (see Table 2.4.4).

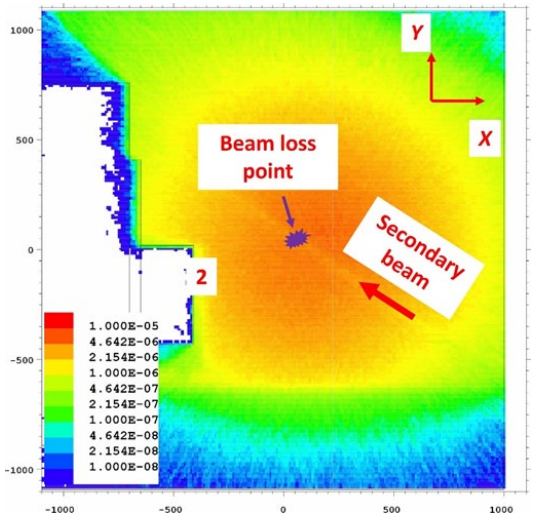

Figure 2.4.6: Prompt gamma dose rate in the MuH2 zone at the height of 7.2 m (pSv per 1 lost positive muon) for a muon beam of 70 MeV/c (see Table 2.4.5)

The MuH2 beamline delivers the beams of muons of both charges with momenta up to 80 MeV/c with the maximum around 26 MeV/c that may be accompanied by electrons or positrons and pions. Due to the mostly lepton nature of the beam the secondary photons clearly dominate the prompt dose rate in the experimental zone. A characteristic two-dimensional distribution of the dose rate in the MuH2 zone from dumping the positive muon beam with the 26 MeV/c momentum is shown in Figure 2.4.5.

As the distribution on Figure 2.4.5 shows the MuH2 experimental zone shall be closed during the beam dumped to the shielding wall. At control point 1 the characteristic dose rate is given in Table 2.4.4. Indeed, the entrance from the MuE4 side shall be confined by a safety door as the dose rate at this point exceeds 10 μSv/h, and at the chicane entrance at the MuE4 side the required dose rate limit is obtained.

Operation of the MuH2 beamline includes the phase of the beam scanning, at which the trajectory of the secondary

Particle	rate, s^{-1}	dose, µSv/h
µ+	5.82E+09	25.4
e+	2.64E+09	10.7
π+	1.27E+09	5.1

Table 2.4.5: The rate of 70 MeV/c muon beam and its accompanying species and prompt gamma dose rate at control point 2 at the hutch entrance resulting from losing the beam in the first separator.

beam will be optically deflected by large angles. In the worst case the beam will interact with the titanium electrode plates of the separators creating the secondary particle source in the center of the MuH2 zone. Figure 2.4.6 shows the two-dimensional distribution of the dose rate above the MuH2 experimental zone from losing the positive muon beam of 70 MeV/c momentum on the left electrode plate of the first separator.

The MuH2 zone shall have the hutch to control the experiment. The characteristic dose rate at control point 2 at one of the considered locations of the hutch is given in Table 2.4.5. As Table 2.4.5 shows, even well above the beam plane at the height of 7.2 m the dose rate during the beam scanning exceeds the limit. This can be mitigated either by confining the passages above the MuH2 zone at beam scanning or by installing an inner concrete bunker inside the MuH2 zone around the separators.

2.4.3 MuH3 radiation shielding

The first two straight sections of the MuH3 beamline share an approximate mirror symmetry with the MuH2 beamline relative to Target H. While not exactly symmetric, this similarity suggests a parallel but somewhat distinct radiation protection approach in this region.

The bulk shielding sections of the MuH3 beamline comprise the initial straight section containing solenoid WSC31 adjacent to Target H, the first magnetic dipole ASP31, the second straight section including solenoids WSP31 and 32, the second magnetic dipole ASP32, and partially, the short third straight section with the solenoid WST31. The horizontal midplane cross-section of the MuH3 shielding configuration is shown in Figure 2.4.7.

As with the MuH2 beamline, radiation transport calculations for shielding assessment are performed using MCNP, with beamline and shielding models converted from STEP geometry files to MCNP format. The GEOUNED utility facilitates this geometry conversion process. We use ADVANTG to obtain weight window grids that are optimized for specific MCNP tallies, such as the dose rates at a set of points.

The bulk shielding consists of steel blocks extending laterally at least 1.5 m from the central axis of the beamline, with the enhanced shielding on the side receiving higher radiation exposure from Target H due to the first dipole bend. Vertically, the steel shielding extends approximately 2.6 m above and 1.5 m below the central axis. Additional radiation attenuation is provided by a concrete roof structure of 3.5 m thickness extending a further 4.5 m in height above the steel shielding, with a 1-m-high access crawlway between the steel shielding and the concrete roof. The shielding geometry incorporates various detailed features.

The downstream sections, encompassing the third magnetic dipole ASH31, beam blocker KSK31, and the first quadrupole triplet QSM31–33, use lighter shielding constructed from concrete. This shielding extends approximately 1 m or more from the central axis of the beamline in both horizontal and vertical directions, and up to 5.7 m upwards. Shielding design above spin rotator 1 is being evaluated, with a 0.5 m concrete

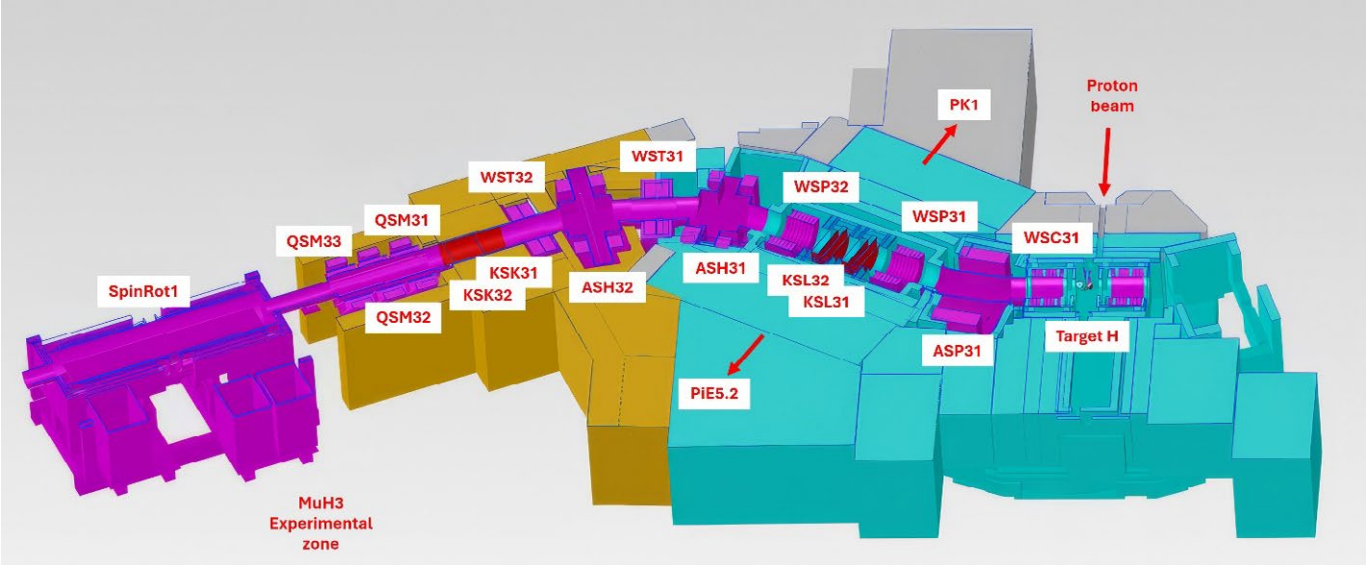

Figure 2.4.7: Horizontal cross-section showing the radiation shielding configuration for the MuH3 beamline. Heavy shielding is concentrated around Target H and throughout the first and second straight sections (steel blocks shown in teal, concrete in gray – subject of further optimization, similar to the MuH2 shielding). Lighter, additional shielding surrounds the third magnetic dipole and extends into the fourth straight section, including the first quadrupole triplet (concrete, shown in orange).

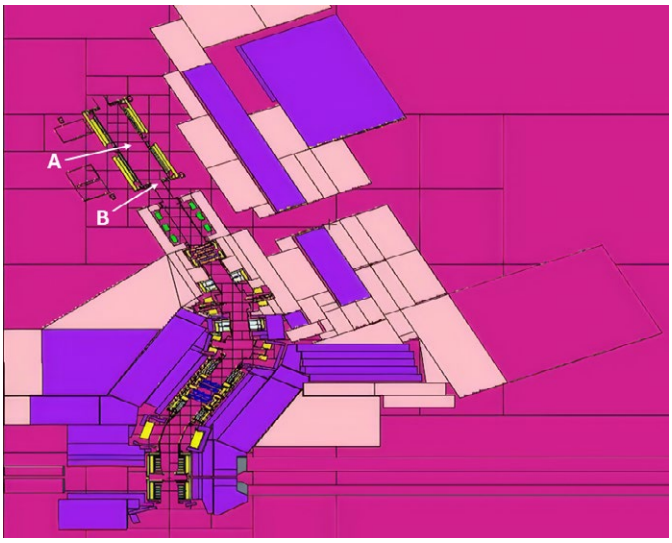

Figure 2.4.8: The horizontal midplane view of the MCNP geometry of the MuH3 beamline and its radiation shielding structures. In this picture, violet is iron, light pink is concrete, yellow is steel, and magenta is air. This model is for radiation shielding studies and is subject to revision. Green labels A and B represent the center and entrance of SpinRot1.

shielding option emerging to mitigate gamma radiation near spin rotator 1 due to the positron component of the beam. The radiation shielding layout for MuH3 is subject to ongoing optimization and revision; this is particularly the case for the concrete shielding area denoted by orange color in Figure 2.4.7.

MCNP simulations using the latest MuH3 radiation shielding model indicate that, for a 3 mA proton current at Target H, the neutron dose rate at the center of SpinRot1 (Figure 2.4.8, label A) is 0.5 µSv/h, with a relative error of 22%. At the entrance of SpinRot1 (Figure 2.4.8, label B), a neutron dose rate of 0.7 µSv/h with a relative error of 31% is expected. These results are consistent with a set of dose rate simulations we have conducted for these points. Currently, we are performing additional simulations with increased computational resources to achieve more precise estimates with lower statistical uncertainties.

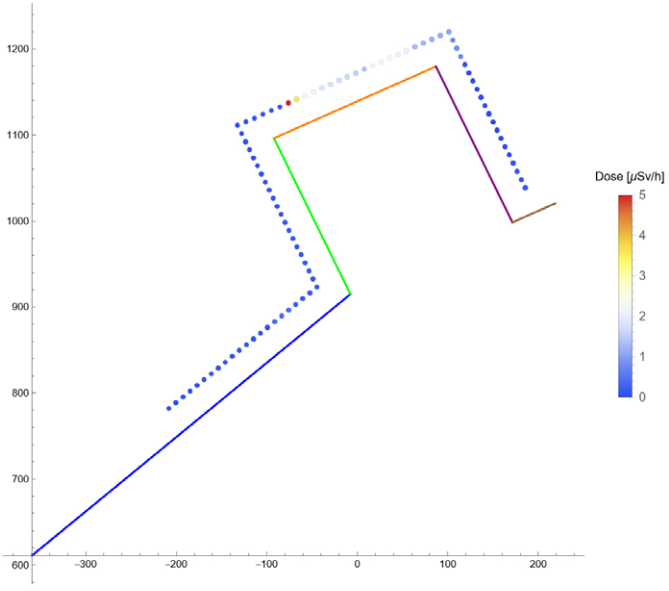

Figure 2.4.9: Dose rates at 30 cm from the shielding wall near ASH32 and QSM31-33.

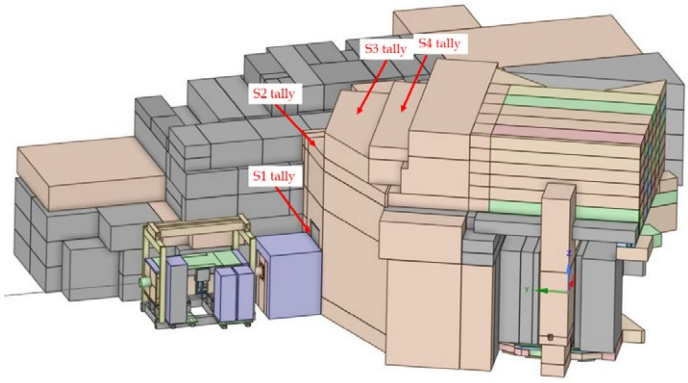

Figure 2.4.10: Positions of tallies S-1, S-2, S-3, and S-4. The tallies are in or near the vertical plane passing through the beamline's centerline at the respective longitudinal position.

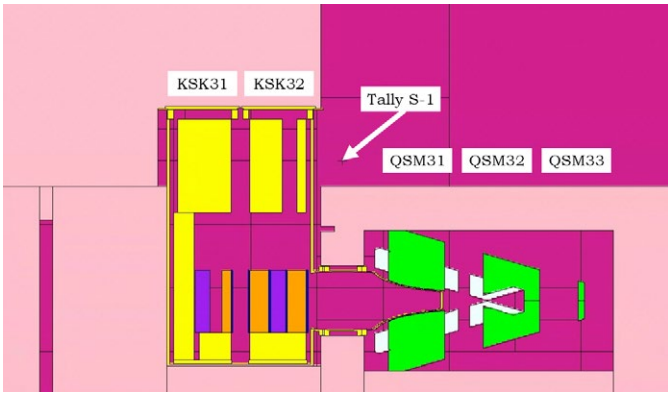

Figure 2.4.11: Tally S-1 above QSM31-33 next to the bulk shielding wall. The tally is in the vertical plane passing through the beamline's centerline.

Furthermore, we evaluated the neutron dose rates across a grid of points at 30 cm from the shielding wall in the experimental area near ASH32 and QSM31-33. The shielding encasement of the QSM31-33 quadrupole triplet is part of the shielding wall for this purpose. The dose rates along the shielding wall do not exceed 51 µSv/h and are subject to decrease in our ongoing studies.

The neutron dose rate at tally S-1 above the radiation shielding enclosure of the QSM31-33 quadrupole triplet next to the bulk shielding wall, as shown in Figure 2.4.10 and Figure 2.4.11, was calculated to be 2.7 µSv/h. At the further tallies S-2 to S-4 (see Figure 2.4.10), the neutron dose rate was calculated to be 25.9, 15.0 and 5.0 uSv/h, respectively. Additional shielding in this area is being considered.

2.4.4 MuE1 radiation shielding after modification

The shielding of the MuE1 beamline has to be modified within the framework of HIMB for integrating the He liquefier, actually located close to Target M, into a stand above the roof

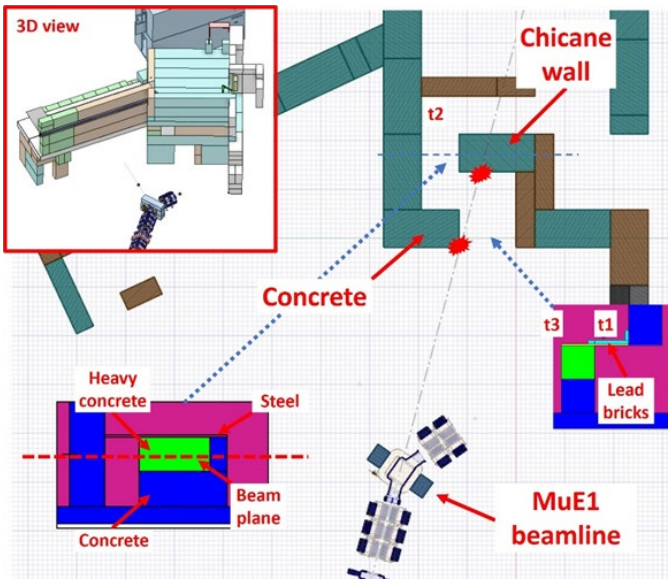

Figure 2.4.12: 3D layout of the new MuE1 entrance chicane (top left) and the cross-sectional view on the beam plane.

of the MuE1 zone. On this occasion of remodeling a second new entrance into the MuE1 experimental zone will be built as shown in Figure 2.4.12. The new entrance will be located in the direction of the unbent MuE1 beam before the last dipole magnet. In the worst-case scenario of the failure of this magnet the secondary beam will continue the straight trajectory and will be lost inside the entrance as depicted in Figure 2.4.12. To mitigate the resulting prompt dose rate around the entrance area, a chicane of normal and heavy concrete with a roof of stainless steel and an additional lead layer is forming the entrance into the MuE1 zone.

Detailed Monte Carlo simulations have been conducted to assess the radiation environment at the new layout of the MuE1 shielding [10]. As in the case of the MuH2 experimental zone, the photons dominate the prompt dose due to the mostly lepton nature of the MuE1 beam. Simulations revealed three hot spots t1–3 with the maximal prompt dose rate among the vertical and horizontal surfaces of the chicane as shown on Figure 2.4.13. The t1 spot is above the passage between the heavy concrete chicane wall and the new opening into the MuE1 zone. The t1 position is shielded by the 5 cm stainless steel plate and the 10 cm lead bricks. The t2 spot is at the beginning of the passage behind the chicane wall. There will be no additional shielding placed. The t3 spot is on the top of the heavy concrete block in the center of chicane. The t3 position is shielded by the same shielding as the t1 position.

Table 2.4.6: Simulated prompt dose rate at the hot spots t1–3.

Hotspot	d, µSv/h
t1	0.9
t2	0.89
t3	0.28

The MuE1 beamline can transport muons and pions of both charges, as well as positrons/electrons. The rates of positively charged particles are about three to four times higher than the rates of the negative ones and so the losses of positive muons, pions and positrons define the dose rate around the shielding. The simulated prompt dose per particle at the hot spots for each of the three positively charged particle types has been multiplied by the largest corresponding particle rate published on the MuE1 PSI public website [SµS – Swiss Muon Source]. The resulting simulated prompt dose rate summed over the three particle types is given for the three hot spots in Table 2.4.6 [10].

2.4.5 Energy deposition in radiation shielding and beamline components

The main part of the energy dissipated from Target H by the secondary particles will be deposited in the elements close to the proton beamline – local shielding of the target and collimators in the proton beamline. Another significant amount of the released energy will be deposited in the coils and yokes of the magnets of the secondary beamlines. These beamline

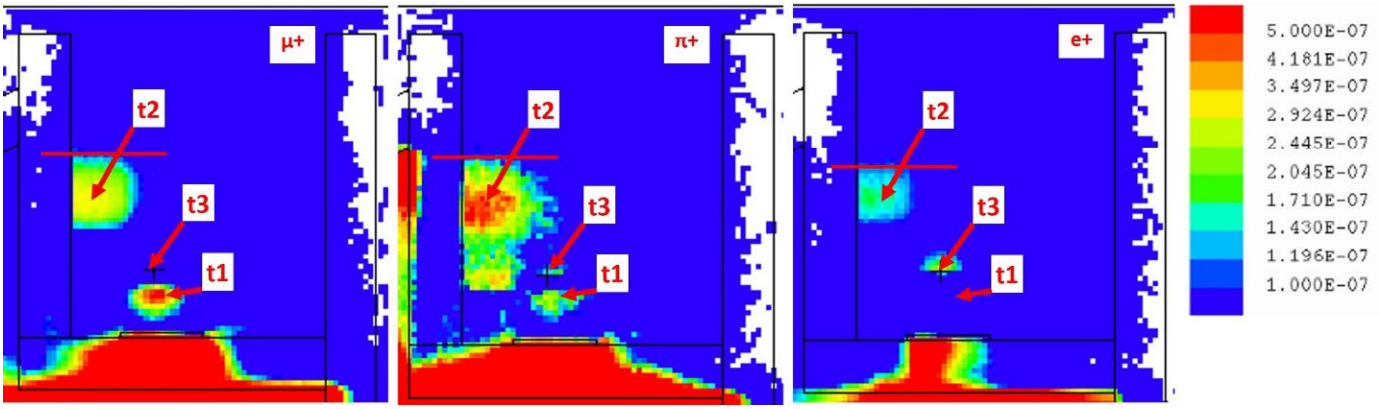

Figure 2.4.13: 2D distribution of the prompt gamma dose rate (pSv/s per one primary particle) for three considered particle types.

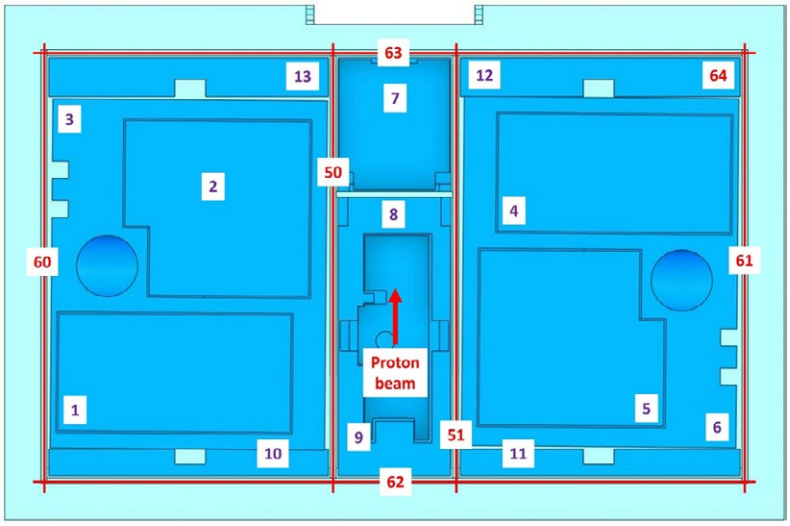

Figure 2.4.14: Position of meshes 50, 51 and 60-64 (red numbers, with mesh 64 at the bottom plate of the vacuum chamber) for scoring the energy deposition density around Target H. Violet numbers 1-13 mark parts of the inserts of the capture solenoids.

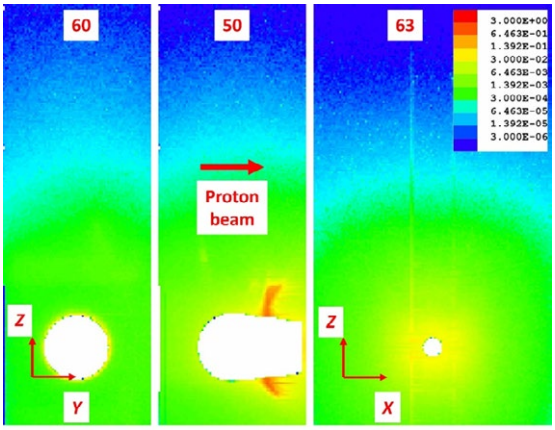

Figure 2.4.15: 2D distributions of the deposited energy density (MeV/cm^3 per 1 proton on the target) for meshes 60, 50 and 63.

components are pre-designed to be actively cooled. The rest of the power will be released in the HIMB vacuum chambers, shielding inserts of the beamline elements and radiation shielding. Estimates of released power in the individual HIMB components, vacuum chambers of Target H, PK2 and MuH2 with the inserts[1], provides input to the design of local cooling and air ventilation systems.

2.4.5.1 Target H

The energy deposited by the secondary particles around Target H has been estimated by placing seven meshes at various boundaries of the Target H vacuum chamber as shown in Figure 2.4.14. Meshes 60-63 were located on four walls of the chamber, mesh 64 at the bottom plate of the vacuum chamber and meshes 50 and 51 at the inner walls between the target insert and the inserts of the capture solenoids.

The height of each mesh was 3 m covering the vacuum chamber from the distance of 90 cm from the floor up to the top of the chamber (along the *Z* axis in Figure 2.4.15). Three characteristic two-dimensional distributions of the deposited energy density are shown in Figure 2.4.15. The size of each mesh cell was 1×1×1 cm^3. Simulated maximal power density and total power integrated in the 1 cm layer of each mesh is given in Table 2.4.7.

The total deposited power was also estimated for each of 13 inserts of the beamline components installed inside the Target H vacuum chamber and is given in Table 2.4.8.

Mesh	Max, W/cm^3	Total, W
50	7.43E-01	155.12
51	6.78E-01	146.25
60	5.76E-02	19.46
61	5.65E-02	15.76
62	2.28E-03	13.76
63	5.27E-02	100.00
64	4.34E-03	25.86

Table 2.4.7: Maximal power density and integrated power in meshes 50, 51 and 60-64.

Insert	W
1	36.24
2	22.90
3	137.54
4	48.22
5	17.77
6	120.16
7	394.20
8	168.11
9	119.10
10	48.79
11	46.19
12	627.98
13	648.18
Total	2435.38

Table 2.4.8: Total power in the inserts in the Target H chamber (see Figure 2.4.14).

[1] For brevity of presentation, further in this chapter the term “insert” refers only to the shielding insert element, without the corresponding beamline element connected to it.

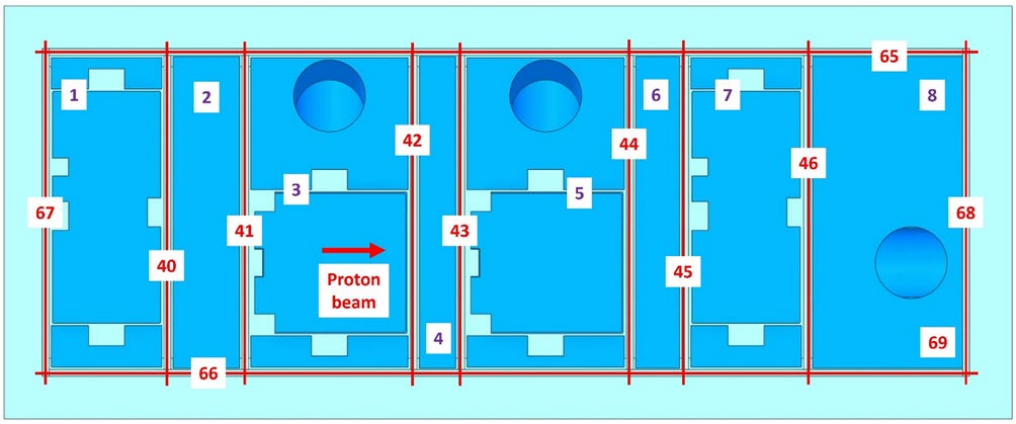

Figure 2.4.16: Position of meshes 40-46 and 65-69 (red numbers, with mesh 69 actually at the bottom plate of the vacuum chamber) for scoring the energy deposition density along the PK2 beamline. Violet numbers 1-8 mark the inserts of the beamline components.

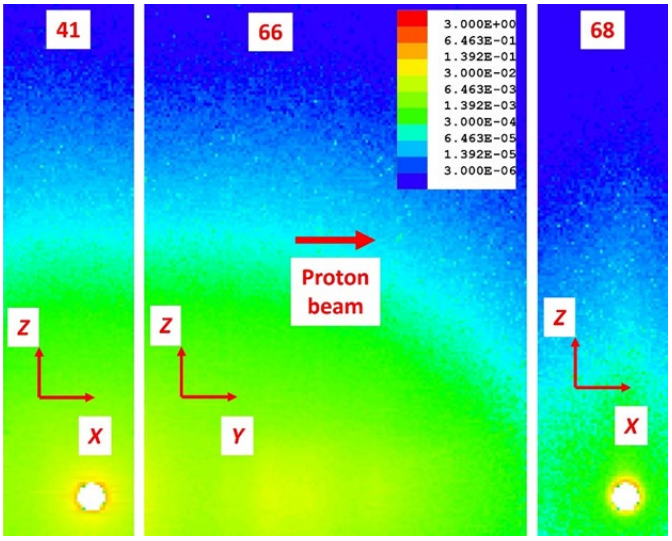

Figure 2.4.17: 2D distributions of the deposited energy density (MeV/cm^3 per 1 proton on the target) for meshes 41, 66 and 68 (in the direction of proton beam).

2.4.5.2 PK2 beamline

In the PK2 beamline the deposited energy has been estimated by placing twelve meshes at various boundaries of the PK2 vacuum chamber as shown in Figure 2.4.16. Meshes 65-68 are located on four walls of the chamber, mesh 69 – at the bottom plate of the vacuum chamber and meshes 40-46 at the inner walls between the shielding inserts of the beamline elements.

The height of each mesh was 2.8 m covering the vacuum chamber from the distance of 1.2 m from the floor up to the top of the chamber (along the Z axis in Figure 2.4.17). Three characteristic two-dimensional distributions of the deposited energy density are shown in Figure 2.4.17. The size of each mesh cell was 1×1×1 cm^3. The simulated maximal power density and the total power integrated in the 1 cm layer of each mesh are given in Table 2.4.9.

The total deposited power was also estimated for each of the 8 inserts of the beamline components installed inside the Target H vacuum chamber and is given in Table 2.4.10.

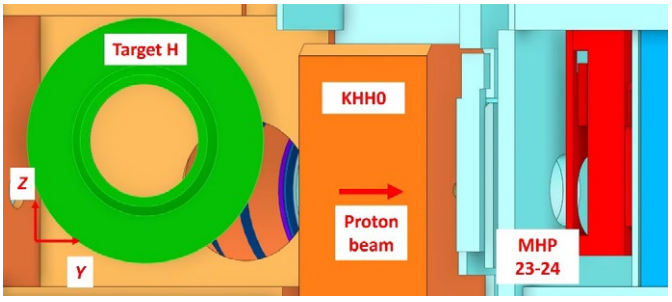

Figure 2.4.18: The MHP 23-24 beam monitor (red) located downstream from the KHH0 collimator.

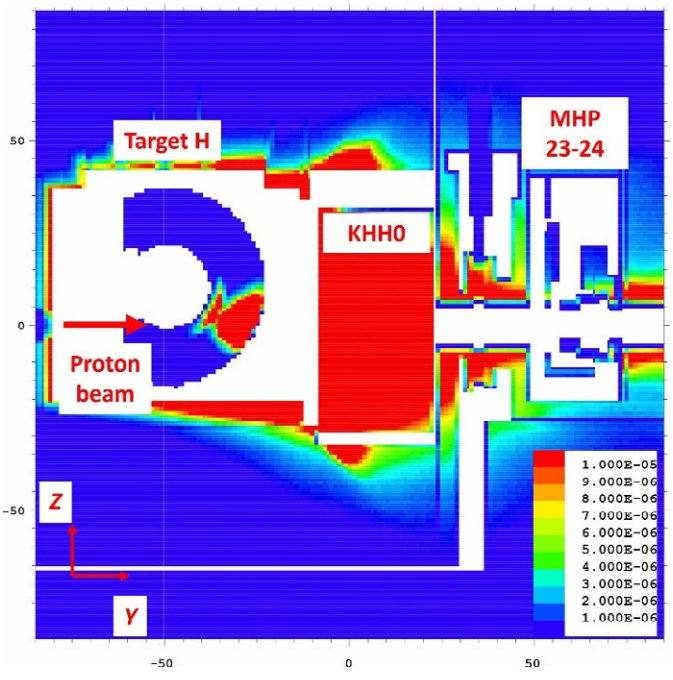

Figure 2.4.19: 2D distribution of the deposited energy density (MeV/cm^3 per 1 proton on the target) around Target H.

Mesh	Max, W/cm^3	Total, W
40	1.40E-02	11.34
41	1.59E-01	53.20
42	2.85E-02	27.35
43	1.71E-01	56.75
44	1.30E-02	12.70
45	3.57E-02	15.85
46	1.81E-02	2.91
65	7.57E-03	43.08
66	1.82E-02	74.89
67	6.83E-02	64.18
68	1.59E-01	10.24
69	3.29E-02	109.35

Table 2.4.9: Maximal power density and integrated power in meshes 40-46 and 65-69.

Insert	W
1	279.52
2	641.01
3	777.99
4	487.55
5	492.49
6	179.63
7	62.37
8	318.58
Total	3239.15

Table 2.4.10: Total power in the inserts in the PK2 chamber (see Figure 2.4.16).

MHP 23-24	
Part	**W**
1	19.7
2	6.5
3	4.9
4	3.8
5	0.6
6	0.6
7	9.7
8	6.4
9	18.3
10	3.0
11	1.0
12	1.4
13	1.2
Total	77.1

MHP 25-26	
Part	**W**
1	7.4
2	2.6
3	2.0
4	3.9
5	0.2
6	0.2
7	5.0
8	1.1
9	13.2
10	2.8
11	0.8
12	0.3
13	0.4
Total	39.9

Table 2.4.11: Total power in the parts of the MHP 23-24 and MHP 25-26 beam monitors.

The total deposited power was estimated specially for the components of the proton beam monitor MHP 23-24 that is located downstream from the KHH0 collimator as shown in Figure 2.4.18. A two-dimensional distribution of the deposited energy density around Target H, the KHH0 collimator and the MHP 23-24 beam monitor is shown in Figure 2.4.19. The total deposited power was estimated for each of the 13 parts of the MHP 23-24 monitor design shown in Figure 2.4.20 and is given in Table 2.4.11. Table 2.4.11 gives also the total power in the parts of the next downstream MHP23B-24B beam monitor that shares the same design as MHP 23-24.

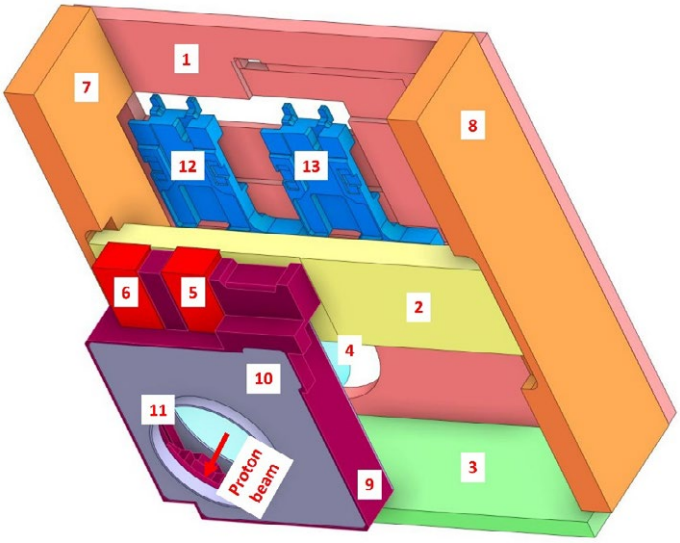

Figure 2.4.20: Parts of the MHP 23-24 design. All parts were simulated as built out of aluminum.

2.4.5.3 MuH2 beamline

Along the MuH2 beamline the energy deposited has been estimated by placing five meshes at various boundaries of the MuH2 vacuum chamber as shown in Figure 2.4.21. Meshes 71 and 73 were located at the start and end of the vacuum chamber, meshes 72 and 74 at the side walls of the chamber, and mesh 75 – along the first intermediate wall after the insert of the first transport solenoid.

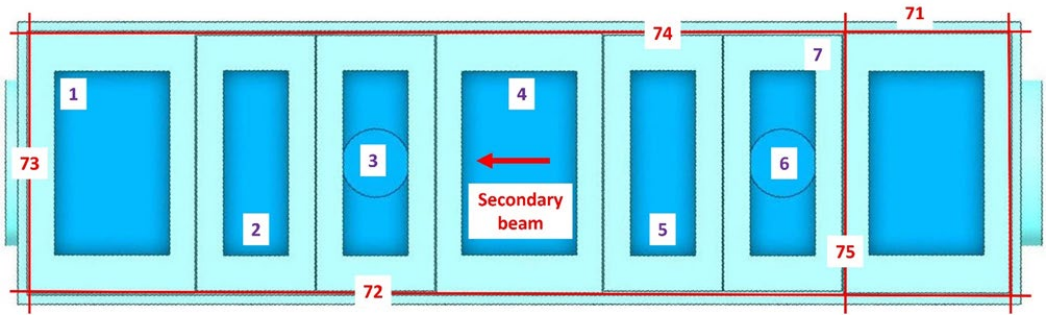

Figure 2.4.21: Position of meshes 71-75 (red numbers) for scoring the energy deposition density along the MuH2 beamline. Violet numbers 1-7 mark the inserts of the beamline components.

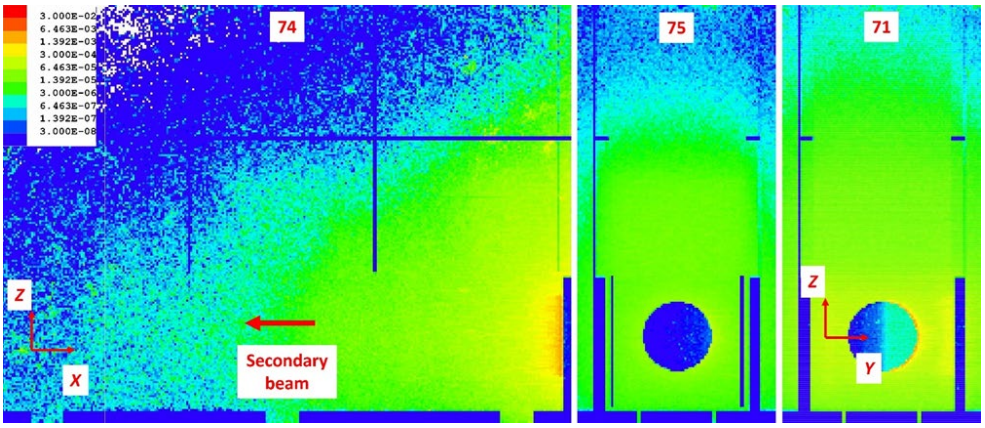

Figure 2.4.22: 2D distributions of the deposited energy density (MeV/cm3 per 1 proton on the target) for meshes 71, 75 and 74 (in the direction of the secondary beam).

Mesh	Max, W/cm³	Total, W
71	2.19E-03	1.23
72	5.37E-04	0.57
73	2.55E-06	0.00
74	4.06E-04	0.58
75	1.47E-04	0.38

Table 2.4.12: Maximal power density and integrated power in meshes 71-75.

Component	W
Target H block, including base plate	6033
MuH beamline, including vacuum chamber and inserts	381
MuH2 shielding	267
Total	6681

Table 2.4.14: Total power deposited in the uncooled HIMB components.

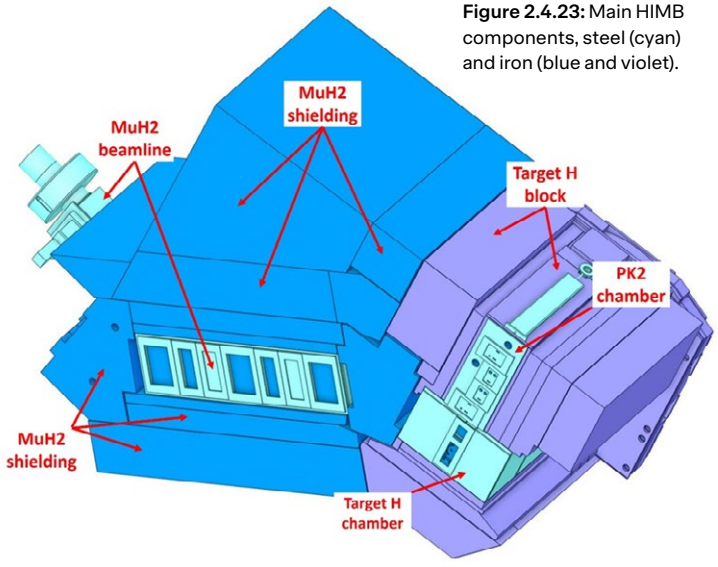

Figure 2.4.23: Main HIMB components, steel (cyan) and iron (blue and violet).

Insert	W
1	0.01
2	0.02
3	0.05
4	0.08
5	0.42
6	0.70
7	1.89
Total	3.17

Table 2.4.13: Total power in the inserts in the MuH2 chamber (see Figure 2.4.21).

The height of each mesh was 4 m covering the vacuum chamber from the floor up to the top of the chamber (along the Z axis in Figure 2.4.22). Three characteristic two-dimensional distributions of the deposited energy density are shown in Figure 2.4.22. The size of each mesh cell was 1×1×1 cm³. The simulated maximal power density and the total power integrated in the 1 cm layer of each mesh 71-75 are given in Table 2.4.12.

The total deposited power was also estimated for each of the 7 inserts of the beamline components installed inside the MuH2 vacuum chamber and is given in Table 2.4.13.

The results obtained for the MuH2 beamline are also taken for the MuH3 beamline due to its almost perfect symmetry with respect to the proton beamline.

2.4.5.4 Other HIMB components

Simulation of the energy deposition in HIMB suggested that the vacuum chambers of Target H and PK2 must be actively cooled. The vacuum chamber and inserts of the MuH2 beamline may not be cooled. The iron shielding block of Target H and the iron shielding around the MuH2 beamline may not be actively cooled either. Figure 2.4.23 shows the location of cooled and uncooled components. The energy deposited in the uncooled components will be released in the environment and shall be taken away by the air ventilation at the target station. The total power deposited in HIMB components that will not be actively cooled is given in Table 2.4.14.

Similar values as for the MuH2 components are expected for the MuH3 beamline.

2.4.6 Absorbed dose

HIMB beamlines shall operate for 20 years without replacement of the beamline components. Coils of the magnets in the Target H block and in MuH2 and PK1 beamlines are the nearest to the beam elements and so will be exposed to the highest secondary particle fluence. The estimate of the absorbed dose rate in the coils of the magnets allows for estimating the life-

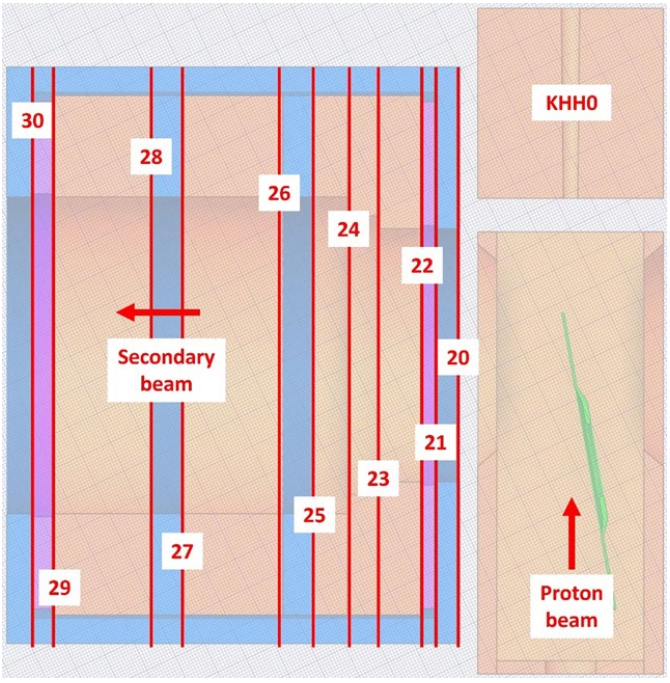

Figure 2.4.24: Positions of meshes 20-30 to score the deposited energy density. For orientation, the target wheel (in green) and the first collimator KHH0 are shown.

time of these components and provides input to the technical design of the magnets.

2.4.6.1 Capture solenoids

Absorbed dose rate in the coils of the capture solenoids inside the Target H block has been estimated by placing eleven meshes at the first 1 cm layer of various parts of magnet assembly perpendicular to the direction of the MuH2 beam as shown in Figure 2.4.24. Meshes 20 and 30 were located at the front and back steel mirror plate, meshes 21 and 29 – at front and back aluminum separators, meshes 22-24, 26 and 28 at the coils 1, 2 and 3, and meshes 25 and 27 – at the inner steel walls of the magnet yoke. Each mesh in the transverse plane fully covers the size of the yoke.

Two characteristic two-dimensional distributions of the deposited energy density are shown in Figure 2.4.25. At the first coil (mesh 22) the distribution of the deposited energy is featured by a clear maximum in the beam plane because of the particles produced in the target in forward direction. At the last third coil (mesh 28) the distribution of the deposited energy becomes almost radially symmetrical.

Simulated maximal absorbed dose rate for each mesh is given in Table 2.4.15. The second column in this Table gives the time in hours after which the absorbed dose level will reach 1 MGy. As can be seen from Table 2.4.15, the level of 1 MGy will be reached in all coils of the capture solenoid in less than 1 day time.

2.4.6.2 Magnets in the MuH2 beamline

For the magnets of the MuH2 beamline it has been assumed that their lifetime will be limited by the lifetime of the epoxy that isolates the coil windings from each other and keeps them in position. The value of 10 MGy has been taken as a limit for epoxy on the non-radiation hard coil assembly [12]. To account for this, the inner 3 cm, closest to the beam, of both dipole and transport solenoidal coils have been simulated as cop-

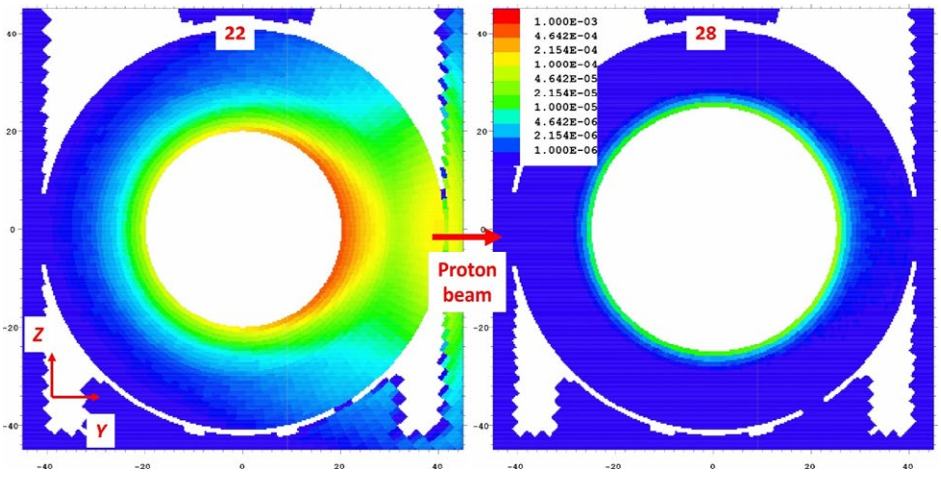

Figure 2.4.25: 2D distribution of the deposited energy density (MeV/cm^3 per 1 proton on the target) for meshes 22 and 28.

Mesh	Max, Gy/s	h(MGy)
20	297.0	0.9
21	203.6	1.4
22	182.0	1.5
23	27.0	10.3
24	4.0	68.6
25	58.5	4.8
26	41.9	6.6
27	17.3	16.1
28	12.9	21.6
29	1.8	156.7
30	11.0	25.3

Table 2.4.15: Maximal absorbed dose rate in meshes 20-30 (see Figure 2.4.24).

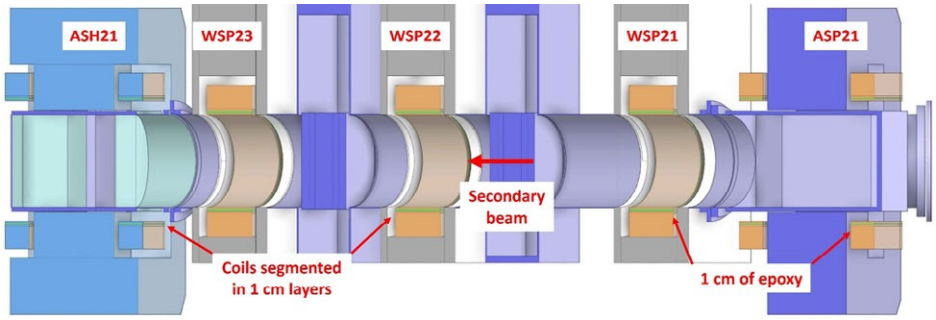

Figure 2.4.26: Layout of magnets in the MuH2 beamline showing the segmentation of coils into copper (brown) and epoxy (green) layers.

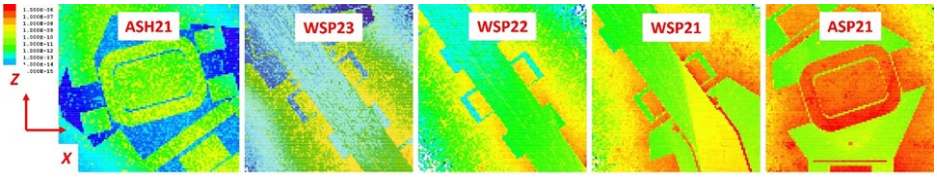

Figure 2.4.27: 2D distribution of deposited energy (MeV/cm^3 per 1 proton on the target) in the 1 cm epoxy layer of the coils (dipoles) and at the beam plane (solenoids) in the MuH2 beamline.

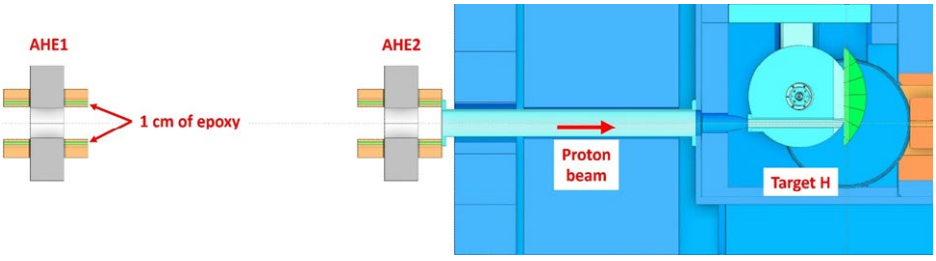

Figure 2.4.28: Two chicane dipole magnets located upstream from Target H with coils segmented in copper (brown) and epoxy (green) layers. Iron shielding of the target block is shown in light blue.

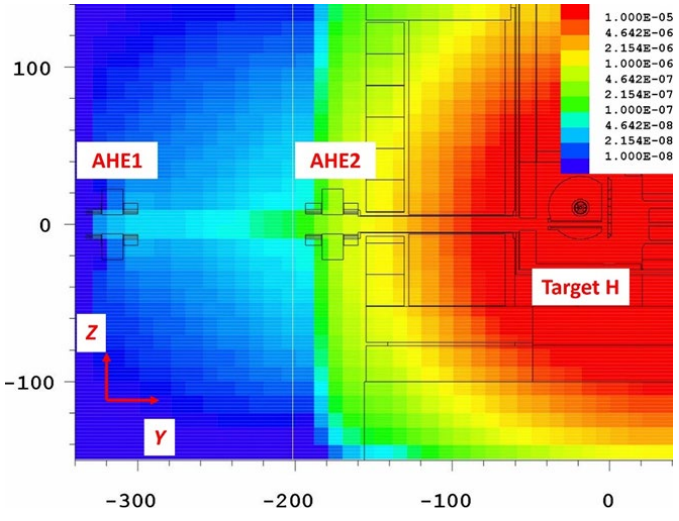

Figure 2.4.29: 2D distribution of deposited energy (MeV/cm^3 per 1 proton on the target) inside and around the Target H block on the vertical beam plane.

per-epoxy-copper sandwich with each layer of 1 cm thickness[2] as shown in Figure 2.4.26.

To capture the maximum of the absorbed dose rate, meshes to score the deposited energy have been placed through the epoxy layer of the dipole coils and at the beam plane for the coils of transport solenoids. Simulated 2D distributions are shown in Figure 2.4.27. The maximal value from the mesh at each magnet is given in Table 15. This Table also gives the time in weeks after which the absorbed dose level will reach the characteristic value of 10 MGy. The results from Table 15 show that in the first dipole magnet ASP21 and in the first transport solenoid the absorbed dose level will exceed this characteristic in less than 2 or 3 years of operation. For the more downstream solenoid magnets and the second dipole the limit will not be reached in 20 years.

2.4.6.3 Magnets in the PK1 beamline

The same model of copper-epoxy-copper sandwich has been applied to estimate the absorbed dose rate in the so-called chicane magnets in the PK1 beamline upstream from Target H, as shown in Figure 2.4.28. These magnets are well protected from the secondary particle flux from the target by iron shielding. Figure 2.4.29 shows the 2D distribution of the energy deposited inside and around the target block. Indeed, in the coils of the chicane magnets the characteristic value of 10 MGy will be reached after more than 20 years of operation as shown in Table 2.4.17.

[2] It should be noted that the thickness of the epoxy does not necessarily reflect the one as built. It was chosen in such a way that sufficient statistics is possible with a reasonable computational effort. The unit Gy normalizes the energy to the volume and removes this dependency.

	Layer	Max, Gy/s w	(10MGy)
ASP21	1st cm	8.08E-01	20
	Epoxy	3.43E-01	48
	2nd cm	6.45E-01	26
WSP21	1st cm	7.96E-01	21
	Epoxy	1.44E-01	115
	2nd cm	3.02E-01	55
WSP22	1st cm	2.21E-02	749
	Epoxy	7.99E-03	2070
	2nd cm	1.70E-02	971
WSP23	1st cm	4.22E-03	3921
	Epoxy	1.34E-03	12357
	2nd cm	3.08E-03	5375
ASH21	1st cm	5.85E-04	28252
	Epoxy	1.99E-04	82976
	2nd cm	5.60E-04	29546

Table 2.4.16: Maximal absorbed dose rate in the coils of magnets in the MuH2 beamline (see Figure 2.4.26).

	Layer	Max, Gy/s w	(10MGy)
AHE1	1st cm	4.31E-02	383
	Epoxy	1.39E-02	1188
	2nd cm	2.95E-02	561
AHE2	1st cm	6.75E-02	245
	Epoxy	1.94E-02	851
	2nd cm	6.62E-02	250

Table 2.4.17: Absorbed dose rate in the coils of PK1 magnets (see Figure 2.4.28).

2.4.7 Activation and remanent gamma dose rate

Target H of HIMB with its primary and secondary beamlines will replace the existing Target M. Operational experience of Target M shows that the components of the primary proton beamline are highly activated, and their handling requires special technique. Also, the service level on the top of the target block hosts equipment that shall be accessible during the regular maintenance. Estimates of the remanent dose rate at the HIMB components due to activation during operation allow for designing the handling tools like an exchange flask and establishing the maintenance procedure.

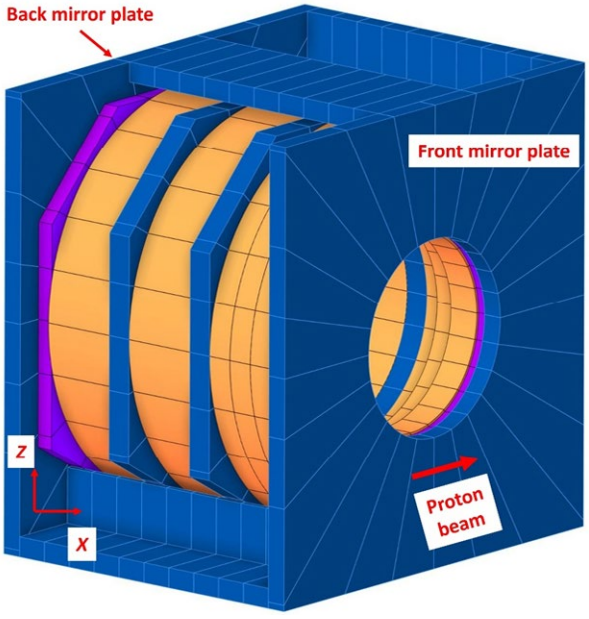

Figure 2.4.30: Model of the capture solenoid (left wall of the yoke removed for presentation reasons): copper coils (orange), aluminum separators (violet) and steel yoke (deep blue).

2.4.7.1 Mirror plates of capture solenoids

For choosing sufficient shielding of the exchange flask containing the capture solenoid, first the activity and second the remanent dose rate after some cooling time has to be calculated. The assembly of the capture solenoid is shown in Figure 2.4.30. To capture the angular distribution of the residual activity, all the elements of the assembly were divided into the 15° segments around the secondary beam axis.

Two-dimensional distributions of the remanent dose rate at the front and back mirror plates of the capture solenoid at the MuH2 beamline after 20 years of operation and 1 month of cooling time are shown in Figure 2.4.31. The maximal dose rate of 38 Sv/h is reached on the front mirror plate on the side of the plate that is downstream from the target. On the back mirror plate the maximal dose rate is factor 50 lower and is equal to 0.82 Sv/h.

2.4.7.2 Vacuum chamber of the MuH2 beamline

The MuH2 vacuum chamber[3] is located downstream from the dipole ASP21 after the first bend of the beam where the radiation environment becomes moderate compared to the Target H region. The fluence of the secondary particle that produces activation decreases by orders of magnitude along the 4.3 m length of the chamber. Different sections of the vacuum chamber will be characterized by the strongly varying remanent dose rate and will require different handling conditions.

[3] This version contains both chambers MuH2.1 and MuH2.2 combined in one.

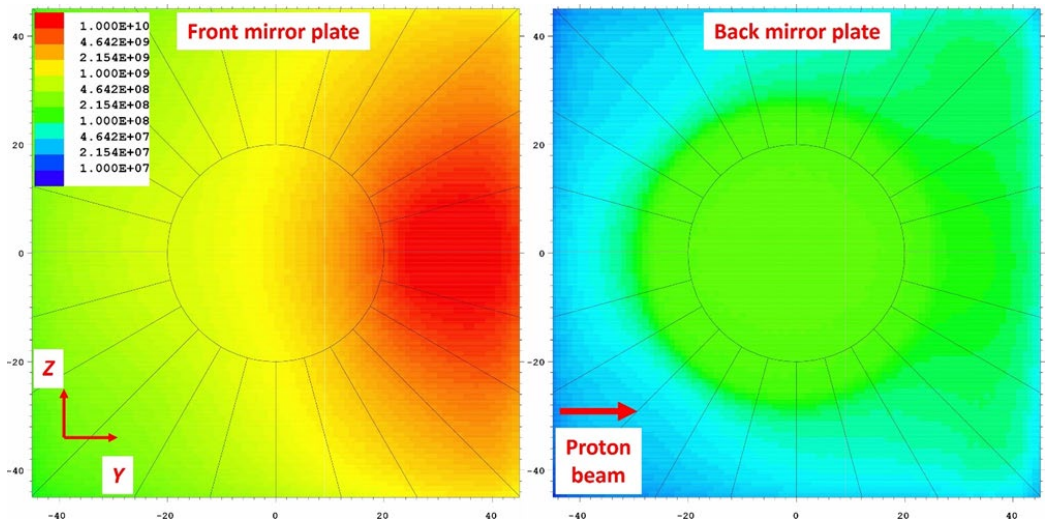

Figure 2.4.31: Remanent gamma dose rate (pSv/s) at the front and back mirror plates of the capture solenoid.

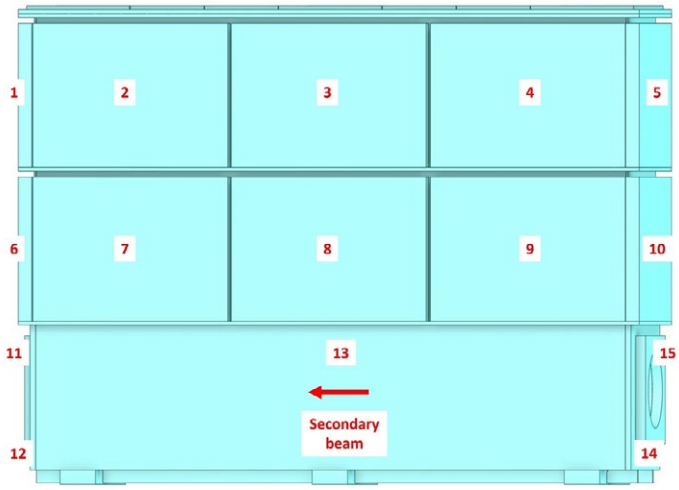

Figure 2.4.32: Parts of the different sections of the MuH2 vacuum chamber.

Part	mSv/h	Part	mSv/h	Part	mSv/h
1	0.1	6	0.6	11	2.4
2	0.1	7	1.2	12	2.2
3	0.0	8	4.7	13	42
4	2.8	9	48	14	360
5	66	10	176	15	470

Table 2.4.18: Contact remanent dose rate for the part of the MuH2 vacuum chamber.

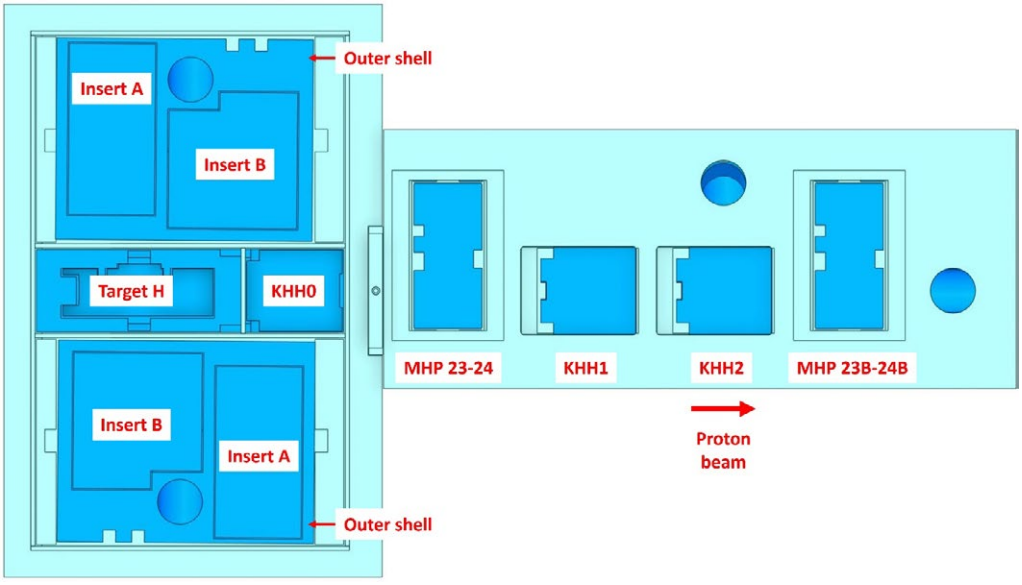

Figure 2.4.33: Inserts of the beamline components in the vacuum chambers at Target H and along the PK2 proton channel (top lids are removed for presentation reasons).

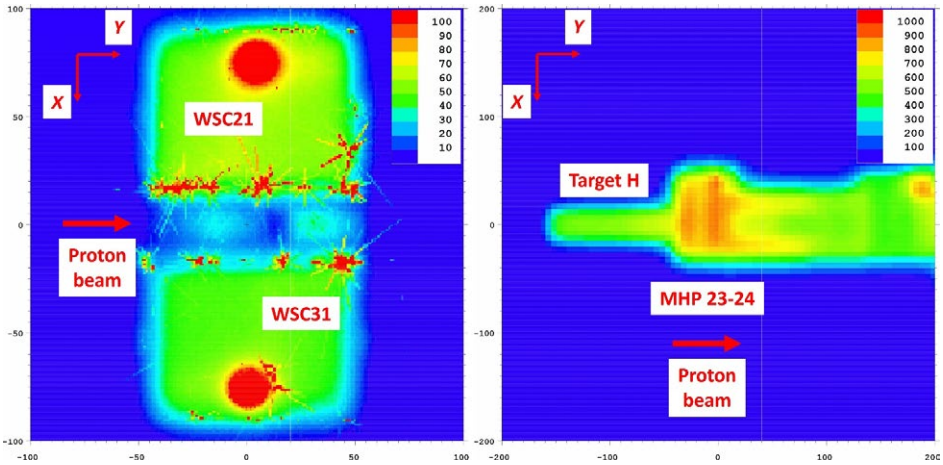

Figure 2.4.34: Remanent dose rate (μSv/h) on the service platform after the activation of capture solenoids and their inserts (left) and inserts of Target H and beamline components of the PK2 proton channel (right, note that the scale is different).

The activation was simulated for the parts of the vacuum chamber that are shown in Figure 2.4.32. The estimated contact remanent dose rate after 20 years of operation and 1 month cooling time is given in Table 2.4.18. Indeed, the variation of the remanent dose rate is more than one order of magnitude, ranging from 100 μSv/h to nearly 0.5 Sv/h, comparing both parts on the top and on the bottom of the chamber, and sections close to the first dipole ASP21 and to the second dipole ASH21.

2.4.7.3 Service platform at the target block

The top of the target block serves as the platform for the service of the beam equipment for the components that are inserted at the beamline through the vertical shafts in the vacuum chambers of Target H and PK2 proton channel as shown in Figure 2.4.33. Inserts A and B together with the shell that surrounds them shield the capture solenoids on both sides of the target. Remanent dose rate on the top of these inserts after 20 years of operation and 1 day of cooling is shown in Figure 2.4.34, left side. As seen from Figure 2.4.34, the remanent dose rate on the service platform above the inserts of the capture solenoids does not exceed 100 μSv/h except the area of the circular openings for the vacuum pumps where the dose rate might reach 1 mSv/h after removal of the pumps.

Beamline components in the vacuum chamber along the proton channel PK2 will be removed together with their inserts. Remanent dose rate on the service platform above the proton channel is estimated also for 20 years of operation and 1 day cooling and is shown in Figure 2.4.34, right side. As seen from Figure 2.4.34 the remanent dose rate above the proton channel reaches the maximal value of 1 mSv/h at the insert of the beam monitor MHP 23-24.

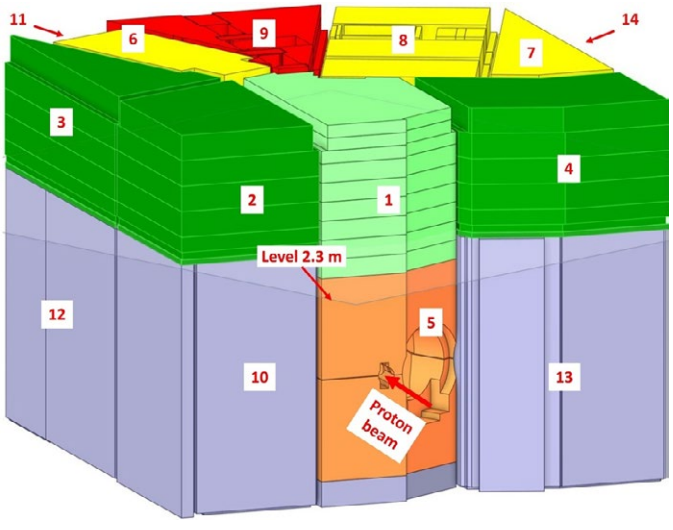

Figure 2.4.35: Parts of the Target M shielding block colored according to the stage of dismantling: part 1 (light green), parts 2, 3 and 4 (deep green), part 5 (orange), parts 6, 7 and 8 (yellow), and part 9 (red). Parts 11 and 14 are not seen as they are beneath parts 6 and 7, accordingly.

2.4.7.4 Target M

Prior to installing Target H, the existing Target M shall be dismantled from the PK2 proton channel. First, target, collimator, and profile scanner inserts will be removed by shielded exchanged flasks. Then, the 14 blocks forming the shielding of the target station M and partly consisting of individual iron plates connected together, are removed in the order shown in Figure 2.4.35. The parts of the shielding will be removed from the target block one after another, partly by remote handling (see Chapter 4.4). To reduce the cost of the IMPACT shielding, the parts of the Target M block that will be less activated will be reused for the shielding of the MuH2 beamline. Highly activated parts will be disposed. The height of the magnet trolleys of the secondary beamlines of 2.3 m is considered as a reasonable estimate of the level that separates the parts of these two categories.

During dismantling, the remanent dose rate in the working area above the Target M shielding block will vary depending on which part will be exposed to the sight. To allow for the planning of dismantling, the remanent dose rate from the individual parts of the shielding block has been calculated using the real beam current profile during the Target M operation

Part	Top d, mSv/h	Max d, mSv/h
1	0.7	35
2	0.4	8.7
3	0.5	9.9
4	0.2	3.4
5	184	1722
6	1.0	29
7	0.2	2.4
8	1.2	492
9	0.6	1296
10	22	83
11	57	1241
12	20	119
13	3.1	46
14	7.1	10

Table 2.4.19: Remanent dose rates on top and the maximal dose rate for each part of the Target M shielding block (see Figure 2.4.35).

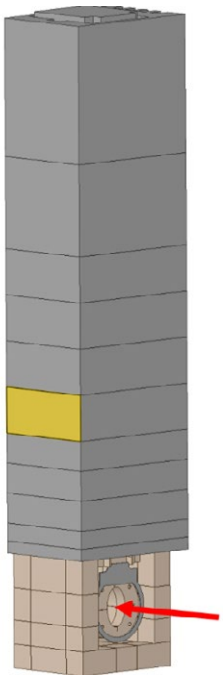

Figure 2.4.36: 3D rendering of the CAD geometry used to compute the activation of the KHE2 local shielding. The proton beam imparting on the collimator is indicated by the red arrow.

since 1974 till the shutdown followed by 90 days of cooling time. The dose rate on top of each part is given in Table 2.4.19. At the start of dismantling with all parts in place, the dose rate is expected on the level of 1 mSv/h. When the top surface of the part 5 will be revealed, the dose rate will reach nearly 200 mSv/h. When the level at 2.3 m will be cleaned, the dose rate is defined by parts 5 and 10–14 till the most highly activated remaining part 9 is completely unshielded.

Parts 1–4 and 6–7 are considered for reusing in the shielding and are placed in specially manufactured containers with sufficient shielding to be handled by personnel. For the design of the containers, Table 2.4.19 provides the maximal dose rate considering all faces of the Target M shielding parts.

2.4.8 HIMB exchange flask

The suitability of the HIMB exchange flask shielding was computationally verified using two activated source objects: the KHE2 collimator local shielding and the HIMB capture solenoid.

The remnant dose rate of both objects was calculated using a multi-step computational approach. In both activation simulations, a fixed proton source was used.

Starting from this proton source, MCNP–extended with the RNUCS patch [13] computed the residual nuclide production rates caused by fast neutrons (E > 20 MeV) and all other particles, along with the low-energy fluxes (E < 20 MeV). This information, together with the operational history, was then passed to the SP-FISPACT code, which is included in the AARE package, to determine the nuclide inventory and the corresponding gamma source.

The activated components were subsequently placed inside the HIMB exchange flask, and a follow-up gamma source calculation was performed. The objective of this step was to calculate the contact dose rate and the dose rate at a 1-meter distance, which should not exceed 2 mSv/h and 0.1 mSv/h, respectively. To improve the variance of the Monte Carlo calculation, the shielding geometry was divided into multiple layers, and the Geometry Splitting variance reduction technique [1] was applied.

The underlying CAD geometries were simplified, cleaned, and subdivided to prevent averaging the gamma sources over coarsely sized volumes. The resulting CAD structures were then converted into MCNP 6.2 models using the GEOUNED code [8].

2.4.8.1 The local shielding of the KHE collimator as the gamma radiation source

Defining the proton source for the collimator was a rather laborious task. First, the phase space of the proton beam at the surface of the collimator was calculated using the beam dynamics code *TURTLE* [14]. The TURTLE output was then converted into an MCNP6.2-readable format via a custom source subroutine. This step was necessary because, due to the use of implicit capture in TURTLE, not all initial proton weights are equal to one. These non-unity initial proton weights cannot be provided through the standard source definition of MCNP6.2.

Implicit capture is a standard Monte Carlo variance reduction technique, where capture events are treated by scattering with a modified weight. When implicit capture is used rather than sampling for absorption with probability $\frac{\sigma_a}{\sigma_t}$, the

particle always survives the collision and is followed with new weight, $w\left(1-\frac{\sigma_a}{\sigma_t}\right)$. Here σ_a and σ_t are the absorption and total cross sections respectively [1].

To assess the effect of the initial source size and the associated source correlations, sources with an increasing number of particles were used to compute the energy deposition in the collimator. Ultimately, it was decided to utilize 70 million source particles provided by TURTLE [14]. It was observed that using at least 30 million particles mitigates the propagation of source correlations caused by under-sampling. These source size effects could be inferred from the statistical checks of the power deposition tally.

The opening of the collimator was approximated by an elliptical cylinder with a cross section

$$\left(\frac{x}{3.1}\right)^2+\left(\frac{y}{5}\right)^2=1,$$

where the dimension of the semi-minor/semi-major axes is centimeters. The CAD geometry used for computing the activation of the KHE2 local shielding is shown in Figure 2.4.36. The high-energy protons from the source strike parts of the collimator, depositing energy and releasing secondary particles.

Using these model assumptions, the total power deposited on the KHE2 collimator was estimated to be 93.5 kW at 2.2 mA on Target E or 1.92 mA on KHE2. The corresponding gamma source of the local shielding was scaled by the ratio of the measured power deposition on KHE to the calculated one: (98.1 kW)/(93.5 kW).

The activation of the shielding is mainly due to neutrons released during the evaporation stage of the nuclear cascade. The local shielding lies outside the line of sight of the forward-peaked high-energy neutrons.

The nuclide inventory of KHE2 was computed assuming 20 years of irradiation at 1.28 mA, followed by a cooling time of 45 days. For this purpose, the AARE package was used. The beam current of 1.28 mA was derived from the following considerations: HIPA operates 8 months per year, and 87.3% of the initial 2.2 mA reaches KHE2.

2.4.8.2 The local shielding of the BHE1 beamdump as the gamma radiation source

In addition to the local shielding of KHE2, the dose rate of BHE1 local shielding was also computed. For this case, the operational history of the beamdump, first part, BHE1 from 2011 to 2017 was considered, followed by a cooling time of 1 week.

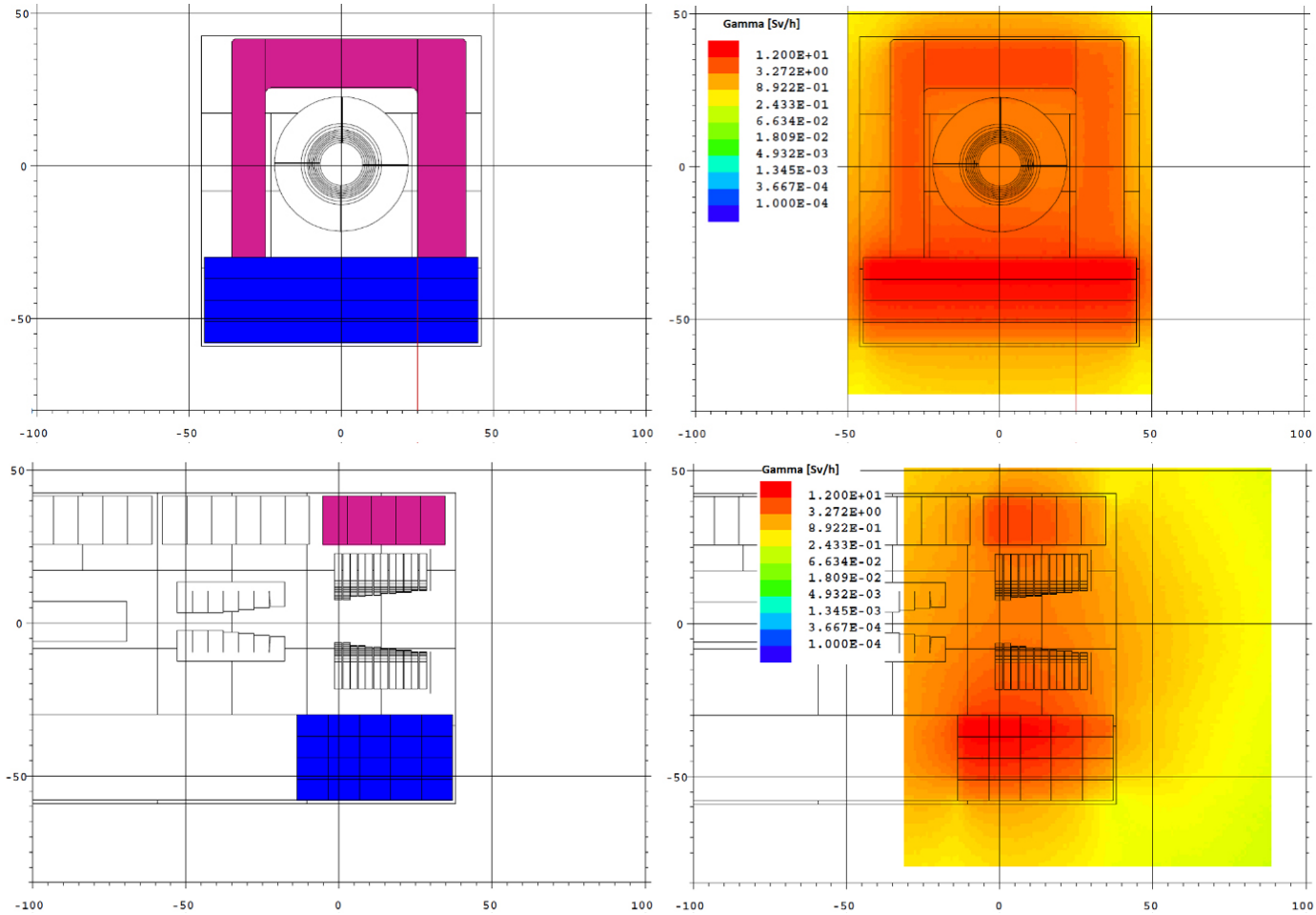

Figure 2.4.37: Remnant gamma dose rate of the BHE1 local shielding. Frontal view (upper row pair) and top view (lower row pair). Each pair of plots shows the computational geometry on the left-hand side (LHS) and the corresponding dose rate map on the right-hand side (RHS).

The proton beam parameters at the surface of the BHE1 were derived using the TURTLE code and provided to MCNP6.2 via a source subroutine.

The purpose of computing the nuclide inventories of both BHE1 and KHE2 local shieldings was to determine which of the two produces a higher remnant gamma dose rate, and to use the more conservative case for verifying the shielding concept of the exchange flask. The resulting dose rate maps are shown in Figure 2.4.37 and Figure 2.4.38. These plots show that, the KHE2 local shielding exhibits dose rates more than four times higher than those of BHE1. Please note that the upper scale limit of the color plot in Figure 2.4.37 is 12 Sv/h, whereas in Figure 2.4.38 it is 40 Sv/h.

Based on the results, it was decided to use the local shielding of KHE2 along with the HIMB capture solenoid for validating the exchange flask design.

Objects other than the local shielding of the BHE1 and the local shielding of KHE2 were replaced with air-filled dummies, since these are not relevant for the exchange flask shielding design.

The next step, after identifying KHE2 as the object with the higher remnant dose rate, was to place it inside the shielding of the exchange flask and verify that the contact (surface) dose rate and the dose rate at 1 meter distance do not exceed 2 mSv/h and 0.1 mSv/h, respectively.

To visualize this effectively, the dose rate scale limits were set to these threshold values. The resulting dose rate maps are shown in Figure 2.4.39.

The dose rate map shows regions where the values are larger than 0.1 mSv/h, however, below the contact dose rate limit of 2 mSv/h. At a distance of one meter from the surface the values of the dose rate are less than 0.1 mSv/h.

2.4.8.3 The HIMB capture solenoid as the gamma radiation source

The dose rate calculation presented in this section uses the HIMB capture solenoid as the source of gamma radiation. The initial proton source was modeled as a pencil beam incident

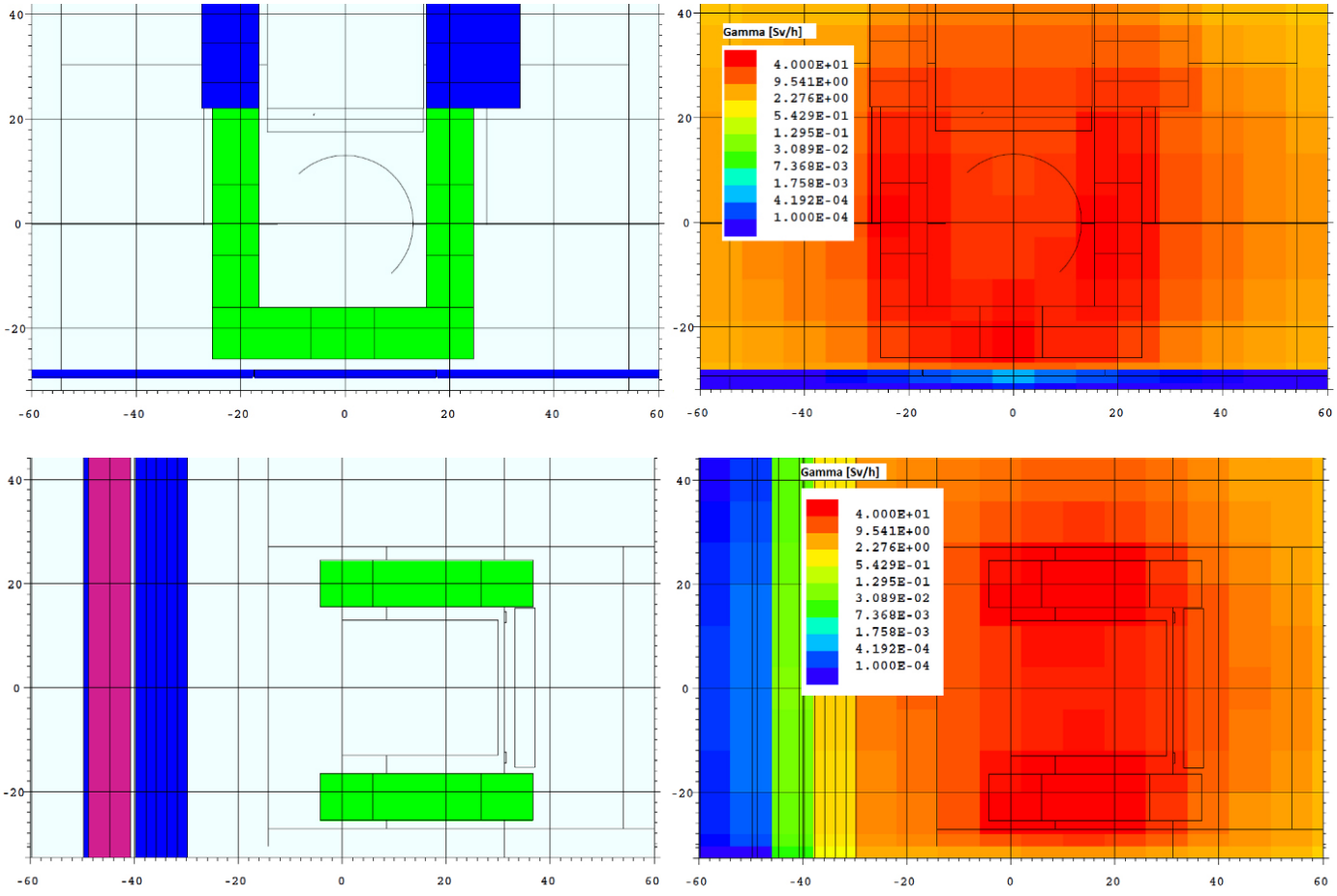

Figure 2.4.38: Remnant gamma dose rate of the KHE2 local shielding. Frontal view (upper row pair) and top view (lower row pair). Each pair of plots shows the computational geometry on the left-hand side (LHS) and the corresponding dose rate map on the right-hand side (RHS).

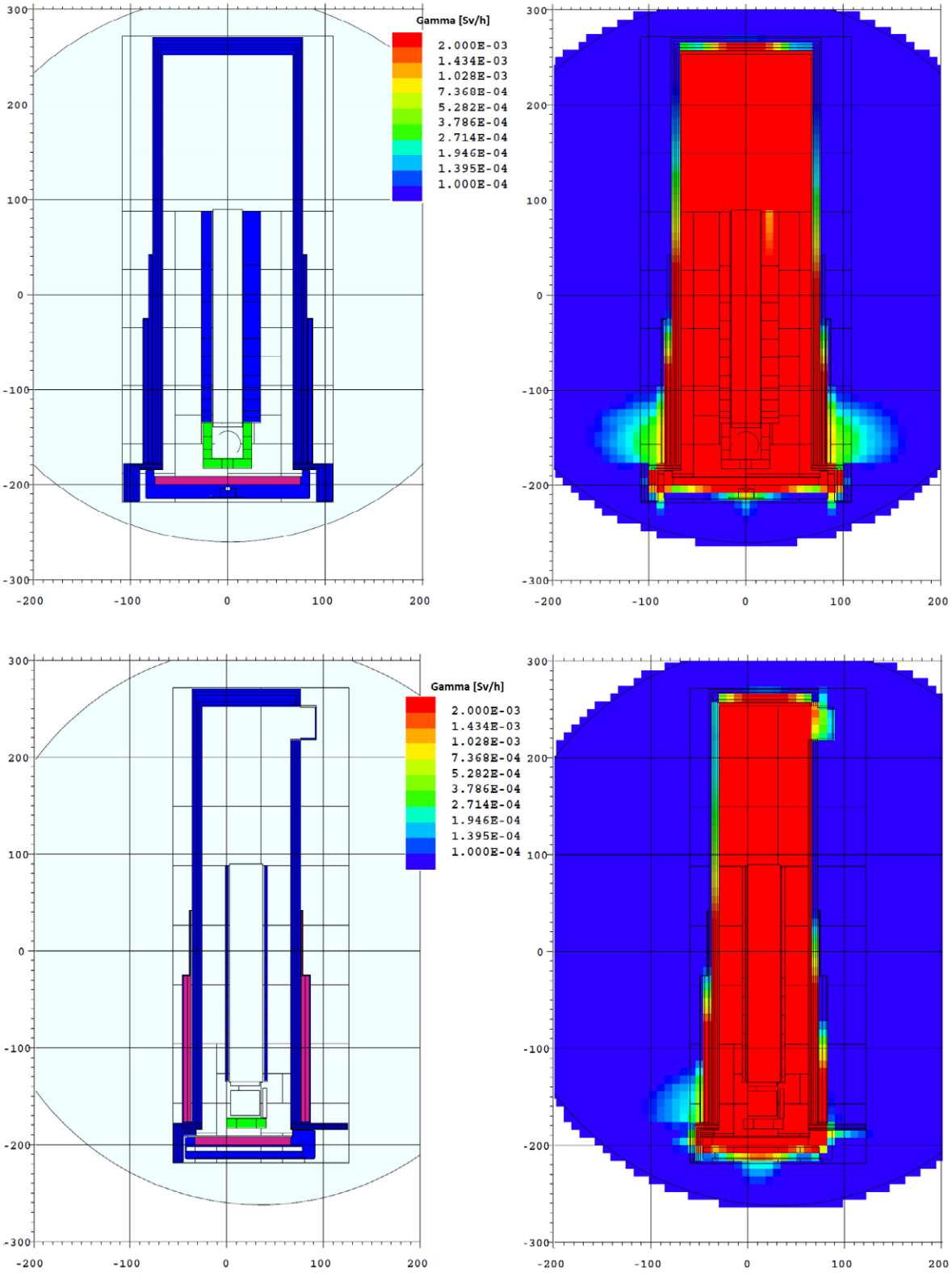

Figure 2.4.39: Dose rate of the KHE2 local shielding placed inside the HIMB exchange flask. Each pair of plots shows the computational geometry (left-hand side, LHS) and the corresponding dose rate map (right-hand side, RHS). The top and bottom pairs of plots represent the front and side views of the geometry, respectively. The dose rate scale limits were set to 0.1 mSv/h and 2 mSv/h.

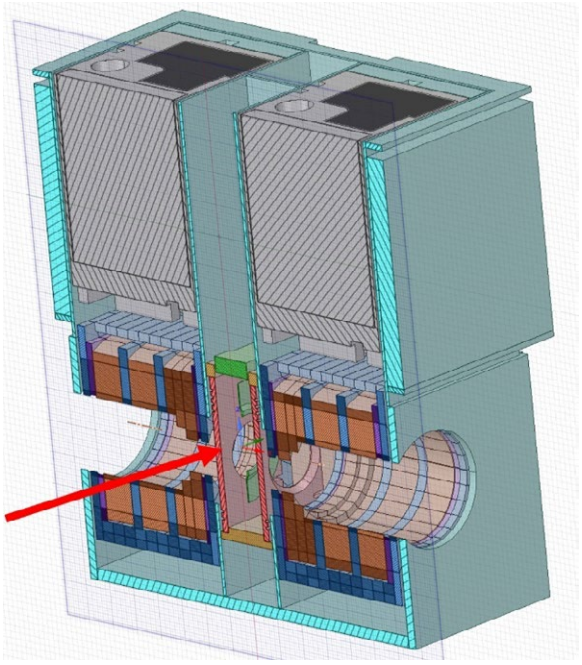

Figure 2.4.40: 3D rendering of the geometry used to compute the activation of the HIMB capture solenoid. The proton beam imparting on the target wheel is indicated by a red arrow.

on the graphite target wheel. To account for the effects of scattered particles, parts of the surrounding structure – including the twin solenoid – were included in the simulation. A 3D rendering of the computational geometry is shown in Figure 2.4.40.

To avoid averaging the activation products over a coarse structure, the HIMB capture solenoid was divided into several smaller sub-volumes. The gamma source of each sub-volume was computed individually and used in the final shielding calculation.

For the operational history, an irradiation period of 20 years with a proton current of 2 mA was assumed. A decay time of 30 days was considered for the decay gamma calculation.

The resulting radiation field within the exchange flask is shown in Figure 2.4.41. The maximum dose rate of about 16.5 Sv/h induced by the capture solenoid supports the assumption that the KHE2 shielding generates a more intense radiation field than both the capture solenoid itself and the local shielding of BHE1.The resulting radiation field outside the exchange flask is shown in Figure 2.4.42. Based on these plots the dose rate outside of the exchange flask is 0.1 mSv/h or less.

2.4.9 References

[1] Pelowitz, D. B. MCNP6 *User's Manual Version 1.0*. LA-CP-13-00634. 2013. LANL. Los Alamos, United States.

[2] Brown, D. A. et al. *ENDF/B-VIII.0: The 8th Major Release of the Nuclear Reaction Data Library with CIELO-project Cross Sections, New Standards and Thermal Scattering Data*. Nuclear Data Sheets 148 (2018). Special Issue on Nuclear Reaction Data, pp. 1–142. 2018.

[3] Petrovic, *C. SP-FISPACT-2001: A computer code for activation and decay calculations for intermediate energies. A connection of FISPACT with MCNPX*. ENEA-RT/ERG, 2001.

[4] Forrest, R. A. *FISPACT-2007: User manual*. Technical Report UKAEA FUS 534. EURATOM/ UKAEA Fusion Association. Abington, UK. 2007.

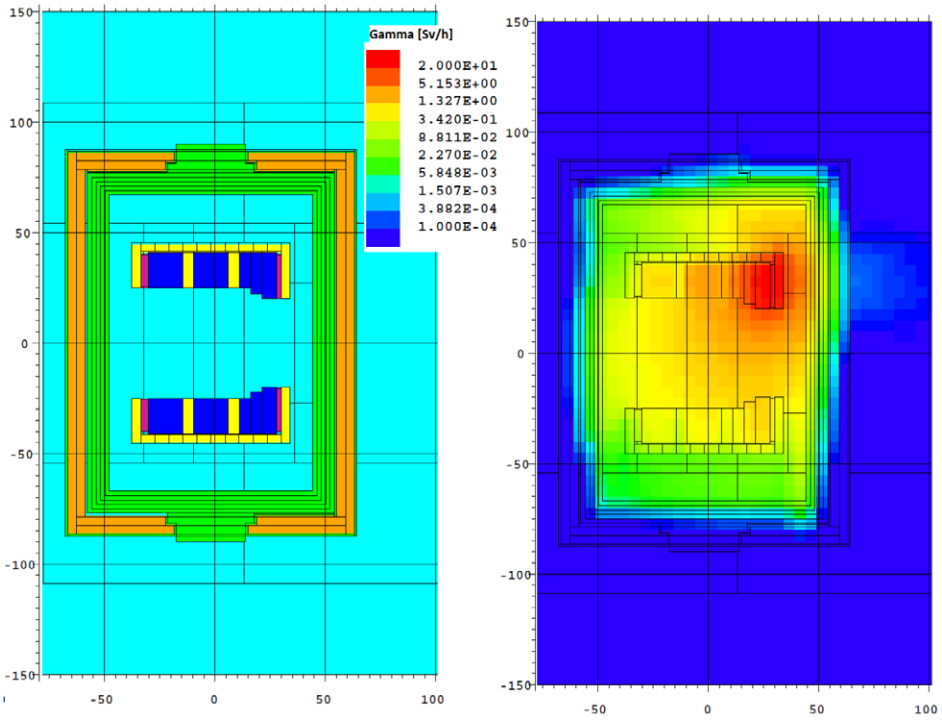

Figure 2.4.41: Top view of the capture solenoid placed within the exchange flask. In this case the upper limit of the dose rate is set to 20 Sv/h to resolve the internal to the exchange flask radiation map. The LHS shows the computational geometry and the RHS shows the gamma dose rate map.

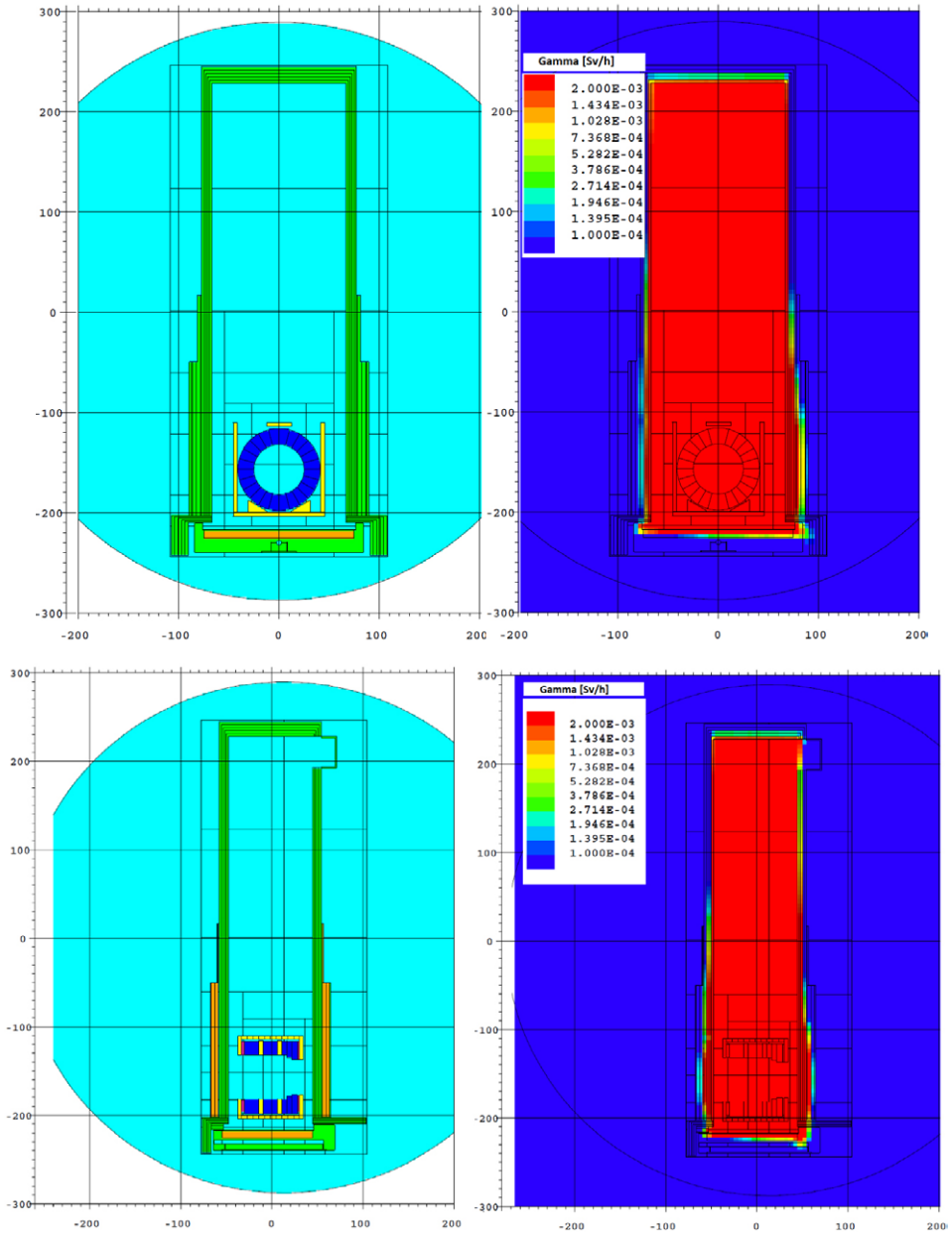

Figure 2.4.42: Dose rate of the capture solenoid, placed within the HIMB exchange flask. Each pair of plots shows the computational geometry (LHS) and the corresponding dose rate map (RHS). The top and bottom pair of plots show front and side views of the geometry respectively. The dose rate limits were set to 0.1 and 2 mSv/h.

[5] Gallmeier, F. X. et al. *An environment using nuclear inventory codes in combination with the radiation transport code MCNPX for accelerator activation problems*. Proc. of the 8th Int. Topical Meeting on Nuclear Applications and Utilization of Accelerators (AccApp'07), Pocatello, USA, July 29–August 2, 2007, pp. 207–211.

[6] Sublet, J.-Ch. et al. *The European Activation File: EAF-2010 neutron-induced cross section library*. CCFE-R (10) 05. CCFE. Culham, UK. 2010.

[7] Wu, Y. *Multi-functional Neutronics Calculation Methodology and Program for Nuclear Design and Radiation Safety Evaluation*. Fusion Science and Technology 74 (2018), pp. 321–329.

[8] Catalán, J. P. et al. *GEOUNED: A new conversion tool from CAD to Monte Carlo geometry*. Nuclear Engineering and Technology (2024), pp. 1738–5733. 2024.

[9] Mosher, S.W. et al. *ADVANTG – An Automated Variance Reduction Parameter Generator*. ORNL/TM-2013/416 Rev. 1. ORNL, United States. 2015.

[10] Chan, H.-W. *PSI internal report TM-81-25-xx*. Paul Scherrer Institut, Villigen, Switzerland. 2025.

[11] *SμS – Swiss Muon Source*. μE1 beam line. [Online] https://www.psi.ch/en/smus/e1.

[12] Kiselev, D. *Absorbierte Energie in Gray für Epoxy-Glas im QTH51*. PSI Memorandum (unpublished). 2012.

[13] Gallmeier, F.X and Wohlmuther, M. *AARE_ACTIVATION Script Version 2.0 User Guide*. https://info.ornl.gov/sites/publications/Files/Pub118703.pdf. 2018.

[14] Rohrer, U. *Graphic Transport/Turtle Framework*. http://aea.web.psi.ch/Urs_Rohrer/MyWeb

[15] ANSYS, Inc. *Ansys SpaceClaim*. [Online] https://www.ansys.com/products/3d-design/ansys-spaceclaim.

3. Technical Design and Simulations

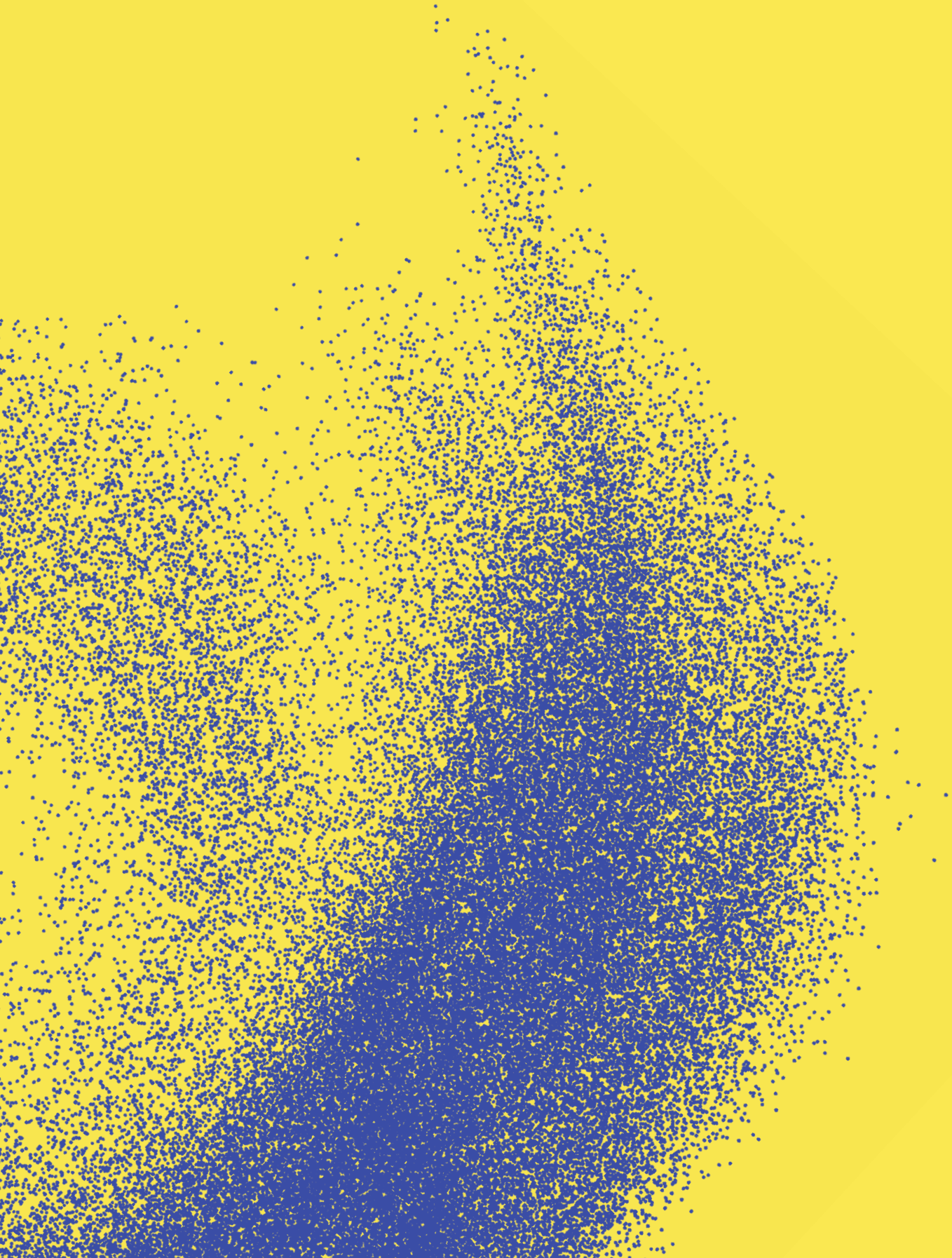

3.1 Target Station H

3.1.1 General Considerations

The development of the new Target Station H is based, wherever possible, on the experience gathered with the 40 mm thick TgE. However, the design of the TgH station is largely constrained by the requirement that the distance between the beam-target interaction point and the upstream end of the capture solenoid magnet of either secondary beam line is set to 250 mm. This ensures a maximum muon capture and transmission towards the experimental areas. For this reason, the TgH vacuum chamber hosts not only the TgH and the KHH0 collimator inserts but also the two capture solenoids. The target geometry employs the "slanted" type successfully adopted since 2019 for TgE [1]. However, with an effective thickness of 20 mm graphite (instead of 40 mm for TgE), the adoption of the slanted concept results in a physical target thickness of only 3.5 mm. Moreover, the maximization of the surface muon production is achieved also through the "extension" of the radial length of the rim tile to the remarkable value of 100 mm.

Strictly speaking, the target station is composed of the target insert, the local shielding, and the collimator KHH0. However, in this chapter, the collimators KHH1/2, belonging to the proton channel 2 (PK2), and the mirror plate of the capture solenoid will be considered as well.

Location	Quantity	Description
1	2	Capture solenoid magnets inserts
2	1	Target H insert
3	1	Local target H shielding
4	3	Copper collimator, KHH0, KHH1, KHH2
5	2	Metal inflatable seal (= pillow seal)
6	2	Beam monitors

Table 3.1.1: List of target station and PK2 inserts.

Figure 3.1.1 and Figure 3.1.2 show a complete overview of the target and PK2 region with and without vacuum chambers.

All inserts are listed in Table 3.1.1.

3.1.1.1 Heat Load

For the components in Table 3.1.2, BDSIM [2] Monte Carlo simulations were performed to assess the power deposition coming from the proton beam as well as from scattered particles. The power depositions for the collimators were checked by MCNP simulations [3]. In addition, the power deposition

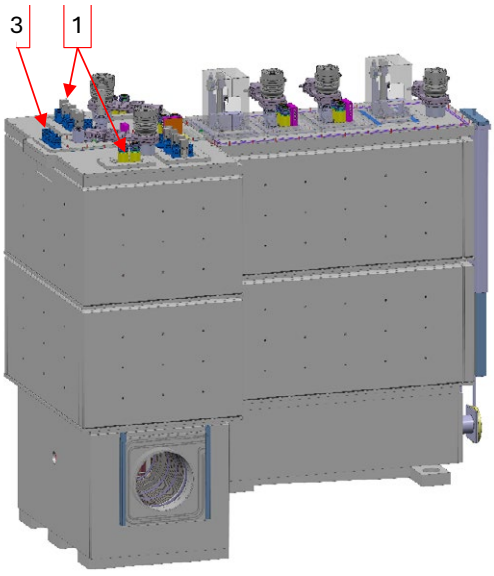

Figure 3.1.1: Target station H and PK2 vacuum chambers.

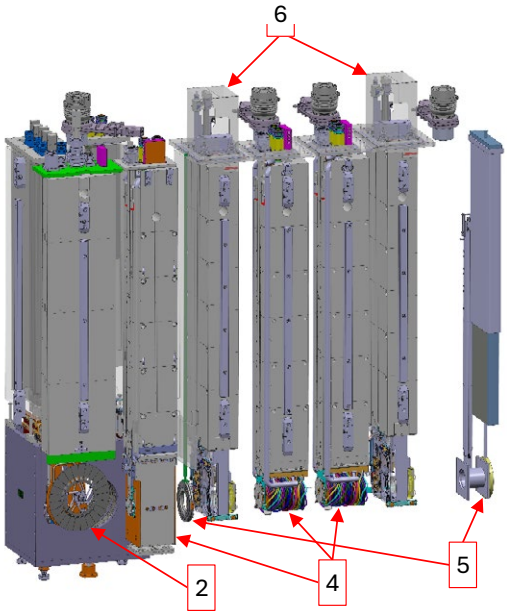

Figure 3.1.2: Target station H and PK2 inserts.

Component	Power deposited by the proton beam and the secondary particles [kW]	Power from the radiating target H [kW]	Total [kW]
Target H	32	–	32
Local Shielding	5	17.5	22.5
Target insert	0.2	6.2	6.4
KHH0	58	0.2	58.2
KHH1	18.2	–	18.2
KHH2	1.7	–	1.7
Mirror plates MuH3	3	0.5	3.5

Table 3.1.2: Summary of heat loads on the components of the target H station for 3 mA proton current.

coming from heat radiated off the target wheel must be considered. All values are summarized in Table 3.1.2.

The power deposition coming from scattered protons and secondary particles produced at the impact point of beam and target is concentrated in forward direction (see Figure 3.1.3).

The detailed power density distributions are presented later in the document for each component. The power deposited by the proton beam on the target wheel has been also calculated adopting the analytical model shown in Chapter 3.1.2.1.3.

3.1.2 Target Insert

Figure 3.1.4 and Figure 3.1.5 show, respectively, the left and the right sides (with respect to the proton beam direction) of the 3D model of the full TgH insert. In Figure 3.1.6, the TgE Insert is shown for comparison. The TgH steel shielding block is divided into four parts. This makes the insert more versatile since, in case of failure of any components, one does not need to dispose of the whole shielding block but only the lower part. Moreover, during disposal, the insert can be easily divided into smaller parts without cutting it. The shielding is equipped with the same guide rails as the TgE insert. This allows to handle the TgH insert by means of the TgE exchange flask.

The bottom part of the target insert is displayed in Figure 3.1.7. The target insert features a back plate behind the graphite wheel (orange in Figure 3.1.5) and a plate above the wheel attached to the steel shielding, the so-called cooling plate (green in Figure 3.1.4). Both plates are made out of copper and function as heat shield, designed to protect the bearings and the surrounding elements from the heat radiated off the target wheel, the four-segment aperture foil (in purple e.g. Figure 3.1.5), the protection collimator, the wires from the various di-

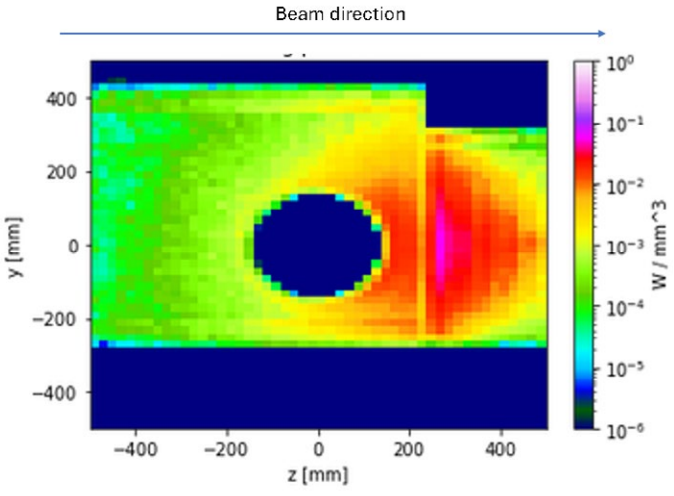

Figure 3.1.3: View of the power deposition in the target H station. On the left, the local shielding with its openings toward the muon beamlines and on the right, the collimator KHH0.

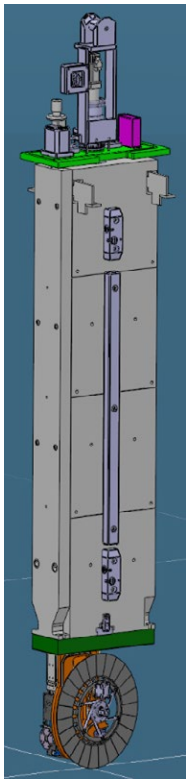

Figure 3.1.4: TgH insert, left side view.

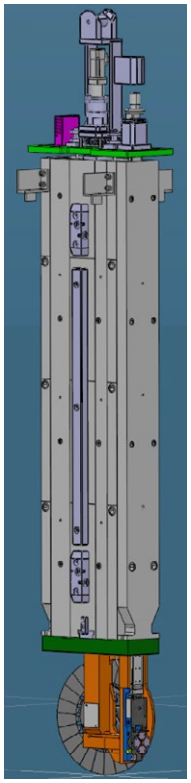

Figure 3.1.5: TgH Insert, right side view.

Figure 3.1.6: TgE Insert.

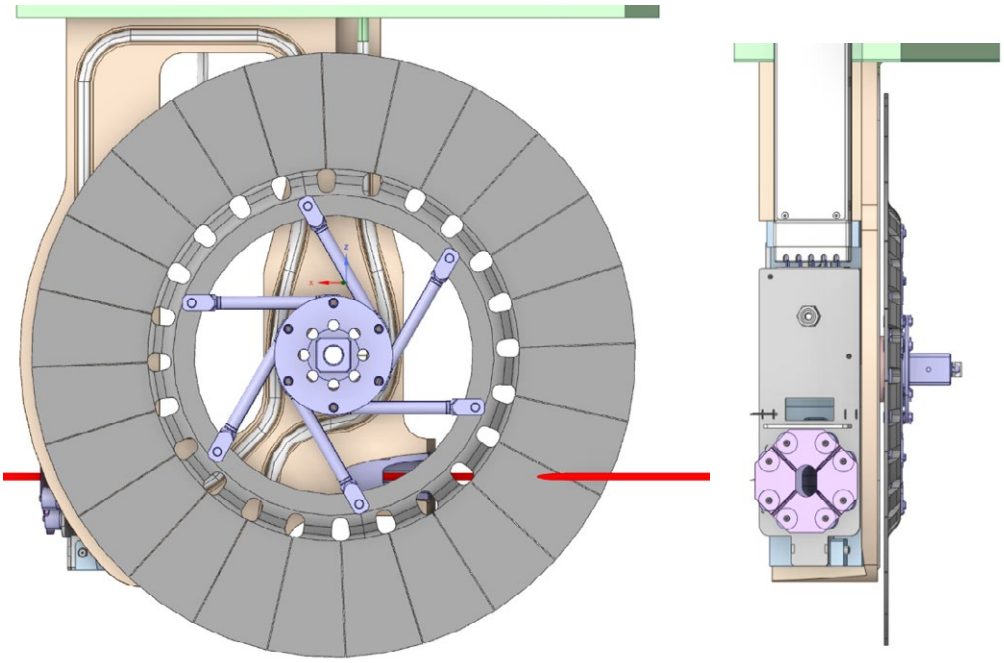

Figure 3.1.7: Side view (left) and back view (right) of the target insert. The red line represents the proton beam path.

agnostics (aperture foil, protection collimator, temperature sensors) and their guiding rail. The parts made from copper are coated with a high-emissivity layer, Al_2O_3-TiO_2 [4] to absorb the heat effectively. This coating already in use at Target E was experimentally compared to a sprayed chrome oxide coating. Both showed high emissivity (ε≈0.8) at the expected operating temperatures (50–250°C), but chrome oxide offered no significant performance advantage, leading to the decision to continue using the existing Al_2O_3-TiO_2 coating. The tests were performed in air and further investigation is on-going in vacuum environment.

Due to the confined space within the target station, a 5 mm gap separates the target rim from the heat shield (see the right side of Figure 3.1.7). The study of the deformation of the target toward the heat shield will be presented later in the document.

Contrary to TgE, the TgH insert is equipped with a diagnostic aperture foil (Figure 3.1.8 and Figure 3.1.9). The foil is composed by four segments, top, bottom, right and left. Each segment collects a signal proportional to the beam displacement (with respect to the ideal beam axis) in the direction of the segment itself. More details about the aperture foil are given in Chapter 3.4.2. The signal wires are mounted on a rail. In the event of a damaged contact or a broken wire, only the rail needs to be replaced. This can be done using the existing exchange flask “drive shaft”.

A Densimet protection collimator is located behind the aperture foil (Figure 3.1.10). It protects the target back plate behind the wheel in the event of a misaligned beam. Information about the collected electric charge and the collimator temperature will be collected in form of signals and made available to the machine protection system, such that a beam interlock is triggered if the reference thresholds are exceeded.

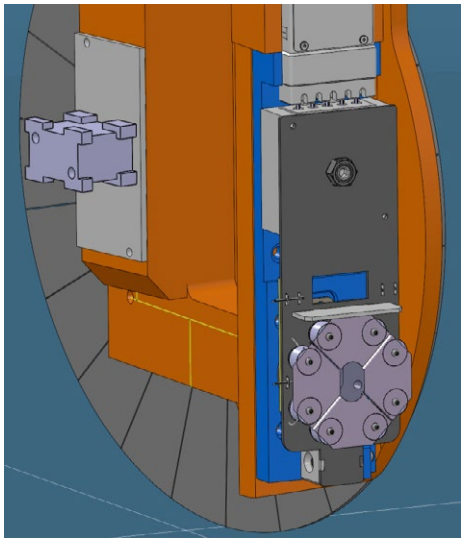

Figure 3.1.8: 4-segment aperture foil.

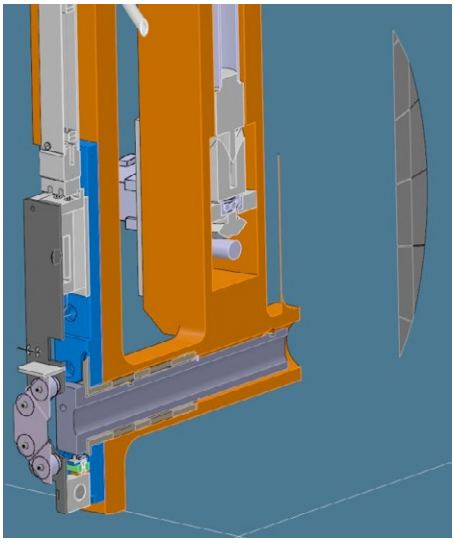

Figure 3.1.9: Cut through the Densimet collimator.

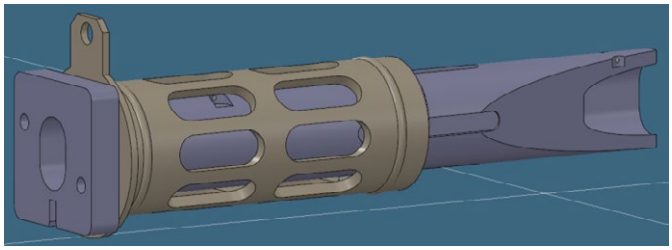

Figure 3.1.10: Densimet® collimator with stainless steel cage. Small spacers made of Al2O3 are located between the collimator and the cage.

3.1.2.1 Target Wheel

Of the two shortlisted target versions in the CDR, V2 (Figure 3.1.11) and V6, version V2 was preferred for Target H [3]. This version comprised two disks and was initially designed to minimize the width of the slits, as the cutting tool dictates a minimum slit size based on its thickness. However, the approach was abandoned for two main reasons:

1. Reducing the slit size below 1 mm would not significantly improve surface muon production.
2. Two-disk designs have thinner bases than single-disk designs, compromising the target's stiffness.

Other factors considered included the orientation of slits and the number of tiles. Given that the impact point is already angled at 30° from the horizontal plane, slanted slits were unnecessary. Additionally, studies were conducted to determine the optimal number of tiles, with findings favoring an increased count to reduce the stresses. This study will be presented later in this document. These considerations lead to the development of three new target versions, called V7, V8 and V9 featuring 12, 18 and 24 tiles respectively (Figure 3.1.12).

Finally, the shape of the hole at the base of the slit of the 24 tiles (version V9) was investigated. A drilled hole version was compared with the cut-out version (Figure 3.1.13) and results are presented later in this chapter.

3.1.2.1.1 Final Design

After accurate evaluation of all simulation results (reported later in this document), the target wheel version V9-cut-out was selected for production. The TgH wheel V9-cut-out is manufactured from a single piece of graphite and includes three primary features:

1. *Beam-interaction tiles:* The 24 tiles interact directly with the proton beam and are separated by 1 mm slits.
2. *Base cut-outs:* Each slit base has a cut-out hole to prevent crack formation. These holes are manufactured with rounded edges to minimize stress concentrations.
3. *Inner ring and spoke assembly:* The inner ring is secured to six spokes made from Inconel 600 (a nickel-chromium-iron alloy), using graphite pins as stable connections that thermally expand with the target.

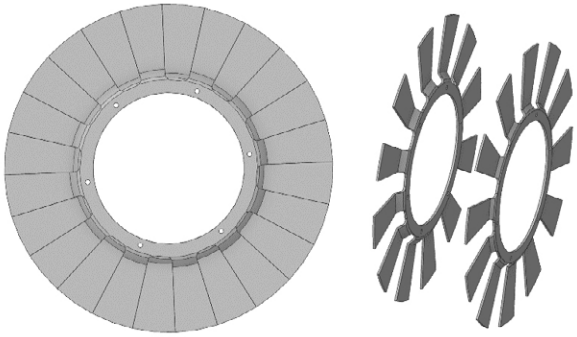

Figure 3.1.11: TgH V2 Model - CDR preferred version.

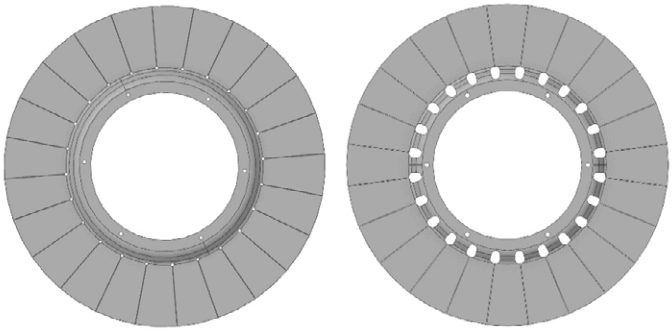

Figure 3.1.13: Models of the V9-drilled (left) and V9-cut-out (right) hole versions.

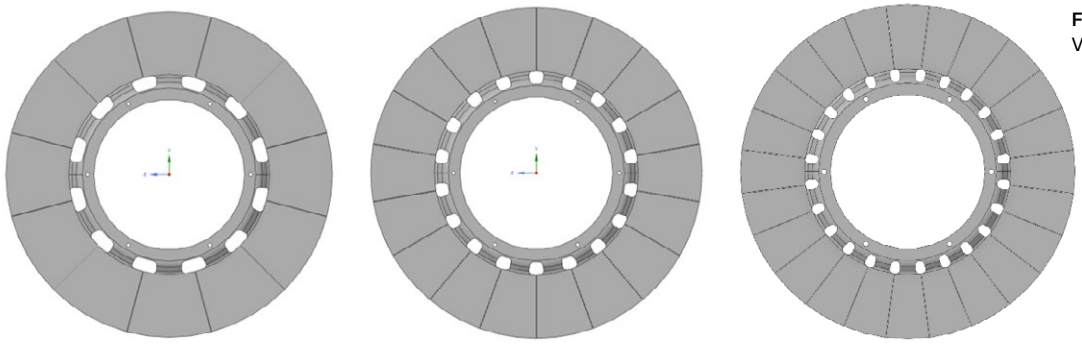

Figure 3.1.12: TgH models V7 (left), V8 (center) and V9 (right).

3.1.2.1.2 Requirements

The requirements for the TgH graphite wheel are reported in Table 3.1.3:

N°	Requirement	Comment
1	$\max(T) < 1700°C$	The maximum temperature max(*T*) in the target must be below 1700°C to avoid excessive loss of material due to sublimation.
2	$\frac{\sigma_I}{\sigma_{UT}} + \frac{\lvert\sigma_{III}\rvert}{\sigma_{UC}} < 1$	The Mohr-Coulomb criteria expressed as stress ratio must stay below 1.
3	$u_\theta < d_{slit}$	The slits must not close.
4	$u_z << d_{heat\ shield}$	The axial deformations must remain well below the distance between the target and the heat shield of the target insert.

Table 3.1.3: Target H thermo-mechanical requirements

3.1.2.1.3 Heat Load

The 590 MeV proton beam, operating at 3 mA, deposits a total power of 32 kW onto Target H [5]. If the target were stationary, this high-power density would lead to overheating and structural damage. To mitigate these effects, the target rotates at a frequency of 1 Hz, distributing the heat along a fixed radius. This rotation frequency is based on operational experience with Target E.

The power distribution is approximated under the assumption that it is uniformly spread along the beam path. The analytical expression for the power density *g*, is given by:

$$g = \frac{dI_{beam}}{dA} \cdot \frac{dE}{dz} \qquad \text{Eq. 3.1.1}$$

Where dI_{beam}/dA is the beam area intensity in mA/mm² and *dE/dz* is the stopping power in MeV/mm. The normalized gaussian distribution of intensity is given by the contour integral of the gaussian on the circular path φ followed by the beam [6]:

$$\frac{dI_{beam}}{dA} = \frac{I_{beam}}{2\pi{\sigma_r}^2} \cdot \oint \exp\left(-\frac{[x-x_0]^2 - [y-y_0]^2}{2{\sigma_r}^2}\right) d\varphi \qquad \text{Eq. 3.1.2}$$

After integration and in polar coordinates $\frac{dI}{dA}$ reads:

$$\frac{dI_{beam}}{dA} = \frac{I_{beam}}{{\sigma_r}^2} \cdot \exp\left(-\frac{r^2 + {r_0}^2}{2{\sigma_r}^2}\right) \cdot I_0\left(\frac{r r_0}{{\sigma_r}^2}\right) \qquad \text{Eq. 3.1.3}$$

Where σ_r is the beam size in the radial direction, r_0 is the beam offset in the radial direction, I_0 is the modified Bessel function of the first kind of order 0.

Figure 3.1.14 shows the main geometrical characteristics of the power deposition on Target H. The beam impinges on the target at an angle α_1=30° from the horizontal plane crossing the center of the target. To increase the production of surface muons, the target is tilted by an angle α_2=10° from the vertical plane. The dashed red circles frame the area of the smeared power density distribution *g*.

No divergence or halo of the beam is considered.

The radial beam size σ_r corresponds to σ_x being projected on the target:

$$\sigma_r = \sigma_x \frac{\cos(\alpha_1)}{\sin(\alpha_2)} \qquad \text{Eq. 3.1.4}$$

As the beam progresses through the target, the gaussian distribution is shifted toward higher radiuses. The location of the beam is corrected using:

$$r_o(z) = r_{impact} + \frac{z}{\tan(\alpha_2)} \qquad \text{Eq. 3.1.5}$$

Finally, the power density distribution of the smeared beam reads:

$$g(r,z) = \frac{I_{beam}}{{\sigma_r}^2} \cdot \exp\left(-\frac{r^2 + r_0(z)^2}{2{\sigma_r}^2}\right) \cdot I_0\left(\frac{r r_0(z)}{{\sigma_r}^2}\right) \cdot \frac{dE(z)}{dz} \qquad \text{Eq. 3.1.6}$$

Figure 3.1.15 shows the analytical power density distribution for σ_x = 0.9 mm on the face where the beam enters and on the r-z cross section. A Python script is used to calculate the distribution and export the data in ANSYS Workbench.

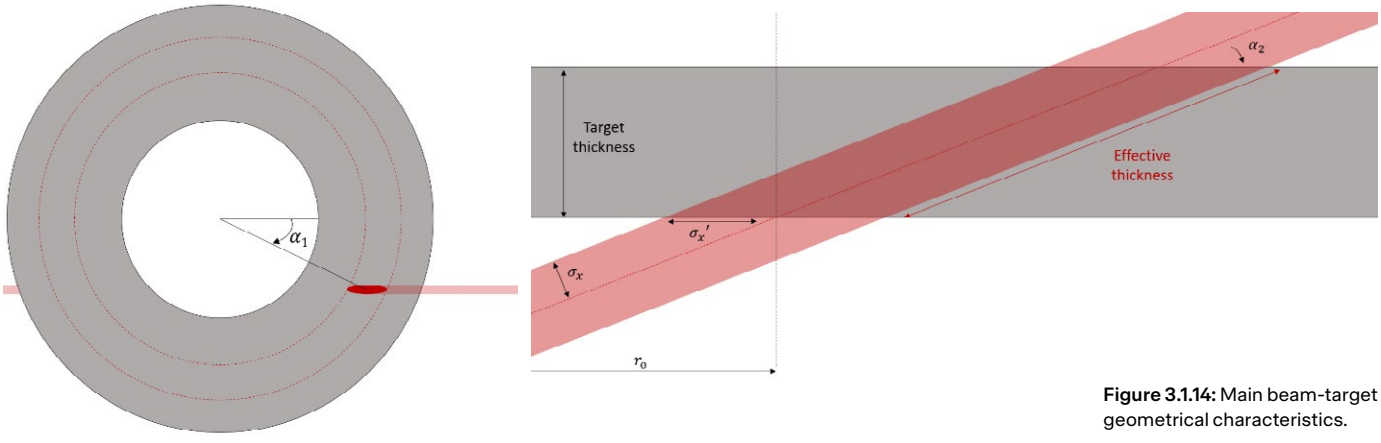

Figure 3.1.14: Main beam-target geometrical characteristics.

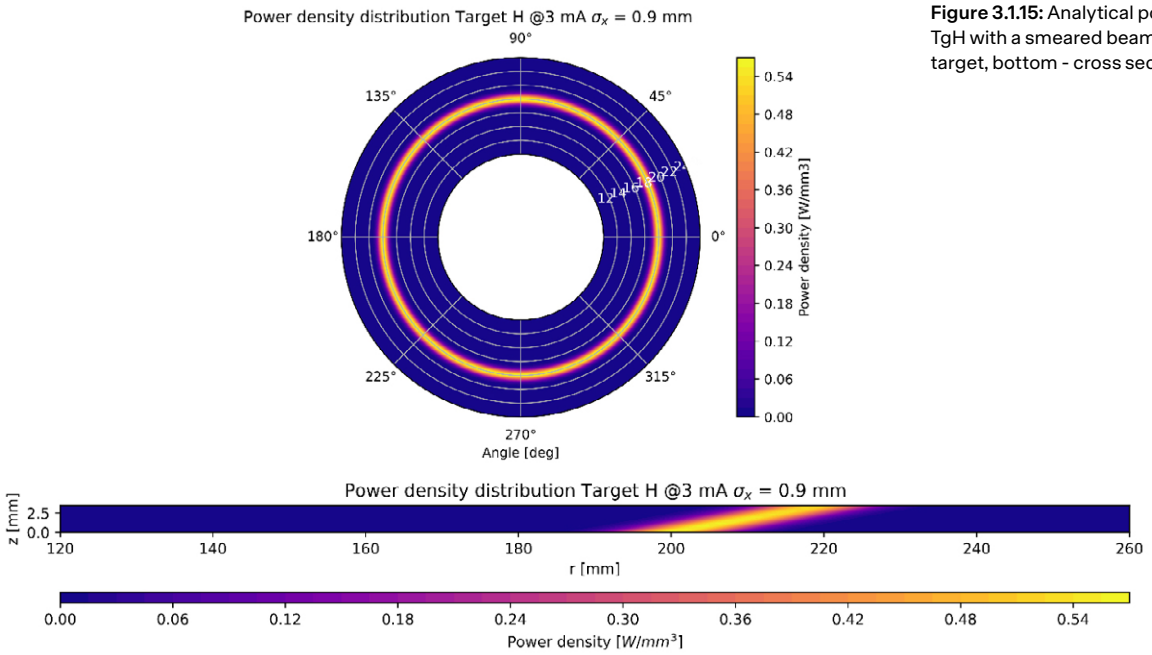

Figure 3.1.15: Analytical power distribution on TgH with a smeared beam: top - front view of the target, bottom - cross section.

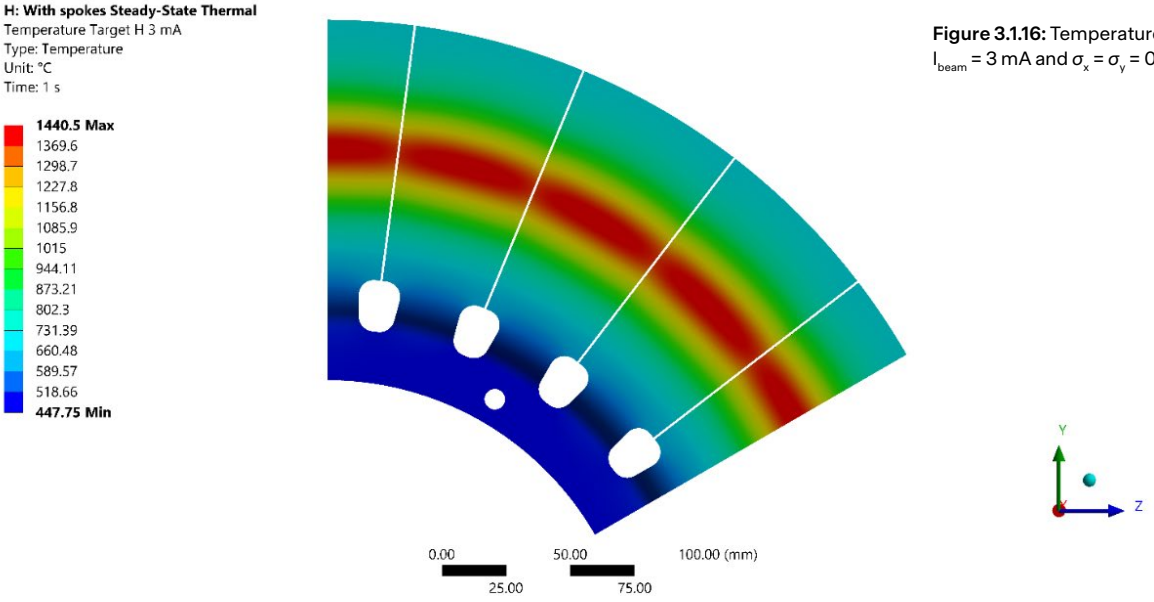

Figure 3.1.16: Temperature contour Target H for I_{beam} = 3 mA and $\sigma_x = \sigma_y$ = 0.9 mm

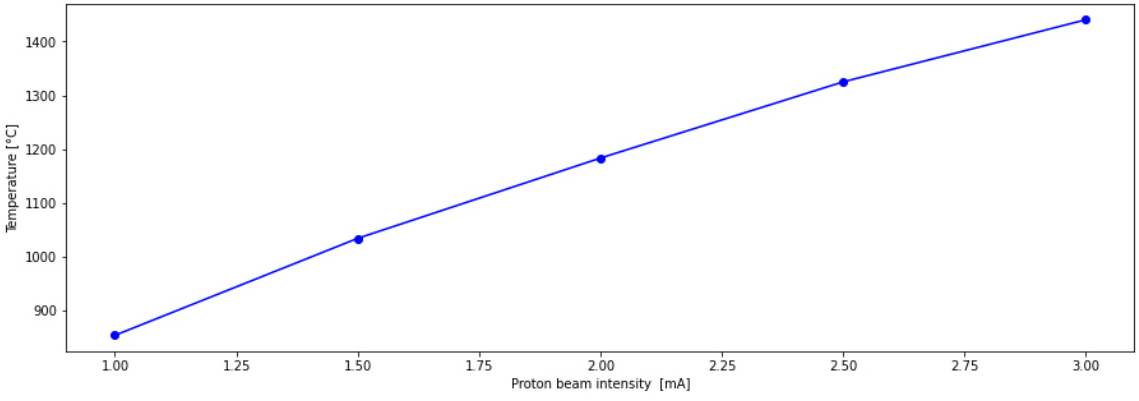

Figure 3.1.17: Maximum temperature on target H plotted against the beam intensity.

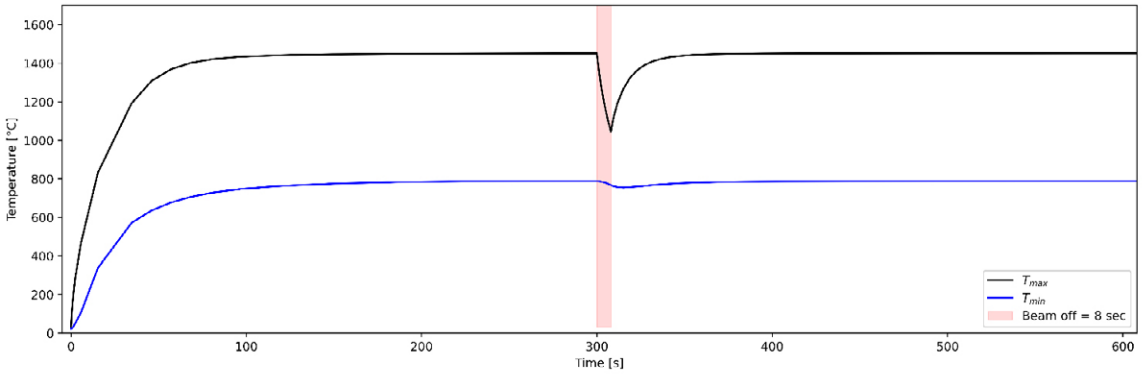

Figure 3.1.18: Maximum and minimum temperature on the target H during a beam cycle (cold start).

3.1.2.1.4 Thermal Simulations

3.1.2.1.4.1 Steady State

The nominal case is given for $\sigma_x = \sigma_y = 0.9$ mm and $I_{beam} = 3$ mA. Figure 3.1.16 shows the temperature distribution of Target H for such case. The requirement N°1 in Table 3.1.3 is satisfied (1440 °C < 1700 °C).

A parametric study was performed with a beam intensity from 1 to 3 mA. The results are shown in Figure 3.1.17.

3.1.2.1.4.2 Transient

A transient simulation was performed using the smeared power deposition to assess the magnitude of the cooling of the target during a UCN kick and with a cold start.

One cycle was simulated and consists of 300-second of beam on target, followed by an 8-second interruption and then another 300-second cycle. These is the worst case with an 8-second pulse to UCN, which means no beam on target H. Every time the beam is on target H, the beam intensity starts immediately at 3 mA.

Figure 3.1.18 shows that the target reaches its maximum temperature at t ≈ 100 s and steady state, when the minimum temperature stabilizes, at t ≈ 160 s, and cools down by about 400°C during the beam kick.

3.1.2.1.5 Structural Simulations

3.1.2.1.5.1 Stress and influence of the number of tiles

The maximum principal stress and the stress ratio are shown in Figure 3.1.19. Requirement n°2 in Table 3.1.3 is satisfied in the tile (0.7 < 1).

The influence of the number of tiles on the stress was studied on three target concepts with 12, 18 and 24 tiles, all separated by 1 mm slits. The results showed that the larger the tile, the higher the stress (Figure 3.1.20). The 24 tiles version was therefore selected.

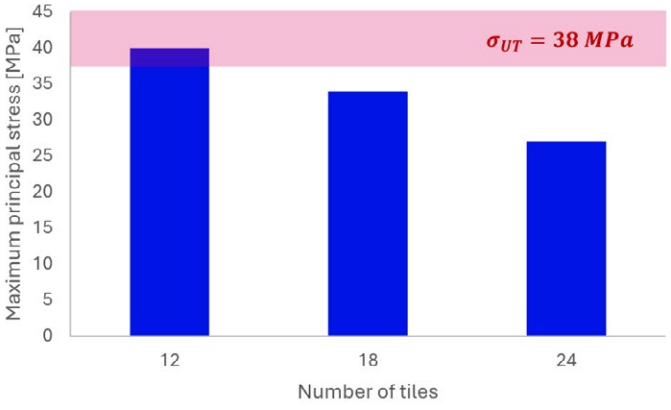

Figure 3.1.20 : Influence of the number of tiles on the maximum principal stress compared to the ultimate tensile strength. [7]

Figure 3.1.19: Maximum Principal Stress (left) and stress ratio criteria (right) in the tile

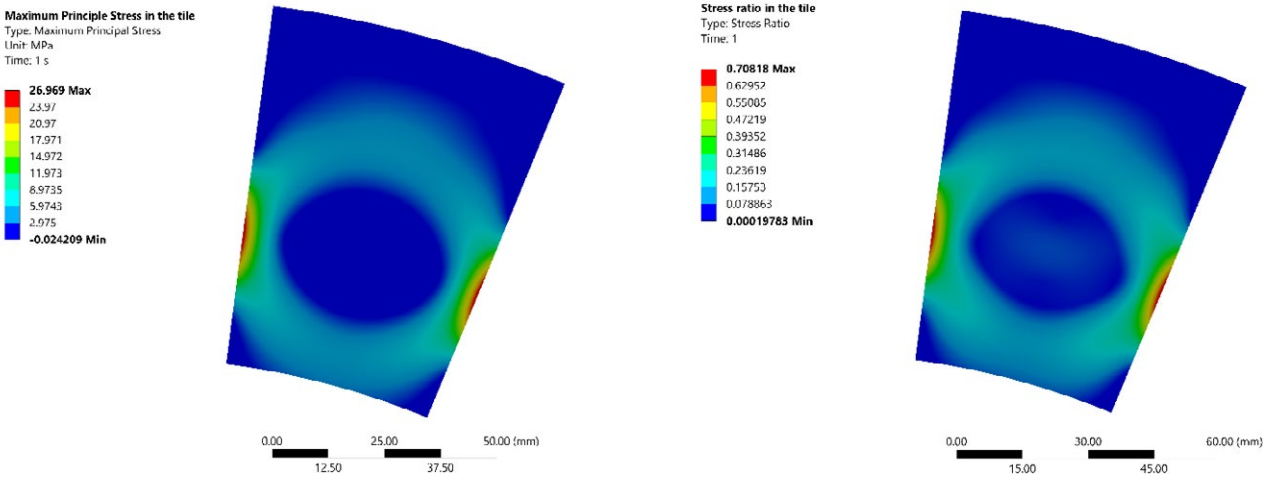

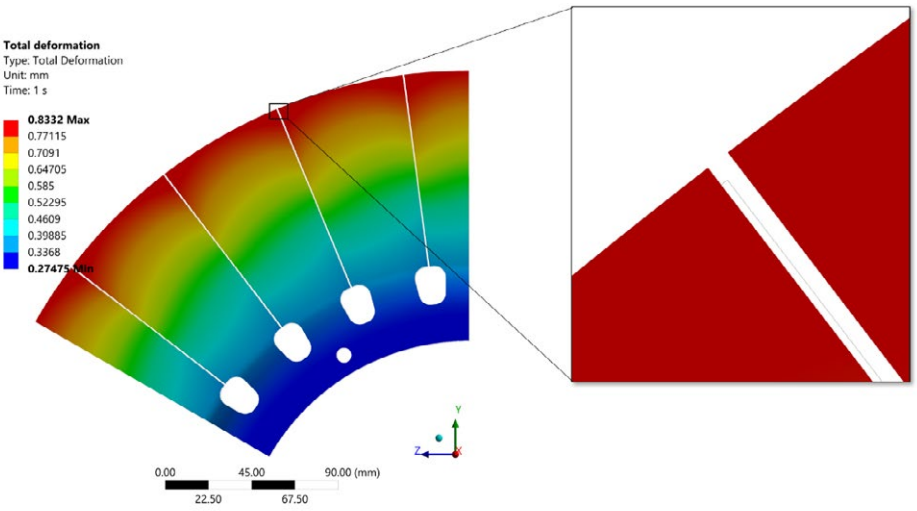

Figure 3.1.21: Total deformation with true scale and close-up view on the tip of a tile. Undeformed frame is also visible as wire frame.

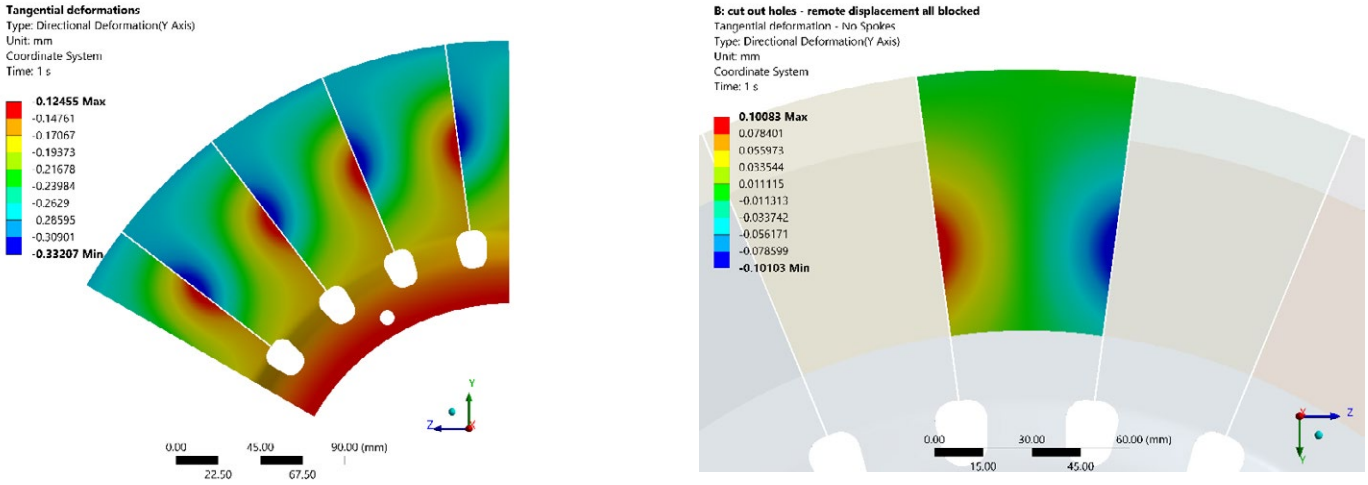

Figure 3.1.22: Tangential deformations with spokes modelled (left) and without the spokes (right)

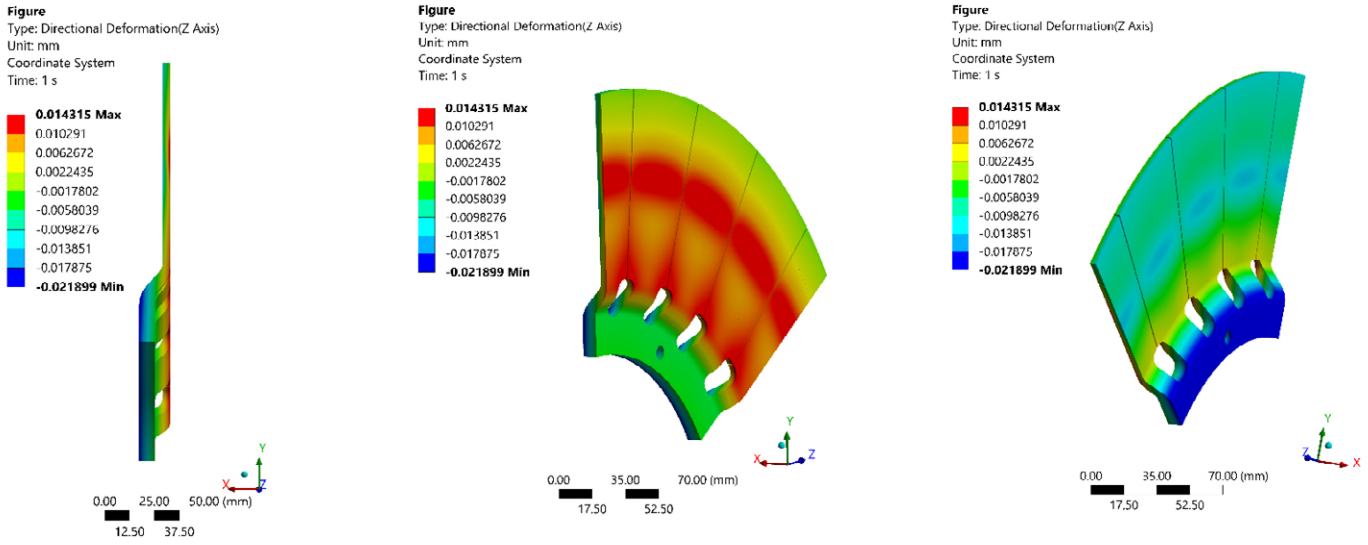

Figure 3.1.23: Axial deformations (-X direction is the where the back plate is located)

3.1.2.1.5.2 Deformation of the target

There is a combination of deformation effects within the target structure, arising from two primary sources: thermal expansion of the target itself and expansion of the spoke. Each of these phenomena can be examined independently, depending on the boundary conditions applied at the spoke-to-target connection:

1. *Thermal expansion of the target only:* If a remote displacement boundary condition is applied, and the spoke is not modeled, only the deformations due to the thermal expansion of the graphite target will be observed. This approach is particularly useful for studying deformation behavior between the slits.
2. *Combined deformation of spoke and target:* If the full spoke-to-target connection is modeled, the entire deformation of the target system, including the effects of the spoke, becomes accessible. This configuration is especially valuable for analyzing deformation toward the cooling plate.

Figure 3.1.21 shows the total deformation of the target, with a close-up view focused on the tip of a tile. The original, undeformed shape is displayed as wire frame for reference. The deformation is primarily characterized by radial expansion, along with a minor rotation around the x-axis.

Plotting only the tangential deformations (normal to the inner surface of the slit) reveals the difference between the model with spokes and the model without spokes. The model without spokes "filters" out the rotation of the target, since the target is free to rotate without the spokes. Otherwise, one would have to plot the deformations in the deformed coordinate system in the model with the spokes. The tangential deformation results indicate that the slit narrows by 0.2 mm, meeting requirement n° 3 in Table 3.1.3 (0.2 mm < 1 mm).

The axial deformations (toward the target back plate) are visible in Figure 3.1.23. The back plate is in the -X direction. The deformation in the direction of the back plate is rather small and is 0.022 mm, which is well below the 5 mm spacing. Requirement n°4 in Table 3.1.3 is therefore met.

3.1.2.1.6 Conclusions

The thermomechanical analysis focused on verifying that Target H meets four requirements under a 3 mA proton beam current:

1. The maximum temperature of the target remains below the sublimation limit of 1700°C, reaching 1440°C, thus preventing excessive material loss.
2. Stress analysis using the Mohr-Coulomb failure theory indicates that the principal stress ratio remains safely below the failure threshold of 1, with a value of 0.7.
3. A detailed study of the thermal expansion and deformations shows that the target's design meets the geometric tolerances for slit width, ensuring that the 1 mm slits close by only 0.2 mm, well within acceptable limits.
4. The axial deformation toward the heat shield is minimal at 0.022 mm, far below the 5 mm threshold.

The study included a comparison of different configurations to minimize stresses and deformations. The model with 24 tiles and cut-out slit bases provided the best results in the simulations, achieving lower compressive stresses than the other design. A parametric study confirmed that increasing the tile count minimized stress concentration.

While the "flat tile" model (CDR model) offers quick estimates with reasonable accuracy for thermal response and stress evaluation, a more complex cyclic-symmetry model with spokes provided a more accurate assessment of structural deformations.

In conclusion, TgH's design meets all thermomechanical requirements under operational conditions at 3 mA, and the findings confirm the suitability of this design.

Figure 3.1.24: TgH drive system.

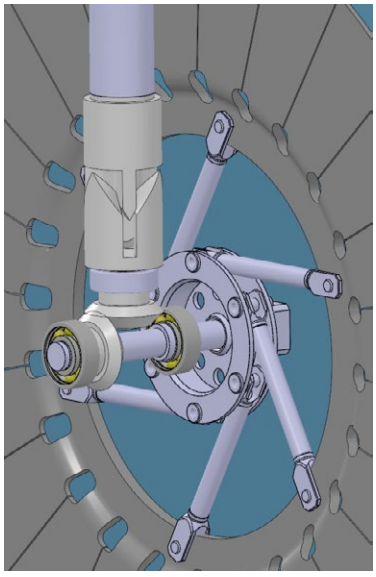

Figure 3.1.25: Angular gear box, TgH

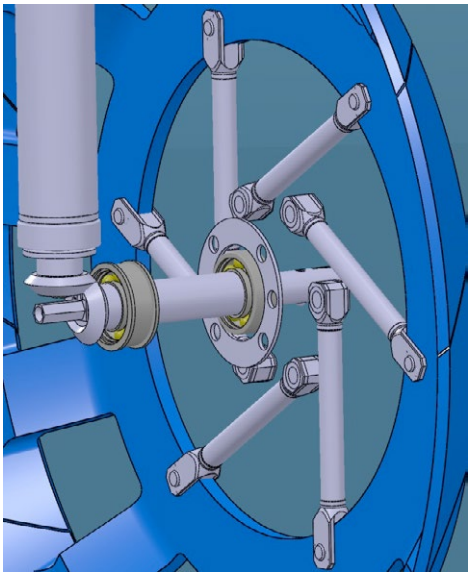

Figure 3.1.26: Angular gear box, TgE

3.1.2.2 Target Drive

Figure 3.1.24 shows the TgH drive system. The initial idea of adopting the drive mechanism of Target E could not be realized, so a different angular gear had to be designed. This allows the vertical drive shaft to be positioned further toward the centre of the insert.

In the TgH angular gearbox, the vertical shaft is located between the bearings, as shown in Figure 3.1.25, while in TgE, the vertical shaft is located behind the bearings (Figure 3.1.26). The same bearing type and size from KOYO are employed both for the TgH and for TgE.

The TgH vertical shaft has also a different design and a special coupling to the bevel gear. For maintenance, the target insert must be transported out of the beam channel into a parking slot by using the target exchange flask E. There, the crane adapter and the servomotor, both on top of the insert, are dismantled. Then the vertical drive shaft must be removed from the target insert by using a small exchange flask “drive shaft”. The crane adapter must be refitted, then the target insert is put back into the target E exchange flask and transferred into the ATEC. There, the graphite wheel must first be removed from the horizontal shaft. The angular gear is held in position by a bracket which must be unscrewed and unplugged (see Figure 3.1.27). On the backside a window is located to which a grasp must be attached (see Figure 3.1.28), which makes it possible to hold the plate with a power manipulator and loosen the screws of the plate with the hand manipulator. It is therefore possible to slide the angular gearbox out of the side of the back plate using the hand manipulator. A new bevel gear can finally be inserted into the back plate and all steps can be carried out in reverse order. The target insert is then pushed back into the parking slot. A new vertical shaft and the servomotor are fitted there. The target insert is now ready for the next beam period.

It is possible to install two versions of a servomotor: the old version, which uses the same motor as Target E (see Figure 3.1.29) and the new version (see Figure 3.1.30), which is a new type of servomotor. The old motor has been used since the 90’s and its availability on the market over the entire HIMB lifespan is not guaranteed.

The new version is manufactured by Beckhoff, it is a servomotor AM8122-1F00-0000 (see Figure 3.1.31), additionally with a planetary gear (Beckhoff AG2250-+PLE60M02-16-0B1-F2, see Figure 3.1.32). To test the resistance to radioactive radiation of the motor, a mock-up was constructed (see Figure 3.1.33). This test contains the servomotor, the gearbox and a rotational inertia mass. One advantage of the new motor is that the speed is monitored using a resolver, eliminating the need for the gold-plated tacho disk required by the old motor.

3.1.2.3 Water Cooling Requirements

Except for the TgH graphite wheel and the protection collimator, all other beam line components examined in this chapter are water cooled and must meet the cooling requirements summarized in Table 3.1.4.

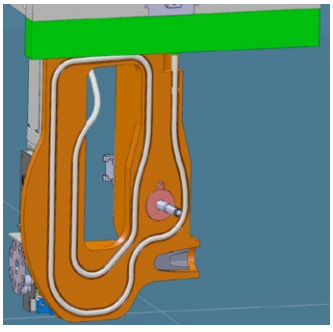

Figure 3.1.27: Frontside without Target Wheel

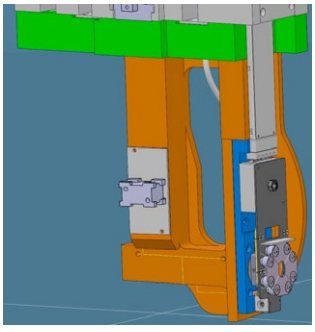

Figure 3.1.28: Cover plate with manipulator grasp

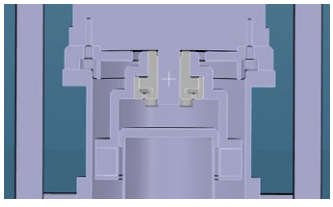

Figure 3.1.29: TgH coupling servomotor old

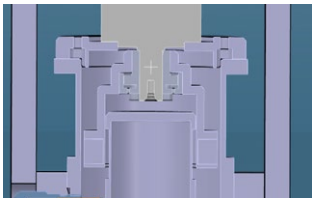

Figure 3.1.30: TgH coupling servomotor new

Figure 3.1.31: Low Voltage-Servomotor AM8122

Figure 3.1.32: Planetary gearbox AG2250

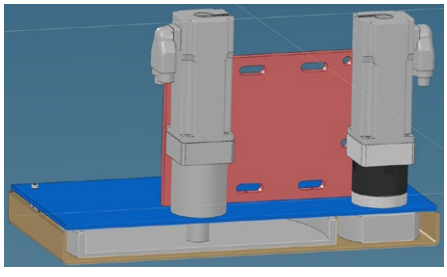

Figure 3.1.33: Motor test, near the beamline

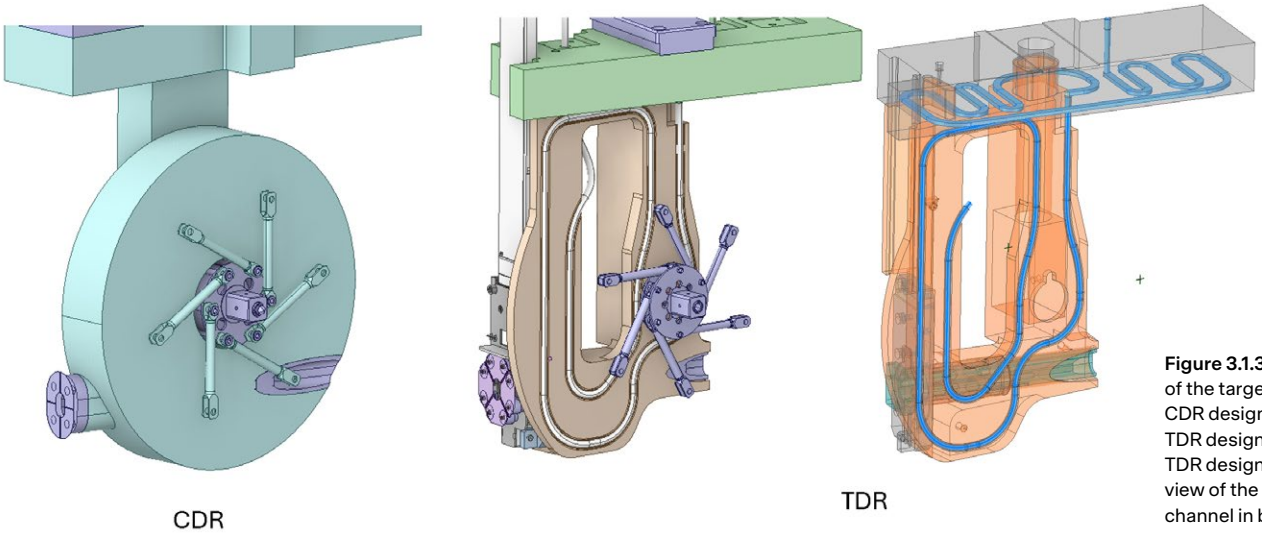

Figure 3.1.34: View of the target insert CDR design (left), TDR design (center), TDR design with view of the cooling channel in blue (right).

3.1.2.4 Back Plate and cooling plate

Figure 3.1.34 shows evolution of the back plate from the CDR to the TDR model. Compared to the CDR, a heat shield was included to protect the wires, the aperture foil and all the components related to the protection collimator. This shield is a protection against the radiated heat from the target. The upper block of the target insert (cooling plate in green) is made of stainless steel 316L *(Important: according to the design office, in May 2025 the upper block material was changed from stainless steel to copper. Nevertheless, stainless steel 316L was employed in all simulations)*. Rectangular channels are milled in the block and covered and welded with a 5 mm sheet of stainless steel 316L. The dimension of the rectangular channel matches the cross section of the circular pipe (50 mm^2).

The main cooling characteristics used in the simulation are reported in Table 3.1.5.

The maximum temperature of the copper body is 107 °C, satisfying R3. The temperature contour is visible in Figure 3.1.35 and Figure 3.1.36.

Component	N°	Requirement description
All	R1	Pressure loss in an insert must be below 2 bars.
	R2	Water velocity must remain below 9 m/s to prevent erosion.
	R3	Copper temperature must remain below 405 °C to avoid creep and material phase transition (reducing thermal conductivity).
	R4	Water surface temperature must remain below 90 °C (boiling temperature at 6 bar) to avoid boiling with sufficient margin.
	R5	Flow regime must be turbulent everywhere Re > 10 000 to ensure good heat transfer.
Mirror plates	R6	The maximum temperature must remain below 80 °C to avoid triggering the magnet's thermal switches.

Table 3.1.4: List of cooling requirements

Cross section	Hydraulic diameter pipes	Heat transfer coefficient	Number of channels	Mass flow rate per channel	Velocity per channel
Circular	8 mm	11 500 $W.m^{-2}.C^{-1}$	1	0.12 $kg.s^{-1}$	2.39 $m.s^{-1}$
Rectangular	6.7 mm	13 800 $W.m^{-2}.C^{-1}$	1	0.12 $kg.s^{-1}$	2.39 $m.s^{-1}$

Table 3.1.5: Main cooling characteristics of the target insert.

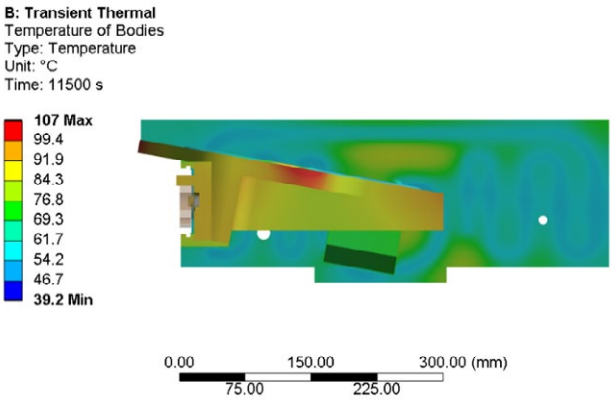

Figure 3.1.35: Target insert – Solid bodies temperature contour (view from below)

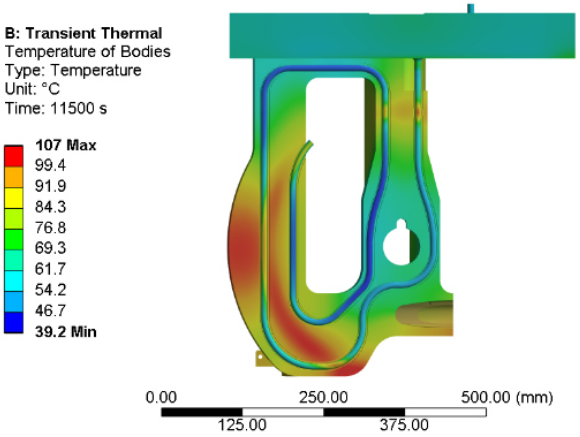

Figure 3.1.36: Target insert – Solid bodies temperature contour (side view)

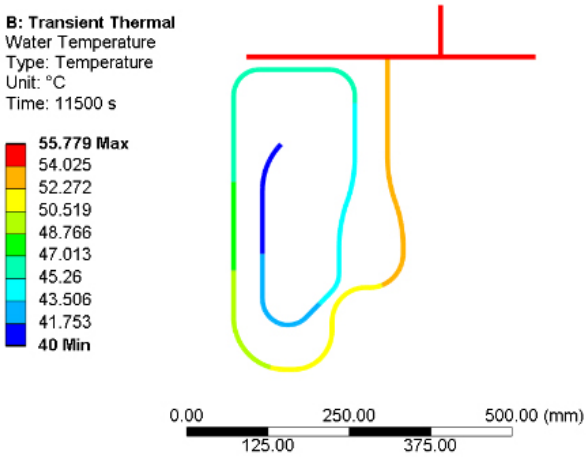

Figure 3.1.37: Target Insert – Water bulk temperature.

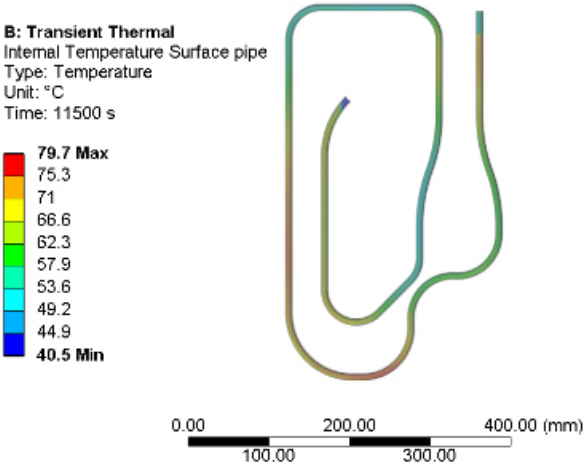

Figure 3.1.38: Target insert – water surface temperature.

The maximum surface temperature of the water is 80 °C, satisfying R4. The maximum bulk temperature of the water is 56 °C.

The main parameters used to calculate the pressure drop are reported in the Table 3.1.6.

At the operating point of 0.12 kg/s, the resulting pressure drop is 0.95 bar, satisfying R1.

3.1.2.5 Protection Collimator

The protection collimator was shortened with respect to what was published in the CDR to reduce the heat load.

Since the protection collimator must trigger the interlock system and absorb the beam in case of missteering, it was checked that with the shortened version the target cannot be bypassed. From upstream aperture constraints, the maximum angle in the horizontal plane is 0.43° and it would need to be above 0.7° to miss the target and hit directly KHH0.

Alumina for the ceramic pads was preferred to MACOR due to its better thermal conductivity as well as its suitability for high temperature applications. The final design reaches a maximum temperature of 154 °C. An overall lower temperature makes the protection collimator more sensitive to the additional power deposition of missteered beam.

Diameter [mm]	Length [m]	Number of elbows 90°	Number of 180° turns
8	8.71	24	8

Table 3.1.6: Target Insert – Parameters for calculation of the pressure drop

3.1.2.6 Temperature Sensors

The target insert is equipped with 11 temperature sensors (TC1-11). Three of them (TC1-3) are located on the protection collimator, while the others are planned for the copper back plate and for the bearing. Figure 3.1.43 shows the position of all sensors while Table 3.1.7 lists the corresponding expected temperatures for beam currents of 2.2 and 3.0 mA.

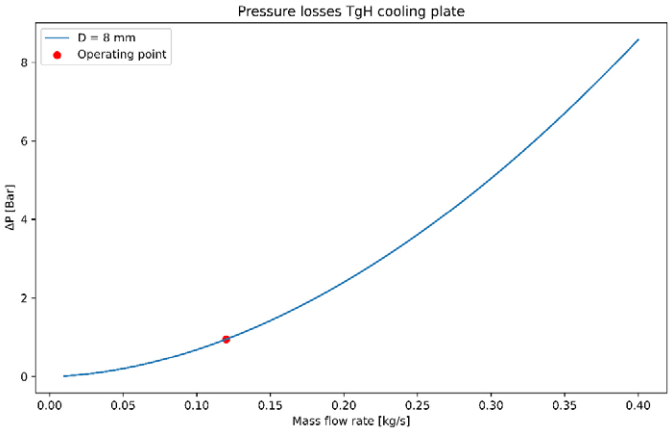

Figure 3.1.39: Target insert - Pressure drop as function of mass flow rate.

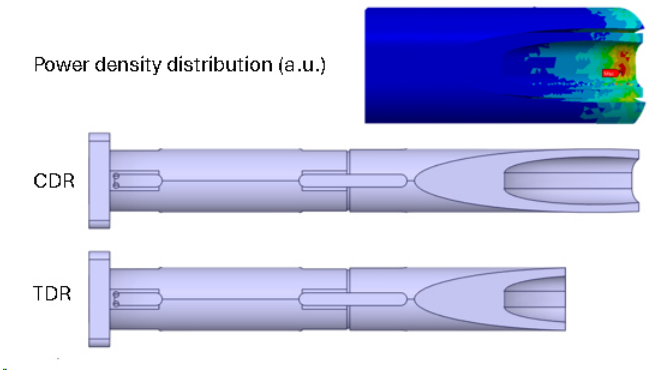

Figure 3.1.40: Shortening of the protection collimator according to the power density hot spot.

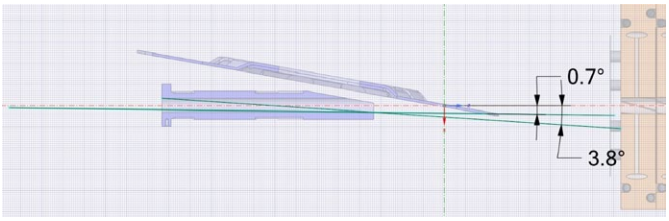

Figure 3.1.41: View of the maximum missteering angle.

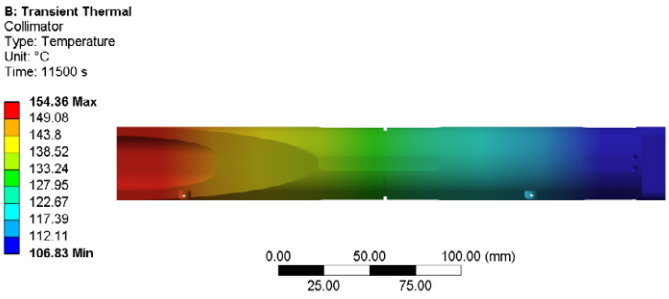

Figure 3.1.42: Temperature contour protection collimator

TC Location	Expected Temperature at 2.2 mA (°C)	Expected Temperature at 3.0 mA (°C)
TC1	119.7	148.7
TC2	119.6	148.5
TC3	94.9	114.8
TC4	85.1	101.5
TC5	78.5	92.5
TC6	–	–
TC7	67.4	77.3
TC8	72.4	84.2
TC9	49.8	53.3
TC10	–	–
TC11	85.2	101.6

Table 3.1.7: List of all TCs located on the target insert and their expected temperature at 2.2 as well as 3.0 mA. TC6 and TC10 temperatures were not simulated because these sensors are located on the bearing.

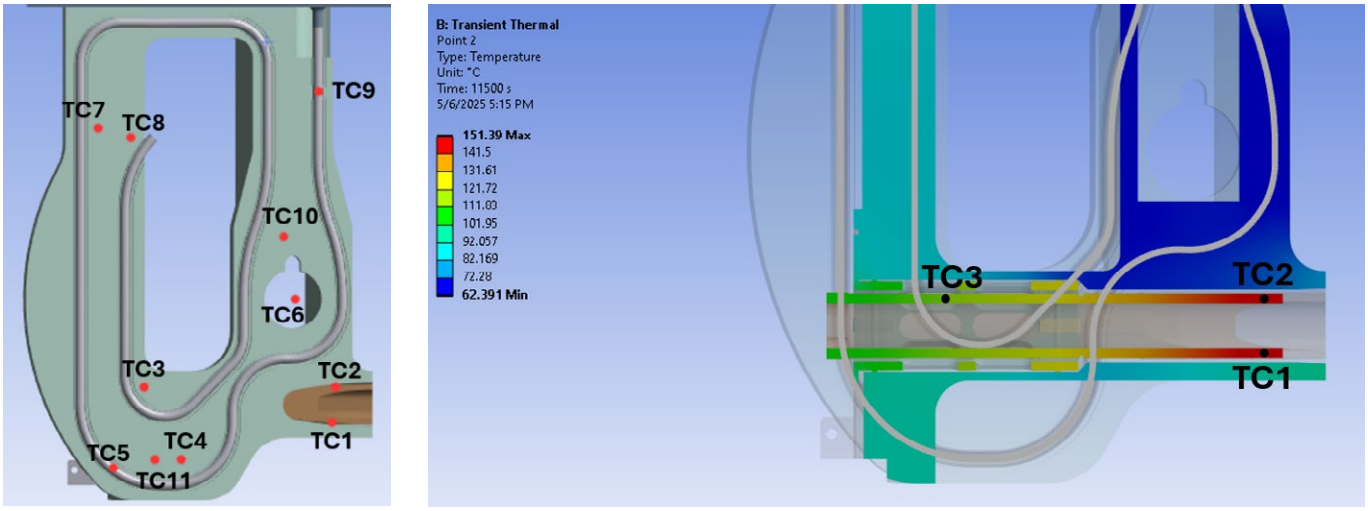

Figure 3.1.43: Position of all temperature sensors on the target insert (left) and location of TC1-3 in the temperature distribution simulation plot (right).

3.1.3 Collimator 0 (KHH0)

3.1.3.1 Mechanical Considerations

The collimator KHH0, consists of a large copper block with a defined opening for the beam (Figure 3.1.44). The large size is necessary to protect the vacuum chamber from particles scattered off TgH and to absorb the 58 kW of deposited power (see Table 3.1.1). The large copper block consists of seven disks. Each disk contains two cooling tubes in counter flow (see Figure 3.1.45). KHH0 is equipped with a 4-sector foil aperture (see Figure 3.1.46). This makes it possible to obtain information about the beam position. As in the case of the TgH insert, the signals are guided by means of an exchangeable rail located on top of the insert.

The special feature of the KHH0 is that the shielding in the vacuum chamber is suspended from the vacuum flange. At the bottom, the copper block stands on three supports, such that the weight of the copper does not only hang on the small points at the top.

The stable connection between the copper body and above steel shielding is ensured by three brackets (Figure 3.1.47). Because the vacuum brazing process softens the copper body, a metal housing has been added (Figure 3.1.48) to support the weight of the copper block itself such that it does not deform under its own weight.

This collimator is also removed by the Target E exchange flask, but the problem here is that the guide rails have no space due to a collision with the vacuum chamber wall and the capture solenoid magnets (see Figure 3.1.49, red rectangle). The exchange flask E works with guide rails that require a cube with rolls along the shielding block. There are U-shaped rails in the exchange flask, that are lowered into the vacuum chamber. When the hoist starts to pull out the beam insert, it must be guided. These rails ensure that the insert is well guided into the flask and does not rotate or shift. The problem is that these rails require space, which is not available with KHH0.

For this problem a removable mechanism is under development, that can be used to guide the collimator into the exchange flask and back into the vacuum chamber (Figure 3.1.50, Figure 3.1.51).

Figure 3.1.44: KHH0 insert.

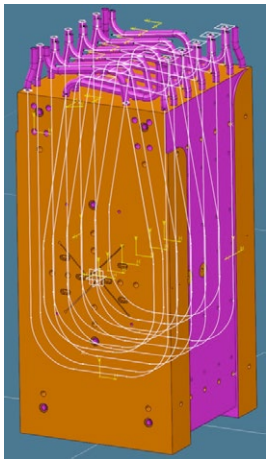

Figure 3.1.45: KHH0 body with cooling pipes

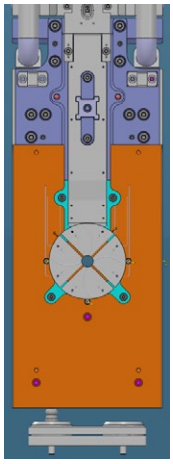

Figure 3.1.46: Aperture foil of KHH0

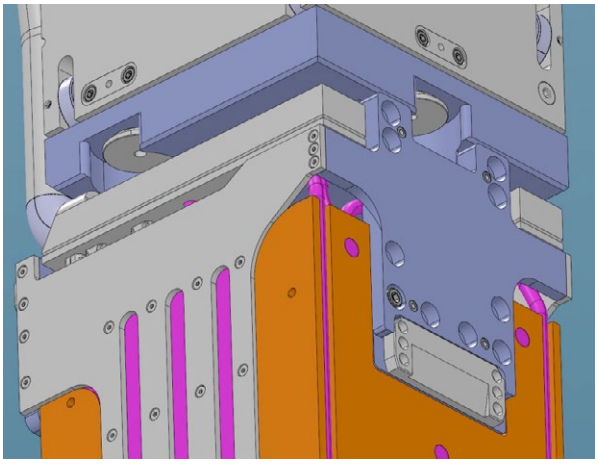

Figure 3.1.47: Hanging bolts

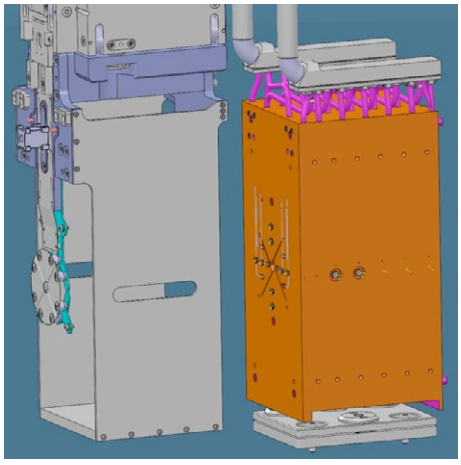

Figure 3.1.48: Support housing

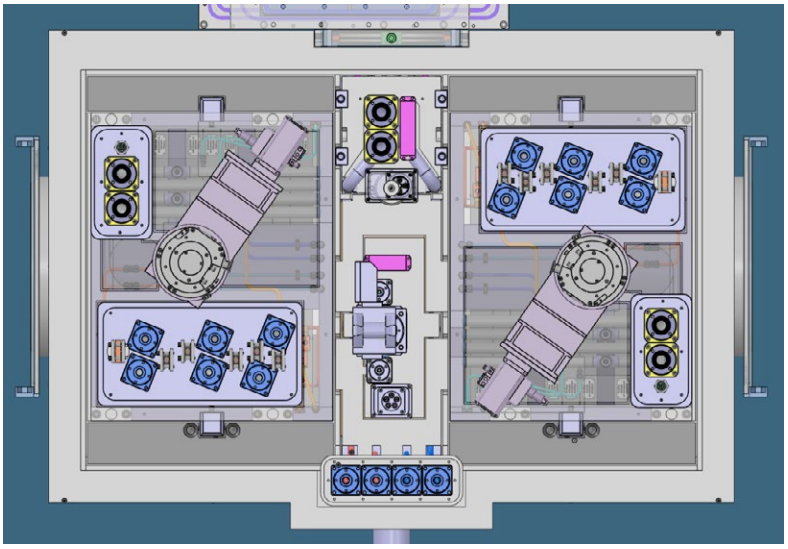

Figure 3.1.49: Target station, view from top

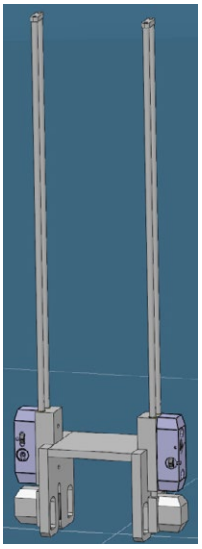

Figure 3.1.50: crane adapter

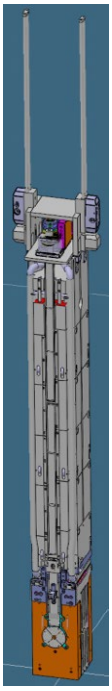

Figure 3.1.51: KHH0 with crane adapter

3.1.3.2 Cooling Aspects and Thermal Simulations

Initially, KHH0 was designed as two separate components: the collimator itself and the cooling plates. This design was inspired by the existing KHE collimators at PSI. However, the limited space between the capture solenoids (±250 mm from the impact point on Target H) presented two challenges:

1. Integrating the cooling pipes and their respective manifolds into both the collimator and the cooling plates proved to be complex from a manufacturing perspective.
2. The gap between the collimator and the cooling plate created a direct view path to the vacuum chamber, which is a non-replaceable component.

To address these issues, the collimator and cooling plates were combined into a single monolithic block made of OFHC copper with 13 cooling channels. This design not only simplifies manufacturing but also shields the vacuum chamber from a significant portion of the power generated by secondary particles and the thermal radiation from the target.

Finally, the cooling pipes are connected in counter flow and expansion slits were added to reduce the stresses. Figure 3.1.52 illustrates the design evolution from CDR to TDR for the collimator KHH0.

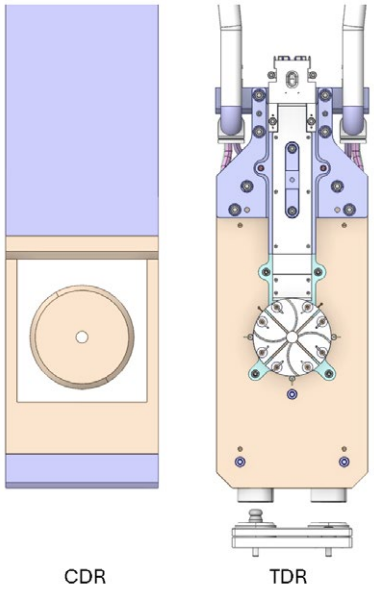

Figure 3.1.52: View of the CDR design of KHH0 (left) and TDR design (right).

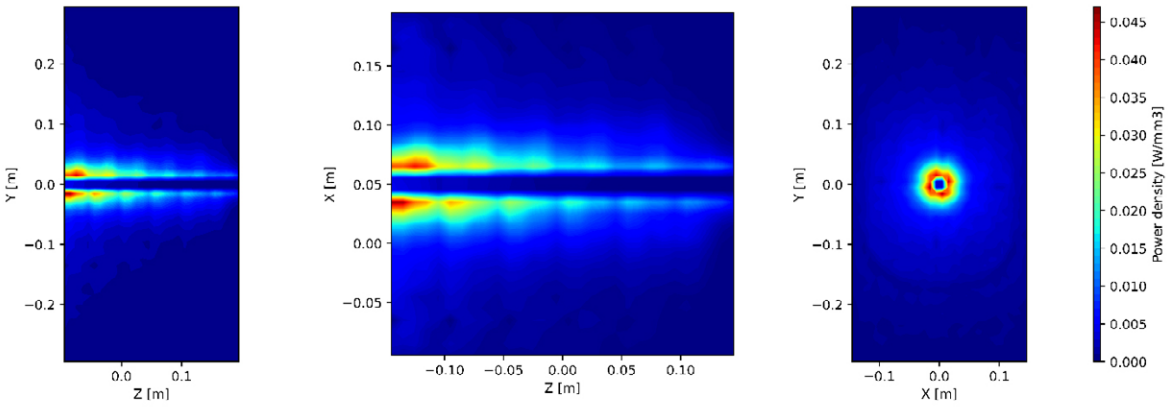

Figure 3.1.53: Power density distribution on KHH0. Cross sections on the YZ and ZX central planes (left and center) and front view on the XY plane (right)

The power density distribution in KHH0 is shown in Figure 3.1.53.

The main cooling characteristics used in the simulation are reported in Table 3.1.8. Two configurations were simulated. A configuration with 12 mm pipes and another with 10 mm pipes showed similar performances.

The results of the thermal simulations for 10 mm pipes are presented in Figure 3.1.54 and Table 3.1.9. The maximum temperature of the copper body is 201 °C, satisfying R3. The maximum surface temperature of the water is 84 °C satisfying R4. The maximum bulk temperature of the water is found at the outlet of the 1st channel located at the front of the collimator: 49 °C.

The results for the 10 mm configuration and the 12 mm configuration are similar, see Table 3.1.9.

Figure 3.1.55 shows the piping system of the KHH0 insert. At the service level, the inlet and outlet consist of two 36 mm pipes. The total pressure loss of the insert is therefore:

$\Delta P_{tot} = 2\Delta P_1 + \Delta P_2$

Diameter pipes	Heat transfer coefficient $W.m^{-2}.C^{-1}$	Number of channels	Total mass flow $kg.s^{-1}$	Mass flow rate per channel $kg.s^{-1}$	Velocity per channel $m.s^{-1}$	Reynolds number
10 mm	11 377	13	2.47	0.19	2.42	24100
12 mm	7 200	13	2.21	0.17	1.51	18000

Table 3.1.8: Main cooling characteristics of the collimator KHH0

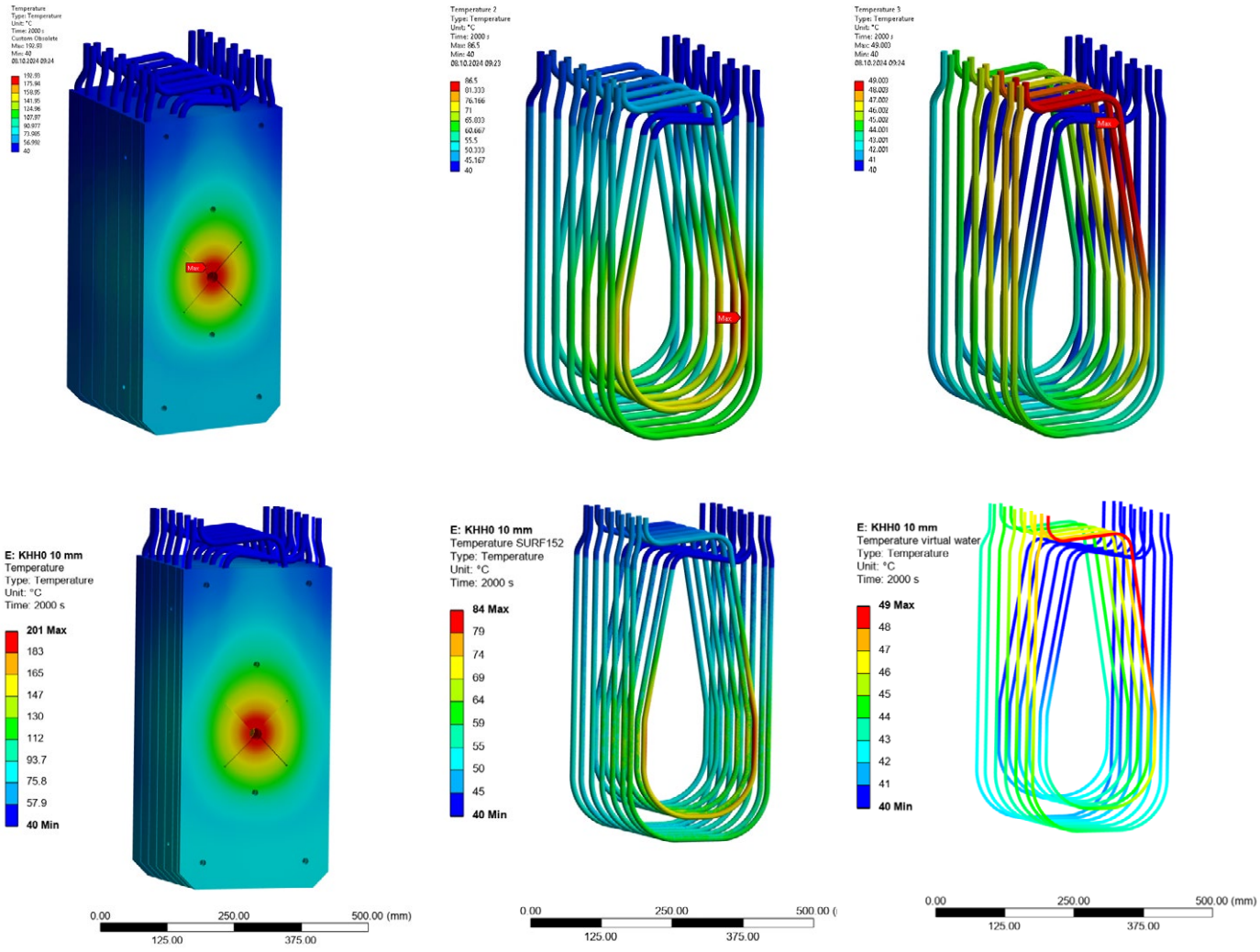

Figure 3.1.54: KHH0 simulation results for 10 mm pipes and v = 2.42 m/s. Temperature contour of the solid bodies (left). Surface temperature of the water (center). Water bulk temperature (right)

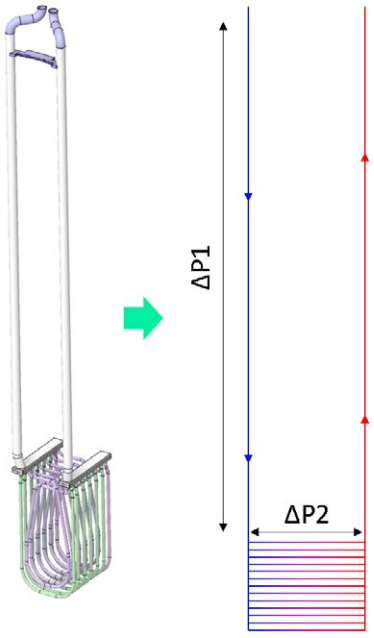

Figure 3.1.55: View of the piping system of KHH0.

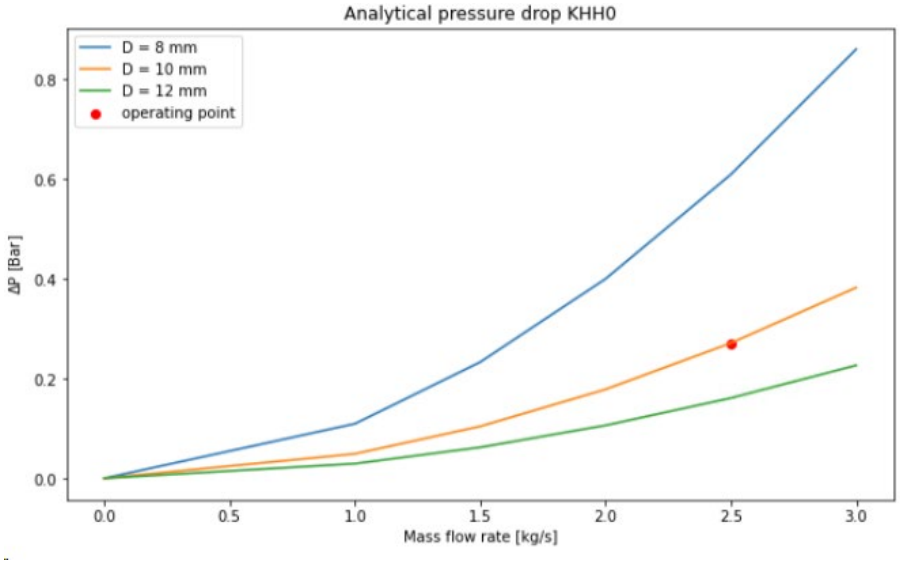

Figure 3.1.56: Pressure drop of KHH0 as a function of the mass flow rate.

Pipe diameter	Maximum solid temperature	Maximum water surface temperature	Maximum water bulk temperature
12 mm	193 °C	86.5 °C	49 °C
10 mm	201 °C	84 °C	49 °C

Table 3.1.9: Comparison of the KHH0 temperature for the 10 mm and 12 mm pipe diameter

	Diameter [mm]	Length [m]	Number of dividing T	Number of converging T	Number of elbows 90°
Branch 1	10	1.327	1	1	2
Branch 2	10	1.498	1	1	6
Main inlet	36	2.2	0	0	3
Main outlet	36	2.2	0	0	3

Table 3.1.10: KHH0 cooling pipes charactristics.

The cooling pipes of KHH0 are in counterflow. To achieve this layout, the purple pipes in the Figure 3.1.55 left are slightly longer and have 4 additional elbows. The main characteristics are presented in Table 3.1.10:

Due to the slight length difference, the flow rates in the branch 1 is 0.198 kg/s and in the branch 2 is 0.186 kg/s. The assumption that all mass flow rates are equal is therefore assumed correct.

The pressure drop as a function of mass flow rate of the total KHH0 insert as seen on Figure 3.1.55 is given in Figure 3.1.56. At the operating point of 2.5 kg/s, the resulting pressure drop with 10 mm cooling channels is 0.27 bar, satisfying R1.

3.1.3.3 Temperature Sensors

It is planned to equip KHH0 with 16 thermocouples (TCs). The KHH0 front plate will host 14 of them at two different depths: TC1-6 (called “outer”) will be located on the upstream face of the collimator, while TC7-14 (called “inner”) will lay 31 mm

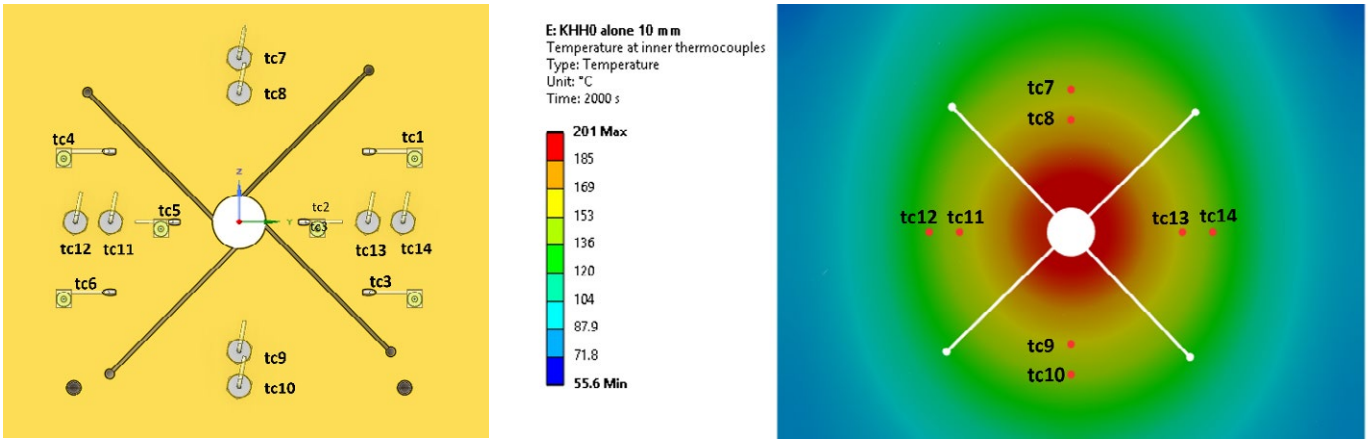

Figure 3.1.57: Location of the outer and inner KHH0 thermocouples (left) and temperate map of the KHH0 plane where the inner thermocouples are located (right).

deeper in the copper body. Figure 3.1.57 shows the location scheme of TC1-14 (left) and the temperature map in the TC7-14 plane (right). The two remaining temperature sensors, TCL1-2 (called "lateral"), will be installed in the second and third collimator disk respectively, as shown in Figure 3.1.58.

These temperature sensors will deliver important information about the beam position during machine commissioning and setup. Moreover, some of the provided signals will be used by the machine protection system. A list of all TCs foreseen in KHH0 along with the corresponding simulated temperature values is presented in Table 3.1.11.

TC Location	Expected Temperature at 2.2 mA (°C)	Expected Temperature at 3.0 mA (°C)
TC1	127.1	158.8
TC2	151.6	192.2
TC3	126.0	157.3
TC4	124.4	155.1
TC5	148.5	188.0
TC6	122.7	152.8
TC7	123.9	154.4
TC8	133.9	168.0
TC9	128.0	160.0
TC10	117.4	145.6
TC11	122.9	153.0
TC12	111.3	137.2
TC13	126.3	157.6
TC14	114.2	141.0
TCL1	122.0	151.8
TCL2	107.4	131.9

Table 3.1.11: List of all KHH0 TCs and their expected temperature values at 2.2 and 3.3 mA.

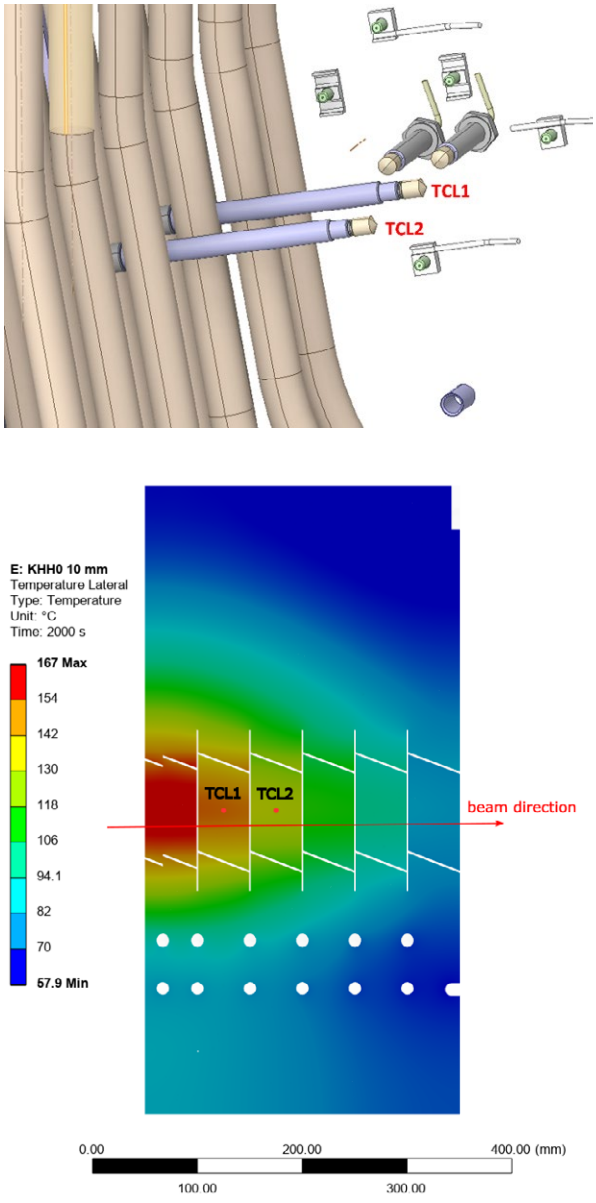

Figure 3.1.58: CAD model showing the location of the two lateral Thermocouples (above) and simulated KHH0 temperature map in the region of interest (bottom).

3.1.4 Capture Solenoid and Mirror Plates

The capture solenoid is treated in detail in Chapter 3.2. There is a direct view angle between the coils of the capture solenoid and the Target H. Therefore, there is an additional heat load on the capture solenoid that comes from the thermal radiation of the target (0.5 kW) on top of the one due to the secondary particles scattered off TgH (3 kW). The main parameters of the simulation are:

- 80°C temperature of the coils
- Emissivity of ε_{coils} = 0.5 which is a conservative value.

The inner surfaces of the capture solenoid are Nickel (coating of the iron parts), Copper or Solder. All of these are reflective materials with low emissivities $\varepsilon_{Ni} \approx \varepsilon_{Cu} \approx \varepsilon_{Solder} \approx 0.05$.

Figure 3.1.59 shows that most of the heat load coming from the thermal radiation of target H is deposited on the first coil. The heat fluxes decrease steeply as the coil is located away from the target. In terms of total power, this results in approximately 1.5 kW with about 500 W deposited on the mirror plate.

The mirror plates are constructed using ARMCO iron and feature four integrated cooling loops:

- 2 × 8 mm loops on the front mirror plate,
- 1 × 8 mm on a side plate,
- 1 × 6 mm on the other side plate.

Initially, the cooling loops were only integrated into the front plate, focusing on the area around the 400 mm muon beamline openings. This design accounted for hot spots caused by the 3 kW power deposition from secondary particles (see Figure 3.1.60), the thermal radiation from the target H, and the relatively low thermal conductivity of iron (67 $W \cdot m^{-1} \cdot °C^{-1}$).

However, after a first round of thermal simulations, a hot spot of approximately 100°C was identified on the side forward plate. To mitigate this issue and prevent triggering the thermal switches, additional cooling loops were added to the side plates (see Figure 3.1.61). These side cooling loops were installed on both sides of the mirror plate, ensuring compatibility with the capture solenoids located on either side of the target station. This design consideration allows a single spare solenoid to be used interchangeably on both sides, despite power deposition occurring primarily in the forward direction.

The difference in diameter between the two side cooling loops (6 mm and 8 mm) is intentional and serves to balance the pressure drop caused by their different lengths. The pressure drop between the loops is equalized, as shown by:

$$\Delta P_{6mm} = \Delta P_{8mm} \qquad \text{Eq. 3.1.7}$$

$$f_{6mm} \cdot \frac{L_{6mm}}{D_{6mm}} \cdot \frac{\rho}{2} \cdot \left(\frac{4 \cdot Q_{6mm}}{\rho \cdot \pi \cdot D_{6mm}^{\,2}} \right)^2 = f_{8mm} \cdot \frac{L_{8mm}}{D_{8mm}} \cdot \frac{\rho}{2} \cdot \left(\frac{4 \cdot Q_{8mm}}{\rho \cdot \pi \cdot D_{8mm}^{\,2}} \right)^2 \qquad \text{Eq. 3.1.8}$$

The mass flow rate in the 8 mm loop is set to 0.1 kg/s, a value assumed across all 8 mm pipes in the coils. Based on

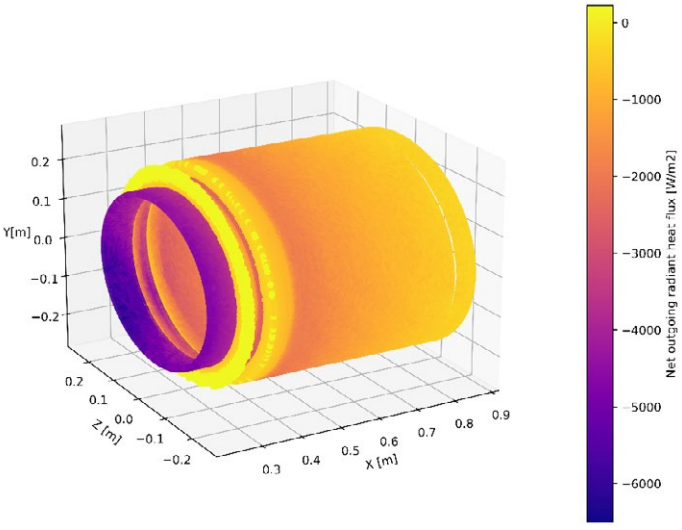

Figure 3.1.59: Net Outgoing radiant heat flux [W/m²] on the capture solenoid.

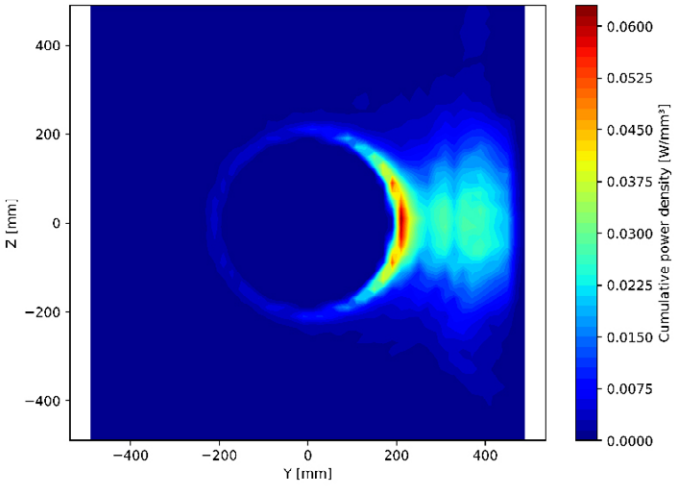

Figure 3.1.60: Cumulative power density distribution over the thickness of the mirror plate.

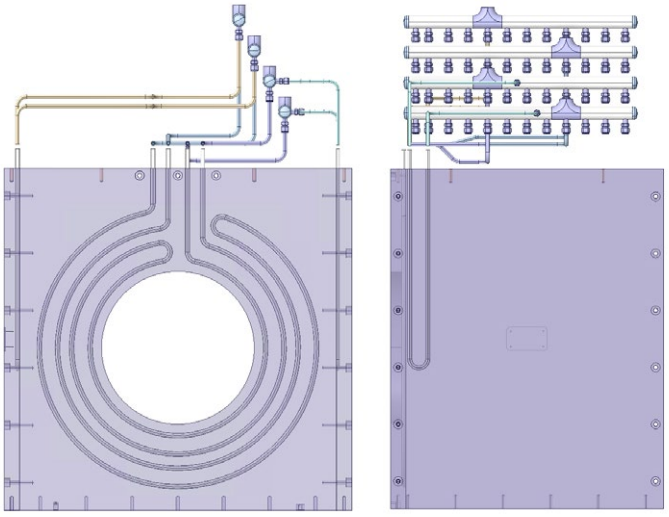

Figure 3.1.61: CAD viewing the mirror plates. View of the front mirror plate with the two cooling loops (left) and view of the side plate with one additional cooling loop (right).

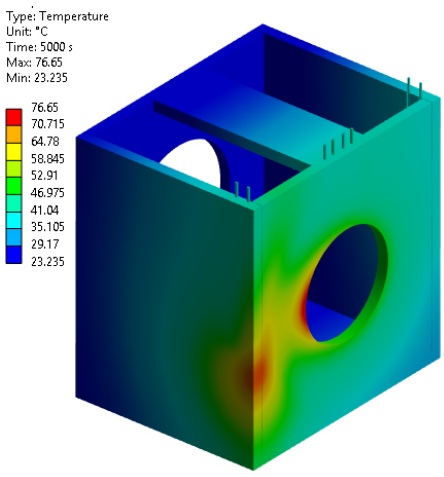

Figure 3.1.62: Mirror plates temperature contour

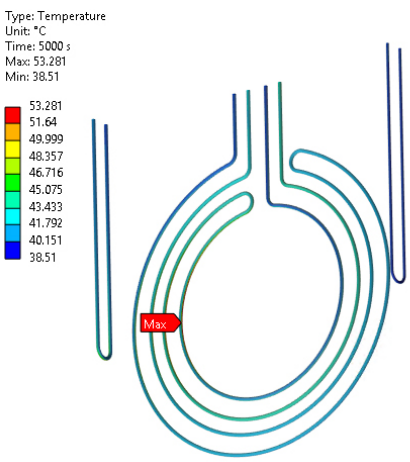

Figure 3.1.63: Water surface temperature contour of the mirror plates

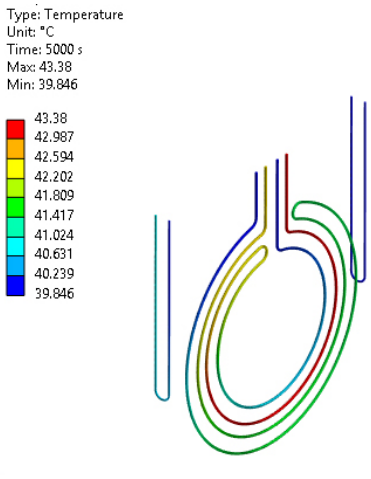

Figure 3.1.64: Water bulk temperature of the mirror plates

Diameter pipes	Length pipe	Number of elbows	Heat transfer Coefficient $W.m^{-2}.C^{-1}$	Friction factor	Mass flow rate per channel $kg.s^{-1}$	Velocity per channel $m.s^{-1}$	Reynolds number
8 mm	3 m	8	9 691	0.028	0.1	2	15 800
6 mm	2.3 m	6	9 829	0.03	0.054	1.9	11 400

Table 3.1.12: Cooling characteristics of the mirror plates

this, the mass flow rate in the 6 mm loop is calculated to be 0.054 kg/s. A summary of the main characteristics is provided in Table 3.1.12.

The results of the thermal simulations are given in Figure 3.1.62, Figure 3.1.63 and Figure 3.1.64. The maximum temperature of the iron body is 76 °C, satisfying R6.

The maximum surface temperature of the water is 53 °C satisfying R4. The maximum bulk temperature of the water is found at the outlet of the channels close to the openings toward the muon beamlines: 43 °C.

The temperature of the mirror plate will be monitored by seven thermocouples (TCs) installed in the region where the hot-spots are expected, namely on downstream half of the mirror plate, as displayed in Figure 3.1.65. The information about the temperature will be useful for three different purposes: beam commissioning/setup of the facility, machine protection, simulation validation. To allow capture solenoid interchangeability for the two secondary beam line (MuH2 and MuH3) left and right of the target station, the TC layout must be symmetric with respect to the vertical middle plane of the magnet. This means that the seven thermocouples shown in Figure 3.1.65

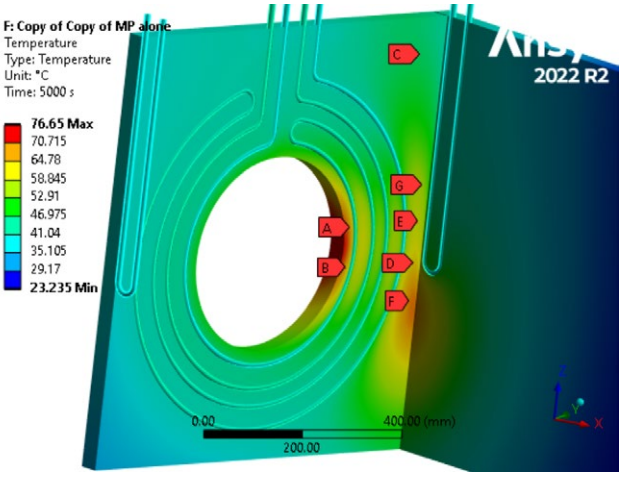

Figure 3.1.65: Location of the thermocouples on the mirror plate (only one half is shown, the others are symmetric).

TC Location	Expected Temperature at 2.2 mA (°C)	Expected Temperature at 3.0 mA (°C)
A	60.5	68.0
B	59.7	66.8
C	44.5	46.1
D	57.6	64.0
E	54.5	59.8
F	60.9	68.5
G	52.2	56.6

Table 3.1.13: Expected temperatures for the different TCs installed on the mirror plate at 2.2 mA and 3.0 mA proton beam current.

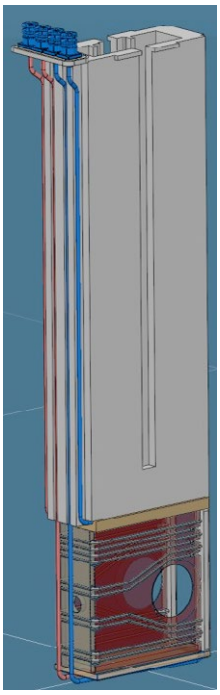

Figure 3.1.66:
Local shielding, TgH

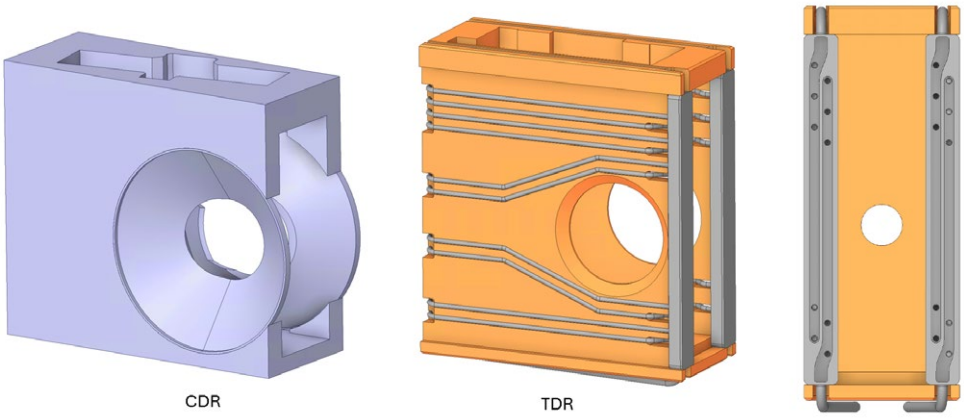

Figure 3.1.67: View of the CDR design of the local shielding (left), TDR design (center), view of the manifolds (right).

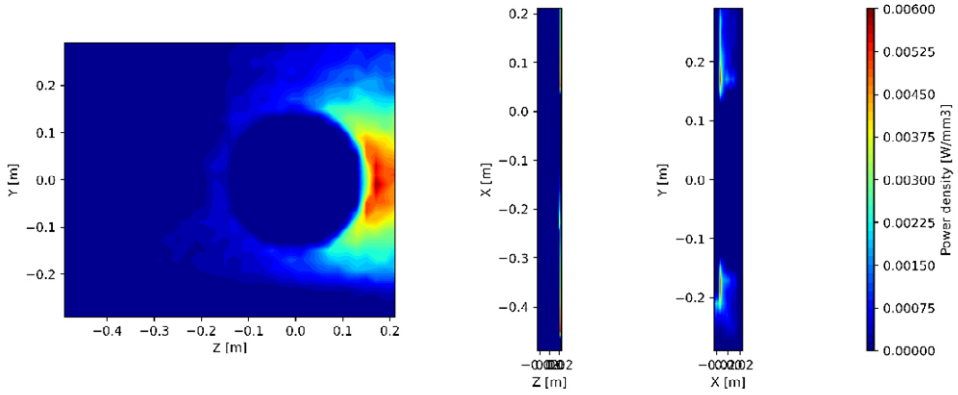

Figure 3.1.68: Power density distribution on the local shielding. Cross sections on the YZ and ZX central planes (left and center) and front view on the XY plane (right)

will be mirrored to the other side of the plate, bringing the total amount of TCs to fourteen. Since there is very little clearance between the target station and the mirror plate, the TCs will be mounted on the mirror plate back surface.

The expected measured temperatures for all TCs have been extracted from the thermal simulations and listed in Table 3.1.13.

3.1.5 Local Shielding

3.1.5.1 Mechanical aspects

Figure 3.1.66 shows the local shielding insert. The local shielding contains the target insert and consists of two main parts: the cooled copper housing at the bottom, which absorbs the thermal radiation from the target wheel, and the steel channel at the top, which holds the copper housing and fills the gap between the TgH and the walls of the vacuum chamber.

Figure 3.1.67 shows the evolution of the local shielding design. In its CDR version, the local shielding included two cones to protect the capture solenoids from the thermal radiation of the target. These cones were removed since they would have needed to be actively cooled and this would have increased the complexity of the design. In addition, due to changes in vacuum chambers and the detailed design of the various components, the dimensions were slightly changed.

Two independent cooling loops are integrated in the local shielding. They can be switched on and off in case of a leakage or malfunction.

3.1.5.2 Energy deposition and thermal simulations

The simulations are performed with only one cooling loop. The power density distribution is presented on Figure 3.1.68.

The main cooling characteristics used in the simulation are reported in Table 3.1.14.

The initial simulations considered the inlet and outlet manifolds to be coated with the Al_2O_3-TiO_2 coating. However,

the temperature would reach almost 200 °C. It was decided to mitigate the temperature on the stainless steel manifolds by removing the coating. The results are visible in Figure 3.1.69 and Figure 3.1.70.

The maximum temperature of the copper body is 143 °C, satisfying R3. The maximum surface temperature of the water is 90.7 °C, slightly over R4. However, the requirement is considered to be satisfied since it is not foreseen to operate at 3 mA only with one cooling loop on the local shielding.

The maximum bulk temperature of the water is found at the outlet of the channels close to the openings toward the muon beamlines of about 52°C.

3.1.5.3 Important note

Although the thermal simulations show that all cooling requirements are satisfied, concern has been recently raised since in

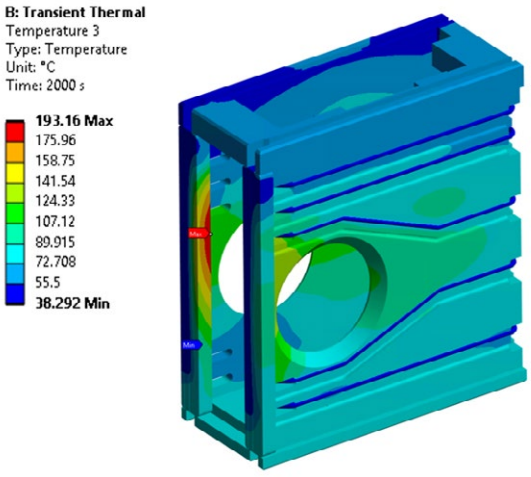

Figure 3.1.69: Local shielding temperature contour with coated manifolds.

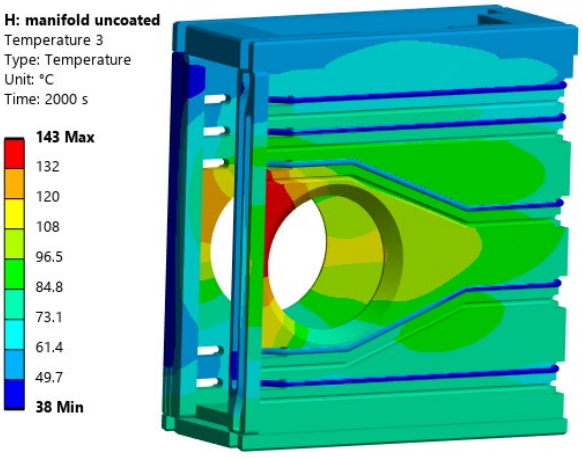

Figure 3.1.70: Local shielding temperature contour with uncoated manifolds.

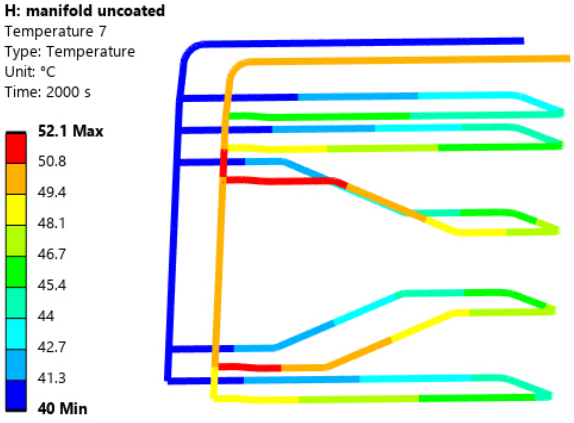

Figure 3.1.71: Local shielding – water bulk temperature contour.

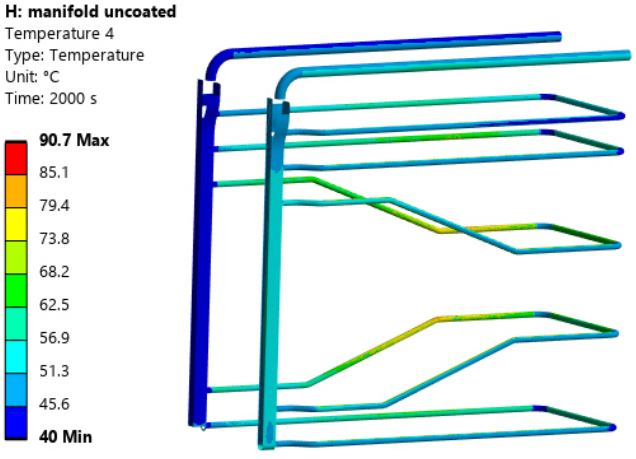

Figure 3.1.72: Local shielding – water surface temperature contour.

Diameter pipes	Heat transfer Coefficient $W.m^{-2}.C^{-1}$	Number of channels	Total mass flow $kg.s^{-1}$	Mass flow rate per channel $kg.s^{-1}$	Velocity per channel $m.s^{-1}$	Reynolds number
10 mm	7 688	5	–	0.12	1.53	15 233
18 mm	9 800	2	0.6	–	2.36	42 314

Table 3.1.14: Main cooling characteristics of one loop of the local shielding

the copper body the water manifolds are in a region of large power deposition from particles scattered off the target wheel. This could lead to hydrolysis with formation of radicals that might induce corrosion of the water pipes. For this reason, it has been decided to update the design of the local shielding model by relocating the manifolds in a region of lower power deposition. The new model will be available by the end of July and the new thermal simulations results are expected by the end of August 2025.

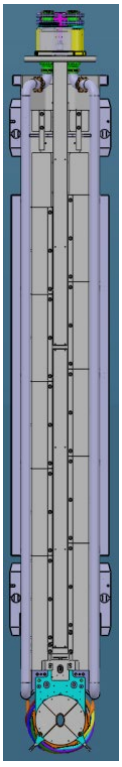

Figure 3.1.73: Collimator KHH1

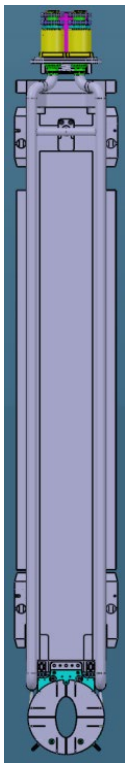

Figure 3.1.74: Collimator KHH2

3.1.6 Collimator 1 (KHH1) and Collimator 2 (KHH2)

Collimator 1 (KHH1) and collimator 2 (KHH2) are similar, only the aperture is different (see Figure 3.1.73). These collimators are constructed in the same principle as the KHE2 collimator, located downstream of TgE (see Figure 3.1.74), which absorbs over 100 kW deposited power and has never experienced any failure in 20 years of operation (being precautionary replaced only once in 2012 by a one-to-one copy of it).

The copper body is manufactured with six copper disks. These are vacuum-brazed to form a single block. Diagnostic thermocouples are also installed (see Figure 3.1.75). Each thermocouple is duplicated to ensure redundancy. There are a few more thermocouples that are used to validate calculation results, that were generated during the design phase. Both collimators have a beam positioning aperture (see Figure 3.1.76). The four aperture segments are located at the top, right, bottom and left ends of the collimator front face (see Figure 3.1.76). The signals are also guided here with the same interchangeable signal rail on the top of the insert as with KHH0.

Each collimator is part of an insert whose shielding consists of small steel blocks (employing the same principle as for the KHH0 and TgH) and equipped with guide rails. This makes it possible to remove KHH1 and KHH2 with the target E exchange flask.

3.1.6.1 PK2 vacuum chamber collimator system

The collimation system downstream of Target H vacuum chamber before the first quadrupole, QHTC13, consists of two OFHC collimators, KHH1 and KHH2, made out of six disks brazed to each other [3]. The cooling system of each collimator

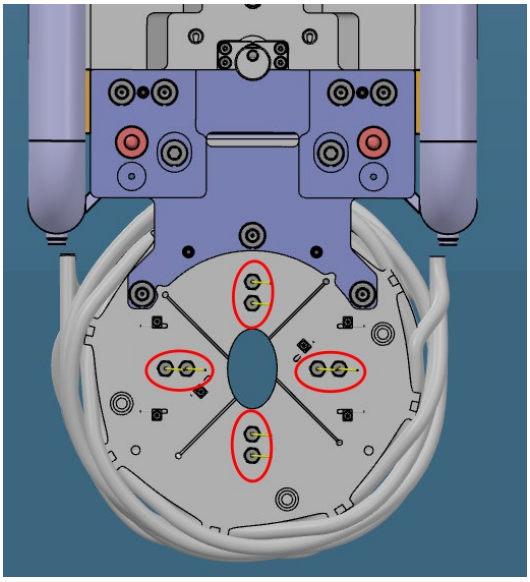

Figure 3.1.75: Thermocouples for beam position shown by the red circles.

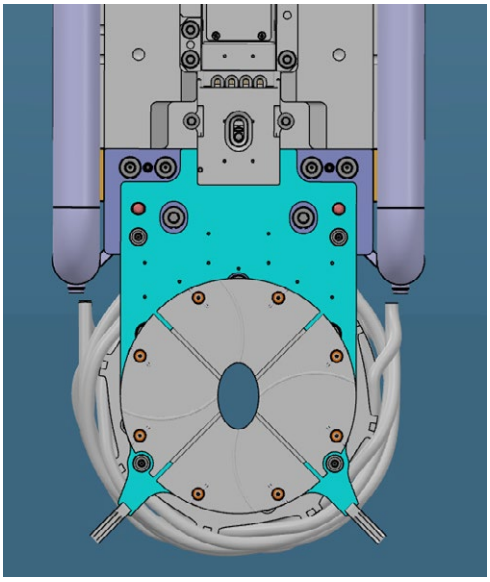

Figure 3.1.76: 4-sector aperture foil located upstream of KHH1 and attached to its insert.

N°	Requirement	Comment
T1	max (T_{Cu}) < T_H (*Cu*)	The maximum temperature max (T_{Cu}) in any solid material must not exceed its homologous temperature T_H.
T2	max (T_{water}) < T_B (*water*)	The maximum temperature in the water max (T_{water}) must not exceed its boiling point T_B (*water*) at any given operating pressure.
T3	$v_{water/Steel}$ < 9 $m.s^{(-1)}$	The water flow on stainless steel must not exceed 9 m/s.

Table 3.1.15: Thermal requirements for KHH1 and KHH2.

is provided by eight helicoidal pipes with an inner diameter of 9 mm made of stainless steel 316L brazed to the main body. The elliptical shapes and apertures of the collimators have been optimized with respect to different parameters such as to reduce the beam size at critical locations of the beamline and to contain at least 2/3rd of the power deposition in its immediate surroundings [3]. ANSYS simulation studies have been then performed to validate the optimized geometry versus thermal and structural integrities.

3.1.6.2 KHH1 thermal analysis

KHH1 and KHH2 have similar geometries [3] but different power depositions due to their relative positions with respect to Target H and to the beamline components between KHH1 and KHH2, which provide more shielding for KHH2. The power depositions on KHH1 and KHH2 have been recalculated with respect to what is published in [3] taking into account the new design of the Target H chamber and beamline elements. For example, collimator KHH0 located in the Target H vacuum chamber now has a monolithic geometry capturing more scattered particles than the previous version [3]. Moreover, the relative positions of KHH1 and KHH2 have been changed with respect to what was specified in [3]. Since the power deposition in KHH1 is still about 8 times bigger than the one in KHH2, only KHH1 was simulated (KHH1 18.2 kW, KHH2 1.7 kW). The same concept for cooling efficiency and structural integrity of KHH1 will be applied to KHH2. The thermal requirements for KHH1 are summarized in Table 3.1.15 following [3]:

The homologous temperature criterium corresponds to a fraction of the melting temperature T_m (≈ 0.5 T_m for metals) above which steady-state creep cannot be ignored. For OFHC, T_H = 405 °C is also the temperature from which the thermal conductivity decreases. The boiling point of water is about 158 °C for a static pressure of 6 bars.

3.1.6.2.1 Materials

All material properties used in the thermal simulations are for non-irradiated virgin materials [8] [9]. The OFHC mass density is assumed to have a constant value of 8'940 kg m^{-3}. Isotropic thermal conductivity and specific heat capacity at constant pressure have a temperature-dependent behavior. Values originate from an experimental investigation performed at PSI and a literature survey [10]. Pipes are made of stainless steel 316L and material data are taken from the GRANTA MDS material database [11]. Pipes are considered to be completely smooth or with 15 µm roughness. Constant fluid properties for the water are taken at 40 °C.

3.1.6.2.2 Power deposition

Monte Carlo calculations for the power depositions in KHH1 and KHH2 were performed using BDSIM software package [2]. KHH1 receives for a proton beam of 3 mA about 18.2 kW

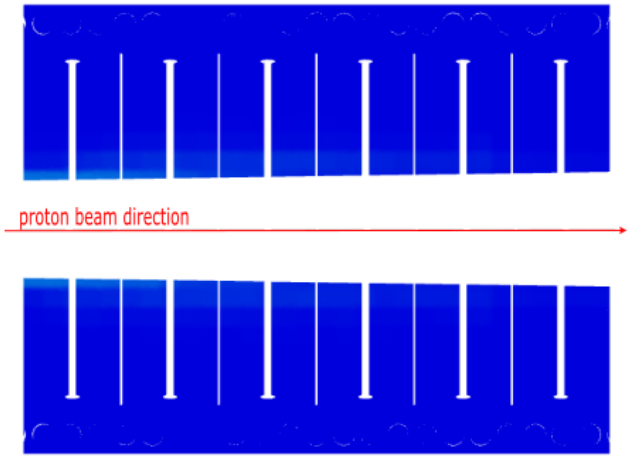

Figure 3.1.77: Power density on the vertical plane passing through the geometrical center of KHH1.

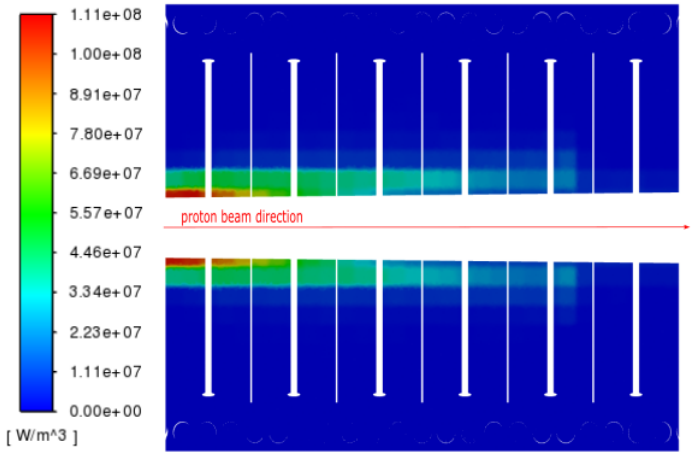

Figure 3.1.78: Power density on the horizontal plane passing through the geometrical center of KHH1.

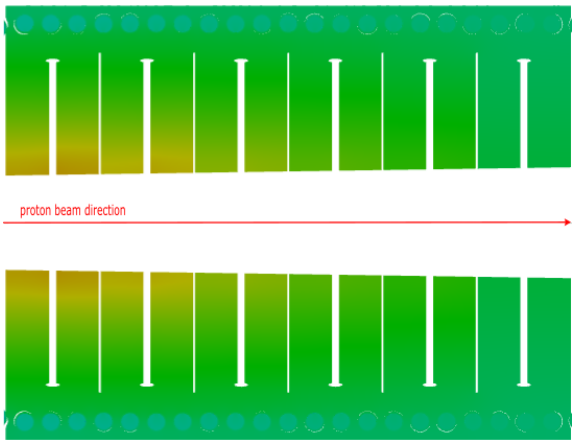

Figure 3.1.79: Temperature distribution on the vertical plane passing through the geometrical center of KHH1.

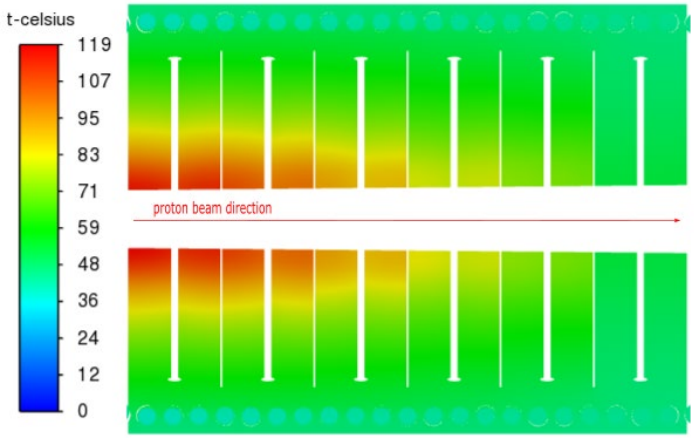

Figure 3.1.80: Temperature distribution on the horizontal plane passing through the geometrical center of KHH1.

and KHH2 receives 1.7 kW. Total power and power distribution are then imported in ANSYS FLUENT for fluid dynamics simulations using profile files and checked against BDSIM data.

In Figure 3.1.78 the power density deposition in KHH1 on parallel and perpendicular planes passing through the geometrical center are shown. The highest power deposition is expected in the first two disks. Comparing Figure 3.1.77 versus Figure 3.1.78, it is also visible that the power density is higher on the horizontal plane with respect to the vertical one. This is due to the power deposition optimization, see Section 8.4.3 in [3], in order to reduce the power received by the quadrupole triplets 1 & 2 from the divergent proton beam.

3.1.6.2.3 Physical model and numerical implementation

The problem consists of a conjugate heat transfer analysis with water in turbulent regime as coolant fluid. The 1 kg/s total inlet water mass flow rate is considered equally distributed in the 8 pipes with an initial 5% turbulent intensity at 40° C. Zero-gauge pressure outlets were implemented, and all outer solid surfaces are considered adiabatic. A constant roughness of 15 µm is set on internal surfaces of the pipes to calculate the pressure drop. This is quite a large value, but it will give a conservative estimate for the sizing of the water pumps needed for the overall IMPACT project. At the inlet, the flow is fully turbulent since the Reynolds number is about 27'000 with an entry water speed in each pipe of about 2 m/s. Contacts between pipes and OFHC body are treated as perfect thermal contacts.

Fluid dynamics simulations were performed using ANSYS FLUENT solver [12] using the Shear Stress Transport model (SST) to account for the turbulent flows in the 8 helicoidal pipes. SST is usually recommended for heat transfer problem [11] and it belongs to the RANS category. The KHH1 body has 10'776'553 elements with a special technique of mesh refinement to reduce the total number of elements, while preserving high accuracy. The mesh has been iteratively refined. Contacts between pipes and KHH1 body are considered as perfect thermal contacts. Several monitor techniques are implemented to check model accuracy, convergence rate and physical quantities such as residual plots, mass imbalance and total heat transfer rate.

3.1.6.2.4 Thermal and pressure results

Temperature distributions are displayed in Figure 3.1.79 and Figure 3.1.80 on the same planes as in Figure 3.1.77 and Figure 3.1.78. The highest temperatures are located on the horizontal plane since the QC13 quadrupole is defocusing on the horizontal plane [3].

The maximum temperature located on the first disk is about 120°C, which is far away from the accepted safety limit of about half melting point temperature in Kelvin (melting point 1083°C). Since the highest temperatures are concentrated in the first two disks of KHH1, the geometry considered for structural analysis will be restricted to the first two disks only. The pressure drop from inlet to outlet in each pipe with 15 µm surface roughness corresponds to about 0.17 bar whereas with no roughness to about 0.15 bar. In Table 3.1.16, requirements vs simulation results are compared showing that the thermal integrity of KHH1 is achieved.

3.1.6.3 KHH1 structural analysis

Thermal load generated by the power deposition from the proton beam at 3 mA causes deformations and stresses in KHH1. In order to access its structural integrity mechanical

N°	Requirement	Simulation results
T1	$\max(T_{Cu}) < T_H(Cu)$	$120\ °C < 405\ °C$
T2	$\max(T_{water}) < T_B(water)$	$49\ °C < 158\ °C$
T3	$v_{water/Steel} < 9\ m.s^{-1}$	$2.5\ m.s^{-1} < 9\ m.s^{-1}$

Table 3.1.16: Requirements vs simulation results comparison.

N°	Requirement	Comment
S1	max (ε_{pl}) < 2%	Low amount of localized plastic strains, ε_{pl}, is allowed for annealed copper
S2	max (σ_{eq}) < σ_U	The maximum equivalent stress, σ_{eq}, should not exceed the ultimate tensile strength (180 MPa) of unirradiated copper, σ_U.
S3	$\Delta l < {}^{d_{slits}}/_{2}$	Slits must not close

Table 3.1.17: Structural requirements

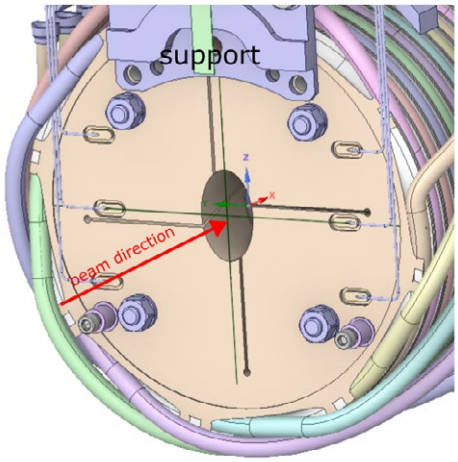

Figure 3.1.81: KHE2 collimator are reference for boundary conditions.

simulations were performed using ANSYS Mechanical [13]. The structural requirements for KHH1 are summarized in Table 3.1.17 [8]:

3.1.6.3.1 KHH1 geometry in structural study

The geometry in the structural analysis consists of the first two consecutive disks of KHH1 along the proton beam direction where the maximum temperature is located. Pipes mimic the real geometry with half pipes brazed inside grooves. Front face slits have a gap of 1.5 mm instead of 1 mm as in the thermal analysis with a tip diameter of 2.5 mm instead of 2 mm. Those differences are the first step in the optimization procedure to avoid closing the slits and reducing elasto-plastic deformations and stresses.

Slit locations and shapes are similar to those in Target E collimator KHE2. In Figure 3.1.81 and Figure 3.1.82, the geometry of KHE2 versus the simplified geometry used in structural analysis are compared. The flange is represented by the magenta surface in Figure 3.1.82. Bolts are provisionally located more outwards in the ANSYS mechanical geometry already accounting for possible redundant thermocouples installation.

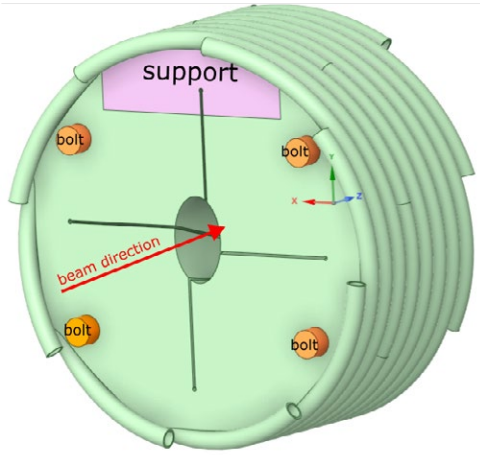

Figure 3.1.82: KHH1 collimator simplified geometry for structural analysis. Magenta surface represents the flange from Figure 3.1.81.

3.1.6.3.2 Materials

Material definitions are the same as for the thermal analysis with the addition of mechanical properties such as tensile yield strength, tensile ultimate strength, isotropic elasticity and multilinear isotropic hardening to account for plasticity. All mechanical properties have constant values except for the hardening, which has been evaluated at 22 °C and 100 °C from 0 [m/m] to 0.074 [m/m] as in [8] [9].

3.1.6.3.3 Physical model and numerical implementation

Simulation results are obtained for a steady-state solution with fixed supports on each inlet and outlet faces of the pipes, frictionless support on the back face of the second disk (structural symmetry) and on the front face at the flange location.

Bolts are modelled with simple geometry without bold pre-tensions because the main regions of interest are close

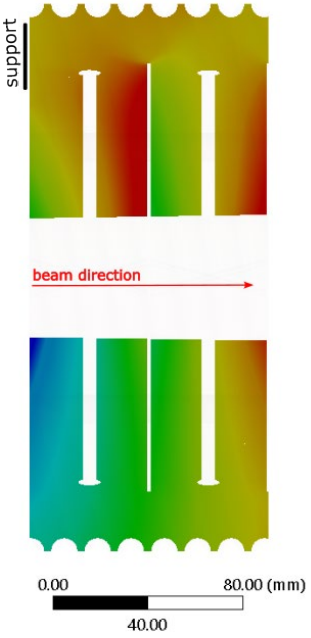

Figure 3.1.83: Directional deformation along beam direction on the vertical plane.

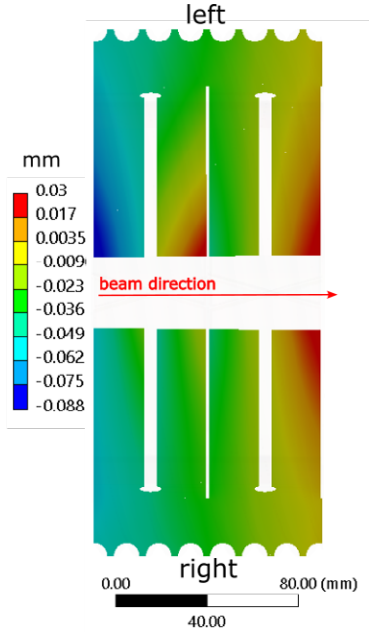

Figure 3.1.84: Directional deformation along beam direction on the horizontal plane.

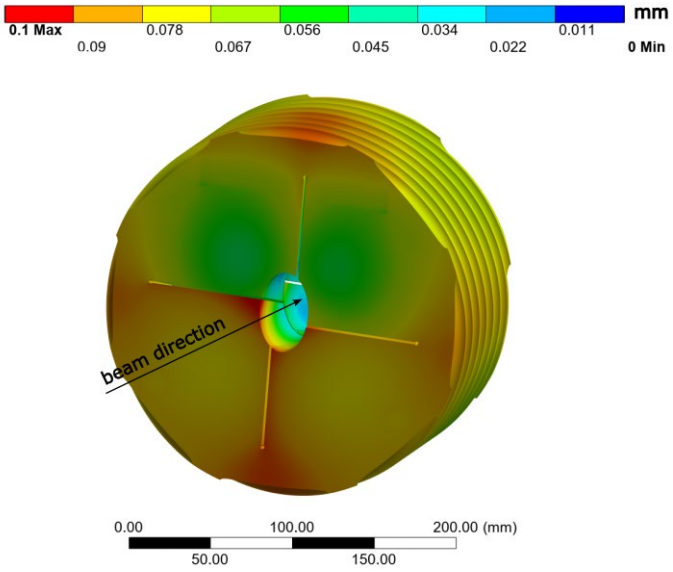

Figure 3.1.85: Total deformation of KHH1.

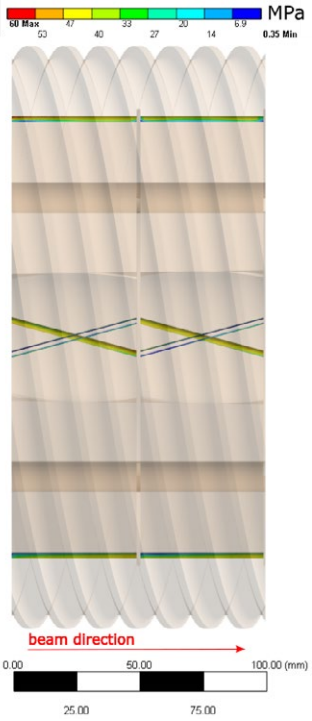

Figure 3.1.88: Stresses at slit locations.

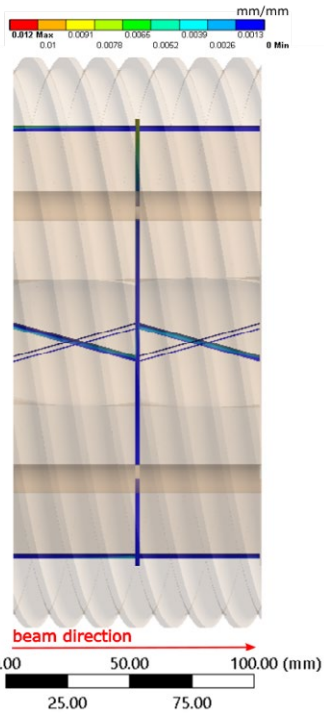

Figure 3.1.89: Plastic deformations at slit locations.

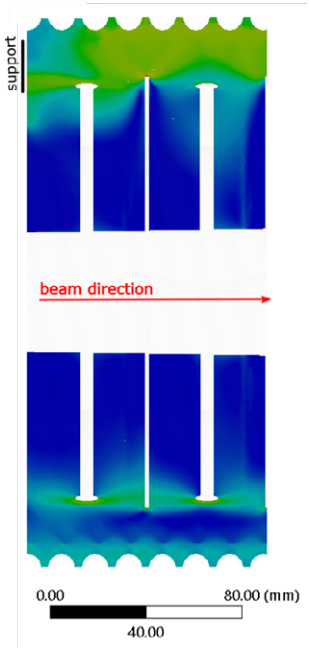

Figure 3.1.86: Stress along beam direction on the vertical plane.

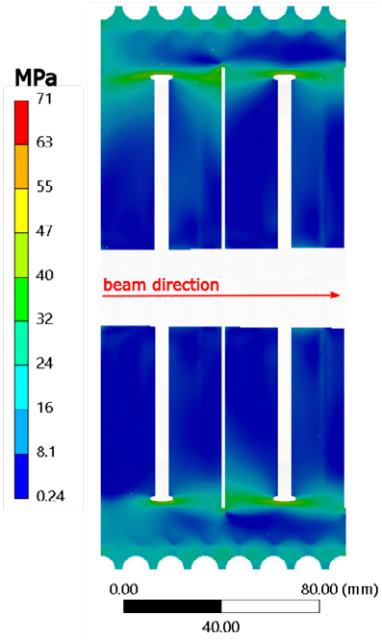

Figure 3.1.87: Stress along beam direction on the horizontal plane.

to the apertures (maximum power deposition) and at slit locations. Furthermore, the technology of fastening and brazing of collimators is well established at PSI and already implemented to other collimators with higher power deposition (KHE2 about 100 kW). A pressure test of 28 bar, 30 min is also applied on the internal surfaces of the pipes.

3.1.6.3.4 Structural results

One of the mechanical requirements is to ensure that all slits remain open during operation at 3 mA proton beam current. Slits will remain open since the maximum perpendicular deformation between the two opposite sides of each slit is at most about 0.08 mm, whereas the gap distance is 1.5 mm. In Figure 3.1.83 and Figure 3.1.84 the directional deformations along the beam direction (Z axis) on the horizontal and perpendicular planes passing through the geometrical center of KHH1 are displayed. Only the body of KHH1 is considered where the slits are located. In the vertical plane (Figure 3.1.83), the presence of the slits causes an asymmetric behavior by preventing perpendicular expansion of the material. Consequently, higher stresses are produced mainly at the slit location between disks, see Figure 3.1.86. On the horizontal plane, directional deformations along Z are also quite small with an absolute maximum value of about 0.09 mm, Figure 3.1.87. The different deformations between left and right parts are due to the fact that slits are not symmetrically distributed, and they cut the body at different angles.

The maximum value of the total deformation in KHH1 body is about 0.1 mm located at the very front of KHH1, see Figure 3.1.85.

The higher stresses of KHH1 body are generally located at slit locations and in the vertical plane, see Figure 3.1.86, a value of 71 MPa is reached at the slit between the disks (maximum stress in full KHH1 body). The yield strength for unirradiated OFHC is about 56 MPa, therefore a certain degree of plastic deformation is expected. In Figure 3.1.87, the stress on the horizontal plane is represented showing maximum values close to the slit locations.

Plastic deformations are expected at each slit location since the local stress exceed the yield point of elastic limit, see Figure 3.1.88 for stresses and Figure 3.1.89 for plastic defor-

N°	Requirement	Simulation results
S1	max (ε_{pl}) < 2%	0.012% << 2%
S2	max (σ_{eq}) < σ_U	71 MPa < 180 MPa
S3	$\Delta l < {}^{d_{slits}}/_{2}$	0.08 mm << 0.75 mm

Table 3.1.18: Requirements vs simulation results comparison.

mations. Nevertheless, plastic deformations remain quite low with a maximum value of 0.012 % well below the requirement for structural integrity.

In Figure 3.1.90 the present design of KHH1 is shown along with thermocouples, actual geometry of cooling pipes, supporting elements, and screws. The slit tip diameters have been increased from 2.5 mm to 4 mm to reduce plastic deformations. Slits through the disks have been rotated by 45° to follow the direction of the aperture foils, not shown in the figure.

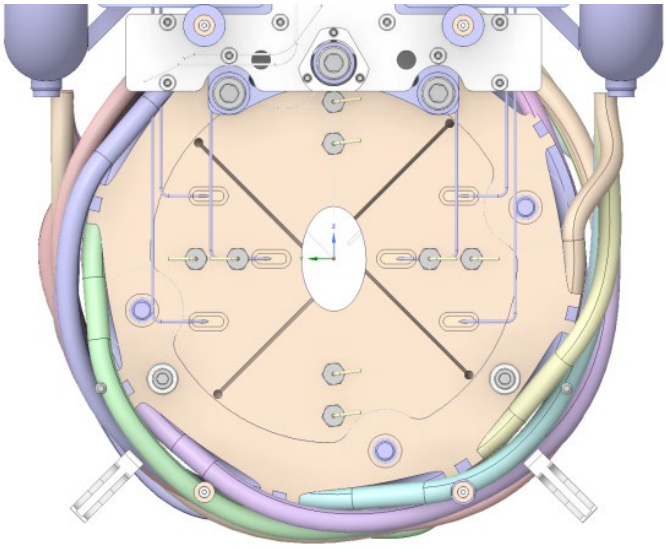

Figure 3.1.90: Present KHH1 design.

3.1.6.4 Conclusions

Thermal simulations of KHH1 have been performed on the geometry optimized with respect to power deposition as in [3]. The maximum temperature of about 120 °C is far below the safety limit of about half melting point temperature for OFHC in Kelvin, i.e. 405 °C. The pressure drop in the stainless steel 316L pipes with 15 µm roughness is only about 0.17 bar. Subsequently, the KHH1 geometry was optimized during the structural analysis to characterize deformation to minimize plastic deformations, which remain well below the accepted limit of 2%.

3.1.6.5 Temperature sensors

As for all other HIPA collimators, KHH1 and KHH2 will be equipped with temperature sensors. Monitoring the collimators temperature will provide important information during beam commissioning and setup. Moreover, the collected data can be employed to validate the simulation results. It is foreseen to install 16 thermocouples (TCs) for each collimator employing the same scheme for KHH1 and KHH2. Six TCs (TC1-6) will be installed on the front face of the first collimator disk as shown on the left side of Figure 3.1.91. TC1-6 are called “outer TCs” since they will be screwed on the surface of the copper body. Eight more TCs (TC7-14) will be still located in the first collimator disc, however not on the upstream face but rather 30 mm deeper into the copper body. For this reason, TC7-14 are called “inner TCs”. Two more TCs (TCL1-2), called “lateral TCs”, will be installed in the 3rd and 4th disc respectively, as

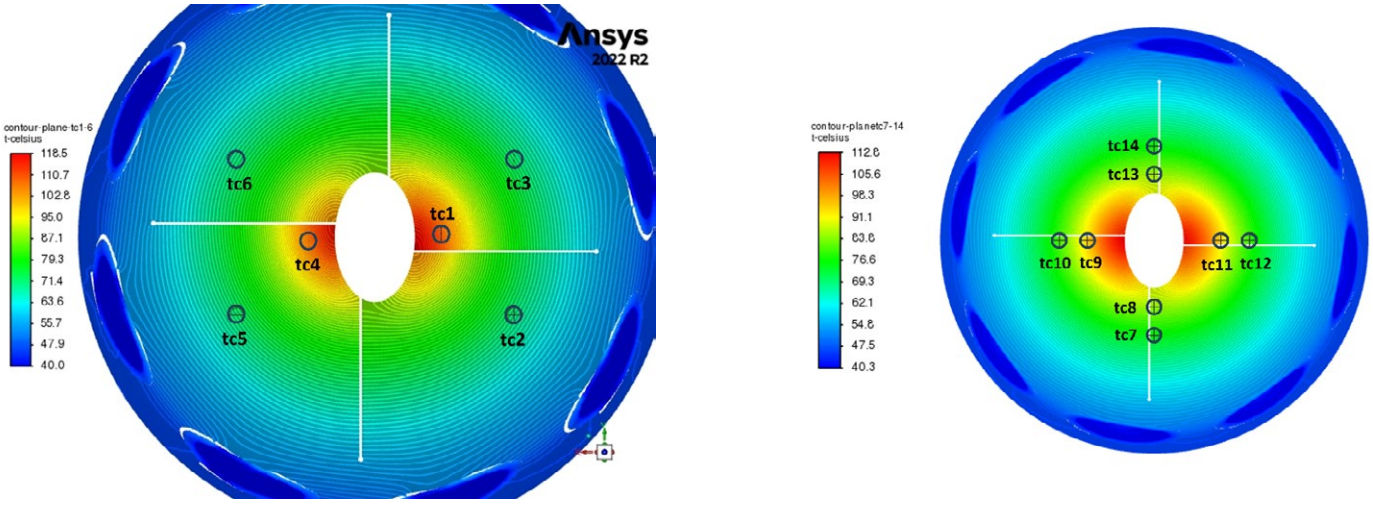

Figure 3.1.91: Location of the outer (left) and inner (right) thermocouples laid on the simulated temperature map of KHH1. Note that the orientation of the four slits will be turned by 45° with respect to this picture, which might slightly change the temperature distribution.

depicted in Figure 3.1.92. Table 3.1.19 lists all KHH1 TCs along with their expected temperature for beam currents of 2.2 and 3.0 mA. No correspondent temperature values are available for KHH2 since no simulation was performed for this collimator because of the much lower power deposition.

3.1.6.6 KHH1 cooling plate

Cooling plates are responsible for absorbing the scattered particles from collimators and cooling the lower part of the collimator inserts, see Figure 3.1.93. Since the deposited power for KHH2 is much lower than the one for KHH1, thermal simulations were performed for the cooling plate of KHH1 only.

3.1.6.6.1 Cooling plate geometry

The geometry used in the thermal simulation comprises only the cooling plate with stainless steel pipe and it was simplified removing holes and screws. The bottom face of the original cooling plate geometry holding the steel pipe with fins open is shown in Figure 3.1.94, whereas Figure 3.1.95 shows the simplified geometry with fins closed. The pipe diameter is 8 mm.

3.1.6.6.2 Materials

The body of the cooling plate is made of OFHC whereas the cooling pipe is made of stainless steel 316L. All material properties used in the thermal simulations are for non-irradiated

TC Location	Expected Temperature at 2. mA (°C)	Expected Temperature at 3.0 mA (°C)
TC1	90.9	109.4
TC2	62.9	71.2
TC3	63.8	72.5
TC4	89.3	107.2
TC5	63.3	71.7
TC6	62.6	70.8
TC7	66.4	76
TC8	73.0	85
TC9	79.6	94
TC10	69.3	80
TC11	80.3	95
TC12	70.1	81
TC13	73.0	85
TC14	66.4	76
TCL1	65.9	75.3
TCL2	62.4	70.6

Table 3.1.19: List of all TCs of KHH1 together with the from simulation expected temperatures at 2.2 and 3.0 mA.

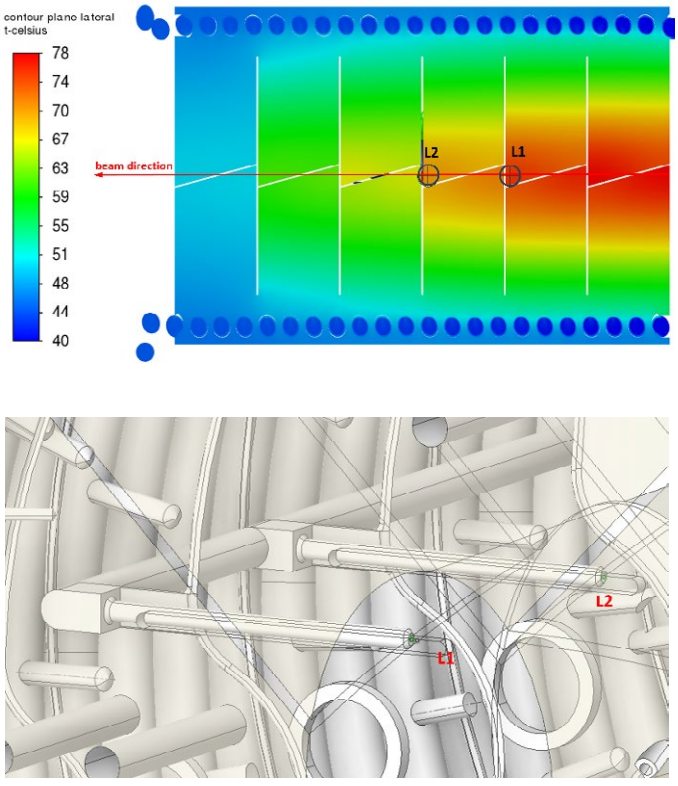

Figure 3.1.92: Location of the lateral thermocouples in KHH1 in the simulated temperature map (top) as well as in the CAD model (below).

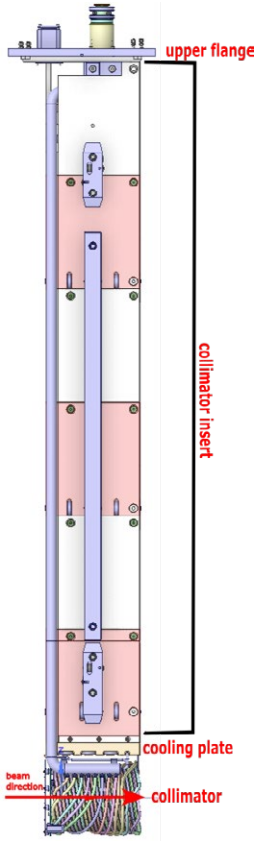

Figure 3.1.93: Lateral view of KHH1 insert, cooling plate and KHH1 collimator.

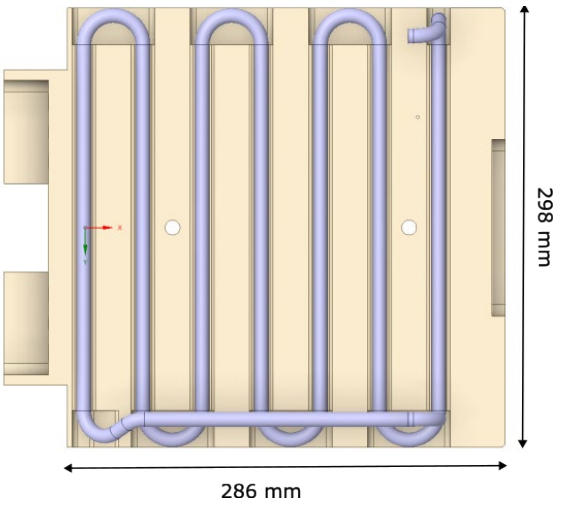

Figure 3.1.94: Bottom face of the original KHH1 cooling plate geometry showing stainless steel 316L cooling pipe, in violet, with fins open.

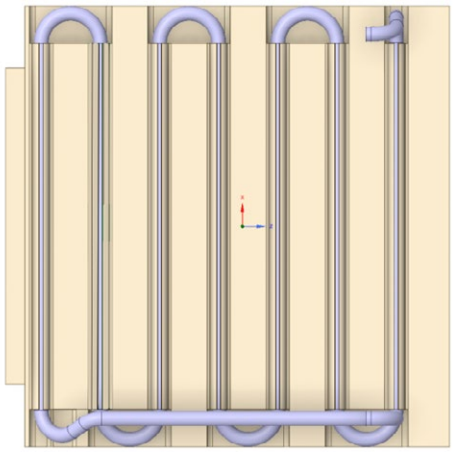

Figure 3.1.95: Bottom face of the simplified KHH1 cooling plate geometry showing stainless steel 316L cooling pipe, in violet, with fins closed.

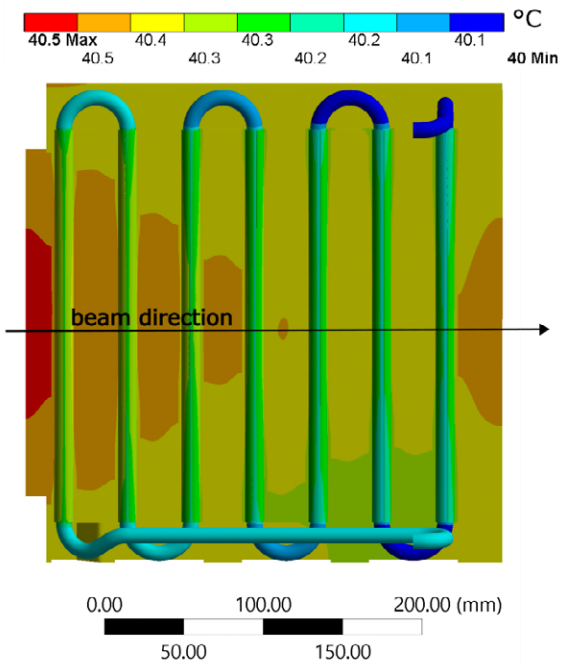

Figure 3.1.96: Temperature distribution at the bottom face of the cooling plate. The proton beam direction is also shown.

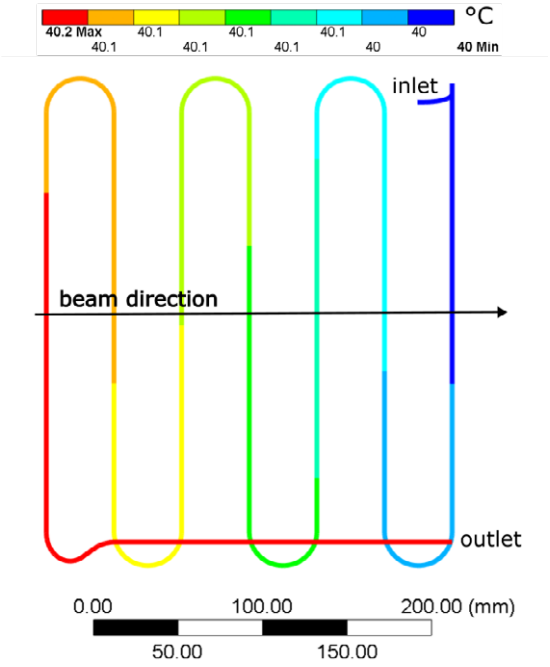

Figure 3.1.97: Temperature distribution in the coolant water from inlet to outlet. The proton beam direction is also shown.

virgin materials [8] [9]. The OFHC mass density was assumed to have a constant value of 8'940 kg m^{-3}. Isotropic thermal conductivity and specific heat capacity at constant pressure have a temperature-dependent behavior. Values originate from an experimental investigation performed at PSI and a survey of literature [10]. Pipes are made of stainless steel 316L and material data are taken from GRANTA MDS material database [11]. Constant fluid properties for the water are implemented.

3.1.6.6.3 Power deposition

Monte Carlo calculations for the power depositions in KHH1 and corresponding cooling plate were performed using BDSIM software package [2] for a proton beam of 3 mA. The cooling plate geometry used in BDSIM calculation is a full block of OFHC, whereas the real cooling plate geometry encompasses pipes, slits, holes, and screws. The calculated power deposition via MC sums up to about 80 W. Since the ANSYS simplified geometry still have cavities and pipe, a constant rescaling factor was used on the top of BDSIM power deposition giving a total value of the imported power of about 70 W.

3.1.6.6.4 Physical model and numerical implementation

The thermal simulation consists of a conjugate heat transfer analysis with water as coolant fluid. The contact between

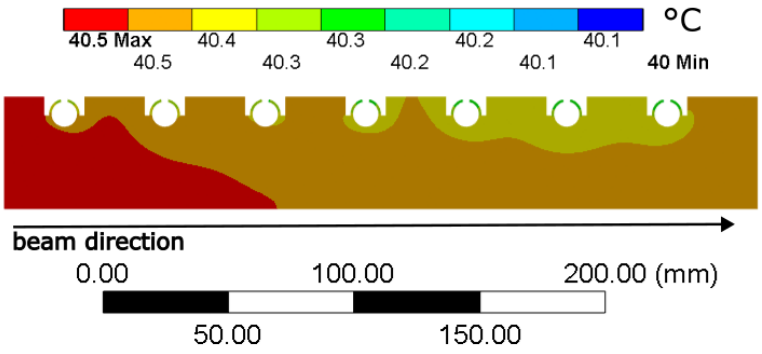

Figure 3.1.98: Temperature distribution on the middle plane cross section of the cooling plate.

stainless steel pipe and cooling plate body is considered perfect. The inlet water temperature is set to 40 °C with an inlet mass flow rate of 0.1 kg/s, which gives an entry speed of 2 m/s. The heat transfer from the cooling plate body to the coolant water through the pipe has a constant heat transfer coefficient of about 0.012 W/mm²C. Zero-gauge pressure outlet was implemented and all outer solid surfaces are considered adiabatic (worst case scenario). Since the deposited power is quite low, the heat transfer simulation between the coolant fluid and the solid body was performed with a special mechanical mesh element, FLUID116, instead of performing a fluid dynamics simulation. FLUID116 elements solve the Bernoulli equation for average properties, and they can reduce the computational time by several orders of magnitude. The solid mesh of the pipes has 5 elements through the pipe thickness to capture the temperature gradient well and a total of 224'675 elements. The cooling plate body has 988'585 solid elements.

3.1.6.6.5 Cooling plate thermal results

In Figure 3.1.96 temperature values are displayed on the bottom face of the cooling plate. The overall maximum temperature reaches 40.5 °C. The temperature distribution in the coolant water is presented in Figure 3.1.97 showing a ΔT of 0.2 °C from inlet to outlet. It is possible to calculate the average ΔT from inlet to outlet at steady-state analytically knowing the water mass flow rate, the water heat capacity, and the deposited power [14]:

$$Q = \dot{m}\, C_p\, (T_{outlet} - T_{inlet})$$

This simple formula gives a temperature difference form inlet to outlet of about 0.16 °C, in agreement with ANSYS calculations.

In Figure 3.1.98 the temperature distribution on the middle plane cross section of the cooling plate is represented. The region of maximum temperature distribution quickly decays along the beam direction.

3.1.6.6.6 Conclusions

Cooling plates are necessary for cooling components of collimator inserts since thermal dissipation by conduction is relatively low due to small contact surfaces between inserts and surrounding elements. Moreover, inserts are not foreseen to be replaced for the expected lifetime of the collimators (more than 30 years) and a cooling concept is then needed to prevent excessive thermal expansion for the guiding system.

3.1.6.7 Terms and abbreviations

OFHC – Oxygen Free High Conductivity Copper
SST – Shear Stress Transport model

3.1.7 Target H temperature monitoring system

The development of the Target H station presents an opportunity to include a temperature monitoring system that will:

- Ensure the integrity of the target, preventing undetected failures.
- Support the study of radiation damage and thermal conductivity loss.
- Validate numerical simulations for thermal and structural behaviour.

A comparable IR monitoring system at J-PARC [15] demonstrated successful temperature monitoring of a muon production target under proton irradiation. The design uses a gold-coated mirror, IR cameras with high resolution, and robust shielding. Lessons from this system influence the proposed design for Target H. The key requirements include:

- An infrared camera: Must operate across a temperature range of 300 °C–1700 °C with ±5% accuracy, 1 mm/pixel spatial resolution, and 24 frames per second minimum.
- Optical components: High IR reflectance/transmittance for mirrors (gold-coated stainless steel) and windows (ZnSe). Germanium lenses.
- Mechanical design: Stable, adjustable, and maintenance-friendly mounts.
- Reflectivity monitoring system: Must include a system to monitor yearly the mirror's reflectivity evolution due to possible graphite deposition.

Ray tracing simulations were performed using ANSYS SPEOS and yielded results meeting the field of view requirement, see Figure 3.1.99–Figure 3.1.101.

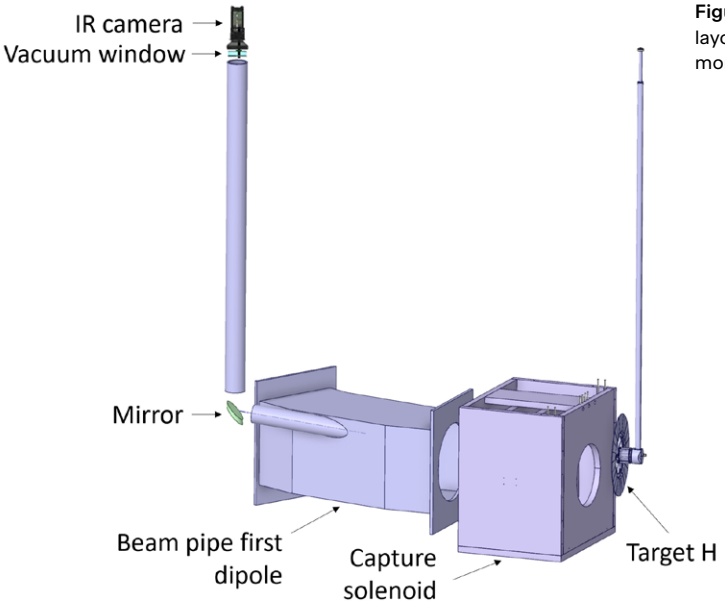

Figure 3.1.99: Basic design layout of the temperature monitoring system.

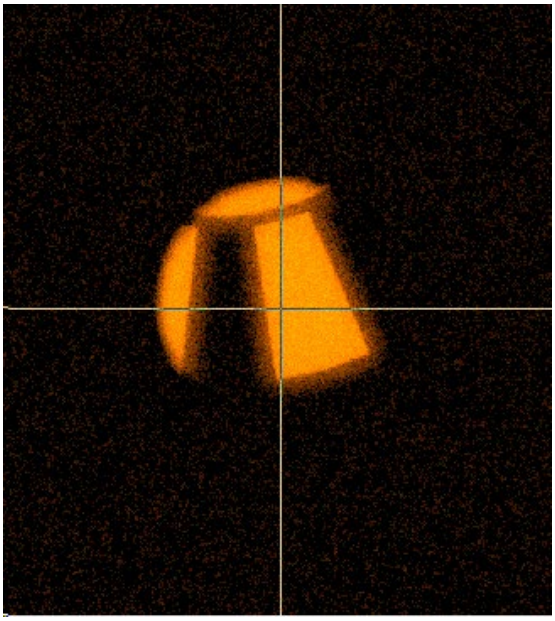

Figure 3.1.100: Irradiance sensor view of the ANSYS SPEOS simulation

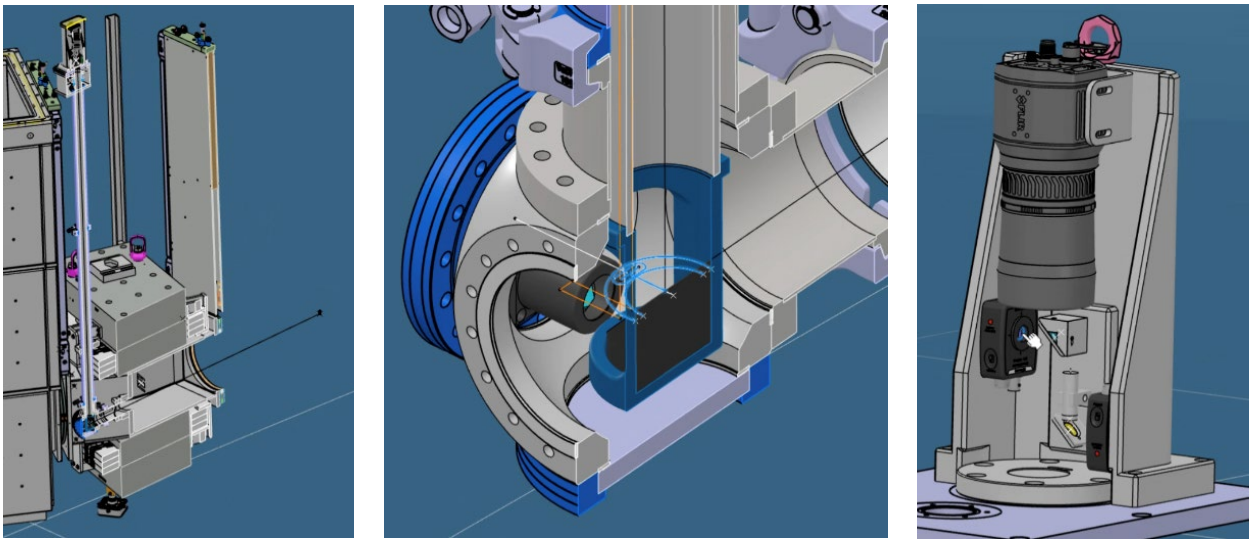

Figure 3.1.101: CAD view of the proposed location behind the first dipole magnet (left) and the camera, mirror, reflector (center) and laser system for reflectivity monitoring (right).

3.1.8 References

[1] D. Kiselev et al., "The PSI Meson Target facility and its upgrade IMPACT-HIMB," in *INTDS2022 30th conf. Int. Nucl. Target Develop. Soc.*, PSI, Villigen, 2023.

[2] L. J. Nevay et al., "BDSIM: An accelerator tracking code with particle–matter interactions," *Comput. Phys. Commun.*, vol. 252, p. 107200, 2020.

[3] R. Eichler, D. Kiselev, A. Knecht, A. Koschik, N. van der Meulen and e. al., "IMPACT conceptual design report.," PSI Bericht, Report No.: 22-01, 2022.

[4] W. Doornenbal, "Experimental thermal analysis of the emissivity of different materials and coatings," 2024.

[5] J. Snuverink, *Private communication*.

[6] T. Reiss, "Simulation of a beam rotation system for a spallation source.," *Physical Review Special Topics-Accelerators and Beams*, vol. 18, no. 4, p. 044701, 2015.

[7] SGL GROUP, *SIGRAFINE R6510 MATERIAL DATA*.

[8] R. P. Martinie, "Cooling and thermo-mechanical design of TATTOOS Beam Dump," PSI, TM-81-23-1283.

[9] R. Martinie et al., "Cooling and Thermomechanical Studies for the IMPACT TATTOOS Beam Dump Design," in *IPAC23*, Venice, 2023.

[10] Deutsches Kupferinstitut, Cu-OFE, 2005.

[11] ANSYS GRANTA, "https://www.ansys.com/products/materials," ANSYS. [Online].

[12] ANSYS FLUENT, "https://www.ansys.com/products/fluids/ansys-fluent," ANSYS. [Online].

[13] ANSYS MECHANICAL, "https://www.ansys.com/products/structures/ansys-mechanical," ANSYS. [Online].

[14] Y. A. Cengel, Heat Transfer A Practical Approach, McGraw-Hill, 2003.

[15] S. Matoba et al., "Development of monitoring system for the muon rotating target at J-PARC using an infrared camera", *J. Phys. Conf. Ser. 2462 (2023) 1, 012031*, DOI: 10.1088/1742-6596/2462/1/012031.

3.2 Magnets

3.2.1 Introduction

3.2.1.1 Background information

The PSI proton accelerator has been in continuous operation since 1972. Both within the main beamline as well as in the secondary beamlines, a total of 350 magnets are currently in operation, including 70 radiation hard magnets.

Thankfully the experience gained in 50 years of operation has been passed down to the engineers presently responsible for magnet concepts and designs. This knowledge has been incorporated in the design of the magnets for the IMPACT project. Both field calculations and mechanical design were performed by PSI staff engineers, and a detailed 3D model of each magnet and a corresponding specification will be submitted to the manufacturer.

3.2.1.2 Challenges

- While classic iron dominated magnets with epoxy coils are mostly state-of-the-art for the suppliers, the number of manufacturers of radiation hard coils is very limited and procurement has proven to be difficult.
- The other main challenge is the tight schedule, since the lead times for magnet production are typically substantial and must be taken into account regarding the main project schedule.

3.2.2 Radiation hard magnets

3.2.2.1 Introduction radiation hard coil

For high radiation environments, PSI has defined a few design principles that have proven to be successful in several decades of operation:

1. No organic materials shall be used
2. The cooling water should not be in contact with the copper conductor (or any other copper material)

Using argument 1, the only available concept for a copper conductor is Mineral Insulated Cable (MIC). Furthermore, the coil body, all connections and all insulation materials must be made of either metal or ceramic. This type of conductor was initially produced by a company named Pyrotenax. Throughout the document, we will use “Pyrotenax” to designate MIC designs and coils. Figure 3.2.1 reports the cross-section of typical MIC cable.

Argument 2 refers to the fact that in a high radiation environment, the water can be ionized and attack the copper surface, leading to substantial corrosion and ultimately to the failure of the magnet. In addition, depending on the acidity of the water, the copper can be further attacked. There are several instances at PSI where long term corrosion has led to a magnet failure, resulting in the replacement of the damaged coil with a new unit. However, the concept of coil replacement is not useful for radiation hard magnets, since even after cooldown the remanent dose is so high that working on the magnet in person is not possible. Thus, contact between copper and water is completely avoided.

Therefore, we have defined a coil cross section that consists of two double pancakes of solid MIC conductor (see Figure 3.2.2); between the two pancakes there is a cooling layer containing stainless steel water pipes and copper inserts for better heat transmission. The whole coil unit is then potted in soft solder to improve both mechanical stability and heat transfer.

Using this concept, a larger coil can be divided into several units, the main advantage being the fact that given the tendency of the MIC cable to be damaged during production, the loss of material and time is reduced with respect to the concept of casting a full coil in one piece. Also, specifically for the solenoids, handling and assembly is easier with respect to having a large and very heavy coil.

Our experience has shown great success of this concept. From the beginning, the concept was integrated into the geometry of the calculation models. One area of concern was the

Figure 3.2.1:
MIC cross section

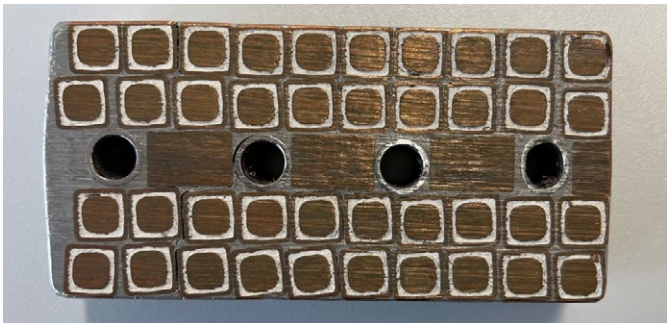

Figure 3.2.2: cross section of coil unit

cooling capacity of the water circuits since specifically the capture solenoid operates continuously at very high currents.

3.2.2.2 WSC – Capture Solenoid

The capture solenoid proved to be the most challenging magnet of the new beamlines. It has the highest radiation load and the highest operating current of all magnets with a peak of about 14.4 A/mm^2 at the nominal cross-section. However, due to manufacturing process, the cross-section might be lower at certain locations. In this case the current density can reach up to 15.5 A/mm^2.

3.2.2.2.1 Mechanical concept

Using the successful PSI concept of double pancake solenoid coil units, a total of nine units were assembled in the model to create a 0.716 m long solenoid with an aperture of 500 mm. The coils are enclosed in an iron yoke. Several geometric features were then defined to fulfill the field requirements. The magnet is inserted directly inside the vacuum chamber to maximize the capture efficiency, and it will operate in vacuum. The integration into the vacuum chamber presented a challenge in terms of connections; this topic is described in Sections 3.9.3 and 3.9.4.

3.2.2.2.2 Field requirements

The capture efficiency can be maximized by inserting the target inside the capture solenoid. However, given the rigorous constraints on the downstream target station E and neutron spallation source SINQ, minimal modifications to the main proton beamline are possible. For this reason, as well as optimal muon production, two identical capture solenoids are placed on either side and as close as possible to the target rather than around it. The magnet operates in vacuum for the same reason. The physical requirements for this design are:

- Overall length as short as possible;
- Produce specific longitudinal gradient field profile;
- Reduced fringe field.

A transmission study of solenoid length versus peak magnetic field strength, showed a 19 % enhancement in absolute transmission with respect to the target comparing a long version with a short one, for the same central magnetic field strength. This may be attributed to the enhanced transmission of divergent particles passing the shorter version in a large phase-space beam. Therefore, the design must provide a very compact magnet, also due to the weight limit. In particular, the crane operates with a maximum weight of 60 t, which must include the magnet, the radiation shielding, and the exchange flask needed for screening the radiation emitted from the magnet if handling is required. The field profile is designed to have a high field at the entrance, maximizing muon capture, and a relatively low field at the exit to ensure proper beam focusing into the next subsequent component. As a result, the capture solenoid exhibits a longitudinal gradient. In particular, the solenoids are optimized for a surface muon momentum distribution peaked at 28 MeV/c. Moreover, the design must assure a limited influence of the fringe field of the capture solenoids to reduce interference on the main proton beam.

During optimization, the following field requirements were found to improve Muon capture:

- A field gradient over the length of the solenoid resulting in three coil packages separated by iron plates;
- A reduced front aperture of 400mm with staggered coils in the first coil package.

The resulting geometric features were integrated into the mechanical model. The upstream iron plate between the target and the coils is called ‘Mirror plate’. It has two main roles: reducing the fringe field of the capture solenoid at the target location in close proximity and protecting the coils form the heat load coming from the target. To this end, the front mirror plate is water cooled.

The first coil is located at 25 cm with respect to the target.

In order to be able to achieve the longitudinal gradient profile the three blocks of coils are fed with different power supplies. The currents flow with different magnitudes in each block of coils (618 A, 20 A, 507 A). However, this was not enough, and two iron blocks were also needed to separate the coils in order to have the required field drop. The longitudinal cross-section of the magnet is shown in Figure 3.2.3.

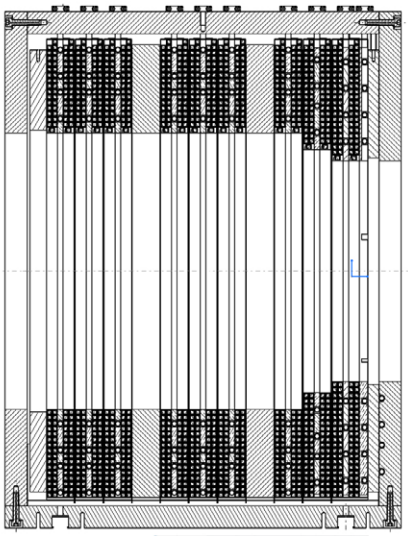

Figure 3.2.3: capture solenoid longitudinal cross section

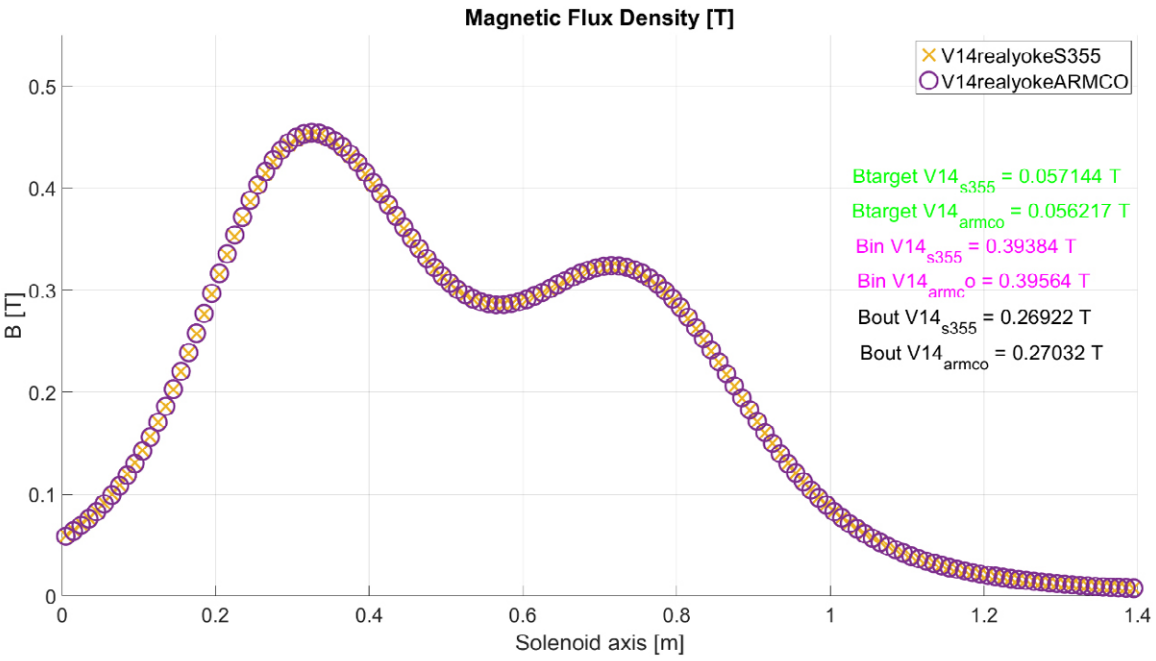

Figure 3.2.4: Axial field of the solenoid for two different iron: S355 and ARMCO.

The field needs to be high at the entrance to capture muons, average at the center for transmission and lower at the exit for having the right focusing into the next magnetic component, as illustrated by the field profile on the axis plotted in Figure 3.2.4. Moreover, the fringe field at the target location needs to be as low as possible, but at the same time a higher field between the target and the solenoid helps improving the capture efficiency. Therefore, the air gap between the first coil and the iron yoke mirror plate (0.035 m), and the mirror plate thickness (0.04 m) were optimized in order to maximize the capture.

3.2.2.2.3 Iron yoke material

Another crucial parameter for the design is the choice of the iron quality. Two types of iron were used and compared to assess the influence of the BH-curve (Induced magnetic flux density B [T] vs applied magnetic field H [A/m]) on the solenoid performance. Figure 3.2.5 reports the BH-curve for the higher quality iron ARMCO (blue) and the lower and cheaper carbon steel S355 in red (widely available on the market).

With respect to the carbon steel, ARMCO is characterized by a higher magnetic saturation and lower magnetic hysteresis. This means that the iron can provide a higher field

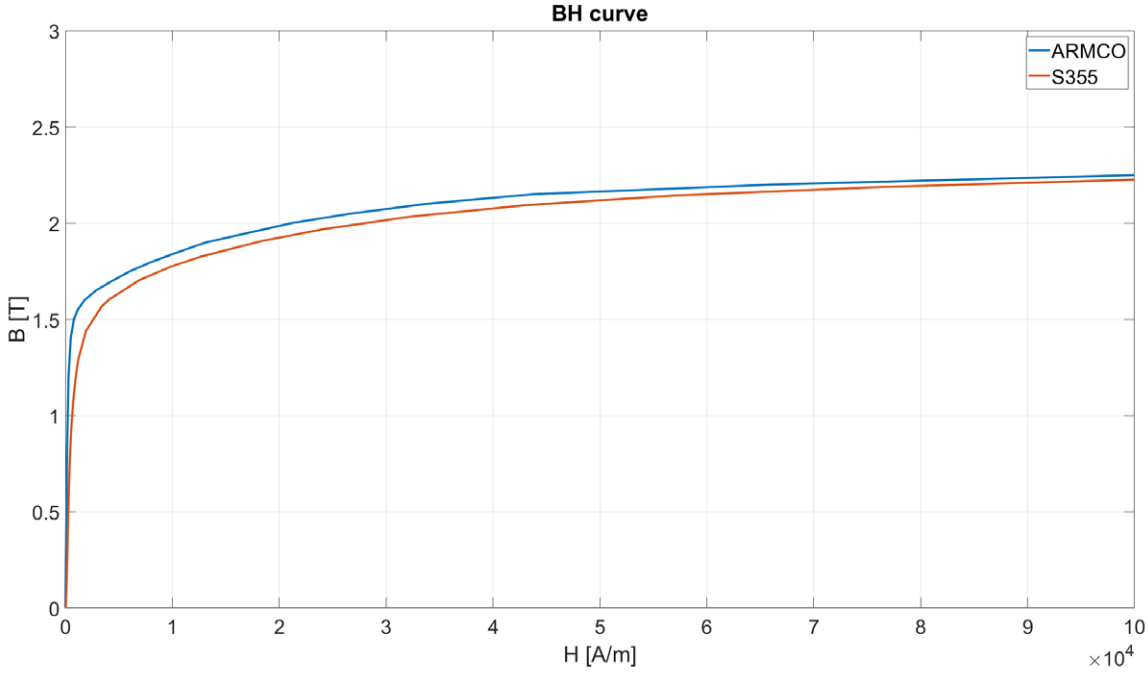

Figure 3.2.5: BH-curves for ARMCO and Carbon Steel S355

for the same current excitation in the case of the ARMCO, because the saturation plateau is reached for higher induced magnetic flux densities. Figure 3.2.4 also shows the comparison between the use of the two different materials. The outcome of this study proved that it is not necessary to work with ARMCO, since the axial field variation inside the magnet is below 0.5 % between the two simulations and the fringe field is 1.5 % higher in the case of S355.

Figure 3.2.6: Field map of the magnetic flux density [T] distribution inside the iron yoke of the capture solenoid performed with COMSOL Multiphysics.

3.2.2.2.4 Key data and requirements WSC21

For MuH2 and MuH3, a total of 2 WSC magnets are required. This paragraph reports the specifications for WSC21, but the same applies to WSC31.

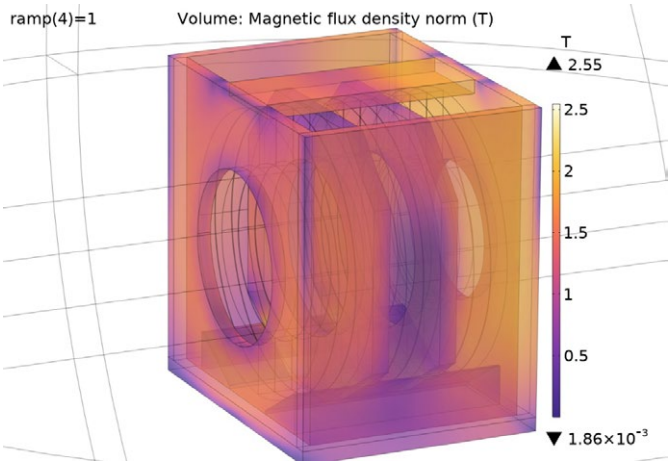

Figure 3.2.6 shows the induced magnetic flux density 3D map inside the iron yoke for the low carbon steel S355.

Basic Parameters WSC21

Main function	Muon, or secondary particle capture element closest to Target H
Dimensions (mm)	716 × 910 × 1532 mm Yoke dimensions 716 × 910 × 935
Material(s)	Magnetic Steel S235 or S355 Mineral-insulated, Radiation-hard Copper Coils + Silver Solder and brazing compound + aluminum fastening plates + ceramic insulators + stainless steel fasteners and water connectors
Weight	4000 [kg]
Most important parts and interfaces (names)	Steel Housing 2× Intermediate Steel Field enhancement Rings 3× coil packages of each 3× coil pancakes Coil pancakes Water cooled coil conductor ends Water cooled iron yoke Temperature sensors on cooling connections and coil body Radiation shielding above the magnet Mechanical interface with exchange flask
Mirror-plates, Coil Dimension & Field Enhancement Rings	• Upstream (US) Mirror-plate (facing Target H) Thickness: 40 mm Aperture: 400 mm Gap to coil Cooling Plate 20 mm • Downstream (DS) Mirror-plate Thickness: 40 mm Aperture: 500 mm Gap to coil 35 mm • Coil Package 1 (US)

	• Cooling Plate attached to Coil 1 thickness 1× 15 mm and Coils 3× 50 mm • Gap between Coils 2 mm *START of Coil 1 MUST be 250 mm +/- 1 mm DS of Target H Centre* Coil1 (US) id: 400 mm od: 820 mm Coil 2 id: 440 mm od: 820 mm Coil 3 id: 500 mm od: 820 mm • Coil Package 2 thickness 3× 50 mm • Gap between coils 2 mm Coil4 (US) id: 500 mm od: 820 mm Coil 5 id: 500 mm od: 820 mm Coil 6 id: 500 mm od: 820 mm • Coil Package 3 (DS) thickness 3× 50 mm • Gap between coils 2 mm Coil7 (US) id: 500 mm od: 820 mm Coil 8 id: 500 mm od: 820 mm Coil 9 id: 500 mm od: 820 mm • 2× Magnet Steel Rings: Thickness: 50 mm Gap to Coils 1 mm Id: 500 mm od: 820 mn
Boundary conditions (constraints)	*START of Coil 1 MUST be 250 mm +/- 1 mm DS of Target H Centre*
Positioning / alignment accuracy	• MIC coil positioning +/- 0.5 [mm] • Magnetic-axis tilt with respect to geometric axis < 2 mr • Adjustable feet
Environment conditions to be considered/ required/specified (temperature, humidity, vacuum, radioactivity, radiation levels, EM fields, vibrations, accidental forces, ...)	• Radiation-harsh Environment, 15.7 [Sv/hr]

Connections / Interfaces / Fabrication

Cooling	• Water-cooling of coils • Radiation cooling (since in vacuum) • 18 loops cooling channels id=8 mm od=10 mm • Flow-rate = 2 m/s • Temperature sensors required • Water flowmeters required • Inlet temperature 40°C • Delta-T 20°C • Volume flow 2.1 l/s • Pressure drop 0.5 bar
Vacuum	Placed in large vacuum tank insert Nominal Pressure < 10^{-5} mb

Power	3 Power Supplies (PS) one for each coil package • All Bipolar switchable PS • Current/voltage monitors • Max. Power (100%) 259 kW • Nominal Power Muons 28 MeV/c 134 kW
Magnetic Field	• Max. Rated Field per coil package 0.45 T • Nominal Surface Muon BFields – Coil package 1 = 0.421 T – Coil package 2 = -0.0012 T – Coil package 3 = 0.277 T
Manufacturing specifications	• Pyrotenax coils • Magnet steel type S235 or S355

Pictures

CAD overview

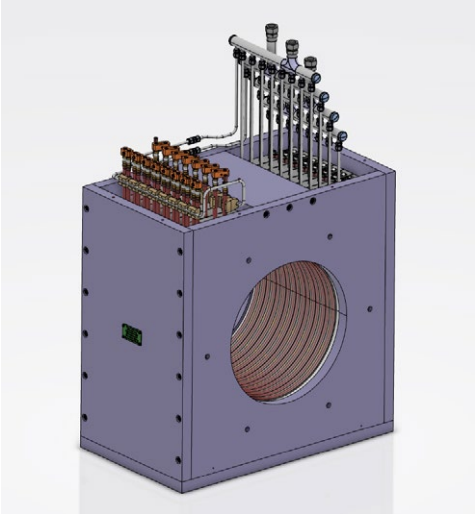

Schematic Layout view

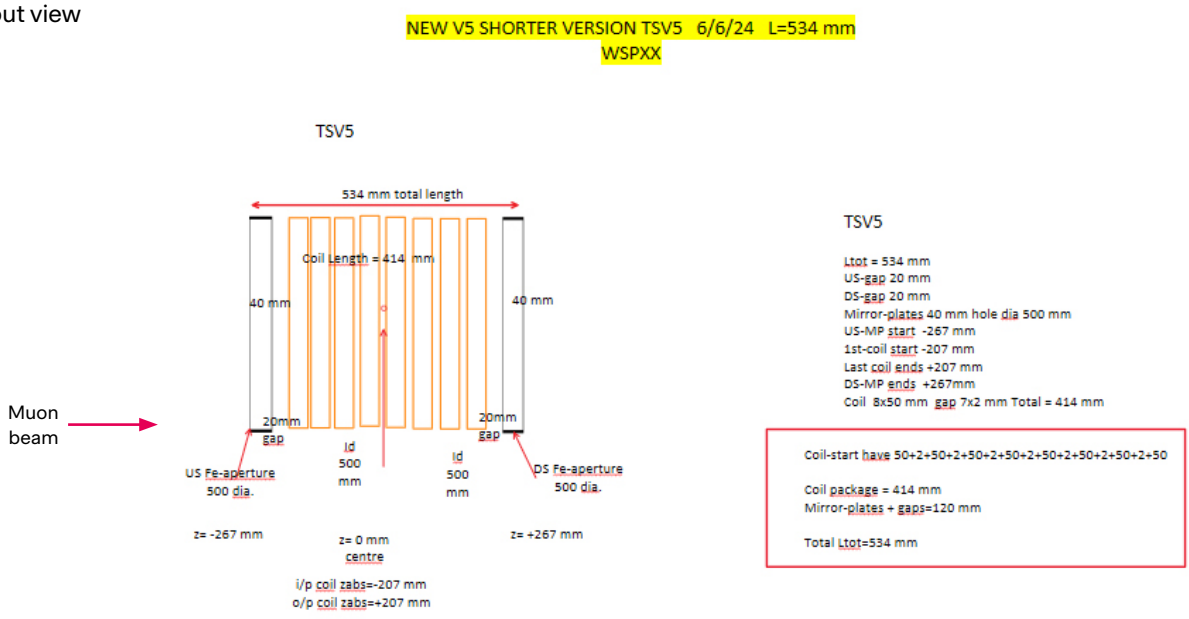

3.2.2.3 WSP – MIC Transport Solenoid

3.2.2.3.1 Conceptual design

Contrary to the capture solenoid, no field gradient was required for the MIC Solenoid WSP, since the main role of the magnet is to focus and transport muons. Therefore, a simple package of eight double pancake units was set into a rectangular yoke. Figure 3.2.7 shows the magnetic flux density distribution at nominal current and the relative material saturation.

3.2.2.3.2 Key data and requirements WSP21

For MuH2 and MuH3, a total of 5 WSP magnets is required. This paragraph reports the specifications for WSP21, but the same applies to WSP22, WSP23, WSP31 and WSP32.

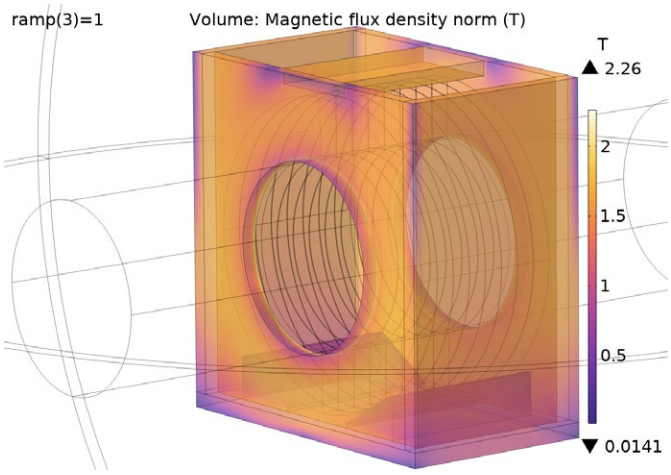

Figure 3.2.7: Field map of the magnetic flux density [T] distribution inside the iron yoke of the MIC transport solenoid performed with COMSOL Multiphysics.

Basic Parameters WSP21

Main function	Muon, or secondary particle Transport element in first straight section after Dipole ASP21
Dimensions (mm)	534 × 910 × 1532 mm Yoke dimensions 534 × 910 × 935 mm
Material(s)	Magnetic Steel S235 or S355 Mineral-insulated, Radiation-hard Copper Coils + Silver Solder and brazing compound + aluminum fastening plates + ceramic insulators + stainless steel fasteners and water connectors
Weight	4000 [kg]
Most important parts and interfaces (names)	Steel Housing 1× coil package of 8x coil pancakes Water cooled coil conductor ends Temperature sensors on cooling connections and coil body Radiation shielding above the magnet Mechanical interface with exchange flask
Mirror-plates, Coil Dimension & Field Enhancement Rings	• Upstream (US) Mirror-plate (facing US) Thickness: 40 mm Aperture: 500 mm Gap to coil: 20 mm • Downstream (DS) Mirror-plate Thickness: 40 mm Aperture: 500 mm Gap to coil 20 mm • Coil Package total length 414 mm Coil1 (US) id: 500 mm od: 820 mm Coil 2 id: 500 mm od: 820 mm Coil 3 id: 500 mm od: 820 mm

	Coil4 id: 500 mm od: 820 mm Coil 5 id: 500 mm od: 820 mm Coil 6 id: 500 mm od: 820 mm Coil7 id: 500 mm od: 820 mm Coil 8 id: 500 mm od: 820 mm Each coil 50 mm long Gaps between Coil 2 mm
Boundary conditions (constraints)	Fit into Vacuum Inserts with Beam-blockers
Positioning / alignment accuracy	• MIC coil positioning +/- 0.5 [mm] • Magnetic-axis tilt with respect to geometric axis < 2 mr • Adjustable feet
Environment conditions	• Radiation-harsh Environment, 2.9 [Sv/hr]

Connections / Interfaces / Fabrication

Cooling	• Water-cooling of coils • Radiation cooling (since in vacuum) • 16 loops cooling channels id=8 mm od=10 mm • Flow-rate = 2 m/s • Temperature sensors required • Water flowmeters required • Inlet temperature 40°C • Delta-T 20°C • Volume flow 2.1 l/s • Pressure drop 0,5 bar
Vacuum	Placed in large vacuum tank inserts • Nominal Pressure < 10-5 mb
Power	1 Power Supply (PS) for coil package • Bipolar switchable PS • Current/voltage monitors • Max. Power (100%) 122 kW • Nominal Power Muons 28 MeV/c 43 kW
Magnetic Field	• Max. Rated Field per coil package 0.45 T • Nominal Surface Muon BField – Coil package = 0.3 T
Manufacturing specifications	• Pyrotenax coils • Magnet steel type S235 or S355

Operation

Expected lifetime	30 years
Spare part policy (redundancies in case of failure)	1 spare for MuH2+MuH3

Pictures

CAD overview

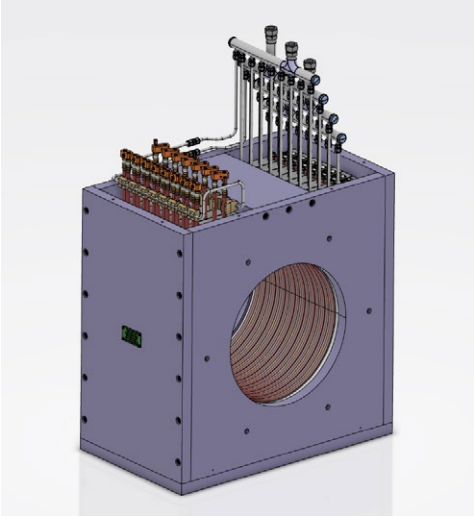

Schematic Layout view

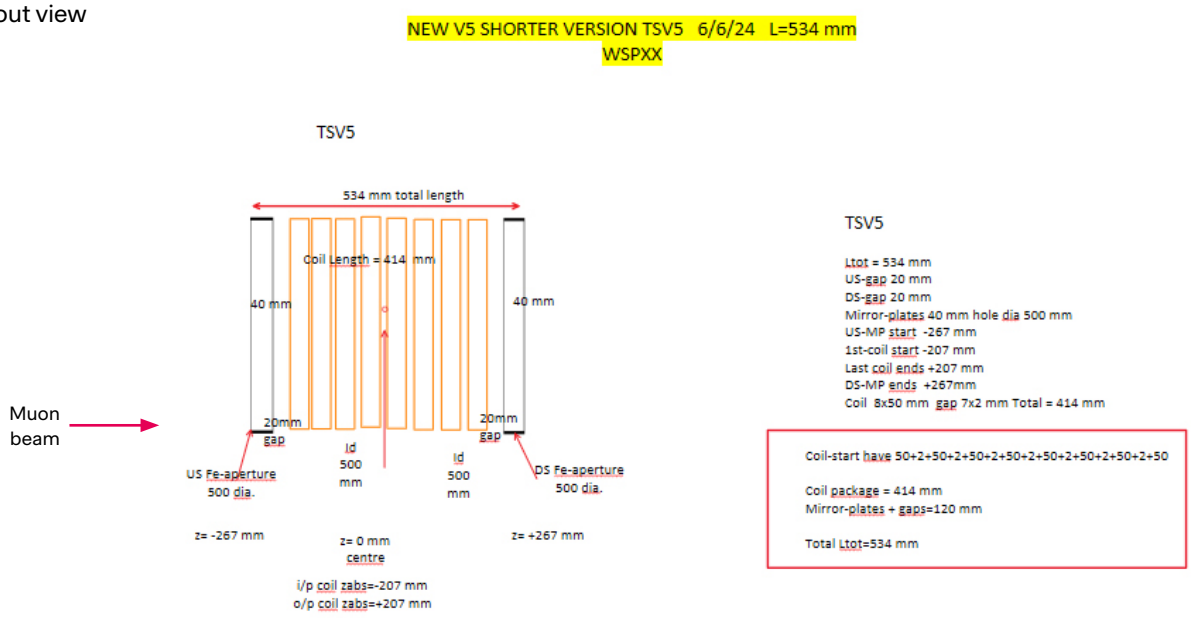

3.2.2.4 ASP – MIC Dipole

3.2.2.4.1 Conceptual Deign

For the MIC dipole, the same concept of coil packages was applied. In total, three packages are stacked and bound by steel bands to form one coil. The yoke and coil geometry are very simple, since the field quality is secondary due to the large aperture.

Figure 3.2.8 reports the magnetic flux density distribution at nominal current for a 35.5 deg bending angle. Except for the yoke corners the yoke is not saturated.

3.2.2.4.2 Key data and requirements ASP21

For MuH2 and MuH3, a total of 2 ASP magnets is required. This paragraph presents the specifications for both ASP21 and ASP31.

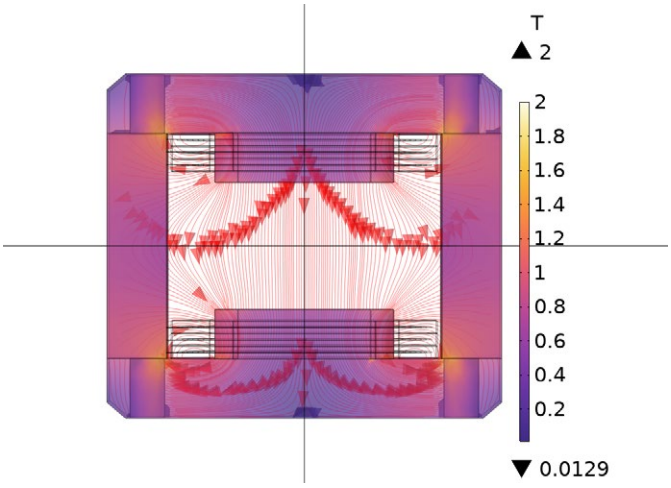

Figure 3.2.8: Field map of the magnetic flux density [T] distribution inside the iron yoke of the MIC dipole performed with COMSOL Multiphysics.

Basic Parameters ASP21

Main function	Radiation hard dipole
Dimensions	1150 × 1910 × 1960 mm 710 × 1700 × 1485 mm
Pole dimension in beam direction	710 mm
Material(s)	Magnetic Steel S235 or S355 Mineral-insulated, Radiation-hard Copper Coils + Silver Solder and brazing compound (MIC) + aluminum fastening plates + ceramic insulators + stainless steel fasteners and water connectors
Weight	12 000 kg
Most important parts and interfaces (names)	Steel Yoke 2× coil packages of each 3× coil pancakes Coil pancakes
Bending angle	36° (ASP21) / 27° (ASP31)
Nominal/maximum field	0.05 (ASP21) / 0.031 (ASP31) / 0.165 T +/- tolerances / uncertainty Maximum from scaling to 80 MeV plus 10 %
Pole gap	550 mm
Field length	1053.5 mm +/- tolerances / uncertainty
Important distances	Gap of 550mm: space for 500mm vacuum chamber
Boundary conditions (constraints)	First dipole after the capture solenoid
Positioning / alignment accuracy	1 mm

Environment conditions to be considered / required / specified (temperature, humidity, vacuum, radioactivity, radiation levels, EM fields, vibrations, accidental forces, ...)	• Radiation-harsh Environment, 15.7 [Sv/hr]

Connections / Interfaces / Fabrication

Cooling water	• Water-cooling of coils • 12 loops cooling channels id=8 mm od=10 mm • Flow-rate = 2 m/s • Temperature sensors required Water flowmeters required
Support structure required for alignment	PSI standard 10 ton feet for alignment
Vacuum chamber	Description, materials, values, ranges
Bipolar power supply	
Diagnostic elements	Temperature sensors (Klixon)

Operation

Expected lifetime	30 years
Spare part policy (redundancies in case of failure)	One complete magnet for two dipoles

Pictures

CAD overview	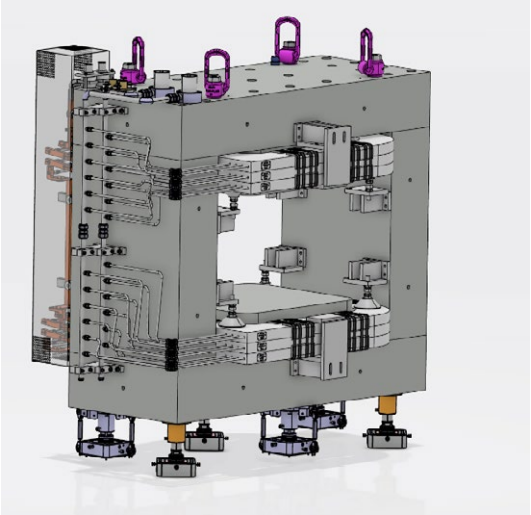

3.2.3 Normal magnets

3.2.3.1 Introduction normal coil

The coils used in the normal magnets are typical state-of-the-art coils. A directly cooled conductor is wrapped in glass fiber and used to wind a coil. The whole unit is then potted in epoxy resin. A typical cross-section is shown in Figure 3.2.9.

In the next paragraphs all epoxy magnets are presented except for the separator described in Chapter 3.8.

3.2.3.2 ASH – HIMB Dipole with Slit

3.2.3.2.1 Conceptual design

Initially, this magnet was a simple square dipole. Due to the limited space in the beamline, it was decided to integrate a slit into the vacuum chamber of the dipole. This in turn required several modifications of the yoke to accommodate the moving parts of the slit perpendicular to the beam direction, as well as the gear drive and motor connection to the service level.

Given the fact that the dipole field is low, it was possible to reduce the cross section of the side yokes to create the necessary space. The side yoke was separated into two side pieces to allow for space in the middle. For the sake of simplicity and reduction of production variations, all three normal dipoles are using the same design even if only two have the slits installed.

Figure 3.2.10 reports the magnetic flux density distribution at nominal current for a 34.4 deg bending angle. Except for the yoke corners the yoke is not saturated.

3.2.3.2.2 Key data and requirements ASH

For MuH2 and MuH3, a total of 3 ASH magnets is required. This paragraph presents the specifications for ASH31 (magnet working without slits), but the same applies to ASH21 and ASH32 (dipoles working with slits).

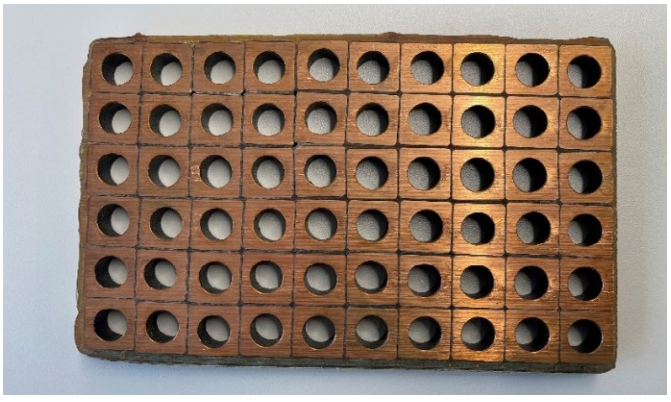

Figure 3.2.9: typical epoxy coil cross section

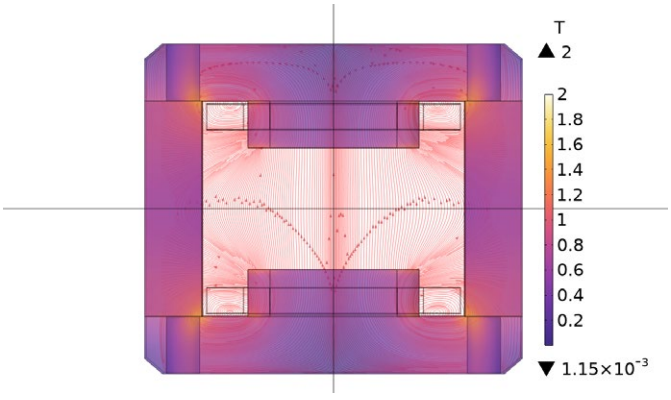

Figure 3.2.10: Field map of the magnetic flux density [T] distribution inside the iron yoke of the dipole performed with COMSOL Multiphysics.

Basic Parameters ASH

Main function	Dipole without slits
Dimensions	1170 × 1942 × 1955 mm Yoke dimensions 710 × 1700 × 1485 mm
Pole dimension in beam direction	710 mm
Material(s)	Magnetic steel S235 or S355 Oxygen-free copper, epoxy impregnated coils Stainless steel, aluminum and G10 parts Beam pipe
Weight	10 000 kg

Most important parts and interfaces (names)	Magnetic steel yoke 2× coil packages of each 5× double pancakes Beam pipe Cooling and power connections

Bending angle	30°
Nominal/maximum field	0.037/0.18 T +/- tolerances / uncertainty Maximum from scaling to 80 MeV plus 10 %
Pole gap	550 mm
Effective field length	1058.55 mm +/- tolerances / uncertainty (from field map)
Important distances	Gap of 550mm: space for 500mm vacuum chamber
Boundary conditions (constraints)	Second dipole in the MuH3 beamline
Positioning / alignment accuracy	1 mm

Connections / Interfaces / Fabrication

Cooling water	• Water-cooling of coils • 5 directly cooled copper conductor circuits id=6 mm • Flow-rate = 1.6 m/s • Pressure drop 8 bar • Volume flow 28 l/min • Temperature sensors required • Water flowmeters required
Support structure required for alignment	PSI standard 10 ton feet for alignment
Vacuum chamber	Description, materials, values, ranges
Bipolar power supply	
Diagnostic elements	Temperature sensors (Klixon)

Operation

Expected lifetime	30 years
Spare part policy (redundancies in case of failure)	One set of spare coils for three dipoles

Pictures

CAD overview

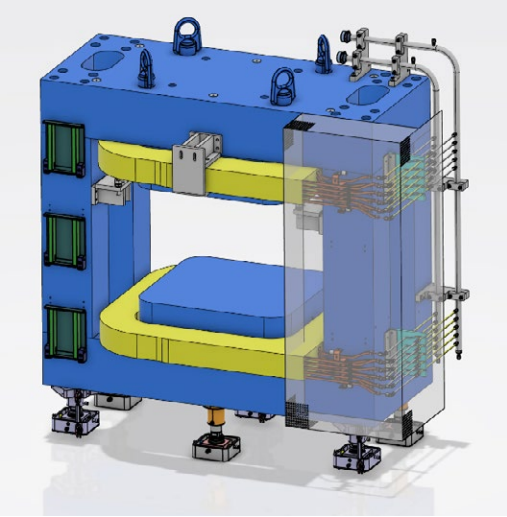

3.2.3.3 WST – Transport Solenoid

3.2.3.3.1 Conceptual design

The solenoid was created using a circular housing with a crosspiece in the middle for stability. In total, two coil units are inserted into the yoke, one from each side. The yoke is then closed with a mirror plate on each side.

The biggest challenge for this magnet was the limited available space in beam direction. For this reason, both the coil length and the yoke length were optimized in order to reduce the fringe field outside the iron yoke. As a result, the mirror plates are highly saturated (Figure 3.2.11), but the magnet still fulfills the beam dynamics requirements.

3.2.3.3.2 Key data and requirements WST21

For MuH2 and MuH3, a total of 8 WSP magnets is required. This paragraph reports the specifications for WST21, but the same applies to the others.

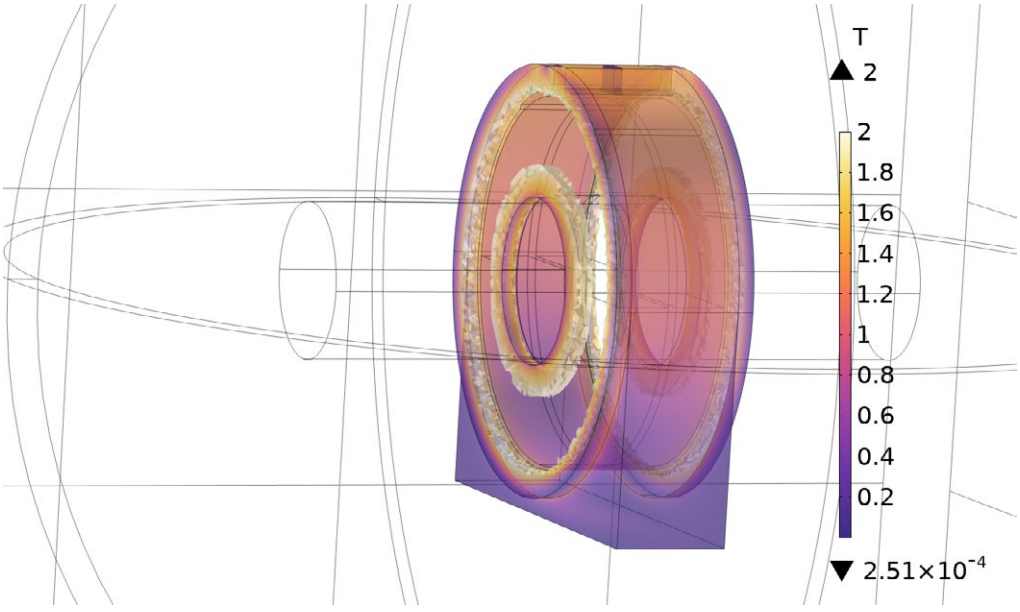

Figure 3.2.11: Field map of the magnetic flux density [T] distribution inside the iron yoke of the transport solenoid performed with COMSOL Multiphysics.

Basic Parameters WST

Main function	Muon, or secondary particle Transport Element in second straight section after Dipole ASH21
Dimensions (mm)	515 × 1508 × 2222 mm Yoke dimensions 465 × 1380 × 1440 mm
Material(s)	Magnetic Steel S235 or S355 Oxygen-free Copper Epoxy impregnated Coils Beam-pipe
Weight	4000 [kg]
Most important parts and interfaces (names)	Steel Housing 2× coil packages of each 6x double pancakes Beam-pipe Support Structure with Adjustable Feet
Mirror-plates, Coil Dimension, beam-pipe	• Upstream (US) Mirror-plate (facing US) Thickness. 50 mm Aperture: 535 mm Gap to coil 6 mm • Downstream (DS) Mirror-plate Thickness. 50 mm Aperture: 535 mm Gap to coil 6 mm • Coil Package 1 total length 163 mm Consisting of 6 double pancakes Id: 552 mm od: 1178 mm • Gap between Coil-packages 27.0 mm • Coil Package 2 total length 163 mm Consisting of 6 double pancakes Id: 552 mm od: 1178 mm
Boundary conditions (constraints)	First solenoid after Dipole ASH21
Positioning / alignment accuracy	• coil positioning +/- 0.5 [mm] • Magnetic-axis tilt with respect to geometric axis < 2 mr

Connections / Interfaces / Fabrication

Cooling	• Water-cooling of coils • 6 directly cooled copper conductor circuits id=8 mm • Flow-rate = 1.6 m/s • Temperature sensors required • Water flowmeters required
Power	1 Power Supply (PS) for solenoid assembly • Bipolar switchable PS • Current/voltage monitors • Max. Power (100%) 77 kW • Nominal Power Muons 28 MeV/c 16.4 kW

Magnetic Field	• Max. Rated Field per coil package 0.55 T • Nominal Surface Muon BField – Coil package = 0.175 T
Manufacturing specifications	• Oxygen-free, Epoxy impregnated Copper Coils • Magnet steel type S235 or S355

Operation

Expected lifetime	Similar to Secondary Beam Quadrupole Magnets > (20-30 yrs)
Spare part policy (redundancies in case of failure)	Possibly 1 spare for MuH2+MuH3

Pictures

CAD overview

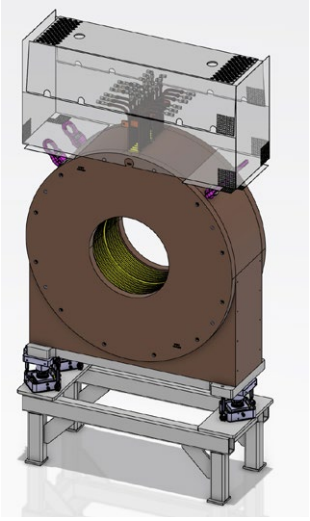

Schematic Layout view

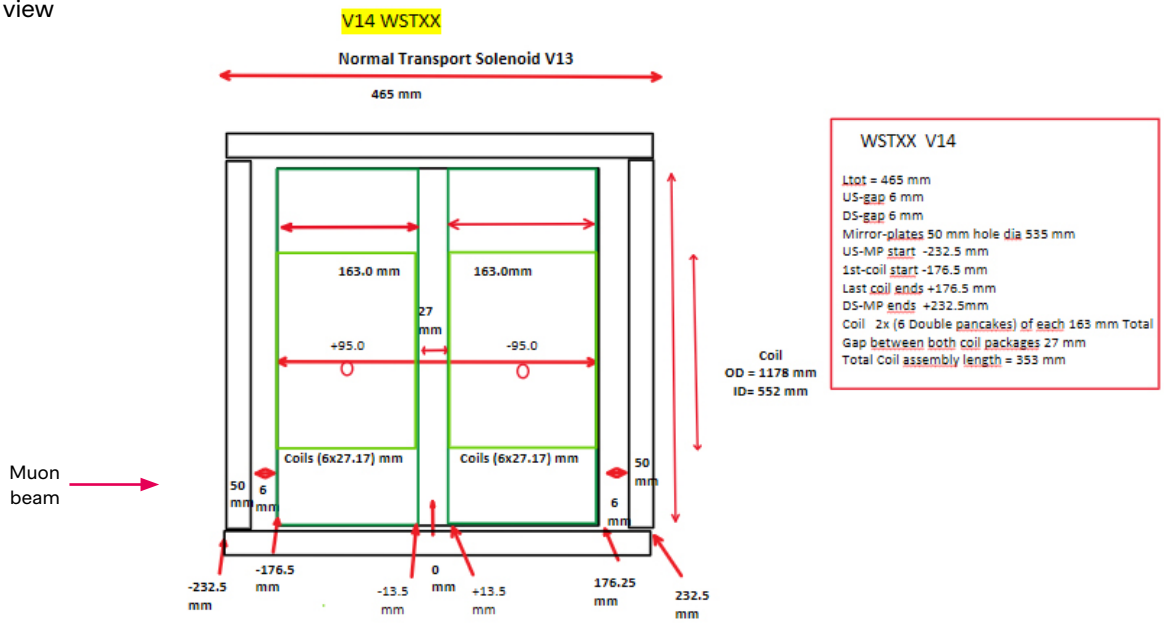

3.2.3.4 AHE - Chicane Magnet

3.2.3.4.1 Conceptual design

The chicane magnets, named AHE1 and AHE2, are required to compensate the vertical deflection of the proton beam at the target due to the horizontal fringe field of the capture solenoids. Since it is planned to mostly operate the two capture solenoid fields in the same direction, the field at the target collision point is substantial. Simulations, reported in Figure 3.2.12, with the two capture solenoids switched on, were performed to assess the integrated fringe field on the main proton beam at the target location to be compensated by the chicane magnets.

Figure 3.2.13 shows the axial field profile of the two capture solenoids of MuH2 and MuH3 when they are both in operation and the fringe field at the target location (x=0m).

At the same time Figure 3.2.14 reports the fringe field in the main proton beam direction that needs to be compensated by adding a vertical deflection beforehand.

Due to the restricted amount of space, the magnets are as compact as possible, but the small and short geometry results in a rather high operating current. Still, by choosing a sufficient conductor size, proper cooling can be guaranteed, and the required operating values can be fulfilled. In particular, the correction of the vertical deflection of the proton beam is done with two chicane magnets having different strengths: 0.097 Tm and 0.054 Tm.

Figure 3.2.15 reports the magnetic flux density distribution inside the iron yoke.

3.2.3.4.2 Key data and requirements AHE1

The specifications were written for both AHE1 and AHE2, but the requirements hereafter refer to AHE1. AHE2 is mechanically identical, only the magnet strength changes.

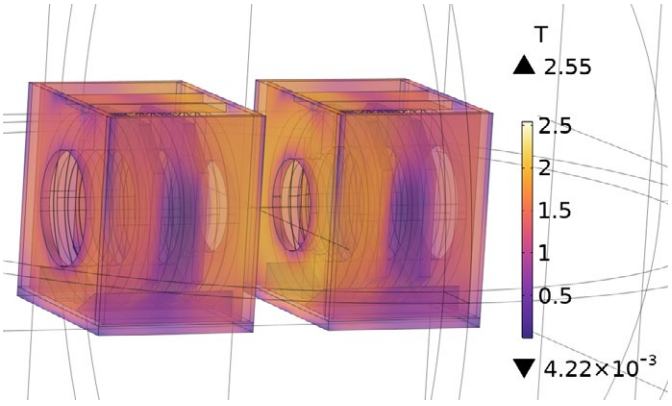

Figure 3.2.12: Magnetic flux density in yoke of MuH2 and MuH3 capture solenoids axes.

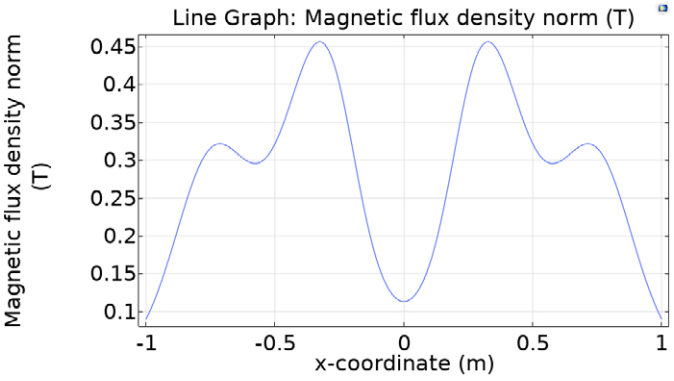

Figure 3.2.13: Magnetic flux density on the capture solenoids axis.

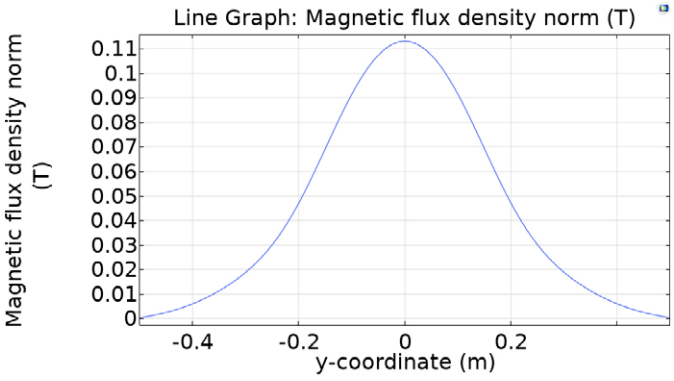

Figure 3.2.14: Fringe field on the main proton beamline of HIPA due to the simultaneous operation of the capture solenoids of MuH2 and MuH3.

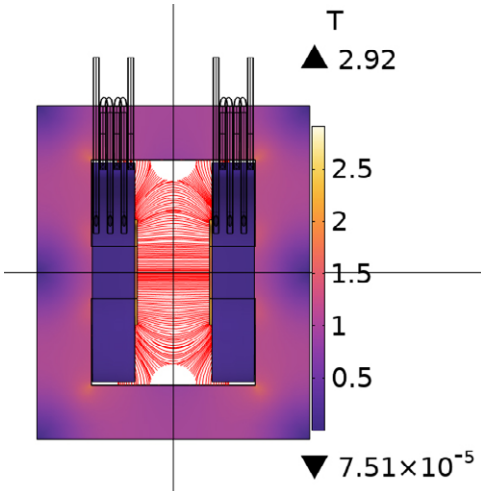

Figure 3.2.15: Field map of the magnetic flux density [T] distribution inside the iron yoke of AHE1 performed with COMSOL Multiphysics.

Basic Parameters AHE1

Main function	Dipole to divert proton beam ahead of target
Dimensions	423 × 653 × 984 mm with cover structure Yoke dimensions 132 × 520 × 554 mm
Pole dimension in beam direction	132 mm
Material(s)	Magnetic steel S235 or S355 Oxygen-free copper, epoxy impregnated coils Stainless steel, aluminum and G10 parts Beam pipe
Weight	600 kg
Most important parts and interfaces (names)	Magnetic steel yoke 2× coil packages of each 4× double pancakes Beam pipe Cooling and power connections
Bending angle	0.024122 rad
Nominal field	0.45442 T +/- tolerances / uncertainty
Pole gap	122 mm
Effective field length	214 mm +/- tolerances / uncertainty
Important distances	Gap of 122 mm: space for vacuum chamber Total length limited according to available space
Boundary conditions (constraints)	Two chicane dipoles form the deviation chicane ahead of target H to compensate for the perpendicular field at the target due to the capture solenoids Space for magnet with coils limited to 340mm
Positioning / alignment accuracy	0.5 mm

Connections / Interfaces / Fabrication

Cooling water	• Water-cooling of coils • 4 directly cooled copper conductor circuits id=6 mm • Flow-rate = 1.5 m/s • Pressure drop 4 bar • Volume flow 5 l/min • Temperature sensors required • Water flowmeters required
Support structure required for alignment	PSI standard 1 ton feet for alignment
Vacuum chamber	Description, materials, values, ranges
Bipolar power supply	
Diagnostic elements	Temperature sensors (Klixon)

Operation

Expected lifetime	30 years
Spare part policy (redundancies in case of failure)	One set of spare coils for two dipoles

Pictures

CAD overview	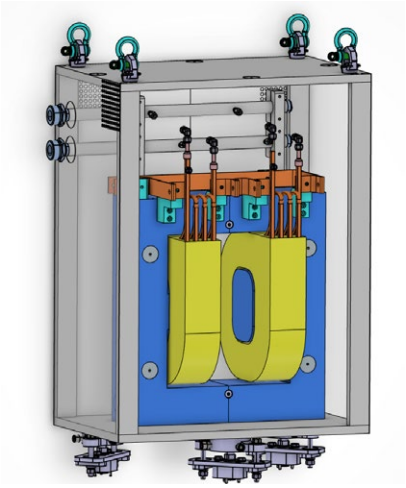

3.2.4 Yoke material of all magnets

Typically, the material used for magnet yokes should be pure iron or low carbon steel. However, during the calculation phase emphasis was placed on regular comparisons of the magnet performance with the use of simple carbon steel. The results showed that while magnet performance is slightly reduced, the resulting properties still fit the requirements set by beam dynamics. Given the fact that the beamlines are in continuous DC operation mode, it was concluded that using carbon steel for the yokes is acceptable.

The main advantage of using carbon steel is the wide availability both in terms of plate and block size as well as much shorter delivery periods. Specifically, the material was defined to be one of the two following:

- S235
- S355

Should the manufacturer be found outside of Switzerland, we expect them to match the Swiss standard for these materials with a corresponding national standard of the country the manufacturer resides in. This should not be a problem since the chosen materials are the most widely available steel grades worldwide.

3.2.5 Materials for components in close proximity to magnets

In order to not spoil the magnetic performance of the magnets described in this chapter, the following table gives the boundary conditions for the materials of components in close proximity to the magnets. The materials given can always been substituted by materials with lower magnetic permeability.

Component	Material
Radiation shielding blocks/ inserts above and below solenoids WSC/WSP and dipoles ASP/ASH	Carbon steel
Shielding block inside TgH vacuum chamber below TgH insert	Stainless steel 304L
TgH/MuH2.1/2.2/3 vacuum chambers	Stainless steel 304L
Large vacuum chamber beam pipes along MUH2/3 and flanges	Stainless steel 316L and 316LN
Pillow seals	Stainless steel 304L
Vacuum chambers for dipoles ASP and ASH	Stainless steel 316L
Shielding between dipoles ASP/ASH and vacuum chambers within the extend of the yoke	Stainless steel 304L
Shielding between solenoids WSP within the extend of the mirror plates	Stainless steel 304L
Beam blockers KSK/KSL	Copper, stainless steel 304L, borated polyethylene
Bellows along beamlines MUH2/3	Stainless steel 304L
Beampipe inside transport solenoids WST	Stainless steel 316L
Vacuum chamber beam blocker KSK and slit system FSVK/FSHK	Stainless steel 304L
Vacuum tank separators	Stainless steel 316L
Beampipe inside chicane magnets AHE	Stainless steel 316L

3.2.6 Magnetic measurement systems & quality control

Quality control: acceptance Tests

- Visual inspection
- Dimensional inspection
- Electrical test
  - Continuity and resistance test
  - High voltage test for insulation
- Water flow measurements

Magnetic measurement system and field quality

The reference magnetic measurement system is the Magnus Field Mapper based on the hall probe sensor for the dipoles. For the solenoids a combination of the translating fluxmeter and hall probe sensors will be used.. For each magnet a 3D map scan will be performed in order to assess the field profile shape, axis position, and the integral field values.

3.3 Power Supplies for Magnets

Most Magnet Power Supplies (PS) for PSI accelerators are generally designed in house, this also includes the digital controllers. Production is outsourced partially, but testing, commissioning and service during the whole lifetime is done in house.

For cases where the PSI-designed portfolio does not cover the needed rating, and an internal development is not reasonable, commercial PS will be used. This is the cases for the PS in the proton beamline (see Chapter 3.3.2)

Many of the PS of the existing PiM1 and PiM3 beamlines have been replaced only few years ago. As these PS are as good as new, we want to reuse them for HIMB to a maximum extent. However, we will need also new PSs.

Some of the PS are very powerful, for cost and space reasons we do not install excessive spare current/voltage. In addition to that the maximum output current is generally limited to approx. 110% of the nominal current, to prevent overload conditions for the feeding transformers.

The magnet PS for HIMB will fulfill the following stability requirements. The values are relative to the nominal current of the Power Supply:

- RMS of the current noise/ripple in the frequency range 10 Hz .... 1 kHz — 200 ppm
- Drift of the mean value of the current over a time span of 100 s .... 48 h — 100 ppm
- Reproducibility after repair/replacement of a Power Supply — 500 ppm

There are several PS needed, that exceed our current design portfolio. We have defined a new converter unit rated 650 A/300 V/1Q to be developed and used for the IMPACT PS and other PS in HIPA. This converter is based on the Infineon IGBT module FF1200R12IE5P. The same IGBT including its gate driver have been used for the design of the SLS Booster Dipole PS already.

This converter unit will be used in two new PS types:

- 650 A/150 V/1Q
- 500 A/250 V/1Q

Both PS are 1Q PS that are equipped with a pole-reversal switch to enable operation with both positive and negative current.

These two PS types will be used in HIMB for totally 6 Capture Solenoid PS and 5 Pyrotenax Solenoid PS. We are aware of the fact that some magnet circuits have very little margin in either voltage or current. However, due to time constraints the new development of these two PS types had to be started well before the final magnet designs were finished (and tolerances could be checked with the manufacturer).

Also, a new converter unit 200 A/100 V/4Q is being developed. This converter unit is based on an Infineon IGBT module FF450R07ME4_B11.

This converter unit will be used in two new PS types:

- 200 A/75 V/4Q
- 200 A/50 V/4Q

These two PS types will be used in HIMB for the ASH-dipoles and QSE-Quadrupoles. Also, they will be used for TATTOOS magnets, and in the future also for the renewal of various PSs in the HIPA.

3.3.1 Digital Power Supply Controller

The first generation of PSI-designed digital power supply controllers (PSC) was designed for SLS about 25 years ago, it is no longer used for new accelerators/beamlines.

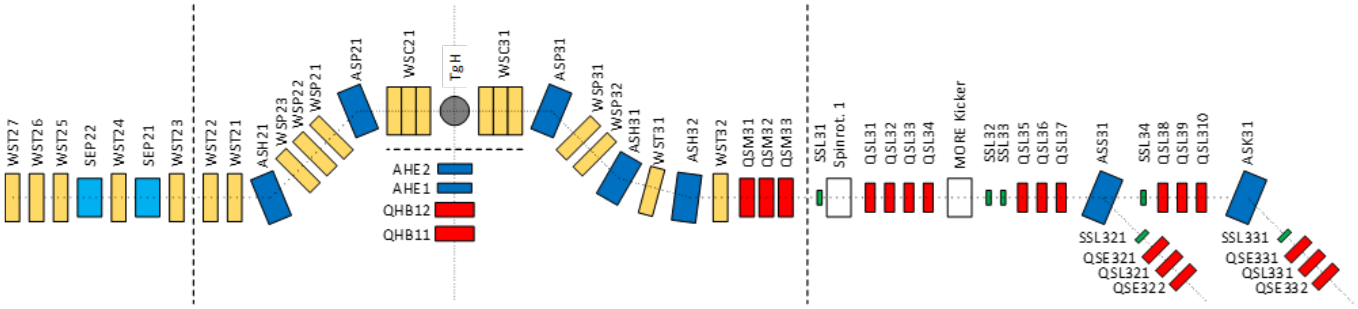

Figure 3.3.1: Schematic overview HIMB magnets/PS

Figure 3.3.2: DPC2-CC Controller card

The DPC controller (2nd generation) was developed for the SwissFEL and is meanwhile well established at PSI (approx. 1'200 units are in service in different accelerators). The controller communicates with the overall control system (EPICS) via a bidirectional optical interface. All existing PS that are reused for HIMB are equipped with the DPC controller. For details refer to [1].

The DPC2-controller (3rd generation) was recently developed for SLS2 and will be the future standard at PSI. Approx. 1'300 PS containing this controller core have been commissioned in the SLS2 lately. Approx. 1'100 cores are integrated in a 5A converter and approx. 200 cores are integrated in a multipurpose controller card (DPC2-CC). All new PS for HIMB are equipped with the DPC2-CC controller card, which provides the following functionality:

- Ethernet interface: This connection can be used by the control system for the operation of the power supply, as well as for remote-diagnostic purposes by the Power Electronics crew.
- Optical interface (POF RX & TX): For legacy reasons, the optical interface can also be used as interface to the control system for the use in older machines (not used for HIMB).
- Optical Trigger: Waveforms can be triggered over this input (not needed for HIMB)
- USB interface: This can be used as a local service interface.
- Scope-Box: This is a service interface. Software-internal signals can be routed to 4 analog outputs for monitoring on an oscilloscope.
- SOM containing a Xilinx UltraScale+ MPSoC: This as a commercially available sub-PCB containing the controller core, optimized for this type of processor. This choice saved development time, and the boards could be developed without needing expertise in the field of processor-close circuit development.
- 1 high precision +/– 10 V analog input (20 bit, 1 MS/s)
- 16 "standard" +/– 10 V analog inputs (18 bit, 200 kS/s)
- 8 digital outputs
- 20 digital inputs
- 15 digital outputs with high time-resolution ("PWM outputs")
- 12 digital inputs with high time-resolution ("PWM feedback")
- 1 PWM-sync interface (1× output, 1× input) to synchronize the PWM phase between two controllers.
- 2 multi-processor links for communication between DPC2-CC processors in a multi-processor system
- External I2C interface
- General purpose data link (e.g., for the connection with the existing AD-card)

3.3.2 Power Supplies for the proton beamline

For the 4 new magnets in the P-channel upstream the Target H, the current and voltage ratings are unfavorable for existing PS designs. Instead, we will use a primary-switched power supply, which is commercially available. If it can fulfill all the

Magnet Name	Winding or Rang	Magnet Type	Section	INom Load [A	UNom Load [V]	RLoad [mOhm]	PS Type	PS Controller	INom PS [A]	UNom PS [V]	PS Polari
QHB11		Quadrupole	1: P-Channel	235	24.2	102.8	Commercial	DPC2 + Commercial	300	30	1Q with PS
QHB12		Quadrupole	1: P-Channel	235	24.2	102.8	Commercial	DPC2 + Commercial	300	30	1Q with PS
AHE1		Chicane weak	1: P-Channel	200	7.8	39.1	Commercial	DPC2 + Commercial	500	20	1Q with PS
AHE2		Chicane strong	1: P-Channel	364	14.2	39.1	Commercial	DPC2 + Commercial	500	20	1Q with PS

Table 3.3.1: Power Supplies for the proton beamline

Magnet Name	Winding or Rang	Magnet Type	Section	INom Load [A	UNom Load [V	RLoad [mOhm]	PS Type	PS Controller	INom PS [A]	UNom PS [V]	PS Polari
WSC21	1	Capture Solenoid RH	2: uH2	618	147.0	237.8	300	DPC2	650	150	1Q with PS
WSC21	2	Capture Solenoid RH	2: uH2	20.25	4.3	212.9	300	DPC2	650	150	1Q with PS
WSC21	3	Capture Solenoid RH	2: uH2	506.75	107.9	212.9	300	DPC2	650	150	1Q with PS
ASP21		Pyrotenax Dipole 35.5°	2: uH2	188	135.8	722.3	74a	DPC	500	160	1Q with PS
WSP21		Pyrotenax Solenoid	2: uH2	402	226.0	562.1	301	DPC2	500	250	1Q with PS
WSP22		Pyrotenax Solenoid	2: uH2	402	226.0	562.1	301	DPC2	500	250	1Q with PS
WSP23		Pyrotenax Solenoid	2: uH2	402	226.0	562.1	301	DPC2	500	250	1Q with PS
ASH21		Normal Dipole 45°	2: uH2	261	77.3	296.2	74a	DPC	500	160	1Q with PS
WST21		Transport Solenoid	2: uH2	450	155.3	345.1	74	DPC	500	160	1Q with PS
WST22		Transport Solenoid	2: uH2	450	155.3	345.1	74	DPC	500	160	1Q with PS
WST23		Transport Solenoid	2: uH2	450	155.3	345.1	74	DPC	500	160	1Q with PS
SEP21		Separator 21	2: uH2	200	42.2	211.2	252	DPC2	200	50	4Q
WST24		Transport Solenoid	2: uH2	450	155.3	345.1	74	DPC	500	160	1Q with PS
SEP22		Separator 22	2: uH2	200	42.2	211.2	252	DPC2	200	50	4Q
WST25		Transport Solenoid	2: uH2	450	155.3	345.1	74	DPC	500	160	1Q with PS
WST26		Transport Solenoid	2: uH2	450	155.3	345.1	74	DPC	500	160	1Q with PS
WST27		Transport Solenoid	2: uH2	450	155.3	345.1	74	DPC	500	160	1Q with PS
Reserve			2: uH2						500	160	1Q with PS

Table 3.3.2: Power Supplies for the MuH2 beamline

requirements, we can use it directly. Otherwise, we can use it with a superimposed current controller implemented in a DPC2-CC controller, and a high precision measuring system. This is a new concept, the evaluation and development are currently in progress.

It must be possible to change the current in the chicane magnets with a current slope of 115 A/s. We can assume that for magnets with iron yokes, the bandwidth is approx. 1 Hz. However, the required bandwidth is 0.02 Hz. Therefore, the magnetic field should follow the current rapid enough.

3.3.3 Power Supplies for the MuH2 beamline

For the *Capture Solenoids*, the new-developed 650 A/150 V PS (see introduction part of Chapter 3.3) can be used.

There is only approx. 5% current margin to the nominal operating current for coil No. 1, and no voltage margin. The voltage margin became smaller and smaller in course of the project and was discussed in March 2025. Since the voltage calculation is based on a worst-case assumption regarding the resistance of the magnet, it was decided to accept this.

The coil No. 2 will carry only small currents. However, we will equip this coil also with the same PS as the other 2 coils to keep full flexibility for the field profile. The PS design must consider low operating points. The stability requirements are 1%, i.e., 0.2 A peak.

For the *Pyrotenax Solenoids* the new-developed 500 A/250 V PS (see introduction part of Chapter 3.3) can be used.

For the two *Dipole Magnets* we can reuse an existing standard PS 2×500 A/160 V. Both dipoles utilize only a fraction of the power capacity, but the reuse of existing PSs is economically efficient.

For the 7 *Transport Solenoids* we can reuse existing standard PSs 2×500 A/160 V. However, the current must be limited to 460 A, to respect the voltage limit of the PS. With that, there is only a 2% current margin to the nominal operating current.

The *Separator Magnets* can be powered by the new-developed 200 A/50 V PS (see introduction part of Chapter 3.3).

Installation: The PS for MuH2 can be installed on the existing platform for the PiM1 PSs. The total required lineup length is approx. 16'750 mm.

The total *Power Demand* of the MuH2 PSs is very high. We assume an average PS efficiency of 90% (realistic estimate) and a power factor of 0.95 (pessimistic estimate). In addition to the magnets, there will be an auxiliary power demand of approx. 50 kVA.

When all magnets work at nominal current (column "I_Nom" in *Table 3.3.2*), the feeding transformer (1'600 kVA) will be loaded with approx. 1'190 kVA (74%). This is not a permanent situation but may happen for several hours or even several days.

However, when all magnets work at maximum current (column "PS Limit" in *Table 3.3.2*), the feeding transformer will be loaded with approx. 1'310 kVA (82%). This situation may happen for max. 5 minutes, when the beamline magnets are cycled all together (worst-case).

System Perturbations: The high power-demand asks for low system perturbations. The PSs are all equipped with 6-pulse diode rectifiers, which offer a good power factor, but generate high harmonic currents. A 6-pulse diode rectifier has a total harmonic current distortion (THDI) of approx. 30%, whereas a 12-pulse rectifier has a THDI of only approx. 10%. A 12-pulse overall system can be achieved by using different transformer winding configurations. 50% of the power must be delivered by Y-system transformers (i.e., Yy6 or Dd0). The other 50% must be delivered by D-system transformers

Magnet Name	Winding or Rang	Magnet Type	Section	INom Load [A	UNom Load [V]	RLoad [mOhm]	PS Type	PS Controller	INom PS [A]	UNom PS [V]	PS Polari
WSC31	1	Capture Solenoid RH	3: uH3	618	147.0	237.8	300	DPC2	650	150	1Q with PS
WSC31	2	Capture Solenoid RH	3: uH3	20.25	4.3	212.9	300	DPC2	650	150	1Q with PS
WSC31	3	Capture Solenoid RH	3: uH3	506.75	107.9	212.9	300	DPC2	650	150	1Q with PS
ASP31		Pyrotenax Dipole 30°	3: uH3	116.25	84.0	722.3	62	DPC	500	120	1Q with PS
WSP31		Pyrotenax Solenoid	3: uH3	402	226.0	562.1	301	DPC2	500	250	1Q with PS
WSP32		Pyrotenax Solenoid	3: uH3	402	226.0	562.1	301	DPC2	500	250	1Q with PS
ASH31		Dipole 34.4° Normal	3: uH3	161.25	49.7	307.9	253	DPC2	200	75	4Q
WST31		Transport Solenoid	3: uH3	450	155.3	345.1	74	DPC	500	160	1Q with PS
ASH32		Dipole 20.6° Normal	3: uH3	105	32.3	307.9	253	DPC2	200	75	4Q
WST32		Transport Solenoid	3: uH3	450	155.3	345.1	74	DPC	500	160	1Q with PS
QSM31		Quadrupole	3: uH3	300	40.4	134.8	62	DPC	500	120	1Q with PS
QSM32		Quadrupole	3: uH3	420	56.6	134.8	62	DPC	500	120	1Q with PS
QSM33		Quadrupole	3: uH3	420	56.6	134.8	62	DPC	500	120	1Q with PS
SSL31y		Steuermagnet	3: uH3	8	4.7	582.3	50	2nd PS on DPC	10	12	4Q
Spinrot1		Dipol Spinrotator 1	3: uH3	470	28.7	61.0	43	DPC	500	80	1Q with PS
QSL31		Quadrupole	3: uH3	50	15.8	315.0	52	DPC	50	24	4Q
QSL32		Quadrupole	3: uH3	50	15.8	315.0	52	DPC	50	24	4Q
QSL33		Quadrupole	3: uH3	50	15.8	315.0	52	DPC	50	24	4Q
QSL34		Quadrupole	3: uH3	50	15.8	315.0	52	DPC	50	24	4Q
Kicker		MORE Kicker	3: uH3								
SSL32x		Steuermagnet	3: uH3	8	4.7	582.3	50	DPC	10	12	4Q
SSL33y		Steuermagnet	3: uH3	8	4.7	582.3	50	DPC	10	12	4Q
QSL35		Quadrupole	3: uH3	50	15.8	315.0	52	DPC	50	24	4Q
QSL36		Quadrupole	3: uH3	50	15.8	315.0	52	DPC	50	24	4Q
QSL37		Quadrupole	3: uH3	50	15.8	315.0	52	DPC	50	24	4Q
ASS31		Dipol Septum 49.5°	3: uH3	380	21.7	57.0	43	DPC	500	80	1Q with PS
SSL34		Steuermagnet	3: uH3	10	5.8	582.3	50	2nd PS on DPC	10	12	4Q
QSL38		Quadrupole	3: uH3	50	15.8	315.0	52	DPC	50	24	4Q
QSL39		Quadrupole	3: uH3	50	15.8	315.0	52	DPC	50	24	4Q
QSL310		Quadrupole	3: uH3	50	15.8	315.0	52	DPC	50	24	4Q
ASK31		Dipol 30°	3: uH3	75	11.3	150.0	53	DPC	100	36	4Q
SSL321		Steuermagnet	3: uH3	10	5.8	582.3	50	DPC	10	12	4Q
QSE321		Quadrupole	3: uH3	60	10.0	166.5	53	DPC	100	36	4Q
QSL321		Quadrupole	3: uH3	40	15.7	393.0	52	DPC	50	24	4Q
QSE322		Quadrupole	3: uH3	80	13.3	166.5	53	DPC	100	36	4Q
SSL331		Steuermagnet	3: uH3	10	5.8	582.3	50	2nd PS on DPC	10	12	4Q
QSE331		Quadrupole	3: uH3	110	18.3	166.5	253	DPC2	200	75	4Q
QSL331		Quadrupole	3: uH3	80	30.1	376.5	53	DPC	100	36	4Q
QSE332		Quadrupole	3: uH3	160	26.6	166.5	253	DPC2	200	75	4Q
WED	High	WED (high)	3: uH3	800	258.4	323.0	79	DPC	800	300	1Q with PS
WED	Low	WED (low)	3: uH3	50	16.2	323.0	79	DPC	50	20	4Q
WEP		WEP	3: uH3	160	48.0	300.0	81	DPC	200	60	4Q

Table 3.3.3: Power Supplies for the MuH3 beamline

(i.e., Yd5 or Dy11). A slight asymmetry between the two systems is acceptable. Simulations and tests have shown that a power share of 33/67% still produces an acceptable THDI of approx. 13%. The existing standard PS 2×500 A/160 V are equipped with transformers with different winding configurations (Dd0 and Dy5). These PS have a nearly perfect power sharing between the two systems. The new PS 650 A/150 V and 500 A/250 V must be equipped with different transformers (i.e., Dd0 for the 650 A/150 V PS and Dy5 for the 500 A/250 V PS). Then we will get a worst-case overall power sharing of 39/61%, which is close enough to the ideal 50/50% share.

Cooling Demand: In the MuH2 beamline there are totally 17 water cooled PS installed. They require 12 water circuits of 10 Liters/Minute or 7 Liters/Minute (total 99 l/min). The total cooling power is approx. 25 kW when all magnets are in their nominal operating point. Worst case, the cooling power is approx. 32 kW (all PS at max. current).

3.3.4 Power Supplies for the MuH3 beamline

For the *Capture Solenoids and Pyrotenax Solenoids* the same PSs are used as for the MuH2 beamline, see Chapter 3.3.3

For the 2 *Transport Solenoids* we can reuse an existing standard PS 2×500 A/160 V, as for MuH2 (see Chapter 3.3.3).

For the *Pyrotenax Dipole* and the *Quadrupoles* QSM31-33 we can reuse two PS 2×500 V/120 V from the existing beamline PiM1.

Various 200A Magnets: There are totally 6 magnets (2 in MuH2 and 4 in MuH3) that require currents up to 200 A. These can be fed by the new-developed 200 A/50 V or 200 A/75 V PS (see introduction part of chapter 2.3).

Various 10 A- 50 A- and 100 A Magnets: There are totally 22 magnets that require a 10 A, a 50 A or a 100 A PS. All of them can be powered by the existing PS in the PiM3 beamline. They are less than 15 years old and are by far not end of life. We expect them to be usable for another 20–25 years.

Special Magnets: The septum magnet, the Spinrotator1 magnet as well as the WED and WEP magnets will be reused together with their PS. These PS are also still in good shape and can be used for another 20–25 years.

Installation: For the PS of the MuH3 beamline a new platform is required. In total, a width of 20'050 mm racks need to be installed on this new platform.

The total *Power Demand* of the MuH3 PSs is very high. We assume an average PS efficiency of 90% (realistic estimate) and a power factor of 0.95 (pessimistic estimate). In addition to the magnets, there will be an auxiliary power demand of approx. 50 kVA.

When all magnets work at nominal current (column "I_Nom" in *Table 3.3.3*), the feeding transformer (1'000kVA) will be loaded with approx. 990kVA (99%). Therefore, it needs to be closely monitored whether this transformer can handle this situation.

However, when all beamline magnets work at maximum current (column "PS Limit" in *Table 3.3.3*), the experiment magnet WED must be off to prevent transformer overload. Then the feeding transformer will be loaded with approx. 840 kVA (84%). This situation may happen for max. 5 minutes, when the beamline magnets are cycled all together (worst case).

As we work very close to the power limits, *a signalization of the actual transformer power and the alarm status shall be available at the beamline control room*. Cycling (or other overload conditions) of the beamline magnets shall only be possible when the WED magnet is off.

System Perturbations: The high power-demand asks for low system perturbations, see Chapter 3.3.3. Also, in MuH3 we will get a worst-case overall power sharing of 45/55%, which is close to the ideal 50/50% share.

Cooling Demand: In the MuH3 beamline there are totally 20 water cooled PS installed. They require 13 water circuits of 10 Liters/Minute or 7 Liters/Minute (total 109 l/min). The total cooling power is approx. 24 kW when all magnets are in their nominal operating point. Worst case, the cooling power is approx. 30 kW (all PS at max. current).

3.3.5 References

[1] M.Emmenegger, H. Jäckle, R. Künzi, S. Richner; *A new generation of digital Power Supply Controllers*; Proceedings of IPAC 2012, Kyoto, Japan, WEDP071. 2012.

3.4 Proton Beam Diagnostics

3.4.1 Beam Position Monitors (BPMs) and Beam Profile Monitors

Close to the targets, BPMs together with profile monitors are inserted into the massive shielding as part of a plug, which also contains shielding. A modular concept has been developed [1] which will be employed for the two new plugs (MHP/S23/24 and MHP/S23B/24B) downstream of Target H. These profile monitors and BPMs with apertures of 102 mm and 132 mm will be the only new profile monitors and BPMs for HIMB. A similar plug (MHP45/46), but with a more demanding larger beam aperture went into operation downstream of Target E in 2024 and shows promising results.

Device	**In-Shielding Monitor Insertion MHP/S23/24 and MHP/S23B/24B**
Reference documents	Drawing 'PRD-00674189 Rev. A' References [1-5]
List of sub-components / sub-systems, which are defined separately:	• read-out electronics (SoM-CAM, DBPM3-HIPA) • motor driver electronics • vacuum chamber • lifting gear • exchange flask H • mounting stand • ATEC support stand and tools

Basic Parameters

Main function	• on-request measurement of horizontal and vertical proton beam profiles downstream of Target H and following collimators (two locations) • permanent measurement of horizontal and vertical beam position in same locations
Design Guideline	• adaptation of modular approach of latest MHP/S45/46 • size compatible with vacuum chambers of MHP23-32 • double seal carrier (not possible in MHP23-32)
Dimensions	• 456 mm × 733 mm × 3265 mm
Weight	• 2300 kg

Material(s)	• shielding: iron (+nickel coating) • monitors: aluminum, stainless steel, aluminium oxide, copper, WS_2 (in ball bearing and signal rail coating) • wires: molybdenum diameter 0.013 mm • in feedthroughs and motor: FeNb, PEEK
Most important parts and interfaces (names)	• wire monitor module (incl. wire holder module) • BPM module • signal rails • shielding block and guiding • vacuum flange and electrical feedthroughs • drive module with magnetic feedthrough • long cables to electronics
Relevant parameters	• beam aperture: 102 mm (23/24) and 130 mm (23B/24B) • BPM position geometry scaling factor[1] 36 mm (102 mm aperture) • BPM signal strength not critical for electronics • simulations with different bunch length show no large influence [5] • Inductive pickup • driver electronics: SoM-CAM + stepper motor driver (backup: MESON)
Boundary conditions (constraints)	• an active cooling of the MHP/S23/24 insertion required because of heating by the beam or secondary radiation, see Section 2.8.1.1 • modules suited to be replaced with manipulator in ATEC • vacuum compatible • very radiation hard at beam height • sufficiently radiation hard at service level • preferably materials not highly activating and suitable for nuclear waste storage
Positioning / alignment accuracy	• initially 1 mm. Thermal environment will influence and might require corrections via temperature measurements. • long-term reproducibility 1 mm • short-term reproducibility 0.2 mm
Environment conditions to be considered (temperature, humidity, vacuum, radioactivity, radiation levels, EM fields, vibrations, accidental forces, ...)	• handling without mechanical shocks (e.g. suited crane) • limited humidity (plugs and cables) • limited dust (vacuum, isolation check) • cable trays to be isolated from vibrations (from e.g. water cooling pipes)

Connections / Interfaces / Fabrication

Relevant connections and interfaces	• to vacuum chamber: double seal carrier (Viton) • to electronics: similar to MHP/S45/46 but preferably ¼'' cables for BPM • electronics connected to run-permit system • compatibility to lifting gear, exchange flask H, mounting stand, ATEC support stand and tools • exchange flask "drive shaft" for signal rails
Manufacturing specifications	similar to MHP/S45/46

[1] Calibration factor to convert unitless signal into mm offset.

Operation

Expected lifetime	• 30 years
Regular maintenance	• check of vacuum tightness • check of signal line insulation • check of BPM electrode configuration by influence test or beam measurement • check of beam position from BPM vs. wire monitor • check of online measured drive forces and signal rail temperatures
Corrective maintenance (repair)	• replacement of defect modules in ATEC • replacement of drive module, signal rails, feedthroughs, and seals at service level
Spare part policy	• all removable modules: 2 sets • material for cables incl. plugs: 2 sets • seals: 5 sets
(Redundancies in case of failure)	• double wires (1 broken wire per plane may be tolerable (if not shorting more wires) • one of the two plugs for the other (not fully redundant)

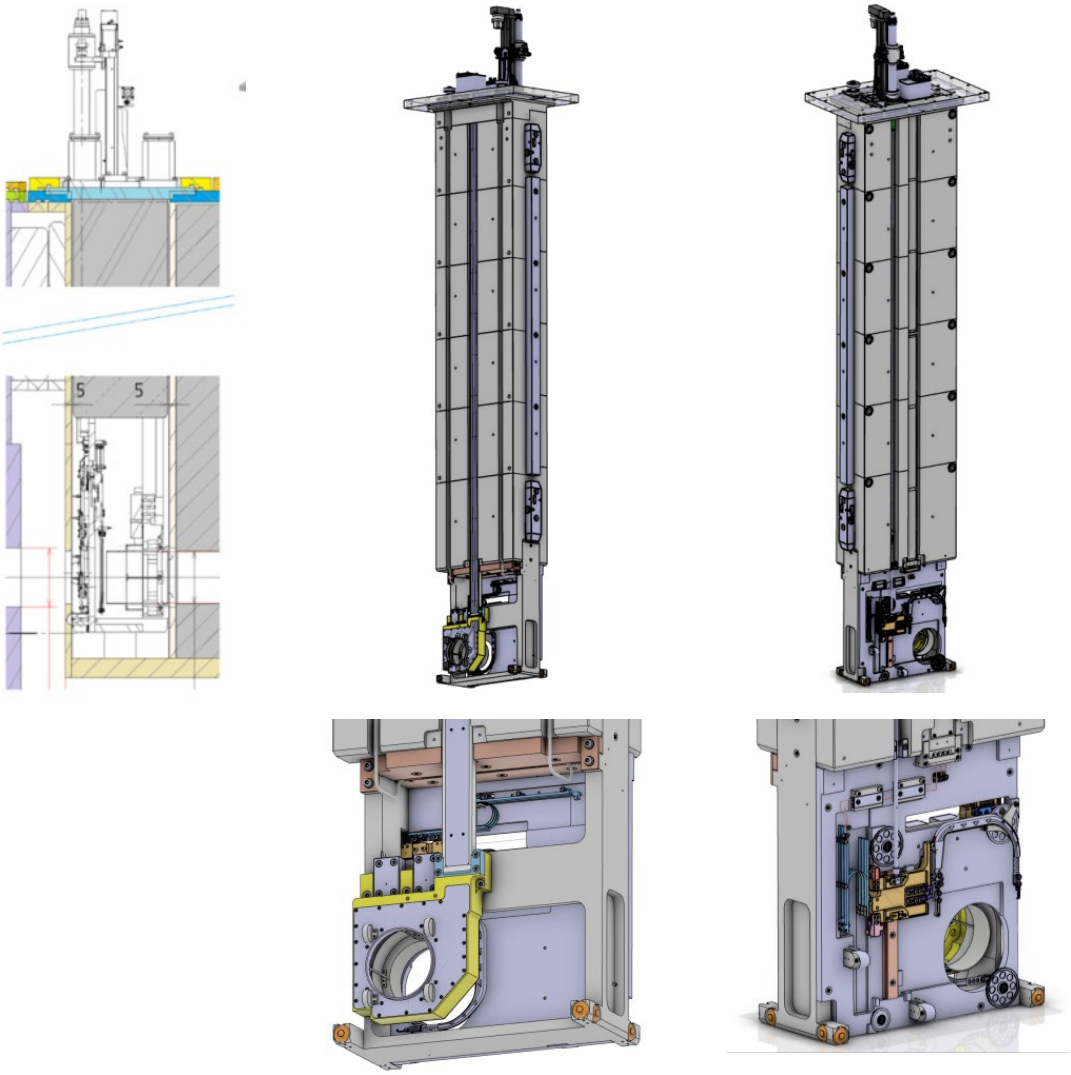

Figure 3.4.1: CAD images of the profile monitor.

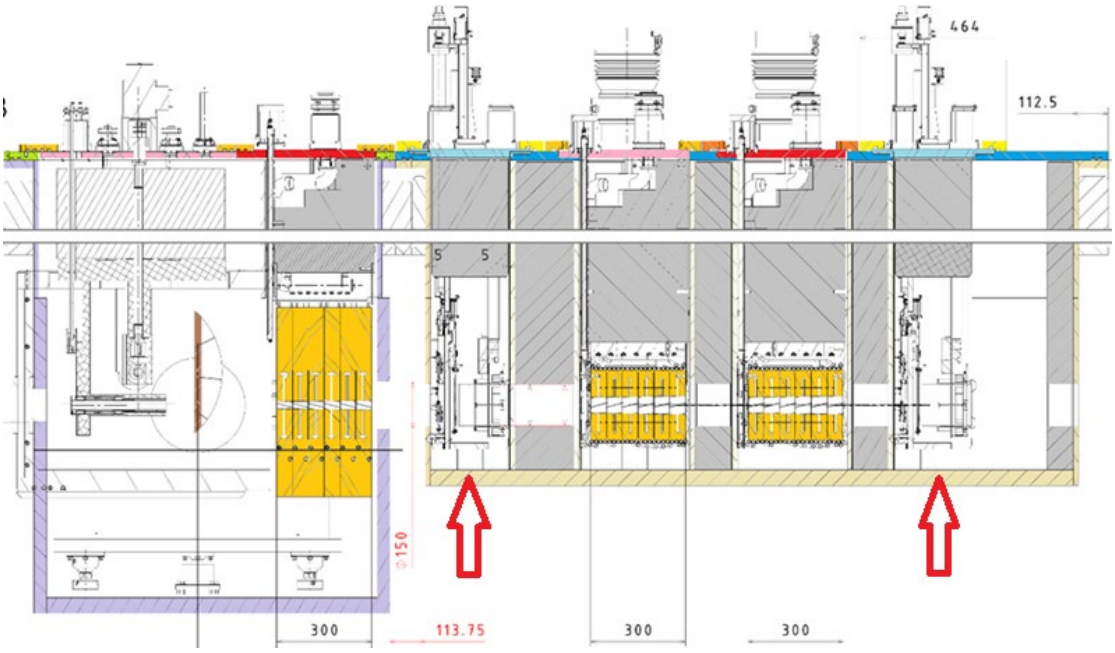

Figure 3.4.2: Location of the two profile monitors along the beam line.

3.4.1.1 Cooling of insertion MHP/S23/24

Todays installed in-shielding profile monitors are completely uncooled, regardless if they are after TgM or TgE. Due to factors as type of design and proximity to the Target H, the monitor requires cooling of its main structures. Its basic design does not deviate from currently existing HIPA designs. Therefore, the monitors hang in the vacuum chambers and have no other contact faces than their flange lid.

As a power deposition of about 280 W takes place in the shielding insert only (see Table 2.4.10, insert 1 in Chapter 2.4.5.2), the whole insert would heat up to a certain unacceptable level. In addition, 77 W is deposited in the first profile monitor (see Table 2.4.11 in Chapter 2.4.5.2). On the bottom side of the shielding a copper plate actively cooled is installed to prevent this. The red arrow in Figure 3.4.3 shows the cooling of the copper plate by a stainless-steel tube soldered to the plate, which cools on the main shielding as well the support frame (yellow arrow) made out of one big aluminum block improving overall heat conduction.

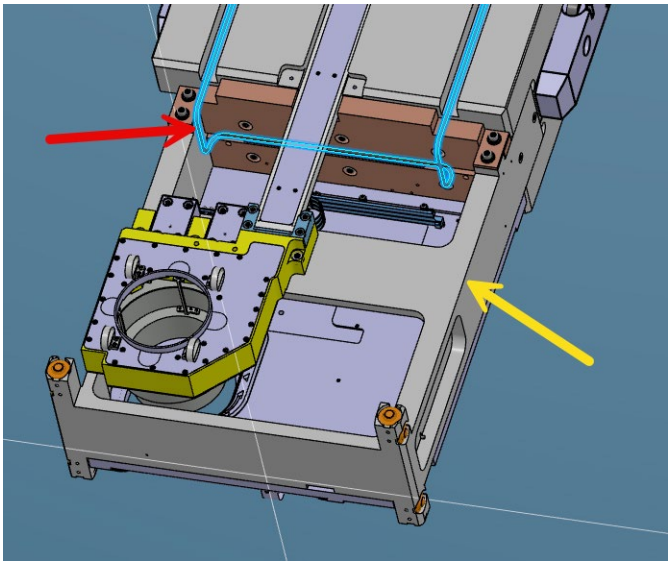

Figure 3.4.3: Lower part of the profile monitor. The arrows are pointing to the cooling pipe and the Aluminum frame.

3.4.1.2 BPM Electronics

The BPM electronics for IMPACT will be based on a new platform called “DBPM3” that is already deployed at SwissFEL and SLS 2.0. For IMPACT, the SLS 2.0 DBPM3 electronics is adapted, changing the working frequency of the RF front-end from 499.654 MHz (beam signal frequency) to 101.26 MHz for IMPACT. For HIMB two pairs of BPMs with these electronics will be installed downstream of Target H. The new electronics will also replace all existing HIPA BPM electronics (“pDBPM1”) in the context of a general upgrade, where the present HIPA BPM electronics generation is now about 20 years old and needs to be replaced due to a limited number of spares and increasing difficulties to repair electronics and obtain obsolete electronics components.

A prototype of the new HIPA/IMPACT DBPM3 electronics has already been tested successfully [7], where the achieved performance meets the requirements. In contrast to the existing electronics, the new DBPM3 electronics can be locked to the machine RF reference clock, thus supporting measurements at lower bandwidth and reduced noise for low beam currents.

For the measurement (see Figure 3.4.4), a centered beam was simulated by splitting RF signals to all four input channels

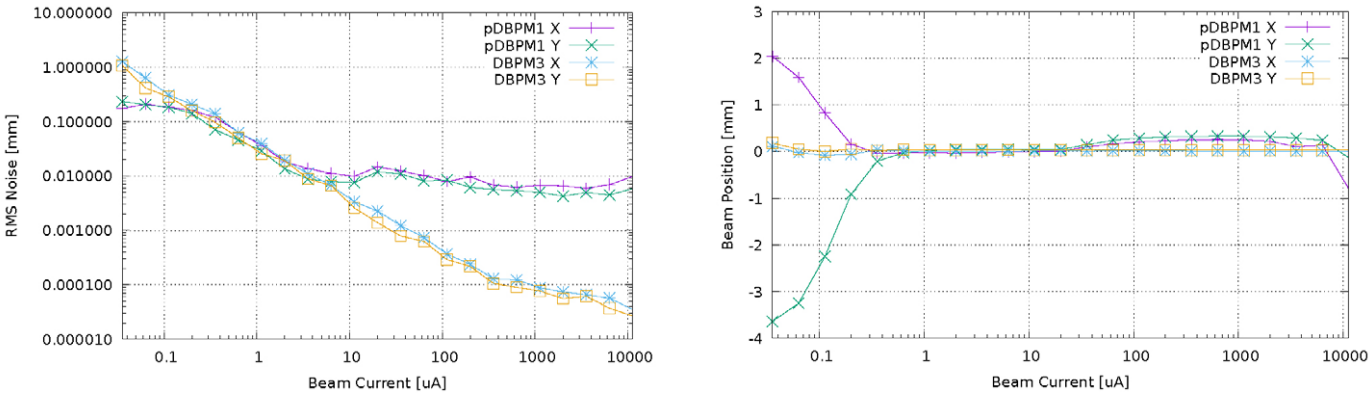

Figure 3.4.4: Noise (left) and beam position readings vs. beam current, measured for the old pDBPM1 electronics and new DBPM3 prototype.

of the electronics. At high beam currents, the DPBM3 noise is much lower. Below 10 µA, noise is limited by thermal RFFE noise. Below 0.1 µA, the pDBPM1 does not provide usable readings anymore, since beam signals are below the noise level and the position readings converge to constant values independent of the real beam position (thus resulting in constant noise and constant readings). In contrast, the DBPM3 electronics still provides usable readings below 0.1 µA, where the noise increases inversely proportional to the beam current.

3.4.2 Aperture Foils

Segmented aperture foils (see also CDR Section 8.5.4.3) are made from thin-sheet metal of nickel or molybdenum and are located at the upstream end of collimators preceding or following targets. At Target H, one preceding collimator (KHBEI) is used to guarantee a defined beam position at the target and to avoid the beam spot on the Cu cooling plate. Three following collimators (KHH0/1/2) are used to clean the scattered beam. The aperture foils MHBEI, MHB0/1/2 are each part of the plug carrying the corresponding collimator.

The foils are divided in 4 sectors with a 45 degrees cross pattern (see CAD picture below) to determine the beam position. The reason for the 45 degrees rotation is that in this way in case of beam losses it is more intuitive for the machine operators to see in which direction the beam should be steered, as the individual tuning knobs can steer up/down or left/right.

At HIPA there is experience with 100 µm nickel and 50 µm molybdenum. 100 µm nickel is chosen on most collimators. Foils with small apertures absorb more energy and heat. For these foils 50 µm molybdenum is chosen, which are more resistant for three reasons: thinner foils absorb less heat; molybdenum survives higher temperatures; Mo foils likely have a higher emissivity (from experience with BX2 the molybdenum foils are blackening in operation). Furthermore, due to the small aperture the mechanical stability for a thinner foil should still be acceptable.

3.4.2.1 4-Segment Aperture Foil MHBEI

Device	**4-Segment Aperture Foil MHBEI**
Reference documents	Drawing PRD-00357781
List of sub-components / sub-systems, which are defined separately:	• protection collimator KHHEI (parent component) • read-out electronics (SoM-CAM) • exchange flask “drive shaft” for signal rail • ATEC handling tools

Basic Parameters

Main function	• permanent measurement of beam loss at four segments • generation of interlock in case of beam loss not as specified (prevents wrong horizontal or vertical beam position and size)
Design Guideline	• similar to existing aperture foils • modular approach for signal rail and contact to collimator
Dimensions	• 280 mm × 96 mm × 65 mm
Weight	• 3 kg
Material(s)	• stainless steel, aluminum oxide • foils: 50 µm molybdenum
Most important parts and interfaces (names)	• aperture foil module • signal rail • feedthroughs • long cables to electronics
Relevant parameters	• foils thickness: 50 µm • foils aperture: as collimator • foil pattern rotated 45° (gap between segments less critical)
Boundary conditions (constraints)	• aperture foil module suited to be replaced with manipulator in ATEC • very radiation hard at beam height • sufficiently radiation hard at service level • preferably materials not highly activating and suitable for nuclear waste storage
Positioning / alignment accuracy	• 0.2 mm relative to collimator
Environment conditions to be considered (temperature, humidity, vacuum, radioactivity, radiation levels, EM fields, vibrations, accidental forces, ...)	• limited humidity (signal rail, plugs and cables) • limited dust (isolation check) • cable trays to be isolated from vibrations (from, e.g., water cooling pipes)

Connections / Interfaces / Fabrication

Relevant connections and interfaces	• to collimator insertion (which is its carrier) • to collimator: contact ensured by gravity • to collimator thermocouple • to electronics: low noise cables similar to e.g. MHI25 • electronics connected to run-permit system • compatibility with exchange flask “drive shaft” for signal rail and ATEC handling tools
Manufacturing specifications	• foils: similar to other aperture foils at 590 MeV or at BX2

Operation

Expected lifetime	• 30 years
Regular maintenance	• check of signal line insulation • check of signal line existence by influence test or beam measurement
Corrective maintenance (repair)	• replacement of defect aperture foil module in ATEC • replacement of signal rail in the field
Spare part policy	• aperture foil module, signal rail, feedthroughs: 2 sets • cables incl. plugs: material for 2 sets
(Redundancies in case of failure)	• partly: collimator KHHEI signal current • partly: collimator KHHEI thermocouple temperature

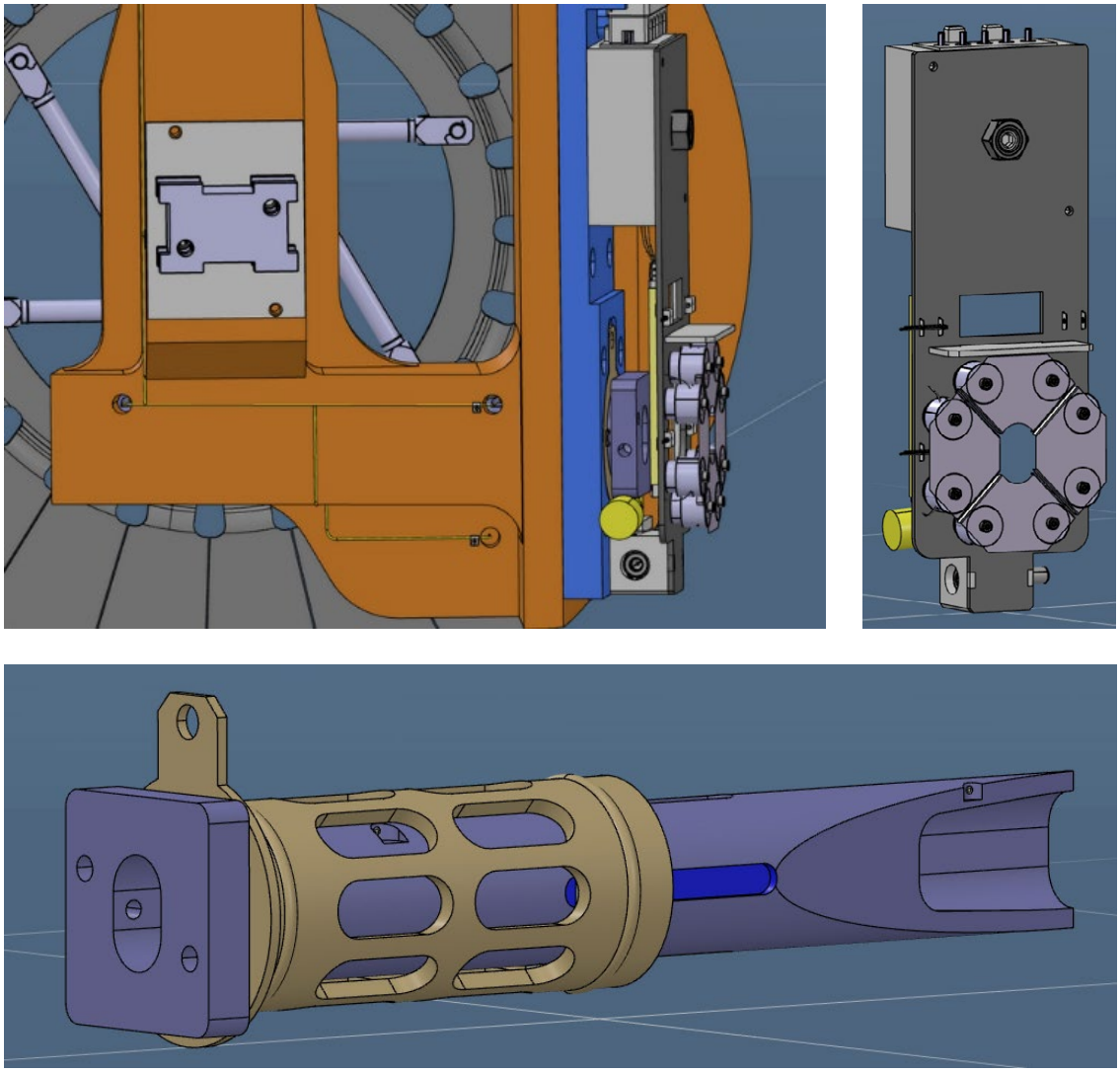

Figure 3.4.5: CAD images of the protection collimator and its aperture foil.

Figure 3.4.6: Thermocouple connection at front face of the protection collimator of Target M. Note that the protection collimator is electrically insulated to be able to measure the proton beam loss current in the collimator.

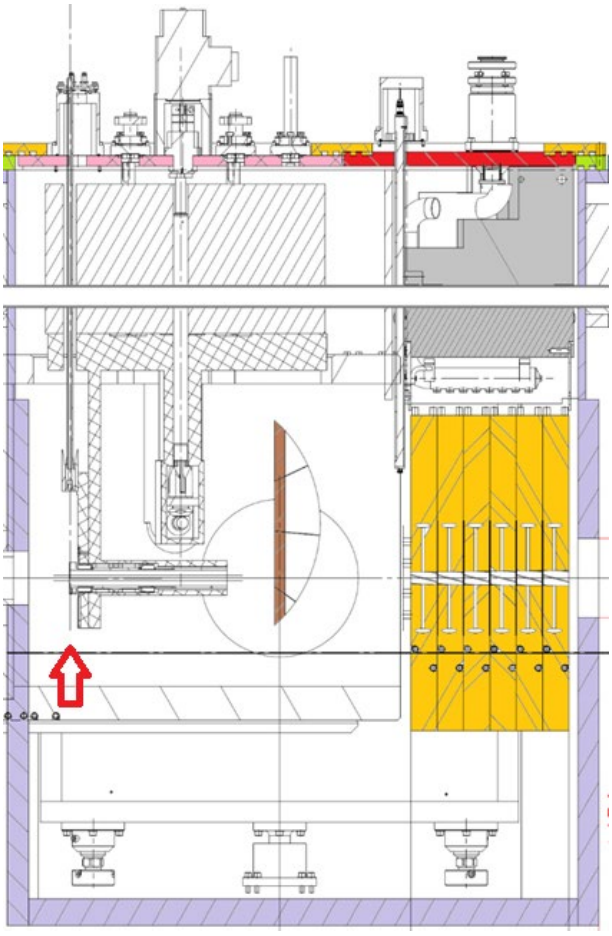

Figure 3.4.7: Location of the MHBEI aperture foil of the protection collimator along the beam line.

3.4.2.2 4-Segment Aperture Foil MHB0

Device	**4-Segment Aperture Foil MHB0**
See documents	Drawing PRD-00662200
List of sub-components / sub-systems, which are defined separately:	• collimator KHH0 (parent component) • read-out electronics (SoM-CAM) • exchange flask “drive shaft” for signal rail • ATEC handling tools

Basic Parameters

Main function	• permanent measurement of beam loss at four segments • generation of interlock in case of beam loss not as specified (prevents wrong horizontal or vertical beam position and size)
Design Guideline	• similar to existing aperture foils • modular approach for signal rail
Dimensions	• 637 mm × 185 mm × 40 mm

Weight	• 4.6 kg
Material(s)	• stainless steel, aluminium oxide • foils: molybdenum
Most important parts and interfaces (names)	• aperture foil module • signal rail • feedthroughs • long cables to electronics
Relevant parameters	• foils thickness: 50 µm • foils aperture: as collimator • foil pattern rotated 45° (gap between segments less critical)
Boundary conditions (constraints)	• aperture foil module suited to be replaced with manipulator in ATEC • very radiation hard at beam height • sufficiently radiation hard at service level • preferably materials not highly activating and suitable for nuclear waste storage
Positioning / alignment accuracy	• 0.3 mm relative to collimator
Environment conditions to be considered (temperature, humidity, vacuum, radioactivity, radiation levels, EM fields, vibrations, accidental forces, ...)	• limited humidity (signal rail, plugs and cables) • limited dust (isolation check) • cable trays to be isolated from vibrations (from, e.g., water cooling pipes)

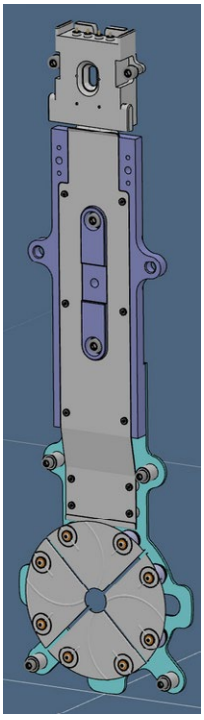

Figure 3.4.8: CAD image of MHB0 aperture foil.

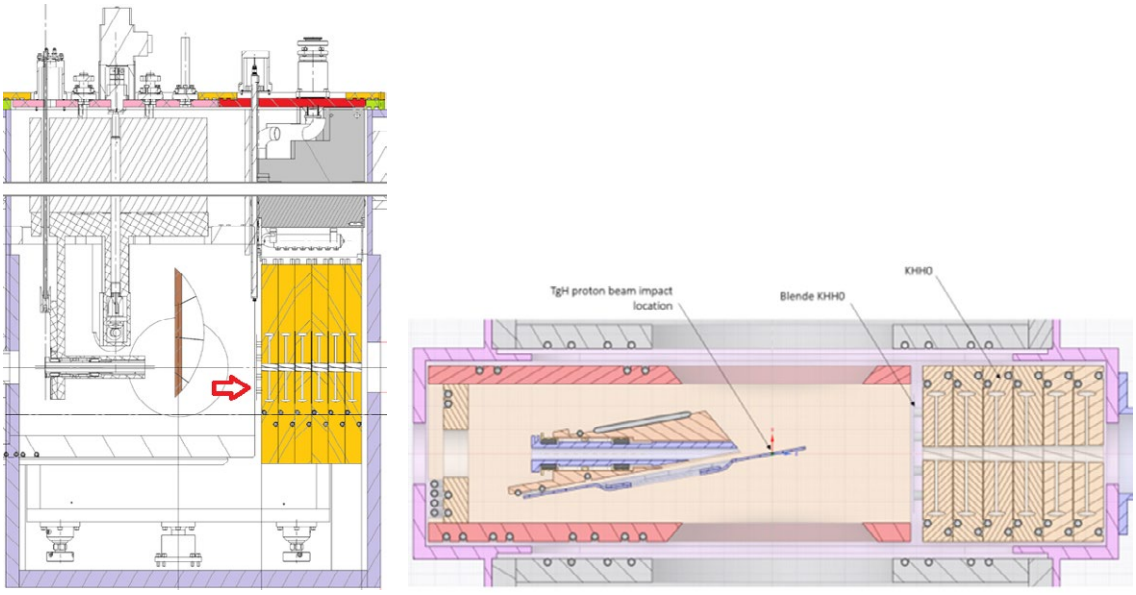

Figure 3.4.9: Side (left) and top (right) view of the KHM0 aperture foil.

Connections / Interfaces / Fabrication

Relevant connections and interfaces	• to collimator insertion (which is its carrier) • to electronics: low noise cables similar to e.g. MHI25 • electronics connected to run-permit system • compatibility with exchange flask “drive shaft” for signal rail and ATEC handling tools
Manufacturing specifications	• foils: similar to other aperture foils at 590 MeV

Operation

Expected lifetime	• 30 years
Regular maintenance	• check of signal line insulation • check of signal line existence • by influence test or beam measurement
Corrective maintenance (repair)	• replacement of defect aperture foil module in ATEC • replacement of signal rail in the field
Spare part policy	• aperture foil module, signal rail, feedthroughs: 2 sets • cables incl. plugs: material for 2 sets
(Redundancies in case of failure)	• partly KHH0 thermocouple temperature • partly: collimator KHHEI

3.4.2.3 4-Segment Aperture Foils MHB1 and MHB2

Device	**4-Segment Aperture Foils MHB1 and MHB2**
See documents	Drawing PRD-00641093
List of sub-components / sub-systems, which are defined separately:	• collimators KHH1 and KHH2 (parent components) • read-out electronics (SoM-CAM) • exchange flask “drive shaft” for signal rail • ATEC handling tools

Basic Parameters

Main function	• permanent measurement of beam loss at four segments • generation of interlock in case of beam loss not as specified (prevents wrong horizontal or vertical beam position and size)
Design Guideline	• similar to existing aperture foils • modular approach for signal rail
Dimensions	• 395 mm x 252 mm x 67 mm

Weight	2.4 kg
Material(s)	• stainless steel, aluminum • foils: nickel
Most important parts and interfaces (names)	• aperture foil module • signal rail • feedthroughs • long cables to electronics
Relevant parameters	• foils thickness: 100 µm • foils aperture: as collimator • alternatively foil pattern rotated 45° (gap between segments less critical)
Boundary conditions (constraints)	• aperture foil module suited to be replaced with manipulator in ATEC • very radiation hard at beam height • sufficiently radiation hard at service level • preferably materials not highly activating and suitable for nuclear waste storage
Positioning / alignment accuracy	• 0.3 mm relative to collimator
Environment conditions to be considered (temperature, humidity, vacuum, radioactivity, radiation levels, EM fields, vibrations, accidental forces, ...)	• limited humidity (signal rail, plugs and cables) • limited dust (isolation check) • cable trays to be isolated from vibrations (from, e.g., water cooling pipes)

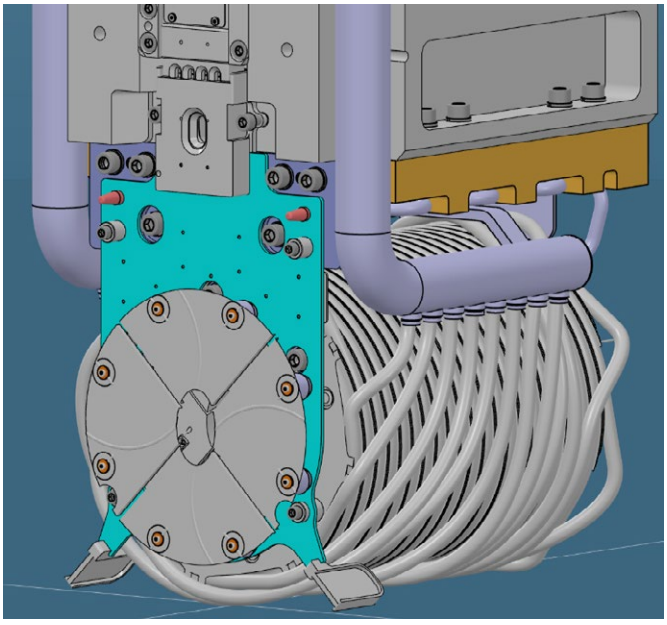

Figure 3.4.10: CAD drawing of the KHM1/2 aperture foil and the KHH1/2 collimator.

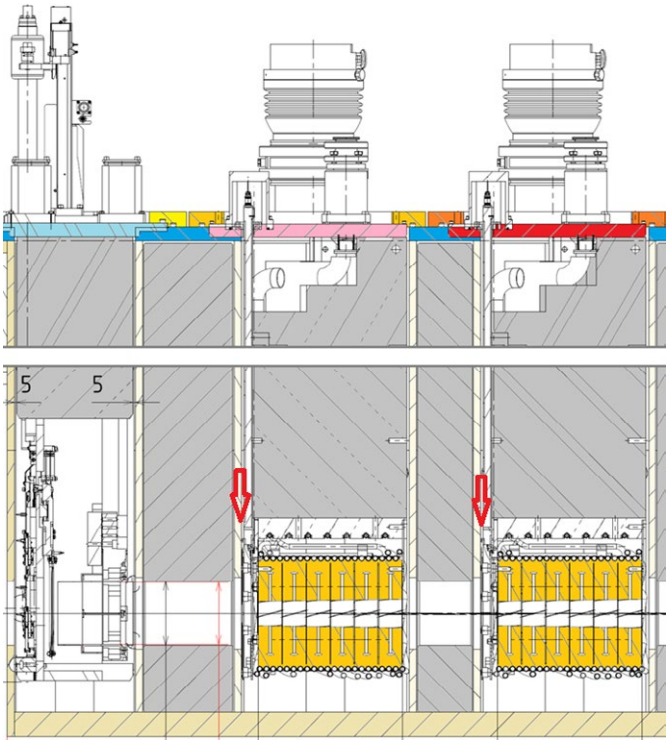

Figure 3.4.11: Location of the two aperture foils KHM1 and KHM2 along the beam line

Connections / Interfaces / Fabrication

Relevant connections and interfaces	• to collimator insertion (which is its carrier) • to electronics: low noise cables similar to e.g. MHI25 • electronics connected to run-permit system • compatibility with exchange flask “drive shaft” for signal rail and ATEC handling tools
Manufacturing specifications	• foils: similar to other aperture foils at 590 MeV

Operation

Expected lifetime	• 30 years
Regular maintenance	• check of signal line insulation • check of signal line existence by influence test or beam measurement
Corrective maintenance (repair)	• replacement of defect aperture foil module in ATEC • replacement of signal rail in the field
Spare part policy	• aperture foil module, signal rail, feedthroughs: 2 sets • cables incl. plugs: material for 2 sets
(Redundancies in case of failure)	• partly MHS23/24 • partly MHB1 for MHB2 and vice versa • partly KHH1 and KHH2 thermocouple temperature

3.4.3 Beam loss monitors

For HIMB, only one of the existing BLM (MHI11) will be replaced by a different type compatible with the design of the monitor plug MHP/S23B/24B and its vacuum chamber. This type of in-shielding ionization chamber is more modular than earlier variants and is in operation in the beam line as MHI25 since 2019.

Device	**In-Shielding Ionisation Chamber MHI11**
See documents	Similar to MHI25 drawing ASM-10002.24.2834 Drawing PRD-00761865
List of sub-components / sub-systems, which are defined separately:	• read-out electronics (SoM-CAM)

Basic Parameters

Main function	• permanent measurement of beam loss • generation of interlock in case of beam loss not as specified
Design Guideline	• copy of MHI25 (modular concept) • possibly unification of signal rail

Dimensions	• ~2900 mm × 98 mm × 35 mm (radius)
Weight	• ~70 kg
Material(s)	• shielding: iron (+nickel coating) • monitor: aluminum, stainless steel, aluminum oxide
Most important parts and interfaces (names)	• ionization chamber (IC) module with cover • signal rail • shielding block • long cables to electronics
Relevant parameters	• active volume as MHI25
Boundary conditions (constraints)	• IC module suited to be replaced with manipulator in ATEC • very radiation hard at beam height • sufficiently radiation hard at service level • preferably materials not highly activating and suitable for nuclear waste storage
Positioning / alignment accuracy	2 cm
Environment conditions to be considered (temperature, humidity, vacuum, radioactivity, radiation levels, EM fields, vibrations, accidental forces, ...)	• limited humidity (IC module, signal rail, plugs and cables) • limited dust (isolation check) • cable trays to be isolated from vibrations (from, e.g., water cooling pipes)

Connections / Interfaces / Fabrication

Relevant connections and interfaces	• to electronics: similar to MHI25 • electronics connected to run-permit system • compatibility to exchange flask
Manufacturing specifications	• similar to MHI25

Operation

Expected lifetime	30 years
Regular maintenance	• check of signal line insulation • check of signal line existence by influence test or beam measurement
Corrective maintenance (repair)	• replacement of defect modules in ATEC • replacement of signal rails in the field
Spare part policy	• complete insertion: 1 (for IC at several locations) • IC module, signal rail: 2 sets • cables incl. plugs: material for 2 sets
(Redundancies in case of failure)	• other loss monitors

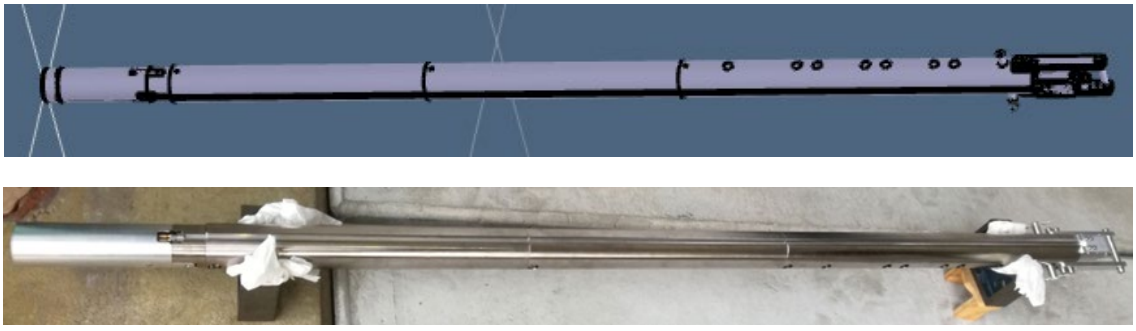

Figure 3.4.12: CAD drawing (top) and photo (bottom) of a beam loss monitor.

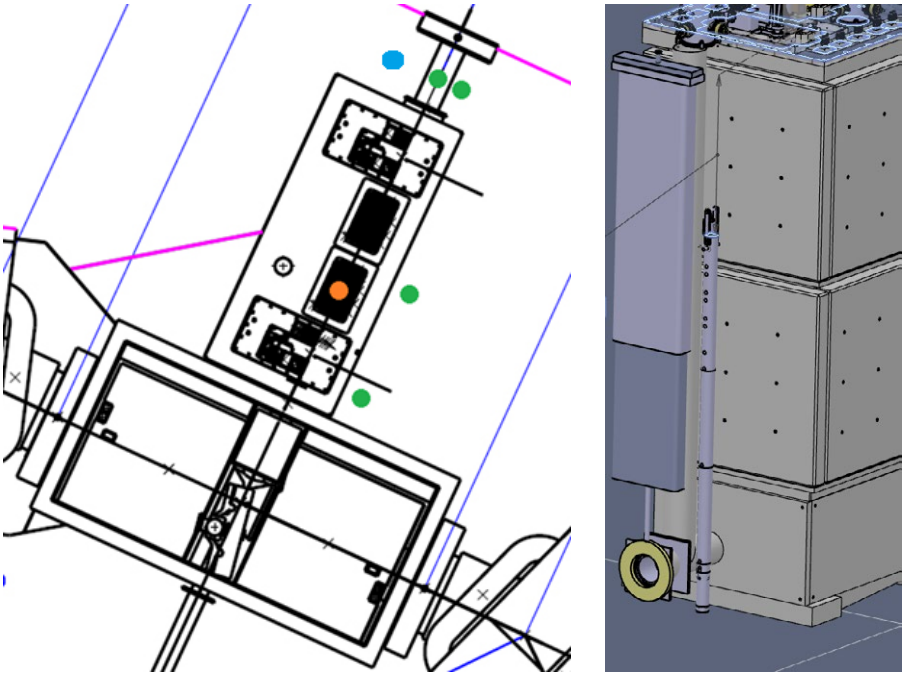

Figure 3.4.13: Left: Top view with new location of MHI 11(blue), behind PK2 vacuum chamber. Current location on top of KHM2 (orange) and other possible considered locations (green). Right: CAD drawing with MHI11, vacuum pump and PK2 vacuum chamber.

3.4.4 References

[1] Dölling, R. et al. 2020, *"Progress of profile measurement refurbishment activities at HIPA"*, Proc. 9th Int. Beam Instrum. Conference (IBIC), p.179-183, https://accelconf.web.cern.ch/ibic2020/papers/wepp33.pdf

[2] Dölling, R. et al. 2019, *"Development of modular spare parts for the profile and position monitors of the 590 MeV beam line at HIPA"*, Proc. 8th Int. Beam Instrum. Conf. (IBIC), p.402-406, https://accelconf.web.cern.ch/ibic2019/papers/tupp035.pdf

[3] Dölling, R. et al. 2022, *"Test of a prototype for modular profile and position monitors in the shielding of the 590 MeV beam line at HIPA"*, Proc. 10th Int. Beam Instrum. Conference (IBIC), p.92-95, https://accelconf.web.cern.ch/ibic2022/papers/mop24.pdf

[4] Dölling, R. 2023, *"Status 590-MeV-BPM, Messungen, Simulationen und weiteres Vorgehen"*, PSI Internal Technical Memo, 'HIPA-DIAGNO-DR84-075.02-07082023 Status 590 MeV BPM.pdf'

[5] Marcellini, F. 2024. *"CST and HFSS simulations of the IMPACT BPM"*, PSI internal presentation, '240705 Marcellini CST and HFSS simulations of the IMPACT BPM.pptx'

[6] Dölling, R. 2019, *"Ersatzteilbaukasten Profil- und Schwerpunktmonitor der 590-MeV-Strahlführung in Abschirmung – Ausgangslage, Zielsetzung, Anforderungen, Randbedingungen, Lastenheft (Update)"*, PSI Internal Technical Memo, 'HIPA-DIAGNO-DR84-055.01-17042019 Lastenheft Ersatzteilbaukasten Update.pdf'

[7] Keil, B., Huber, P. 2024. *"Developing a new beam position monitor electronics for HIPA, The PSI High Intensity Proton Accelerator"*, Proc. IPAC'2024, Beijing, China, 2024, TUP20.

3.5 Accelerator Control System and Network

The control system is a central part of any large research facility. It provides an abstraction layer between the underlying facility, and the functionality required by both technical staff and the end users. A few key aspects of a good control system are reliability, security, and ease of use. Furthermore, due to the long productive life expected of a large research facility, maintainability, and modularity with clear interfaces for future upgrades are particularly important.

IMPACT, as the rest of HIPA, follows a network distributed heterogeneous control system. The core units are input output controllers (IOCs), monitoring and processing variables representing logic and physical properties of the machines. Workstations in different control rooms execute software to tune, monitor, analyze and visualize the different parameters of the accelerator and its experiments. The different devices are segregated for safety and stability reasons between a machine network and an office network, connected via gateways and with different access rights for the various resources.

3.5.1 Requirements and Challenges

The control system must fulfill the needs of beamline users, control room operators, beamline scientists and be manageable by the available engineering manpower. Additionally,

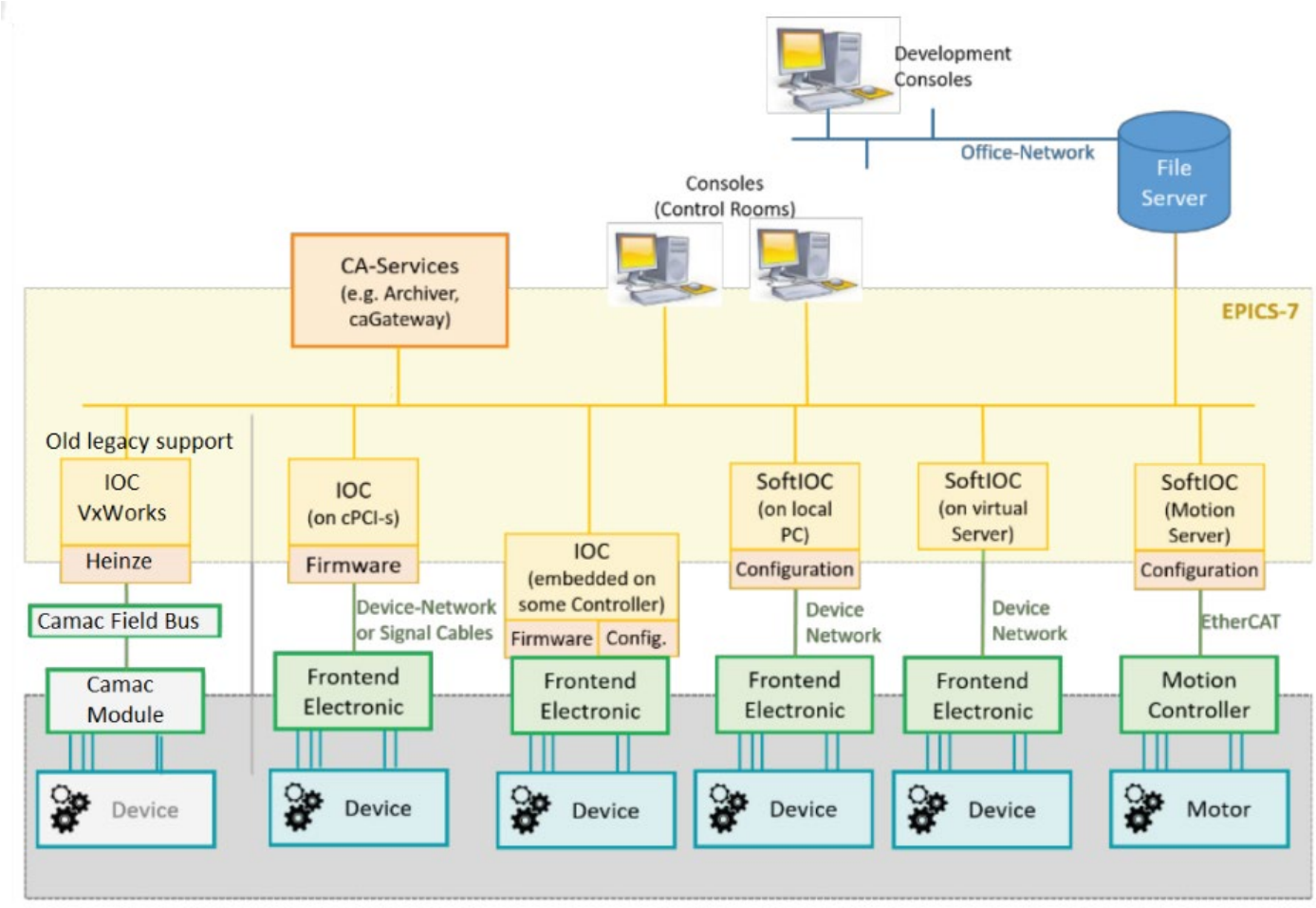

Figure 3.5.1: EPICS architecture for IMPACT and HIPA.

it needs to be tightly integrated with the existing HIPA infrastructure, which itself is made of different layers due to its historical development. Therefore, the main requirements are:

- Modular and incrementally upgradeable to allow for easy and concentrated maintenance.
- Scalable and easily extendable to provide opportunity for new ideas and solutions.
- Reliable to enable stable operation.

The main challenge of the IMPACT project for the control system is the integration into the existing control systems of the proton accelerator, providing backwards compatibility with legacy components until they are successively renewed during future upgrades. Therefore, the IMPACT control system will be rooted in the existing system while at the same time growing to accommodate new possibilities and developments.

3.5.2 Software

The control system is distributed and based on EPICS, which stands for Experimental Physics and Industrial Control System. For IMPACT and HIPA in general we use channel access process variables (PVs), which are units of information with different read, write and type properties used to distribute the many parameters of status and control of the machine. Those variables can be read and modified instantaneously, archived for later use, or visualized on displays, for which caQtDM is used. For more details, please refer to the technical note on the control system for HIPA [1], Sections 2.1.1. to 2.1.3.

The PVs originate in IOCs. They are control units meant to process certain input variables and produce output values required to visualize, regulate, or otherwise control parts of the machine.

There are *hard* and *soft* IOCs. The hard IOCs are electronic pieces of hardware equipped with a processing unit, network connectivity and typically a bus and or a physical interface to sensors, actuators, or other subordinated devices. Hard IOCs come in different form factors, some are standalone and some feature some sort of bus connection such as VME, CAMAC, OpenCPSI-S, uTCA and others.

The so-called soft IOCs instead are application specific programs that run on physical or virtualized servers, each with their own IP. They implement an EPICS interface for different applications without the need of a physical interface, for example controlling devices connected to the network or performing calculations. An overview of the different EPICS components can be found in Figure 3.5.1.

There are several operating systems (OS) in use for HIPA, mainly Linux and VxWorks. (see HTN [1], Section 2.2). For IMPACT the expected standard OS will be Linux, be it in the form of a virtualized soft IOC or embedded in a hardware IOC, if there are special requirements for the interface to physical signals.

3.5.3 Hardware

The main hardware platforms will be VME for motor control (MESON) and magnet control (DPC2), OpenCPSI-S for accelerator signal distribution, SoM-CAM for current acquisition, and WAGO for temperature measurement. The hardware platforms are briefly described below. For more thorough descriptions of the various hardware types and boards, refer to the technical note [1] Section 2.3.

3.5.3.1 VME

VME stands for Versa Module Europa and is the most commonly standard used for controls hardware in HIPA. VME is used for hardware IOCs, as well as carrier boards for different applications such as motion control, data acquisition, power supply control and others. However, VME architecture is an outdated technology. For the IMPACT project, whenever possible, we will be using newer hardware IOCs such as OpenCPSI-S and virtualized soft IOCs as standard solutions.

3.5.3.2 OpenCPSI-S

OpenCPSI-S stands for Open Common Parallel Serial Interconnect Solution. It is PSI variant of the industry standard CompactPCI Serial (CPCI-S) which is a computer bus interconnect standard that uses serial point-to-point connections for communication among the system's boards. OpenCPSI-S is compatible with CPCI-S and we can therefore also use and mix commercial products in this system.

Compact PCI Express hardware is currently used in HIPA for RF subsystems only, and not part of the general control system. It is planned to use OpenCPSI-S hardware for the new accelerator signal distribution system nodes. In the future, OpenCPSI-S will eventually replace VME based systems.

3.5.3.3 SoM-CAM

The SoM-CAM is a multi-channel high-dynamic range current amplifier and digitization box, with built-in signal processing, networking capabilities, and hardware expansion slots. Its operating system is Linux, running an EPICS IOC. It can operate stand-alone or in a series-connected network with other SoM-CAMs to form a virtual backplane. It is provided in a 1U 19" rack mount housing.

The feature set and flexibility of the SoM-CAM will make it a key component for current measurement and data processing for diagnostic sensors at HIPA. It will replace all legacy CAMAC-based current amplifier boards, other miscellaneous electronic boards, and their respective CAMAC crates. Hence it will unify most HIPA diagnostic electronics, simplify installation, setup and maintenance, and boost reliability.

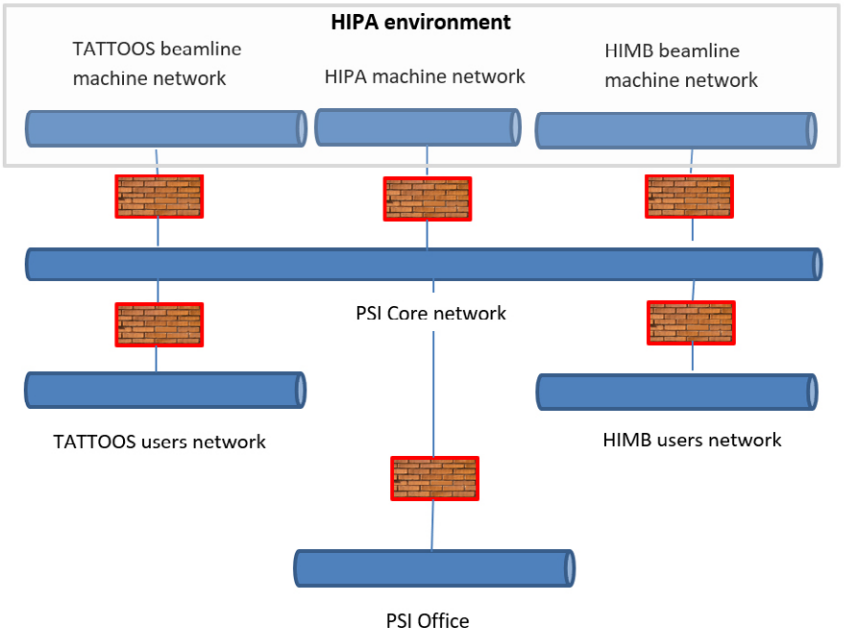

Figure 3.5.2: IMPACT proposed Ethernet controls network infrastructure

It will increase functionality while maintaining the existing level of machine protection.

The SoM-CAM features twelve galvanically isolated current measurement inputs that cover the range from 10 pA to 10 mA. Its bandwidth is up to 50 kHz. It can also apply bias voltages to the inputs to reduce undesired effects due to secondary electron emission or thermo-electron emission, depending on the sensor. In addition, hardware expansion modules can provide digital inputs and outputs or generate high-voltage bias voltages, which are required for ionization chambers, for example.

3.5.3.4 WAGO

WAGO IO systems are input/output peripherals with programmable logic control capability (PLC). PSI uses the WAGO "I/O-SYSTEM 750". It is widely used at PSI as a standard, cost-efficient low speed, no real time data acquisition, such as to measure temperature and pressure. Data is streamed through a simple Ethernet port via Modbus TCP as binary and analog values to a soft IOC. On this soft IOC the channels are converted to EPICS process variables.

3.5.4 Network Infrastructure

The controls network infrastructure is divided, as in the case of all PSI accelerators, between a general PSI Office network and its own facility machine network, with dedicated network attached storage, environment variables and physical resources. IMPACT new experimental areas, MuH2 and MuH3, will be segregated from the rest of the machine network, as it is currently the case. The traffic is controlled with the use of gateways. The proposed network distribution is described in more detail in the technical note [1] Section 2.4.1 and visualized in Figure 3.5.2. The EPICS protocol runs on the Ethernet controls network.

Besides the controls network there will also be the beam diagnostics network, the accelerator signal distribution network, and the interlock network. These are described below in Section 3.5.5 "Subsystems".

3.5.5 Subsystems

The main common and facility subsystems and their solutions for IMPACT are briefly described below. For more thorough explanations, please refer to the technical note on the control system for HIPA [1] Chapters 3 and 4.

3.5.5.1 Timing

There are currently no requirements on time synchronization above repetition rate of 1 Hz. In case of future need for synchronization faster than 10 Hz, there are two standard solutions supported at PSI: The Timing and Event System by Micro-Research Finland and an OpenCPSI-S based hardware implementation.

3.5.5.2 Motion Control

For motion control there are different technical solutions depending on the application. For beam profile monitors with stepper motors, there are the existing VME based MESON, and in the future Beckhoff-based ECMC, possibly synchronized with SoM-CAM for data acquisition.

3.5.5.3 Accelerator Signal Distribution

The purpose of the accelerator signal distribution is to broadcast select machine information with very low latency to certain time-critical machine diagnostics and to user beamlines. The main signals of interest are the proton beam current at various locations, the machine RF (50.6 MHz), and UCN kick timing signals. The currently installed accelerator signal distribution is based on an electrical distribution network. This legacy system will be replaced by a digital system based on a fiber optic network and digital end-stations. It will later be expanded and partially rerouted to accommodate new elements for IMPACT.

3.5.5.4 Temperature Measurements

All temperature measurements are performed with WAGO systems. Temperature sensors are thermocouples for good accuracy and radiation hardness.

3.5.5.5 Cameras

At HIPA the cameras are not attached to the control system but handled separately by the users with standalone computers.

3.5.5.6 Magnet Control

The control system interface to the power supply controllers provides EPICS integration of the magnet power supplies and depending on the model also interface to the interlock network. For new magnets of IMPACT these control system interfaces will be available:

- CPSI-S CIO board with MIO rear transition module supporting six POFs for up to six power supply controllers. An EPICS IOC will run on the CIO board. The CIO board will be directly connected to the EPICS network. It can generate interlocks through its connection to the interlock network. This solution supports all types of power supply controllers, i.e. Multi-IO, PSC, DPC, and DPC2.
- Soft IOC for power supply controller which have a network interface, i.e. DPC2 (same as for SLS). Soft IOCs do not support interlocks.

The selection of power supply controller type for each magnet depends on the requirements of the magnet power supply and the need for interlock. For description of the magnet power supplies and the power supply controllers see Chapter 3.3 “Power Supplies for Magnets”. For description of the purpose and function of interlocks see the subsequent Section 3.5.5.9 “Machine Protection System”.

3.5.5.7 Vacuum and Cooling

Vacuum and cooling control will be based on Siemens PLC, where each PLC is interfaced by a dedicated soft IOC using the S7 protocol and the field bus will be Profinet.

3.5.5.8 Diagnostics

The read-out electronics for beam profile monitors (Section 3.4.1), aperture foils (Section 3.4.2) and beam loss monitors (Section 3.4.3) is SoM-CAM, which is described briefly above in Section 3.5.3.3 and in detail in the technical note [1]. The Read-out electronics for the beam position monitors (Section 3.4.1) is DBPM3-HIPA, which is described in Section 3.4.1.2.

The SoM-CAMs and the DBPM3-HIPA are connected to EPICS via the controls network. The SoM-CAMs are also connected to the beam diagnostics network in a mixed ring/star topology using fiber optic links (virtual backplane). Each SoM-CAM also has a direct connection the interlock network via a fiber optic link.

3.5.5.9 Machine Protection System

The machine protection system stops the beam to prevent damage to the machine in case of anomalies, malfunctions, or any other unsafe condition. Interlock signals are collected from more than 1200 measurement points, mainly from the beam loss monitors and magnet power supply control system interfaces, by the interlock network and processed by USI2 VME boards to generate the beam stop signal. The beam stop signal generation is a complex algorithm of weighted thresholds, and suppressed and unmasked inputs, which depend on the machine operation modes.

For historical reasons, in this TDR the terms “machine protection system”, “interlock system”, and “run-permit system” are used as synonyms.

3.5.5.10 Target H

The target is controlled by a stand-alone PLC with PSI-made logic. It provides an EPICS interface, with basic commands such as start, stop, and monitor.

3.5.6 References

[1] CAS AEK Electronics and Controls, “Control System for HIPA,” Paul Scherrer Instiute (PSI), Villigen, Switzerland, Technical Note, v1.7, Aug. 2024. Available: Alfresco, https://i.psi.ch/78o (TN_HIPA_Control_Systems_v1-7.pdf).

3.6 Slit Systems

Slit systems are typically used along the secondary beamlines to shape the size and divergence of the beam, adjust its intensity, and tune the momentum acceptance. We foresee three new slit systems: Two along the MuH2 beamline and one in the new part of the MuH3 beamline.

3.6.1 FSH21 / FSH31

The first slit systems FSH21 and FSH31 will be installed in both beamlines within one of the bending magnets itself. This slit system will allow to control the intensity and shape of the momentum acceptance. However, it should be noted that due to the extremely high acceptance and transmission of the solenoidal channel, with limited momentum resolution, only a limited tuning of the momentum acceptance will be possible. The whole slit system will be placed in the vacuum chamber of the magnet ASH21 & ASH32 (Figure 3.6.1). The drive consists of a stepper motor for each plate which moves the jaws via a gearbox (Figure 3.6.2) and can position them with an accuracy of approx. +/- 0.5 mm. A reference run of the limit switches is necessary to determine the exact and absolute position. A 10-turn potentiometer provides additional safety and control over the absolute position of the plates.

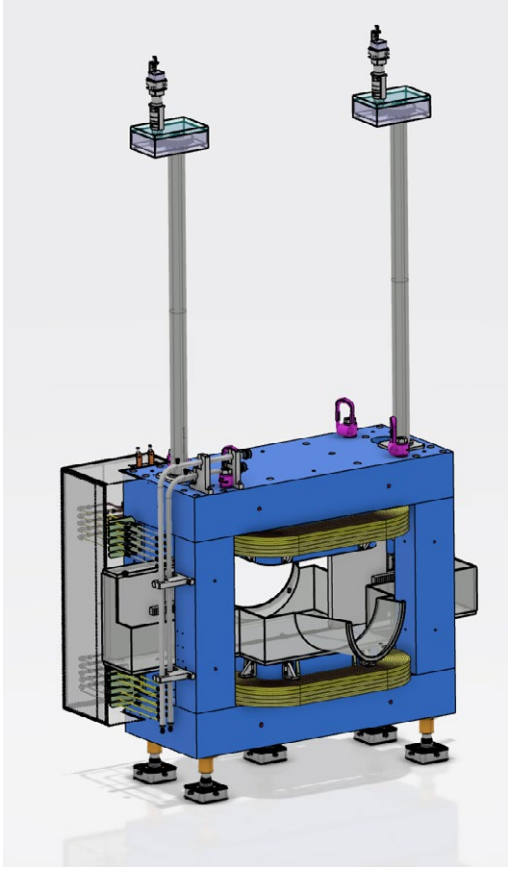

Figure 3.6.1: FSH21 / FSHK31 with vacuum chamber and dipole magnet

Figure 3.6.2: FSH21 / FSH31 mechanical principle

FSH21 / FSH31

Main function	Horizontal slit system	
Dimensions	Tank complete (L×W×H): Only collimator mechanic: Drive with extension: Collimator plate length	1491×2270×3417 mm 270×2124×500 mm 240×350×2898 mm 40 mm
Location	Within the Bending dipole magnet ASH21 & ASH32 in MuH2 & MuH3	
Jaws/plates	OFHC copper thickness 40 mm or Densimet with 20 mm thickness	
Drivetrain	Stepper motor located on the service level	
Functionality	Two independently movable plates that can move from the center of the magnet to fully open. A small gap of a few mm in the closed position is acceptable.	
Boundaries	Minimal slit opening: Maximal slit opening:	< 5 mm 500 mm
Alignment accuracy	+/- 0.5 mm position reproducibility	
Limit switch detection	Inside of Vacuum: proprietary end switches Outside of vacuum: Siemens Sirius (3SE5)	
Position detection	Relative position based on the steps of the stepper motors. Absolute position by a 10-turn Vishay potentiometer (502-21103).	
Control system	Beckhoff slit control system	
Environment conditions	Vacuum pressure foreseen: Max ventilation pressure: He Leak rate: Radioactivity: Sealing: Transport: Magnetisms:	$< 10^{-6}$ mbar 1.2 bar $< 10^{-8}$ mbar l s^{-1} activation expected metal together with dipole No iron or steel parts
Expected lifetime	30 years +	
Maintenance	Vacuum: Slit system:	Annual pump service The vacuum group offers an on-call service and a large spare parts pool. Maintenance free Major repairs are only planned during the annual shutdown. The control unit offers compensation options for limit switches or potentiometer failure. Service only during office time.

3.6.2 FSVK21 / FSHK21

The second slit system will be located at the end of the MuH2 beamline and allow to adjust and shape the beam spot upstream of the final focus.

The design of the slit systems will follow the existing designs used at the other secondary beamlines adapted to the larger aperture of MuH2 and MuH3. It is made from a 40 mm thick copper plate (alternatively 20 mm Densimet). The whole slit system will be placed in its own vacuum chamber (Figure 3.6.3) The drive consists of a stepper motor for each plate which drives the plates via a gearbox (Figure 3.6.4) and can position them with an accuracy of approx. +/- 0.5mm. A reference run to the limit switches is necessary to determine the exact and absolute position. A 10-turn potentiometer provides additional safety and control over the absolute position of the plates.

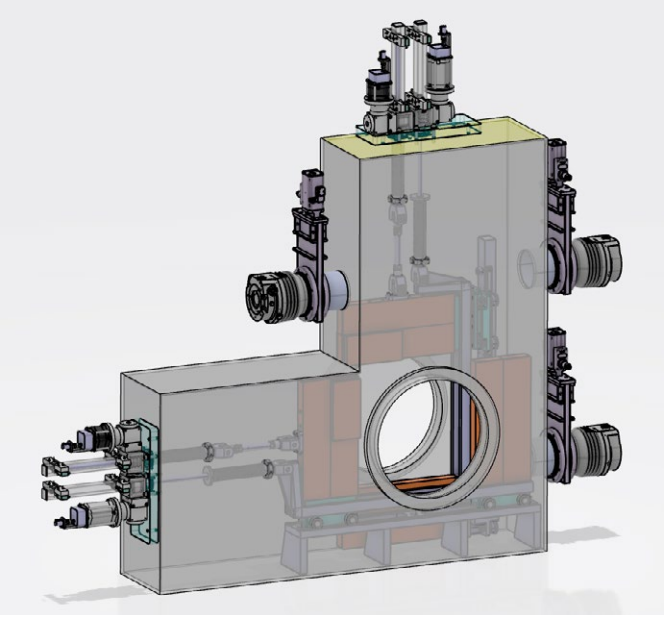

Figure 3.6.3: FSVK21 / FSHK21 with vacuum chamber

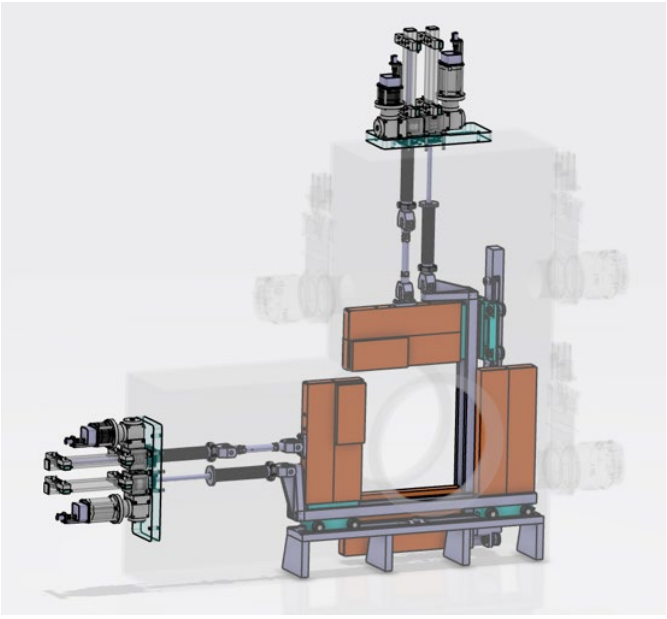

Figure 3.6.4: FSVK21 / FSHK21 mechanical principle

FSVK21 / FSHK21

Main function	Horizontal and vertical slit system	
Dimensions	Tank complete (L×W×H): Collimator plate length:	536×2605×2224 mm 40 mm
Location	Standalone after the separator right before the last magnet of the beamline	
Jaws/plates	40 mm thick OFHC copper or 20 mm thick Densimet	
Drivetrain	Stepper motor drive for each collimator plate	
Functionality	Four independently movable plates that can move from the center of the magnet to fully open. A small gap of a few mm in the closed position is acceptable.	
Boundaries	Minimal slit opening: Maximal slit opening:	< 5 mm 500 mm
Alignment accuracy	+/- 0.5 mm position reproducibility	

Limit switch detection	Outside of vacuum: Siemens Sirius (3SE5)	
Position detection	Relative position based on the steps of the stepper motors. Absolute position by a 10-turn Vishay potentiometer (502-21103) for each axis (plate)	
Control system	Beckhoff slit control system	
Environment conditions	Vacuum pressure foreseen: Max ventilation pressure: He Leak rate: Radioactivity: Sealing: Transport:	$< 10^{-6}$ mbar 1.2 bar $< 10^{-8}$ mbar l s^{-1} ow, no activation expected Viton O-ring Crane lifting
Expected lifetime	30 years +	
Maintenance	Vacuum: Slit system:	Annual pump service The vacuum group offers an on-call service and a large spare parts pool. Maintenance free Major repairs are only planned during the annual shutdown. The control unit offers compensation options for limit switches or potentiometer failure. Service only during office time.

3.6.3 Slit motion control

In HIPA there are many motors which are used to open a gap for the beam. 4 motors (top, bottom, left and right) move e.g. a densimet plate (tungsten alloy) so that a gap in the beam path is opened. Another variant of opening a gap is to use 2 oval plates which can be moved against each other.

Controls are used for slits (uncooled densimet plates PSI abbreviation FS, see Figure 3.6.5), movable collimator jaws (water-cooled with copper plates in the proton beam, PSI abbreviation KHN) and degraders (retractable plastic filter plates in the secondary areas, PSI abbreviation DSC).
A so-called slit control ("Spaltsteuerung") is currently being used for this. These have been in use for many years. If there are defects, it is becoming increasingly difficult to repair the components, because spare parts are no longer available, and the technology is outdated. By using state-of-the-art technology, we are well prepared for the next 20 years.

Several areas in HIPA have already been updated with a new PLC. The slit control at MuH2 (PiM1) and MuH3 (PiM3) will also be renewed.

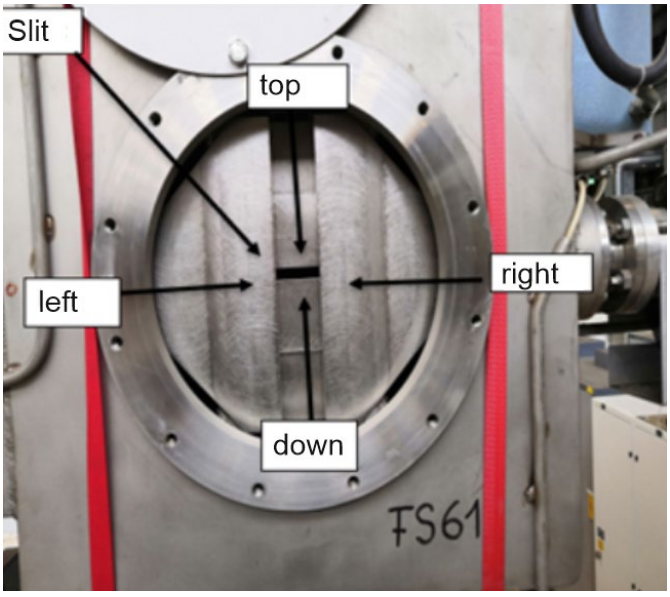

Figure 3.6.5: Slit FS61 as an example.

3.7 Beam Blocker

The position and shielding effect are determined by simulation and calculations within Chapters 2.1 and 2.4.

Two large 320-mm thick beam blockers (“KSL”) made of copper and stainless steel will be installed after the first dipoles ASP21 (MuH2) and ASP31 (MuH3). They are named KSL21/22 and KSL31/32 (Figure 3.7.1). Another two 320-mm thick beam blockers (“KSK”, Figure 3.7.2) made of copper, 5% borated polyethylene and stainless steel will be installed after the second/third bending magnets ASH21 & ASH32. The exact composition is shown in Figure 3.7.3.

The beam blockers will be designed based on the existing installations adapted to the larger aperture sizes of the MuH2 and MuH3 beamlines. As one of the new safety functions, the blockers will be driven directly and not by chains as in the currently used beam blockers. This, combined with safety-related limit switches makes sure that the beam blockers will close in case of a failure. Both beam blocker types will be inserted into a big vacuum chamber, while the KSL type can be taken out via the service level, the KSK is accessible directly after the removal of the shielding blocks.

As an additional measure for fire protection and vacuum reasons, the polyethylene must be enclosed in a vacuum-tight housing.

Figure 3.7.1: KSL beam blocker

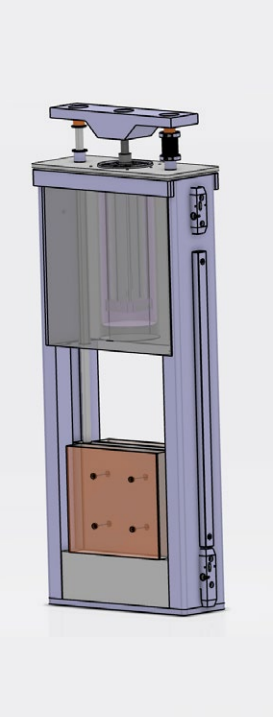

Figure 3.7.2: KSK beam blocker

Figure 3.7.3: Structure & materials of the beam blockers

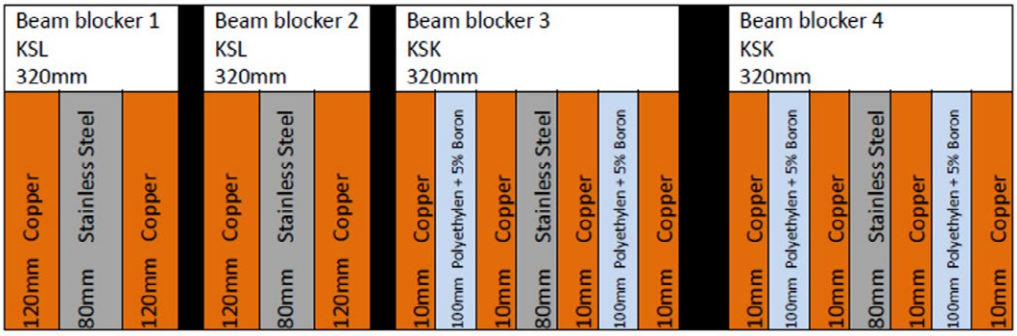

Material	Thickness	Material density	Shielding aquivalent S=794.08g/cm²
Copper	560mm	8.93g/cm³	500.08g/cm²
Stainless Steel	320mm	7.90g/cm³	252.80g/cm²
Polyethylene + 5% Boron	400mm	*1.03g/cm³	41.20g/cm²

3.7.1 KSL21 / KSL22 / KSL31 / KSL32

KSL21 / KSL22 / KSL31 / KSL32

Main function	Safety element for blocking off the beam in the area during accelerator operation.	
Dimensions	Beam blocker (L×W×H): Beam Blocker open: Shielding block thickness:	372.5×1000×3448 mm 372.5×1000×3948 mm 320 mm Cu 120mm / Fe 80mm / Cu 120 mm
Location	After the first dipole magnets	
Blocker plates	Copper - stainless steel - copper	
Drivetrain	Pneumatic cylinder	
Functionaltity	The beam blocker is closed in the rest position and closes automatically by gravity if it is not actively held open. It can only be opened if the PSYS control unit allows it.	
Boundaries	Closed in its rest position, actively opened Safety performance Level E is targeted for the design	
Limit switches	Detection outside of vacuum: Siemens Sirius (3SE5); two independent end switches	
Control system	PSYS control system	
Environment conditions	Vacuum pressure foreseen: Max ventilation pressure: He Leak rate: Radioactivity: Sealing: Transport: Closing time:	$< 10^{-6}$ mbar 1.2 bar $<10^{-8}$ mbar l s^{-1} activation expected metal exchange flask +/- 15 s
Expected lifetime	30 years +	
Maintenance	Drive system: The Beam blocker can only be repaired when the accelerator is switched off. In the event of a failure, the next steps must be planned together with the operators and the radioprotection personnel. Personal safety always remains the top priority. Service only during office time.	Maintenance free, durable, oversized elements foreseen

3.7.2 KSK21 / KSK31

KSK21 / KSK31

Main function	Safety element for blocking off the beam in the area during accelerator operation.	
Dimensions	Beam blocker (L×W×H): Shielding block thickness:	715×945×2215 mm 480 mm
Location	After the bending magnets ASH21 & ASH32	
Blocker plates	Copper – 5% borated polyethylene – copper - stainless steel – copper – 5% borated polyethylene - copper	
Drivetrain	Pneumatic cylinder	
Functionality	The beam blocker is closed in the rest position and closes automatically by gravity if it is not actively held open. It can only be opened if the PSYS control unit allows it.	
Boundaries	Closed in its rest position, actively opened Safety performance Level E is targeted for the design	
Limit switches	Detection outside of vacuum: Siemens Sirius (3SE5); two independent end switches	
Control system	PSYS control system	
Environment conditions	Vacuum pressure foreseen: Max ventilation pressure: He Leak rate: Radioactivity: Sealing: Transport: Closing time:	$< 10^{-6}$ mbar 1.2 bar $< 10^{-8}$ mbar l s^{-1} activation expected metal crane +/- 15 s
Expected lifetime	30 years +	
Maintenance	Drive system: The Beam blocker can only be repaired when the accelerator is switched off. In the event of a failure, the next steps must be planned together with the operators and radioprotection personnel. Personal safety always remains the top priority. Service only during office time.	Maintenance free, durable, oversized elements foreseen

3.8 Separator

3.8.1 Introduction

Electrostatic separators, which work according to the Wien filter principle, are required to filter the particle beam. Briefly explained, the different particles pass between the two electrode plates and are deflected by the electric field. The deflection is canceled for the desired particle type through a perpendicular magnetic field sensitive on the velocity of the particles.

For more details see IMPACT CDR [1], Chapter 7.5 Particle Separation Process: Separator and Spinrotator.

An electrode length of 1900 mm is required for sufficient separation, but this must be divided between two separators, as the beam has to be refocused with a solenoid in between.

3.8.2 Key data and requirements

Basic Parameters

Main function	Crossed-field electric/magnetic Wien-filter to separate unwanted background particles from wanted beam particles via velocity selection	
Dimensions (mm)	Tank & Magnet (L×W×H):	1691×2440×2212 mm
	Only tank (L×W×H):	1691×2022×2013 mm
Material(s)	Magnetic Steel Frame & Shielding:	Steel S235
	Electrodes:	Titanium
	Coils for Dipole:	Copper OFHC
	Vacuum Tank:	Stainless steel 316L
	Isolator:	aluminum oxide ceramic
Weight (without LLA)	Magnet	11.090 t
	Chamber with electrodes	2.200 t
	High voltage Power supplies	2×0.600 t
	High voltage resistor	2×0.330 t
	Control rack	0.350 t
	Vacuum components	0.200 t
	Gate valve NW500	0.235 t
	Cables	0.200 t
	Platform	1.760 t
	Total	**17.895 t**
Most important parts and interfaces (names)	• Steel Housing • 2× Vertical Dipole Magnets with water cooling • 2× moveable Titanium Electrodes • 2× stepper motor drive & transmission (NEFF) & linear bearings	

	• 2× high voltage feedthrough • 2× high voltage resistor • 2× high voltage power supplies • Large Vacuum Tank • Vacuum pump unit • 4× Adjustable 10 t feet's between support structure and ground. • 3× Adjustable 1 t feet's between support structure and vacuum tank • Support Structure with resistors, HV power supplies, control rack and opening for a solenoid. • Load Lifting Atachment (LLA)
Functionality	The high-voltage field deflects all particles to the side. The magnetic field, perpendicular to the electric field, directs the desired wanted particles back onto the beam axis at the appropriate speed.
Boundary conditions (constraints)	Beamline height: 1500 mm Gap between electrode: 300–450 mm Electrode length: 950 mm Electrode height: 630 mm Max E-field inside vacuum tank: 60 kV/cm Nominal high voltage: 2×320 kV Max. high voltage (pos/neg): 2×350 kV E-field (HV) distance 450mm: 15.55 kV/cm E-field (HV) distance 300mm: 23.33 kV/cm Integral E-field (HV) @450mm: 1477.7 kV Integral E-field (HV) @300mm: 2216.6 kV Highly polished HV-parts: Ra 0.1 µm Dipole B-field: > 0.04 T

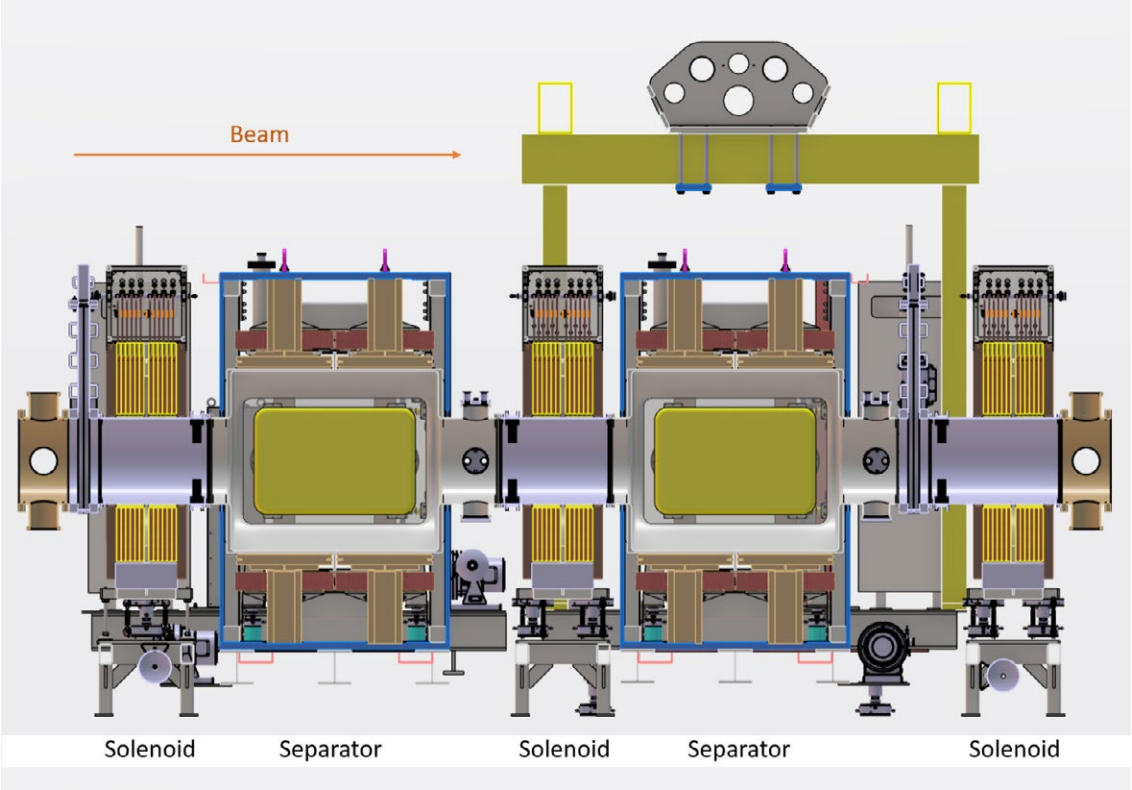

Figure 3.8.1: The picture shows the beam section (cut open along the beam axis) with the two separators and the necessary solenoids and vacuum valves on both ends.

Positioning / alignment accuracy	• Coil positioning +/- 0.5 mm • Electrode positioning reproducibility +/- 0.2 mm • Electrodes must be parallel • Magnetic-axis tilt with respect to geometric axis < 2 mr • Magnetic axis & electrostatic axis 90° to each other	
Environment conditions to be considered/ required/ specified (temperature, humidity, vacuum, radioactivity, radiation levels, EM fields, vibrations, accidental forces, ...)	Vacuum pressure foreseen: Max ventilation pressure: He Leak rate: Sealing: Radioactivity: X-ray: EM fields: Vibration: Transport:	$< 10^{-7}$ mbar 1.2 bar $< 10^{-8}$ mbar l s^{-1} Viton O-ring low activation expected with high voltage switched on with Magnet switched on Scroll vacuum pump (absorber) Load Lifting attachment (LLA)

Connections / Interfaces / Fabrication

Cooling	Magnet:	• Water-cooled coils • Delta T 2K • Delta P 3bar • Flow speed = 1.7 m/s • Volume flow = 40 l/min • Temperature sensors required • Water flowmeters required
	Turbo pump:	• Water cooling (redundancy air cooling) • Demineralized water
Power	1× Power Supply (PS) for Dipole Coils • Bipolar switchable PS • Maximum current 200 A (Nominal up to 200 A) • Maximum voltage 50 V (Nominal up to 39 V) • Maximum power 7.8 kW @ 200A/39V 1× Positive High Voltage Power Supply • Max. voltage 350 kV (nominal 320 kV) • Max. current 1 mA (nominal < 0.005 mA) • Max. Power 350 W 1× Negative High Voltage Power Supply • Max. voltage 350 kV (nominal 320 kV) • Max. current 1 mA (nominal < 0.005 mA) • Max. Power 350 W	
Magnetic Field	• Max. B-Field > 44 mT @ 200 A • Surface Muon B-Field max = 36 mT • Magnetic Housing Thickness 20 mm • R-Load: 195 mΩ (4 Coils)	

Electric Field dependent on variable electrode gap between 300–450 mm	Max. high voltage (pos/neg): • E-field (HV): • Integral E-field (HV): Nominal high voltage (pos/neg): • E-field (HV): • Integral E-field (HV):	2×350 kV 15.55–23.33 kV/cm 1477.7–2216.6 kV 2×320 kV 14.22–21.33 kV/cm 1351.1–2026.6 kV
Manufacturing specifications	For vacuum components • only vacuum-compatible materials (no silicones) may be used in the production process. Attention: many polishes have silicates as binders • after production, all components should be vacuum-cleaned and the sealing surfaces protected against damage. More information, see Chapter 3.9.4	
Load Lifting Attachment (LLA)	Color: Crane spreader beam: Attachment to crane hook: Attachment to platform: Capacity K+P bolt system: Weight Traverse Frame concept: Lifting capacity LLA: Mounting on crane hook: Test: Documentation:	yellow concept K+P bolt system bolted connection 22 t 2 t 20 t from ground by hand official external certification Instruction manual

Operation

Expected lifetime	30 years +	
Regular maintenance	Vacuum: HV System: Resistors: Gap drive: Magnet:	Annual pump service Reconditioning Maintenance free, durable Maintenance free, durable, oversized elements foreseen maintenance free
Corrective maintenance (repair)	Vacuum: HV System: Resistor: Gap drive: Magnet: LLA:	The vacuum group offers an on-call service and a large spare parts pool. all important parts on stock because of long delivery time. Service only during office time. 1:1 replacement Service only during office time. all important parts on stock because of long delivery time. Service only during office time. Coil, water hose on stock. Service only during office time. Annual inspection for recertification
Spare part policy (redundancies in case of failure)	Spare parts should be kept in stock on a risk-based basis.	

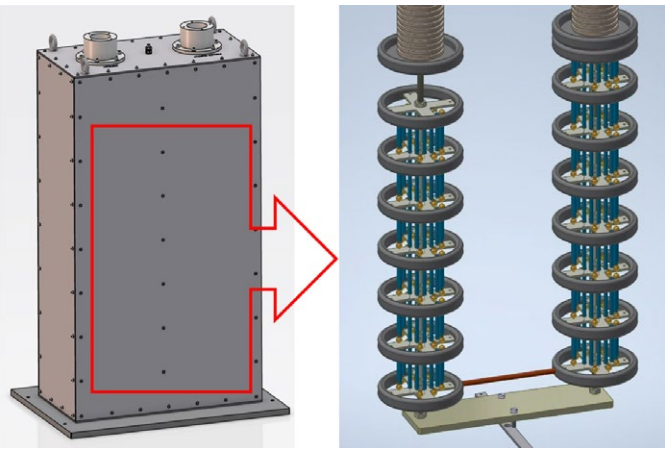

Figure 3.8.2: (Left) Concept model of the HV resistor, (Right) Internal structure of the HV resistor with exponentially increasing individual resistors in series, [pictures by Heinzinger 14.04.2025]

3.8.3 High voltage part

3.8.3.1 High voltage power supplies

The high voltage is to be generated by one positive and one negative 350 kV supply unit. They should each be housed in a 19" cabinet that can be bolted to the base frame. The electrical connection to the system is to be made using commercial Essex cables and plugs.

3.8.3.2 High voltage resistor

Series resistors are to be installed between the high-voltage power supply and the electrodes for damping in case of a discharge. The resistors use a silicone casting as insulation material. This solid insulator has a much better dielectric strength than oil. The resistors are connected to commercial, oil-free Essex sockets.

The resistance of the resistor is in the order of 5 MΩ. The resistor cascade is divided into two parts. On the side of the high voltage tank the resistances are exponentially increasing, on the HV device side the large resistances are planned. The foreseen dimensions are (L×W×H) 645×300×1200 mm, the weight more than 300 kg.

Tests with up to 385 kV (+10%), short-circuit tests and power tests up to 385 W (+10%) are planned with the high-voltage resistors in summer 2025.

3.8.3.3 High voltage feedthrough

Prototypes for oil-free 350 kV vacuum feedthroughs, which are compatible with Essex connectors, are already in production at PSI.

The HV bushing is a large, brazed assembly consisting of isostatically pressed sintered aluminum-oxide ceramic, which has vacuum-brazed elements at both ends. The production of the ceramic is very complex, time-consuming and cost-intensive.

The total weight of the ultra-high voltage bushing is 32 kg and the length is 654 mm. This assembly is permanently attached to the large rectangular separator flange and, unlike the electrodes, does not move. The voltage contact is realized by a spring, the length of which is adapted to the distance between the electrode and the HV feedthrough. The electrodes have pot-shaped holders with a cone in the center. This cone centers the spring and prevents it from buckling.

3.8.3.4 High voltage electrodes

To fulfil the various separation requirements, the distance between the electrode plates can be adjusted between 300 and 450 mm. On each side there is a stepper motor and lifting gear unit that can move the titanium electrodes in a controlled manner.

Titanium is the optimum high-voltage electrode material, as it forms an insulating oxide layer like aluminum but also has a hardness similar to that of stainless steel.

The electrodes are manufactured in a lightweight design to minimize their weight and keep the load and torque at the fixing points of the ceramic rods as low as possible. This is achieved by milling pockets within the two titanium plates,

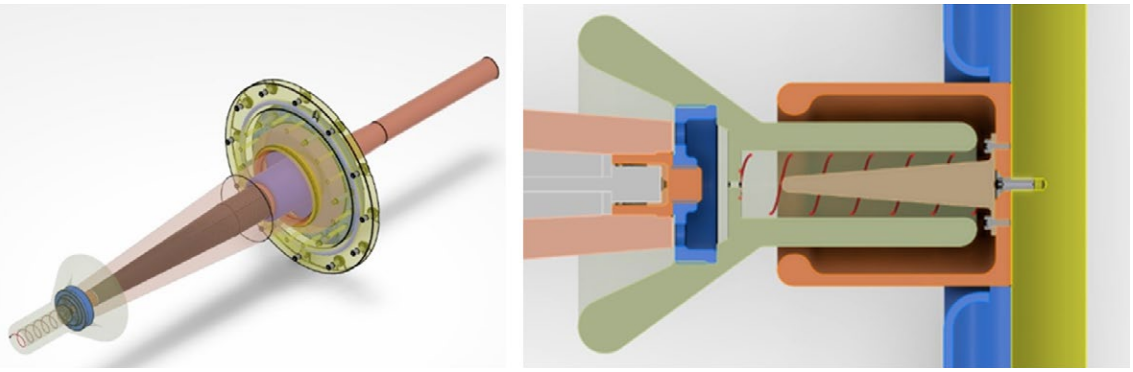

Figure 3.8.3: (Left) HV-350 kV-Feedthrough, oil free, compatible with Essex connectors; (Right) Electrical spring HV contact between Feedthrough and electrode plate.

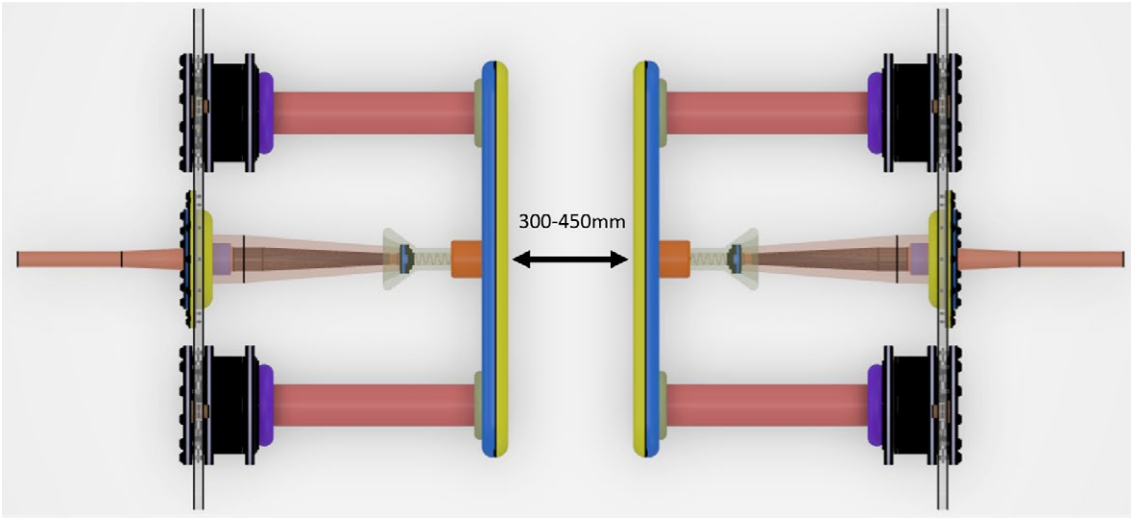

Figure 3.8.4: Top view on the electrodes, feedthrough, isolator and mechanical fixation

which are then welded together. Like the HV bushings, the ceramic retaining rods are made of isostatically pressed aluminum oxide. They are clamped to the ends of the insulators as a fastening method. This design has been successfully used in other separator and spin rotator devices in recent years. The clamping must be concealed from high voltage with polished cover components.

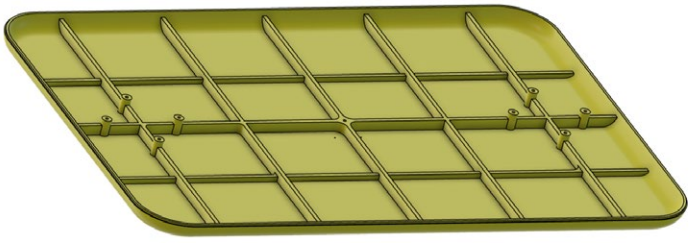

Figure 3.8.5: View onto the electrode plate to see the rip structure for stabilization and lightweight construction.

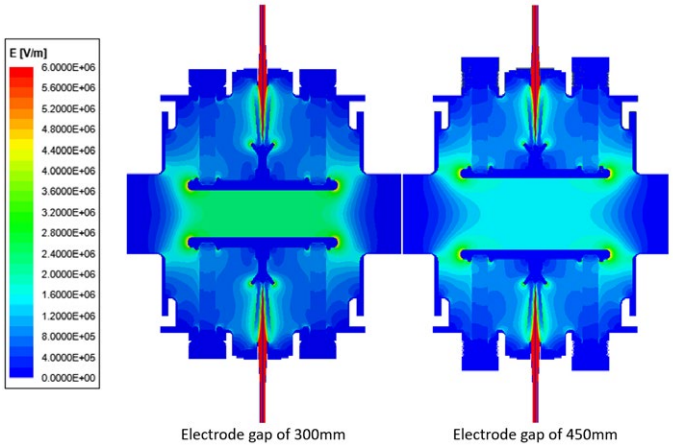

Figure 3.8.6: Top view on the high voltage simulation with the different gaps between the electrode plates.

3.8.3.5 High voltage simulation

The distances and radii are dimensioned so that we do not exceed the maximum E-field of 60 kV/cm anywhere in the vacuum tank.

Figure 3.8.6 shows the electric field distribution with a gap between the electrodes of 450 mm, the picture on the right shows the situation with a gap of 300 mm. The increase in the field between the electrodes with a small gap can be seen from the color code.

The green color between the electrode plates of the left tank shows an HV E-field of 2.4×10^6 V/m, the more turquoise color of the right tank shows between the electrode plates an HV E-field of 1.6×10^6 V/m. At the corners of the electrode plates, you can see the field peaks in yellow and red. Thanks to the radii, these remain below the maximum specified HV E-field of 6×10^6 V/m. The HV -plugs and cables in the vacuum feedthroughs (Figure 3.8.4) are purchased parts from Essex and are specified for 350 kV. In our simulation, these are modelled as dummies and therefore Figure 3.8.6 might not reflect the real situation.

3.8.4 Vacuum part

3.8.4.1 Vacuum vessel

The vacuum tank is a round tube made of internally polished stainless steel, which has a DN500 connection flange for the beamline at both ends. The connection piece is extended on one side so that the vacuum system can be directly connected to the beam axis. On both sides it has large rectangular flanges with double seals, where the electrode plates including drive and HV feedthrough are mounted sideways as a complete unit.

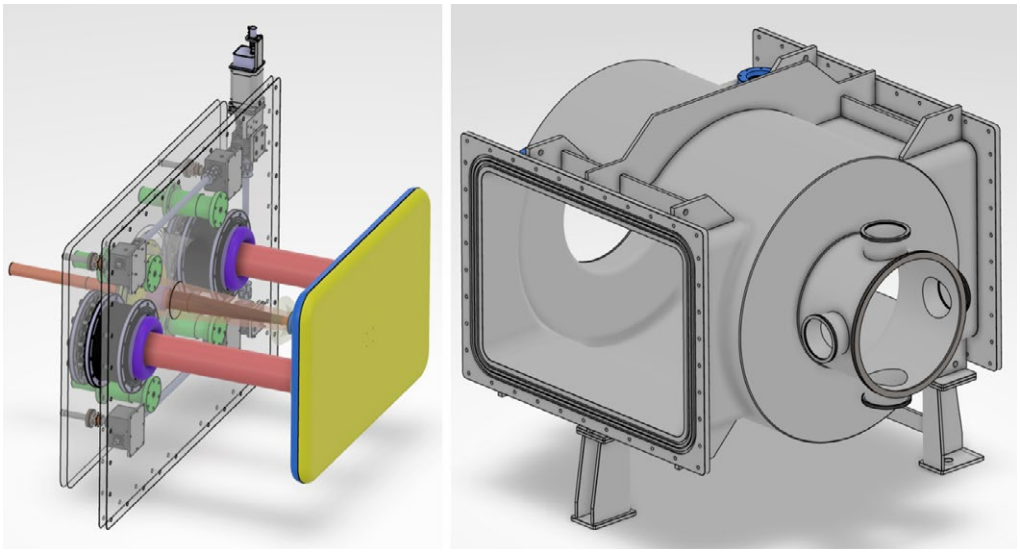

Figure 3.8.7: (Left) Flange as complete Assembly with HV-Electrode, drive and feedthrough; (Right) Vessel with support legs

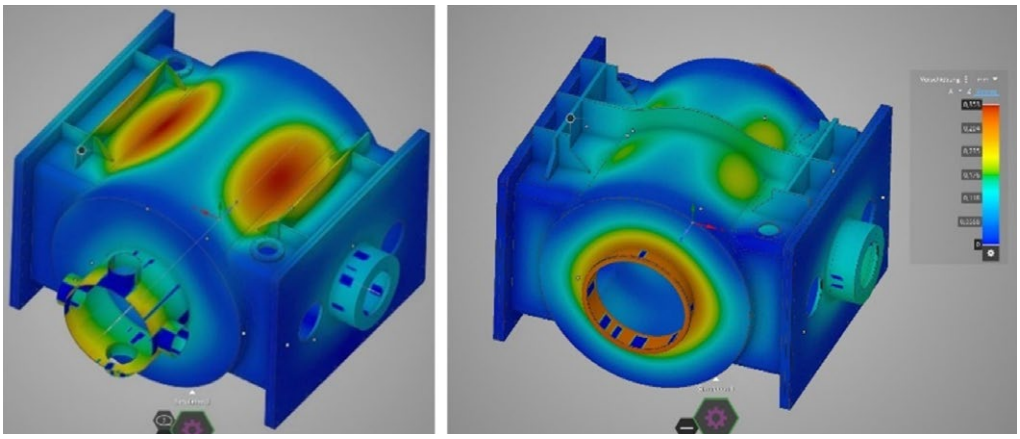

Figure 3.8.8: (Left) High mechanical material tension in the tank wall due to the vacuum force inside. (Right) Reduced mechanical material stress in the tank wall due to reinforcement by the rib.

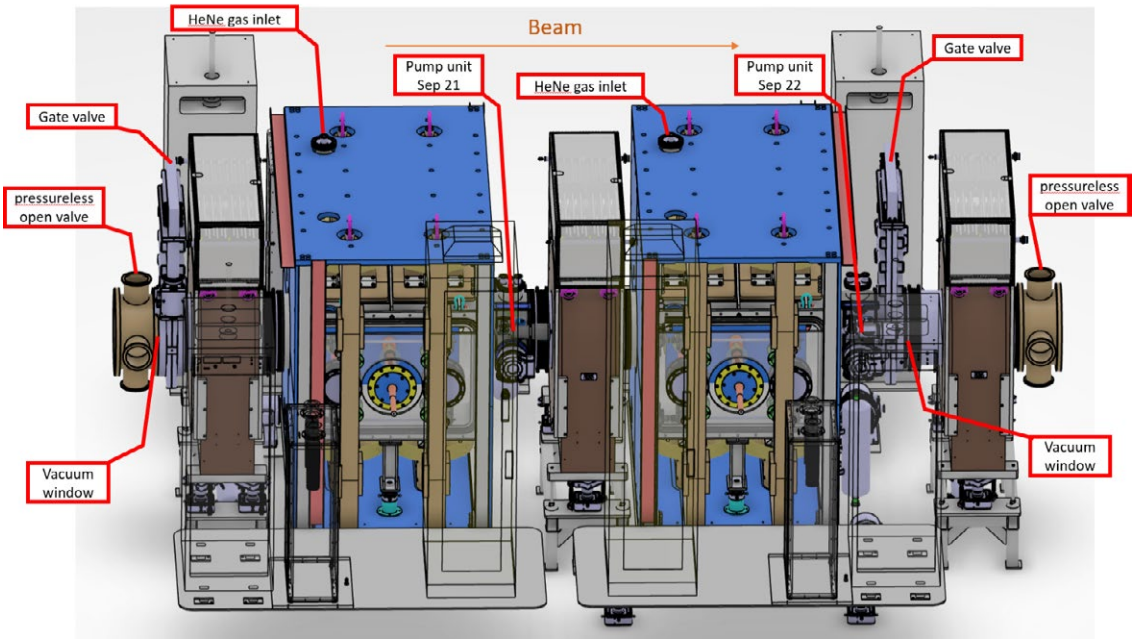

Figure 3.8.9: Separator assembly with the labeled vacuum components or the foreseen installation location.

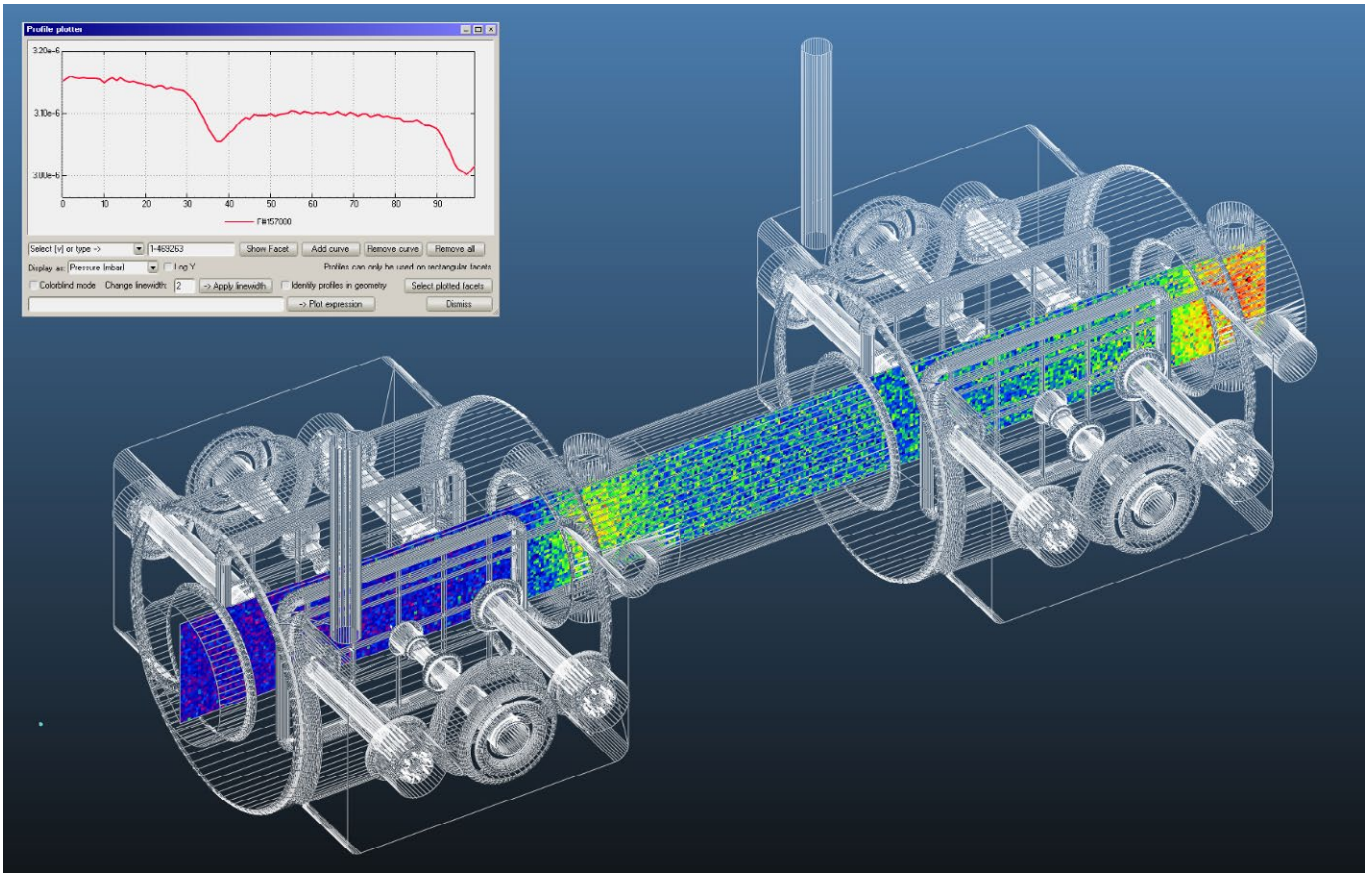

Figure 3.8.10: Vacuum simulation.

The chamber has various welded reinforcing elements as strength simulations had shown that these were necessary. In the following simulation images, you can see the material displacement due to the high vacuum in the chamber. Without reinforcement, we have a deflection of 0.6 mm on the chamber wall (left). With reinforcing rib, the displacement at the same point is < 0.1 mm (right).

The separator tank is supported on three legs, which in turn are mounted on levelling feet for exact alignment with respect to the magnet and the beamline.

3.8.4.2 Vacuum system

Together with the center solenoid, the two separators form a separate vacuum section. It is sealed off on both the inlet and outlet sides with 500 mm vacuum valves. During beam operation they are in the open position, but for service and safety reasons the valves close automatically and stand the difference vacuum to atmospheric pressure. Each separator has its own pumps, sensors and valves, which are controlled by a common PLC system.

During high-voltage operation, we are planning a HeNe gas atmosphere at a pressure of 10^{-4} mbar. For this purpose, a three-position slide valve is installed upstream of the turbopump to dose the suction power.

For enclosing the protection gas, we plan to install at the outside of the valves 3 µm Mylar foils to separate the vacuum if the valves are open. The foils cannot withstand atmospheric pressure. The foils must be specially protected with a pressure less open valve to ensure that the same pressure prevails on both sides in the event of closed valve, a power failure, compressed air failure or vacuum less condition.

For details on the design of a PSI standard pumping unit, see Chapter 3.9.7.

3.8.4.3 Vacuum simulation

The tanks of the separators are very large volumes with large, outgassing surfaces. The vacuum of 3×10^{-6} mbar achieved in the simulations after 24h is slightly worse than the $< 10^{-7}$ mbar required in the specifications. However, it can be assumed that the surfaces are additionally cleaned by the high-voltage conditioning. From experience with other separators, the vacuum pressure decreases by up to half an order of magnitude.

Figure 3.8.10 shows the pressure distribution along the central plane in the separator. The two light areas are due to the pumps at these locations. In the diagram next to it, these can also be recognized as lower pressure values.

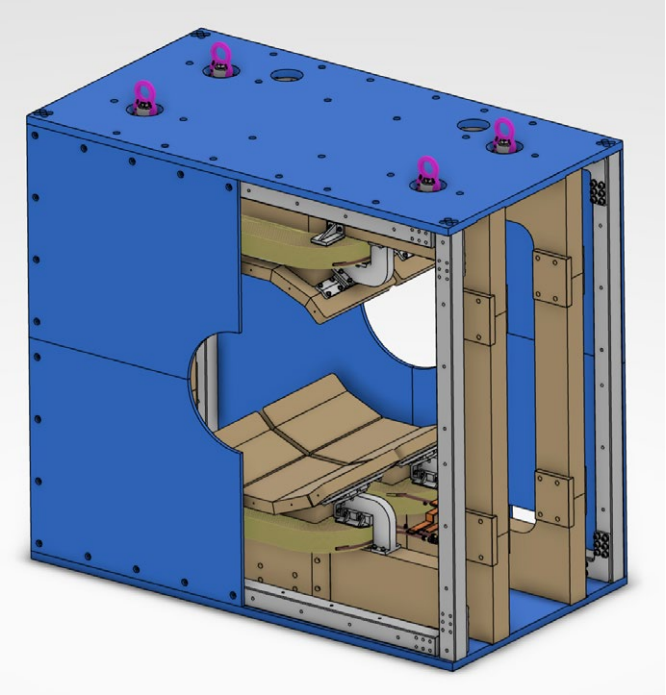

Figure 3.8.11: Iron Body of the separator magnet. Part of the front mirror plates is not shown for viewing, that we can see the detail structure inside.

3.8.5 Magnet

A double dipole encloses the vacuum tank. They are electrically connected and form a single unit in operation. The iron body is made up of several steel plates.

In the case we have to open the tank during beam time, the upper mechanical structure of the magnet can be lifted off. The tank can then be lifted out of the magnet for repair.

The complete magnet weighs 11 tons including the coils. The poles are segmented and mould themselves to the curves of the tank to create an almost homogeneous magnetic field between the electrode plates.

The maximum B-field of the magnet is 44 mT at 200 A. A maximum of 36 mT is required for the planned operation with muons. The highest field is only required in special cases and running at the smallest electrode setting.

The simulation (Figure 3.8.12) shows the saturation of the iron. The Magnet will operate at constant field. In order to ensure that the field is reproducible within line requirements, the demagnetisation protocol can setup when shutting down the magnet. Figure 3.8.12 shows also the B-field in the separator along the beam axis.

The magnetic field is limited by mirror plates along the beam path.

3.8.6 Magnet power supply

A separate 200 A/50 V power supply is provided for each separator magnet. More details can be found in Chapter 3.3.3.

3.8.7 Separator control system

3.8.7.1 High voltage system

A Compact Rio controller with Lab View Code is planned for controlling the high voltage, as has been currently used on other separators at PSI.

The controller handles communication with the HV devices, vacuum system, dose rate measurement and displays all values graphically. However, only the high voltage can be controlled by the user. Automated procedures are available for conditioning.

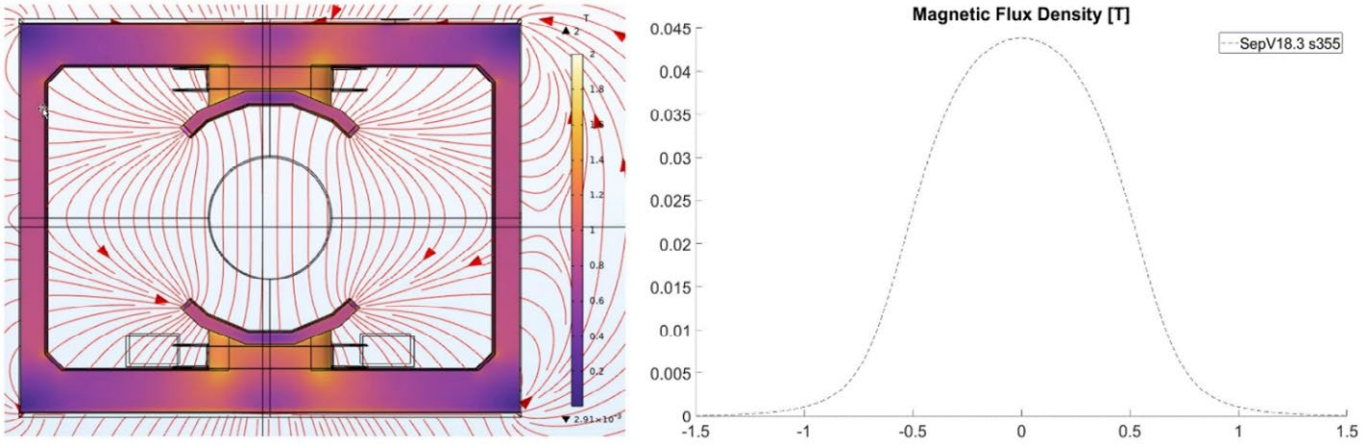

Figure 3.8.12: (Left) Iron saturation simulation model; (Right) Magnet peak field of the final design

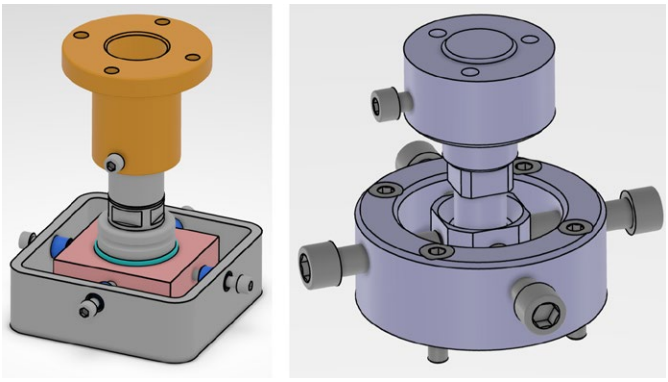

Figure 3.8.13: (Left) 10t PSI standard feet (Drawing number: PRT-06.3.007D); (Right) 1t PSI standard feet (Drawing number: ASM-50004.28.831A)

3.8.7.2 Electrode position control

The stepper motor drive of the electrode plates is also to be operated with the High voltage Compact Rio controller. In the HIPA system, a stepper motor-driven slit system (FSH51) is currently operated with a C-Rio controller. In terms of control technology, this offers many synergies. Only integrating this into the separator control system requires additional effort.

3.8.7.3 Interlock and dependence with other systems

There are three permanently wired interlocks to the high-voltage devices. If communication with the control unit is no longer possible, there is a red emergency button at the area entrance that can be used to switch off the high voltage.

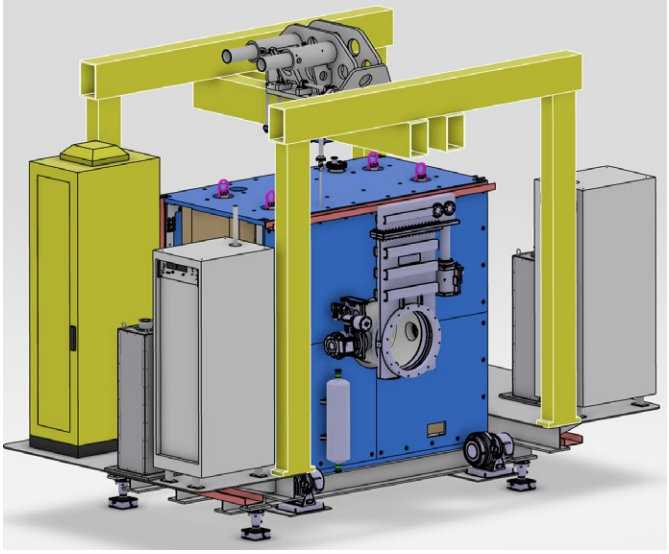

Figure 3.8.14: Load Lifting Attachment (LLA). In yellow the crane crossbeam, above, gray the adapter for attaching to the 60t crane hook.

The high voltage can only be switched on if the vacuum is better than 1×10^{-4} mbar, or 1×10^{-3} mbar for inert gas operation. If the vacuum exceeds these limits during operation, the high voltage is switched off.

There is a dose rate measuring device close to the separator that measures the X-ray radiation and emits a visual and acoustic alarm if it is exceeded. In the event of a malfunction, the high voltage is switched off or cannot be switched on.

3.8.8 Adjustment

Four 10 t feet are provided between the floor and the separator base frame. These are required to compensate for mechanical tolerances and to adjust the entire separator to the beam axe.

Three 1 t feet are provided for the alignment between the magnet and the electrode plates in the vacuum tank.

3.8.9 Load Lifting Attachment (LLA)

It is intended that one and the same load lifting attachment can be used for both separators to be able to transport the separators on the crane. The LLA should be permanently mounted on one of the two separators. See the yellow frame in the following picture.

Structurally, the LLA is a traverse that is mounted on the base frame with fixed, load bearing supports. A bolt system must be provided as a connection to the crane hook. As this is above 4 meters high, it should be possible to operate and lock it with a crank system.

In addition, auxiliary frames are provided for attaching the electrodes to the vacuum cover. This also serves as a LLA for inserting the assembly into the vacuum tank.

3.8.10 References

[1] Eichler R., Kiselev D., Koschik A., Knecht A., van der Meulen N., Scheibl R., et al., *IMPACT conceptual design report*, Villigen PSI: Paul Scherrer Institut; 2022. PSI Bericht: 22-01.

3.9 Vacuum System, Chambers and Controls

3.9.1 Overall Concept for the Vacuum System at HIMB and HIPA

The renewal of the target station and the associated beamlines represents a highly complex construction in terms of vacuum systems compared to the existing setup. The primary challenges are the large volume to be pumped and the overall conductance of the construction. The vacuum concept is based on components and systems that have proven effective at HIPA over many years.

Pumping large volumes is a well-established process at HIPA, particularly due to the large volumes of Injector 2 and the ring accelerator. However, pumping a system with such low conductance is a new challenge. The radiation-hard Pyrotenax coils have so far only been used outside the beamline.

The vacuum system consists of the following components and subsystems:

Chambers and Beamline
The chambers of the target station, including the PK2 chamber, MuH2 and MuH3 chambers, along with the remaining pipes and chambers of the beamline (see Chapter 3.9.3), form the volume to be evacuated. Various components are installed in these chambers, which significantly contribute to the low overall conductance of the system. Due to their size, enormous forces act on the chambers, which must be compensated. All chambers and components installed in the vacuum must be manufactured and cleaned according to vacuum technical standards.

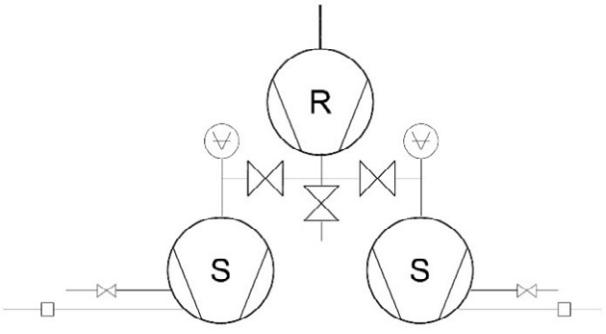

Figure 3.9.1: Pre Vacuum Layout

Pillow Seals
A special component to highlight is the pillow seal, which is explained in more detail in Chapter 3.9.5. This technology has been successfully used since the construction of HIPA and has been continuously developed. Pillow seals enable the assembly and disassembly of two chambers while maintaining a vacuum-tight connection between them. The seals are entirely metallic and can be remotely operated, enabling their use under high radiation conditions.

Pumping System
The pumping system is divided into two subsystems:

1. Primary Vacuum System
   - This subsystem is characterized by high pumping speed enabling the large volume to be pumped down to a pressure of < 1E-1 mbar within a reasonable time. It consists of a Roots pump and two pre-stage screw pumps, following the proven system used in Injector 2 (Figure 3.9.1).

2. Turbo Pump System
   - This system pumps the volume to the final vacuum pressure. The central component is the turbomolecular pump, which requires a primary vacuum pressure of < 4 mbar. The primary vacuum is provided by a buffer system.
   - A 20-liter buffer tank, separated from the primary pump (scroll pump) by a valve, ensures this supply. The primary pump reduces the buffer tank pressure to < 1E-1 mbar, after which the valve to the primary pump closes, and the pump is switched off. The turbomolecular pump channels residual gases into the buffer tank until it reaches a pressure of 4 mbar. The process then repeats. This approach reduces the operating hours of the pre-pump and saves energy (Figure 3.9.2).

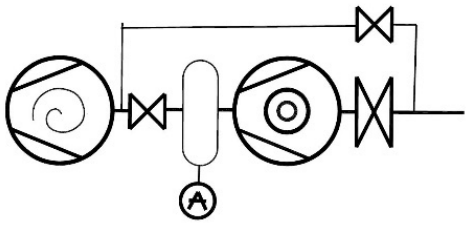

Figure 3.9.2: Turbopump System Layout

The turbo pump system is modular and distributed throughout the facility, available in various sizes of turbomolecular pumps.

Measurement System

The measurement system monitors the pressure in the new target station, the beamlines, and the pre-vacuum system. It is divided into several subsystems:

1. Pressure Measurement in the Target Station and Beamlines
   - This subsystem uses Pirani gauges (measurement range up to 1E-3 mbar) and Penning gauges (up to 1E-9 mbar). These gauges are installed on each chamber with a turbo pump system.

2. Pressure Measurement in the Primary Vacuum System
   - This subsystem is required to control the logical processes via the PLC (programmable logic controller).

3. Measurement for Nitrogen Venting
   - This subsystem reliably tracks the pressure progression up to atmospheric pressure. Additionally, it includes an atmospheric pressure switch to detect when atmospheric pressure is reached during the ventilation process.

Nitrogen Venting System

The nitrogen venting system is used to fill the evacuated volume with nitrogen, preventing water from entering the chambers. This ensures the chambers reach their final vacuum pressure more quickly after evacuation. The system is structured as follows:

- A central nitrogen supply line feeds the system, separated from the venting system by a main valve.
- The line is secured by an overpressure valve.
- Each chamber to be vented has a separate valve connecting it to the central line.
- A purging function allows cleaning of the line between the main valve and the chamber valve via an additional valve that opens to the outside.
- After the venting process, another valve ensures the chamber is open to the outside. This prevents the formation of under-pressure caused by molecular adsorption from surfaces that have been under vacuum.

3.9.1.1 Vacuum Layout Target Region

(see Figure 3.9.3)

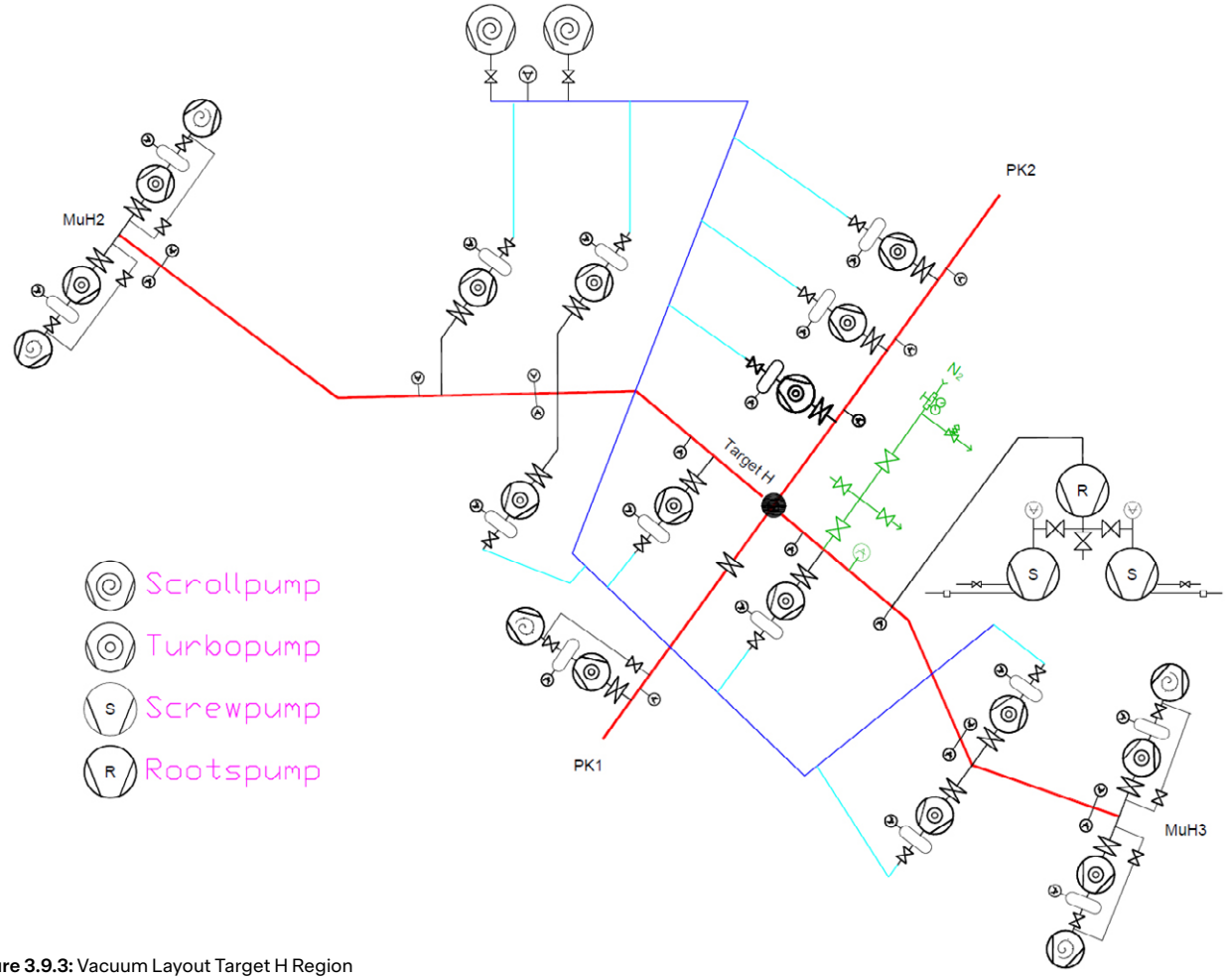

Figure 3.9.3: Vacuum Layout Target H Region

3.9.2 Vacuum System Simulations

Several simulations were conducted as part of the vacuum system design. These included determining the achievable final pressure using Monte Carlo simulations and calculating the pump-down time for the entire volume to estimate the time required to reach the final vacuum.

Determining the Achievable Final Vacuum
Monte Carlo simulation software MolFlow+ developed by CERN for vacuum simulations was used. The vacuum system was modeled and optimized iteratively. Each time an optimization was performed, the simulation was repeated until the optimal vacuum system layout was identified.

Procedure

1. Basic Parameters - Desorption
   Stainless steel was defined as the material for surface outgassing rates (desorption). Other materials like copper, normal steel nickel coated etc. have similar outgassing rates, but would enhance preparation and computational time for the simulation. A safety margin was considered due to unresolved design model details by setting a range between optimistic and pessimistic desorption rates. This range corresponds to experimentally measured outgassing rates of stainless stell after one hour (pessimistic) and after ten hours (optimistic):
   - Stainless steel outgassing rate after 1 hour: 3×10^{-8} mbar l/s/cm^2
   - Stainless steel outgassing rate after 10 hours: 8×10^{-9} mbar l/s/cm^2

2. Creating the Simulation Model
   At the time of creating the simulation model, the construction model was not yet fully developed and detailed. This did not pose a challenge, as the model had to be significantly simplified for the simulation software. The focus was on creating an envelope model that abstracted the geometry of the space to be evacuated and made it suitable for calculations.

   The process began with simplifying the construction model to generate a negative volume of the space to be evacuated. This volume model was then converted into an envelope model, which could be processed by the simulation software Molflow+. This process had to be repeated several times due to optimizations and adjustments to the construction model.

3. Parameterizing the Simulation Model
   The parametrization of the model is crucial for the simulation results. All surfaces of the model had to be assigned the previously determined desorption rates. Additionally, pumping speed, also referred to as sticking factors for the pumps, were defined. The software simulates the path of molecules from desorption on the surfaces to removal by the pumps.

   The resulting residual gas fraction in the system represents the achievable pressure. To visually display the pressure profile and distribution in the system, a detector layer was defined, which counted the penetrating molecules and derived the pressure from this data. The simulation ran until enough hits were recorded on the detector layer to achieve an accuracy of ± 0.1%.

4. Data Evaluation
   Once the simulation collected sufficient data on the detector layer, a pressure distribution matrix was created. This matrix showed the pressure profile along the beam path. From this data, pressure curves of the beam path were visualized.

5. Iterative Development Process of the Vacuum System
   In the first simulation round, a simple configuration of pumps was chosen. Initial results showed that it would be

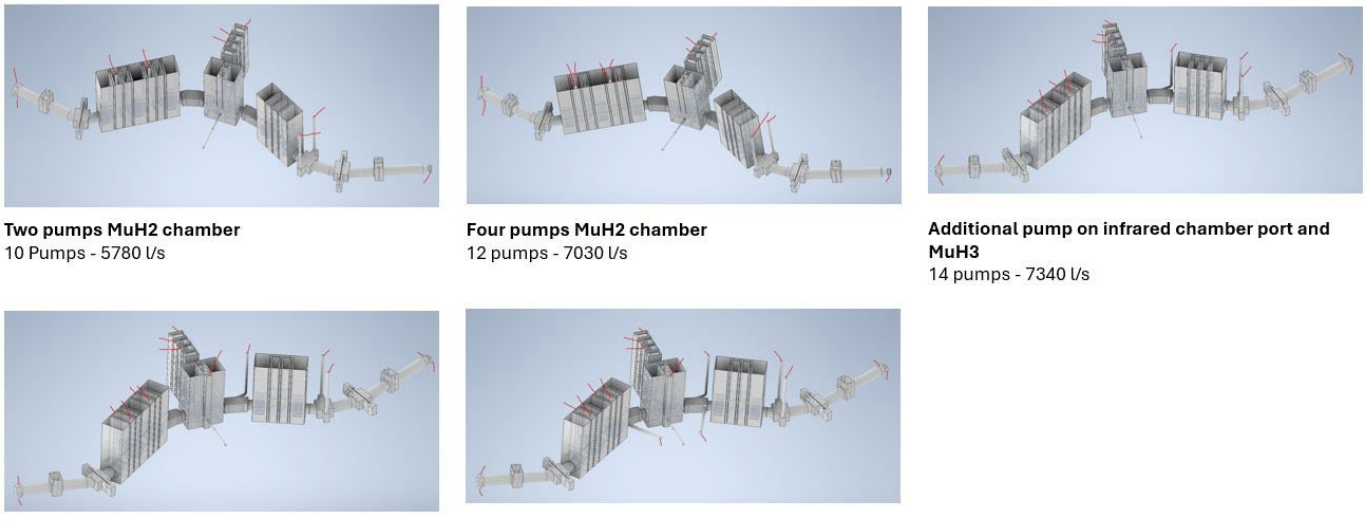

Two pumps MuH2 chamber
10 Pumps - 5780 l/s

Four pumps MuH2 chamber
12 pumps - 7030 l/s

Additional pump on infrared chamber port and MuH3
14 pumps - 7340 l/s

More suction speed MuH3, additional pump on target chamber
15 Pumpen - 8900 l/s

Additional pumps on dipole chambers
17 Pumps - 10150 l/s

Figure 3.9.4: Model Variants

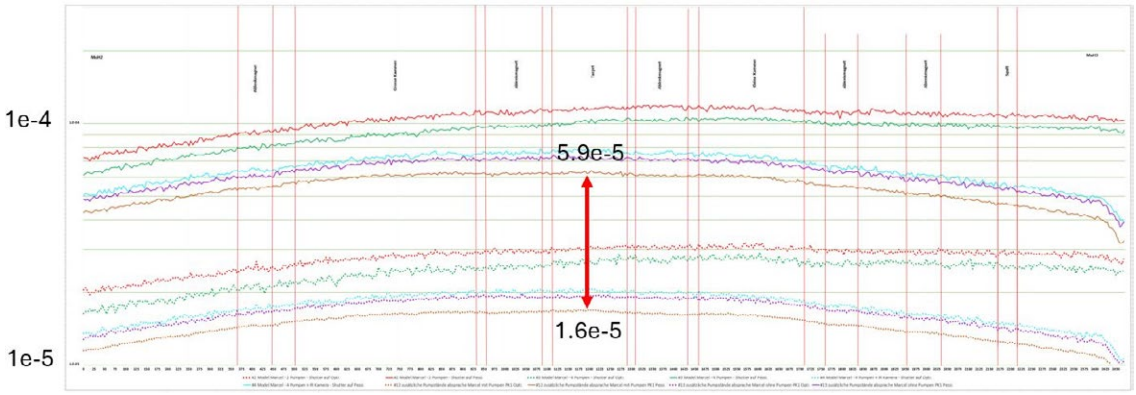

Figure 3.9.5: Pressure curve first simulation series. Different colors represent pumping variants (red 10, green 12, blue 14, violet 15, brown 17 pumps).

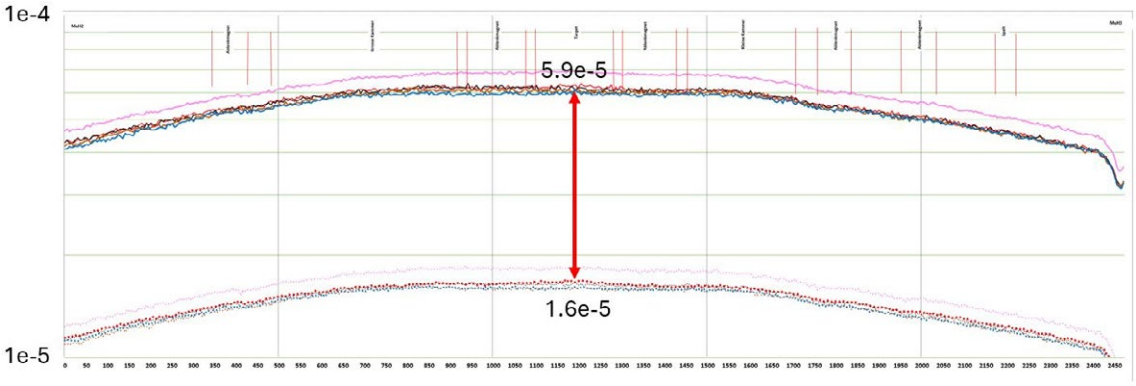

Figure 3.9.6: Pressure curve second simulation series. Different colors represent pumping variants (red 10, green 12, blue 14, violet 15, brown 17 pumps).

challenging to achieve the desired pressure of <1E-5 mbar at the target. Pressures on current targets are: Target E = 9E-6 mbar and Target M = 1.5E-5 mbar. Adjustments were made to the pump configuration and pumping speed. Additionally, the positioning of additional pumps was examined to optimize the pressure profile.

This iterative process continued until further changes to pump performance and position brought no significant improvements. The vacuum system was then optimized for total conductance, positively impacting the achievable final pressure. However, this optimization must be further pursued during the detailed design of the vacuum chambers and verified by a final simulation.

Results of the Simulation for Achievable Final Vacuum

The simulation results show the achievable final pressure in the system, considering the optimizations to minimize total conductance and improve pressure distribution.

Figure 3.9.5 shows how the achievable pressure has developed through the iterative development process. The different colors represent the variants shown in Figure 3.9.4. Red 10 pumps, green 12 pumps, blue 14 pumps, violet 15 pumps, brown 17 pumps.

Figure 3.9.6 shows how the improvement in achievable pressure has stagnated despite the increase in suction power. This clearly indicates that the overall conductance of the system determines the pressure.

Pump-Down Time Determination

To calculate the required pump-down time, the pressure range from atmospheric pressure (1000 mbar) to the final vacuum (1E-5 mbar) was divided into different flow range. The relevant ranges are laminar flow (1000 mbar to approximately 1E-2 mbar), molecular flow (below 1E-2 mbar), and the transition range, which includes Knudsen flow. The transition range was not considered in this analysis. In addition, the desorption factor comes into play in the molecular flow range from 1E 4 mbar.

Pump-Down Time in the Laminar Flow Range

The pump-down time in the laminar flow range depends on factors such as the volume to be evacuated, the pumping speed of the primary vacuum pumps, the length and cross-section of the lines, and the temperature.

Since pre vacuum pumps do not provide constant suction capacity in the laminar range, the change in suction capacity across different pressure ranges was considered. The pressure decays exponentially in the laminar regime and so the pumping duration can be estimated by Equation 3.9.1.

The calculation determined a pump-down time of approximately 2000 seconds (~ ½ h) to evacuate the volume from 1000 mbar to 0.1 mbar.

$$t = \frac{V}{S} \cdot \ln\left(\frac{p_0}{p_1}\right)$$

Equation 3.9.1: Formula for pump-down time in the case of Laminar flow.

Pump-down time in the molecular flow range without desorption

In the molecular flow range, where turbomolecular pumps operate at a constant pumping speed, the total conductance of the system was considered.

The pump-down time up to a pressure of 1E-4 mbar, where the outgassing of the surfaces becomes relevant, was calculated to be about 15000 seconds (about 4 hours).

Pump-down time in the molecular flow range with desorption to final pressure.

In the molecular flow range, desorption of the surfaces becomes relevant from a pressure <1E-4 mbar. Since the surface area in the vacuum is so large in this vacuum system, it takes a long time until the final pressure is reached. This can take 1–2 days.

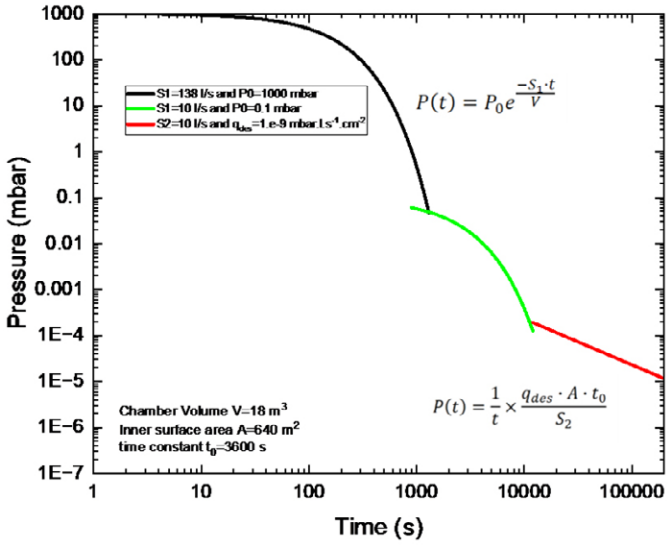

Figure 3.9.7: Formula for total conductance calculation

Total Pump-Down Time

The total time to evacuate the volume from 1000 mbar to 1E-5 mbar is thus approximately 5.5 hours. This time serves as a reference and can be adjusted under real conditions depending on the final system parameters.

3.9.3 Vacuum chambers

3.9.3.1 Introduction

The current system around TgM consists mainly of two larger vacuum chambers, namely the TgM chamber and the vacuum chamber for a profile monitor and two collimators located downstream in the proton channel (PK2).

3.9.3.2 Implementation

Size and position of the vacuum chambers are determined by the placement of the components described in Chapters 2.1, 2.2 and 3.10. The main requirements are listed below:

- Position of the capture solenoid magnets to the target (+250 mm)
- Position of the collimator KHH0 to the target (+250 mm)
- Positions of the collimators KHH1 and KHH2 (limited free positioning, max. +300 mm)
- Space conditions in the former areas PiM1 (new MuH2) and PiM3 (new MuH3)
- Requirements for beam dynamics (solenoid magnet distances, deflection angle)
- Requirements related to radiation protection and maintenance (especially at the so-called service level +2.5 m above the beam)

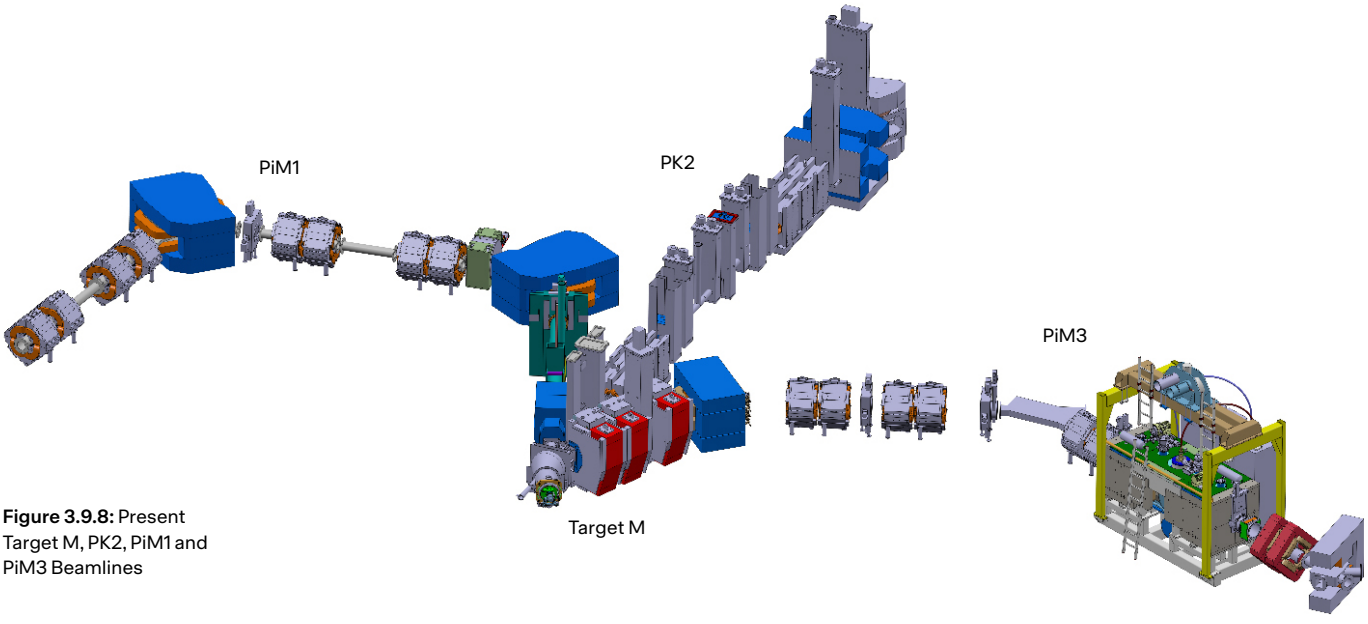

Figure 3.9.8: Present Target M, PK2, PiM1 and PiM3 Beamlines

Considering the requirements outlined above – including the dimensions of the new inserts to be placed within the chambers, the current manufacturability standards for vacuum chambers, the need for flexibility, and the desired minimum space between the components – a larger unified chamber design was implemented. This approach contrasts with the traditional PK2 concept (see Figure 3.9.9), which featured numerous smaller chambers positioned in close proximity.

A similar system is currently in use at the HIPA facility's Beamdump BHE, featuring a large vacuum chamber capable of housing multiple inserts within a compact space, see Figure 3.9.10.

BHE chamber (10002.24.300) L × B × H:
2 m × 1 m × 3.6 m, m = 4000 kg

As a result, the TgH region now comprises a total of five large vacuum chambers, see Figure 3.9.11 and Figure 3.9.12. Notably, the MuH2.1 and MuH3 chamber in the MuH2 and MuH3 areas are identical.

Chamber	Size (L×W×H)	Empty weight *	Full weight **	Incl. Inserts like TgH, MHP, KHHx, ...***
TgH	1.4×2×3.3	15 t	24.5 t	55.3 t
PK2	2.3×0.9×2.1	13.2 t	29.3 t	38.4 t
MuH2.1 / 3	2.6×1.3×3.3	17.5 t	39 t	63.5 t
MuH2.2	1.6×1.3×3.3	12.5 t	23.5 t	38.3 t

* welded chamber + external shielding
** welded chamber + external shielding + inside fillers, guiding and internal shielding
*** welded chamber + external shielding + inside fillers, guiding and internal shielding + inserts

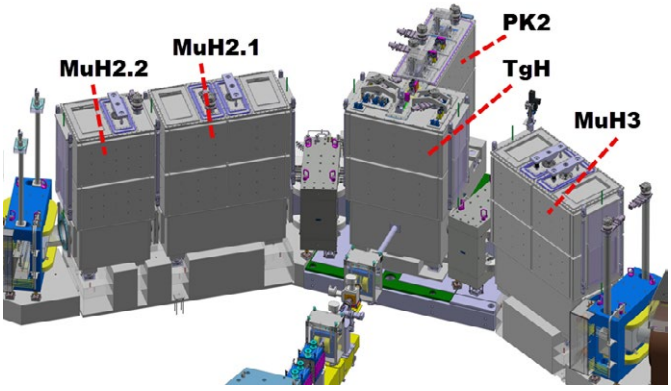

Figure 3.9.11: New large vacuum chambers for HIMB ('big five').

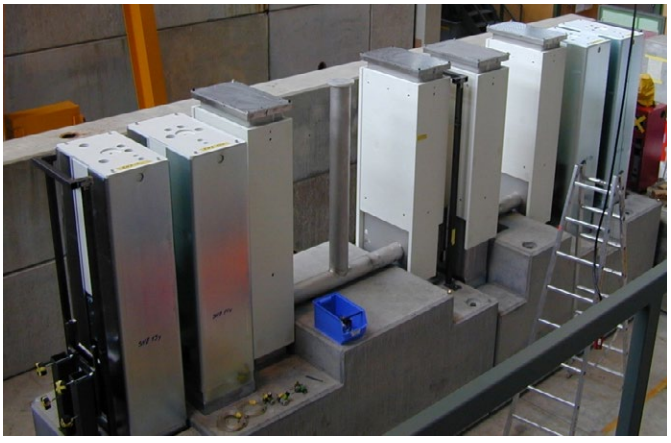

Figure 3.9.9: PK2 Vacuum Chamber during pre-assembly

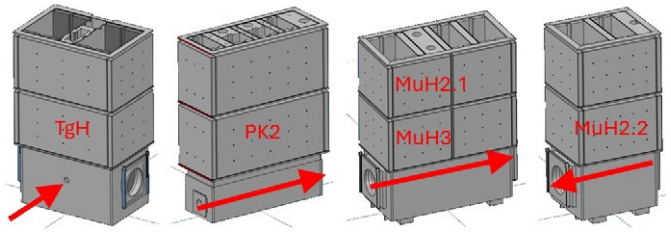

Figure 3.9.12: Large vacuum chambers for HIMB.

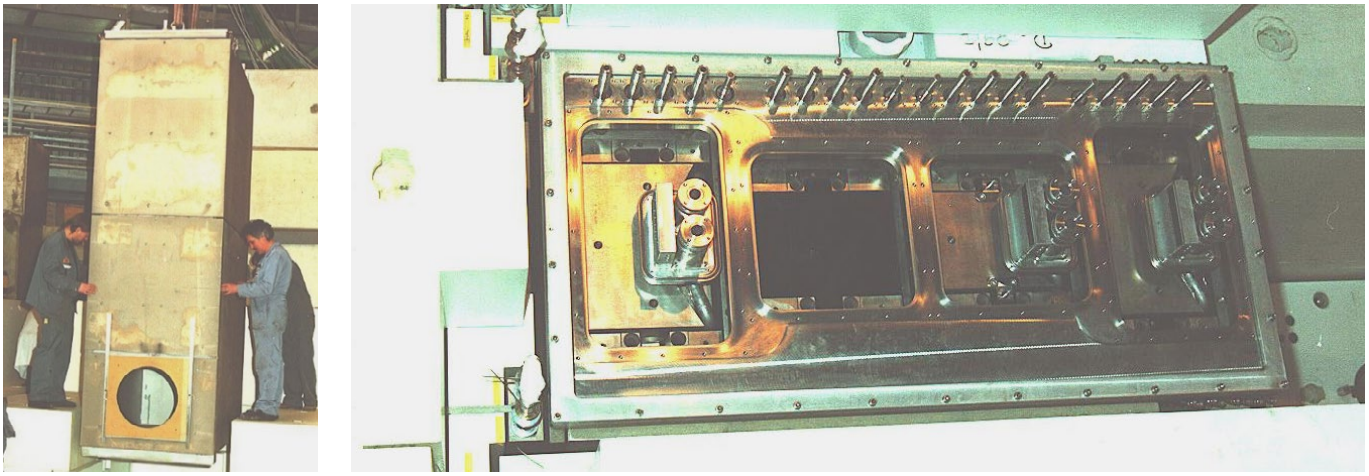

Figure 3.9.10: Beamdump BHE Vacuum Chamber

The 4 large vacuum chambers were also analyzed under consideration of aspects and limitations such as

- Mechanical deformation due to vacuum forces
- Mechanical deformation due to dead weight and payload
- Mechanical deformation due to temperature differences/ heating
- Transport and handling (non-activated chambers)
- Transport and handling (activated chambers) including a later disposal in the ATEC facility
- Manufacturability
- Dismantling / disposal
- Replacement of the vacuum chambers in the event of a leak

This required consideration of factors such as the maximum load capacity of the WEHA hall crane (60 tons) and the capabilities of the current ATEC facility (12 tons, size restrictions/ space conditions and tools in the ATEC).

The externally attached shielding in the upper part of the large chambers ensures that the chambers are not bent by the vacuum forces. The standard wall thickness of each chamber is 15 mm, with a minimum wall thickness of 40 mm in the area of the beam.

3.9.3.3 Basic Parameters

Basic Parameters Vacuum Chambers

Main function	Vacuum containment for various devices
Dimensions (mm)	various
Weight	various
Material(s)	316L = 1.4404 1.4435 to be used for chambers IN magnets such as the transfer solenoid or dipole chambers Weldings 1.4439 (for 1.4435 chambers) Internal shielding S235 or S355, nickle plated External shielding S235 or S355, nickle plated Permeability for base material and weldings <1.02
Positioning / alignment accuracy	Large structures must meet beamline tolerances. It was commonly understood and agreed, rotation around vertical axis is one of the most important tolerances to look at (angles). • +/- 0.5 mm for DN500 • +/- 0.3 mm for DN320 • +/- 0.1 mm for DN160
Vacuum	• Nominal Pressure < 10^{-5} mbar • Double sealing as a standard on inserts • Double sealing *with intermediate vacuum* only on main flanges of the big chambers, also applicable for MuH2/MuH3 chambers
Internal shielding	• Target chamber (Target slot) internal shielding especially requires “black” painting
Manufacturing specifications	• Vacuum tight welded, min. > 10^{-7} mbar • He-Leakage rate < 2×10^{-8} mbar l/s • Spezifische Ausgasrate < 1×10^{-9} mbar l/s/cm^2 • Welding material • Welding quality and inspection

3.9.3.4 Interfaces

The connection to the supports and girders below is achieved using 50-ton feet, which ensures proper adjustment and positioning. Further details can be found in Chapter 3.10 on girders and adjustment.

The chambers are equipped with measurement points on the flange cover (top cover, main cover) for the survey of the chamber, allowing for optimal positioning within the specified tolerances. Each flange cover is positioned roughly first and then the position is fixed precisely and reproducible with 2 mandrels. This applies to both the main covers and the respective insert covers. This ensures repeatability of the positions in the tenth of a millimeter range.

Wherever possible, there are guide elements for the inserts in the chambers to guarantee alignment and first positioning of the inserts. These guide elements are also used to install and remove the inserts using the exchange flask. They are compatible with the exchange flask of TgH and TgE.

Removal of the local shields / guides in the chamber: All parts are secured and positioned in the chambers via bolts and pins in the base plate and main cover of the vacuum chambers and have corresponding holding points for load handling devices.

3.9.3.5 Cooled chambers

The backside of the TgH chambers, approximately +/-500 mm above and below the beam, will be cooled along its entire length. The flange facing the PK2 chamber will also be cooled to prevent excessive heat in the pillow seal installed between the TgH and PK2 chambers.

At the PK2 vacuum chamber, the front flange, along with the front and side walls at beam level, are cooled. The cooling parameters for these components are similar to those of the TgH. In addition, the inserts for the profile monitor and KHH1/2, as well as the internal shielding, are cooled near the beam.

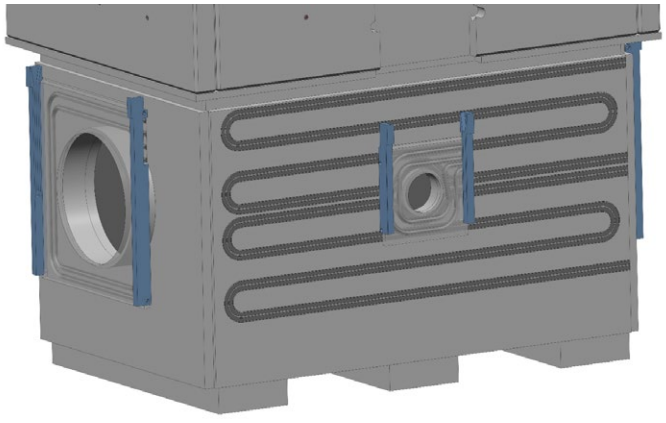

Figure 3.9.13: Target H cooled side walls

The cooling of the side walls as well as the cooling of the ground plate is still under development, for both the TgH chamber and PK2 chamber.

Details concerning the cooling simulations can be found in Chapter 3.9.3.6.

3.9.3.6 Thermomechanical simulation

Thermomechanical models for the MuH2.1/MuH3, TgH and PK2 chamber were created based on the latest CAD models with ANSYS Workbench 2024R2. Power deposition in the MuH2.1/MuH3 chamber is negligibly small - approximately 50 W for a chamber weighing 8 tons, with additional 11 tons of external and 21 tons of internal shielding. External shielding plates which are considered as load-bearing elements provide additional stiffness through bolted connections to the chamber walls. Payload accounts for the weight of components that do not contribute to the stiffness of vacuum chamber.

Energy deposition in TgH chamber is described using seven meshes representing the chamber walls and the bottom plate, as described in Chapter 2.4.5.1. The 2D power density distribution is mapped onto 3D finite element models, resulting in a constant power density across the wall thickness. The total power in the inserts after mapping is compared with the value calculated in the Mont-Carlo (MC) simulation, as shown in Table 3.9.2. If the total power in ANSYS thermal model after mapping is lower, the power density will be scaled up to match the source data given by MC simulation. The total power in TgH chamber of 4.5 kW comprises of power deposition of following components:

Total power in the inserts

Chamber incl. external shielding	1'487	W
Guiding rails (4×)	1'371	W
shielding floor (3×)	556	W
Inserts Cap. Sol. 1	197	W
Inserts Cap. Sol. 2	186	W
Inserts KHH0	384	W
Inserts Target	287	W *(partially water-cooled)*
Total	4'468	W

Table 3.9.2: Total power in the inserts in the target H chamber

This procedure is used to determine the power deposition in the MuH2.1 chamber, based on energy calculation described in Chapter 2.4.5.3 MuH2 beamline. The power deposition in the PK2 chamber is derived based on Chapter 2.4.5.2 PK2 beamline, with a total power of 5.5 kW comprising:
Chamber incl. external shielding ~2'100 W
Guiding rails and internal shielding ~3'400 W

Chamber	Size (L×B×H) [m]	chamber [ton]	external shielding [ton]	Payload [ton]	Total [ton]	Power deposition [kW]
TgH	1.4×2×3.3	7.5	9.5	41	58	4.5
PK2	1.9×1.1×2.9 (current) 2.3×0.9×3 (FEA)	6	9	24	39	5.5
MuH2.1/3	2.6×1.3×3.3	8	11	46	65	0.05

Table 3.9.3: Main parameters of vacuum chamber finite element models

Thermomechanical finite element models include only mechanical components of vacuum chambers. Components with dedicated water cooling, such as the target, collimators and magnets as well as inserts for profile monitors etc., are excluded from thermal model but their mass is accounted for in the mechanical models.

3.9.3.6.1 Mechanical calculation of MuH2.1/3 chamber

Remote displacements are defined in local coordinate systems. The single foot at the upstream end is fixed in all three translational degrees of freedom (DOF), while all rotational DOFs remain free. At the two downstream feet, the DOF along the x-axis is released to allow for thermal expansion (Figure 3.9.14). External shielding plates are connected to the chamber walls via bolted connections, with frictionless contact modelled between them.

Figure 3.9.15 shows the deformation and von Mises stress in the MuH2.1/3 chamber under mechanical loads, including gravity, vacuum and bolt pretension. The deformation in the chamber is below 0.40 mm, and the von Mises stress is below 60 N/mm2, demonstrating a stiff chamber with a sound mechanical design.

3.9.3.6.2 Conceptual design of water cooling for PK2 and TgH chambers

The cooling design of PK2 and TgH chambers is still under development. As highlighted in Table 3.9.3, the finite element model was created based on a previous version of CAD model.

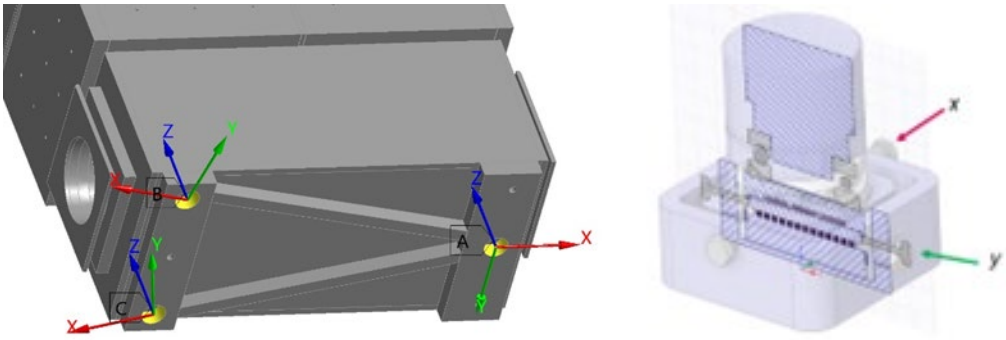

Figure 3.9.14: Boundary conditions MuH2.1/3 chamber (left) and foot (right)

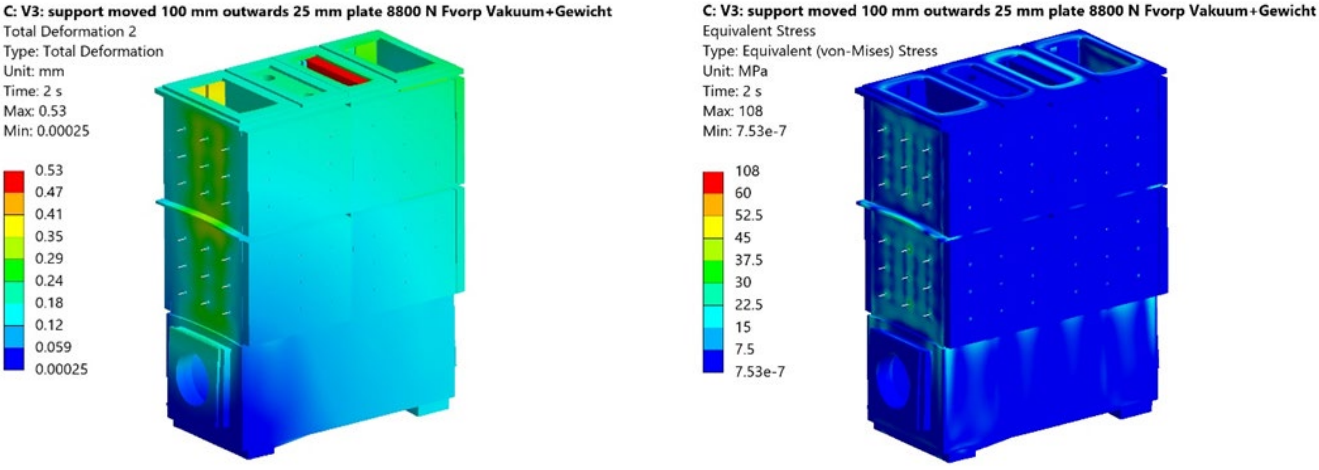

Figure 3.9.15: Muh2.1/3 chamber under gravity, vacuum and bolt pretension. Left: deformation in mm, Right: von Mises stress in N/mm^2

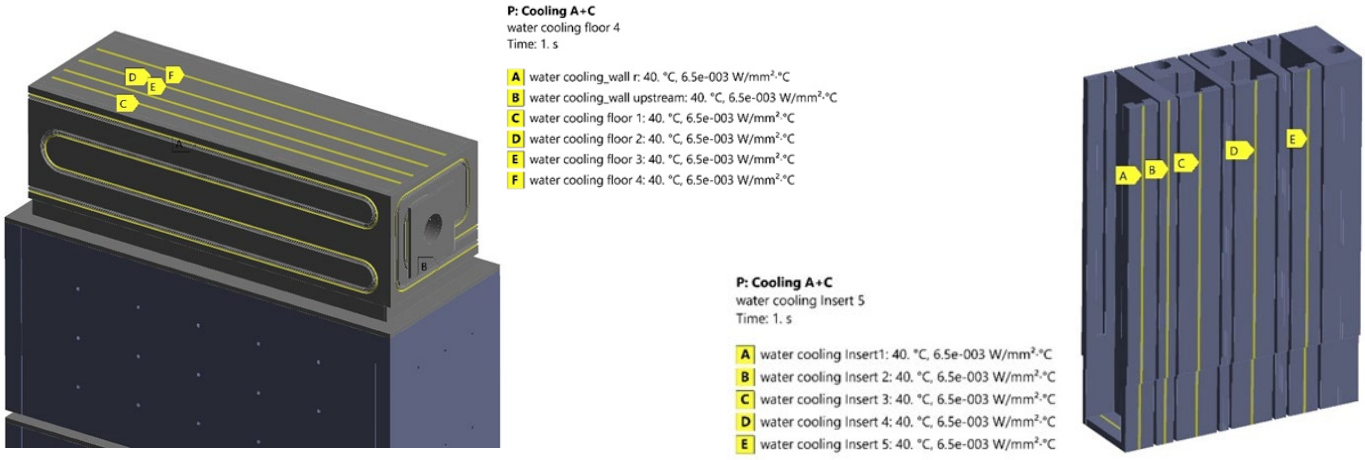

Figure 3.9.16: Water cooling simulation PK2 chamber. Top: in-air cooling channels on the chamber; Bottom: in-vacuum cooling surfaces on the insert.

In the latest CAD design, the chamber is shorter, slightly lower, and broader. The total weight and power deposition for both versions of the chamber are comparable. The in-vacuum cooling design of guiding rails and internal shielding contains a lower section made of OFE copper with a stainless-steel water pipe brazed in place. The upper section is made of structural steel. The in-air water cooling could be based on a welded design with a groove and cover plate, or alternatively on the current HIPA water cooling solution, which uses thermally sprayed aluminum (TSA) coatings to provide a good thermal contact between the stainless-steel water pipe and the chamber wall. *The pipes are mechanically fixed, e.g. by welding.*

3.9.3.6.3 Thermal calculation of PK2 and TgH chambers

Preliminary cooling simulations were performed by defining the water inlet temperature as 40 °C with a heat transfer coefficient of 6'500 W/m²K, which is reduced by 20% for an assumed water pipe with a diameter of 8 mm and water velocity of 1.5 m/s. Inside the chamber, all guiding rails and the first shielding plates were treated as water cooled.

The shielding blocks, which are assumed to have no water-cooling in this simulation, are cooled by radiative heat transfer to the chamber walls directly facing it. The emissivity of steel is assumed to be 0.4. This value is conservative for oxidized stainless and structural steels but not for polished steel. The radiative heat transfer surface to ambient is modelled to consider walls which are parallel to tunnel and also floor facing steel girder, with an equivalent emissivity 0.25 and an ambient temperature 40 °C. Internal inserts are considered to have thermal contact with bottom plates, represented by a thermal contact conductance of 300 W/m²K, to allow for heat transfer between them. When insert is cooled by water, the heat transfer through thermal contact is negligible.

Figure 3.9.16 shows the thermal model of water cooling for PK2 chamber. The lower part of the longitudinal walls, the front wall facing the TgH chamber and the bottom plate are water-cooled. All guiding rails and one internal shielding block are also designed to be water-cooled.

Figure 3.9.17 presents the temperature distribution in PK2 chamber and inserts. Temperature as high as 103 °C is calculated in the shielding block which is not cooled in the current thermal model. In the updated CAD design, all shielding blocks will be water-cooled, which is expected to reduce the maximum temperature below 100 °C. The very last shielding block will be moved out of the vacuum chamber.

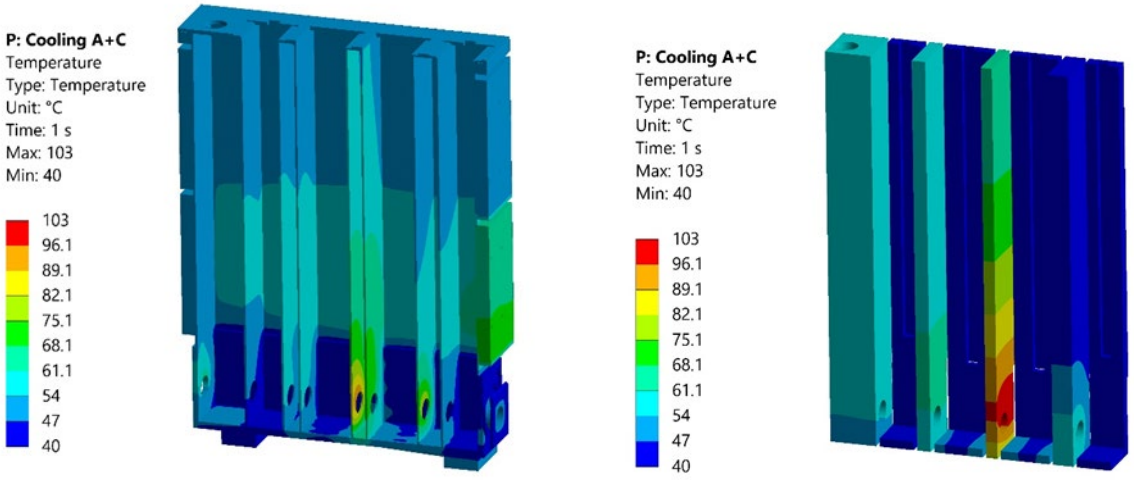

Figure 3.9.17: Temperature distribution [°C] in PK2 chamber. Left: T in PK2 chamber; Right: Temperature in guiding rail and shielding blocks.

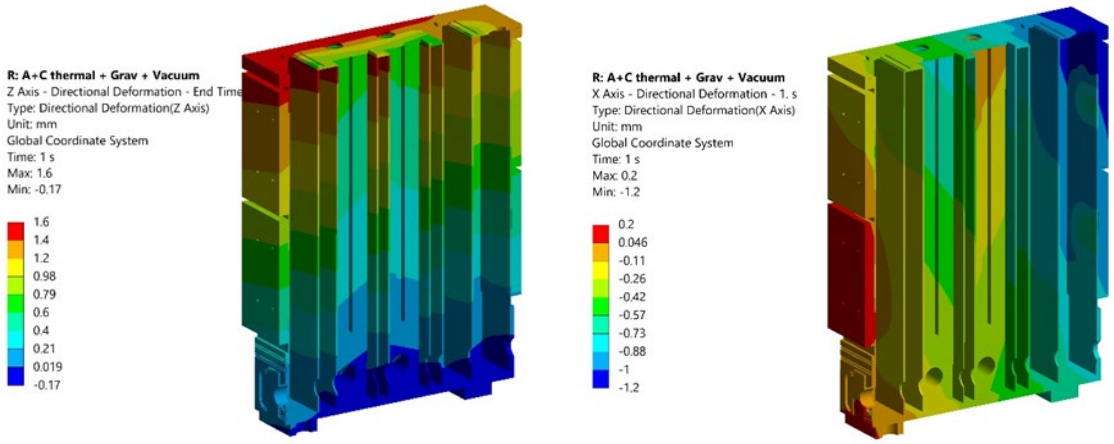

Figure 3.9 18: PK2 chamber: Deformation under thermal, gravity and vacuum loads. Left: vertical deformation in mm; Right: deformation in beam direction in mm.

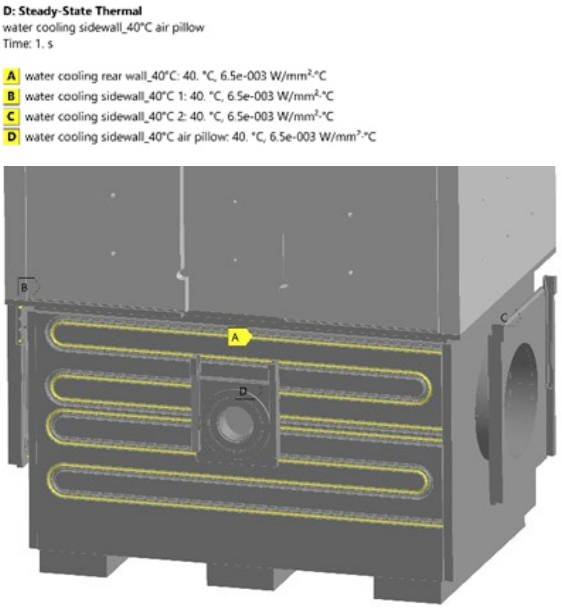

Figure 3.9.19: TgH chamber water cooling in the rear wall and flanges only.

Figure 3.9 18 illustrates that the thermal expansion of the chamber is 1.6 mm in the vertical direction and 1.2 mm in the longitudinal direction. Since the inlet water temperature is defined as 40 °C, a temperature increase from ambient (22 °C) to the operating temperature of 40 °C will induce a thermal expansion of approximately 1 mm for the 3 m-high stainless steel chamber.

In the current thermal model of TgH chamber only the lower part of longitudinal walls and flanges for pillow seals are considered to have water-cooling (Figure 3.9.19). Cooling design still has to be performed.

The large HIMB chambers demonstrate a stiff design under vacuum and payloads conditions. The current state of preliminary thermal analysis shows that water cooling is required for TgH and PK2 chambers. Appropriate water cooling is capable of keeping the chamber temperature below 100 °C. Final simulation will be performed once the cooling design is finalized.

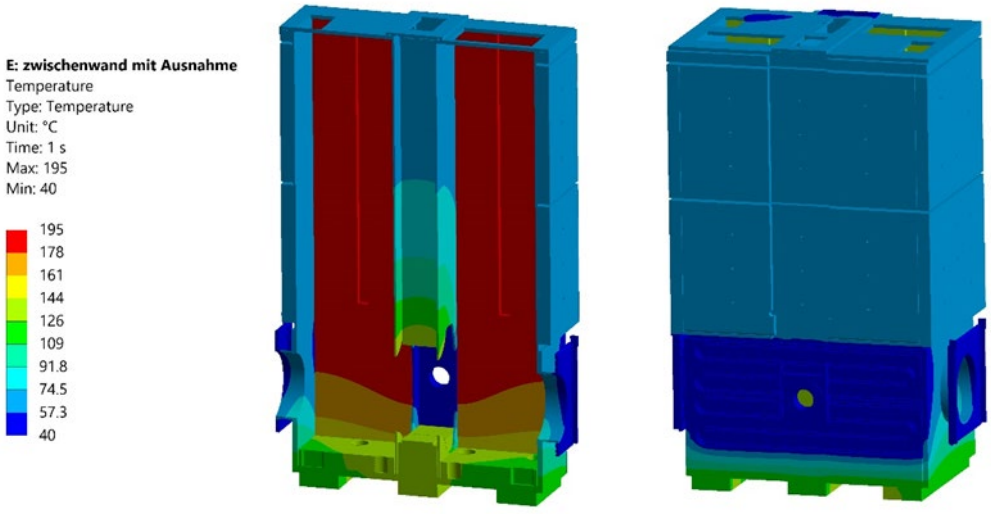

Figure 3.9.20: Temperature in the TgH chamber, guiding rails need water cooling.

3.9.3.7 Non-cooled chambers

Particularly for the large chambers, the MuH2-3 / MuH2 chambers will not be cooled externally. Similarly, any chambers not mentioned in the previously listed chapter will not be cooled, either internally or externally.

3.9.3.8 Additional chambers

The chambers in Table 3.9.4 generally have similar main dimensions, with a width, length, or height of approximately 1.5 to 2 meters, and their empty weight is typically around 600 kg.

ASP21
PRD-00431567

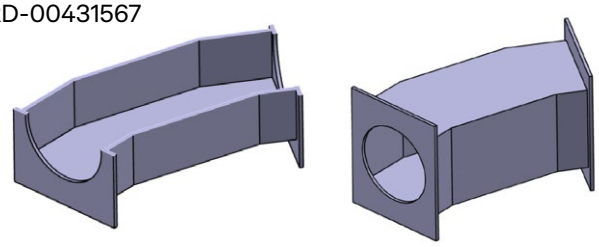

ASH21
PRD-00431571

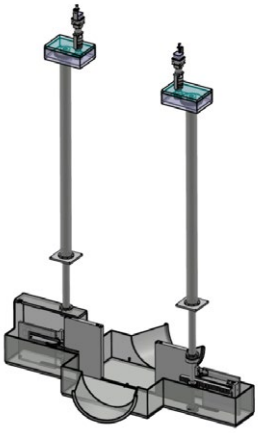

WST..
PRD-00592388 (type 1 without bellow)

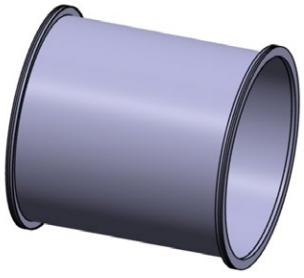

Attention: The second flange has to be welded on site, when the chamber is already in the Solenoid Magnet.

WST..
PRD-00433688 (type 2 with bellow)

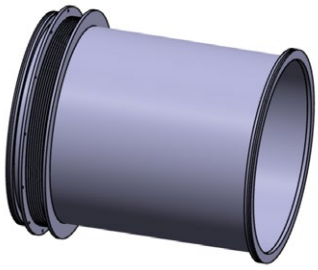

Attention: The second flange has to be welded on site, when the chamber is already in the Solenoid Magnet.

KSK21

FSV/HK21

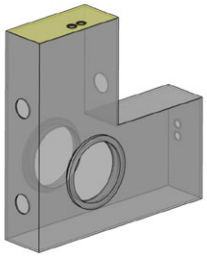

ASP31
PRD-00597814

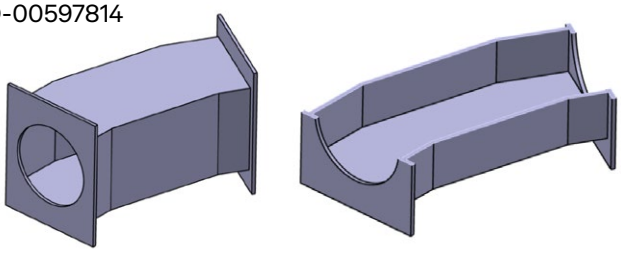

MHW1
IR Camera
PRD-00608238

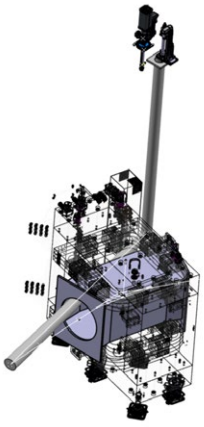

ASP32 PRD-00603543	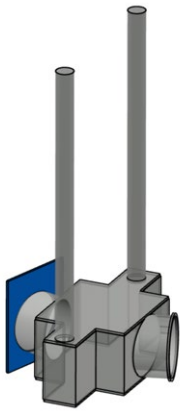
ASH31 PRD-00603545	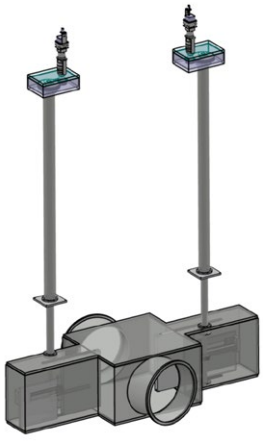
Separator PRD-00677987	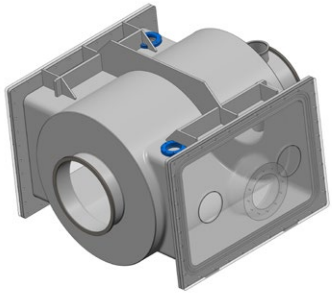

Table 3.9.4: List of other vacuum chambers

3.9.4 Vacuum-Specific Requirements

The vacuum technical system includes the large chambers (TgH, PK2, MuHx, MuH2), the dipole chamber, the shutter chamber, and various connecting pipes. These components must meet all vacuum technical requirements in their manufacturing, cleaning, and sealing to ensure the flawless operation of the overall system.

3.9.4.1 Manufacturing Requirements

The manufacturing of the components must be specially adapted to the requirements of vacuum operation, in particular:

- Machining:
  - Wet machining processes must use silicone-free lubricants.
  - If possible, machining should be performed “dry” to minimize contamination.
- Sealing Surfaces:
  - Grinding directions must be concentric and free of transverse grooves.
  - Sealing surfaces must be continuously protected during transport and storage to prevent damage.
  - Surface roughness Ra: ≤ 1.6 µm.

3.9.4.2 Cleaning and Washing

Thorough cleaning is crucial to eliminate contaminants that could impair vacuum operation. The requirements include:

- Mechanical Components:
  - Degrease without residue and clean with a neutral rinsing agent.
  - Clean channels, blind holes, and threads to be free of grease and residues.
- Avoidance of Residues:
  - No drips or cleaning agent residues should remain on the workpieces.
- Handling After Cleaning:
  - Cleaned workpieces may only be touched with gloves.
  - Subsequently, the components must be protected from contamination.

3.9.4.3 Welding Requirements

Welding techniques have a significant impact on the tightness of the components. The following guidelines apply:

- Weld Execution:
  - A vacuum-side weld is always preferred and must be continuous and tight.
  - The vacuum-technical outer weld should be executed intermittently.
  - Welds made from the outside must be welded in such a way that a flawless root is formed on the vacuum side.
- Post-Processing:
  - Weld seams must not be reworked to avoid compromising tightness.
  - Oxide layers should not be removed, e.g. by stainless steel brushing. This should avoid that contaminants are introduced into the surface.
- Cleaning Before Welding:
  - Workpieces that are difficult to clean after welding must be thoroughly cleaned before the welding process.

3.9.4.4 Helium Leak Test

The leak tightness test is conducted according to the European Standard EN 1779 and is a central quality proof for vacuum technical systems:

- Prerequisites:
  - Execution only by specially trained personnel.
  - Use of certified testing equipment and detailed documentation.
- Procedure:
  - The helium leak test is performed after welding and before further processing steps.
  - External companies can be commissioned with the testing if necessary.
- Documentation:
  - Test certificates and reports must be included with the accompanying documents.
- Limit Value:
  - The maximum integral leak rate is $< 1 \times 10^{-7}$ mbar l/s.

3.9.4.5 Sealing Systems

Both standardized and specific sealing systems are used to seal the vacuum system, adapted to the respective operating conditions.

- Standard Flange Connections:
  - ISO-KF small flange (ISO 2861) and ISO-K clamp flange (ISO 1609) for general applications.
  - Variants:
    - With elastomer seals for low ionizing radiation.
    - With pure aluminum edge seals for high ionizing radiation.
    - With Helicoflex seals for high ionizing radiation combined with thermal load.
- Specific Sealing Systems (Figure 3.9.21):
  - Used for lid seals of large chambers and inserts.
  - Integration of installation grooves for O-rings:
    - O-Ring Dimensioning:
      - Di 35–140 mm: Cord diameter ø5.33 mm.
      - Di 140–500 mm: Cord diameter ø7.00 mm.
      - From Di 500 mm: Cord diameter ø10.00 mm.
    - O-Ring Compression: 30%
    - Maximum Groove Fill Factor: 95%
- Sealing Systems with Intermediate Vacuum(Figure 3.9.22):
  - For the lid seals of large chambers (e.g., MuH3, MuH2) and the insert seals, double seals with intermediate vacuum are used. This configuration significantly improves tightness and increases safety.
- Simple Sealing Systems in Special Applications (Figure 3.9.23):
  - Insert seals and lid seals where a double seal is not possible due to space constraints, such as on the TgH and PK2 chambers, are designed as specific single seals.

3.9.4.6 Bellows

In this project, membrane bellows are used to flexibly connect vacuum chambers or pipelines and fulfill specific requirements for separation and compensation. The main function is to enable the separation of chambers or pipes when necessary to create space for the removal or installation of individual components. The bellows absorb axial movements: they can be deliberately compressed to create space for maintenance work and expand again after decompression without losing their original shape or tightness. This facilitates handling and access to hard-to-reach components. Additionally, the membrane bellows compensate for slight misalignments between the connected components. Such misalignments can arise, for

Figure 3.9.21: Schematic illustration Single seal

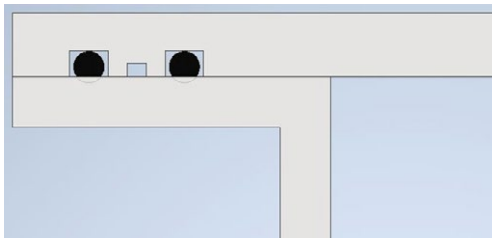

Figure 3.9.22: Schematic illustration Double seal

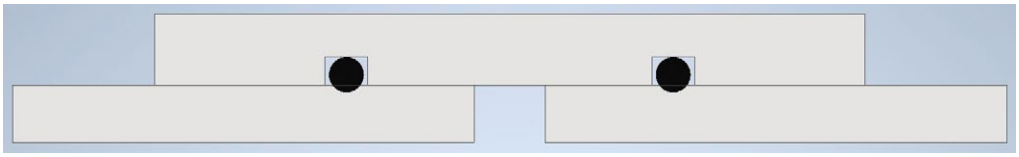

Figure 3.9.23: Schematic illustration seal carrier

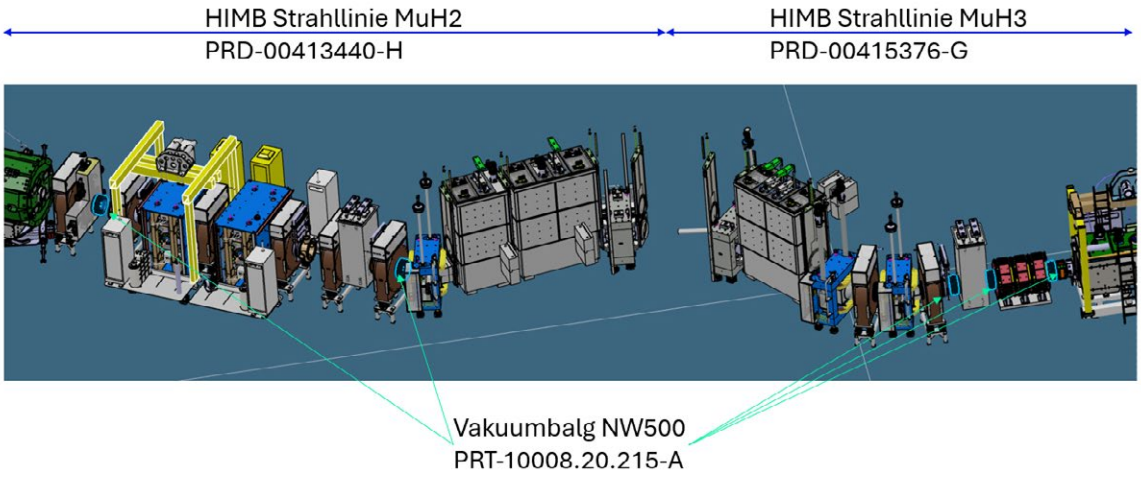

Figure 3.9.24: Overview of bellow positions.

example, due to assembly deviations or thermal expansions. The bellows are mainly used as independent components but can also be directly attached to pipe constructions.

3.9.5 Pillow seals (KD)

In the following chapter, the pillow seal will be referred to by the abbreviation KD.

3.9.5.1 Introduction

The pillow seal technology was developed at PSI in partnership with the company MEWASA for the construction of the HIPA (High-Intensity Proton Accelerator) and has been continuously optimized over the years. These seals, specifically designed for use under intense ionizing radiation, enable a vacuum-tight connection between two chambers while allowing assembly and disassembly without the need for on-site manual work on the flange.

A key advantage of the pillow seal is its purely metallic construction, eliminating the need for maintenance, as required with elastomer seals. Additionally, this design ensures high reliability and durability, even under extreme operating conditions.

3.9.5.2 Pillow seals P-Channel & secondary beamlines

Pillow seals are situated between the beamline components and guided into position through a housing box and placed into the flanges. Each arrow in Figure 3.9.25 above indicates one pillow seal: dashed arrows point to the existing DN160 seal, dotted arrows point to the new DN160 seal, while solid

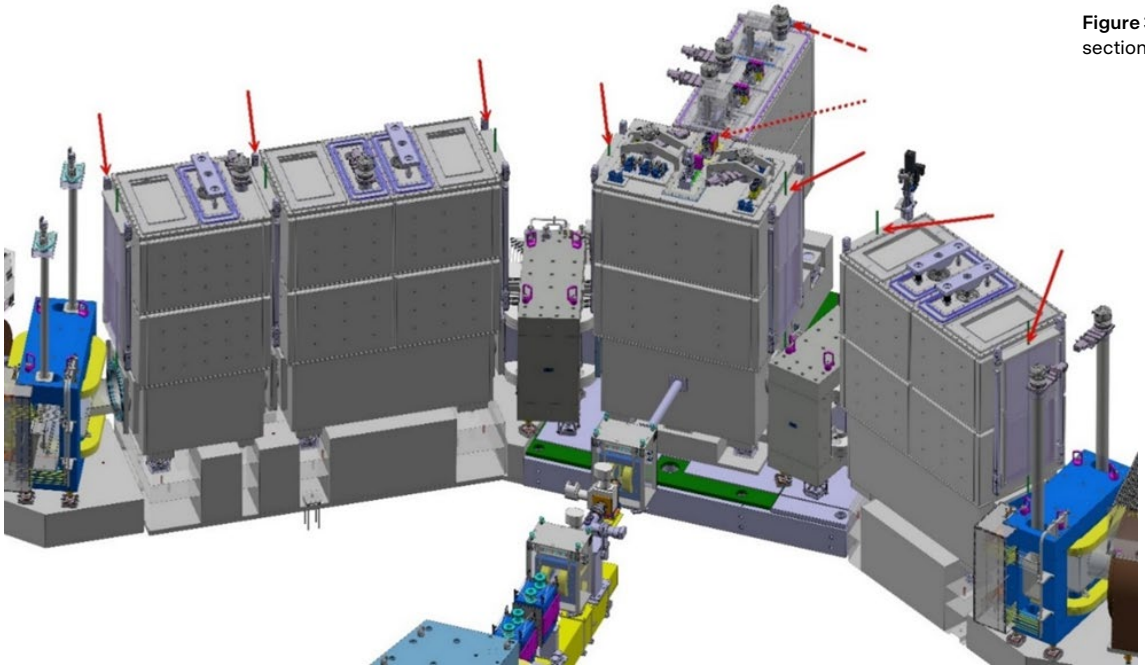

Figure 3.9.25: Overview Target H section with Pillow Seals

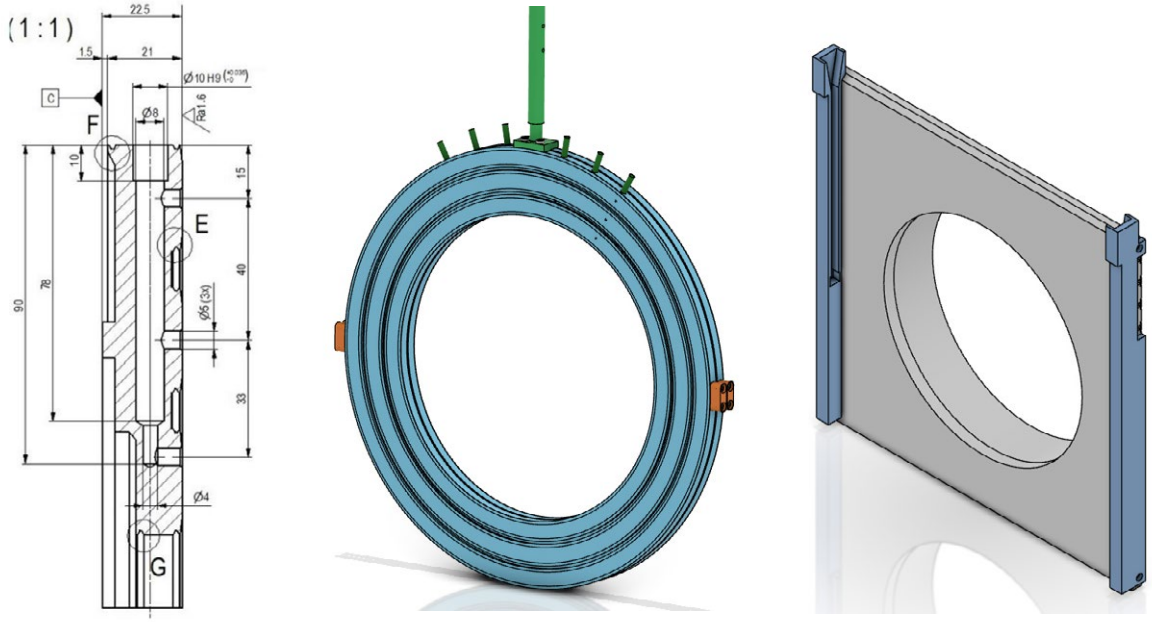

Figure 3.9.26: Pillow Seals and Housing box KD500

arrows indicate the DN500 seals. In the secondary beamlines are seven pillow seals with the nominal diameter of DN500 in place, along with two pillow seals with the nominal diameter of DN160 in the proton channel.

The pillow seal itself is a purchased component from MEWASA. The following drawing and 3D image illustrate such a purchased DN500 seal. It consists of two discs connected by bellows. Each disc has two intermediate vacuum grooves and three welded foil layers on the surfaces, which are pressurized once the seal is in position. Pressure is also applied between the discs, causing the pillow seal to expand and press against the flanges in the beamline. The seal requires support in the form of pressure and vacuum lines. It is made entirely of stainless steel.

The housing boxes for the pillow seals are designed and manufactured by PSI. In first place they act as a lift-transporting the seal to its installation site while protecting it from scratches. Secondly, they act as a shielding to the service level. Once the seal reaches its designated location in the beamline, it is guided out of the housing box and placed directly into the guides at the sealing flanges. The positioning is also integrated into the flange guides. *The flange surface must be polished in a circular direction*.

There are two types of housing boxes because radiation exposure varies along different sections of the beamline, and some pillow seals need to be removed from their position using an exchange flask. In such cases, the load-bearing tool and guides are adapted to the design of the exchange flask. For certain pillow seals, as well as for collimator 0 (KHH0), standard guides cannot be mounted on the left and right due to space constraints. Therefore, grooves are milled into the shielding body instead of attaching guides with screws.

On the load-bearing tool, guide blocks are installed to create a form-fit connection between the C-groove of the

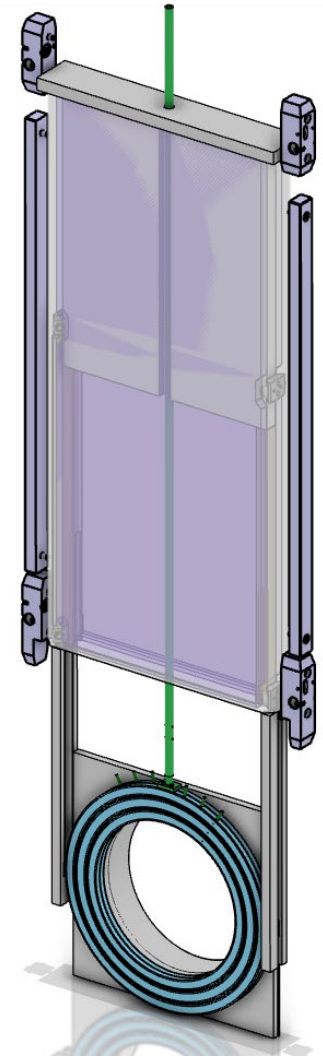

Figure 3.9.27: Pillow Seal KD500 with guide blocks

	KD160	KD500
Outer diameter	310 mm	720 mm
Inner diameter	162 mm	500 mm
Thickness (vented)	35 mm (geometrically, a minimum of 32 mm would be possible)	46 mm
Thickness (inflated)	38 mm	52 mm
Flange distance	35–38 mm	46–52 mm
Stroke	3 mm	6 mm
Leak rate (with separate pressure supply)	$10^{-7}/10^{-8}$ mbar l/s	$10^{-7}/10^{-8}$ mbar l/s
max. angular misalignment	0.3°	0.5°
Flange surface	Groove direction concentric	
Flange surface roughness	Ra 0.1 (MEWASA's specifications)	Ra 0.1 (MEWASA's specifications)
Flange flatness	0.02 mm (MEWASA's specifications)	0.02 mm (MEWASA's specifications)

Table 3.9.5: Specifications Pillow Seals

exchange flask and the guide grooves in the shielding body. When the insert is pulled into the exchange flask, the guide blocks slide down along the rods in the groove. This ensures that the insert is guided at the top and in the middle section of the shielding body, preventing it from swinging inside the exchange flask.

Table 3.9.5 gives some specifications for the Pillow Seals KD160 and KD500.

3.9.5.2.1 KD160 pillow seal

In the following the KD160 pillow seal is described, which is positioned solely between the TgH and PK2 chambers. Functions are illustrated in Figure 3.9.28. The installation situation is depicted in Figure 3.9.29 and an overview is shown in Figure 3.9.30.

Both flanges, the one on the TgH chamber and the one on the PK2 chamber, are cooled to prevent the KD160 from heating up.

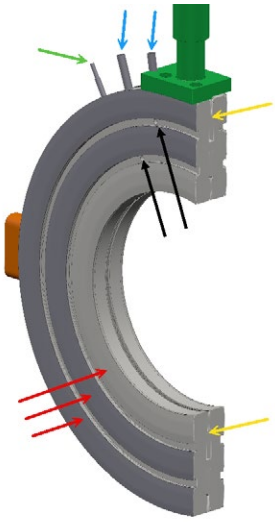

Figure 3.9.28: View of KD160:
Green: Compressed air connection
Red: Three cushions inflated via the green compressed air connection
Yellow: Bellows with three membrane pairs
Blue: Intermediate vacuum connections
Black: Two areas for intermediate vacuum

Figure 3.9.29: KD160 installation situation at target chamber.

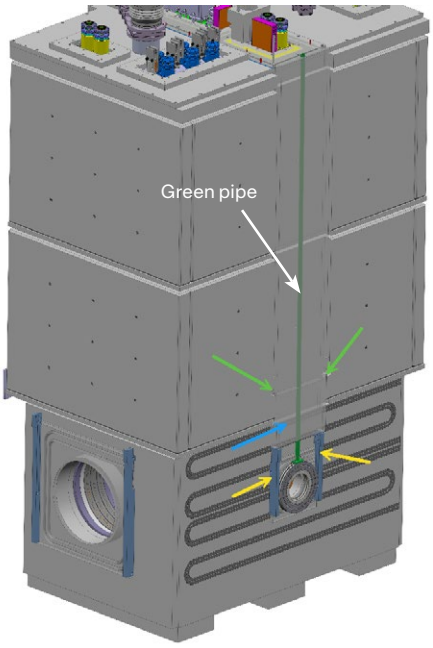

Figure 3.9.30: KD160 overview
Green: Shows the load-bearing points on the insert
Blue: Shows the protected "storage position"
Red: Shows the load-bearing tool, which makes the KD160 transportable for the exchange flask

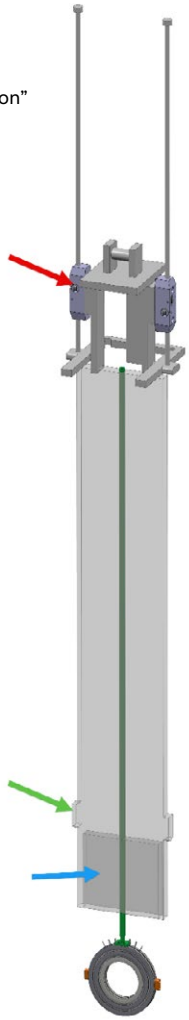

KD160 installation situation (see Figure 3.9.29)

Green: The shielding of the vacuum chamber TgH is milled in a channel shape on the backside to create space for a pillow seal, without increasing the distance between the TgH chamber and the PK2 chamber. The housing box will be centered directly on the backside of the TgH chamber itself. The insert is guided all around with ball pressure bushings, which have been widely used in HIPA, to prevent any collision between the chamber and the insert.

Yellow: The pillow seal is centered using the guiding slides, which are attached to the flange of the chamber. just like with the other KDs, ensuring it is controlled and placed in its final position without causing scratches on the KD or flange surface.

Blue: The area shown here is the fully protected "storage position" of the KD. In this zone, the KD is also guided and fully enclosed by a shell. To move it to this position, the green pipe is pulled and blocked on the service level, as done previously.

3.9.6 Valves, Pumps

3.9.6.1 Pumps

3.9.6.1.1 Introduction

- Objective and Context:
  The pumping system is designed for evacuating a volume of nearly 18 m^3. It combines multiple pump types to meet the requirements for rapid and efficient pressure reduction as well as the generation of stable high vacuum.
- Application Area:
  The area of application includes use in highly sensitive radiation environments, which places specific demands on the pump design and electronics.

3.9.6.1.2 System Description

The pumping system consists of a combination of various pump types, each fulfilling specific functions:

1. Screw Pumps and Roots Pump (Rough Vacuum):
   - Task: Pre-evacuating the large volume (18 m^3) to the rough vacuum range.
   - Types:
     - Two screw pumps for primary pumping.
     - One Roots pump for further pressure reduction and increased pumping speed.
2. Scroll Pumps (Pre-Vacuum):
   - Task: Creating and maintaining the necessary pre-vacuum for the turbomolecular pumps.
3. Turbomolecular Pumps (High Vacuum):
   - Task: Achieving high vacuum down to 1E−5 mbar.
   - Special Feature: Use of external electronics due to high radiation exposure.

3.9.6.1.3 Operating Principle

1. Evacuation of Rough Vacuum:
   - The rough vacuum evacuation is performed using a combination of screw pumps and a Roots pump, arranged in series and operating simultaneously.
   - The screw pumps handle pressure reduction from atmospheric pressure to the range of 1E−2 mbar.
   - The Roots pump operates in parallel to efficiently further reduce pressure and increase pumping speed.
   - This combination is necessary because the Roots pump can only operate safely at a maximum differential pressure of 85 mbar. The screw pumps reduce the inlet pressure of the Roots pump, ensuring it remains within its optimal operating range.
2. High Vacuum Generation:
   - High vacuum is achieved by turbomolecular pumps, which reduce system pressure to 1E−5 mbar.
   - A stable primary vacuum pressure of at least 10 mbar is required for the operation of the turbomolecular pumps. This is provided by scroll pumps, which generate and maintain the pre-vacuum.
   - Scroll pumps are thus essential for the operation of the turbomolecular pumps. Without a sufficiently low primary vacuum, the turbomolecular pumps cannot operate.

3.9.6.1.4 Radiation Resistance

- Screw, Roots, and Scroll Pumps:
  - Must be equipped with a 3-phase motor.
- Turbomolecular Pumps:
  - Are equipped with external electronics to ensure no sensitive electronics are installed directly on-site.

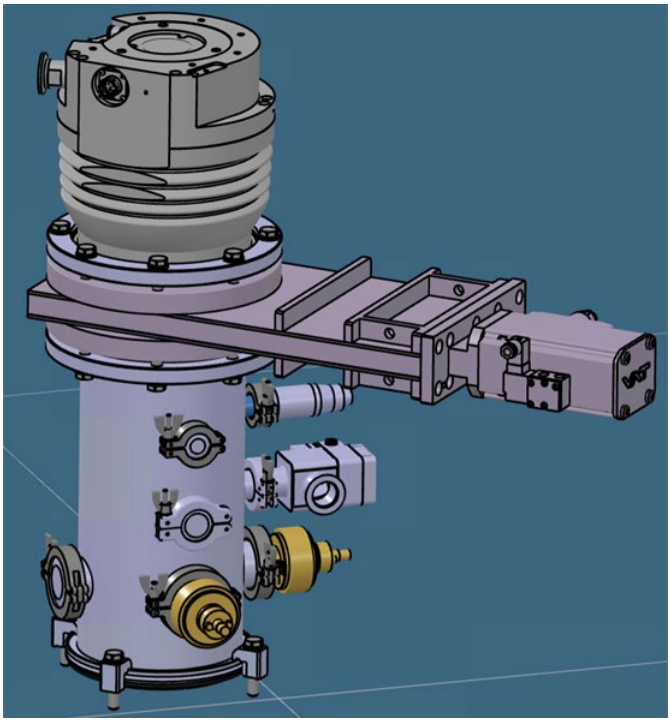

Figure 3.9.31: Illustration of pumps and valves.

- This prevents electronic components from being damaged by ionizing radiation in the operating environment.
- The pump itself remains fully operational as radiation-sensitive control and regulation components are spatially removed and operated outside the radiation area.

3.9.6.1.5 Technical Specifications

- Screw Pumps:
  - Pumping Speed: 100 m^3/h
  - Ultimate Pressure: 1E−2 mbar
- Roots Pump:
  - Pumping Speed: 500 m^3/h
  - Pressure Range: 1E−2 mbar
- Scroll Pumps:
  - Pumping Speed: 15 m^3/h
  - Ultimate Pressure: 1E−2 mbar
- Turbomolecular Pumps:
  - Pumping Speed: 700 l/s
  - Ultimate Pressure: 1E−9 mbar

3.9.6.2 Valves

3.9.6.2.1 Introduction

- Objective and Context:
  Gate valves and angle valves are essential components in the system, enabling safe control and separation of different pressure and beam path areas. They are used to secure the beam path, establish connections between chambers and pumps, and control logical processes in the pre-vacuum area.

3.9.6.2.2 System Description

The valve system includes three different types assigned specific tasks within the facility:

1. Large UHV Gate Valves (Series 19.2, VAT):
   - Task:
     - Separation of the beam path into different sections at the separators (Chapter 3.8.4.2).
     - Ensuring that beam path areas can be independently isolated.
   - Features:
     - High vacuum tightness with low leakage rates.
     - Designed for large flange diameters and frequent opening and closing.
2. UHV Gate Valves Between Chambers and Turbomolecular Pumps (Series 10.8, VAT):
   - Task:
     - Separation of chambers from turbomolecular pumps.
     - Allowing replacement or maintenance of pumps without affecting the chambers.
   - Features:
     - Compact design for use in tight spaces.
3. Angle Valves in the Pre-Vacuum System (Series 24.4, VAT):
   - Task:
     - Control of logical processes in the pre-vacuum area.
     - Blocking and releasing lines for pressure regulation.
   - Features:
     - Fast switching times.
     - Robust and maintenance-friendly.

3.9.7 Vacuum control systems (VCS)

3.9.7.1 Introduction

The new HIMB vacuum control system will replace the Target M and a part of the p-channel vacuum control system (VCS). The existing VCS for the p-channel is based on the Siemens S7-300 series and MP270 / MP277 operator panels and has been in use since 1993 for the vacuum systems of HIPA and Proscan. The plan is to upgrade the VCS of the entire p-channel to the new Siemens S7-1500 series and simultaneously switch the network from MPI/Profibus to Profinet. All passive measurement cells will be connected to the new TPG500 with Profinet and all turbopumps will be equipped with the new TCP350PN controller for Profinet.

The new p-channel VCS consists of five main sections:

1. Main Beam p-channel ring to target E (p-channel1, target H, and p-channel2)
2. UCN
3. MuH2 (former piM1)
4. MuH3 (former piM3)
5. TATTOOS (new line)

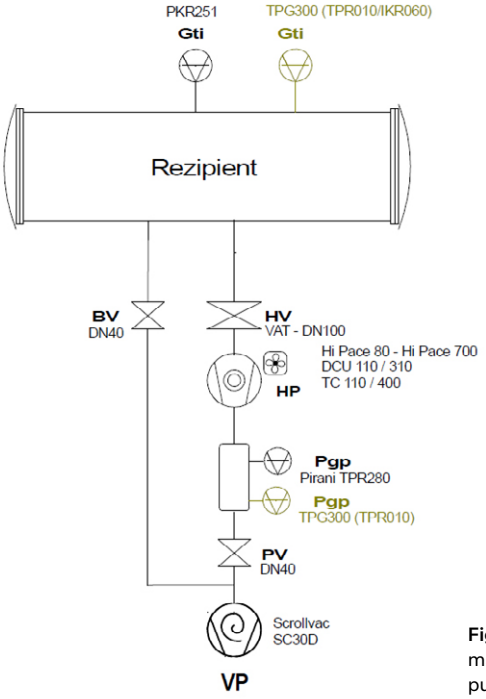

Figure 3.9.32: Schematic of a standard pump station.

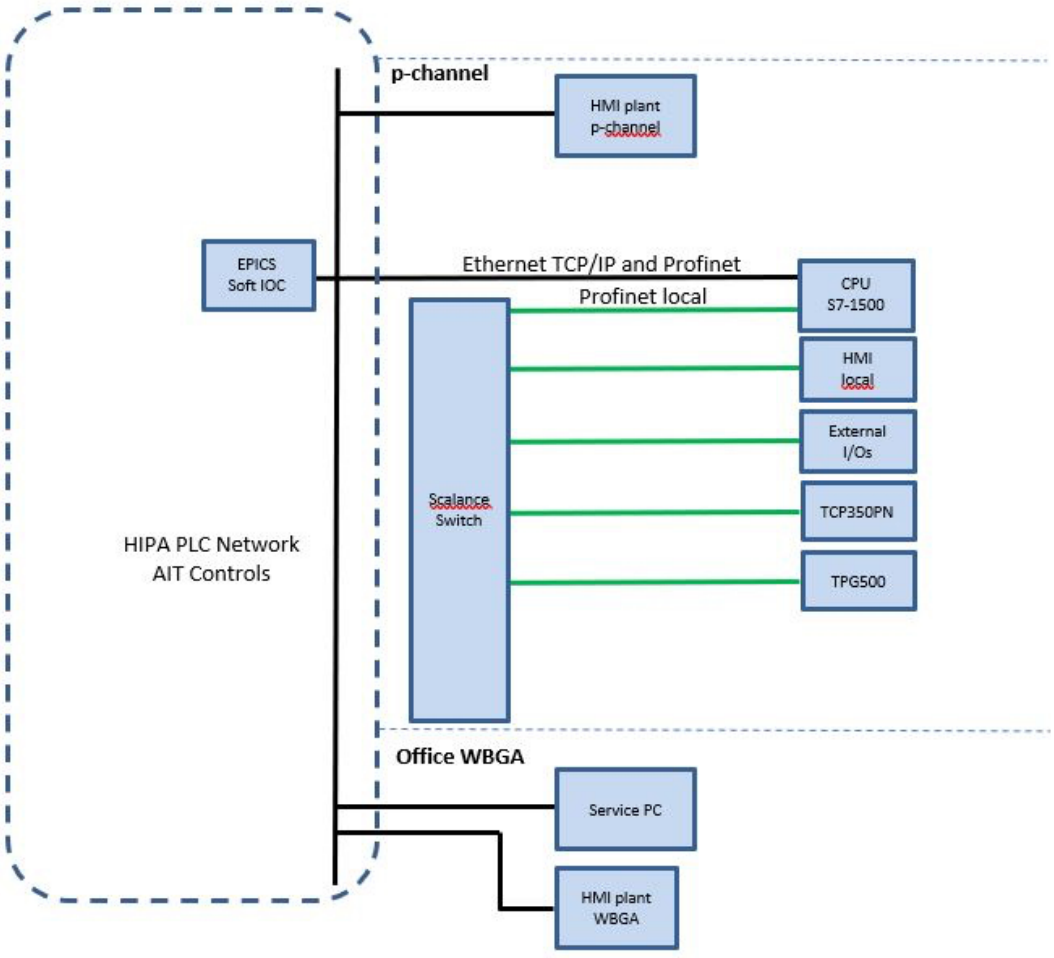

Figure 3.9.33: Network Architecture (green: Local Internal Network)

3.9.7.2 Special Functions

- Central pre-vacuum pumps for some of the pump stations.
- Automatic target H venting with nitrogen.
- Fast closing valve in the beam path to UCN.
- Test routine for fast closing valves.
- Pillow seals for EHT, HIMB, and UCN.

The VCS monitors and controls vacuum systems in distinct vacuum areas, each with independent vacuum pumping systems. The system ensures that valves between neighboring areas remain closed unless there is a sufficiently good vacuum on both sides. Vacuum pressure is measured by vacuum gauges, which trigger interlock signals and close the valves between areas if necessary.

3.9.7.3 Functional Description of a standard pump-station used in the HIPA plant

That principle will be used for the HIMB project.
Short function description:

- The *primary vacuum pump (VP)* starts and evacuates the pipes.
- The *PV valve* opens, and the buffer is pumping down to 2e-3 mbar.
- The *PV valve* closes, and the turbomolecular pump (HP) starts.
- Then the *BV valve* opens and evacuates the recipient during the startup of the turbo pump.
- The *BV valve* closes once the recipient reaches < 1 mbar.
- As soon as the turbomolecular pump reaches 97% of its speed and the recipient vacuum is <= 1 mbar, the *HV valve* opens and pumps the recipient further down to the high vacuum.
- After that, the buffer is pumped between 4 mbar and 2e-3 mbar.

The buffer function is used to reduce the running hours of the pre-vacuum pump. Is the buffer pumped (< 2e-3 mbar), then the valve PV will be closed, and the pump stops delayed after 30 minutes. The delayed stop is used to get out the moisture and to dry the pump.

3.9.7.4 Network Architecture

The network of the p-channel is structured as follows (see Figure 3.9.33):

- *Hipa PLC Network (VLAN):* Ethernet TCP/IP communication with EPICS. (CPU X2)
- *Hipa PLC Network (VLAN):* Profinet communication between plant HMIs and plant CPUs. (CPU X2)

- *Local Internal Network:* Profinet for HMI, I/Os, TCP350PN, and TPG500. (CPU X1)

The network diagram provides a conceptual overview and does not include every single component.

3.9.7.5 Measuring Instruments and Control

For pressure measurements during operation, *cold cathode vacuum gauges* (type IKR60 - Pfeiffer) with a lower measurement limit are employed. *Pirani gauges* (type TPR10 - Pfeiffer) are used to monitor pumping and venting phases (see Chapter 3.9.1). The *TPG500 vacuum gauge controller* is used to read these different gauges. The controller can read up to four gauges, depending on the inserted measuring cards. The *PLC* reads the values via the Profinet connection and sends them to the HMI's, EPICS, and can also be used for interlocks.

Turbomolecular pumps are initially controlled by *Pfeiffer TCP350PN* controllers. The *PLC* reads the status of the TCP-350PN and sends commands to the controller via Profinet. Data from the pumps are processed and evaluated in the PLC program. The PLC also sends the information to the HMI's and the EPICS.

3.9.7.6 Control System and Programming

The control system will be based on the *Siemens S7-1500 series*. The individual vacuum areas are connected via a Profinet network with external I/O's. A *soft IOC* ensures communication between the PLC and the EPICS control system. Programming, maintenance, and service of the PLC system are carried out via a Windows PC and the *TIA Portal* programming environment.

All data from the Profinet devices and the IO's are collected and processed in the PLC. The PLC is connected to the soft IOC and the EPICS user interface. The PLC send and receives data to/from the EPICS over the soft IOC's. For safety reasons we have other user interfaces such as plant Human Machine Interfaces (HMI's) and local HMI's. If the connection to EPICS is lost, the machine can still run and be controlled and monitored from the plant and the local HMI.

For safety reason all machines in the HIPA plant can run independent and have therefore its own local HMI. The local HMI is only used for the specific machine and on that HMI it's also possible to control all machine parts in manual mode (e.g. open/close valves for tests). Some special functions (like venting) are only located on the local HMI. The special functions and the manual mode can only be accessed with username and login to prevent unauthorized manipulation.

All HIPA vacuum plc's and plant HMI's are connected to the redundant HIPA plc network vlan, which is maintained from the AIT. If for any reason the AIT HIPA plc network has a failure, the machine can still run and be controlled from the local HMI. The local HMI is located out in the plant and in the electrical cabinet of the corresponding machine.

The plant HMI are used to control and monitor the whole HIPA in automatic mode. For controlling and monitoring the P-channel and HIMB, the screens and the fault messages will be integrated in those plant HMI's.

3.9.7.7 Interlocks and Safety Functions

The VCS includes numerous integrated functions, with several examples listed below:

- A vacuum interlock signal is generated when a valve is closed, causing a beam trip.
- Separate interlock signals are sent to different systems (cooling water...).
- When the fast valve closes in the UCN, the beam is dumped.
- Release signals for the upstream and downstream vacuum areas.
- Status information is sent to other systems, such as the *Machine Interlock System*.

3.9.7.8 Summary

The new Vacuum Control System (VCS) for HIMB will be based on a modern Siemens S7-1500 architecture and will ensure a full migration of the existing p-channel VCS to Profinet communication. This new system will provide robust network and measurement systems to precisely monitor and control vacuum conditions, as well as ensure safety interlocks for the HIMB operation.

3.10 Girders & Support Structures

3.10.1 Concept of support structures

The support structures and adjustment mechanisms, which are used, are proven steel frames (supports) or iron blocks (girders), whereby the girders also serve as radiation protection for the floor. As a result, they are utilized in various components that are exposed to high levels of radiation.

When it is feasible, an effort is made to reuse the current support structures for components that are reused. The adjustment mechanisms are manually adjustable with a threaded rod for vertical adjustment and adjusting screws (usually 4 pieces) for horizontal adjustment.

Adjustment mechanisms typically have an accuracy of less than +/- 0.5 mm and an adjustment range of at least +/- 10 mm, which satisfies component requirements.

Pictures of the support and the girder with adjustment mechanism are shown in Figure 3.10.1–Figure 3.10.3.

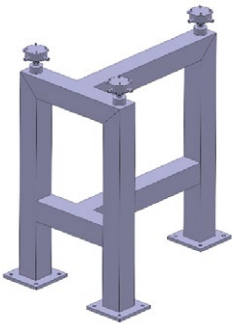

Figure 3.10.2: Steel frame support

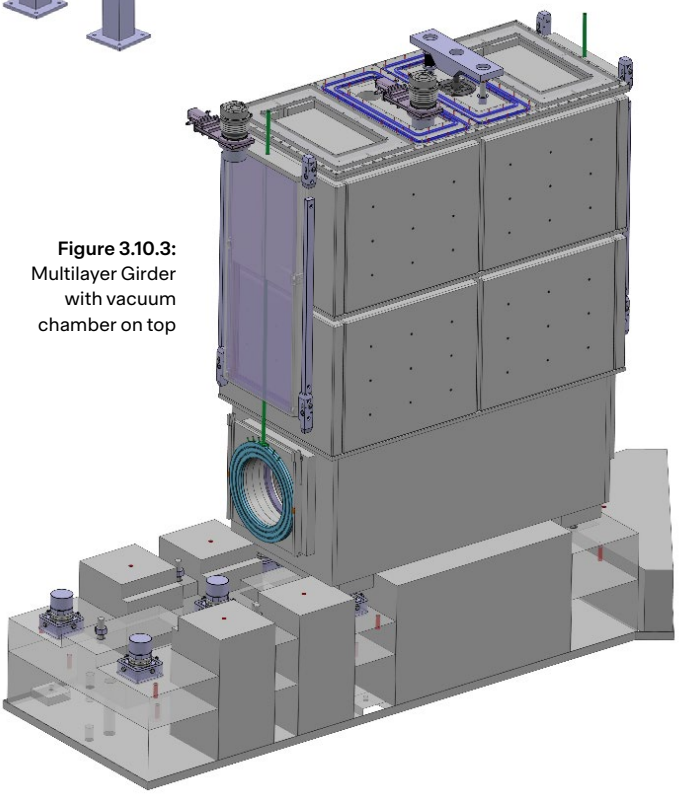

Figure 3.10.3: Multilayer Girder with vacuum chamber on top

3.10.2 Adjustment mechanisms

10 t feet

The10 t HIPA standard and adjustable feet (Figure 3.10.4), which are used at the HIPA facility, are primarily used for the solenoid magnets or other components.

The maximum weight of the 5 large vacuum chambers, including their inserts, is between 40 to 70 tons each. As a result, a new foot had to be developed, as the normal PSI standard feet only allow a load of 10 t per foot.

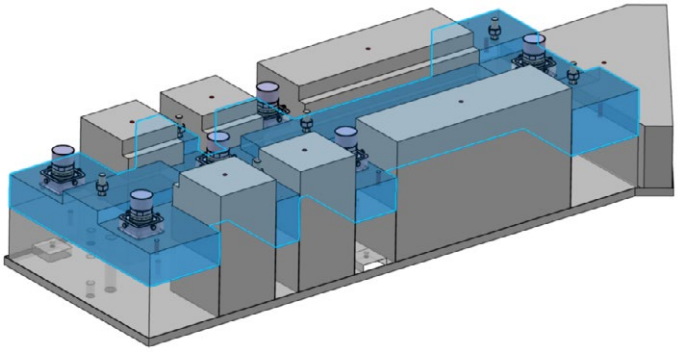

Figure 3.10.1: Multi-layer girder

Figure 3.10.4: PSI standard 10 t foot.

50 t feet

The green marked area represents the area of the saw thread with diameter D=155 mm with pitch P=6 mm. The many fine holes represent a labeled scale with 6° per step (6 mm stroke / 60 steps per revolution = 0.1 mm stroke per 6° in Z direction).

The overhead crane with a load of 60 t is used for the adjustment (XYZ) so that the entire load does not have to be adjusted manually. The 4 adjusting screws (XY) have an M20×1.5 mm thread. The positioning in XY allows a maximum of 9 mm.

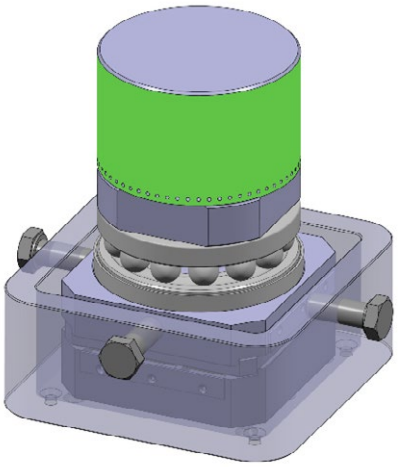

Figure 3.10.5: Newly developed 50 t foot.

Auxiliary support feet

As an additional support for the large vacuum chambers, a smaller foot will be placed underneath the chambers. These feet can take up to 1/10 of the load of the 50 t feet and should help to stabilize the chamber and prevent it from bending. In order to allow the chamber to expand, in case of thermal expansion, a small copper plate will be place between bolt and girder. Figure 3.10.6 shows the positions of the 50 t feet and the smaller auxiliary support feet.

3.10.3 Installing the support structures

All girders and supports will be installed with assistance from the surveying group, which uses a laser tracker and the adjustment mechanism to ensure the precise positioning of the components. Following the procedure:

- All supports, girders and, where possible, the components have to be equipped with measuring points.
- The girder is coated with formwork oil on the underside and around the lower edge so that the mortar does not adhere to the girder. In addition, a plastic sheet must be placed between the girder and the hall floor to ensure that the mortar cannot set with the girder, in addition to the formwork oil.
- The first step is to position the girder (+/-1 mm XYZ), with the horizontal alignment being the most important. The girder is shimmed with “small” aluminum or steel plates of different thicknesses in the millimeter range until they are level within the required tolerance. The shimming should guarantee a maximum distance of 40 mm and a minimum distance of 6 mm from the hall floor.
- A frame is placed around the girder to prevent the mortar from leaking out.
- PCI Repaflow mortar (shrinkage-compensated) is used to undercast the girder. The girders may have several filling holes, which ensure good large-area casting. An area of approx. 0.4 m×0.4 m can be covered with one filling hole.
- If necessary, the girders are multi-layered due to the ATEC weight restriction (crane load <12 t) and a next girder would be placed on top of the one on the ground. The other layers are pinned with large pins so that the upper layers remain in position relative to the base.
- The components are then mounted on the girders, where intended, at an appropriate distance from the target without girders, on their support structures or directly on the

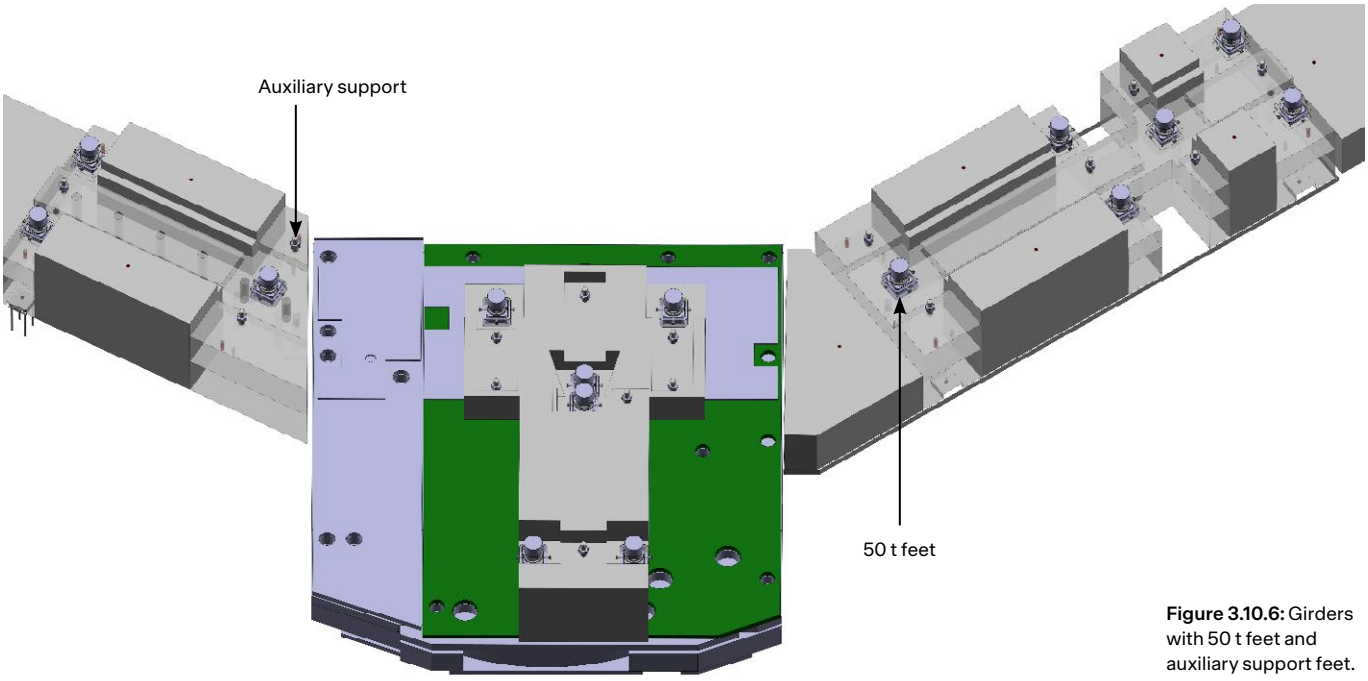

Figure 3.10.6: Girders with 50 t feet and auxiliary support feet.

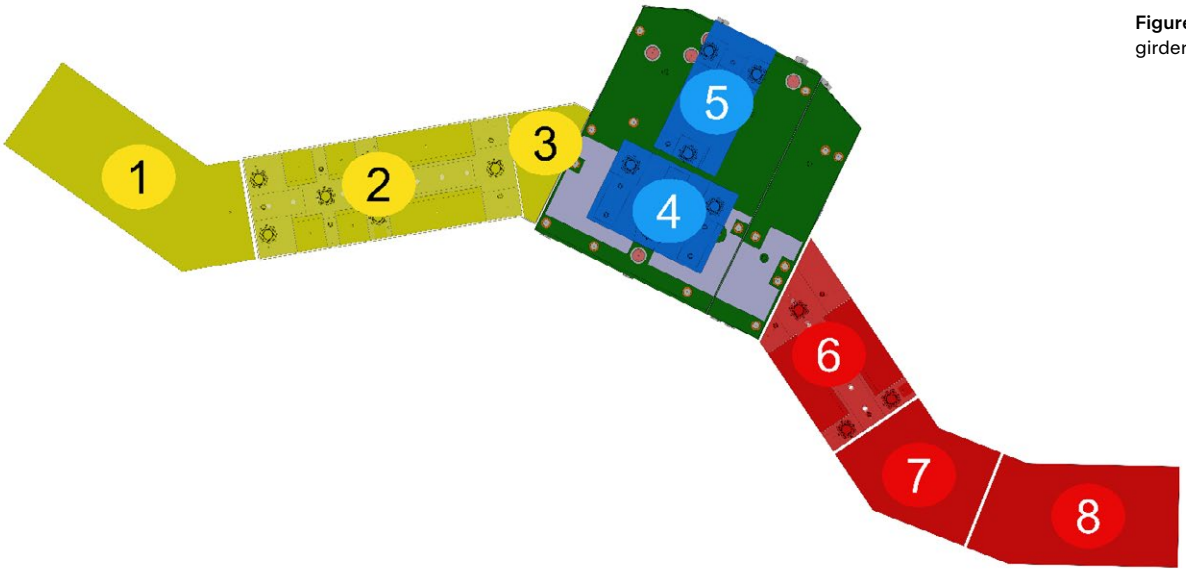

Figure 3.10.7: Overview of girders in the HIMB area.

adjustment mechanisms and precisely measured and adjusted.

- After mounting the local shielding, the components are measured again and readjusted if necessary.

3.10.4 Dismantling the support structures

In the case the girders and supports have to be dismounted or disposed later, a certain design was defined in order to facilitate this process. Therefore, all support structures are dimensioned (size and weight) so that they can be dismantled or separated either on site or at the ATEC facility.

3.10.5 Support structure overview (proton/secondary beamlines)

In Figure 3.10.7 an overview of all girders needed for the two secondary beamlines MuH2 and MuH3 as well as the p-channel are given. The numbers point to the girder in Table 3.10.1. Altogether eight adjustable girder structures are needed to support the vacuum chambers and dipoles,

3.10.6 References

[1] Construction drawing 3073_WEHA, floor loads, IMPACT-EXT-25-07241_3073_WEHA_Bodenplatte_Achse_13-19.

[2] Construction drawing 3073_WEHA, maximum floor loads, IMPACT-EXT-25-07242_WEHA-max Bodenbelastungen

[3] Data sheet, concrete painting, IMPACT-EXT-25-07243_TechnicalDataSheet_StoPox_WL_100_0202_DE_03_01

[4] Data sheet, iron painting, IMPACT-EXT-25-07244_T_Rucoplast_2K-Grundierung_03.2021

[5] Data sheet, iron painting, IMPACT-EXT-25-07245_T_Rucopur_3000_glanz_und_seidenglanz_2023

[6] Data sheet, Zementärer Vergussmörtel, IMPACT-EXT-25-07246_PCI_Repaflow®_Technisches_Merkblatt__DE

MuH2 (1)	MuH2 (2)	MuH2 (3)	TgH (4)	PK2 (5)	MuH3 (6)	MuH3 (7)	MuH3 (8)
Slit Dipol - KV	MuH2.1, MuH2.2 chamber	Pyortenax Dipol	Traget chamber	PK2 chamber	MuH3 chamber	Dipol+ Solenoid	Dipol-KV
PRD-00700318	PRD-00758210	PRD-00615558	PRD-00701068	PRD-00701067	PRD-00758211	PRD-00700319	PRD-00758212

Table 3.10.1: Overview of beamline, devices and respective girder drawing number. : First row: Beamline with number in brackets, which point to the location in Figure 3.10.7. Second row: Device on girder. Third row: drawing number.

3.11 Exchange Flask H

As the inserts of the beamline are radioactively activated by the proton beam, it is necessary that they are designed for remote handling. It is already mentioned in the CDR (2022) it is planned to handle as many beamline inserts as possible with the existing target-E exchange flask. Some inserts are too large for this exchange flask, therefore they have to be handled with the new HIMB exchange flask, for example the capture solenoid magnet.

3.11.1 Flask H

The exchange flask H serves as a safe transport medium for activated inserts that need to be removed from the beamline. Inspections and replacement of components make it necessary to remove the inserts from time to time and transport them safely through the experimental hall (WEHA). The flask is well shielded and encapsulates the insert that contamination is avoided during transport and the dose rate to people is well reduced (see also Chapter 2.4). The components intended for the HIMB exchange flask can have a total height of approx. 3450 mm and weight up to almost 14.5 t (Table 3.11.1). The dimensions of the exchange flask are determined by the size and mass of the largest and heaviest inserts but are limited in height by the space available within the experimental hall due to the maximum height of the indoor crane and the highest point of the infrastructure over which the transport medium must be moved.

The total height of the exchange flask is 5450 mm (Figure 3.11.1), although the effective height on the hook of the hall crane between the lowest edge of the construction and the lower edge of the hall crane is 4935 mm (Figure 3.11.2). The highest position to which the overhead crane can be moved is 13.2 m and the highest point over which transportation must take place is 7.5 m, resulting in a clearance of 5.70 m.

The weight of the exchange flask is limited by the hall crane capacity of 60 t, which, after deducting the weight of the heaviest insert, defines the maximum weight of the flask.

A total of 17 inserts are provided for the exchange flask H, 6 of them come from the existing target station E system and are therefore fixed in their design, and 11 further new inserts for HIMB (Table 3.11.1). Although the new exchange flask H is able to accommodate all of the aforementioned inserts, Target H and all collimators are taken up with exchange flask E in order to transport them into the ATEC via the lock. The infrastructure of the lock is currently not designed for the conditions of the new transport medium.

Focus of the exchange flask H development is mainly on picking up the large and heavy inserts like the capture solenoids. However, due to their size, these must be introduced via the ATEC roof by removing segments from it, which makes this process more elaborate, but counts to the routine operations.

The activation of the inserts determines the shielding material thickness of the exchange flask and therefore also the weight. Among the HIMB components the capture solenoid with a dose rate of about 16.5 Sv/h (see Chapter 2.4.7.1) was identified as the insert with the highest activation. Particularly due to its large weight and the weight limit of the exchange flask, this component is the most critical, regarding the required shielding thickness. According to UraM Art. 35[2], the dose rate must not exceed 2 mSv/h at the surface of the exchange flask and 0.1 mSv/h at a distance of one meter. These values are achieved by using an additional 100 mm thick shielding consisting of a 80 mm lead layer encased in steel.

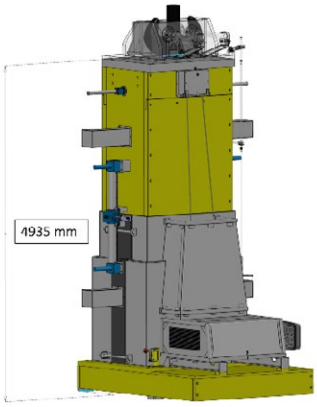

Figure 3.11.1: Effective height underneath the crane hook of exchange flask H.

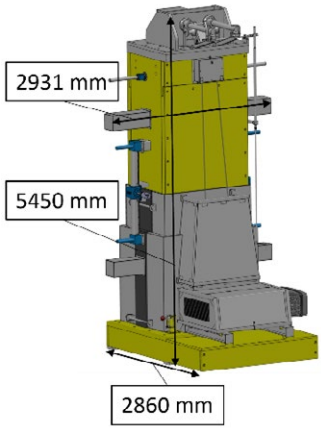

Figure 3.11.2: Basic dimensions of the exchange flask H.

[2] In fact, the UraM Art 35 does not apply here, because the exchange flask is not used outside of the zone. Therefore, it should be seen as an recommendation rather than a hard limit.

Name	Number	Revision	Existing Stock	HIMB	Expected Exchange Interval	Activation	Total Weight	Hight	Width	Depth
Local Shielding - BD1	ASM-10002.24.1703	-.1	X		1/ 20+ Years	< 40 Sv/h	5090,5	3360	900	450
	ASM-10002.24.1741	-.1								
Local Shielding - BD2/3	ASM-10002.24.2200	-.1	X		1/ 20+ Years	< 40 Sv/h	8761,6	3360	900	515
	ASM-10002.24.2199	-.1								
Local Shielding - BD1	ASM-10002.24.1741	-.1	X		1/ 20+ Years	< 40 Sv/h	5100,4	3360	900	450
	ASM-10002.24.2330	-.1								
Local Shielding - Cross-slotted collimator	ASM-10002.24.2108	-.1	X		1/ 20+ Years	ca. 40Sv/h	4172,1	3163,5	780	329,25
Local Shielding - TgE	ASM-10002.24.2092	-.1	X		1/ 20+ Years	< 40 Sv/h	4397,4	3188	780	525
Local Shielding - KHE2	PRD-00687658	-.1	X		1/ 20+ Years	< 40 Sv/h	2754,2	2710	610	440
TgH	PRD-00610196	A.1		X	1/Year	<16 Sv/h	1525,5	3255,15	585	304,4
KHH0	PRD-00660114	-.1		X	1/ 10 Years	<16 Sv/h	1701,4	3131	330	417
KHH1/KHH2	PRD-00635260	-.1		X	1/ 10 Years	<16 Sv/h	2026,4	2977,95	405	412
MHP/MHS 23/24A//MHP/MHS 23/24B	PRD-00674189	-.1		X	1/ 10 Years	<16 Sv/h	2299,2	3270	606	373
WSP21/22/23//31/32	PRD-00624823	B.1		X	1/ 20+ Years	<16 Sv/h	6999,4	3415,65	910	534
KSL21/22//31/32	PRD-00747008	-.1		X	1/ 20+ Years	<16 Sv/h	4698,4	3448	1010	396,5
WSC21/WSC31	PRD-00627853	A.1		X	1/ 15 Years	approx. 16 Sv/h	14710,6	3422,85	1010	739
KD21/22/23/24//KD31/32/33	PRD-00735385	-.1		X	1/ 20+ Years	<16 Sv/h	276,4	3165,75	954	140
KSK21/22//31/32	PRD-00670839	-.1		X	1/ 20+ Years	<16 Sv/h	2810,9	2483	1010	396,5
KDH 21/KDH22	PRD-00643498	-.1		X	1/ 20+ Years	<16 Sv/h	333,2	n/a	455	50
Local Shielding - TgH	PRD-00694258	-.1		X	1/ 20+ Years	<16 Sv/h	2299,9	3131,35	334,4	918,8

Table 3.11.1: List of all inserts intended for the exchange flask H.

The carrier housing, into which the inserts are pulled, has already a wall thickness of 100 mm steel. This means that both elements together form a 200 mm thick shield consisting of steel and lead in the area of maximum radiation (Figure 3.11.3).

The front and rear sides of the chassis are bolted to the carrier housing, allowing the internal components of the exchange flask to be accessed for maintenance by removing the plates after the shielding has been removed first. On the rear side of the exchange flask, at the height of the highest

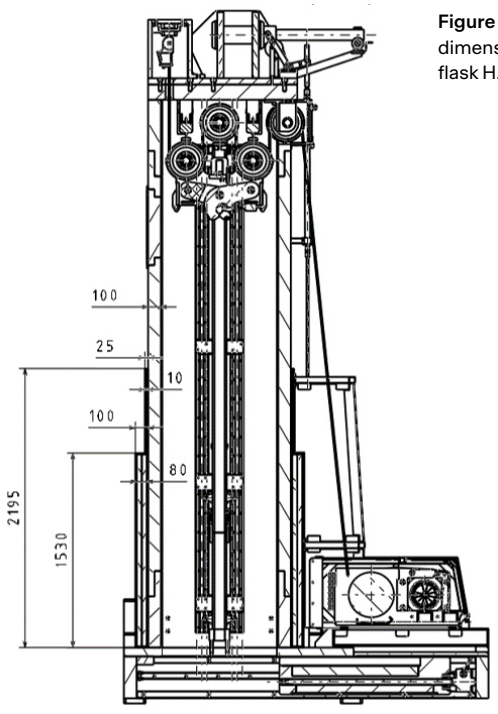

Figure 3.11.3: Shielding dimensions of the exchange flask H.

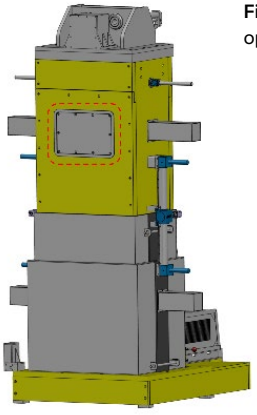

Figure 3.11.4: Inspection opening

gripper position, there is an inspection opening through which inspections can be carried out (Figure 3.11.4).

A rail system is used for the safe installation and removal of the new inserts into and out of the system. It can be moved vertically and connected to the vacuum chambers via locating pins, thus creating a seamless transition. The transition from the lowest edge of the insert to the upper inner edge of the local shielding is particularly critical, as this represents a potential risk of collision. The rail system is designed in such a way that its path from the interior extends over the closure lid, the contamination protection, the bridge and the distance between this and the local shielding (Figure 3.11.19). This kind of rail system is already used in the Target E exchange flask and has proven its worth there. Each of the inserts has a different width, which means that the rail system must be adjustable over this dimension. For this reason, a stepless system is provided for exchange flask H, which can be moved between a track width of 304.4 mm and 1010 mm by using spindle lift drives on both sides (Figure 3.11.5).

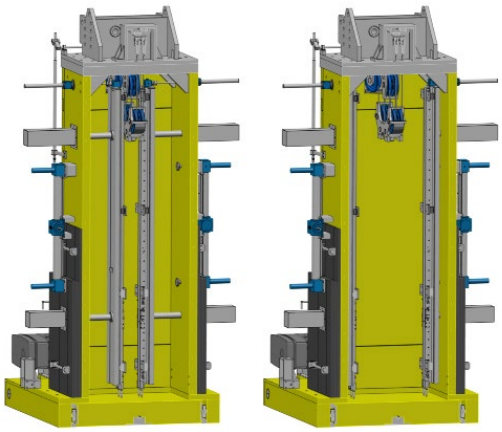

Figure 3.11.5: Adjustable track width

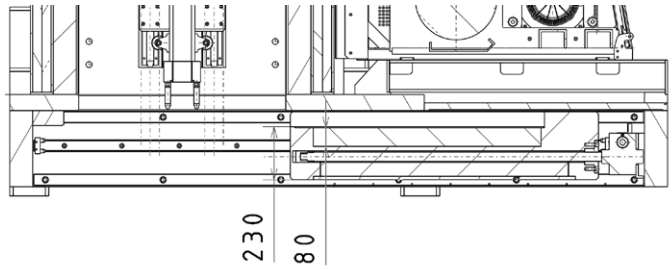

Figure 3.11.6: Exchange flask H closure.

The lower side of the exchange flask can be closed thanks to a 230 mm thick steel lid with an 80 mm lead layer movable via a spindle lift drive. It shields the surroundings from the inserts (Figure 3.11.6 and Figure 3.11.19) and protects it from contamination.

The exchange flask is transported using the previously mentioned 60 t indoor crane. The connection to the hook of the crane is achieved via a coupling system, which is similar to the one used in the target E exchange flask and is closed exclusively by manual force with a crank (Figure 3.11.7 and Figure 3.11.8).

To lift the inserts out of the beam line, the current concept provides a pulley construction (Figure 3.11.9-Figure 3.11.12) whose drive, together with the cable drum, is located outside the closed exchange flask. Due to the large weight of the inserts and the limited space inside the exchange flask, a fourfold pulley block (Figure 3.11.9) with two driven ropes is planned, with which the rope force can be reduced to one eighth of the weight force of the inserts. This enables the use of a lighter and smaller cable winch. Furthermore, thinner steel cables allow for more compact deflection pulleys, which results in a more compact overall design of the exchange flask. The rope ends are connected outside the chassis. Load cells are located there, which detect the weight of the insertion

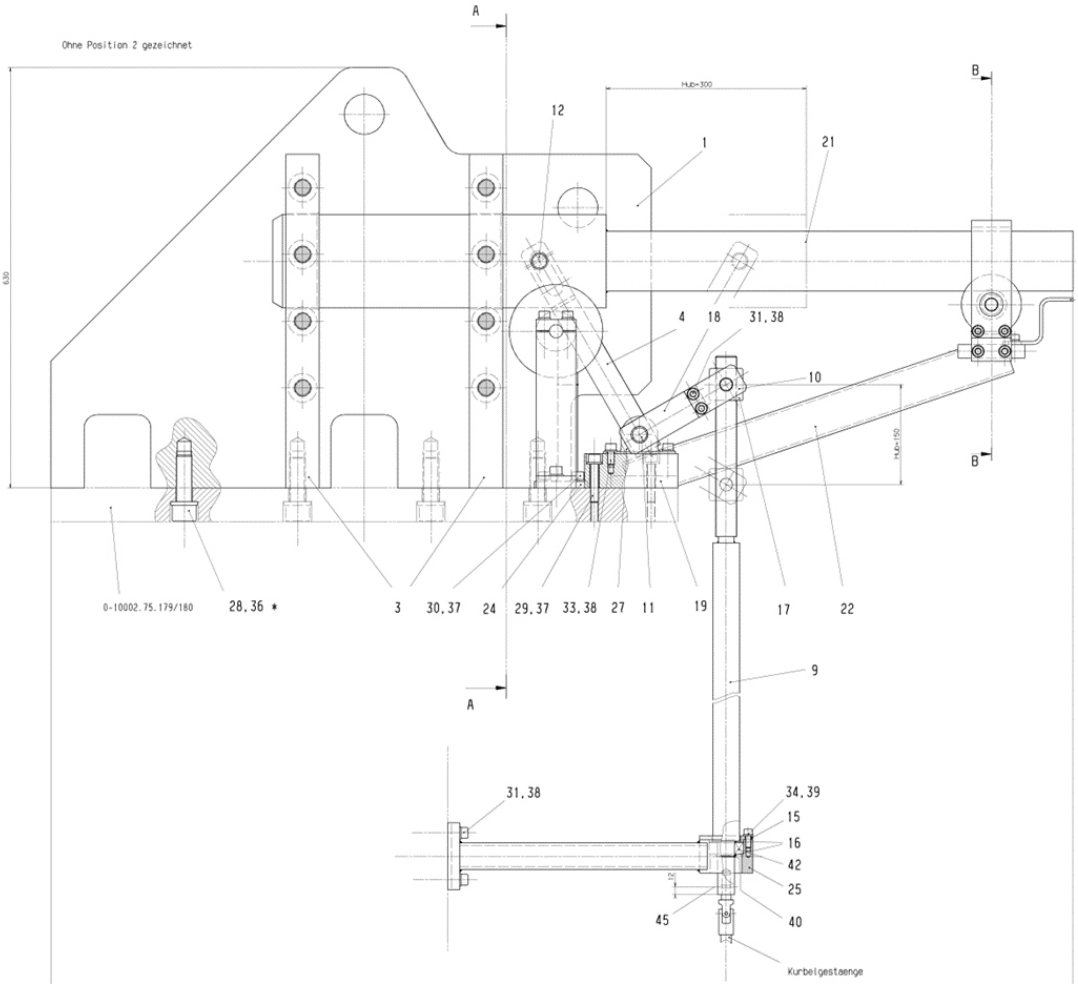

Figure 3.11.7: Coupling system for hall crane.

Figure 3.11.8: Hall crane coupling with exchange flask E.

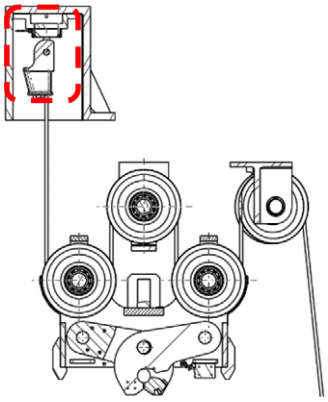

Figure 3.11.9: Pulley construction

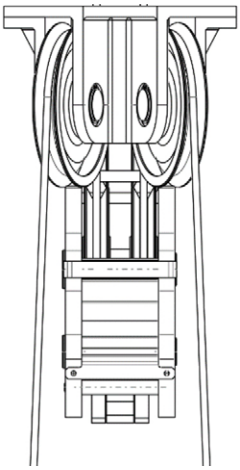

Figure 3.11.10: Rotated deflection pulleys

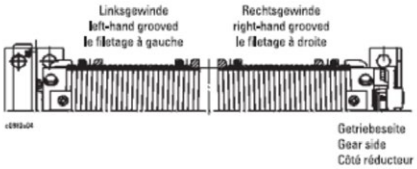

Figure 3.11.11: Rope drum

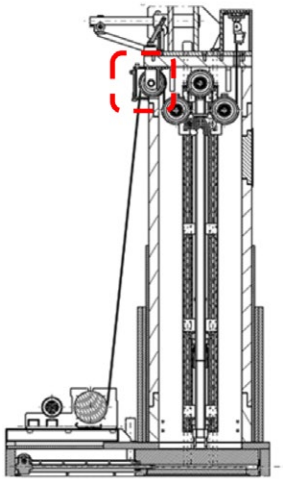

Figure 3.11.12: Position of deflection pulley

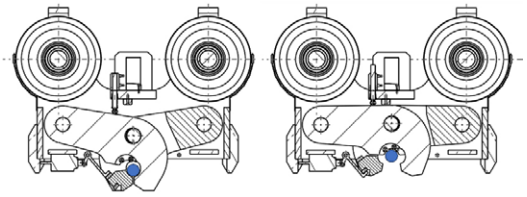

Figure 3.11.13: Opened and locked position of the gripper.

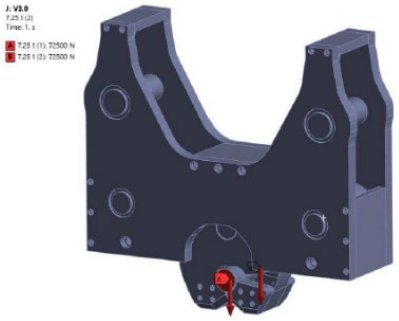

Figure 3.11.14: Force introduction into the gripper.

and ensure a shutdown in the event of a slack rope, i.e., a large difference in rope force (Figure 3.11.9).

The steel cables are guided into and out of the exchange flask via a deflection pulley, the axis of which is level with the outer chassis wall (Figure 3.11.12). There they end on a double-grooved cable drum with counter-rotating winding (Figure 3.11.11). These deflection pulleys are also rotated by 20° around the Z axis in order to allow a rope entry angle of +/-3.5° on the deflection pulleys when the rope is winding or unwinding on the drum (Figure 3.11.10).

The cable winch itself has an additional brake on the cable drum, which should be seen as an additional safety feature. In the event of a power failure, the load can be lowered by manually releasing the hoist brake.

In order to transport the insert, an interface is required in the form of a load handling device with a coupling bar to which the gripper of the wire rope hoist system can attach. The gripper used in exchange flask H is a purely mechanical system in which the gripper claws grip around the coupling bolt of the traverse and remain closed due to self-locking caused by the weight of the inserts.

The jaws can only be opened by releasing the gripper from the suspended load by using pairs of rollers on the upper sides of the jaws, which rest on the coupling bar when the gripper is set down (Figure 3.11.13). This position is then secured by a latch so that the gripper remains in the open position and can be removed from the traverse. When the gripper is in the closed position, this latch, which is controlled by a lifting magnet, additionally secures the gripper claws against unintentional opening.

3.11.1.1 Calculation model of the gripper

Based on the gripper model (PRD-00721026), a FEM calculation was performed to determine the forces induced in the gripper through the pin at the load attachment point by a load of 145'000 N, caused by the heaviest insert (approx. 14.5 t) (Figure 3.11.14).

The gripper is equipped with a total of four rope pulleys, each with a diameter of 300 mm, over which two steel ropes run. These four pulleys rotate on two bolts with a diameter

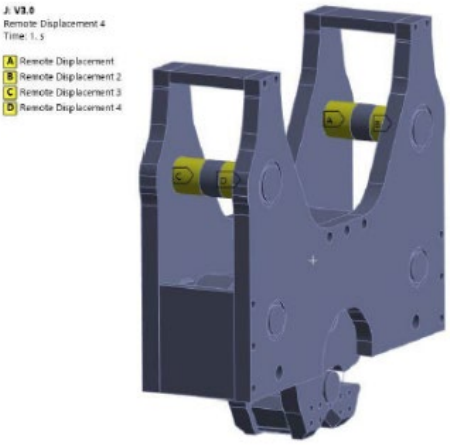

Figure 3.11.15: Constraint points of the model.

of 60 mm, which are fixed to the gripper housing. At these points, the structure is constrained via displacement conditions (Figure 3.11.15).

This results in a maximum displacement of the gripper jaws of 0.49 mm and 0.07 mm in the housing itself (Figure 3.11.16).

The resulting stresses are primarily concentrated in the areas of the jaws where the load is introduced via the coupling pin of the load attachment device and in the rotation areas (Figure 3.11.17). The stresses in these areas reach up to 125 N/mm². Local stress peaks arise due to the bending behavior of the pins, with values of up to 495 N/mm² calculated at the edges of the bearing points. However, these have no impact on the overall strength of the gripper and can be neglected.

In the pins themselves, a stress of up to 148 N/mm² is expected (Figure 3.11.18).

Based on the expected stresses in the gripper, a safety factor of at least 5 can be ensured with the appropriate material selection according to EN 13001.

3.11.1.2 Motion sequence of exchange flask H

The numbers in Figure 3.11.19 refer to the following description:

1. Adjusting the rail system to the correct track width according to the inserts.
2. Opening the lid.
3. Lowering the extendable rail system.
4. Lowering the gripper and coupling.
5. Pulling up the gripper together with the insert.
6. Raising the rail system while simultaneously raising the gripper/insertion.
7. Closing the lid

The transport of the exchange flask (Figure 3.11.20) is carried out via the hall crane. Despite the removal of the shielding blocks, obstacles within the experimental hall of 7.5 m height must be crossed.

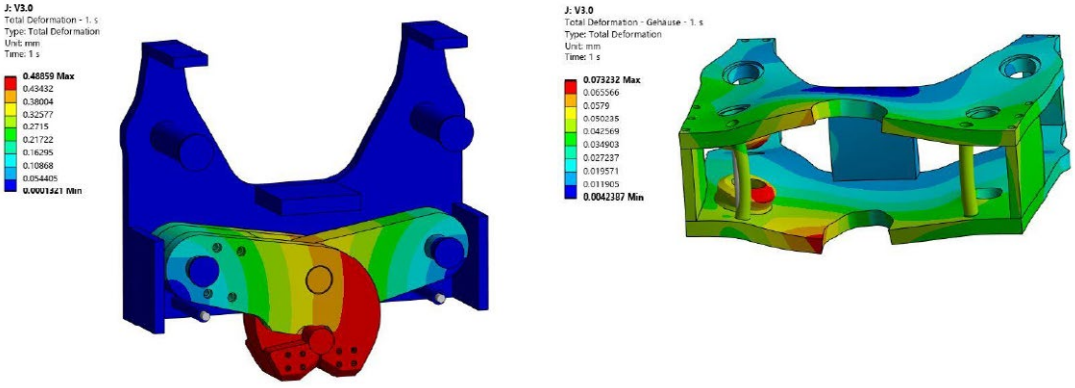

Figure 3.11.16: Deformation of the gripper (left) and housing (right) under maximum load.

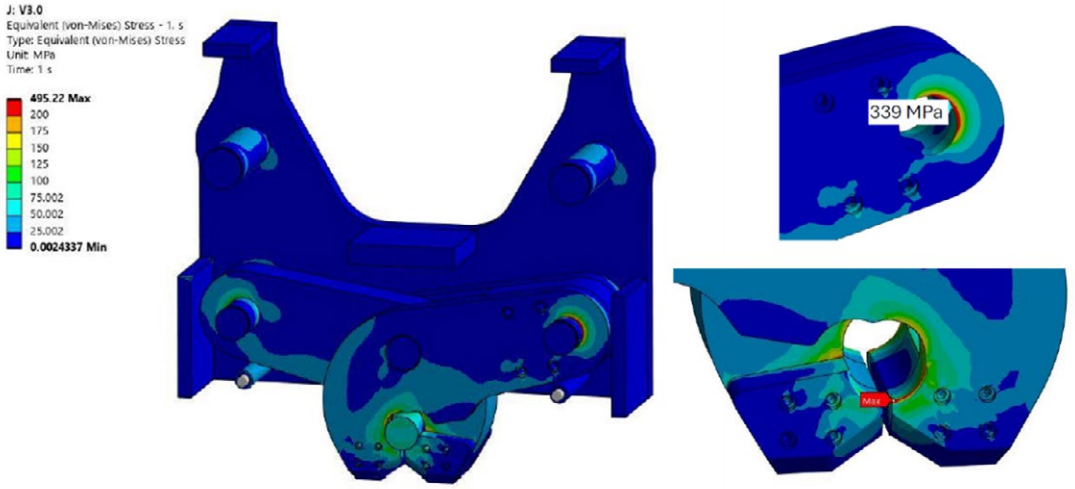

Figure 3.11.17: Stress distribution within the gripper.

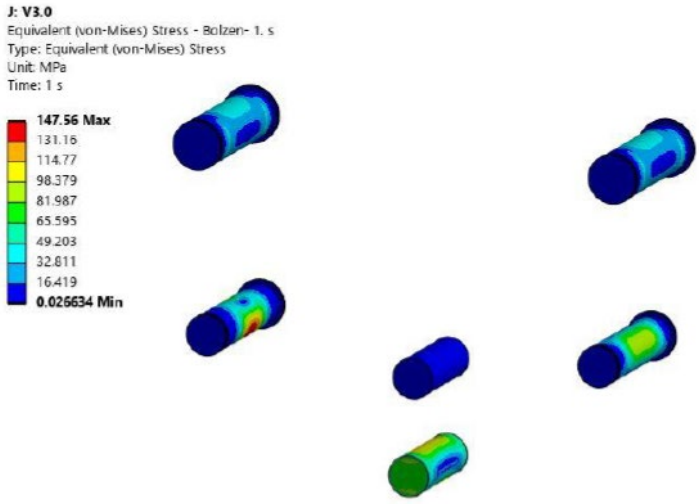

Figure 3.11.18: Stresses within the pins.

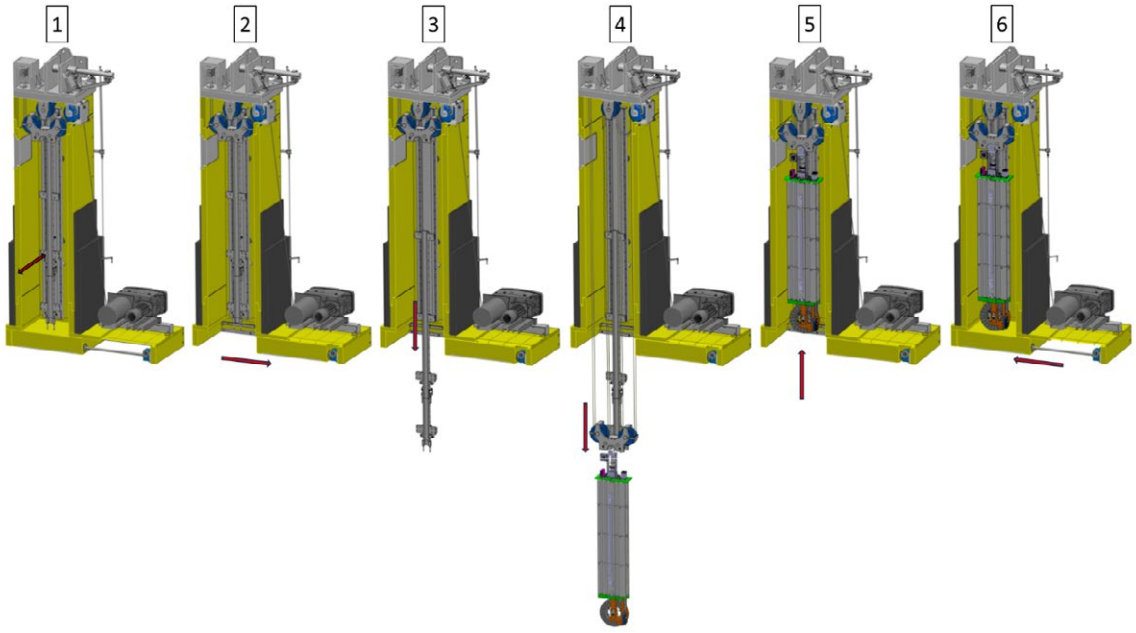

Figure 3.11.19: Motion sequence of exchange flask H.

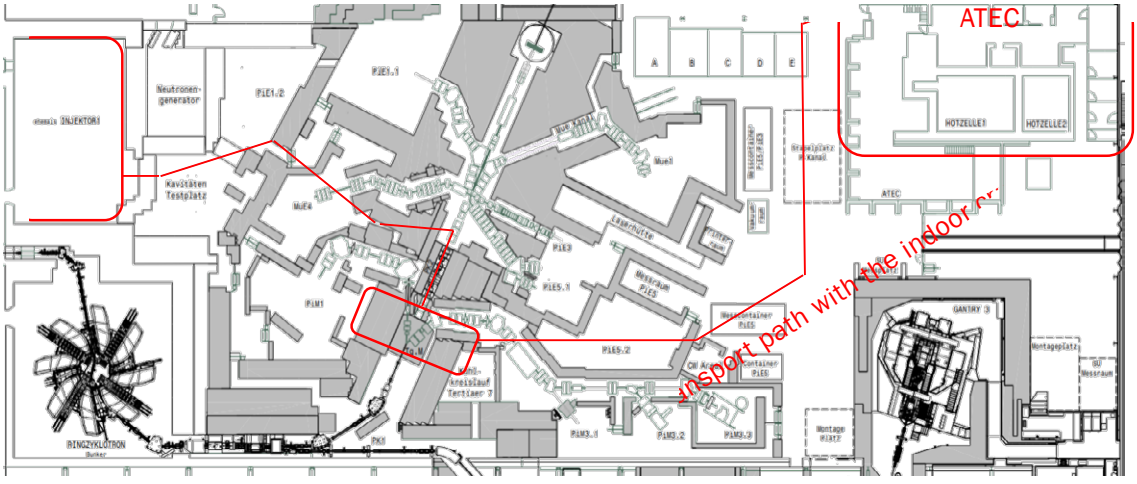

Figure 3.11.20: Transportation route and operating areas of exchange flask H.

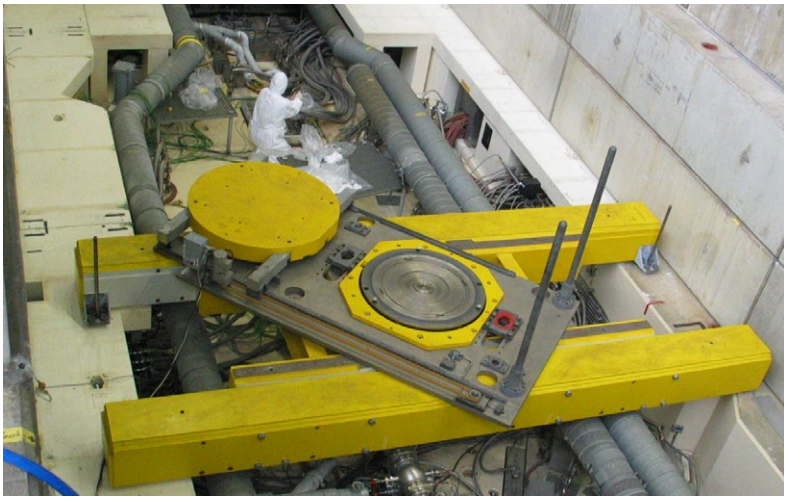

Figure 3.11.21: Bridge element for spanning the infrastructure above the beamline.

Figure 3.11.22: Exchange Flask on its bridge.

The transport of the exchange flask takes place both between the ATEC and the inserts, as well as to the area of the former Injector 1, where nowadays parking slots for the inserts are located. Two additional parking slots will be installed for the target H insert.

On the beamline the concrete shielding blocks are removed in advance up to the service level, where the inserts can be accessed. Here the flask support structure, the so-called bridge (Figure 3.11.21, example photo), offers a suitable surface where the flask can be positioned above the corresponding insert.

3.11.2 Bridge

As mentioned in Chapter 3.11.1, a structural element is required for the placement of the exchange flask H, which spans the infrastructure on the service level. This structure is called bridge and already conceived in a similar form for the exchange flask of target E (Figure 3.11.22).

The bridge for target H exchange flask is designed in such a way that it can be converted into two variants (Figure 3.11.23), called small and large. This is necessary to position it along the proton channel as well as in the secondary areas (Figure 3.11.24). However, the conversion from one variant to the other also means that specific parts are required according to the width spanning above the proton channel and the secondary areas respectively (Table 3.11.1). These specific parts represent the connecting elements between proton channel and the muon beamlines, which are the same in both variants. A variant for both sections is not possible due to the boundary conditions of the shielding.

Both bridge variants have a levelling system located in the common parts. This system is used to compensate for potential height differences at the contact points of the bridge, which are located left and right from the beamline (Figure 3.11.23).

Levelling is achieved via spindle lifting gears at the beam ends, which are operated by a ratchet via their drive pivot if required (Figure 3.11.25). The height of the support surface can thus be varied by pressing the bridge upwards or by lowering it.

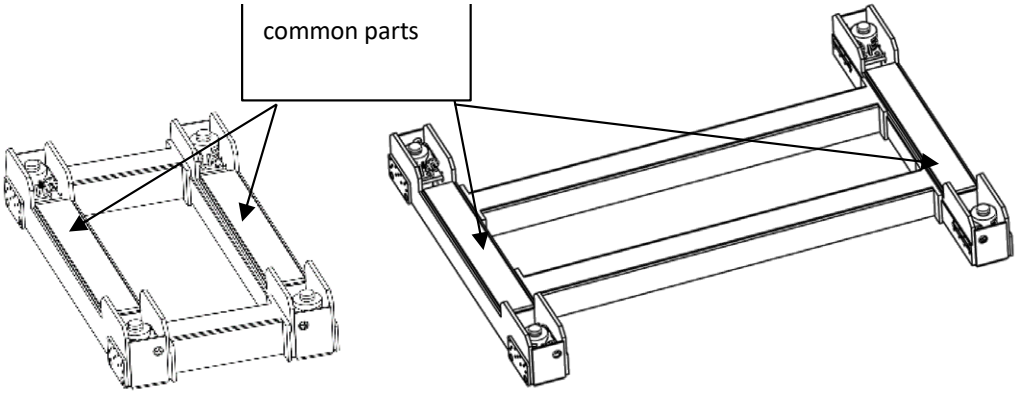

Figure 3.11.23: Small and large variant for exchange flask H.

	Element	Common Part	Specific Part		Length in mm	Width in mm	Height in mm	Weight in kg
Small Variant				(mounted)	4350	2227.5	700	**7975**
	Proton channel	x			4350	495	700	3261
	Connecting Elements		x		1267.5	700	420	727
			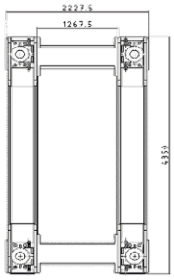					
Large Variant				(mounted)	5890	4350	700	**11479**
	Proton channel	x			4350	495	700	3261
	Connecting Elements		x		4930	700	420	2479
								

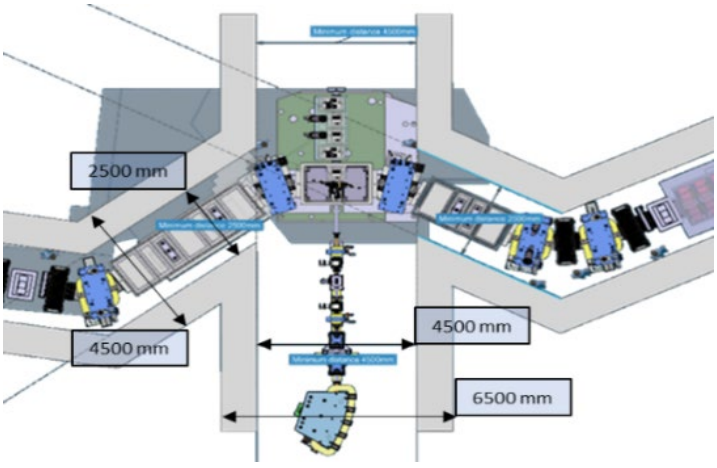

Figure 3.11.24: Schematic representation of the proton channel and secondary areas.

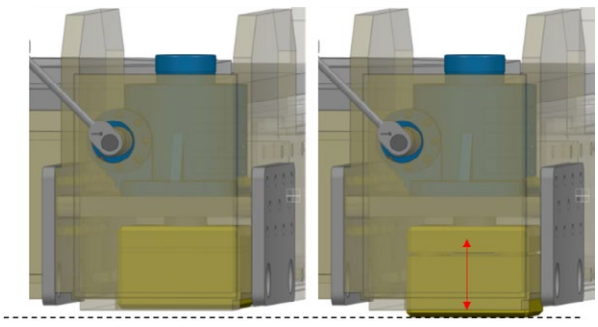

Figure 3.11.25: Height adjustment via spindle drive.

Height adjustment is necessary to ensure that the exchange flask is in a vertical position above the inserts.

To ease the positioning of the exchange flask above the insert, levelling lasers are attached to the beams, which can be used to position the bridge on the shielding blocks according to the location of the inserts. The correct position is approached using reference markers and the alignment of the laser lines with the hall crane. The position of the bridge can thus be arranged correctly in the X and Y axes, as well as around the Z axis (Figure 3.11.26).

The exchange flask itself is guided into the correct position via long positioning pins so that it finally stands on form-fit feet with the base (Figure 3.11.27). The alignment of the exchange flask to the bridge and thus also to the insert is defined by an attached plate. The positioning pins, the feet for the form-fit and a closure lid are located on this plate. A cover is also provided on the bridge to shield the surroundings from an open radiation source created by removing an insert from the beam line. This lid is opened after the exchange flask has been set down. Once the insert has been safely removed from the system and encapsulated by the exchange flask closure lid, the lid on the bridge is also closed (Figure 3.11.28). Not shown is the contamination protection between the bridge and the service level. It is connected to the exhaust air system and protects the surrounding from contamination, particularly when the insert is pulled into the exchange flask.

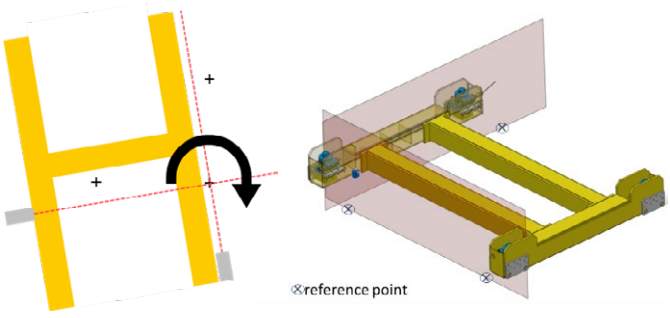

Figure 3.11.26: Positioning supported by leveling lasers.

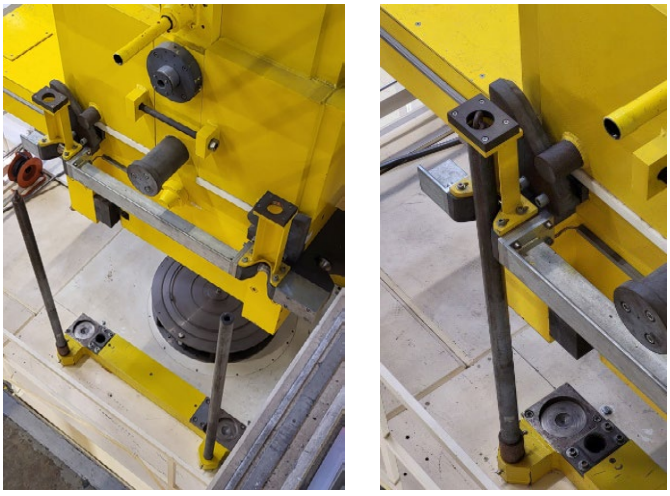

Figure 3.11.27: Positioning pins.

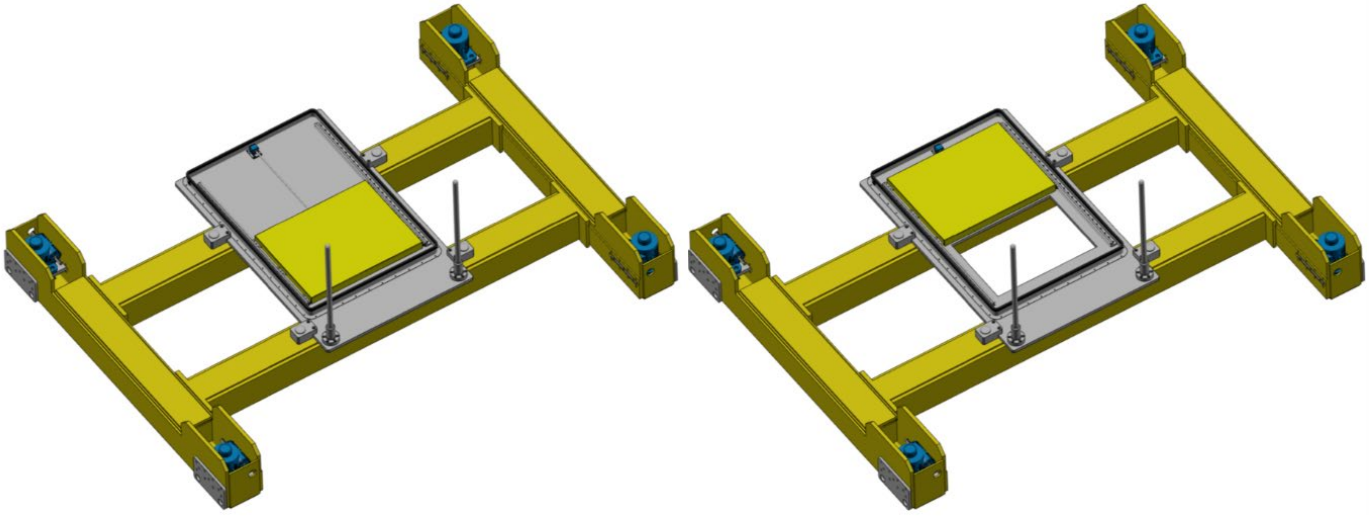

Figure 3.11.28: Lid system.

3.12 Machine Safety

Machines and systems must meet operational safety requirements and product safety. This requires consideration of numerous rules and guidelines (e.g., EN ISO 12100, machine safety, etc.). A PSI process consultant advises the project team on the process flow and document creation. It is recommended to start the preparation of the documents in the concept phase with the defined PSI standard documents. The individual documents for each component serve as the foundation for the overall assessment documentation for the facility and necessitate a thorough understanding of standards, regulations and specific facility knowledge. Furthermore, the design, implementation, commissioning, and operation of the system are based on these documents and measures.

The new EU Machinery Regulation (2023/1230) replaces the previous EU Machinery Regulation 2006. Suppliers, manufacturers who are tasked by PSI to procure or manufacture machines with a planned commissioning date at PSI after January 20, 2027, must design and validate the machines in accordance with the essential health and safety requirements in Annex III of the EU Machinery Regulation 2023/1230. This also applies to PSI internally manufactured machines. The new EU Machinery Regulation was published in the Official Journal of the European Union and came into effect on July 19, 2023. On January 20, 2027, the transition period ends and reaches its final validity.

Table 3.12.1 lists all beamline components, which need a machine safety or system assessment.

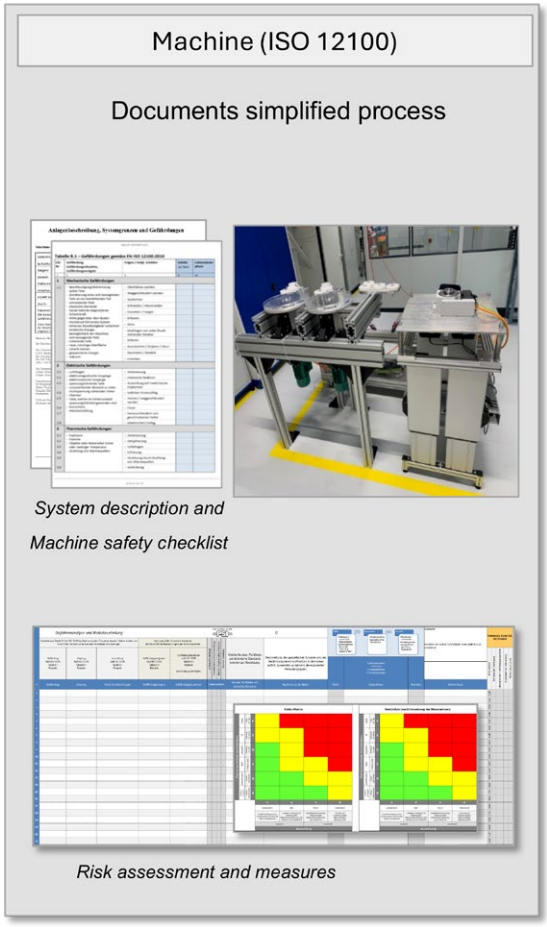

Figure 3.12.1: Individual assessment, example of a "HTS Coil Winding"

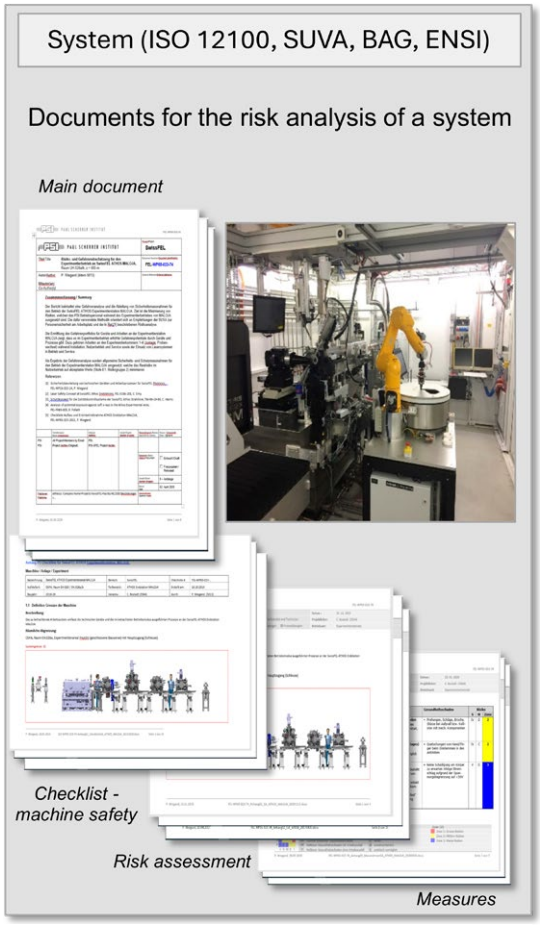

Figure 3.12.2: System assessment, example of "SLS Beamline 10SA PX II Experiment and optics hutch"

HL Name	Name	Installation region
Target - Insert		
TgH	TgH - Target H Insert	Target H -region
TgH	TgH - Target H local shielding	Target H -region
Exchange flask		
	Exchange Flask HIMB	
	Bridge for exchange flask	
Collimator - Insert		
KHH0	KHH0 - Collimator incl. diag. foil	Target H -region
KHH1	KHH1 - Collimator incl. diag. foil	PK2 - Beamline after TgH
KHH2	KHH2 - Collimator incl. diag. foil	PK2 - Beamline after TgH
Profile monitor - Insert		
MHP S23/24	MHP S23/24 - Profile monitor	PK2 - Beamline after TgH
MHP S23B/24B	MHP S23B/24B - Profile monitor	PK2 - Beamline after TgH
Magnet - Insert		
WSC	WSC - Capture solenoid	Target H -region
WSP	WSP - Pyrotenax solenoid	MuH2 - Shielding area
WST	WST - Transport solenoid	MuH2 - Shielding area
WSP	WSP - Pyrotenax solenoid	MuH3 - Shielding area
WST	WST - Transport solenoid	MuH3 - Shielding area
Pillow seal - Insert		
KDH21	KDH21 - Pillow seal NW160	PK2 - Beamline after TgH
KD	KD - Pillow seal NW500	MuH2 - Shielding area
KD	KD - Pillow seal NW500	MuH3 - Shielding area
Beam blocker - Insert		
KSL	KSL - Beam blocker (long)	MuH2 - Shielding area
KSL	KSL - Beam blocker (long)	MuH3 - Shielding area
KSK21	KSK21 - Beam blocker (short)	MuH2 - Shielding area
KSK31	KSK31 - Beam blocker (short)	MuH3 - Shielding area
Ionisation chamber		
MHI11	MHI11 - Ionisation chamber	PK2 - Beamline after TgH
Slit system - incl. magnet		
ASH21 /FSH21	ASH21 / FSH21 - Dipole with slit system	MuH2 - Shielding area
ASH32	ASH32 - Dipole with slit system	MuH3 - Shielding area
FSK21	FSK21 - Slit system	MuH2 - Shielding area

HL Name	Name	Installation region
Magnets		
WST	WST - Transport solenoid	MuH2 - Shielding area
ASP21	ASP21 - Pyrotenax dipole	MuH2 - Shielding area
APS31	ASP31 - Pyrotenax dipole	MuH3 - Shielding area
ASP31	ASP31 - Dipol with pump	MuH3 - Shielding area
AHE1	AHE1 - Chicane magnet 1	PK2 - Beamline before TgH
AHE2	AHE2 - Chicane magnet 2	PK2 - Beamline before TgH
SSL31	SSL31 - steering magnet	MuH3 - Shielding area
Separator		
Sep	Sep - Separator	MuH2 - Shielding area

Table 3.12.1: Component list HIMB.

4. Dismantling, Installation and Safety

4.1 Current Experimental Hall (WEHA) Layout

The current layout of the experimental hall (WEHA) is illustrated in the Figure 4.1.1. The yellow lines represent the beamline directions. The dashed lines are beamlines, which will not be refurbished and therefore are not part of the project. However, some beamlines will be affected due to the reconstruction of the northern area of the WEHA or from the relocation of the Helium liquefier (Cryoplant). Within the HIMB project the beamlines PiM1 and PiM3 will be replaced as well as the target station M.

All areas which are going to be dismantled or relocated are indicated in yellow. As part of the reconstruction of the northern area, the neutron bunker and RF test facility will be dismounted, and the latter rebuilt. Furthermore, several infrastructures like the cooling circuits 7 and 4 of the adjacent building WNAA (Figure 4.1.1) as well as the helium liquefier will be relocated. A detailed explanation can be found in Chapter 4.2.

Since the remodeling of the WEHA required for installing HIMB is a major effort, the work is split to the two regular shutdowns 2025 and 2026 before the one-year-long shutdown 2027, in which the removal of target M and the HIMB installation will take place.

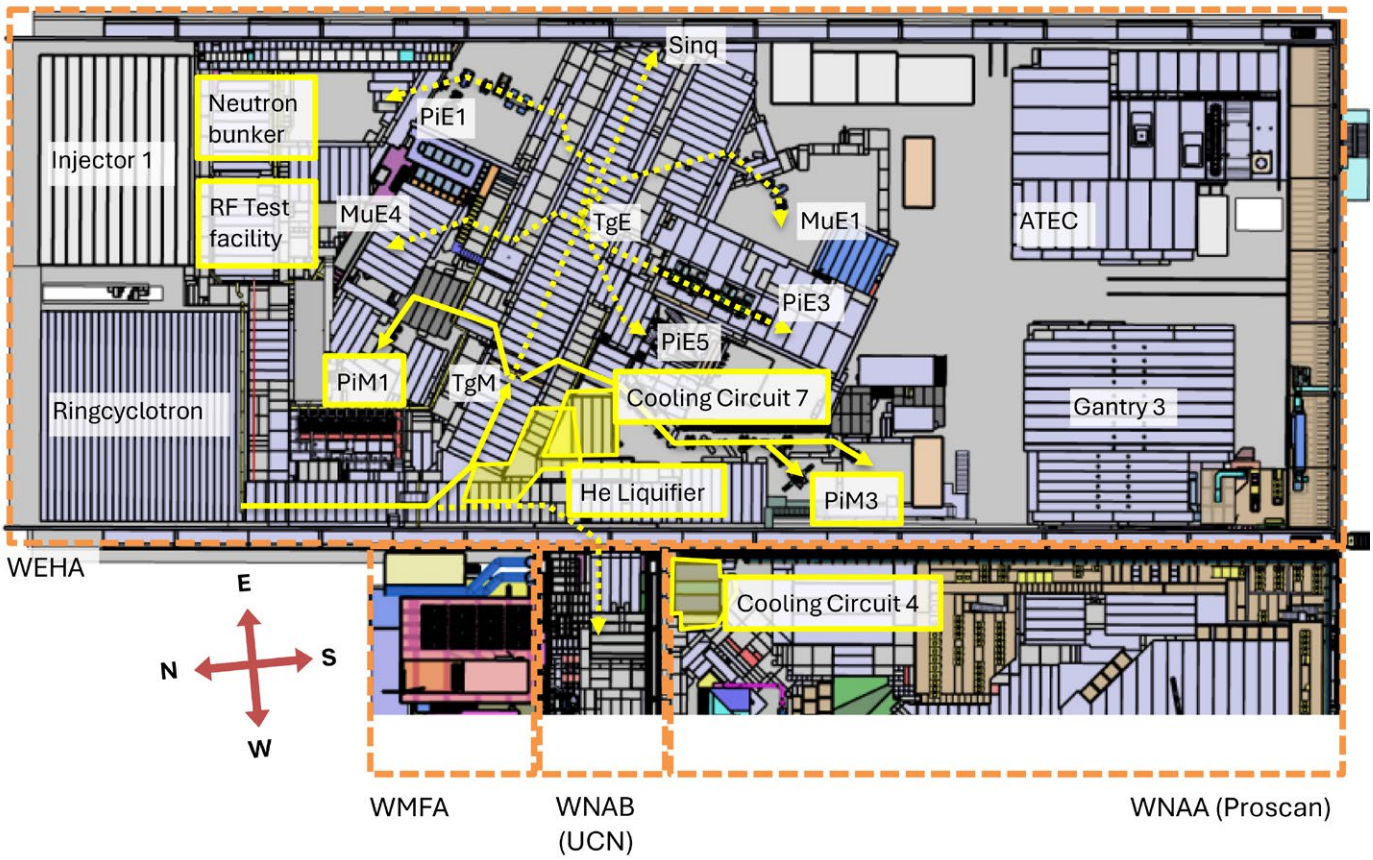

Figure 4.1.1: Current situation of the WEHA. The dashed orange lines indicate different buildings.

4.2 New Experimental Hall (WEHA) Layout

Figure 4.2.1: Overview WEHA after 2028.

4.2.1 Overview of the Areas

Figure below illustrates the experimental hall (WEHA) after all modifications in 2028. This illustration provides an overview of all areas and supports the understanding of the explanations in the following chapters.

4.2.2 WEHA Exp. Areas remodeling

4.2.2.1 North Area

Since the new MuH2 Beamline does not fit into the current experimental area, the layout must be modified. This change also has an impact on the surrounding areas. These changes provide the chance to reorganize the entire northern region, eliminating outdated areas and improving the current emergency route situation to satisfy modern safety requirements (see Chapter 4.6.). In Figure 4.2.2 the existing beamline in PiM1 (grey shaded line) with the current area layout and the new beamline MuH2 is illustrated.

In the following a short explanation about the current and new situation of each area within the northern part of the experimental hall (WEHA) is given.

4.2.2.2 East Wall

In Figure 4.2.3 the present situation is shown. Through the east wall (red circled area in Figure 4.2.4), a new escape route will

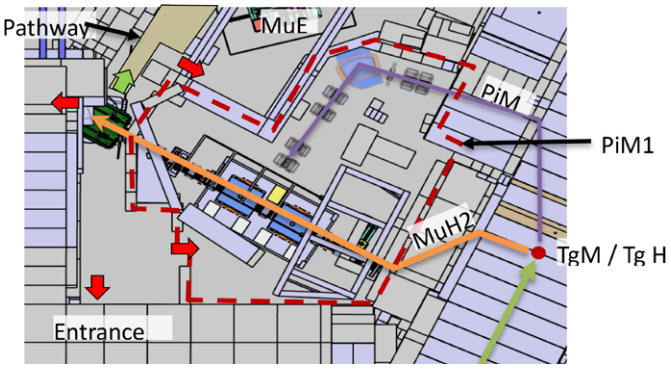

Figure 4.2.2: Current PiM1 area (red dashed) with new beamline MuH2 (orange line).

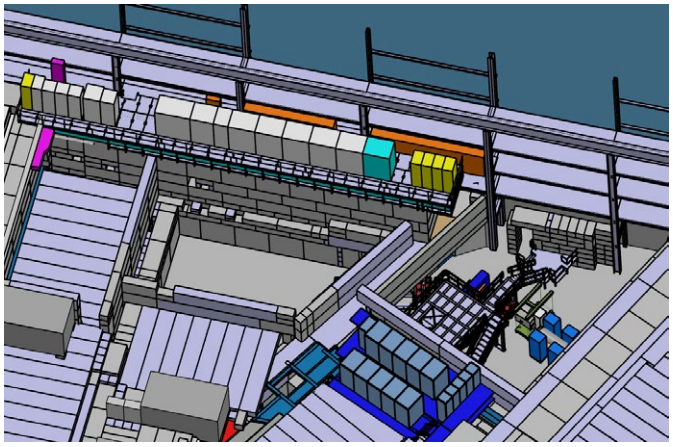

Figure 4.2.3: Current situation of the east wall

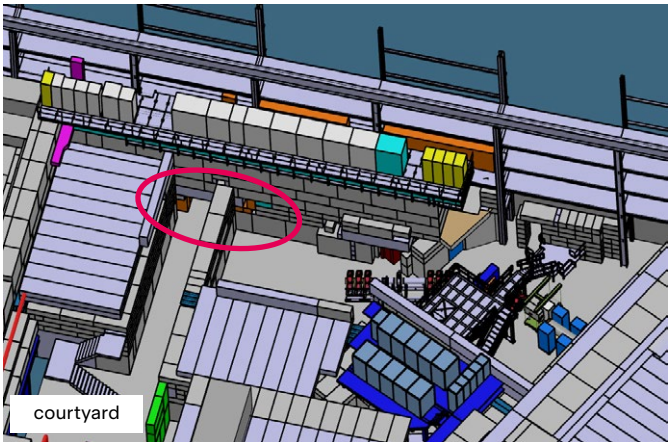

Figure 4.2.4: After final remodeling of the east wall

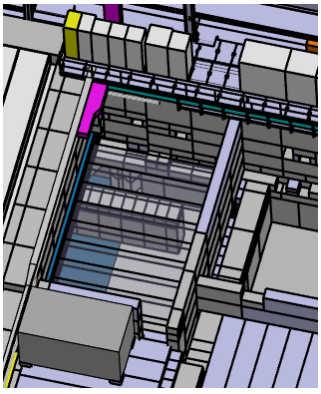

Figure 4.2.5: Current situation of the Neutron bunker

Figure 4.2.6: After final conversion to new RF test facility

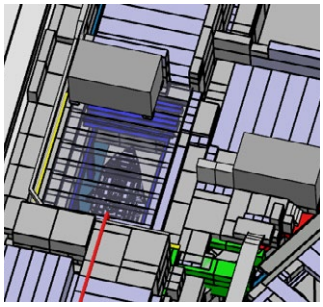

Figure 4.2.7: Current situation of the RF test site

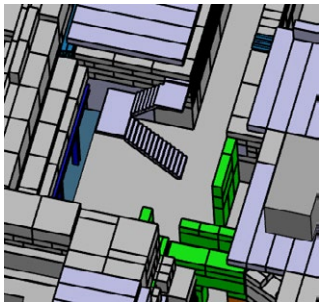

Figure 4.2.8: After final remodeling to the new inner courtyard

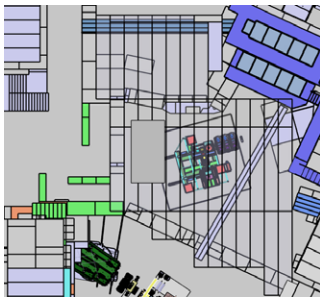

Figure 4.2.9: Current situation of the area MuE4

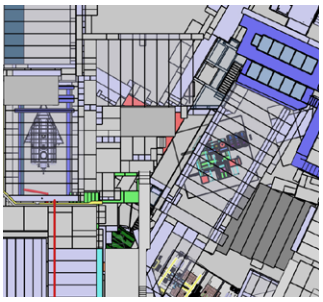

Figure 4.2.10: After final remodeling of the area MuE4

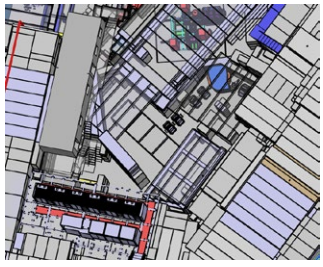

Figure 4.2.11: Current situation of the area PiM1

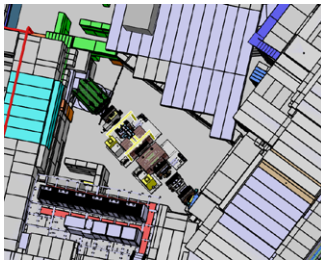

Figure 4.2.12: After final remodeling of the area MuH2

be established. This will enhance the accessibility and escape route situation in the northern areas. The courtyard, which serves as a loading area for experiment supplies, provides access to all experimental areas (see Figure 4.2.4).

Neutron Bunker

The 14 MeV neutron generator in this bunker (Figure 4.2.5) will move to another building outside the WEHA. Therefore, the inner labyrinth and the associated offices will be removed (Figure 4.2.6) to make space for the RF test facility. To access this area the existing bunker door will be refurbished and reused.

RF test facility

Due to the relocation of the current RF test facility (Figure 4.2.7), this newly available space can be used as an inner courtyard (Figure 4.2.8) as loading area from the hall crane or for handling, smaller pre-assemblies, and general accessibility improvements.

Beamline areas

Figure 4.2.9 shows the crowded situation around the MuE4 area. The part of the wall close to the new courtyard of the MuE4 site will also be rebuilt (Figure 4.2.10). The new entrance from the East to the WEHA will be accessible from the inner courtyard.

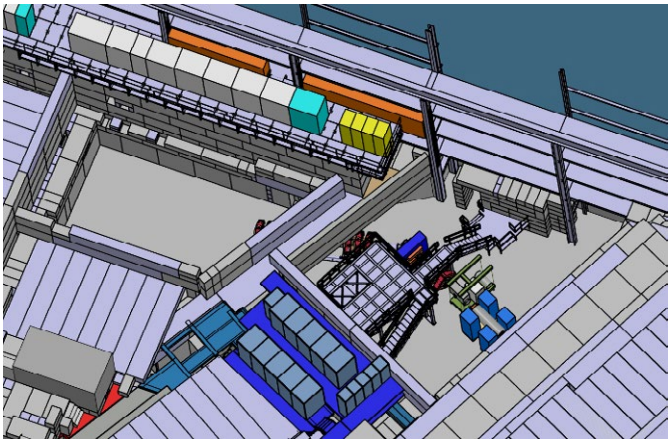

Figure 4.2.13: Current situation of the area PiE1

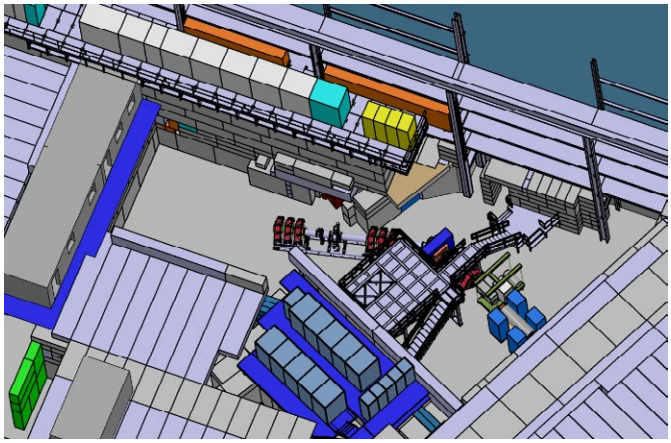

Figure 4.2.14: After final remodeling of the area PiE1

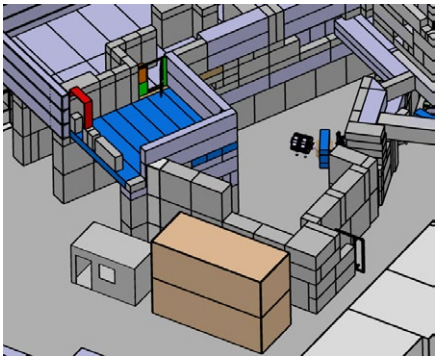

Figure 4.2.15: Current situation of the area MuE1with hutches in the front.

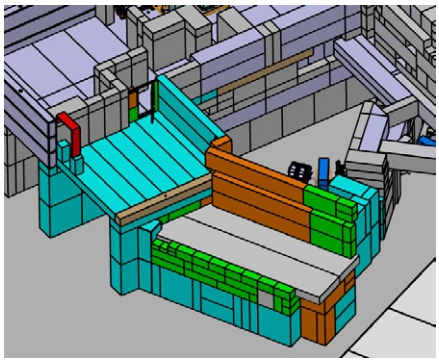

Figure 4.2.16: After final remodeling of the area MuE1 (before the installation of the cryogenic platform)

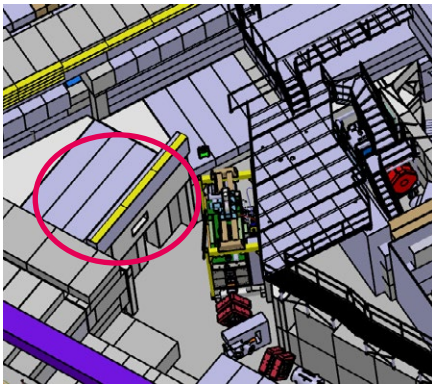

Figure 4.2.17: Current situation of the tertiary cooling circuits 7 bunker

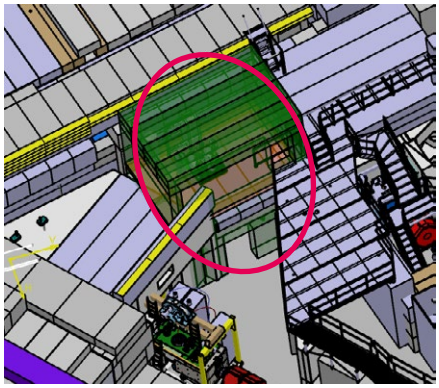

Figure 4.2.18: After final installation of the new combined bunker tertiary cooling circuits 4 and 7

The installation of the new MuH2 beamline for HIMB requires adjustments to the existing PiM1 area (Figure 4.2.11) to accommodate the new conditions. Additionally, the corner of the ring bunker wall will be modified to provide more space. A new access point to the area will be established, leading from the inner courtyard (Figure 4.2.12).

The PiE1 area (Figure 4.2.13) is also impacted by the modifications. Due to the addition of a new corridor serving as an escape route, the length of the area will be reduced. However, 0.5 meters of the east wall will be partially removed, which will expand the experimental space. The area will still have two access points, but the pathway above the area will be removed (Figure 4.2.14).

4.2.2.3 South Area

In the south area smaller changes at the MuE1 area due to the movement of the cryostation are performed. Moreover, a new bunker for two water cooling circuits (read in the following) is planned. Nowadays these cooling circuits are located at different places, the new situation will provide a centralized solution and more important shorter pipe lengths to the components to be cooled.

MuE1 area

The MuE1 area (Figure 4.2.15) is being transformed to serve as the future location for the cryostation, however, will not reduce

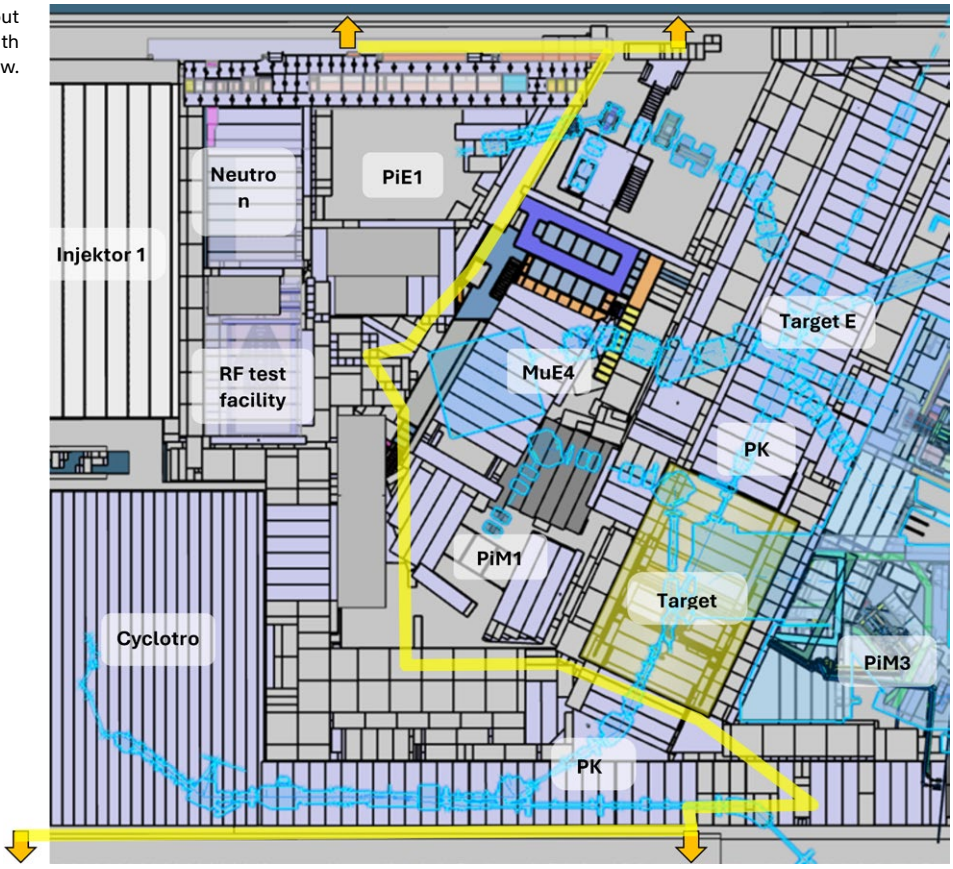

Figure 4.2.19: Current layout of northern areas in WEHA with existing pathways in yellow.

the existing area for the experiment. As part of the conversion, a new side entrance will be added to the south wall (Figure 4.2.16).

Water cooling circuit bunker

The two tertiary cooling circuits 4 and 7 will be set up together at a new location. The current tertiary 7 circuit (Figure 4.2.17) will have to make space for the new HIMB MuH3 beamline. After the remodeling the two water cooling circuits are stacked one onto another. The tertiary 7 will be located at the floor level and the tertiary 4 in the upper level (Figure 4.2.18).

4.2.3 Emergency exit paths

Currently there are various areas in the northern part dedicated to experiments and RF test site. In addition, there are still some leftovers from shielding constellations of former experiments. Within IMPACT the PiM1 beamline will be disassembled and replaced with the new MuH2 beamline. As explained in Chapter 4.2.2.1 the layout of the experimental area will change. Consequently, the safety guidelines for emergency exit routes must be adhered to, according to which the emergency route to the next fire protection section must not exceed 35 meters if there is one entrance only. With two entrances 50 meters are allowed.

In Figure 4.2.19 the current situation and pathways are shown. With the new inner courtyard and the new passageway in the east wall, a new escape route will be established in the northern area (Figure 4.2.20). The length of the escape route (Table 4.2.1) has been significantly decreased because the new fire protection section starts at the beginning of the corridor. Furthermore, instead of using various staircases, the escape routes from the inner courtyard are now solely on the ground floor.

Area	Stair steps	New fire section [m]	10% reserve [m]
RF test facility	0	21.8	24.0
PiE1	0	18.8	20.7
PiE1 (2nd exit, WNHA)	0	13.0	14.3
MuE4	0	27.9	30.7
MuH2	0	31.0	34.1
Courtyard	0	12.5	13.8
Office container	30	25.6	28.2

Table 4.2.1: Length of the escape routes in the northern areas after the modifications in 2028.

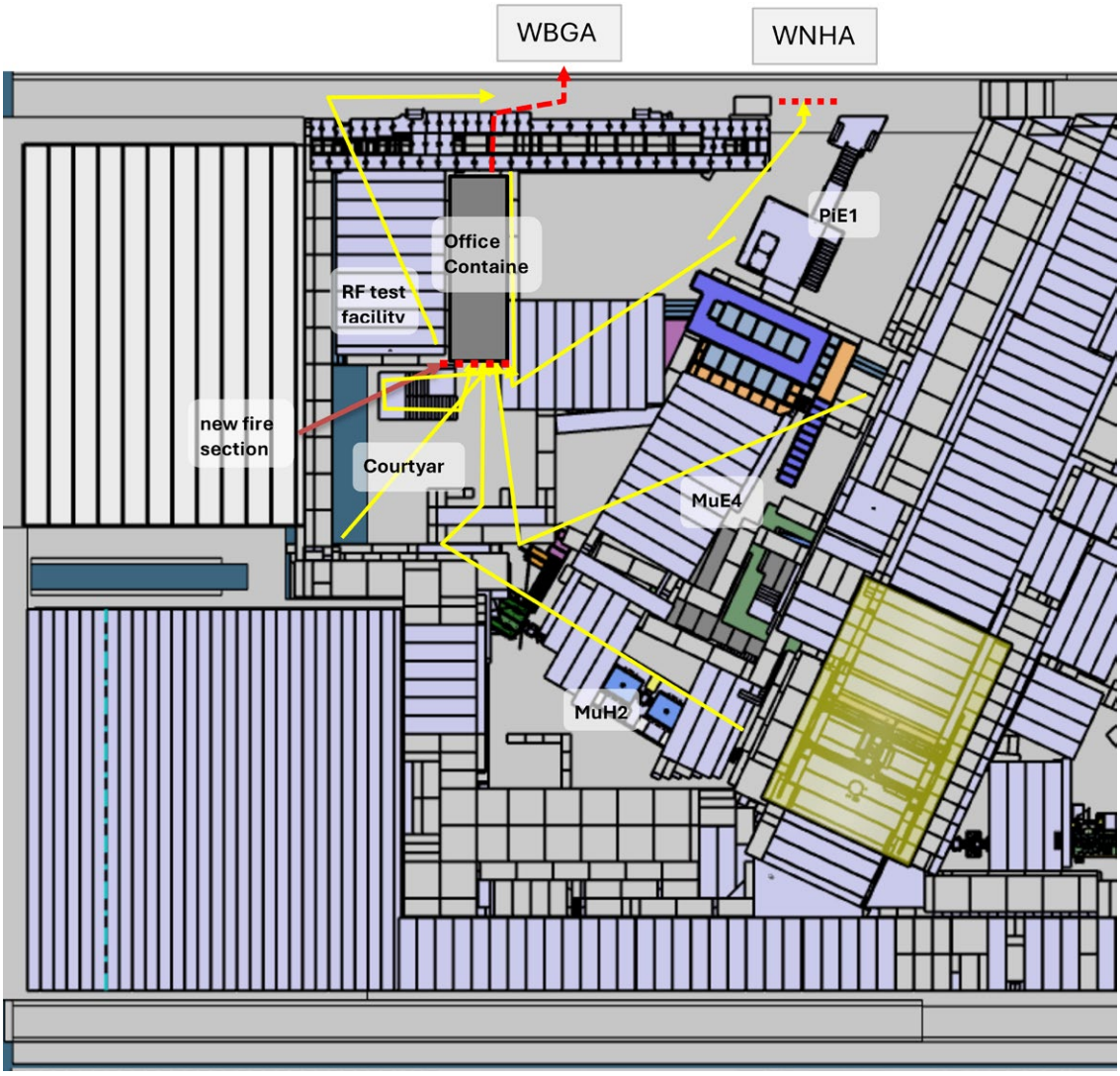

Figure 4.2.20: New layout of northern area with pathways in yellow.

4.2.4 Target and Beamline Shielding

The shielding consists of both steel and concrete layers. Steel shielding is typically placed near components that emit the highest radiation, such as targets and collimators. Currently, the proton beamline and target stations within the PK2 section are shielded with steel, surrounded by a broad layer of concrete shielding.

The current shielding design will undergo changes to allow the first sections of the MuH2 and MuH3 beamlines to be accessible from above for maintenance after removing some shielding. This modification also affects the design of the shielding above these sections, requiring it to be accessible with the hall crane and equipped with roof beams similar to those in the existing P-channel.

Figure 4.2.21 shows the current shielding situation with the new beamlines MuH2 and MuH3. The concrete blocks are shown in grey and the iron beams in blue. The green area indicated in Figure 4.2.21 has to be reshuffled from the ground to provide space for the new shielding design.

As outlined in the shielding simulations in Chapter 2.4 the area around the target chamber and the first sections of both beamlines MuH2 and MuH3 must be shielded with steel and concrete. As a result of the top-access design for maintenance and the significant steel shielding requirements, the current p-channel concrete shielding must be entirely reconstructed from the ground up. The Figure 4.2.22 shows the size of the new steel shielding, without any additional concrete shielding, within the WEHA.

Some of the old Target M steel shielding will be reused for shielding reducing the amount of radioactive waste and steel resources. In order to handle these activated elements, they will be put into steel containers (Figure 4.2.23) during the remote dismantling of Target M. These steel containers will have walls as thick as necessary to lower the dose rate on the outer side, to allow safe working conditions with compliant exposure rates in their surroundings.

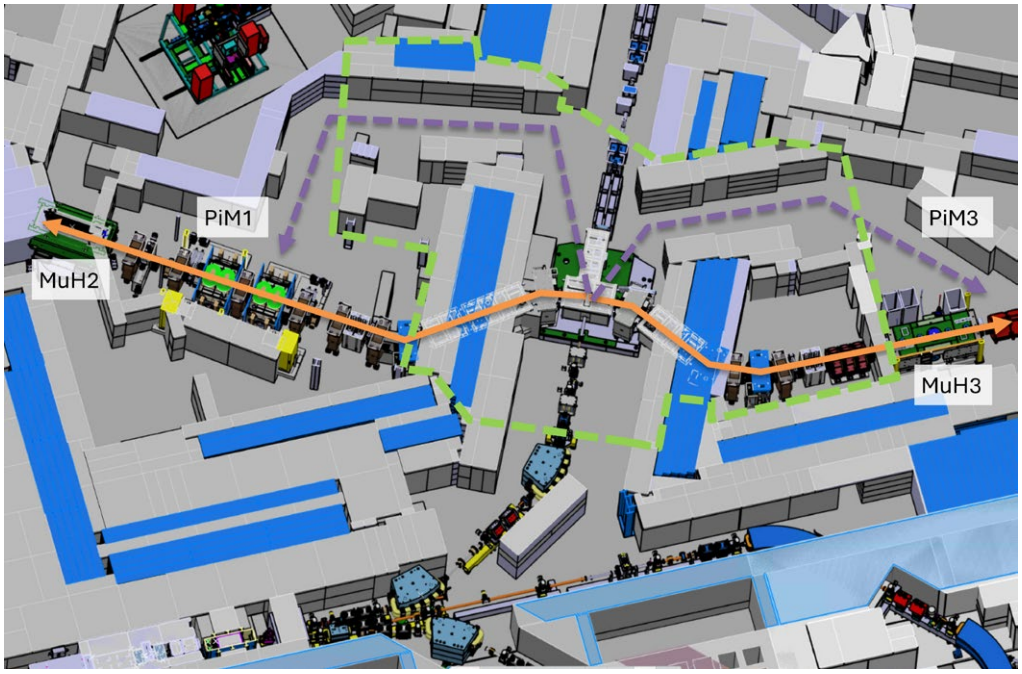

Figure 4.2.21: Current shielding situation with the new beamlines MuH2 and MuH3 in orange. Dashed violet current beamline PiM1 and PiM3.

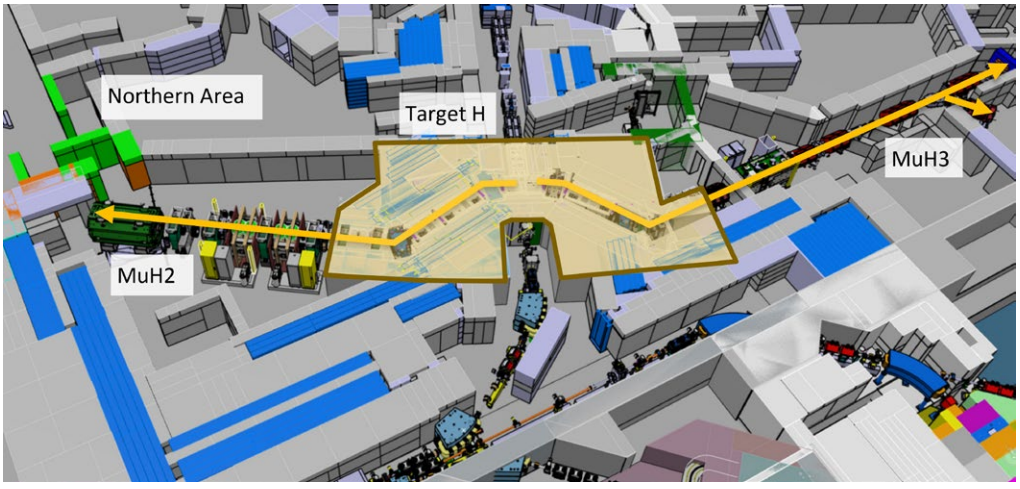

Figure 4.2.22: Size of the new steel shielding in yellow.

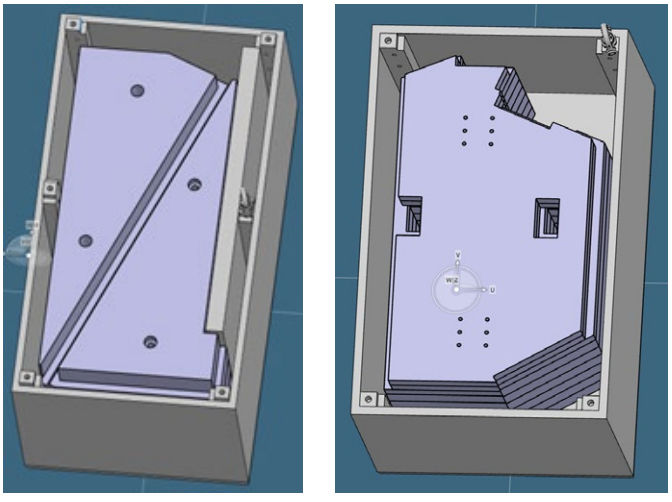

Figure 4.2.23: Steel container with old Target M shielding

4.3 Infrastructure

4.3.1 Electrical Installations and Cabling

4.3.1.1 Power distribution and energy supply

The currently installed power in the experimental hall WEHA is sufficient. The main energy distribution for the WEHA building will remain at its present position. Because of the new building planned for TATTOOS, three existing transformers for WEHA have to be relocated and will be installed on a new podium.

For the HIMB project, new power distributions in each of the new experimental areas have to be installed. The existing main distributions need to be updated based on the new area and infrastructure design. The individual experimental areas must be supplied independently of each other.

4.3.1.2 Cabling and installation

A high number of existing cables need to be replaced. Many cable trays, some cables and other infrastructure components have to be adapted to the new layout of the affected area.

The entire electrical installation from the proton beamline up to the experiments must be completely reconnected and rewired. That means also removing of the old cables and cable trays and installing new ones.

All cables associated with the new areas and beamlines have to be changed or replaced and need to be shielded according to EMC requirements. This results in an increase of cabling volume by approximately 1/3 for the new muon beamlines, and respective requirements for additional space on the cable trays. The individual experimental areas and its infrastructure must be cabled independently of each other. The associated control racks must be redesigned in accordance with latest standards. Some systems need more space for their control racks. This space must be provided with new platforms. Figure 4.3.1 and Figure 4.3.2 show the present situation of already densely filled infrastructure platforms and cable trays in the WEHA.

4.3.2 Cooling System

In order to obtain space for the systems, components and building infrastructures, extensive dismantling and relocation work in the area of the cooling system is necessary. In general, the cooling station has to be relocated as the new muon beamlines cross the space of the existing installation. Most

Figure 4.3.1: Full rack platform at the WEHA building westside.

Figure 4.3.2: Filled and partially filled cable trays and a lot of old cables near the PiM1 experimental area.

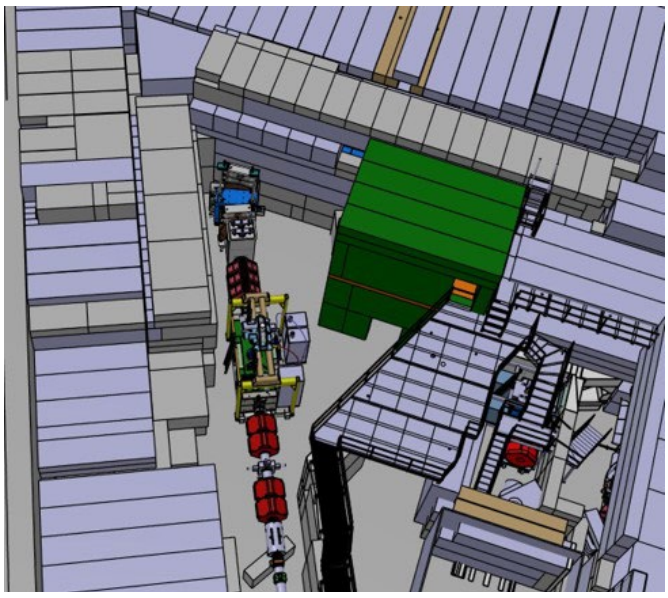

Figure 4.3.3: New location of the tertiary 4/7 cooling circuits (green), see also Chapter 4.2.2.3.

of the components have been in service for approximately 15 years; selected components may have a residual life of further 15 to 20 years.

For the HIMB project, a new and tailored cooling infrastructure has to be designed. Focus is set on the beam path components, the beam dump and the experimental facilities. The new cooling system is planned and built taking energy and efficiency optimizations into consideration. As far as possible, the existing cooling circuits and components will be reused or modified. The existing cooling supply of the Target M is assigned to the cooling circuit tertiary no. 7 and the existing cooling water distributions are reassigned. The connections for cooling of the consumers are renewed. Due to space constraints, the tertiary cooling circuit no. 7 is being rebuilt at a new, suitable location (Chapter 4.2.2.3), where also the cooling circuit tertiary no. 4 will be located, presently situated in WNAA (see Figure 4.1.1 in Chapter 4.1). The situation of the new location is shown in Figure 4.3.3.

The existing, well-preserved main components such as pumps, heat exchangers, filters, control valves are partially activated or contaminated and will be reused to minimize waste. As part of the energy optimization and the relocation, the existing 20-year-old control system will be replaced and redesigned according to the current state of the art and the electrical cabling will be completely exchanged.

4.3.3 Cryogenic System

The main topic regarding cryogenic systems is the reuse of the 1990 Sulzer helium liquefaction plant at a new location in the WEHA and the installation of a second liquid nitrogen (LN2) feed to increase supply security. Parts were already installed a few years earlier but will be completed by the extension of the LN2 line between MuE1 and the SINQ wall.
New cryogenic He supply station:

- Saves space: including counting houses and service caves.
- Suitable for the current cold box (horizontal position) and the future one (upright position).
- Ground filling: less crane usage than before.
- Top filling: for Dewars that need to be transported by crane anyway.

4.3.3.1 He liquefaction

The plant will be around 40 years old when HIMB goes into operation. To ensure continued high-availability operation, various components will need to be renewed. However, we know that some critical components in the cold box can no

Figure 4.3.4: New cryogenic He supply station including cold head workshop and counting rooms.

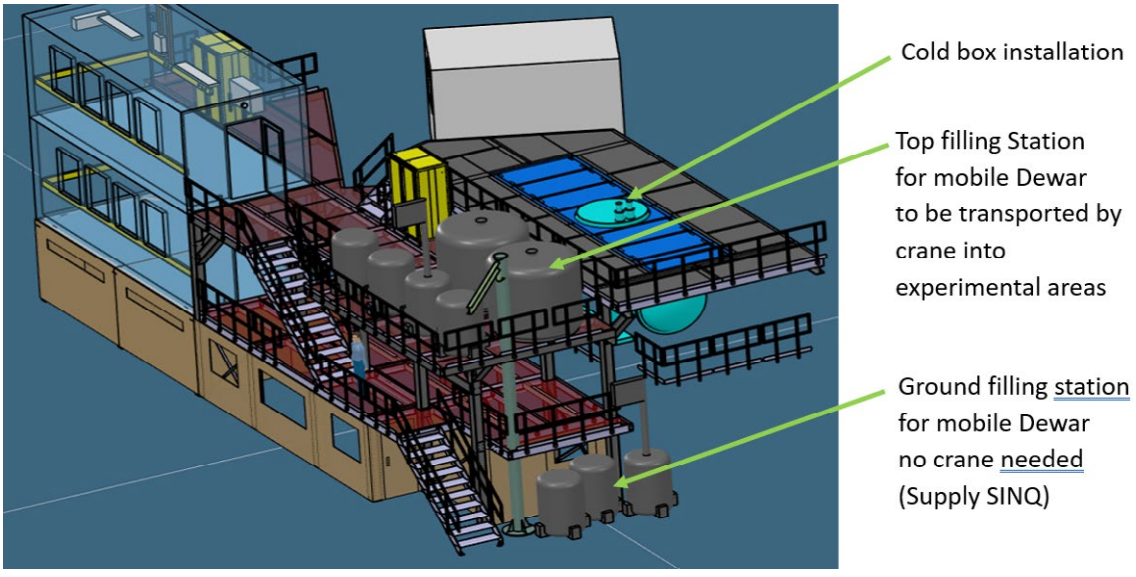

longer be manufactured identically due to the lack of documentation from the manufacturer. Additionally, the unit had a crack in the vacuum envelope about 10 years ago. Due to the high investment for a new cold box, it was decided to take this risk.

4.3.3.2 Upcoming work on the liquefaction plant

- A multi-story steel structure must be designed and fabricated, on which the liquefaction plant will be installed.
- An existing breakthrough to the tunnel under the WEHA will be used to supply the cold box at the new location in order to route the helium lines from the compressors in the WKSA building and the required infrastructure to the liquefaction plant. This includes warm helium, nitrogen, cooling water with emergency backup, helium recovery, compressed air, and electricity.
- The two existing 2000 litres dewars must be installed with new transfer lines.
- Two new transfer lines must be designed and installed for helium transfer into the mobile dewars.
- The transfer line from the cold box to the BTS Magnet must be planned and fabricated. Due to the challenging path through the shielding of the experiments, it must be a flexible design with a length of about 30 m. The length of the line could be problematic for operation, as the heat input in such flexible lines is significant. The boundary conditions need to be clarified.
- To connect the MuE1 experiment, the existing transfer line will be partially reused to reduce financial costs. The line to the BTS Magnet is more complex and, therefore, much more expensive.
- To improve reliability, all cabling on the cold box will be renewed. Additionally, a terminal cabinet that is no longer needed, will be rebuilt.
- Critical sensors and actuators will be replaced with new standard modules.
- The vacuum and pump-purge system will be renewed, and the piping must be restructured. As a result, it will also be necessary to switch the ports of the cold box to accommodate the new situation.
- The control cabinet and the PLC will remain largely unchanged to save additional costs.

4.3.3.3 Other upcoming work

- The cold head overhaul workshop, currently located around the existing liquefaction plant, must be rebuilt, and installed at the new location in the premises beneath the new liquefaction plant.
- The LN2 lines in the WEHA, which are currently supplied by only one tank at the WBGB building (T2), will need to be partially renewed and extended.
- New automatic filling stations for LN2 will be installed in the experimental areas to reduce the time spent in the zone and increase the efficiency of the experimental work.

4.3.3.4 Conclusions concerning cryo-systems

The planned upgrades and changes are shown in Figure 4.3.5. These modifications will result in a safer and more redundant supply of liquid nitrogen, as well as easier handling and a modernized infrastructure for the distribution of liquid helium.

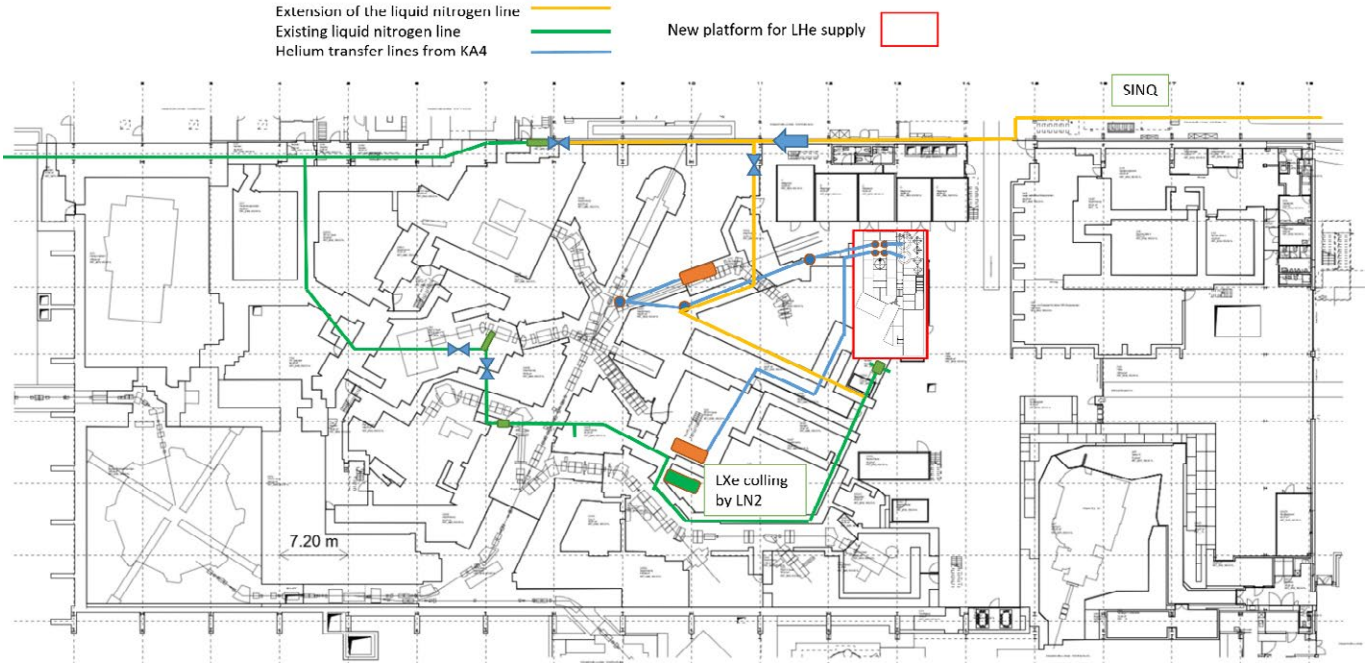

Figure 4.3.5: Overview of the liquid nitrogen and helium distribution in the experimental hall after the planned upgrades and infrastructure changes.

4.3.4 HVAC

4.3.4.1 Current System

The HVAC system consists of an air-cooling system above the steel shielding of the proton channel and an air extraction to maintain a certain level of under pressure in the channel. The installation is soon at end-of-life and therefore a total replacement of the present system including controls is foreseen. The existing components must be removed and if required decontaminated.

4.3.4.2 Low Pressure Staging Concept & Realisation

During operation, the negative pressure within the channel will be achieved via air connection ducts linked to the central exhaust air system of the WEHA. The negative pressure can be regulated through automatic or manual adjustment of the exhaust airflow. Due to various leakages in the channel's shielding, a high exhaust airflow is required to maintain sufficient negative pressure. Identifying and mitigating these leaks is a key objective for further planning.

To enhance air circulation and cooling efficiency within the channel, modifications to the air circulation system will be implemented.

During maintenance, the ventilation and air-conditioning system will be deactivated, and the airflow to the central exhaust air system will be shut off.

Additionally, the existing air-cooling system of PiM1 will be replaced and resized to meet the required cooling load (see Table 2.4.14 in Chapter 2.4.5).

4.3.5 Compressed Air

Pressurized air will be fed by the existing campus wide network with industrial standard compressors. The compressed air with a nominal pressure of 6 bar. Fluctuations of +/- 0.5 bar as well as fluctuations in relative humidity are possible. Various quick coupling connections will be installed.

4.3.6 Central Building Control System (GLS)

The HVAC and cooling systems are connected to the technical building control system in order to monitor the systems and to alert the responsible service unit in case of failure. In case of extensions and replacements of control systems, those interfaces and schematics have to be adapted, implemented and tested. Generally, the system allows to archive all the monitored data points and to retrack the status of the controlled systems as required.

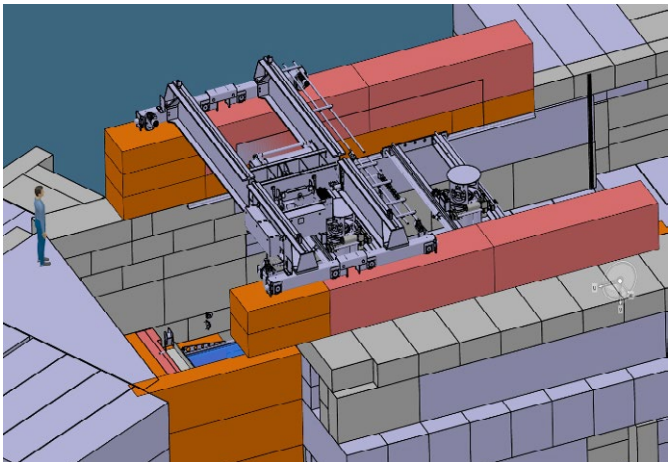

Figure 4.3.6: Crane and Powermanipulator; Tg M Dismantling.

4.3.7 Cranes and Handling Tools

The experimental hall WEHA is equipped with a portal crane featuring two hoisting devices (60 t and 10 t). This crane enables the transfer of items from the Ring bunker and Injector1 bunker to the southern entrance of the hall. Additionally, the crane allows to move items into the active materials storage WAKA. For the loading and unloading of components from WAKA, an additional crane (3.2 t) is available.

The southern section of the experimental hall is equipped with a rail system and transport trolley. This trolley can move components, such as concrete blocks, with a total weight of approximately 100 t in or out of the hall. While most lifting devices (LLA) are already available, some require modification or new procurement.

Various forklifts (1.5 t, 3 t, 20 t) are available for transferring components.

For the dismantling of Target M an additional crane with a load capacity of 32 t (Figure 4.3.6) will be installed in the p-channel within a contamination protection enclosure. The detailed steps of the dismantling procedure are described in Chapter 4.4.5.

4.4 Logistics, Dismantling, Assembly and Installation

4.4.1 Storage and Pre-assembly Areas

To support the project's preparation and storage requirements, suitable sites at PSI and potentially external locations must be defined and reserved. A dedicated material storage area will be established to serve as a primary reception point for a significant amount of incoming material, reducing administrative and monitoring efforts. The external hall ELMA in Kleindöttingen (9 km from PSI), is suitable for most of the new components (area 2'250 m^2; two 12.5 t cranes). A comparison with previous large-scale PSI projects shows that half of ELMA is sufficient for material storage. In addition, the need for storage space was verified with PSI specialist groups and the assumptions were confirmed.

Furthermore, during the long shutdown several areas on the west campus, and more importantly in the WEHA are reserved for short-term storage, logistics and storage of radioactive material. Some parts of the existing beamline will be stored for later re-installation, some will be kept as spare, and the rest will be stored within radiological monitored areas for later disposal. Figure 4.4.1 shows an illustration with the potential spaces needed for the project. A list of all potential spaces with the foreseen usage scenario is given in Table 4.4.1.

Pre-assembly will take place in ELMA, PiA and WEHA, though it is constrained by the crane's lifting capacity and hook height. For heavy components, such as the large vacuum chambers and their inserts, WEHA is the only feasible option for pre-assembly. However, the hall is already heavily utilized and could become a bottleneck for pre-assembly operations. As a result, the newly available spaces created through the reconstruction of the north area, as detailed in Chapter 4.2, will be utilized for pre-assembly and logistical operations during the long shutdown.

4.4.2 Work prior to long-shutdown

Prior to the long shutdown, several tasks are planned to reduce the workload during the shutdown period. The two primary

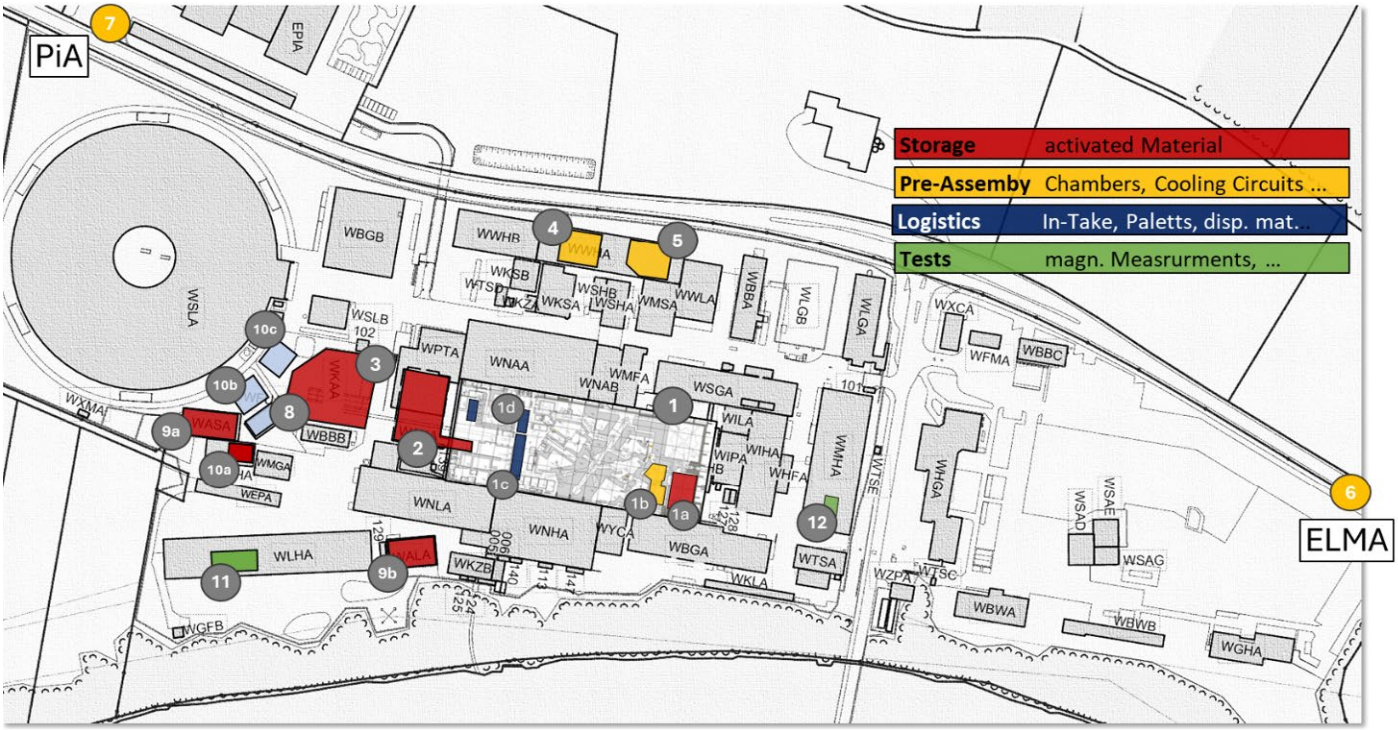

Figure 4.4.1: PSI West Campus.

No	Area	m^2	Components	Usage	Status	Remark
1a	WEHA- Inj.1 Bunker	200	5 Parkierzellen; Tg.M/H containers; Iron-beams	temp. storage of highly activated material	okay	3 existing
1b	WEHA-ex. Neutron Bunker	160	target-H station	pre-assembly	okay	floor load capacity 18.5 t/m^2
1c/d	WEHA	200		logistic area; handling of heavy components	okay	60 t crane
2	WAKA	160	activated and reusable parts	temporary storage	okay	
3	WKAA	100	PK-roof-shielding	temporary storage	okay	
4	WWHA-11	200	separators	preassembly	okay	20 t crane
5	WWHA-A5	250	el. racks and cooling circuits	Pre-assembly of cooling circuits and electro-racks	okay	5 t crane
6	ELMA	1100	magnets and general project parts	magnets pre-assembly storage shelfs for general project use	okay	rent extended until Sep.2031; floor load capacity 4 t/m^2
7	EPiA	200	all inserts	assembly	okay	20 t crane
8	WFUA	100	new cables	storage for new cables	okay	
9	WXHA	100		temp. storage	tbd	
10	Tent	190	material from Target-M removal	not or low activated material for later disposal	tbd	no shielding needed
11	WLHA	50	magnets	magnetic measurements	tbd	
12	WMHA	30	Tg.H	test stand	okay	
13	tbd	tbd	material from Target-M removal	activated material for later disposal (that needs shielding)	tbd	covered concrete-iglu with drain-safe bottom
14	tbd	160	Exchange flask (Tg.H & inserts)	assembly area incl. material storage	tbd	60 t crane; assy in 2H2026

Table 4.4.1: Overview Estimated Area Needs. See Figure 4.4.1.

modifications to be completed beforehand include relocating the cryostation and implementing changes to the northern area of the p-channel.

4.4.2.1 Croystation Movement

The cryostation relocation is necessary to free up space adjacent to Target M. In 2025, the new location in the MuE1 area is prepared by modifying the layout and the construction of a new platform, see Figure 4.4.2. By end of 2026 or before the long shutdown, the helium transfer lines and the cryostation must be fully operational.

4.4.2.2 North Area reconstruction

In the northern area of the p-channel, several modifications are planned as outlined in Chapter 4.2.2. These changes aim to enhance emergency exit routes, as detailed in Chapter 4.2.3. However, the reconstruction will be executed in different phases as shown in the illustration below. The aim is to free up the

space and prepare an area for the pre-assembly of the new target H station, see Figure 4.4.3. This process must be finished until the second quarter of 2026. After the long shutdown the new RF test site and the new inner courtyard will be set up.

4.4.2.3 Beamline dismantling

As a preparatory measure for the long shutdown, both PiM1 and PiM3 beamlines are scheduled to be dismantled in advance. This involves removing all infrastructure and beamline components, except for the beamline section mounted on the trolleys, see the subsequent Chapter 4.4.3.

4.4.3 PiM1, PiM3.x dismantling

The PiM1 beamline as well as the PiM3 beamline are planned to be dismantled before the long shutdown. However, all com-

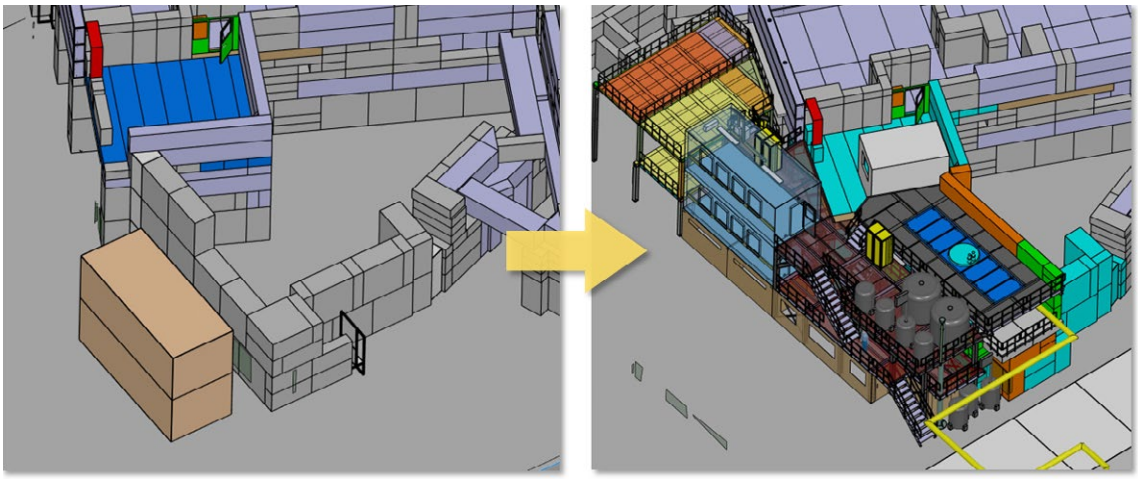

Figure 4.4.2: Cryostation movement before long shutdown.

Figure 4.4.3: Step by step site preparation for the pre-assembly of the Target H station.

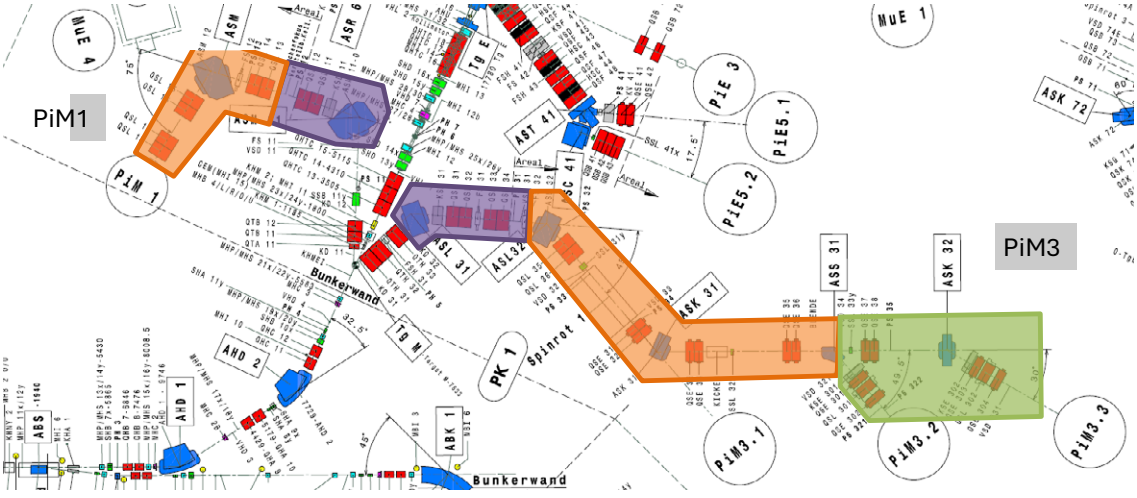

Figure 4.4.4: PiM1 and PiM3 Beamline. Orange: Parts will be removed before long shutdown. Purple: Components on trolleys, to be removed in long shutdown. Green: Parts will remain.

ponents on the trolleys, which are underneath of the p-channel shielding cannot be dismounted prior to the long shutdown. Figure 4.4.4 illustrates both beamlines, PiM1 and PiM3, whereas the orange parts are removed before the long shutdown and the purple part indicate all components on the trolleys. The green part will remain and will not be removed during the long shutdown.

4.4.3.1 PiM1

Following is a list of the tasks that need to be executed before and during the shutdown in order to dismantle the beamline PiM1.

Before long shutdown (September–October 2026)

Within the area PiM1 (Figure 4.4.5)
1. Close and disconnect beam blocker KSD11.
2. Remove experiment and area equipment.
3. Dismount area cooler.
4. Dismount steel platform 1.
5. Disconnect beamline elements ASM11 – QSL18 and dismount infrastructure.
6. Remove roof PiM1.

Outside area
1. Disconnect all power supplies (PS) and dismount power supply platform PiM1.
2. Store PS and platform for reuse.
3. Remove all cables and cooling lines.

Within the area MuE4
1. Stop beam operation MUE4 and close and disconnect beam blocker KV61 and KV62.
2. Remove roof MuE4.
3. Remove QSL 13 -QSL18.
4. Stop operation liquid Nitrogen to MuE4.
5. Remove wall between PiM1 and MuE4.
6. Install rail system.

Outside area
1. Disconnect hutches MuE4 and PiM1.
2. Dismount hutches, store MuE4.
3. Remove obsolete walls.

At the start of the long shutdown (January 2027)
1. Unseal the p-channel and break vacuum.
2. Drive trolley out of the tunnel.
3. Remove infrastructure connections on the trolley.
4. Remove iron bricks and concrete stones.
5. Remove beamline elements.
6. Remove trolley (Figure 4.4.6)
7. Remove rail system.
8. Remove FS11.
9. Seal or close with shielding the tunnel.

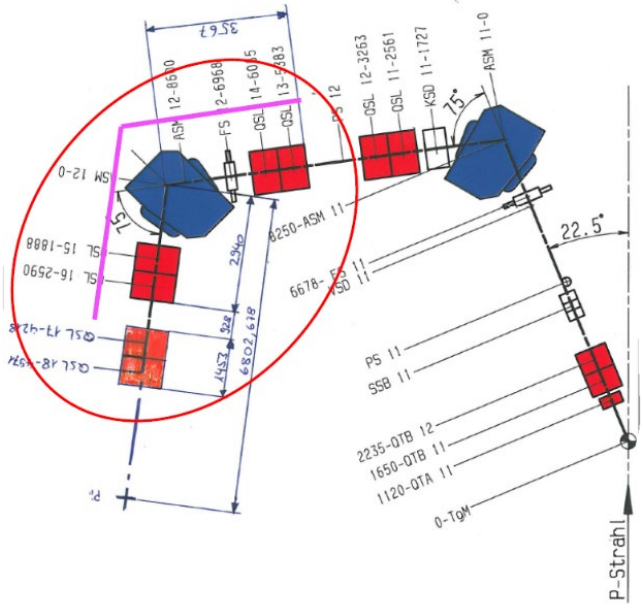

Figure 4.4.5: PiM1 beamline, first steps of removal.

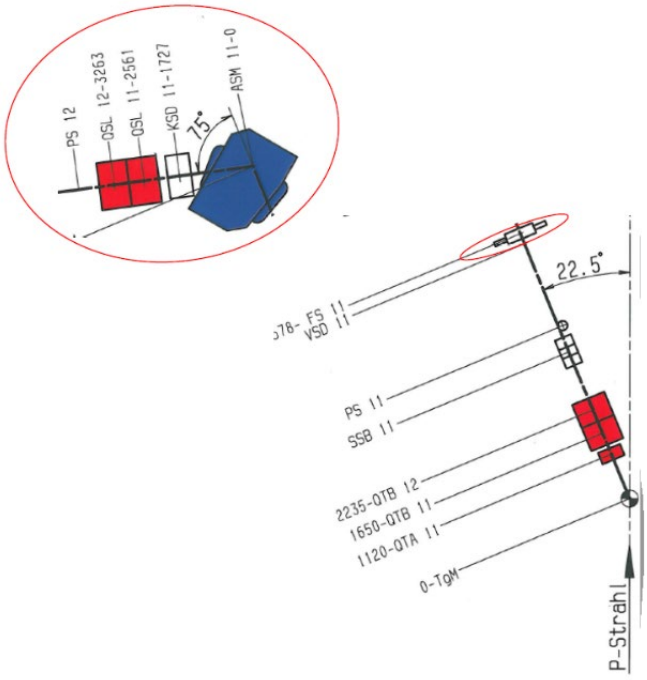

Figure 4.4.6: PiM1 Beamline, trolley removal.

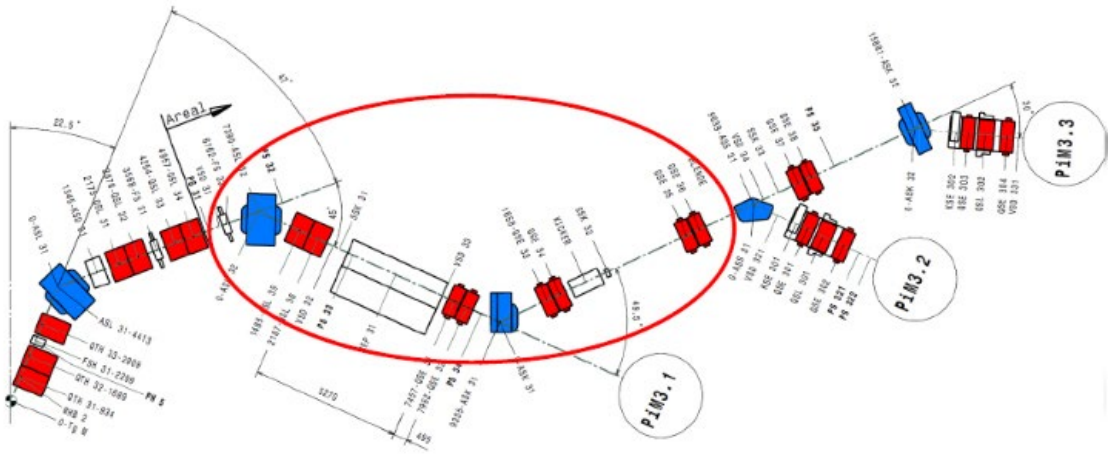

Figure 4.4.7: PiM3 Beamline, first steps of removal.

4.4.3.2 PiM3

Below is a list of the tasks that need to be executed before and during the shutdown in order to dismantle the beamline PiM3.

Before long shutdown (December 2026)

In the area (Figure 4.4.7)
1. Close and disconnect beam blocker KSD31.
2. Disconnect beamline elements FS32 –QSE36 and dismount electrical and cooling infrastructure.
3. Open vacuum connections FS32 –ASS31.
4. Remove all beamline elements FS32 –QSE36.
5. Install rail system.

Outside area
1. Open roof above ASL32/FS32.
2. Remove power supplies.
3. Remove power supply platform.
4. Remove all cables and cooling lines.

At the start of the long shutdown (January 2027)
1. Unseal the p-channel and break vacuum.
2. Take out the pillow seal and close the target vacuum.
3. Drive trolley partial out of the tunnel.
4. Remove infrastructure connections on the trolley.
5. Remove iron bricks and concrete stone.
6. Remove beamline elements.
7. Remove trolley (Figure 4.4.8).
8. Remove rail system.
9. Seal or close with shielding the tunnel in the p-channel.

4.4.4 PK1 Dismantling

The PK1 beamline is located in the north-western area of the WEHA experimental hall and connects the Ring cyclotron with the current Target M. The last part of the PK1 beamline from AHD1 to the shielding block of the target station M, illustrated in Figure 4.4.9, must be dismounted in order to remove the Target M

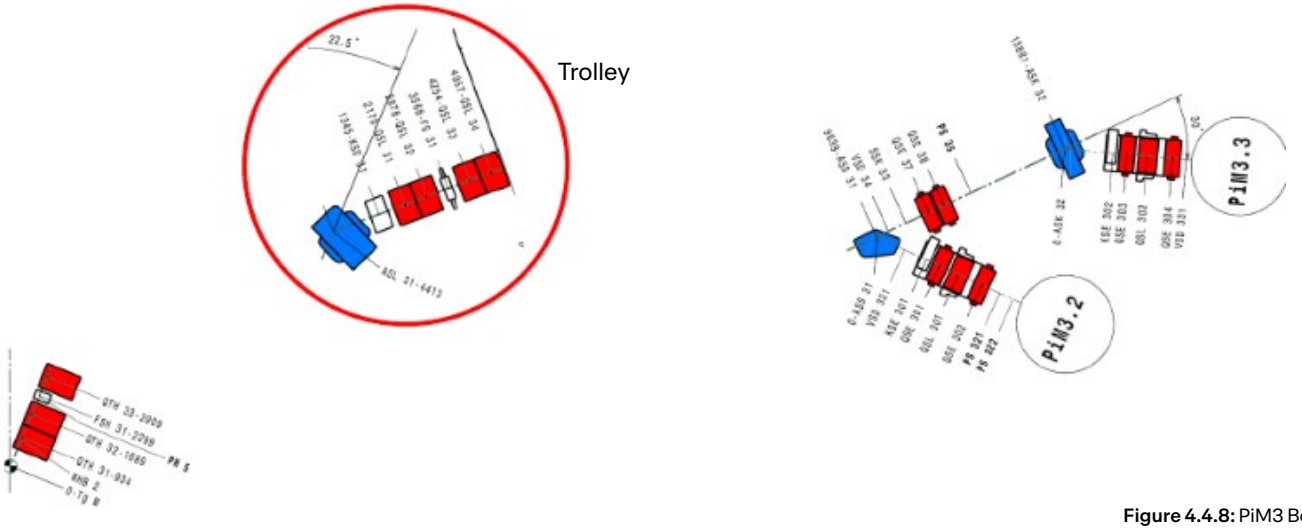

Figure 4.4.8: PiM3 Beamline, trolley removal.

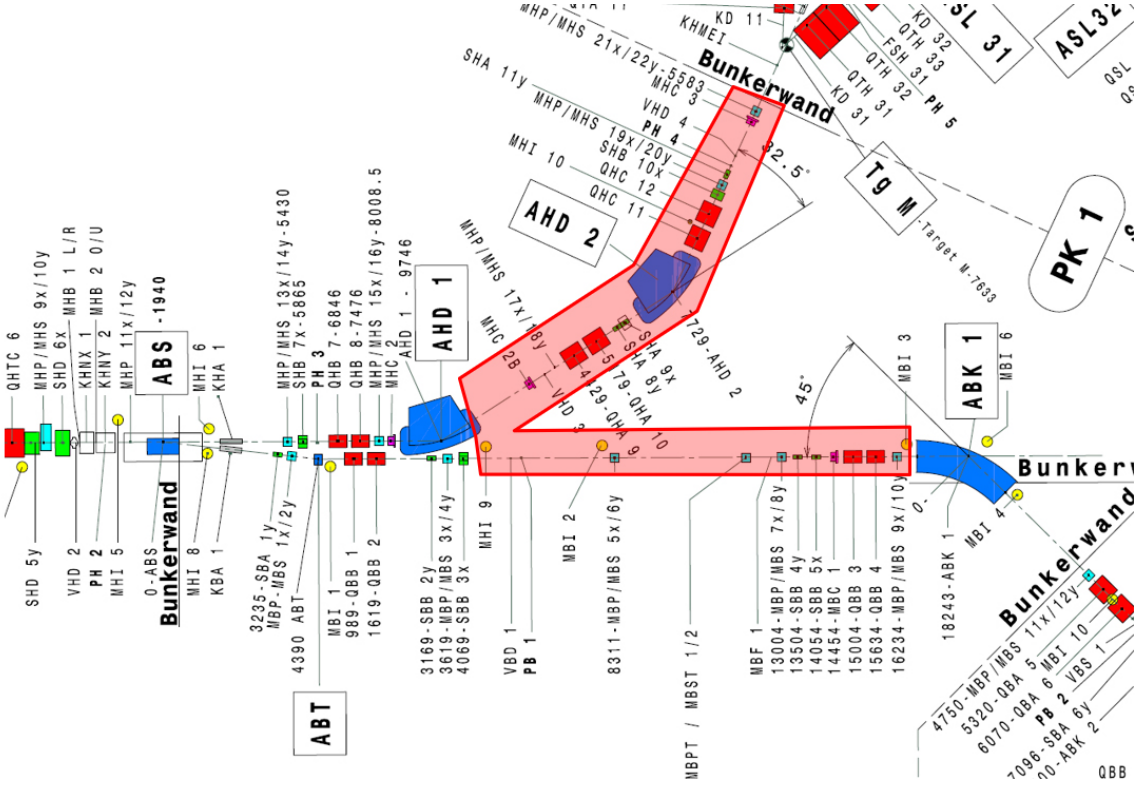

Figure 4.4.9: Part PK1 of the p-channel.

shielding in a contamination protection by manipulators. Many components in PK1 are highly activated, therefore have to be stored in WAKA or the Injector 1 bunker for a later reinstallation. A large part of the beam components will be reused.

The beamline will be dismounted for the following reasons:

- Construction of contamination protection and an airlock system for the dismantling of target station M.
- The UCN beamline is rewired from the WNAB building.
- Dismantling and construction of infrastructure facilities along the beamline. Coordination with the setup of the beamline for TATTOOS in 2029 required.

The beam components are dismantled at the vacuum system seals. The roof above the proton channel PK1 consists of concrete beams, which are removed with the hall crane of the experimental hall WEHA. The beamline components will be removed with the hall crane, all lifting devices and attachments are available.

4.4.5 Target M dismantling

4.4.5.1 Preparatory Work

The dismantling of the current Target M will be partially carried out via remote control. Before the dismantling of the target

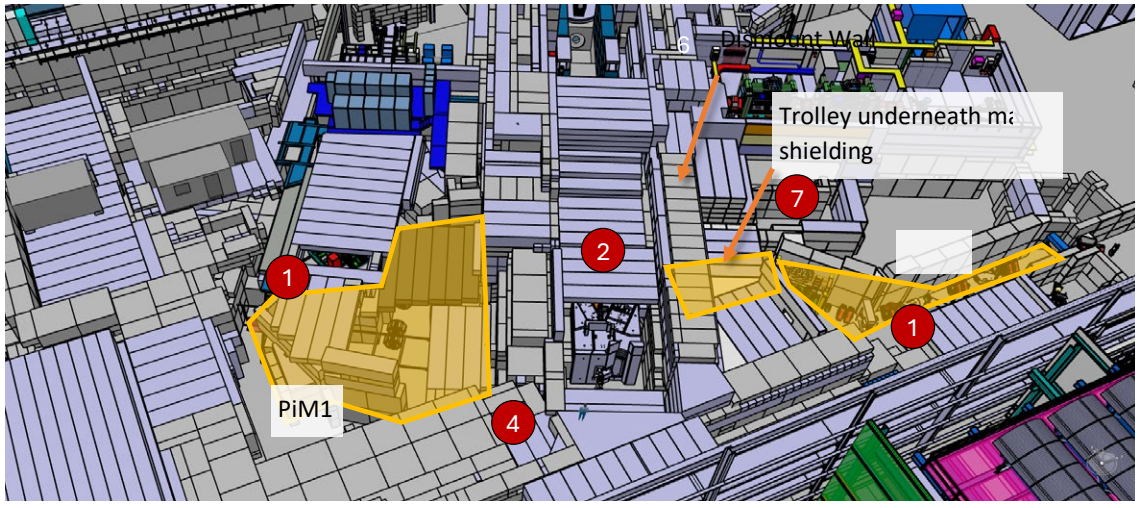

Figure 4.4.10: Overview of WEHA about target station M dismounting preparatory steps by numbers.

Figure 4.4.11: Target M exchange flask.

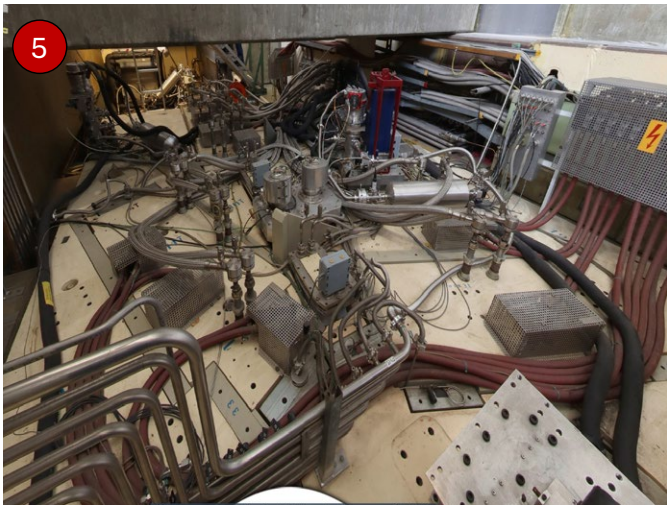

Figure 4.4.12: Target M service level.

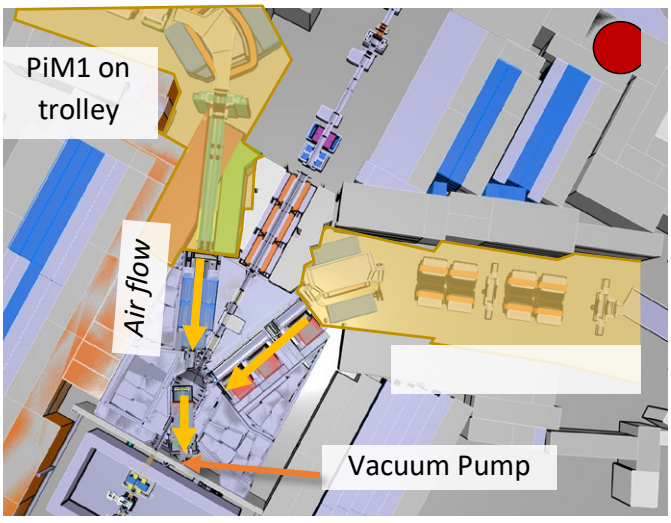

Figure 4.4.13: Air lock system.

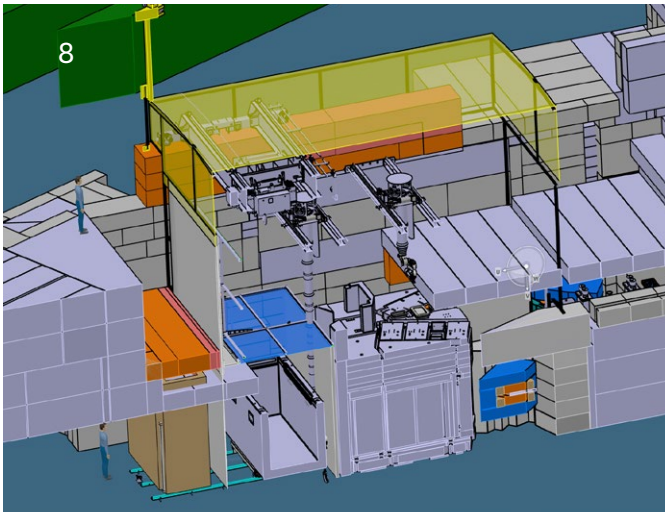

Figure 4.4.14: Contamination protection enclosure.

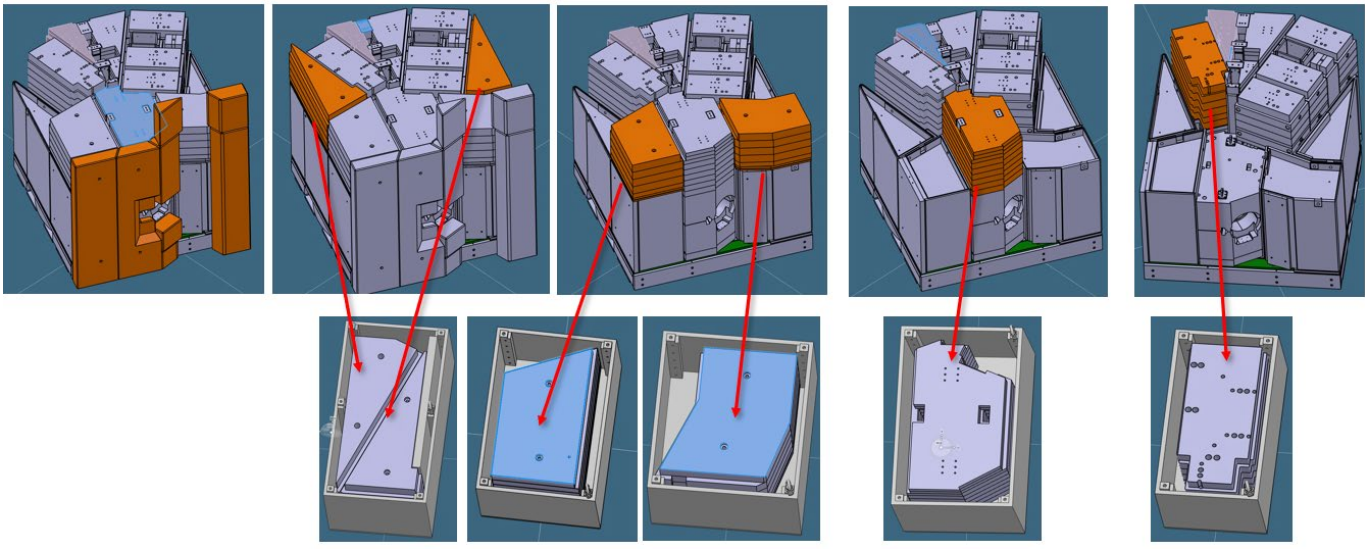

Figure 4.4.15: Procedure of Target M shielding dismantling.

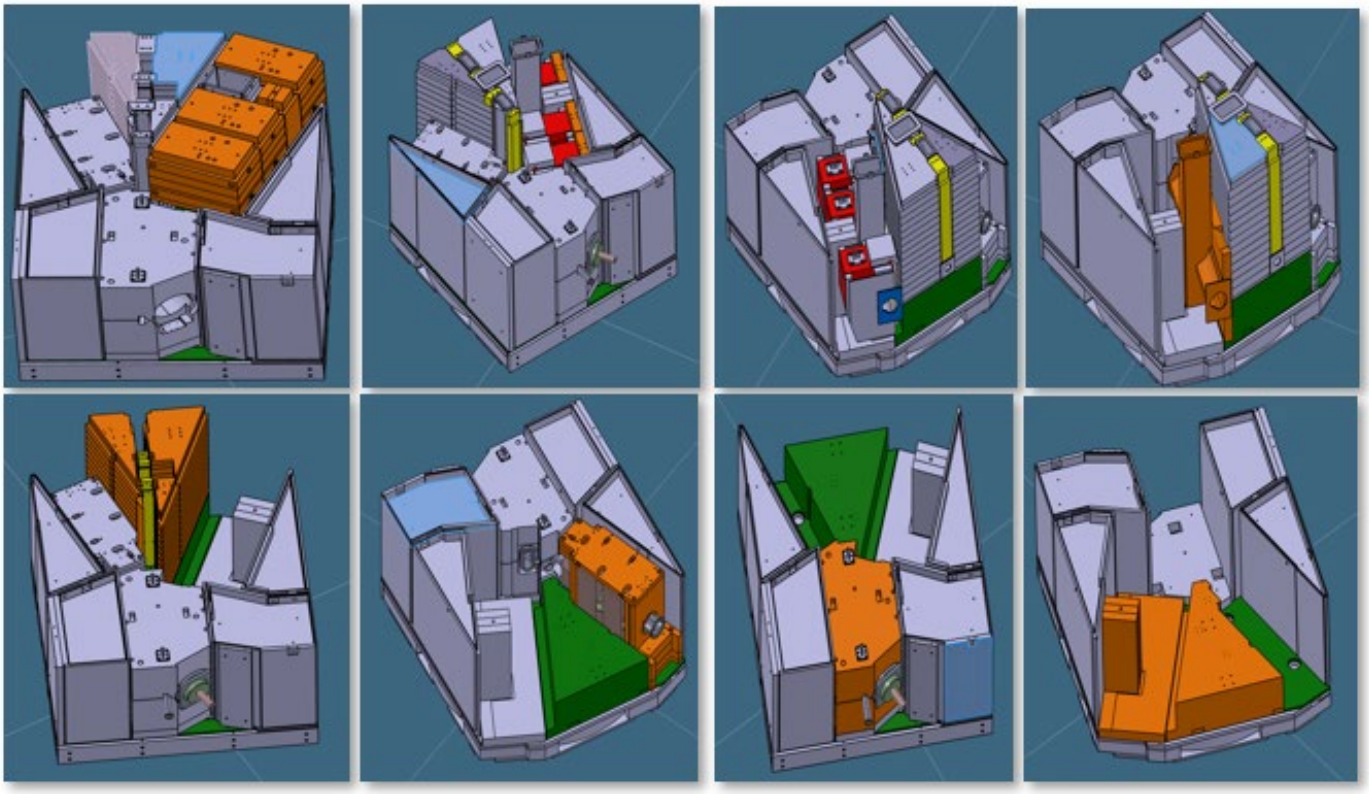

Figure 4.4.16: Procedure of Target M shielding dismantling, remote handling.

station, the following preparatory tasks are planned, see also Figure 4.4.10 - Figure 4.4.14:

1. Dismantling the PiM1 and PiM3 areas (scheduled before the long shutdown in 2027).
2. Removing concrete roof beams above the target station M.
3. Dismantling Target M, the two collimators, the BPM/profile monitor MHS/S23/24 and the slit FS31 using the three exchange flasks. The components will be temporarily stored in the parking slots.
4. Dismantling PK1 (see detailed steps in Chapter 4.4.4)
5. Dismantling infrastructure on the service level.
6. Removing the southern shielding walls.
7. Dismantling the PiM1 rail system and installing the lead glass window. Subsequently, the shielding wall will be rebuilt up to the crane height.
8. Setting up contamination protection, including a crane, power manipulator, camera system, airlocks, and lock system with trolley (Figure 4.4.14).
9. Connecting the ventilation system to the vacuum chambers.

4.4.5.2 Dismantling of the Target M Station

The target station can essentially be divided vertically into two levels. The upper level primarily consists of steel shielding, which will be reused. The plan involves manually attaching the components within the contamination-protection enclosure to the crane and placing them into customized steel containers which are sufficiently shielded as illustrated in Figure 4.4.15. These shielding containers will become part of the new shielding for Target H.

4.4.5.3 Remote-Controlled Dismantling

After the removal of the upper layer, the remote-controlled dismantling process starts.

The dismantling of Target M takes place within a contamination-protection enclosure (Figure 4.4.14) and is partially done via remote control. For this process, an additional crane with a load capacity of 32 t will be installed in the p-channel. Additionally, a power manipulator currently in use in Service Cell 2 at ATEC will be set up within the contamination-protection enclosure. For remote-controlled handling, the camera system from Service Cell 1 will be utilized. Furthermore, the installation of a lead glass window in the southern shielding wall is planned, which serves as redundance to the camera system.

The dismantling sequence follows the original assembly order from approximately 40 years ago (Figure 4.4.16). The planned steps are as follows:

1. Dismantling of the PiM1 section, including the vacuum chamber.
2. Dismantling of the section leading to PK2.
3. Dismantling of the PiM3 section.
4. Dismantling of the target vacuum chamber, including shielding.

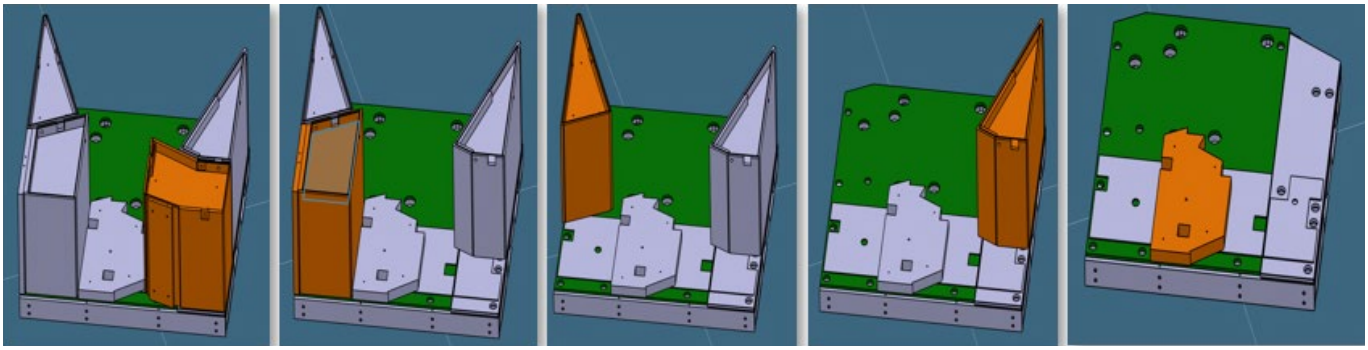

Figure 4.4.17: Procedure of Target M shielding dismantling, parts manually attached to crane.

After the remote-controlled dismantling of the beamlines, shielding components on the lower level will remain (Figure 4.4.17). These components are also planned to be manually attached to the crane within the contamination-protection enclosure. They will then be placed into additional steel shielded containers, which will be integrated into the new shielding for Target H.

For the dismantling of the target station, the following shielding containers will be manufactured or procured:

- Approximately 12 steel containers for the reuse of components.
- Approximately 7 concrete containers for the temporary storage of components until disposal.

4.4.6 Pre-Assembly

In preparation for the long shutdown, the components are pre-assembled and tested to minimize installation time during the shutdown. Pre-assembly will also help to identify any before unknown problems with the components or the installation process.

There will be three different assembly locations. In the external hall (ELMA), all magnets will be pre-assembled and stored until pre-installation. In the new workshop of the Park-Innovare building (PiA), all inserts, e.g. Target H, collimators, monitors, etc., will be pre-assembled and tested. Finally, the newly gained area in the experimental hall (WEHA) is used

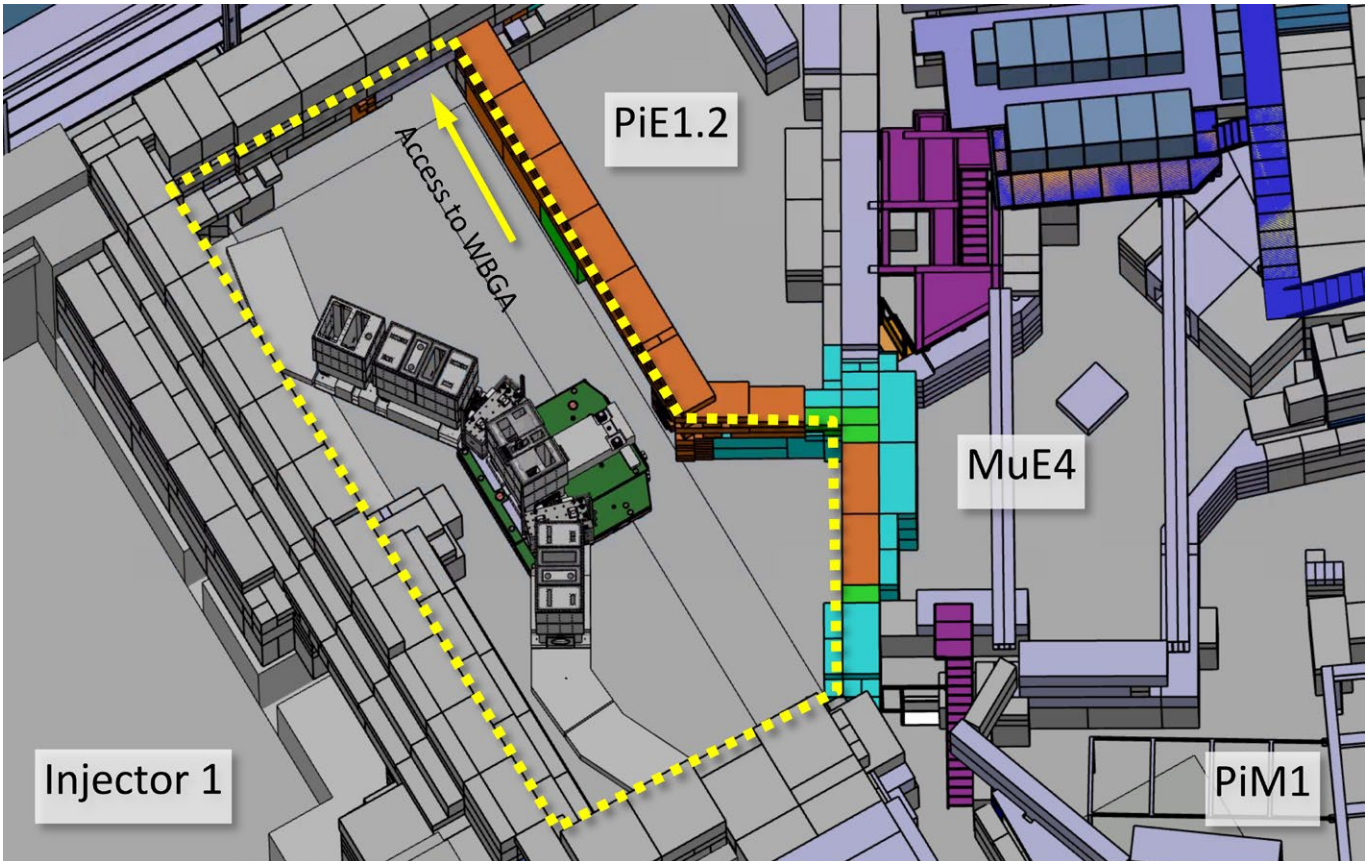

Figure 4.4.18: Pre-assembly area of the target station H.

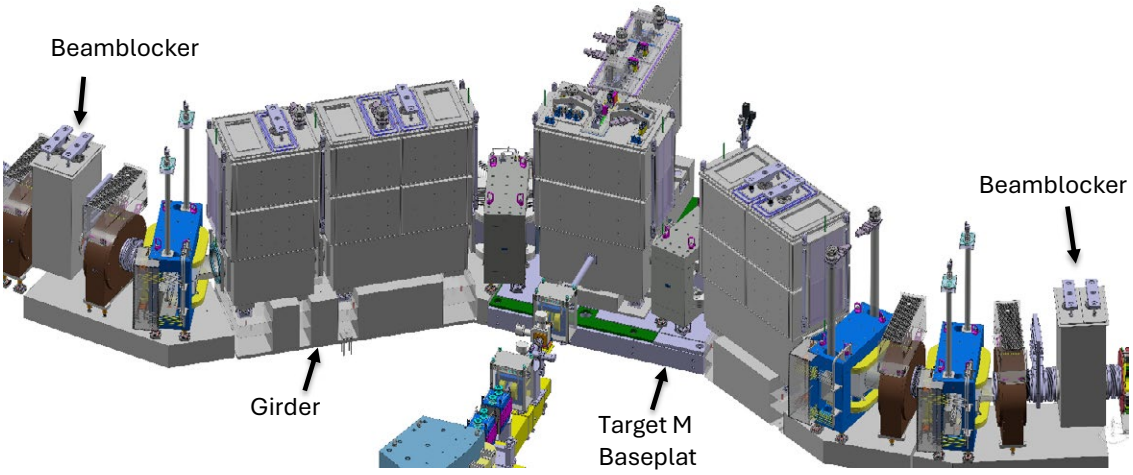

Figure 4.4.19: New target station H and beamlines.

to pre-install the entire Target H station without surrounding shielding, see Figure 4.4.18. This includes the assembly of the girders, the large vacuum chambers and all inserts (including magnets).

Pre-assembly of the Target H station, as shown below, will begin in the second quarter of 2026. During the pre-assembly phase, the installation procedure for all inserts will be tested. The inserts will be pre-aligned so that less time is needed for alignment in the later installation phase. In addition, the vacuum chambers with all inserts will be pumped down to test the vacuum pressure.

4.4.7 Installation of new Target Station and Beamlines

As soon as the existing Target M, the beamlines PiM1 and PiM3 and the surrounding shielding are dismounted, the new Target station H and the Beamlines can be installed. The first components to be installed are the girder / baseplates underneath the large vacuum chambers. The existing Target M baseplate will be reused. All components within the main shielding of the p-channel will be supported by girders that extends up to the chambers of the KSK beam blockers, see Figure 4.4.19.

As a first installation step, the floor will be prepared, the holes will be drilled and the girder can be installed, as explained in Chapter 3.10. Once the girder is aligned, the Target H vacuum chamber will be positioned first. Subsequently, the inserts, such as Target H and both capture solenoids, will be installed in the chamber and their alignment will be checked for discrepancies. It is crucial to do this before any other larger vacuum chambers or the first dipoles are installed, since later there is no chance to check this on site. In the following steps, the dipoles and the PK2 chamber, along with their inserts, will be installed using the same procedure. Next, the large vacuum chambers for both beamlines MuH2 and MuH3, along with their dipoles, solenoids, and beam blockers, will be mounted on top of the girders.

Before the remaining parts of the beamlines (see Figure 4.4.20) will be installed, the complete main shielding of the p-channel will be put into place. This includes the steel shielding near the large vacuum chambers as well as the concrete shielding. However, the roof beams above the large vacuum chambers will remain open until the new exchange flask H and the existing exchange flask E is tested with all foreseen inserts. In the meantime, the PK1 beamline can be installed as the final component within the shielding. Since it is still activated, this approach helps minimizing the dose rate for workers on site. In parallel, cables and signals from all monitors. thermoelements etc are checked in the WEHA as well as in the accelerator control room. After carefully checking the water supply, the magnets are powered on.

Finally, the concrete roof beams will be put in place and the functioning of the PSYS checked. Closing all four beam blockers in MuH2 as well as in MuH3, HIPA beam operation to target station E and beamdump or SINQ, respectively, should be possible as soon as the approval of the Federal Office for Public Health (BAG) for beam operation has been granted. The beamlines MuH2 and MuH3 continue with installation and first commissioning of magnets, separators, and beam pipes within their experimental area.

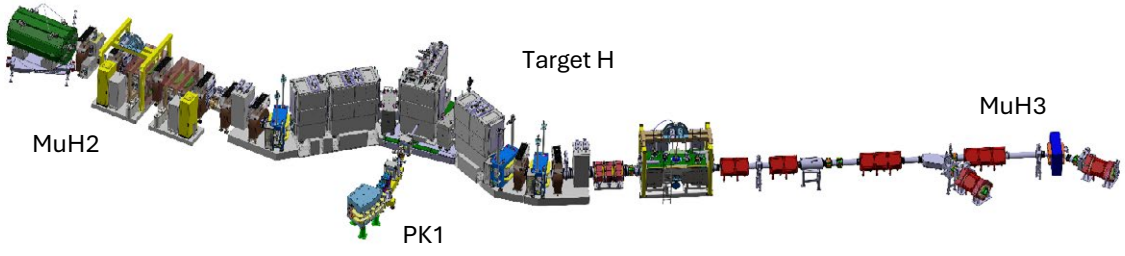

Figure 4.4.20: New target station H and beamlines MuH2 and MuH3.

4.5 Survey and Alignment

4.5.1 Alignment concept

The measurement and alignment are based on an existing measurement network and is mainly using 3D measurement methods. The new beamline components, such as base plates, target chambers, magnets and individual components are prepared, pre-assembled and aligned in designated pre-assembly areas. These modules are then transported to the target area, checked and finally aligned.

4.5.2 Coordinate system

The basis for the measurement and alignment is the right-handed coordinate system defined by the construction. The zero point of this coordinate system is the center of the ring accelerator at the level of the beam plane (Figure 4.5.1).

The axis alignment is based on the existing reference system, with the X-axis pointing in the longitudinal direction of the hall (South/Villigen) and the Y-axis in the transverse direction of the hall (East/Aare). The Z-axis points vertically upwards. This reference system forms the interface between survey and construction.
Where useful and appropriate, different coordinate systems can be used (i.e. beam-based systems, girder-related systems, etc.). To avoid confusion these will be labeled and/or explicitly explained/defined.

4.5.3 Survey network

The coordinate system is represented by survey reference marks designed for a 1.5-inch CCR measuring reflector.

The existing fiducials form the basis of the survey network (Figure 4.5.2). That network will be extended by new installations of fiducials.

The new points are mainly attached to the walls or cemented into the foundation at ground level (Figure 4.5.3).

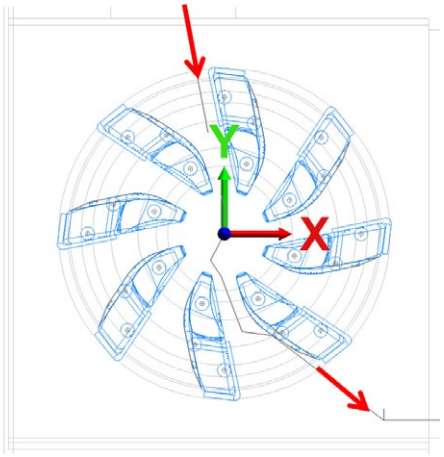

Figure 4.5.1: Coordinate system IMPACT

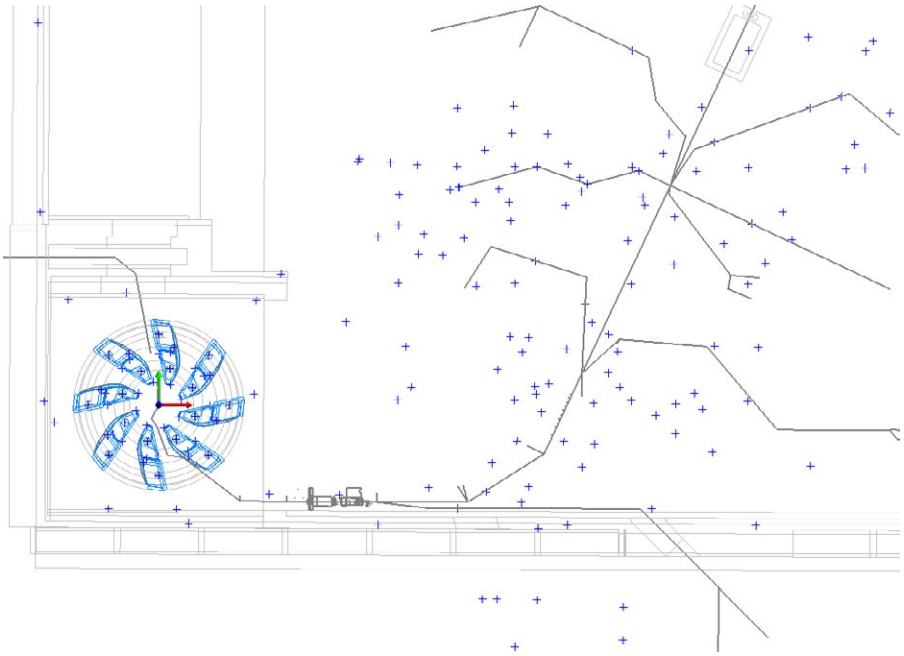

Figure 4.5.2: Sample of existing fiducials in WEHA.

4.5.4 Instrumentation

Devices of the highest accuracy are available for the measurements. Measurement and adjustment are based on 3D measuring methods, mainly using Laser trackers. Other devices such as theodolites, total stations and precision levels are used where necessary and appropriate (Table 4.5.1).

4.5.5 Software

The Spatial Analyzer (NewRiverKinematics Data-Capturing, Calculations, Reporting) surveying program, which has the required device interfaces, is used for measurement data acquisition and adjustment. The WinGeonet software (SLAC Computation and Graduation-Adjustment for Alignment-Network) for network adjustments and height calculation is used.

Figure 4.5.3: Wall and floor installations.

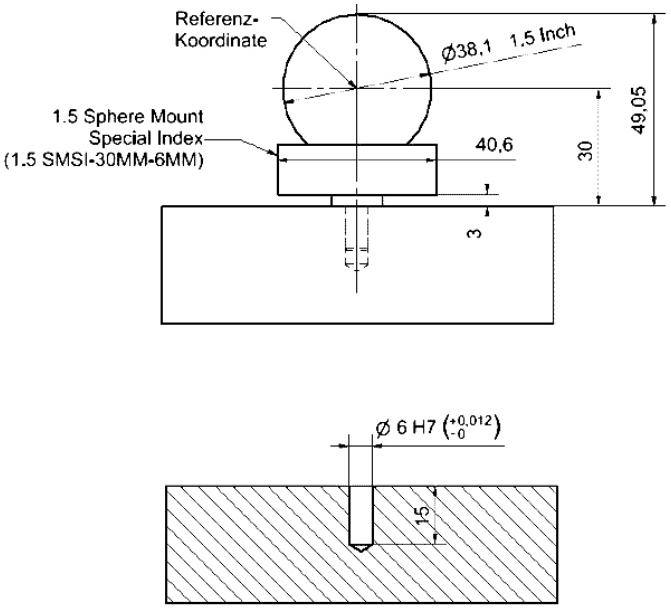

Figure 4.5.4: 6 mm hole (ø 6mm, H7) for the use in combination with 1.5-inch CCR reflector and adapter (LEICA, Hubbs)

Instrument	Typical Range[m]	Accuracy (2σ)	Task
Lasertracker HEXAGON AT960-LR, LEICA AT901	0 m–15 m (max. 60 m)	Ux,y,z = ±15 µm + 6 µm/m	Network Measurement, Alignment
Lasetracker LEICA AT401	1.5 m–15 m (max. 80 m)	Ux,y,z = ±15 µm + 6 µm/m	Network Measurement, Alignment
Theodolite Totalstation LEICA-TDA5005	1.5 m–100 m (max.600 m)	Angular: 0.15 mgon (0.5“) => 0.1 mm/40 m Distance: 0.2 mm+2 ppm => 0.3 mm/40 m	Network Measurement, Axis-Alignment
Theodolite LEICA -TM5100A	0.5 m–20 m	Angular: 0.15 mgon (0.5“) => 0.1 mm/40 m	Axis-Alignment, Auto-Collimation
Precision Level WILD N3	0.6 m–10 m	±0.2 mm/km (optical/analog)	Network Measurement, Height transfer
Precision Level ZEISS DiNi11T	5 m–10 m	± 0.3 mm/km(Barcode/digital)	Network Measurement, Height transfer

Table 4.5.1: Surveying instrumentation (specification and application for IMPACT).

4.5.6 Fiducials on components

The positioning and alignment (6 degrees of freedom, 3 translations, 3 rotations) of the beam components is defined by fiducials on the components. These (min. 4) fiducials are necessary for components with accuracy requirements < 0.5 mm. The measuring spheres can be placed in the 6 mm (H7) reference hole by using an existing measuring adapter (Figure 4.5.4).
Simple components such as blocks, frames, pumps and pipes do not require fiducials. Rough positioning and control is carried out by measuring the external geometry (cylinders, circles, edges, corners, planes).

4.5.7 Alignment tolerances

Different accuracies are required for the individual work steps and procedures for system installation. The highest accuracies are required for the beam components and the surveying network during pre-assembly and alignment and installation of the infrastructure. Alignment tolerances are summarized in Table 4.5.2.

Component	Alignment tolerances (2σ)	Instrument
Floormarkings for holes, axis-markings	± 0.5 mm	Laser tracker, Theodolite
Alignment of Base-Plates, blocks, support- frames, columns	± 0.5 mm	Laser tracker, Precision-Level
Alignment network reference-points (local accuracy for typical working range 10 m)	± 100 µm (≙ 10 ppm)	Laser tracker, Theodolite, Precision-Level
Pre-assembly tolerances of components	± 50 µm (transversal, vertical) (≙ 10 ppm) ± 0.5 mm (longitudinal)	Laser tracker
Final alignment (final Position)	± 100 µm (transversal, vertical, longitudinal) (≙ 10 ppm)	Laser tracker

Table 4.5.2: Alignment tolerances.

4.6 Radiation Protection and Safety

4.6.1 Radiation protection

The operation of the HIPA facility falls into the scope of Swiss legislation. Among other guidelines, beam operation must be in accordance with the Radiological Protection Act RPA [1], the Radiation Protection Ordinance RPO [2], the guideline ENSI-G12 [3], the BAG license A-60891-76 and PSI internal guidelines. The general radiation protection aspects and some specific requirement for the dismantling process were already discussed in the CDR and are not repeated here.

4.6.1.1 Radiation protection planning during installation and assembly

The radiation protection personnel collaborate with the technical staff of PSI to assess the risks and the doses of the personnel performing the installation and assembly. If required, optimization measures are defined together to reduce the doses and comply to the radiation protection requirements.

In the next chapters, the results of the radiation protection planning are presented, based on the results of the Monte Carlo simulations carried out by the responsible specialist group. Where simulations are not available or do not deliver the required information, radiation protection mappings were performed. These assessments are considered sufficiently conservative.

For the personnel the following monitoring is planned:

- Dosimeter: All persons involved are equipped with a personal and approved dosimeter in accordance with RPO art. 61.
- Electronic personal dosimeter (EPD): EPDs enable direct reading and documentation of the doses after each work step. The doses are entered into a database and compared with the planned doses.
- Tritium monitoring: Regular or ad hoc urine samples to detect tritium incorporation will be performed. In addition, regular incorporation monitoring for Co-60 is carried out.
- Triage monitoring: Control measurements using a large component measuring station (HPGe) after the work has been completed or if incorporation is suspected. If incorporation is confirmed, a recognised whole-body measurement is carried out by the authorised dosimetry service at PSI East.
- Dose rate measurements, wipe tests, nuclide and activity determinations and the collection of aerosol samples are carried out regularly. Additionally, the cabin of the indoor crane is equipped with a dose rate probe to warn the crane operator of increased radiation levels.

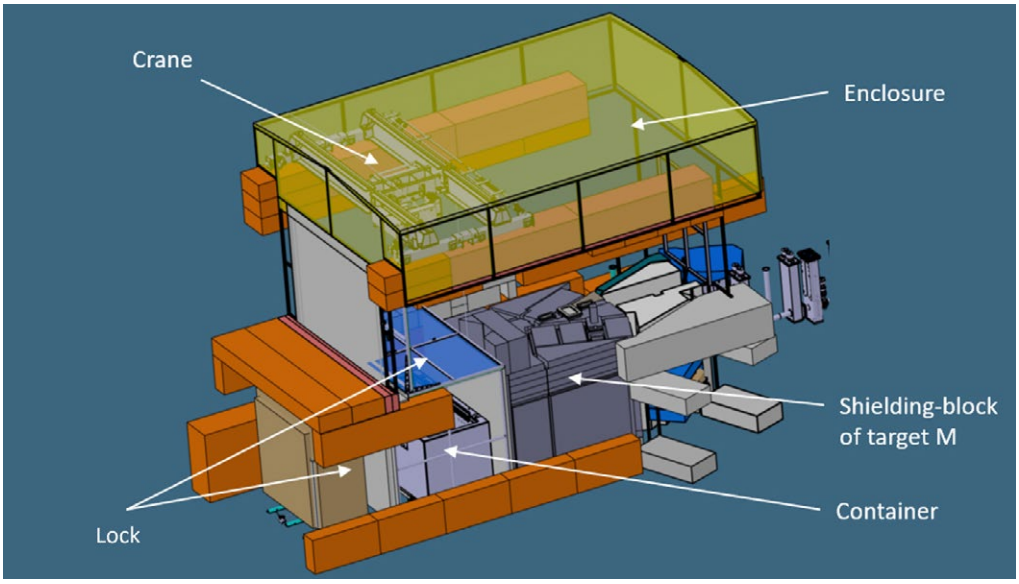

Figure 4.6.1: 3D layout of the main elements foreseen for the removal of target M and implementation of target H.

Work step	Dose in man-mSv
Removal Target-M	0.3
Removal of collimator KHM1	0.7
Removal of collimator KHM2	0.7
Expansion of profile monitor MHP 23/24	0.6
Removal of infrastructure at operating level	5.4
Removal of the cushion seals	1.0
Removal of target block elements	0.8

Table 4.6.1: Dose assessment for the Target M disassembly.

Special attention must also be paid to controlling the material flow. Suitable measures will be taken to prevent the mixing of activated and inactive material. It must also be avoided that activated or contaminated material leaves the controlled area without being released by the radiation protection personnel.

4.6.1.2 Dose assessment of Target M disassembly

The radiation protection planning for the removal of the Target M region includes a large number of safety-relevant measures and work steps. Firstly, the Target M is removed and transported to a parking slot. The collimators KHM1 and KHM2 and the profile monitor MHP23/24 are then removed and transferred to the ATEC. The infrastructure on the service level ("Bedienebene") is completely dismantled to make room for both crane and manipulator. As visible in Figure 4.6.1, an enclosure (zone type IV) and the necessary personnel and material gateways are built to prevent the spread of contamination, with the service level being covered with concrete shielding blocks to reduce the dose rate. The Target M shielding-block is dismantled in stages and the segments are filled into containers. These latter are then decontaminated, inspected, and transported for interim storage. The dose estimate shows that the largest individual and collective doses are expected to be 1.50 mSv and 9.45 man-mSv (Table 4.6.1), respectively. To ensure safety, all persons involved are continuously monitored for incorporation and are equipped with both personal and electronic dosimeters. In addition, regular aerosol monitoring is carried out to detect air contamination at an early stage.

4.6.1.2.1 Optimisation

The most important measures to reduce the doses to the personnel are:

- Shielding of the service level: after dismantling the infrastructure, the service level is covered with 0.5 m × 1 m × 6 m concrete blocks, which reduce the dose rate of the target station by a factor 80. This measure reduces the doses during the construction of the enclosure and the dismantling of the target station.
- Use of "DeconGel": the decontamination agent "DeconGel 1128 Spray" is used to bind contamination and prevent dispersion. It can be sprayed onto heavily contaminated components; when it dries, it forms a plastic matrix that safely binds the contamination.
- Change of personnel: individual doses can be minimised by regularly changing personnel during work. By assigning different employees alternately to the exposed tasks, the exposure is evenly distributed, and the radiation dose to each individual is reduced. This strategy helps to ensure compliance with the limit values for individual doses and to protect the health of employees.
- The dose-relevant works will be remotely carried out by employing crane, power manipulators, and a camera system.

4.6.1.2.2 Intervention thresholds – Target M disassembly

Intervention thresholds serve as tools for radiation protection optimization purposes. If a threshold is reached, the situation – including the remaining work and the current radiation protection measures – will be reassessed to determine whether additional or more effective protective measures are necessary to complete the activities safely.

Individual dose: 1.2 mSv
Collective dose: 7.6 man-mSv
Others:

- Exceeding the contamination values according to the RPO, annex 10.
- Deviation from the planned work steps.
- Hazard to conventional occupational safety.

4.6.1.3 Dose assessment of Target H installation

4.6.1.3.1 Dose assessment

The radiation protection planning for the installation of the new Target H includes different work steps. The main dose contribution is the residual dose rate from the existing activated components. To date, both simulation and experimental results on the residual dose rate are not available. Preliminary dose estimates rely therefore on the experience gained by the operational radiation protection group with similar projects. Dose estimates will be corrected as soon as updated information will be provided. Due to the fact, that the most highly activated components will already be removed before the installation of Target H, the collective dose is estimated in the order of 1.2 man-mSv.

4.6.1.3.2 Optimization

Although the estimated collective dose is relatively low, further optimisation can be achieved for the individual doses.

These latter can be minimised by regularly changing personnel during work. By assigning different employees alternately to the exposed tasks, the exposure is evenly distributed, and the radiation dose of each individual is reduced. This strategy helps to ensure compliance with the limit values for individual doses and to protect the health of employees.

4.6.1.3.3 Intervention thresholds – Target H installation

Individual dose: 0.4 mSv
Collective dose: 1.0 man-mSv
Others:

- Exceeding the contamination values according to the RPO, annex 10
- Deviation from the planned work steps
- Hazard to conventional occupational safety

4.6.1.4 Dose assessment for the dismantling of the beamline in p-channel 1 (PK1)

As mentioned in Chapter 4.4.4, beamline components from AHD1 to the shielding block of the target station M, will be dismounted to allow for the removal of target M itself (see Figure 4.4.9 in Chapter 4.4.4). These elements will be provisionally stored in the WAKA facility. The freed space will be mostly used to host the lock ("Schleuse") and the container handling systems. In addition, part of the p-channel 1 (PK1), which will later steer the beam to TATTOOS, might be dismantled already in parallel to the work required for HIMB.

4.6.1.4.1 Dose assessment

The radiation protection planning for the dismantling of the beamline in p-channel 1 comprises a variety of safety-relevant measures and work steps. First, the highly activated components are removed and transferred to ATEC. When the beamline is ventilated, tritium is removed via a filter system over a long period of time. The beamline is dismantled in stages and the various components transferred to WAKA. The dose estimate shows that the largest individual doses are expected to be in the order of 2.0 mSv and the collective doses in the order of 13.8 man-mSv. To ensure safety, all persons involved are equipped with personal and electronic dosimeters (i.e., EPD) and continuously monitored for their accumulated dose. In addition, regular aerosol monitoring and permanent workplace monitoring for tritium are carried out in order to detect air contamination at an early stage.

4.6.1.4.2 Optimisation

Due to the rather long estimated dismantling times directly in contact with the beam line, higher doses are expected. The individual dose needs therefore be carefully optimized. This will be achieved by regularly changing personnel during work. By alternately assigning different employees to the exposed tasks, the exposure is evenly distributed, and the radiation dose of each individual is reduced. This strategy helps to protect the health of employees and to ensure compliance with the limit values for individual doses.

4.6.1.4.3 Intervention thresholds – dismantling of PK1

Individual dose: 2.0 mSv
Collective dose: 11.0 man-mSv
Others:

- Exceeding the contamination values according to the RPO, annex 10
- Deviation from the planned work steps
- Hazard to conventional occupational safety

4.6.1.5 Dose assessment of dismantling of secondary beamlines

4.6.1.5.1 Dose assessment

The radiation protection planning for the dismantling of PiM1 and PiM3 beamlines includes different work steps. The main dose contribution is the residual dose rate from the existing activated components. The estimated collective dose is 15 man-mSv.

4.6.1.5.2 Optimisation

Although the estimated collective dose is already low, given the fact that many people will be involved, further optimisation can be achieved for the individual doses through personnel rotation.

4.6.1.5.3 Intervention thresholds – dismantling of secondary beamlines

Individual dose: 1 mSv
Collective dose: 10 man-mSv
Others:

- Exceeding the contamination values according to the RPO, annex 10
- Deviation from the planned work steps
- Hazard to conventional occupational safety

4.6.1.6 Dose rate measurements

From a radiation protection point of view, IMPACT needs different dose rate measurements. These can be distinguished by the following two main purposes:

1. Normalization of Monte Carlo simulations

Calculations using multi-purpose radiation transport codes like MCNP or FLUKA are commonly used to investigate the radiological situation for future experiments and to optimize the shielding configuration (see Chapter 2.4). The obtained results depend on a geometrical model and a reliable radiation source term. Whereas a detailed geometric model is usually available from design drawings, source term related information like

beam loss scenarios is difficult to evaluate. For this reason, measurement campaigns with a comparable irradiation situation using the existing facility are used to normalize the results of simulations. In the most straightforward way this is done by comparing measured dose rates to simulated ones.

2. Verification of the compliance with limits

As part of the licensing process for operating new facilities, the compliance with dose rate constraints given by [2;4] must be verified by dedicated measurement campaigns. These are based on survey instruments, suitable for the expected radiation fields, intensities, representative measurement conditions and experimental conditions.

There is a broad portfolio of different survey instruments devices with individual properties available at PSI. However, for the requirements described above, the following survey instruments, depending on their sensitivity to the particle type, are mainly used:

Neutron radiation
Extended range REM counters [5] are routinely used for measurements of the dose rate arising from neutron radiation. A device suitable for the expected radiation field is the LUPIN 5401 BF3-NP PSI [6]. These survey instruments cover an energy range from thermal to a few GeV and are capable to discriminate an intense photon background [7]. Dose values can be acquired for time intervals of 50 ms. The LUPIN uses a cylindrical proportional counter filled with BF_3. It has a nominal sensitivity of 2 cts per nSv and a moderator optimized for dose indications in terms of ambient dose equivalent H*(10).

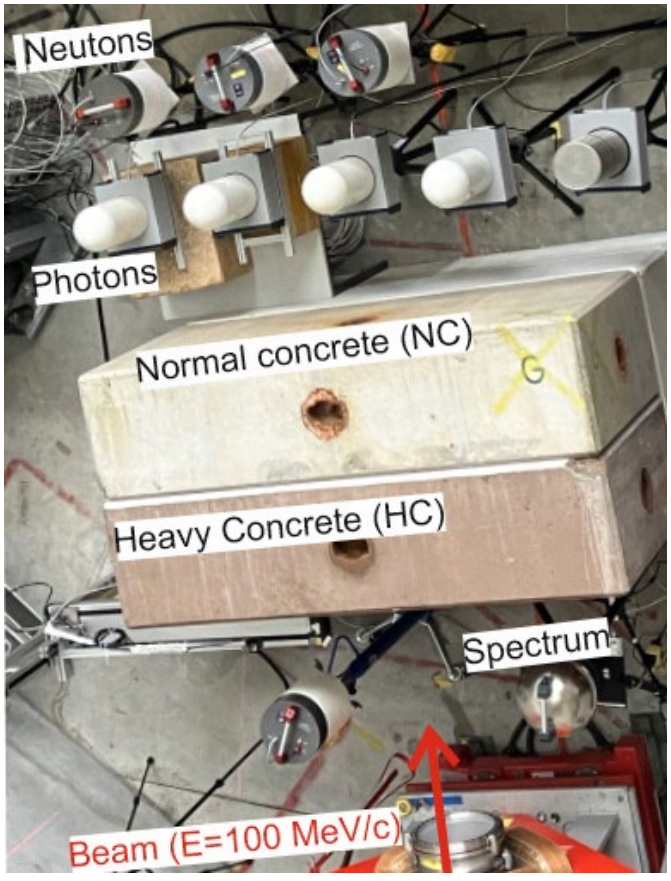

Figure 4.6.2: Measurement setup in the PiE1-exerimental area to verify attenuation factors for different shielding compositions for a symmetric detector positioning behind a combination of normal (NC) and heavy concrete (HC) shielding. The beam direction is indicated by the red arrow.

Photon radiation
The dose arising from photons are surveyed using an environmental γ-radiation monitoring unit of type NAUSICAA ICP-T (referred to as "NAUSICAA") [8]. The unit consist of a high-pressure ionization chamber, filled with a mixture of Argon (8 atm) and Xenon (2 atm) combined with an electrometer covering 7 decades and a CPU-based acquisition and control unit. This type used for the measurements is suitable for photon fields with dose rates from 10 nSv/h to 100 mSv/h and energies up to 10 MeV. Dose values are acquired for time intervals of 1 s.

Each instrument is calibrated in the neutron (photon) field produced by an AmBe (^{137}Cs) source at the Calibration Laboratory of PSI, which is accredited by the Swiss Accreditation Service SAS (SCS0075).

In the case that spectral information is needed, for neutrons an extended range Bonner Sphere spectrometer [9] and for photons high purity Germanium HPGe-semiconductor detectors are available.

In addition, a process for measurement setup and data evaluation has been established and already applied during several measurement campaigns used to verify results of Monte Carlo simulations, for example for measurements of attenuation factors in PiE1 (Figure 4.6.2).

4.6.2 Personnel Safety System (PSYS)

Areas that are used for production and transfer of ionizing radiation must be surveyed according to the Swiss Radiation Protection Ordinance RPO [2] and SnAV [10]. Therefore, the access to these areas will be controlled by a person-safety-system (PSYS). These systems ensure safe conditions while access is possible and prevents access during beam operation. The basic conditions are specified in an internal document [11].

Two of the affected areas of the reconstruction activities within the HIMB project are the experimental areas MuE1 and MuE4. The general PSYS specifications for these areas will not change, but there will be adaptions in the respective amount and locations of entrance doors. Therefore, the positions of the components for the PSYS, such as safety tour and emergency switches, will have to change.

The three areas that belong to the (actual) PiM3 beamline will need a completely new PSYS installation, as these control systems are technically not up to date. The functionality of these new PSYS must suit the general concept and basic conditions as described in [11]. According to the results of the

necessary risk assessment, the major safety functions concerning radiation protection are:

- No beam, while access is possible
- No access during beam operation
- Immediate termination of beam, when emergency switch is pushed

The main machine components to avoid beam inside an accessible area are beam stoppers, appropriate to the beam conditions. In case of failure of these machine components, an escalation of the alarm to the main beam stopper ("BW2") of HIPA will prevent major impact on people.

Due to legal constraints, some additional functions are needed as well:

- Ensure, that no person is inside the area, when beam operation is allowed. This is ensured by passing a safety tour before beam operation is possible.
- Signalization of (possible) beam operation inside and outside the area
- Acoustic warning before and during beam operation

The possible impact of the identified risks to people working inside the area will determine the required level of safety (performance level) of the used components of the safety system.

Additional risks may be included in the safety system PSYS which may come up when the risk analysis is performed.

4.6.2.1 Control unit for PSYS

The Personnel Safety System (PSYS) is based on PLC systems. It controls access to the experimental areas, so that no people can enter the area if dangerous levels of radiation (or other hazards) can occur and ensures that no potentially harmful manipulations can be executed if people are present.

The reconstruction of the experimental areas in the WEHA for the HIMB project requires a new Personnel Safety system for one beamline, that includes up to 3 experimental areas (PiM3-Areas) and adjustments of the layout in some other areas. In particular, additional side and escape doors have to be added to comply with current regulations.

4.6.3 Work Safety

Most safety related functions at PSI are centralized in the department "Radiation Protection and Safety" (ASI). As part of the Center of Corporated Services, ASI is separated from the research laboratories and operation of facilities. This organizational setup ensures adequate segregation of duties.

The groups of the ASI section "Betriebsstrahlenschutz" have a mandate to supervise the radiological situation at the accelerator facilities and the handling of potentially activated or contaminated material. Subject matter experts on various topics of conventional safety, e.g. fire protection, lasers, chemicals or cryogenic gases are either part of the ASI organization or attached to the respective line organizations.

The responsibility for conventional safety lies within the line organizations. The design and build process for new or modified components must include an adequate risk assessment, according to [12] which is based on ISO 12100 and other standards. The line organization have appointed coordinators to assist the designers in this process and to liaise with the respective subject matter experts. Regular planning meetings are used to coordinate on site activities and to identify work related hazards.

4.6.4 References

[1] Swiss Federal Council. 1991. *Radiological Protection Act (RPA).* SR 814.50 Switzerland, 22. March 1991.

[2] Swiss Federal Council. 2017. *Radiological Protection Ordinance (RPO).* SR 814.501 Switzerland, 26. April 2017.

[3] ENSI-G12. 2021. *Anlageninterner Strahlenschutz, Richtlinie für die schweizerischen Kernanlagen*.

[4] Swiss Federal Council. 2017. *Verordnung des EDI über den Umgang mit radioaktivem Material (UraM).* SR 814.554 Switzerland, 26. April 2017.

[5] C. Birattari et al., *"An extended range neutron rem counter"*, Nuclear Instruments and Methods in Physics Research A, Vol. 297, Issues 1–2, 1990, pp. 250-257, ISSN 0168-9002, https://doi.org/10.1016/0168-9002(90)91373-J.

[6] LUPIN 5401 BF3-NP. ELSE Nuclear. *PSI – User Manual (Rev.10).*

[7] M. Caresana et al., *"A new version of the LUPIN detector: improvements and latest experimental verification"*, Rev. Sci. Instrum., vol. 85, no. 6, p. 065102 (8 pp.), 2014. https://doi.org/10.1063/1.4879936

[8] NAUSICAA 5301 IC / IC-PF. ELSE Nuclear. *User Manual (Rev.2).*

[9] Wiegel, B. and Alevra, A. V., *"NEMUS – the PTB Neutron Multisphere Spectrometer: Bonner spheres and more"*, Nuclear Instruments and Methods in Physics Research A, Vol. 476, No. 1–2, pp. 36–41, 2002. doi:10.1016/S0168-9002(01)01385-7.

[10] Swiss Federal Council. 2017. *Verordnung des EDI über den Strahlenschutz bei nichtmedizinischen Anlagen zur Erzeugung ionisierender Strahlung (SnAV).* SR 814.501.51 Switzerland, 26. April 2017.

[11] TM-96-03-04 – Schutzkonzept der Personensicherheitsanlage des HIPA-Beschleunigeranlage des PSI West; A. Fuchs, C. Harm; 12.12.2018. PSI internal document.

[12] PSI-PB-9670-214 – Einsatz und Betrieb von am PSI hergestellten und eingesetzten Geräten und Anlagen zu Forschungszwecken; W. Rendler; 08.05.2025. PSI internal document.

4.7 Disposal

4.7.1 Radiological characterization

In the context of the IMPACT project, radiological characterization will be performed on materials originating mainly from the experimental hall (WEHA). In carrying out the comprehensive radiological characterization campaign, PSI must comply with the Swiss legislation, namely the Radiation Protection Ordinance RPO [1] and the guideline ENSI-B04 [2].

The key aspects of radiological characterization are the identification of the activity, dose rate and surface contamination of the most relevant radionuclides in a given material. The values of these quantities determine the disposal scenario, as described in the RPO [1]. The disposal scenarios of interest for the materials considered in the present campaign are free release (clearance), recycling, deposit in a decay storage and landfilling.

For the free release (clearance) of a given material, the following three conditions from RPO art. 106 must be met:

1. The specific activity of each radionuclide must be below the nuclide-specific clearance limit "LL" detailed in annex 3 of the RPO [1] or the total activity of the sample must be below LL·1000 g.
2. The maximum ambient dose rate at a distance of 10 cm from the surface must be less than 0.1 μSv/h (net of background radiation).
3. The surface contamination for each radionuclide must be below the nuclide-specific surface contamination guidance value "CS" detailed in annex 3 of the RPO [1].

If these conditions are fulfilled, the material can be exempted from mandatory licensing and supervision by the Federal Office of Public Health (FOPH), and it can be disposed without specific restrictions. For materials – particularly metals and concrete – with a specific activity lower than 10 LL, recycling according to RPO art. 115 can be possible. Another option is the disposal on a landfill according to RPO art. 114. For both options dedicated guidelines from the FOPH exist and must be followed.

Materials that will meet the clearance or recycling criteria after a maximum decay period of 30 years can be stored in decay storages compliant with RPO art. 117 [1]. At PSI dedicated buildings exist for such a storage.

It is fundamental to quantify different types of material that will be subject to radiological characterization and to have radiation protection concepts to carry them out. These materials originate from structures in the WEHA that need to be dismantled or modified for the HIMB project. Specifically, they include components from the muon beamlines PiM1 and PiM3, the proton beam sections, the helium liquefication plant, the water-cooling loop "Tertiary circuit 7", and potentially concrete shielding blocks.

An estimate of the various materials to be characterized is given in Table 4.7.1, based on inputs from technical personnel involved in the facility decommissioning. These materials are most likely not radioactive waste. Additionally, about 5000 t of concrete blocks and 4000 t steel will be moved within the project. The largest share will be used for remodeling purposes

Item	Material	Estimated weight [t]
Components from experimental areas and cooling circuit 7 (pipes, valves)	Stainless steel	7
Ventilation pipes (PK2) and materials from experimental area dismantling (steel sheets, cable racks)	Steel	21
Flexibles hoses	Plastics	2
Valves for rubber hoses	Brass	1
Cable material	Copper, PVC	9
Installation material (steel sheets, plugs, etc.)	Steel, aluminum	7

Table 4.7.1: Overview of the material to be radiologically characterized for the IMPACT project. "PK2" is denoted as a part of the proton beam channel.

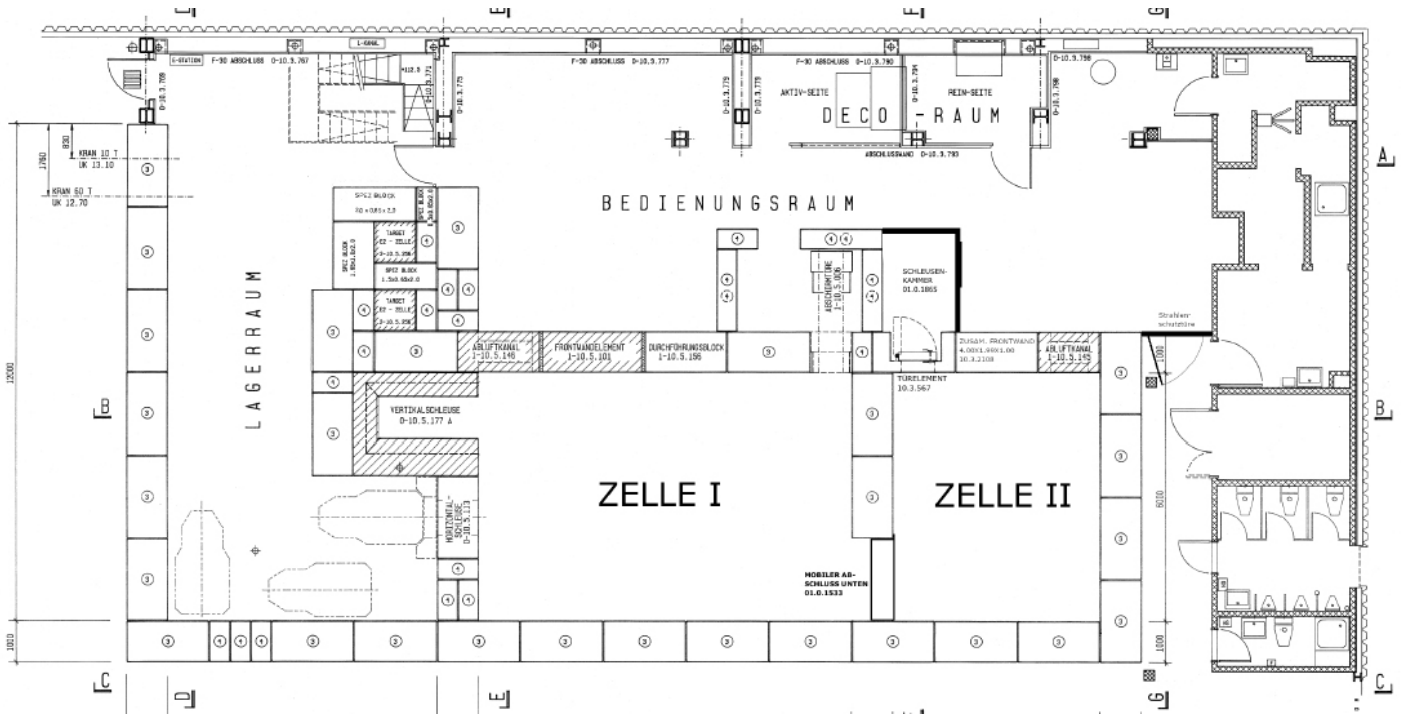

Figure 4.7.1: Layout of the ATEC facility.

within the IMPACT project and will either be reused or stored at PSI for future projects.

Based on experience at the HIPA facility, the main radionuclides to be expected in the materials reported in Table 4.7.1 are Be-7, Na-22, Na-24, Mg-25, Al-26, Cl-36, Ti-44, Fe-55, Co-57, Co-60, Ni-63, Sb-124, Eu-152, Eu-154, Hg-194, Pb-202 and Bi-207.

The necessary measurements for the radiological characterization will be carried out following the guideline ENSI-B04 [2]. The measurements will be mainly performed in a dedicated PSI building, the "Freimessgebäude" WMGA building. The core resources of WMGA are two 4π clearance monitors: a 440 l chamber with 6 plastic scintillators (model Mirion RTM661/440Inc), generally used for samples up to 30 kg, and an 1800 l one (model Ludlum HWM-1800) with 24 plastic detectors, calibrated for different weights and material types. The chambers are calibrated using reference nuclide vectors enabling the accurate determination of the specific activity. The 1800 l chamber was upgraded by PSI by inserting a characterized HPGe spectrometer to perform a complementary, online gamma spectrometry of the investigated sample to check the used nuclide vector.

PSI can rely on a series of already available radiological characterization concepts of specific materials listed in Table 4.7.1 (e.g., for cables materials and different calibrations of the clearance monitors). Additionally, new concepts can be developed to address the specific requirements of the IMPACT project.

4.7.2 Waste package specifications

During the operation of HIPA different types of radioactive waste, e. g. targets, shielding, magnets, cables etc. are going to be produced. Vast majority of the waste materials are expected to be steel (normal and stainless) and copper. From long-time experience with the operation of accelerator facilities at PSI, it is foreseen to dispose these materials taking existing waste package specifications into account.

For example, waste package type 13 exists already which can be used for operational accelerator waste and for spallation targets or collimator parts (type of waste package J-P-010008/10 and -12/14).

According to the Swiss Nuclear Energy Ordinance ("Kernenergieverordnung" KEV, Art. 54 Abs. 6) [3] the Swiss Federal Nuclear Safety Inspectorate (ENSI) is in charge to define the requirements and scope for the conditioning of radioactive waste within a guideline. The conditioning of radioactive material has thus to comply with the aspects of the guideline ENSI-B05 "Requirements for the conditioning of radioactive waste" [4] where details and requirements regarding the conditioning process and its approval are defined. Disposal pathways are described in a waste package type specification which must be approved by ENSI. In such a specification several aspects must be addressed regarding the conditioning of radioactive waste, e. g.:

- conditioning procedures
- disposal concept

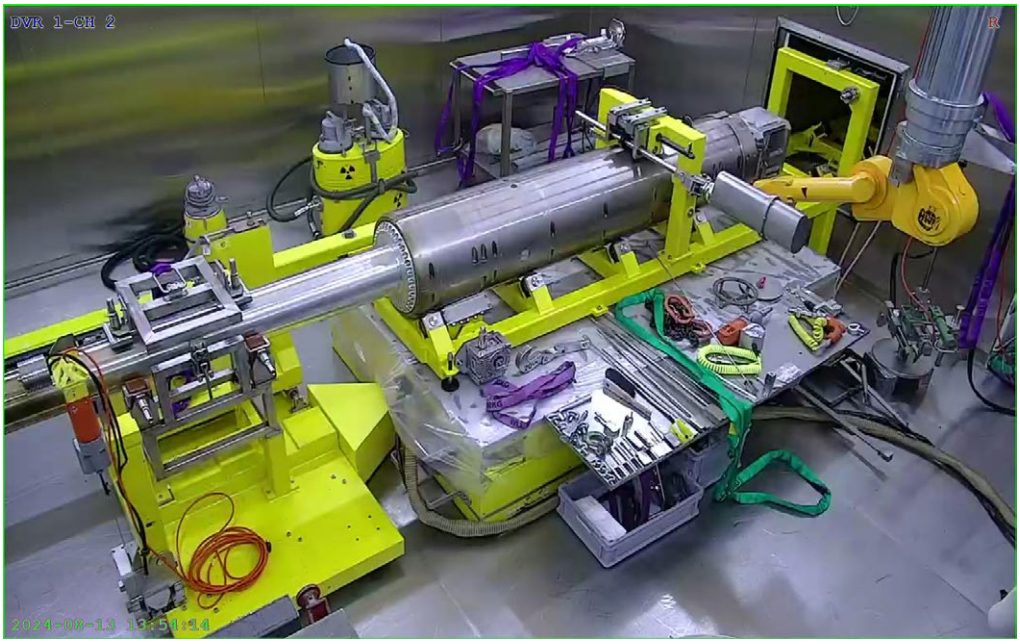

Figure 4.7.2: Treatment of a highly activated part within the Service Cell 1.

- robustness of the concept
- waste product
- waste package and its components
- quality management and time frame of conditioning
- suitability for transport, interim storage and final disposal of the type of waste package

To fulfill these criteria and to be able to dispose radioactive waste as a predefined or future waste package type, a detailed knowledge on the characteristics (e. g. nuclide and material inventory, nuclide and material quantities, dose rates, production rates, waste volumes, etc.) of the current or future waste is crucial.

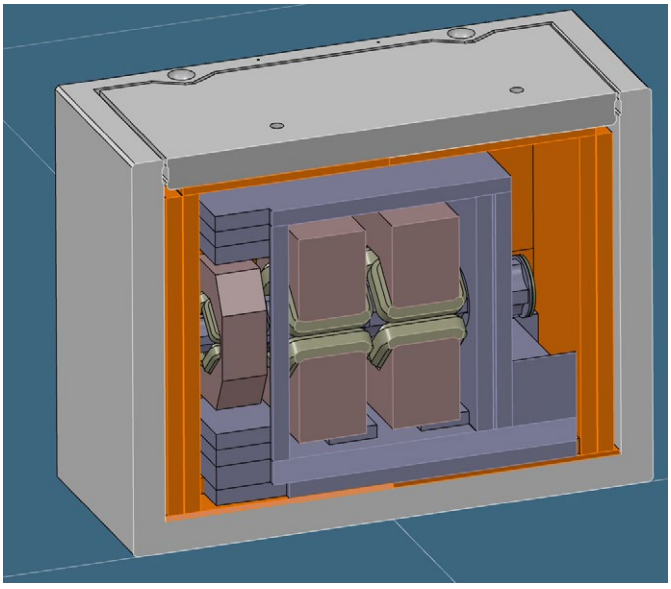

Figure 4.7.3: Example of a concrete container.

As the federal waste collection facility, PSI administers several types of waste package specifications and disposal concepts which give numerous opportunities to dispose various types of radioactive waste. If required, PSI also has the expert knowledge to develop innovative concepts and to launch an approval process for a new waste package type specification.

4.7.3 Processing of highly activated parts in ATEC for disposal

4.7.3.1 Description of the ATEC facility

The ATEC is located in the south-eastern corner of the experimental hall WEHA and is designed for handling highly activated and/or contaminated components from the HIPA facility. The ATEC area includes an operator room (Zone II) and two service cells (Zone IV), see Figure 4.7.1.

The two service cells are equipped with a movable roof made of concrete shielding blocks. From the operator room, work in the two service cells can be remotely controlled using various auxiliary devices such as cranes, power manipulators, hand manipulators, camera systems, bandsaws, ventilation systems, and more.

There is a storage area in the North of Service Cell 1 for exchange flasks as well as airlock systems that connect Service Cell 1 with the exchange flasks. Additionally, in the eastern section, there is a DECO room with a decontamination facility for cleaning smaller components.

Access to the ATEC area is provided through the personnel airlock located South of Service Cell 2.

4.7.3.2 Insertion of Components into the Service Cells

The insertion of components into the service cells can be carried out as follows:

- Service Cell 1: Components can be fed through the horizontal and vertical lock-systems using exchange flasks. Larger components can also be inserted via the opened roof.
- Service Cell 2: Components can only be inserted via the opened roof.

4.7.3.3 Disposal of Components

Within the service cells, components designated for disposal are disassembled or cut into smaller pieces. These components are then placed into standard concrete containers (KC-T12 and KC-T30). The process of disposing of components in concrete containers is a well-established process, see for example in Figure 4.7.2.

All the material from the dismantling of Target M is temporarily stored in the Injector 1 bunker. It also contains the vacuum chambers and shielding parts that are no longer used and cannot be reused in the new shielding of Target H. As most of these parts are too large to be stored in a standard large concrete container, newly constructed concrete containers have to be purchased, see an example in Figure 4.7.3. After the HIPA plant restarts user operation, the ATEC facility begins the disposal process of the Target M components. The entire process will take years and has not yet been defined in detail. The injector 1 bunker will be kept reserved until all material has been disposed. A facility near the ATEC site is available for final conditioning with concrete mortar of the radioactive waste in the standard containers. This facility can process 12–16 containers per year.

4.7.4 References

[1] Swiss Federal Council. 2017. Radiological Protection Ordinance (RPO). SR 814.501 Switzerland, 26. April 2017.

[2] ENSI-B04. Eidgenössische Nuklearsicherheitsinspektorat. Befreiung von Kontroll- und Überwachungsbereichen sowie Materialien von der Bewilligungspflicht und Aufsicht. November 2018.

[3] Swiss Federal Council. 2004. Nuclear Energy Ordinance (NEO) / Kernenergieverordnung (KEV). SR 732.11 Switzerland, 10. December 2004.

[4] ENSI-B05, Richtlinie für die schweizerischen Kernanlagen – Anforderungen an die Konditionierung radioaktiver Abfälle.

[5] IMPACT Conceptual Design Report, PSI Bericht Nr. 22-01, ISSN 1019-0643, 2022

PSI in brief

With 2300 employees and an annual budget of 460 million Swiss francs, PSI is the largest research institute for natural and engineering sciences in Switzerland. It is the central location of Switzerland's large research facilities. As part of the ETH Domain, PSI is a key pillar in the Swiss research landscape and conducts cutting-edge research in the fields of Future Technologies, Energy and Climate, Health Innovation and Fundamentals of Nature.

By collaborating with industry, PSI strengthens the innovative power of Switzerland as a business location. Additionally, through the founding of spin-offs, PSI transfers its latest scientific findings directly into the economy. PSI is already investing today in the experts of tomorrow: around a quarter of PSI employees are postdoctoral researchers, PhD students or trainees.

Paul Scherrer Institute PSI
Forschungsstrasse 111
5232 Villigen PSI
Switzerland
www.psi.ch